

Lecture Notes in Civil Engineering

Kasinathan Muthukkumaran
Balunaini Umashankar
N. Kumar Pitchumani *Editors*

Earth Retaining Structures and Stability Analysis

Proceedings of the Indian Geotechnical
Conference 2021 Volume 6

 Springer

Lecture Notes in Civil Engineering

Volume 303

Series Editors

Marco di Prisco, Politecnico di Milano, Milano, Italy

Sheng-Hong Chen, School of Water Resources and Hydropower Engineering,
Wuhan University, Wuhan, China

Ioannis Vayas, Institute of Steel Structures, National Technical University of
Athens, Athens, Greece

Sanjay Kumar Shukla, School of Engineering, Edith Cowan University, Joondalup,
WA, Australia

Anuj Sharma, Iowa State University, Ames, IA, USA

Nagesh Kumar, Department of Civil Engineering, Indian Institute of Science
Bangalore, Bengaluru, Karnataka, India

Chien Ming Wang, School of Civil Engineering, The University of Queensland,
Brisbane, QLD, Australia

Lecture Notes in Civil Engineering (LNCE) publishes the latest developments in Civil Engineering—quickly, informally and in top quality. Though original research reported in proceedings and post-proceedings represents the core of LNCE, edited volumes of exceptionally high quality and interest may also be considered for publication. Volumes published in LNCE embrace all aspects and subfields of, as well as new challenges in, Civil Engineering. Topics in the series include:

- Construction and Structural Mechanics
- Building Materials
- Concrete, Steel and Timber Structures
- Geotechnical Engineering
- Earthquake Engineering
- Coastal Engineering
- Ocean and Offshore Engineering; Ships and Floating Structures
- Hydraulics, Hydrology and Water Resources Engineering
- Environmental Engineering and Sustainability
- Structural Health and Monitoring
- Surveying and Geographical Information Systems
- Indoor Environments
- Transportation and Traffic
- Risk Analysis
- Safety and Security

To submit a proposal or request further information, please contact the appropriate Springer Editor:

- Pierpaolo Riva at pierpaolo.riva@springer.com (Europe and Americas);
- Swati Meherishi at swati.meherishi@springer.com (Asia—except China, Australia, and New Zealand);
- Wayne Hu at wayne.hu@springer.com (China).

All books in the series now indexed by Scopus and EI Compendex database!

Kasinathan Muthukkumaran ·
Balunaini Umashankar · N. Kumar Pitchumani
Editors

Earth Retaining Structures and Stability Analysis

Proceedings of the Indian Geotechnical
Conference 2021 Volume 6

Editors

Kasinathan Muthukkumaran
Department of Civil Engineering
National Institute of Technology
Tiruchirappalli, India

Balunaini Umashankar
Department of Civil Engineering
Indian Institute of Technology Hyderabad
Sangareddy, Telangana, India

N. Kumar Pitchumani
AECOM India Pvt. Ltd.
Chennai, India

ISSN 2366-2557

ISSN 2366-2565 (electronic)

Lecture Notes in Civil Engineering

ISBN 978-981-19-7244-7

ISBN 978-981-19-7245-4 (eBook)

<https://doi.org/10.1007/978-981-19-7245-4>

© The Editor(s) (if applicable) and The Author(s), under exclusive license to Springer Nature Singapore Pte Ltd. 2023

This work is subject to copyright. All rights are solely and exclusively licensed by the Publisher, whether the whole or part of the material is concerned, specifically the rights of translation, reprinting, reuse of illustrations, recitation, broadcasting, reproduction on microfilms or in any other physical way, and transmission or information storage and retrieval, electronic adaptation, computer software, or by similar or dissimilar methodology now known or hereafter developed.

The use of general descriptive names, registered names, trademarks, service marks, etc. in this publication does not imply, even in the absence of a specific statement, that such names are exempt from the relevant protective laws and regulations and therefore free for general use.

The publisher, the authors, and the editors are safe to assume that the advice and information in this book are believed to be true and accurate at the date of publication. Neither the publisher nor the authors or the editors give a warranty, expressed or implied, with respect to the material contained herein or for any errors or omissions that may have been made. The publisher remains neutral with regard to jurisdictional claims in published maps and institutional affiliations.

This Springer imprint is published by the registered company Springer Nature Singapore Pte Ltd.

The registered company address is: 152 Beach Road, #21-01/04 Gateway East, Singapore 189721, Singapore

Contents

1	Incorporation of Surrounding Rock Layer Presence in the Design of Underground Cut and Cover Box Structure	1
	Chiranjib Sarkar, Ankit Som, and Ganesh Deepak Kanchuboyina	
2	Elastic–Perfectly Plastic Behavior of Lower Siwalik Sandstones	13
	D. V. Sarwade, Pankaj Kumar, K. K. Mishra, P. Senthil, and Hari Dev	
3	Effect of Volume Loss During Tunnel Construction on the Ground Surface	23
	Rahul Shakya and Manendra Singh	
4	Crack Growth in Rocks with Pre-existing Flaws Subjected to Uniaxial and Biaxial Compression	31
	G. Sivakumar and V. B. Maji	
5	Parametric Study on the Performance of Temporary Secant Pile Wall	45
	V. J. Gowthaman and C. Anburaj	
6	Numerical Analysis of Ground Settlement Induced by Shallow Tunnels	55
	R. Rajaraman and Gundeti Sumanth Kumar	
7	Seismic Assessment of Horseshoe-Shaped Tunnel Using a Pseudo-Static Approach	65
	Ambika Srivastav and Neelima Satyam	
8	Effects of the Shield Driving on Soil Arching Around the Tunnel ...	75
	M. Vinoth and M. S. Aswathy	
9	Stability Analysis of Overburden Dump Slope—A Case Study of Marki Mangli-I Coal Mine	83
	S. S. Geete, K. H. Singh, A. K. Verma, T. N. Singh, and P. P. Dahale	

10	Living Soil Nails to Prevent Shallow Landslides in Lateritic Soil Slopes	101
	D. Anand Praveen and P. V. Divya	
11	Restoration Measures of Landslide Affected Valley Slope—A Case Study of Tindharia Area Along NH 55 in West Bengal	113
	Avik Kumar Mandal, S. Sailesh, Pradyot Biswas, and Atanu Adhikari	
12	Effect of Hysteretic SWCC on Marappalam Rainfall-Triggered Slope Failure	139
	Nallabothula Mounika, Ammavajjala Sesha Sai Raghuram, B. Munwar Basha, and Arif Ali Baig Moghal	
13	Effect of Antecedent Uniform Rainfall Pattern on the Stability of a Typical Northeastern Slope	149
	Sreeram Shruthija and Sudheer Kumar Yamsani	
14	Response of Isolated Shallow Footing on Sloping Ground with Dynamic Loading	161
	Saumitro Mandal, Aniket Chanda, and Arghadeep Biswas	
15	Detection, Monitoring, and Early Warning of Landslides Using In-Situ Ground-Based Monitoring Techniques: A Review	169
	Shreya Maheshwari and Riya Bhowmik	
16	A Comprehensive Review on Rainfall-Induced Slope Failures: Mechanism, Models, and Influencing Factors	177
	Vineet Gajamer and Abhishek Kumar	
17	Optimum Thickness of Veneer Cover Soil of MSW Landfill for Stability Against Uplifted-Floating Failure	187
	Dabbiru Soujanya and B. Munwar Basha	
18	A Concise Review of State-of-the-Art on Landslide Monitoring and Warning System in India	197
	Shikha Sharma, Naresh Mali, and Venkata Uday Kala	
19	Probabilistic Slope Stability Analysis of Bioreactor Landfills	207
	Ankit Goel, Subhadeep Metya, and Gautam Bhattacharya	
20	Experimental Investigation of Pull-Out Resistance of Grouted Soil Nails—A Critical Review	219
	Ruchita Salvi and Ashish Juneja	
21	Reduction of Surface Erosion of Soil Slopes Using Alkali Activated Binder Treated Jute Fibers	231
	Gunde Sachin Chakravarthy and Anasua GuhaRay	

22 Parametric and Stability Analysis of Landslide Near Somwarpet, Coorg District, Karnataka 241
 Anand. M. Hulagabali, V. Shilpa, N. C. Shobharani, G. S. Vasundhara, and M. L. Prashanth

23 Dynamic Stability and Landslide Simulations in Hilly Regions of Kerala 251
 Geethu Maria Joseph and K. Ranga Swamy

24 Historical Development of Landslide Early Warning System (LEWS): A Review 263
 Prashant Sudani, K. A. Patil, and Y. A. Kolekar

25 Study on Design of Reinforced Earth Retaining Wall with Copper Slag as Fill Material 279
 C. N. V. Satyanarayana Reddy, R. Dhanunjay Kumar Reddy, and M. Nagalakshmi

26 Multi-Approach Global Stability Assessment of Soil Nail Walls 291
 Vikas Pratap Singh

27 Finite Element Analysis of Back-To-Back Mechanically Stabilized Earth Wall 303
 K. A. Aboorvaraj, P. V. Premalatha, and A. Karthikeyan

28 Behavior of Diaphragm Wall in Semi Top-Down Construction Method: A Case Study 313
 C. Vimala, P. V. S. R. Prasad, and Madan Kumar Annam

29 Review of Use of Asphaltic Concrete Core in Earthen/Rock Fill Embankment Dam 323
 Satyajit Roy, V. K. Jain, Manish Gupta, and R. Chitra

30 Construction of Diaphragm Wall for Seawater Intake Pump House 337
 B. Govind Raj, Madan Kumar Annam, and Bairagi Kondapalli

31 Seismic Stability of Reinforced Soil Wall Using Horizontal Slice Method: Effect of Surcharge on Cohesive-Frictional Soils 345
 M. C. Venkatasubbaiah and G. V. Narasimhareddy

32 A Comparative Study on the Stability Analysis of Tailings Pond Embankments Under Transient and Steady-State Seepage Conditions 357
 Surender Singh, Abhishek Kumar, and T. G. Sitharam

33 Structural Behavior of Partial Seepage Barriers for Variations in Depth of Pervious Stratum 369
 S. Sivakumar, P. V. Premalatha, and N. Almas Begum

34	Performance Evaluation of Scrap Rubber-Sand Mixture Reinforced with Geogrids as a Backfill Material in Retaining Walls	383
	K. P. Anjali and Renjitha Mary Varghese	
35	Behavior of Cantilever Concrete Diaphragm Wall Under Sequential Excavation of Front-Fill Soil: A Numerical Study	395
	Abhijit Debnath and Sujit Kumar Pal	
36	Gabion Walls—A Remedial Measure for Slope Stabilization	409
	Blacinta Pereira and Wilma Fernandes	
37	Stability Enhancement of Railway Embankment Using Geosynthetic Layer	421
	Furquan Ahmad and Pijush Samui	
38	Numerical Analysis of Earthen Embankment Resting on Soft Clay Deposit	429
	Anand M. Hulagabali, R. Srujana, A. V. Rachana, and M. Y. Longkumer	
39	Study on Soil–Panel Interaction on the Performance of MSE Wall	447
	Anand M. Hulagabali, C. H. Solanki, and G. R. Dodagoudar	
40	Effect of Different Compressible Inclusions on Lateral Earth Pressure Reduction in Rigid Retaining Wall	457
	L. Anandha Raj and M. Muttharam	
41	Restoration of Breached Ash Dyke Embankment in Constrained Site Conditions	467
	Vinod Kumar Mauriya	

About the Editors

Dr. Kasinathan Muthukkumaran is currently Professor in Civil Engineering at National Institute of Technology, Tiruchirappalli, India. He obtained Ph.D. in Soil-Structure Interaction and Marine Geotechnical Engineering from Indian Institute of Technology Madras. He has published more than 150 papers in international and national journals and conferences. He has completed 5 R&D (including ISRO—**Chandrayaan-2 Mission project**) and 70 major consultancy projects in Geotechnical Engineering and published two patent including “**Moon Soil**” (A Method for Manufacture of Highland Lunar Soil Simulant). He has guided 10 PhD scholars and 6 more are in progress, 5 MS (by research) and more than 40 M.Tech. students in Geotechnical and allied research areas. He is the **Founder Chairman** of Indian Geotechnical Society (IGS-Trichy) Trichy Chapter. He is a member of Technical Committee (TC-301 on “**Preservation of Historic Sites**”) of International Society for Soil Mechanics and Geotechnical Engineering. Prof. Muthukkumaran area of research is in geotechnical engineering, which includes pile foundation, soil-structure interaction, marine geotechnics and foundations, field instrumentation, geotechnical physical modeling, ground improvement and forensic geotechnical engineering. He has received DST Young Scientist Award, IGS- Smt. Indra Joshi Biennial Award and Keynote Paper Award—GEOMATE Conference 2015 at Osaka, Japan. He is an Associate Editor of *Australian journal of Civil Engineering* and serving editorial board member of several journals. Prof. Muthukkumaran has significant administrative contribution as Estate Officer, Associate Dean (Planning and Development), Member of Buildings and Works Committee and Member of **Board of Governors (BoG)** of National Institute of Technology, Tiruchirappalli and Member of Buildings and Works Committee, IIM Trichy. He has received **NIT Trichy Achiever Awards** for research publications, research projects, maximum citation and consultancy projects.

Dr. Balunaini Umashankar is Professor in the Department of Civil Engineering, Indian Institute of Technology (IIT) Hyderabad. He has been with IIT Hyderabad since 2009 after completing his Ph.D. from Purdue University. He did his Bachelors from S V University in 2000 and Masters from IIT Kanpur in 2002. He specializes in

geotechnical engineering with research focus on geosynthetics in pavements, reinforced earth structures, foundation engineering, recyclable materials in geotechnics and soil-structure interaction. He is presently involved with research to use drone technology to monitor geoinfrastructre facilities. He has been involved with several research projects funded by National Highway Authority of India (NHAI), Ministry of Road Transport and Highways (MoRTH), Neyveli Lignite Co. Ltd. (NLC), Department of Science and Technology (DST), etc. He is a technical advisor to the Irrigation and CAD Department, Government of Telangana, for the recently concluded project in the State—‘The Kaleshwaram Lift Irrigation Project’.

Dr. N. Kumar Pitchumani is Regional Director at AECOM India Pvt. Ltd., heading the Geotechnical Engineering business line and involved in the analysis and design of the geotechnical components of large infrastructure projects, especially underground metros. He brings in 28 years of professional experience in the field of geotechnical engineering, encompassing teaching, research, consulting, analysis and design in various aspects of geotechnical engineering. His experience includes foundation designs for various types of structures in the transportation and marine infrastructure projects. He has been responsible for various projects involving ground improvement of soft clays and reclamation fills. Dr. Kumar did his Bachelors in Civil Engineering at VJTI Mumbai in 1987 and then his M.Tech. and Ph.D. in Geotechnical Engineering at IIT Kanpur in 1989 and 1992, respectively. Prior to moving into the industry, he started his career with National Institute of Rock Mechanics and then as Assistant Professor at IIT Madras. Since 1999, he has been in the Consulting Industry with L&T Ramboll, L&T ECC and COWI before joining AECOM in 2011. He has around 40 publications in journals and conferences. He is also Adjunct Professor at IIT Madras, disseminating his industrial experience to the student community. He is Chartered Engineer with the Institution of Engineers, London.

Chapter 1

Incorporation of Surrounding Rock Layer Presence in the Design of Underground Cut and Cover Box Structure



Chiranjib Sarkar, Ankit Som, and Ganesh Deepak Kanchuboyina

Introduction

Underground construction is generally carried out by two methodologies, namely: tunneling and cut and cover. Depending on ground conditions, tunneling methodology is subdivided into Tunnel Boring method and New Austrian Tunneling method, whereas cut and cover methodology is subdivided into top-down and bottom-up construction. In top-down construction, temporary and permanent support can be integrated into one earth retaining structure. On the other side, bottom-up construction requires separate temporary earth retaining structural arrangement to provide support during excavation and construction period. Top-down construction with diaphragm wall is mainly chosen when there is presence of soil strata. Bottom-up construction is mainly preferred in mixed ground condition or if there is presence of rock layer [1]. In a metro corridor in congested locations, soldier and secant piled walls are mainly provided as temporary earth retaining arrangement due to limited space availability [2]. Bottom-up construction with soldier pile support arrangement is generally chosen when water table is below base slab level. Secant pile support arrangement is chosen when water table is at shallow depth. Waler and strut or ground anchor system is further provided to support soldier piled and secant piled walls laterally. Thus, bottom-up construction, as earth retaining arrangement, requires additional time and activities leading to higher costs. Hence, it is necessary to have an innovative practice beyond the common and conventional methods in design/construction with site-specific considerations and design input parameters. Structural design of a cut and cover station situated in mixed ground condition of

C. Sarkar (✉) · A. Som
AECOM India Private Limited, New Town, Kolkata 700156, India
e-mail: chiranjib.sarkar@aecom.com

G. D. Kanchuboyina
AECOM India Private Limited, T. Nagar, Chennai 600017, India

Chennai Metro Project Phase-II alignment corridor has been referred for the present case study. Construction of underground station in mixed ground condition is quite tough, uneconomical, and time consuming with conventional methods. Grade (IV) or better charnockite rock is encountered within the excavation depth of Thiruvanmiyur station. Due to difficulty of excavation in hard strata as well as self-standing nature of rock, diaphragm walls with shear pins embedded into rock strata have been adopted. This arrangement reduces the requirement of temporary earth retaining support arrangement like soldier pile, secant pile, etc. Therefore, it helps to save time, manpower and material costs by 15–20%. Due to varying rock level along the station alignment, diaphragm walls, cast in panels, terminate at different depths. The above-mentioned arrangement has been adopted to ensure adequate stability. Furthermore, stitch walls have been provided as connection between station diaphragm wall and station base slab using open excavation method. Entire sequence of construction has been modeled and analyzed in PLAXIS 2D [2] software for checking of structural design, stability, ground deformation, etc. On the other hand, service stage model has been developed in STAAD.Pro V8i [3] to check for serviceability criteria of the structure.

Project Location and Station Description

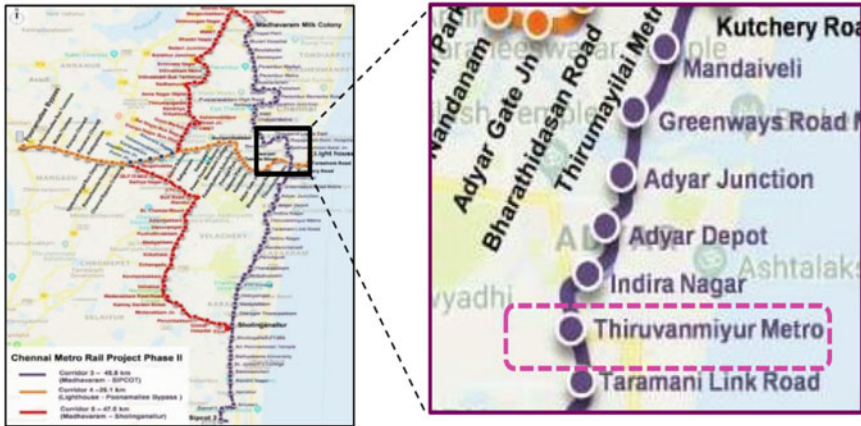
The city of Chennai is situated near 13° North Latitude and 80° East Longitude and stretches over a length of 19 km along the Coromandel Coast with an area of 172 km². Entire Phase-II work of Chennai Metro Rail Limited (CMRL) is divided into three lines, i.e., Corridor 3, Corridor 4 and Corridor 5. Thiruvanmiyur station (Ch. 24,804.002) lies in Chennai Metro Phase-II Corridor 3. AECOM is the Detailed Design Consultant (DDC) for CMRL Corridor 3. The horizontal alignment for Thiruvanmiyur station is shown in Fig. 1.1.

Thiruvanmiyur metro station comprises three levels of slabs supported on two diaphragm walls on both sides. Length of the station is 152 m, height is 16.5 m, and width of the station varies from 20.35 m in the middle of station to 24.05 m at the ends. Three-dimensional (3D) view of the entire station box for Thiruvanmiyur station is shown in Fig. 1.2.

Geotechnical and Geological Conditions of Project Location

The geology of Chennai comprises mostly sand deposits, clay, granite, gneiss, and traces of shale and sandstone. The city is classified into three regions based on geology i.e., sandy areas, clayey areas, and hard rock areas.

For the Thiruvanmiyur station, the subsurface strata at the site consist of cohesionless soil, cohesive soil, and weathered rock. Depth-wise and strata-wise summary



(A) CMRL Project Phase II Corridor

(B) Location of Thiruvanniyur station

Fig. 1.1 Location plan of Thiruvanniyur underground metro station

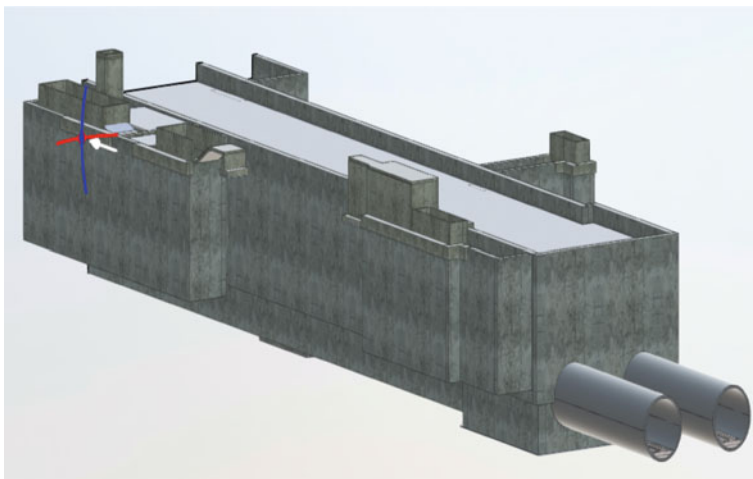


Fig. 1.2 3D view of the entire station box for Thiruvanniyur station

of station design parameters (SPT: standard penetration test, C' : effective cohesion, Φ' : effective angle of internal friction, Y : bulk density, E' : drained modulus, E_{rm} : rock modulus, ν : Poisson's ratio) for soil and rock are presented in Table 1.1. Geotechnical profile's longitudinal section with superimposed station box outline for Thiruvanniyur station is shown in Fig. 1.3.

Ground water level observations during drilling of boreholes indicate that the ground water table varies from 1.25 to 4.4 m ground level.

Table 1.1 Depth-wise geotechnical parameters for Thiruvanniyur station

Soil type	Depth m	SPT	C' kPa	Φ' deg	γ kN/m ³	E' kPa	E_{rm} MPa	ν
Filling material	0–1.5	12	–	30	18.0	18,000	–	0.3
Medium silty sand	1.5–12.0	30	–	32	19.0	27,500	–	0.3
Charnockite G(V)	12.0–15.0	–	61	48	20.0	–	348	0.3
Charnockite G(III)	15.0–27.0	–	252	67	24.0	–	4665	0.2
Charnockite G(II/I)	27.0–40.0	–	758	71	25.0	–	19,890	0.15

Model of the Case Study

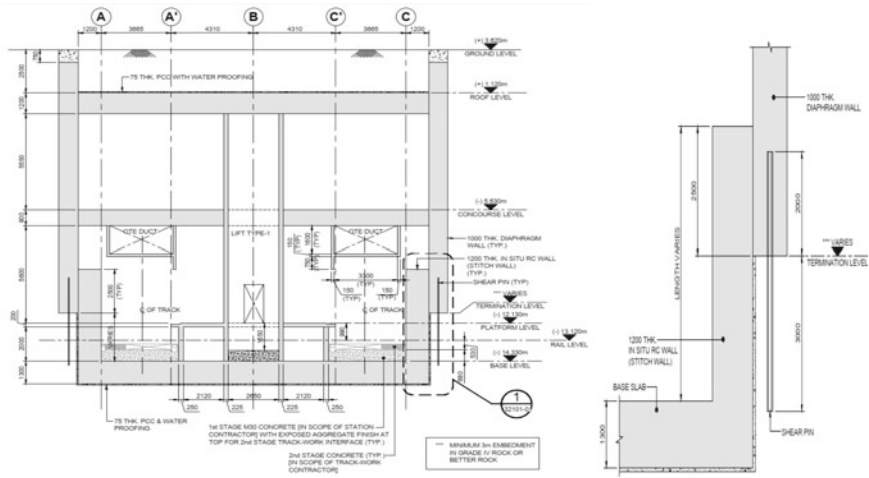
Due to varying rock layer along the station alignment, the following conditions are considered:

- Case 1 (rock layer at base level): diaphragm wall terminates at least 3 m below base slab
- Case 2a (rock layer more than 3 m below concourse slab): diaphragm wall terminates above base slab and more than 6 m below concourse slab
- Case 2b (rock layer within 3 m below concourse slab): diaphragm wall terminates within 6 m below concourse slab.

Shear pin is required in Case 2a and Case 2b. A reinforced concrete stitch wall is further provided as a connection between diaphragm wall and station base slab. Diaphragm walls (D-Walls) with shear pins embedded in rock strata and stitch wall connections with diaphragm wall for Thiruvanniyur station are shown in Fig. 1.4.

Construction Stage Analysis

Top-down stations are supported by temporary 2 levels of conventional steel strutting system and permanent slabs during excavation. The entrances/shafts are constructed with bottom-up sequence. The entrances/shafts are supported by temporary 2 levels of conventional steel struts during excavation. To reduce the effect of unbalanced load, entrance excavation should commence only after concourse slab of station is constructed. Different stages of construction sequence of typical top-down station with entrance modeled in PLAXIS 2D [4] are shown in Fig. 1.5. The constitutive model contains simple graphical inputs for different stages of construction. Mohr–Coulomb method of soil model is used in finite element-based software PLAXIS 2D [4].



(A) Station typical Cross Section

(B) D- wall with shear pin and stitch wall

Fig. 1.4 Diaphragm wall with shear pin and stitch wall connection for Thiruvanniyur station

Service Stage Analysis

The diaphragm walls are modeled as two-dimensional frame elements supporting the roof slab, concourse slab, and base slab which in turn provide lateral restraint to the diaphragm walls. The crack width on the external and internal faces of the diaphragm walls has been limited to 0.25 mm for serviceability limit state. Besides this, it has also been checked against ultimate limit state. The thickness of diaphragm walls has been taken as 1000 mm for main station and 800 mm for entrances/shafts. To incorporate the varying nature of rock layer, two extreme cases have been considered, namely Case 2a and Case 2b. In both the cases, minimum overlap of 2.5 m between the D-Walls and the stitch walls has been considered for the connection. The details are illustrated in Fig. 1.6. The crack width on the external and internal faces of the 1200-mm-thick stitch walls has been limited to 0.25 mm and 0.3 mm, respectively [5]. Three-dimensional, (3D) cross-sectional view of the station showing connection between D-Wall with stich wall from Revit BIM [6] structural model is shown Fig. 1.7.

Stability Analysis

The complete cut and cover station structure has been checked against flotation considering water table at ground level. Toe stability has also been checked from PLAXIS 2D model. Factors of safety for both flotation and toe stability have been

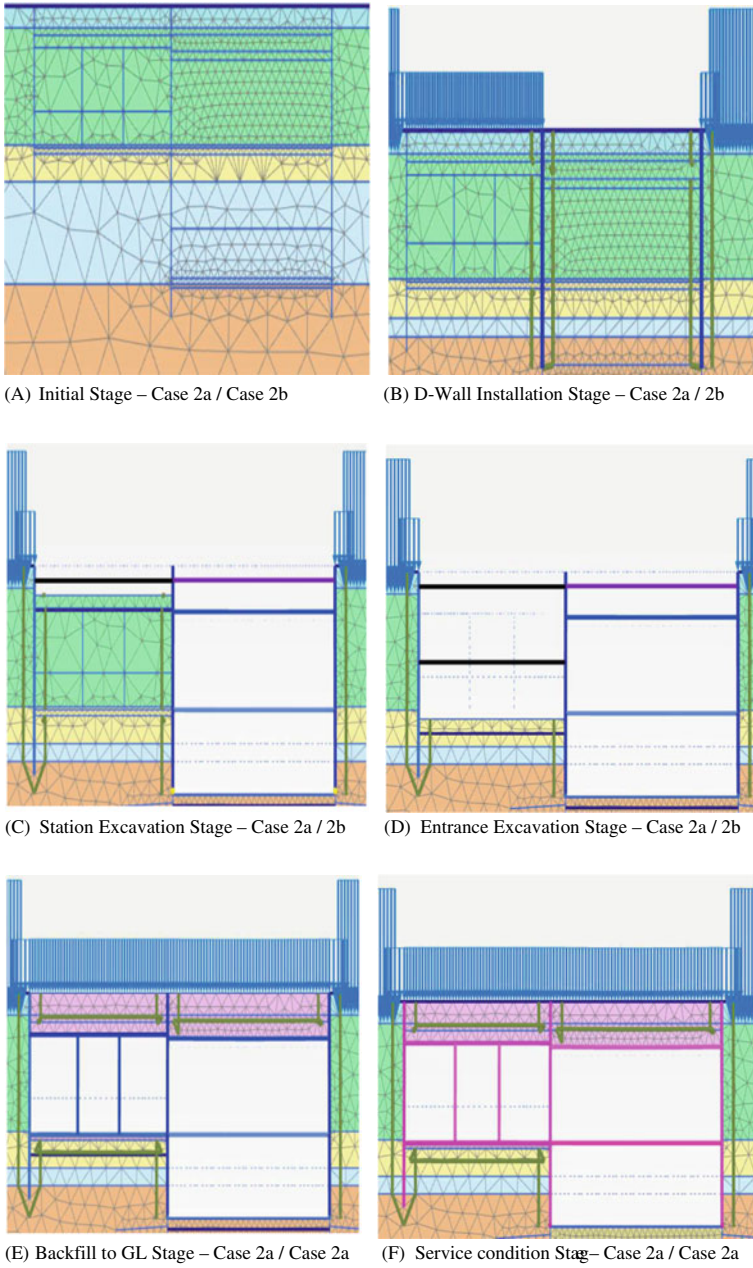


Fig. 1.5 PLAXIS model cross section for top-down station with entrance

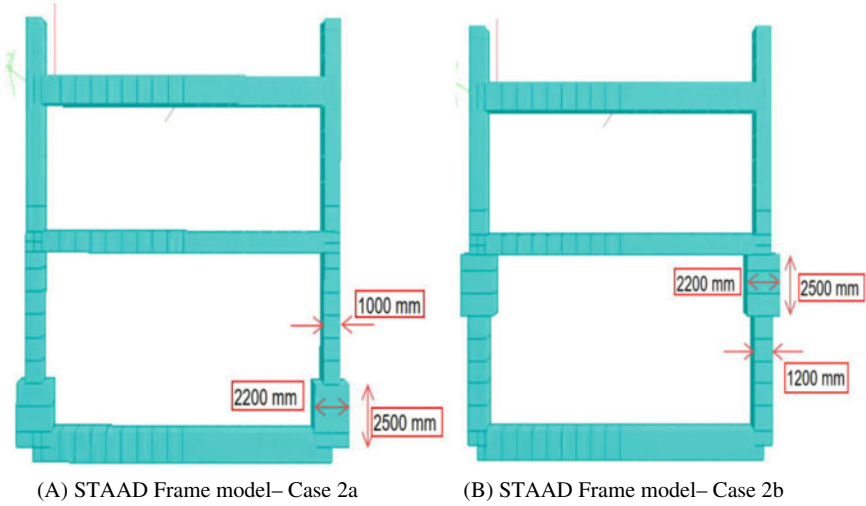


Fig. 1.6 STAAD two-dimensional frame models showing case 2a and case 2b

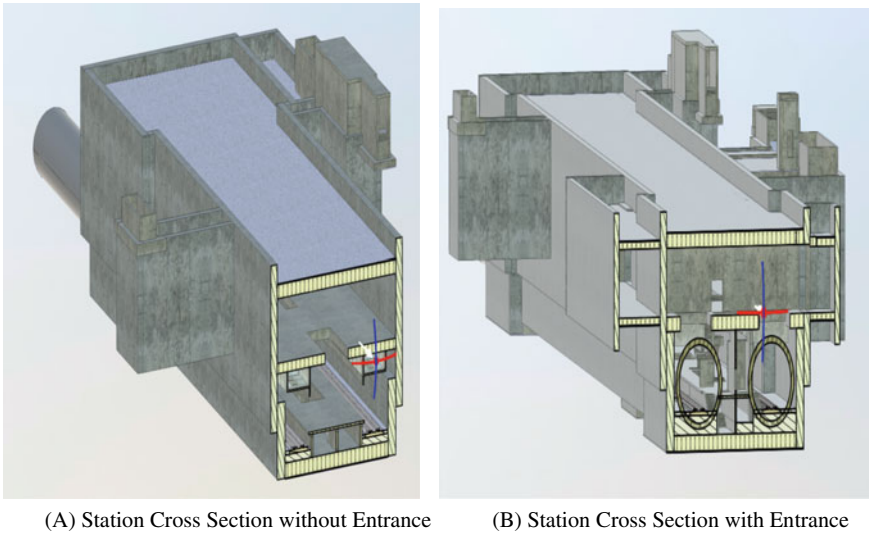


Fig. 1.7 3D cross-sectional view of station from Revit BIM service model

found well within the limiting values. Toe stability factor curve from output envelop of PLAXIS 2D model is shown Fig. 1.8.

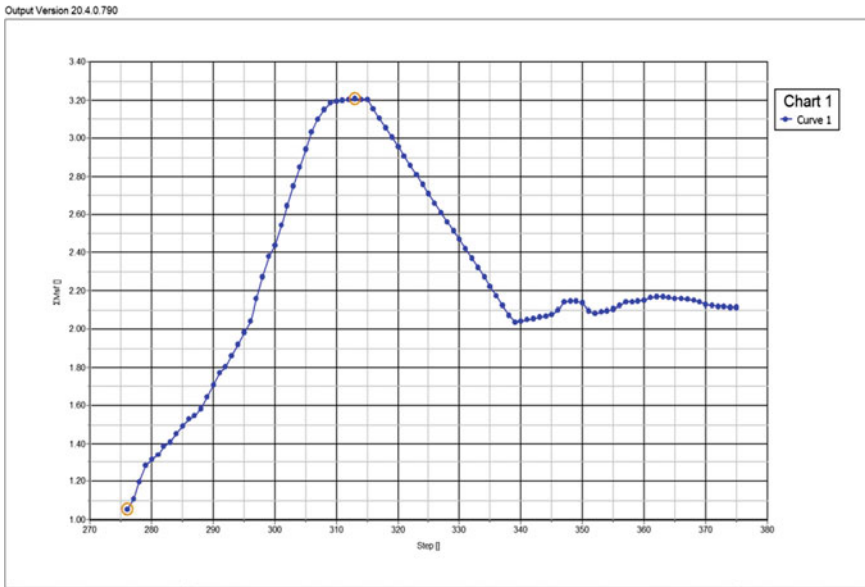


Fig. 1.8 Toe stability factor curve from PLAXIS 2D model

Discussion on Analysis and Results

As outcomes of model analysis, ground settlement, lateral deformation of diaphragm walls, bending moments, and shear forces of diaphragm walls have been estimated. Ground stability has been ensured by checking ground surface settlements with respect to the limiting value. Ground settlement curve from output envelop of PLAXIS 2D model is shown Fig. 1.9.

Horizontal deflection of diaphragm walls in different stages of excavation at different depths of the diaphragm wall has been plotted. Stability and safety of adjacent structures have been ensured by checking deflection of diaphragm walls and by performing a building damage assessment which is beyond the scope of this paper. Figure 1.10 shows the sequential deflection curve of diaphragm wall for different stages of excavation till final excavation level (FEL), strut levels, and slab levels.

Bending moment and shear force diagrams of diaphragm walls have been plotted for different stages of excavation, backfill, and service condition. Structural reinforcement concrete design of diaphragm walls has been done with respect to the envelop for different stages. Figure 1.11 shows the bending moment and shares force envelop for different stages of excavation till final excavation level (FEL), strut levels, and slab levels.

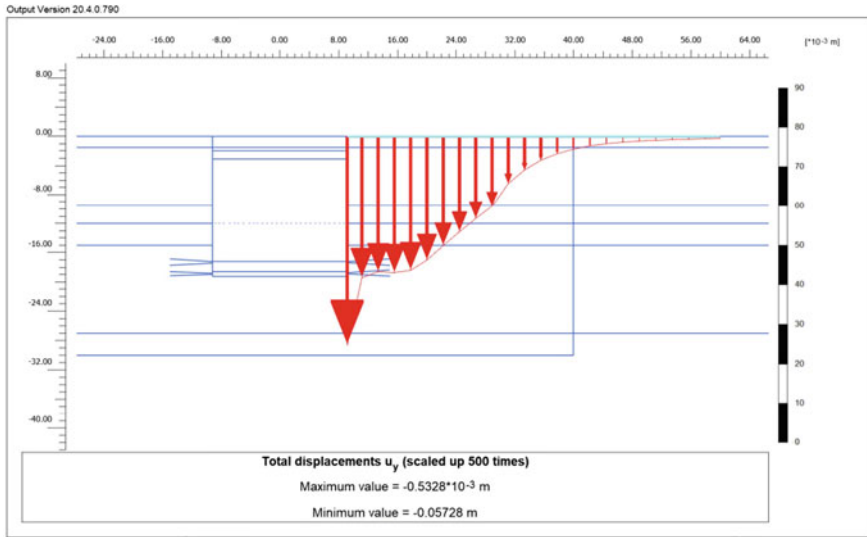


Fig. 1.9 Ground settlements curve from PLAXIS 2D model

Conclusion

Construction of underground cut and cover box structure in mixed ground condition is quite difficult, uneconomical, and time consuming with current conventional methods. The present case study describes an unconventional approach in design and construction of underground cut and cover box structure in mixed ground condition. Unconventional and innovative technical solutions many times save project from long standstills.

Structural design of Thiruvanmiyur station which falls in mixed ground condition of Chennai Metro Project Phase-II alignment corridor has been referred here. Due to difficulty in excavating hard rock strata, an arrangement of shallow diaphragm walls (terminated above base slab level) with shear pins embedded into rock strata with stitch walls has been adopted. This arrangement reduces the requirement of temporary earth retaining supports like soldier piles, secant piles, etc. Therefore, it helps in saving time, manpower, and material costs of temporary earth retaining supports.

Entire sequence of construction stages has been analyzed in finite element-based numerical model for checking of structural design, stability, ground deformation, etc. The present case study may be useful to the practicing engineers as a good reference for similar situations and to simplify the design.

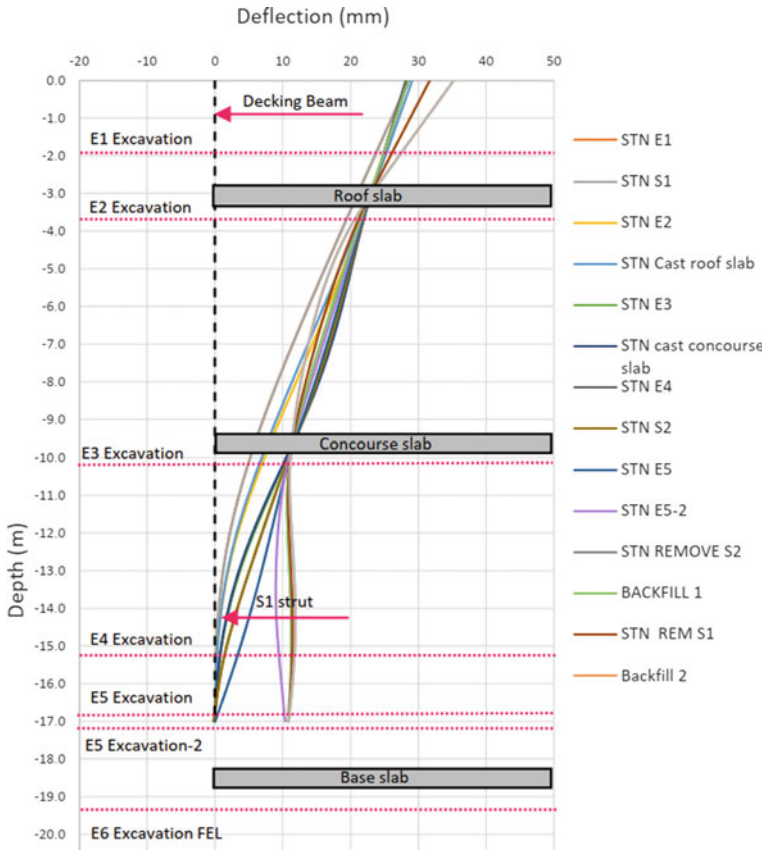
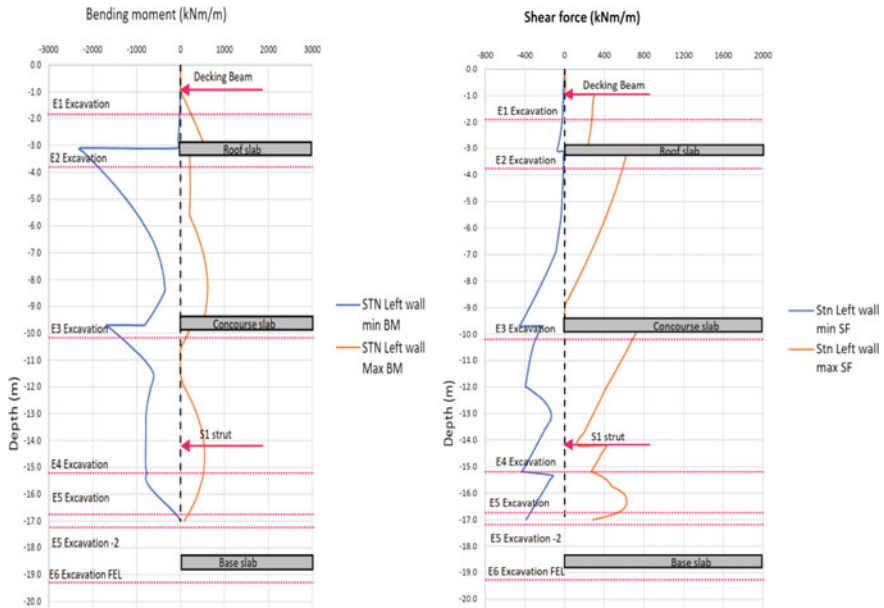


Fig. 1.10 Deflection of diaphragm wall for different stages of excavation at different depths



(A) Bending moment diagram of D-Walls

(B) Shear force diagram of D-Walls

Fig. 1.11 Bending moment and shear force diagram of D-walls for different stages of excavation, backfill, and service condition

Acknowledgements The authors acknowledge the support from the entire team involved in the project of Chennai Metro Rail Corporation Corridor 3.

References

1. Singh B, Goel RK (2006) Hudson JA (ed) Tunnelling in weak rocks. Elsevier geo-engineering book series, 1st ed, vol 5. Elsevier Science
2. Vanuvamalai A, Jaya KP (2018) Design analysis of an underground tunnel in Tamilnadu. Arch Civ Eng 64(1):21–39. <https://doi.org/10.2478/ace-2018-0002>
3. Bentley Systems (2015) V8i SELECT series 6. STAAD.Pro. Retrieved from https://communities.bentley.com/products/ram-staad/b/analysis_and_design_blog/posts/staad-pro-v8i-select-series-6
4. Bentley Systems (2019) PLAXIS 2D. Plaxis connect. Retrieved from <https://communities.bentley.com/products/geotech-analysis/w/plaxis-soilvision-wiki/46022/plaxis-connect>
5. Chennai Metro Railway Limited (2019) Design manual: structural—underground station structures (Phase II corridor 3)
6. Autodesk (n.d.) Revit BIM. Retrieved from <https://www.autodesk.in/products/revit/overview>

Chapter 2

Elastic–Perfectly Plastic Behavior of Lower Siwalik Sandstones



D. V. Sarwade, Pankaj Kumar, K. K. Mishra, P. Senthil, and Hari Dev

Introduction

Direct shear test on rock mass is important, as they provide design parameters required for civil structures founded on or constructed in rock mass. This method is quite popular among practicing engineers for determination of cohesion and friction angle of rock over rock and concrete over rock interfaces [1, 2]. Same rock type may have significantly different shear strength parameters depending upon site-specific geological characteristics [3, 4]. Hence, it is essential to conduct in-situ shear tests to determine cohesion and friction angle of the rock mass. The kind of arrangements for testing in drifts and open trenches has been discussed by some researchers, viz Singh [1], Sarwade et al. [5], and Ramana et al. [6].

Peak and residual shear strengths of rock mass are evaluated by in-situ shear tests on rock mass, as a function of normal stress to the sheared plane. The peak and residual, cohesion 'c', and friction angle ' ϕ ' are determined by linear regression on the respective normal stress versus shear stress plot. These values are used in stability and numerical analysis of dam foundations and limit equilibrium analysis of slope stability problems, etc. [7]. For conducting tests, the application of normal stress is decided based on stress to be expected due to the proposed structure, subjected to practical limitations.

While conducting the in-situ shear tests, normal stress is kept constant throughout the test and shear stress is increased gradually to measure the displacement. As the test continues, the shear stress reaches highest level which is considered to be peak shear stress, and after that, the shear stress suddenly reduces (even after continuous application of shear load) as the block starts moving. At the end of the test, the

D. V. Sarwade (✉) · P. Kumar · K. K. Mishra · P. Senthil · H. Dev
Central Soil and Materials Research Station, Olof Palme Marg, Hauz Khas, New Delhi 110016,
India
e-mail: sarwade77@gmail.com

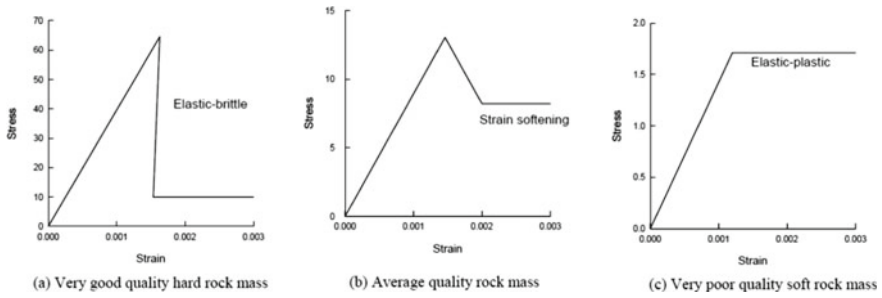


Fig. 2.1 Post-failure behavior of rock mass

shear stress remains same, which is considered to be residual shear stress. Hence, from each shear test, peak and residual shear stresses are measured at the constant normal stress [8]. However, in some cases, only peak shear stress is observed and it remains at almost same stress level with continuous displacement and residual shear stress cannot be distinguished, which is due to progressive failure or elastic–perfectly plastic behavior of rock mass. Similar types of results were encountered in the past study [9, 10]. Generally, rock mass can show three types of post-failure behavior, viz. elastic-brittle, strain softening, and elastic–perfectly plastic as shown in Fig. 2.1 [11].

In this paper, a case study of progressive failure is observed for moderate to poorly cemented sandstone of lower Siwalik. It is clearly evident from Fig. 2.1 that the progressive failure or elastic–perfectly plastic behavior corresponds to poor quality of rock masses, which means rock mass continues to deform at a constant stress level.

Study Area

The proposed Adi Badri Dam Project envisages construction of 33.4 m high and 160 m long concrete gravity dam across Somb Nadi for revival of holy Sarasvati River and a barrage and a pipeline of length 8.82 km. The impounded water shall be carried through open channel/pipeline through gravity to the downstream artificial reservoir to feed the water into Sarasvati River. The catchment area of Adi Badri Dam is 29.50 km².

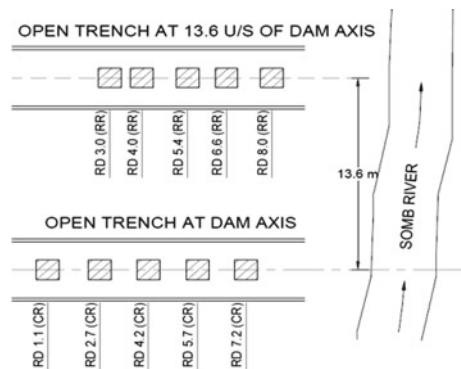
The project area falls under lower Siwalik, which are soft rocks having alternate bedding of sandstone, siltstone, and clay stone. Rock mass exposed in the area is highly to moderately jointed sandstone with bands of mudstone (1–10 m thick). The attitudes of joints are varying due to warping and folding. The rock mass falls in poor category, i.e., Class-IV as per RMR classification. The rock is classified as fine to medium grained poorly to moderately cemented gray silty sand rock. The permeability of rock mass is ranging from 10⁻⁴ to 10⁻⁵ cm/s [12, 13].

In-Situ Shear Testing

Two open trenches of 2.2 m width and 1.8 m depth with 9 m length each were excavated parallel to the dam axis, of which one is excavated along dam axis and another was excavated at 13.6 m upstream side of dam axis on left bank at riverbed level (Fig. 2.2). Rock mass encountered in these trenches is sandstone. Five in-situ shear tests on concrete over rock (CR) were conducted in the trench at dam axis, and five in-situ shear tests on rock over rock (RR) were conducted in the trench located 13.6 m upstream side of dam axis on the left bank riverbed level of River Somb [14].

In-situ shear tests were conducted following the suggested methods by ISRM and Indian Standards [15, 16] in open trench, and normal loading reaction was taken from kentledge arrangement made of ISMB girders and sand bags. An innovative design was made at site to arrange the ISMB girders in such a way that the dead load was equally transferred on three testing blocks in single loading of gunny bags, meeting the load requirements from top. The blocks and top reaction pads were kept parallel to avoid eccentric normal loading, whereas side reaction pads toward upstream direction, concentric with blocks. Normal load was applied by 200 T capacity hydraulic jack, and MS columns were used to make contact of jack with top reaction pad. Shear load was applied by another hydraulic jack of same capacity placed between block and side reaction pad, at an angle of 15° with the horizontal so that the line of action of applied force should pass through the center of gravity of the test block. An angle of 15° with the horizontal was achieved with the help of an arrangement made by two specially designed wooden wedges. A typical sketch of equipment setup for testing in open trenches is shown in Fig. 2.3. Photographs of test in progress are shown in Fig. 2.4. Each block was tested at different normal stress but it was kept constant during the test. The displacements of the blocks were measured with help of four dial gauges in normal direction and three dial gauges in shear direction. Normal load and shear load on the blocks were measured using load cum pressure gauges. The readings of dial and pressure gauges were recorded up to failure and continued even after the failure to obtain residual shear strength.

Fig. 2.2 Sketch showing of in-situ shear test locations



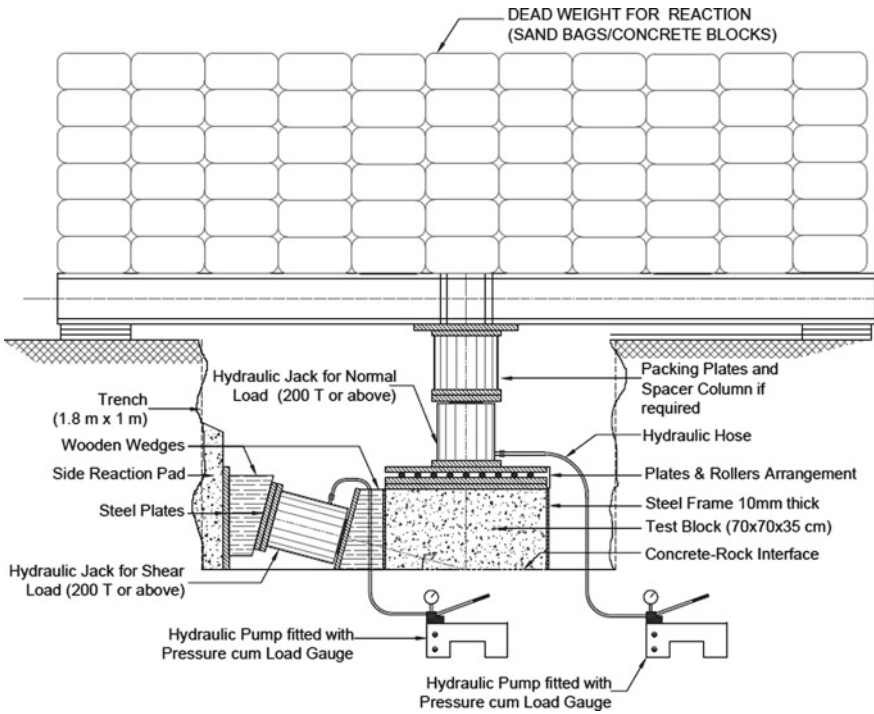


Fig. 2.3 Typical sketch showing equipment setup for shear tests in open



(a) SHT at RD7.2 m



(b) Normal Loading arrangement

Fig. 2.4 In-situ shear test in progress at site

Calculation and Interpretation

Normal stress and shear stress are calculated from normal load and shear load applied during the test using equations Eqs. 2.1 and 2.2:

$$\text{Shear Stress, } \tau = \frac{P_s}{A} = \frac{P_{sa} \cos \alpha}{A} \quad (2.1)$$

$$\text{Normal Stress, } \sigma_n = \frac{P_n}{A} = \frac{P_{na} + P_{sa} \sin \alpha}{A} \quad (2.2)$$

where P_{sa} = shear load applied, P_s = shear load, P_n = normal load, A = area of sheared surface corrected to account for shear displacement, P_{na} = normal load applied, and α = applied shear force at an angle 15° .

$P_{sa} \sin \alpha$ is a reduction factor, applied to reduce normal load for each increment of shear load in order to maintain the normal stress constant. The peak and residual shear stress recorded at failure and after failure for each block is plotted against the respective normal stress, and the best fit curve is plotted using linear regression method. From the best fit curve (straight line), cohesion ‘ c ’ and friction angle ‘ ϕ ’ of rock mass are calculated.

Rock Over Rock Interface (RR)

Five in-situ shear tests on rock over rock interface were conducted in the open trench located 13.6 m upstream side of dam axis at riverbed level on left bank of River Somb. The tests were conducted at applied normal force of 10, 15, 20, 30, and 40 T. The test results of direct shear tests on RR interface are given in Table 2.1.

Shear stresses and shear displacement at respective normal stresses are plotted in Fig. 2.5. The graph of shear stress against normal stress is used for deriving cohesion (c) and friction angle (ϕ) is shown in Fig. 2.6. Photographs of overturned blocks are shown in Fig. 2.7.

Table 2.1 Observation/findings of tests on rock over rock interface

RD	Sheared area, cm ²	Normal load, T	Shear load, T	Normal stress, MPa	Shear stress, MPa
3.0	5349	10	14	0.18	0.25
4.0	5484	40	34	0.72	0.59
5.4	5465	20	26	0.36	0.45
6.6	4878	30	34	0.60	0.66
8.0	6103	15	12	0.24	0.19

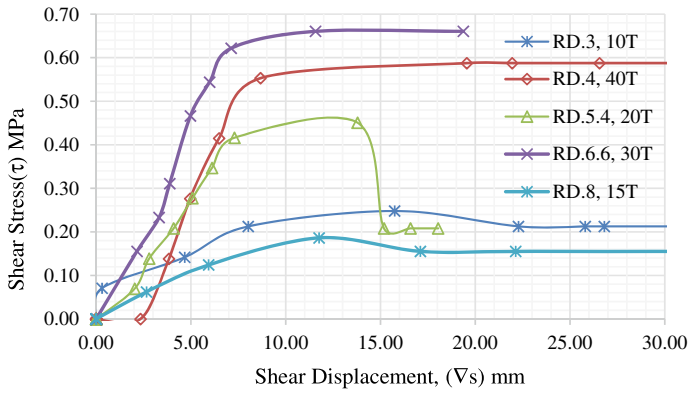


Fig. 2.5 Plot of shear stress versus shear displacements for RR interface

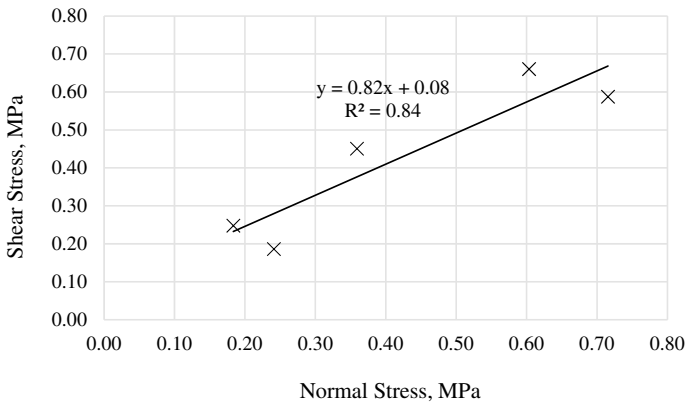


Fig. 2.6 Plot of shear and normal stress for RR interface

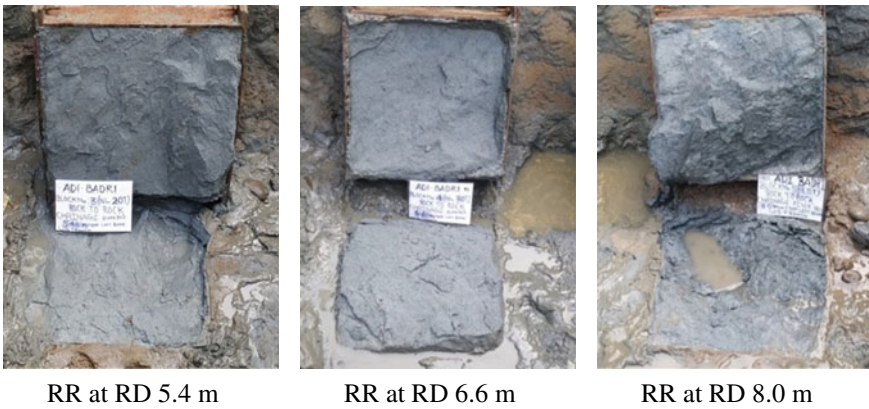


Fig. 2.7 Photographs of overturned sheared blocks of RR interface

It is seen from Fig. 2.5 that there is no clear distinction between peak and residual shear stress in all blocks except for test at RD 5.4 m, which is due to formation of key/depression along the shear plane (Fig. 2.7). However, in other test blocks, significant asperities/undulations/shear key/depressions along the shear plane were not present. Therefore, the shear strength parameters in peak and residual are same. During testing, it was observed that after reaching peak stress level, it remained same even with the continuous application of shear load, and the block movement was observed. This type of shearing can be termed as progressive shearing and elastic–perfectly plastic behavior of rock mass as the rock mass continues to deform at a constant stress. After overturning the blocks, actual sheared area is considered for computation of shear stresses from the applied loads (Fig. 2.7).

All the test data have been considered for linear fitting to evaluate cohesion (c) and friction angle (ϕ) of rock mass at dam site (Fig. 2.6), which were determined as 0.08 MPa and 39° , respectively.

Concrete Over Rock Interface (CR)

Five numbers of in-situ shear tests were conducted on concrete over rock interface at the location of dam axis trench excavated on riverbed level at left bank of River Somb. The tests were carried out at applied normal loads of 10, 15, 20, 30, and 40 T.

The test results of in-situ shear tests on concrete over rock interface are given in Table 2.2. Shear stresses versus shear displacements at respective normal stresses are plotted in Fig. 2.8. From the plots of shear stresses against respective normal stresses, cohesion (c) and friction angle (ϕ) were derived as shown in Fig. 2.9. After overturning sheared blocks, actual area was measured to compute stresses from applied loads. Photographs of overturned blocks are shown in Fig. 2.10.

It is seen from Fig. 2.8 that there is no clear distinction between peak and residual shear stress in all blocks except the test at RD 4.2 m, which is due to asperities and undulation along the shear plane (Fig. 2.10). However, in other test blocks, significant asperities/undulations/shear key/depressions along the shear plane were not present. Therefore, the shear strength parameters in peak and residual are same and only peak

Table 2.2 Observations/findings of tests on concrete over rock interface

RD	Sheared surface, cm ²	Normal load, T	Shear load, T	Normal stress, MPa	Shear stress, MPa
1.1	4900	10	10	0.20	0.19
2.7	4900	15	12	0.30	0.23
4.2	4900	40	36	0.80	0.70
5.7	5220	30	34	0.56	0.62
7.2	4900	20	22	0.40	0.43

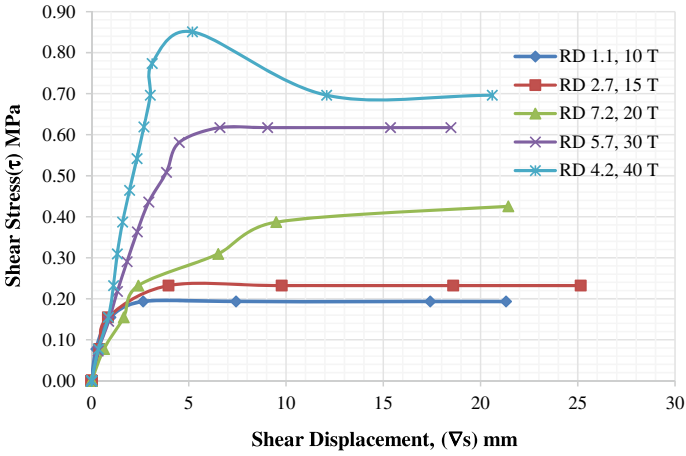


Fig. 2.8 Shear stress versus shear displacements plot for CR interface

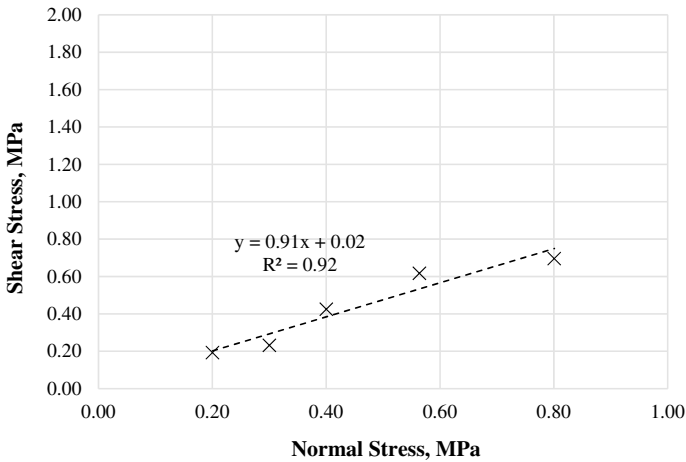


Fig. 2.9 Plot of shear and normal stress for CR interface

values have been reported. This is a typical progressive shearing and elastic–perfectly plastic behavior of rock mass.

All the test data have been considered for linear fitting to find out friction angle (ϕ) and cohesion (c) of rock mass at dam site (Fig. 2.9), which are determined as 42° and 0.02 MPa, respectively. Due to the nature of shearing behavior, the parameters for peak and residual are same. Photograph of overturned CR blocks is shown in Fig. 2.10, and it can be seen that the shearing has taken place along the concrete interface.

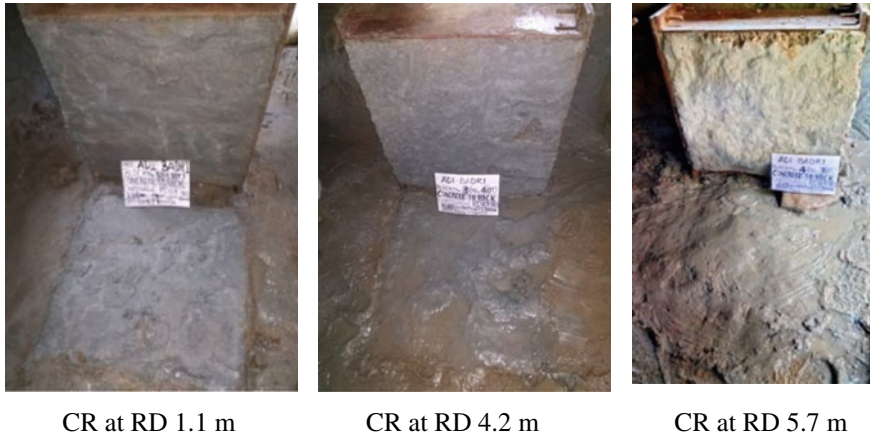


Fig. 2.10 Photographs of overturned sheared blocks of CR interface

Conclusion

In-situ shear tests were conducted at dam site of Adi Badri Dam Project across Somb River for obtaining shear strength parameters. Five numbers of shear tests were conducted on both the interfaces of rock over rock and concrete over rock, in the open trench at the riverbed level. The tests were carried out at applied normal loads 10, 15, 20, 30, and 40 T.

- The rock mass encountered in the open trenches at the dam site of Adi Badri is moderate to poorly cemented sandstone of lower Siwaliks.
- The cohesion (c) and friction angle (ϕ) for rock over rock interface were found to be 0.08 MPa and 39° , respectively, whereas for concrete over rock interface found to be 0.02 MPa and 42° as peak shear strength parameters. The residual parameters for rock over rock as well as concrete over rock interface were not distinguished.
- In the present study, test results revealed progressive failure and elastic–perfectly plastic behavior of rock mass, that means the rock mass continues to deform at a constant stress level for both RR and CR blocks.
- The shear strength parameters for peak and residual state are same for the sandstone due to soft nature of rock mass and absence of significant asperities/undulations/shear key/depressions along the shear surface.

References

1. Singh R (2009) Measurement of in-situ shear strength of rock mass. *J Rock Mech Tunnell Technol* 15(2):131–142

2. Chawre B, Yadav RP, Mishra KK (2014) In situ shear strength parameters—a case study. *J Eng Geol* XXXIX(1)
3. Ramana GV, Pathak S, Dev H (2016) Shear strength parameters of granite rock-mass: a case study. In: IGC-2016, 15–17 Dec 2016, IIT Madras, Chennai, India
4. Senthil P, Sarwade DV, Dev H (2021) Direct shear test on quartzite rock mass: evaluation of rock joints and interfacial shear strength parameters. *ISRM (India) J* 10(1):22–31
5. Sarwade DV, Senthil P, Dev H (2020) Evaluation of shear strength parameters for design of dam for a drinking water project—a case study. *Int J Eng Res Technol (IJERT)* 9(3), March 2020
6. Ramana GV, Pathak S, Dev H, Singh R, Gupta VK (2014) Shear strength of Deccan granite rock mass in open trench. In: INDOROCK-2014, 5th Indian rock conference on underground construction for hydropower, mining & infrastructure, 12–14 Nov 2014, New Delhi, vol I, pp 279–288
7. Bakhtiyari E, Almasi A, Cheshomi A, Hassanpour J (2017) Determination of shear strength parameters of rock mass using back analysis methods and comparison of results with empirical methods. *Eur J Eng Res Sci* 2(11), November 2017
8. Dev H (2017) Shear strength of rock mass—interpretation and analysis. *J Eng Geol* XLII(1)
9. Singh S, Sarwade DV (2009) Interpretation of shear strength parameters of rock mass, GEOTIDE, IGC-2009, Guntur, India
10. Singh R, Sarwade DV (2015) Evaluation of shear strength parameters in jointed rock mass. *J Rock Mech Tunnell Technol* 22(1):21–36
11. Hoek E (2000) Rock engineering course notes, pp 182–185
12. GSI Report (2018) A note on the geological/geotechnical investigations of the proposed Adi Badri project, Near Adi Badri, District Yamuna Nagar, Haryana, Geological Survey of India, Chandigarh
13. SGS Report (2018) Report on geological exploration by diamond core drilling of NX drill holes at Adi Badri dam area Locations, Jagadari, District Yamuna Nagar, Haryana, M/s Shivalik Geotech Services
14. CSMRS report: report on in-situ shear strength parameters of rock mass at dam site of Adi Badri dam project, Haryana. Central Soil and Materials Research Station, New Delhi, No. 02/RM-F/CSMRS/E/12/2020-21, December 2020
15. (1996) IS 7746: Indian standard code of practice for in-situ shear test on rock. Bureau of Indian Standards, New Delhi
16. Ulusay R, Hudson JA (eds) (2007) *ISRM: the complete ISRM suggested methods for rock characterization, testing and monitoring: 1974–2006*. International Society for Rock Mechanics

Chapter 3

Effect of Volume Loss During Tunnel Construction on the Ground Surface



Rahul Shakya and Manendra Singh

Introduction

Quick populace development in metropolitan regions has brought about a huge lack of ground spaces for construction. To decrease surface traffic volume needs, tunnels are constructed underneath the ground surface. There can be ground movements and damage to existing buildings and other structures due to the construction of the tunnel below the ground surface. It ought to be controlled to adequate levels. The subsurface excavation occurs for the construction of the tunnel, due to which ground movement occurs inward to the tunnel because of the expulsion of soil from the tunnel segment. The volume of the completed void in every case is not exactly the volume of eliminated soil. The volume of the finished void is always smaller than the volume of removed soil. Therefore, volume loss occurs during the construction of tunnel. The volume loss (V_L) is defined as the ratio of the extra volume of excavated soil (ΔV) to the volume of finished void (A_f) per unit length [1].

$$\text{Volume Loss}(V_L) = \frac{\Delta V}{A_f} * 100 \quad (3.1)$$

Previous studies showed that the value of volume contraction mainly depends on two factors. The initial one is geotechnical and topographical attributes of soil, and the subsequent factor is the method of excavation. Numerous examinations have been done around this problem, and the conclusion from the studies suggests that the lower and higher value of volume contraction is 0.2% and 2%, respectively.

The volume loss can be defined with the help of three components, which include face loss, tail loss, and shield loss. Formula for the total volume loss is given in

R. Shakya · M. Singh (✉)

Department of Civil Engineering, National Institute of Technology Hamirpur, Hamirpur, Himachal Pradesh 177005, India
e-mail: manendra@nith.ac.in

Eq. 3.2 [1].

$$V_L = V_{Face} + V_{Shield} + V_{Tail} \tag{3.2}$$

where V_{Face} , V_{Tail} , and V_{Shield} are the face loss, tail loss, and shield loss, respectively.

For the value of V_{Face} , V_{Tail} , and V_{Shield} , Loganathan [2] gave the analytical methods which are related with the empirical parameters and obtained from soil’s properties. There are few restrictions of this solution since certain parameters are reliant upon the observational values and are related to high uncertainty. The magnitude of volume loss, V_L , depends primarily on the geotechnical properties of soil and method of construction of tunnel. Peck [3], Cording and Hansmire [4], O’Reilly and New [5], Attewell et al. [6], and Mair [7] have reviewed the value of volume loss from tunneling projects. Clough and Schmidt [8] studied a tunnel in clay and suggested a relationship, based on the closed-form solution of a cavity in linear elastic–perfectly plastic conditions. According to a symposium submitted in London related to the settlement of bored tunnels [9], the value of volume loss was generally between 1 and 2%, and in one case, it was observed as 3%. It was also observed that NATM method was the most effective method for controlling the ground movement.

Problem Description

A typical section of DMRC (Delhi Metro Rail Corporation) has been considered for analysis, which is situated on the yellow line, as shown in Fig. 3.1. The geometric and other details of the problem have been obtained from Yadav [10] and have been presented in Table 3.1.

The soil was obtained from the excavation of DMRC tunnels through the alluvium deposits, known as Delhi silt. For the present study, the elastic modulus (E) of Delhi

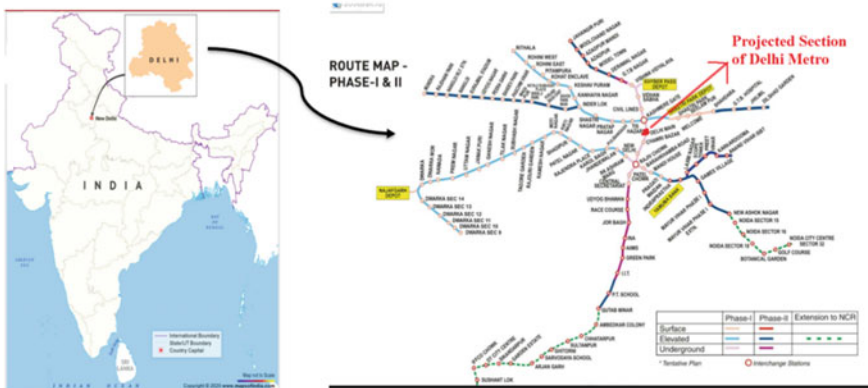


Fig. 3.1 Alignment plan for phase 1 and phase 2 of Delhi metro project [10]

Table 3.1 Geometric and other details of tunnel [10]

Properties	Value
Diameter of tunnel	6.4 m
Overburden depth	28.8 m
Thickness of RC liners	0.28 m
RC liner's elastic modulus (E_C)	$3.16 * 10^7$ kPa
Poisson's ratio	0.15

silt varied with depth according to the following relation [10].

$$E = 1.22 + 0.83(z) \quad (3.3)$$

where z is the depth of the soil layer.

In-situ unit weight, γ_{bulk} , and saturated unit weight, γ_{sat} , were found to be 18.33 kN/m^3 and 21.35 kN/m^3 , for the entire soil layer, respectively. No water table was experienced. The value of Poisson's ratio is 0.25. The value of cohesion has been considered as zero, and the value of friction angle (ϕ) and dilation angle (ψ) is 35° and 5° , respectively, for entire soil layer. The value of K depends on the friction angle ($K = 1 - \sin\phi$). Friction angle was same for entire soil layer. Therefore, value of K will remain same for the entire soil layer.

Numerical Modeling

For the simulation of problem, PLAXIS 2D software was used. Plane strain analysis has been carried out. For the discretization of the domain of soil layer, 15-noded triangular elements have been used. Horizontal domain of the soil should be greater than the twenty times of diameter of tunnel [11]. Therefore, soil domain for the current study has been taken as $128 \text{ m} \times 78 \text{ m}$. Figure 3.2 shows the geometry of physical model. Some critical points of tunnel like crown, invert, and springing points have also been depicted in Fig. 3.2. Elasto-plastic behavior of soil has been simulated using MC (Mohr–Coulomb) yield criterion. Elastic behavior of tunnel has been taken for both elastic and elasto-plastic analysis. In finite element mesh, the nodes were restrained in the horizontal direction while in vertical direction remains free to move, whereas the bottom boundary was restrained in horizontal as well as in vertical direction also. Top boundary was free against the displacement in both directions.

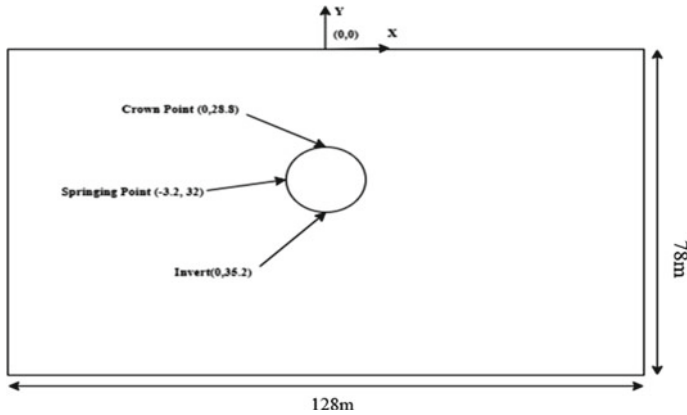


Fig. 3.2 Geometry of physical model

Results and Discussion

Elastic Analysis

The ratio of final vertical stress after the construction of tunnel to the initial stress before the construction of tunnel at any point surrounding the tunnel is known as vertical stress concentration. Figure 3.3 shows the vertical stress concentration along the horizontal axis of the tunnel. It can be observed that the vertical stress concentration has the maximum value at $r/a = 1$, and after that, it starts to decrease up to $r/a = 4$; thereafter, it becomes constant. From Fig. 3.3, it can be concluded that vertical stress concentration increases with increase in volume loss especially near the periphery of tunnel. The results have been compared with Terzaghi and Richart [12] solutions, as shown in Fig. 3.3. It can also be concluded from Fig. 3.3 that PLAXIS model has the same value of vertical stress concentration as Terzaghi and Richart [12] for volume contraction of 2%. Therefore, for this site, volume loss of 2% should be taken for the elastic analysis.

Figure 3.4 depicts the vertical displacement along the transverse axis of the tunnel. From Fig. 3.4, it can be noticed that vertical displacement was found to be maximum near the tunnel. Vertical displacement has decreased with increase in the ratio of r/a and becomes almost zero at $r/a = 4.5$. Results obtained by numerical analysis have been compared with Pender's closed-form solutions [13]. From Fig. 3.4, it can also be stated that Pender's solution overestimates the vertical displacement; therefore, numerical analysis is very essential for analyzing the behavior of soil-tunnel system.

Table 3.2 represents the maximum horizontal displacement (U_X) and vertical displacement (U_Y) in soil as well as in tunnel for different values of volume contraction. It can be observed from Table 3.2 that the maximum displacement in soil remains constant, whereas settlements in tunnel increase slightly with increase in the value of volume contraction.

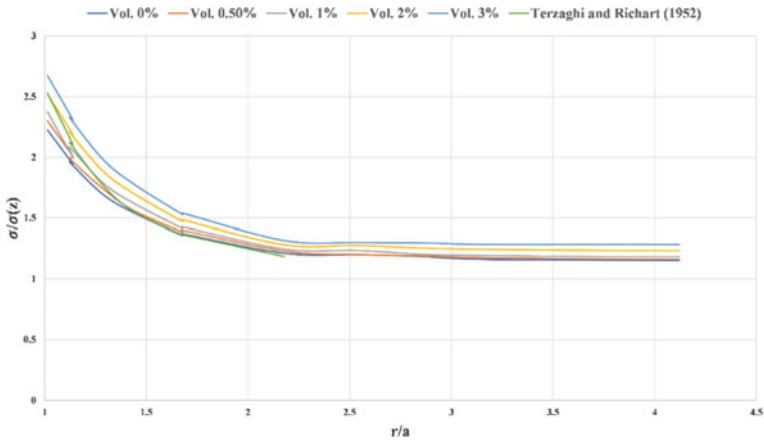


Fig. 3.3 Vertical stress concentration along the transverse axis of the tunnel (where 'a' and 'r' are the radius of the tunnel and radial distance along the axis of tunnel, respectively)

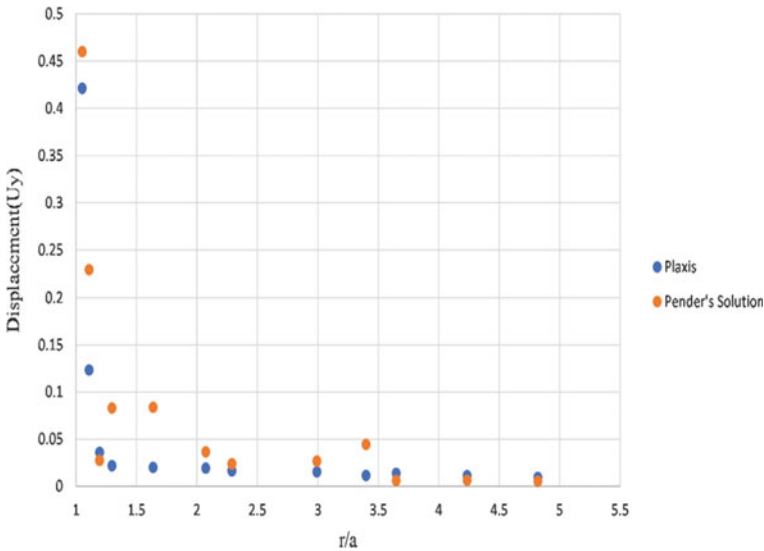


Fig. 3.4 Vertical displacement along the horizontal axis of the tunnel

Elasto-Plastic Analysis

Figure 3.5 shows the variation of vertical stress concentration along the transverse axis of the tunnel for the elasto-plastic behavior of soil. From Fig. 3.5, it can be concluded that the soil nearby the tunnel entered into the plastic zone and the value of vertical stress concentration drops down less than unity. The value of this stress

Table 3.2 Maximum displacement in soil-tunnel system elastic behavior of soil

V_L (%)	Soil		Tunnel	
	U_X (mm)	U_Y (mm)	U_X (mm)	U_Y (mm)
0	19.31	66.39	18.99	67.59
0.5	19.31	66.39	19.37	67.95
1.0	19.31	66.39	19.75	68.32
2.0	19.31	66.39	20.5	69.04
3.0	19.31	66.39	21.34	69.77

ratio has increased to maximum value up to a certain distance from the tunnel, and this distance is known as elasto-plastic radius. Beyond elasto-plastic radius, the value of stress concentration started to decrease up to certain distance and thereafter becomes constant at a distance. The vertical stress concentration has decreased with increase in volume loss, as shown in Fig. 3.5. It can also be observed from Fig. 3.5 that for the volume contraction of 3%, the stress concentration follows the trend with Bray’s closed-form solutions [14]. Therefore for this site, volume loss of 3% should be taken for the elasto-plastic analysis.

The values of maximum displacements in soil as well as in tunnel for different values of volume contraction have been tabulated in Table 3.3. From Table 3.3, it can be stated that the maximum displacements in soil and tunnel have increased significantly with increase in volume loss.

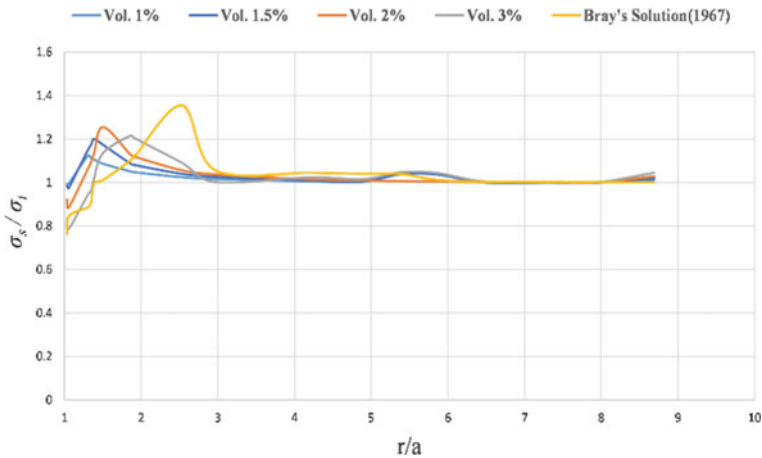


Fig. 3.5 Vertical stress concentration along the transverse axis of the tunnel for the elasto-plastic behavior of the soil

Table 3.3 Maximum displacement in soil-tunnel system for elasto-plastic behavior of soil

V_L (%)	Soil		Tunnel	
	U_X (mm)	U_Y (mm)	U_X (mm)	U_Y (mm)
1.0	8.6	56.97	17.21	56.06
1.5	13.11	60.46	20.16	60.27
2.0	21.66	63.67	25.01	64.43
3.0	38.53	70.79	38.52	72.08
1.0	8.6	56.97	17.21	56.06

Conclusion

From this study, the following outcomes were obtained.

1. For elastic behavior of soil, vertical stress concentration has increased with increase in volume loss. The results are well matched with Terzaghi and Richart solutions for volume loss of 2%. Therefore, for this site, volume loss of 2% should be taken for the elastic analysis and for elasto-plastic behavior of soil the vertical stress concentration has decreased with increase in volume loss. For the volume contraction of 3%, the stress concentration follows the trend with the Bray's closed-form solution.
2. For elastic behavior of soil, effect of volume loss on maximum displacement in soil was negligible, whereas settlement in tunnel has increased slightly with increase in the value of volume contraction, whereas for elasto-plastic behavior of soil, maximum displacements in soil and in tunnel increased significantly with increase in volume loss.

References

1. Golpasand MRB, Nikudel MR, Uromeihy A (2016) Specifying the real value of volume loss (V_L) and its effect on ground settlement due to excavation of Abuzar tunnel, Tehran. *Bull Eng Geol Env* 75(2):485–501
2. Loganathan N (2011) An innovative method for assessing tunnelling-induced risks to adjacent structures. In: PB 2009 William Barclay Parsons fellowship monograph 25. Parsons Brinckerhoff Inc, pp 92
3. Peck RB (1969) Deep excavation and tunneling in soft ground. In: Proceedings of the 7th international conference on soil mechanics and foundation engineering. State of the art Volume. Mexico, pp 225–290
4. Cording EJ, Hansmire WH (1975) Displacements around soft ground tunnels. In: Proceedings 5th pan American conference soil mechanics and foundation engineering, Buenos Aires, vol 4, pp 571–633
5. O'Reilly MP, New BM (1982) Settlements above tunnel in the United Kingdom—their magnitude and prediction. In: *Tunnelling*. The Institution of Mining and Metallurgy, London
6. Attewell PB, Yeates J, Selby AR (1986) Soil movements induced by tunnelling and their effects on pipelines and structures. Blackie and Son Ltd., Glasgow

7. Mair RJ (1996) General report on settlement effects of bored tunnels. In: International conference of geotechnical aspects on underground construction in soft ground, London, UK, pp 43–53
8. Clough GW, Schmidt B (1981) Design and performance of excavations and tunnels in soft clay
9. Leblais Y, Bochon A (1991) Villejust tunnel: slurry shield effects on soils and lining behavior and comments on monitoring requirement. *Tunnelling* 91:65–77. London, UK
10. Yadav HR (2005) Geotechnical evaluation of Delhi metro tunnels. Ph.D. thesis, Department of Civil Engineering, IIT Delhi, India
11. Amorosi A, Boldini D (2009) Numerical modeling of the transverse dynamic behavior of circular tunnels in clayey soils. *Soil Dyn Earthq Eng* 29(6):1059–1072
12. Terzaghi K, Richart FE (1952) Stresses in rock about cavities. *Inst Civ Eng*
13. Pender MJ (1982) Elastic solutions for a deep circular tunnel. *Geotechnique* 30(2):216–222
14. Brown ET, Bray JW, Ladanyi B, Hoek E (1983) Ground response curves for rock tunnels. *J Geotech Eng* 109(1):15–39

Chapter 4

Crack Growth in Rocks with Pre-existing Flaws Subjected to Uniaxial and Biaxial Compression



G. Sivakumar and V. B. Maji

Introduction

Rock mass generally exhibits discontinuities and is mostly seen in the upper earth crust's region which varies from micromillimeter to kilometer in length. Based on the International Society for Rock Mechanics (ISRM), major types of discontinuity observed in rock mass are faults, fractures/fissures, joints, bedding planes, and cleavage. According to An et al. [1] in the field cases of massive rock slopes and underground tunnels, the fracture is most commonly observed for non-persistence fracture. Studies on fully persistence fractures are well defined by many literatures, whereas the non-persistence fracture needs more study to understand their failure mechanism. Slope failure observed in the field is discovered from complex interaction between non-continuous fractures and brittle propagation through intact rock (see Fig. 4.1a). In underground tunneling and mining, a new microlevel fractures are expected to develop around the excavated portion (see Fig. 4.1b).

Researchers in the past decades attempted to study the behavior of newly developed cracks from pre-existing fractures by performing experimental and numerical studies. Initial experimental studies are performed on a single flaw or double flaw specimens having parallel configurations [3–9] on rock (Limestone, Marble, Sandstone) and rock like materials (Plaster of Paris, gypsum). Based on the observations, tensile crack is the first primary crack observed from the flaw tips. The cracks were observed to propagate in a stable manner toward the loading direction, making a curvilinear path. Subsequently, shear cracks are observed as a shear zone near to the flaw tip. The cracks are observed to be visible once the material is about to reach its

G. Sivakumar (✉)

Assistant Professor, Indian Institute of Technology Jammu, Jammu, Jammu and Kashmir, India
e-mail: sivakumar.g516@alumni.iitm.ac.in

V. B. Maji

Professor, Indian Institute of Technology Madras, Chennai, Tamil Nadu, India

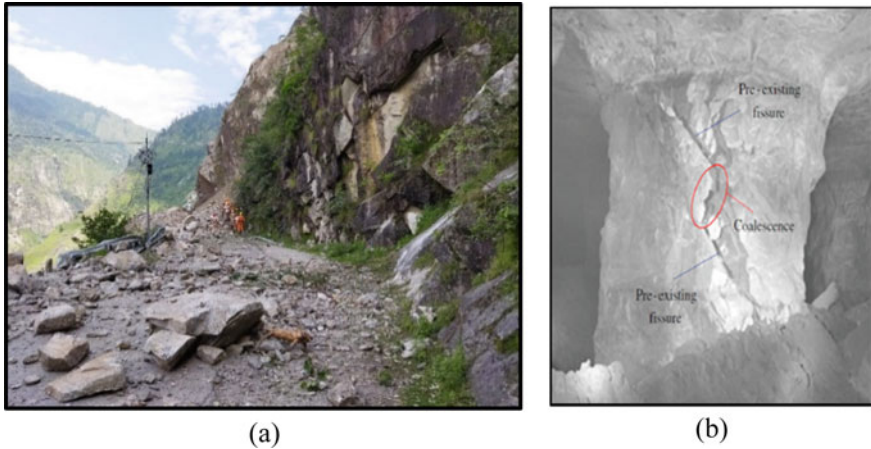


Fig. 4.1 Common failure in rock mass due to presence of discontinuity: **a** landslide in Kinnaur district (Himachal Pradesh) and **b** pillar fissure in United States [2]

peak limit, and the crack is observed to grow in an unstable manner after the peak. There are also subsidiary cracks (far-field cracks, extension cracks) which depending upon the material type, they may or may not influence the tensile/shear cracks for material failure [8, 10–12]. The specimen is mostly observed to fail by fully developed wing crack under uniaxial compression. However, the studies were performed when the flaw surface is considered as open, whereas in the field, the surface mostly has narrow or closed flaw surfaces. According to Shen et al. [6] and Wong and Chau [7], there will be friction that exhibits between the flaw surfaces for a narrow/closed condition. The effect of friction alters the behavior of crack type and its propagation when compared to open flaw configurations. Also, the growth of tensile crack was observed to subside when subjected to lateral confinements. Experimental studies under biaxial conditions [10, 13] reveal that in specimens observed, there is a reduction in the tensile crack and a more dominant presence of shear zone/crack influences the material failure.

Therefore, in the present study, an attempt is made to study the behavior of crack growth for a flaw having narrow condition when subjected to uniaxial and biaxial conditions. Also, previous studies on specimens having double flaws were carried out by considering parallel arrangements [6, 10]. Very limited studies are performed to study the crack growth and coalescence between the two flaws having non-parallel arrangement [12, 14]. Hence, a study for double flaws having non-parallel configuration is considered to understand the crack types and their coalescence nature when subjected to uniaxial as well as biaxial loading conditions. Generally, the crack initiation and their coalescence behaviour are easy to monitor if the propagated cracks are stable. However around the material peak limit, the initiation and coalescence path are difficult to observe from experimental studies. With the advancement in numerical methods like Finite Element Method (FEM), Discrete

Element Method (DEM), Hybrid Finite-Discrete Element Methods (FDEM), and Displacement Discontinuity Method (DDM), the crack growth can be studied. For realistic simulation of progressive failure of the discontinuity medium flow through the continuum medium intact rock, the Extended Finite Element Method (XFEM) is most widely adopted. The model was used in conjunction with the Cohesive Zone Model (CZM) by many researchers [11, 12, 15, 16]. Hence, the study is further extended to numerical methods to study the systematic behavior of crack growth.

Experimental Study

From previous literature, it is understood that the material at a discontinuity flaw angle of 45° is most favorable geometry, where the crack initiates sooner than the other flaw angle [11, 12, 16]. For the present study, the geometry of the specimen is carried with a single flaw of 45° angle and a double flaw having non parallel configuration, where one flaw is horizontal and another flaw inclined at 45° angle. The study was carried on both geometries to understand the crack growth behavior under uniaxial and biaxial compression. Specimens are prepared using artificial rock material gypsum, and the reason to adopt gypsum is making of narrow flaws and geometrical arrangement is much easier.

Sample Preparation and Testing

The samples are prepared by mixing S-35 grade gypsum and Plaster of Paris at a ratio of 3:1 in a dry state, and water is added at 35% of the total mix [12]. The specimens are made into slurry once the gypsum is mixed with water and later transferred into the mold for curing. For creating a narrow flaw, a metal shim of a very smooth surface having a thickness of 0.1 mm is used. The specimen is cured for 20–30 min, and then, the metal shim is removed when the gypsum is still in semi-solid condition and kept for curing in an oven for 24 h at 40°C . After oven drying, the specimen is kept at room temperature for complete curing for four days. Testing is carried out after 5 days of complete curing. The physio-mechanical properties of the material are determined as per ISRM suggested methods (see Table 4.1).

The dimensions of the specimens for uniaxial compression are 76.2 mm (width) \times 152.4 mm (height) \times 30 mm (thick) for a single flaw specimen (SF45U) (see Fig. 4.2a). In the case of non-parallel flaw arrangement (NP45U), two metal shims are used to create one horizontal and one inclined flaw underneath the horizontal flaw (Fig. 4.2c). For biaxial compression, the dimensions of the specimens changed into 125 mm (width) \times 150 mm (height) \times 30 mm (thick) for single (SF45B) and double flaw specimens (NP45B) (see Fig. 4.2b, d). The increase in the width of the specimen takes care of crack types not to get influenced by the effect of surface degradation at sides due to lateral confinement [17].

Table 4.1
Physio-mechanical properties
of gypsum

Property	Value
Density, ρ (kg/m ³)	1550
Young's modulus, E (GPa)	1.037
Poisson's ratio, ν	0.39
Uniaxial compressive strength, σ_c (MPa)	15.49
Tensile strength, σ_t (MPa)	1.11

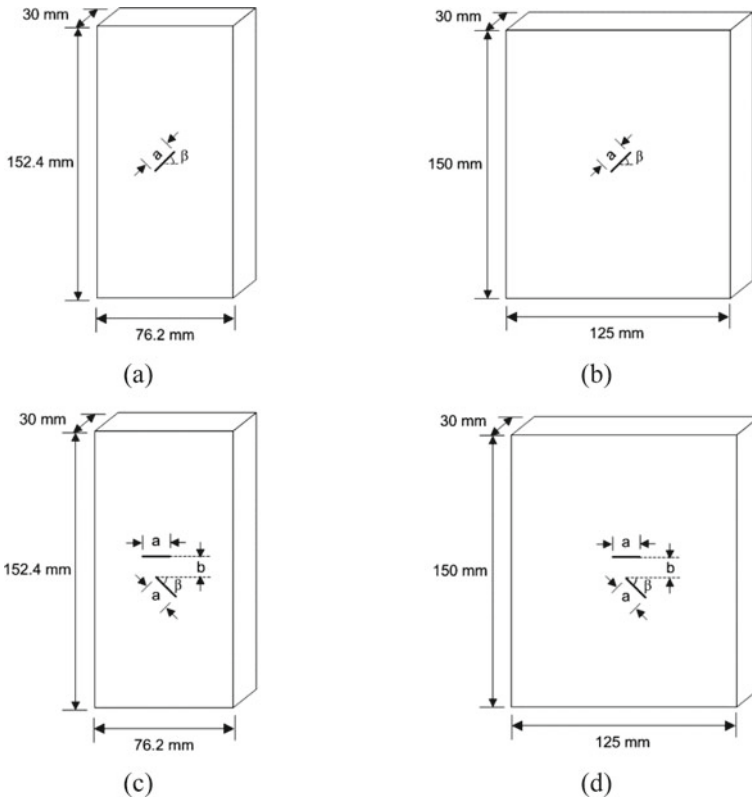


Fig. 4.2 Sample prepared for testing **a** SF45U, **b** SF45B, **c** NP45U, and **d** NP45B

The prepared specimens will be tested using 500 kN uniaxial testing (UT) compression machine available in Geotechnical Engineering Division, IIT Madras. The testing is performed until it reaches its complete failure under a displacement loading rate of 0.031 mm/min. The corresponding crack stresses at different stages of its growth are monitored using a datalogger (see Fig. 4.3). In the case of biaxial compression, the lateral confinement applied using air compressor and the specimen is arranged in such a way that the material undergoes by plane stress condition (see Fig. 4.4). The condition is achieved by modifying the conventional triaxial cell

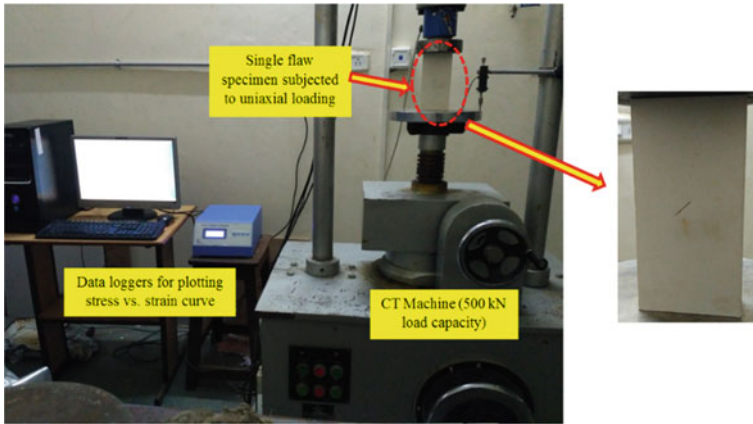


Fig. 4.3 Uniaxial compression testing machine [12]

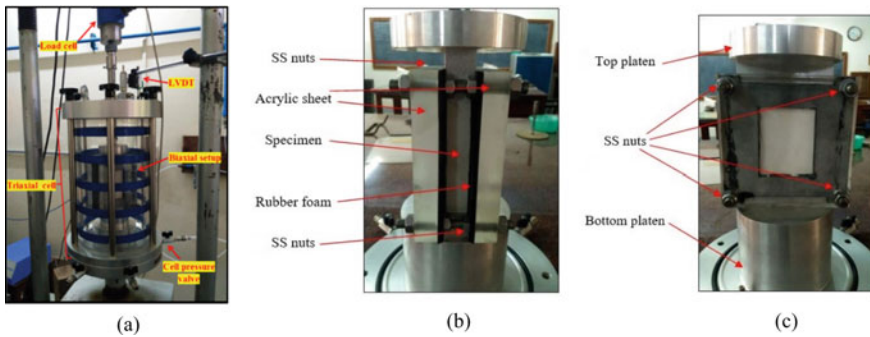


Fig. 4.4 **a** Modified triaxial setup for biaxial loading, **b** cross-sectional view, and **c** front view of specimen with center opening for monitoring the crack growth during testing [18]

(2000 kPa capacity). The confinements at two different levels 0.65 MPa and 1.24 MPa and deviatoric loading are applied from the UT machine.

Experimental Results

Single flaw. The final failure patterns obtained for a single flaw under uniaxial and biaxial compression are shown in Fig. 4.5. Specimens exhibit predominant tensile failure at both side of the flaw tips when subjected to uniaxial loading during the initial stages of the crack development. The tensile cracks (*T*) are observed to initiate in oblique direction to the flaw surface. The initiated cracks propagate in a stable manner and orient toward the compressive loading direction, making a curvilinear path.

Subsequently, shear crack (*S*) appears in the coplanar direction from the flaw surface. The crack extends in length almost half width of the flaw surface. When the material reaches its peak limit, the growth of wing crack subsides, whereas the propagated coplanar gets deviated and extends (*Ext*) in a direction parallel to wing crack. The crack gets extended in an unstable manner at an angle of 55° and propagates toward the material boundary causing ultimate material failure. Due to narrow flaw aperture, the surface gets closed and experiences slippage at the time of crack initiation. The slippage at the crack tip further induces higher stress concentration at the tip, leading to subsequent spalling in the flaw surface (see Fig. 4.5).

The failure of the specimen under biaxial compression is mostly affected by the tensile crack of wing propagation. The increase in the ratio between width of the specimen to flaw length causes the material to not exhibit shear cracks. The initiated wing crack will attain a curvilinear path and propagate directly toward the direction of major compressive loading. Also, the cracks do not get influenced by the presence of the external far-field cracks (*F*) unlike in uniaxial compression. The effect of lateral confinement affects the propagation direction of tensile crack. The path was found to slightly deviate away from the major compressive direction and tends toward the lateral confinement direction, when the confinement increases. Figure 4.6 shows the tensile crack initiation and peak stress observed for different confinement levels. Both crack initiation stress and peak stress were observed to increase with the increase in confinement. And the difference between these two stresses becomes narrow with an increase in confinement.

Double flaw. Figure 4.7 shows the final failure patterns observed for double flaw specimens with confinements of 0, 0.65, and 1.24 MPa. The tensile crack from the horizontal flaw was observed to initiate oblique to the flaw surface, irrespective of the confinements. For a uniaxial condition (0 MPa), the first crack of tensile nature (*T*) is observed from the inner tip of the inclined flaw which propagates toward the horizontal flaw forming coalescence. Simultaneously, another tensile crack is observed from outer tip of the horizontal flaw. With further loading, the propagated crack moves toward the right tip of the horizontal flaw and meets the horizontal flaw. At the coalescence stage, a new tensile crack is observed from left tip of the horizontal flaw. Also, a shear crack (*S*) is observed from outer tip of the inclined flaw. The wing crack propagation was found to orient toward the loading direction

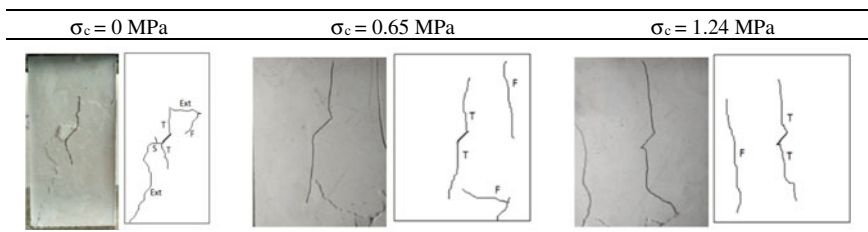
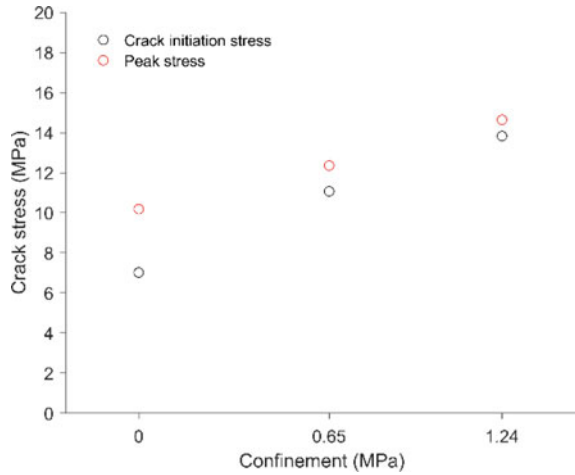


Fig. 4.5 The observed failure pattern for single flaw specimens subjected to a uniaxial compression (0 MPa) and biaxial compression, b 0.65 MPa, and c 1.24 MPa confinements

Fig. 4.6 Crack initiation and peak stress observed for different confinements on a single flaw specimen



reaching its material strength, whereas the initiated shear crack was observed to propagate toward horizontal boundary. Additional subsidiary crack (*F* and *Ext*) is observed from the developed crack after peak stress. The shear crack was found to extend (*Ext*) in the direction of loading and later toward the far-field cracks (*F*) from the boundary.

In case of biaxial compression, the tensile crack is first observed from the outer tip of the inclined flaw. The observed crack from outer tip of the inclined and horizontal flaws was found to be propagating toward the direction of major compressive loading direction for 0.65 MPa confinement. However, for 1.24 MPa confinement loading, the direction of the tensile crack from the horizontal flaw was found to deviate away from the major loading direction. The coalescence between the inclined flaw and horizontal flaw is generally formed by the propagation of the tensile crack from inner tip of the inclined flaw in both uniaxial and biaxial compression. In uniaxial compression, additional coalescence which may be shear nature is observed forming between the horizontal flaw at its right tip and the inclined flaw at its outer tip. For biaxial compression, coalescence is observed forming between the inner tip of

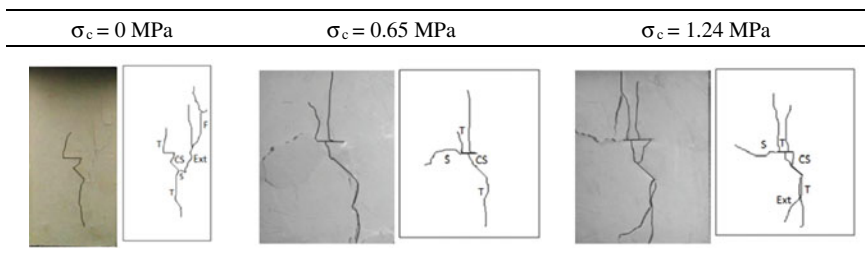
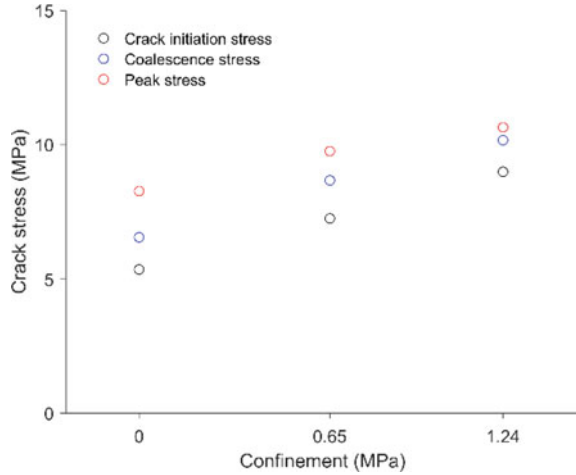


Fig. 4.7 The observed failure pattern for double flaw specimens subjected to a uniaxial compression (0 MPa) and biaxial compression, b 0.65 MPa, and c 1.24 MPa confinements

Fig. 4.8 Crack initiation and peak stress observed for different confinements on a non-parallel double flaw specimen under confinements 0, 0.65, and 1.24 MPa



the inclined flaw which later propagates and forms linkage with a horizontal flaw but toward the mid-section of the flaw surface. The shear cracks are observed from the horizontal flaw at left tip for biaxial condition due to higher compressive stress concentration. Due to this concentration, a spalling is observed at that region for 0.65 MPa confinement along with shear crack. For higher confinement 1.24 MPa, the shear cracks extend relatively more length compared to lower confinements. However, the crack growth dissipates before reaching the specimen boundary and the material failure does get influenced by propagated tensile cracks.

The behavior of crack stress at initiation (due to tensile crack), coalescence, and peak with respect to different confinements (0, 0.65, and 1.24 MPa) is shown in Fig. 4.8. The crack stresses were observed to initiate with an increase in lateral confinement. The coalescence stress is observed after tensile crack initiation stress, subsequently followed by peak stress. In case of higher confinement loading (1.24 MPa), the crack and coalescence stress becomes closer to the peak stress with an increase in flaw angle.

Numerical Study

For the present study, the numerical model is carried out as two-dimensional problems by considering plane stress state conditions. The type of the element used for this model is CPS4R, a 4-node bilinear plane stress quadrilateral, and is solved using reduced integration method. The analysis is carried out in dynamic implicit quasi-static procedure, and the corresponding mesh is shown in Fig. 4.9. The size of the element is chosen based on mesh optimization study. The dimension of the model for the single and non-parallel double flaw is kept analogous to the experimental study (see Fig. 4.9). The boundary conditions of the model are made in accordance with

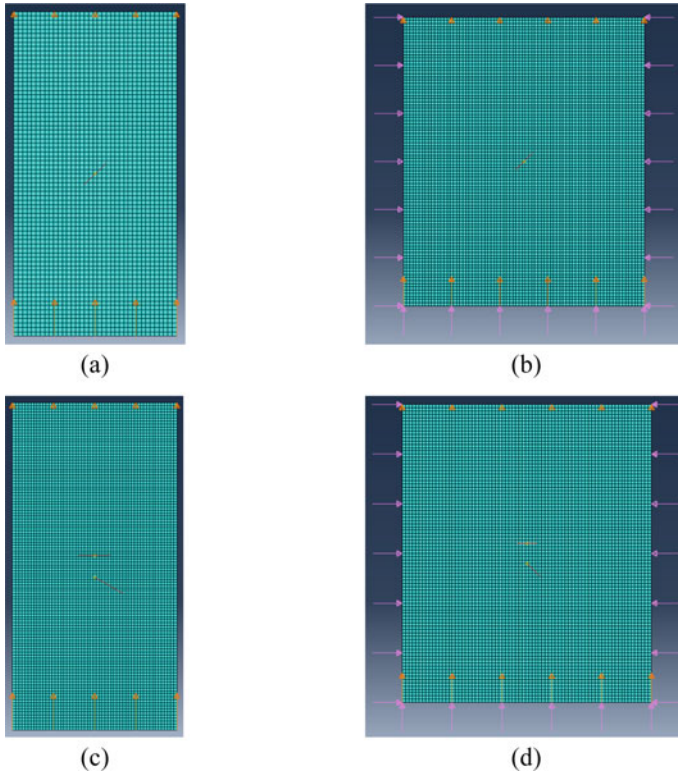


Fig. 4.9 Geometry of the specimen **a** SF45U, **b** SF45B, **c** NP45U, and **d** NP45B

the laboratory tests, where the loading is applied at the bottom end with a loading rate of 0.031 mm/min as applied during laboratory studies. The top end is restrained in the y direction and the movement in the x direction is not restricted so as to allow free crack propagation.

Material Model and Input Parameters

In the present study, the numerical analysis considers the discontinuity in a continuum medium where the rock is expected to behave in elasto-plastic manner. Cohesive Zone Model (CZM) is adopted to model the discontinuity which could be used in conjunction with elastic-plastic model. The model follows the concept of fracture mechanics, where damage evolution around discontinuity (pre-existing flaw) after crack initiation is studied [11, 12, 15, 16]. The adopted model is combined with XFEM approach using FE tool “ABAQUS”, where the mesh refinement around existing discontinuity can be avoided. Table 4.2 shows the list of material input

Table 4.2
Physio-mechanical properties
of gypsum [12]

Property	Value
Young's modulus, E (GPa)	1.037
Poisson's ratio, ν	0.39
Tensile strength, σ_t (MPa)	1.11
Tensile stress for mode I (MPa)	1.087
Shear stress for mode II (MPa)	1.56
Relative displacement under mixed mode (μm)	8
Kinetic friction coefficient	0.28
Penalty stiffness (GPa/m)	1.037×10^2

parameters used in the numerical model. The basic physio-mechanical properties are adopted from the experimental studies based on Table 4.1. The determination of CZM parameters for gypsum material is found from the fracture toughness test (see Table 4.2). The toughness test is carried out under two different modes (mode I and mode II), where the crack tip stresses and damage evolution after crack initiation are calculated [12]. CZM assumes the kinetic friction coefficient [11, 12] across the discontinuity that governs both tangential and normal behavior when it undergoes slipping after reaching its threshold limit. In addition, contact stiffness or penalty contact (K_p) is used to ensure there is no penetration between two elements at the flaw surface. As per Mahabadi et al. [19], the value of stiffness generally lies in the range from 1 to 1000 times of the Young's modulus (E), and for the present study, the value is taken as 100 times of Young's modulus (E) based on back analysis [12].

Numerical Results

Single flaw. The failure pattern observed in the numerical analyses on a single flaw under different confinements is shown in Fig. 4.10. From the numerical analysis, the growth of the tensile crack is clearly seen to propagate from the flaw tips to the material boundary. The specimens did not have significant subsidiary cracks in model, and the ultimate failure of the specimen is influenced by the fully developed tensile crack. The visibility of the shear crack is not observed in the numerical model. However, based on the maximum principal stress (S_{\max}) contour, the possible formation of shear crack can be seen in low strength material by very thin line band close to the flaw tip. According to the stress contour, these band in yellow where possible movement due to shearing can be expected. These shear bands were observed to appear along with the wing crack, and their growth subsides within the material boundary.

The initiated tensile crack under biaxial compression propagates toward the direction of major compressive loading direction under both confinements. However, there is a little deviation of the propagated path which slightly seems to orient away from

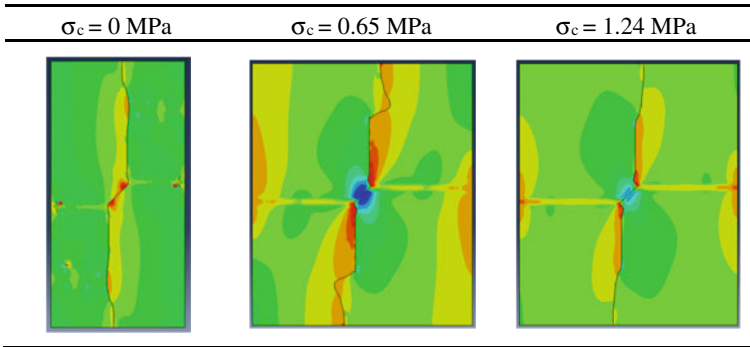
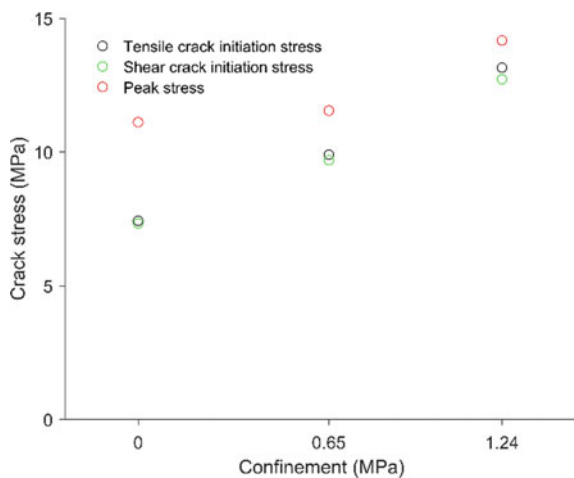


Fig. 4.10 Failure pattern observed from S_{max} stress contour in ABAQUS for gypsum under different confinements of single flaw angle specimen

that path with an increase in confinement. Based on S_{max} contour, compared to uniaxial compression, a much pronounced tensile nature band is observed in quasi-coplanar direction from the flaw surface. From experiment observation, the shear crack is developed and observed to be propagating due to the effect of confinement. Due to lateral confinement, the stress concentration on the flaw surface is higher compared to uniaxial condition. This causes a higher stress to initiate the sliding between the flaw surfaces. Thus, higher crack initiation stress is observed compared to uniaxial compression (Fig. 4.11). Formation of shear band is observed at the same stress level of tensile crack initiation according to S_{max} stress contour. However, under 1.24 MPa confinement, the shear stress is relatively observed prior to tensile crack when compared to other lower confinement. Similar to the experimental study, the difference between the peak stress and crack initiation stresses reduced with an increase in confinements.

Fig. 4.11 Crack initiation due to tensile and shear crack and peak stress observed for different confinements on a single flaw specimen



Double flaw. The failure pattern observed for non-parallel double flaws is represented in Fig. 4.12 for different confinements. The sequence of the formation of the tensile cracks was clearly identified in the numerical analysis. Under uniaxial compression, the initial formation of tensile cracks is observed from the inclined flaw at the both tips. Similar to the experiments, the initiated tensile crack from the inner tip of the inclined flaw propagates toward the horizontal flaw which leads to formation of tensile nature coalescence. A slight difference in position of coalescence with respect to the horizontal flaw is observed in the model. The position of coalescence is toward the midportion of the horizontal flaw where initiated wing crack from inner tip of inclined flaw less curvilinear compared to experiments. Based on S_{max} , the formation of thin red band is observed for NP45 model between the right tip of the horizontal and outer tip of the inclined flaw. According to the contour, the red color indicates material exceeding the tensile value and is analogous to experiments. This additional coalescence is observed to be in tensile nature. After coalescence, a new wing crack from horizontal flaw appears from either the left or right tip or mixed of both. The initiated wing crack along with outer tip of the horizontal flaw propagates toward the loading direction.

In case of biaxial compression, the tensile crack growth is limited within the material boundary and the length of propagated crack becomes smaller with the increase in confinement. Based on maximum principal stress contour, a heavy stress concentration of high compressibility is observed at horizontal flaw tips. Also, a thin band formation between inner tip of the inclined and the horizontal flaw which represents the possible formation of crack is observed from the experiment study. The tensile crack propagated from the horizontal flaw clearly shows the deviation of propagation path from major principal loading direction particularly in 1.24 confinement.

The crack initiation stress due to tensile and shear crack together with coalescence and peak stress is shown in Fig. 4.13. The numerical model could differentiate the coalescence stress corresponding to tensile crack and shear crack from S_{max} stress contour. Similar to the single flaw configuration, the shear crack is observed to initiate at the same stress level of tensile crack. However, when lateral confinement

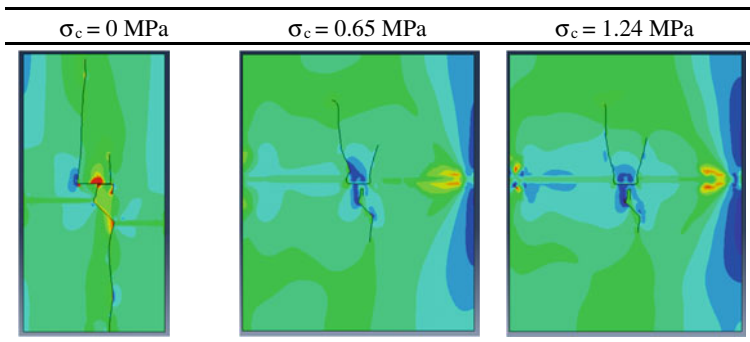


Fig. 4.12 Failure pattern observed from S_{max} stress contour in ABAQUS for gypsum under different confinements for non-parallel double flaw angle specimen

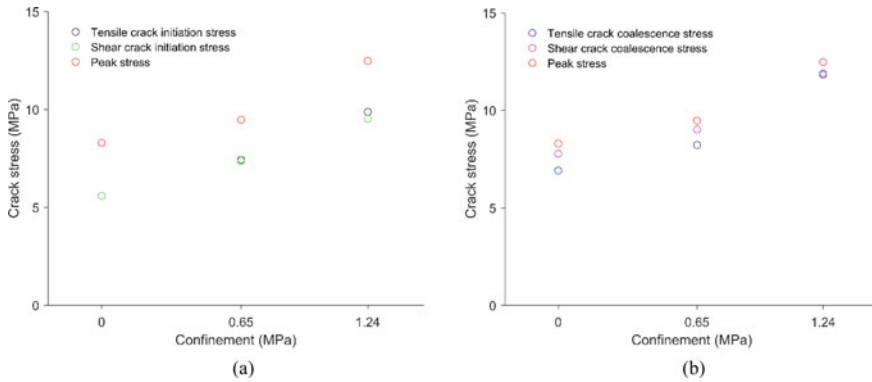


Fig. 4.13 **a** Crack initiation (tensile and shear) and **b** coalescence stresses (tensile and shear) compared with peak stress under different confinements for double flaw specimens

is applied, the shear crack appears prior to tensile crack. The coalescence stress due to tensile crack from the inner tip of the inclined flaw and horizontal flaw is prior to second coalescence. The secondary coalescence is observed between the right tip of horizontal flaw to the outer tip of the inclined flaw. However, for 1.24 MPa, the difference between these two coalescence stresses becomes narrow and appears closer to peak stress.

Summary and Conclusion

The crack growth behavior and its failure pattern are studied for a flaw having narrow flaw configuration on single and double flaw arrangements. The experimental study is conducted on both uniaxial and biaxial loading conditions at a flaw angle of 45° . Subsequently, numerical analysis is performed to predict the initiation and coalescence based on tensile and shear crack based on maximum principal stress contour. Based on observation for a single flaw specimen, the following conclusions are drawn:

- The tensile crack and shear crack are observed to initiate at the same level. However, with the increase in confinement, the shear crack is observed prior to tensile crack.
- The direction of tensile crack propagation path was found to be deviating away from major loading direction with an increase in lateral confinement. This phenomenon was clearly observed for the double flaw specimen on horizontal flaw.
- The length of tensile crack is limited within the material boundary for lateral confinement. Also, the coalescence due to tensile and shear crack was observed to initiate closer to the material peak with increase in confinement.

The present study is limited to the single flaw angle since the scope is to understand the crack growth under different uniaxial and biaxial loading configurations. The behavior of crack propagation and failure can be studied by extending for other flaw angles with further new geometrical arrangements. Thus, by understanding the crack growth and its stress behavior, one could successfully model the safe and economic design for rock mass having severe discontinuities.

References

1. An X, Ning Y, Ma G, He L (2014) Modeling progressive failures in rock slopes with non-persistent joints using the numerical manifold method. *Int J Numer Anal Meth Geomech* 38:679–701
2. Esterhuizen GS, Dolinar DR, Ellenberger JL (2011) Pillar strength in underground stone mines in the united states. *Int J Rock Mech Min Sci* 48(1):42–50
3. Lajtai EZ (1974) Brittle fracture in compression. *Int J Fract* 10(4):525–536
4. Ingraffea AR, Heuze FE (1980) Finite element models for rock fracture mechanics. *Int J Numer Anal Meth Geomech* 4:25–43
5. Huang J, Chen G, Zhao Y, Wang R (1990) An experimental study of the strain field development prior to failure of a marble plate under compression. *Tectonophysics* 175:269–284
6. Shen B, Stephansson O, Einstein HH, Ghahreman B (1995) Coalescence of fractures under shear stresses in experiments. *J Geophys Res* 100(B4):5975–5990
7. Wong RH, Chau KT (1998) Crack coalescence in a rock-like material containing two cracks. *Int J Rock Mech Min Sci* 35(2):147–164
8. Wong LNY, Einstein HH (2009) Systematic evaluation of cracking behavior in specimens containing single flaws under uniaxial compression. *Int J Rock Mech Min Sci* 46(2):239–249
9. Yang SQ, Jing HW (2011) Strength and crack coalescence behavior of brittle sandstone samples containing a single fissure under uniaxial compression. *Int J Fract* 168:227–250
10. Bobet A, Einstein HH (1998) Fracture coalescence in rock-type materials under uniaxial and biaxial compression. *Int J Rock Mech Min Sci* 35(7):863–888
11. Sivakumar G, Maji VB (2018) A study on crack initiation and propagation in rock with pre-existing flaw under uniaxial compression. *Indian Geotech J* 48(4):626–639
12. Sivakumar G, Maji VB (2021) Crack growth in rocks with pre-existing narrow flaws under uniaxial compression. *Int J Geomech* 21(4):04021032
13. Petit JP, Barquins M (1988) Can natural faults propagate under mode II conditions? *Tectonics* 7(6):1243–1256
14. Lee H, Jeon S (2011) An experimental and numerical study of fracture coalescence in pre-cracked specimens under uniaxial compression. *Int J Solids Struct* 48:979–999
15. Gonçlaves da Silva B, Einstein HH (2013) Modeling of crack initiation, propagation and coalescence in rocks. *Int J Fracture* 182:167–186
16. Xie Y, Cao P, Liu J, Dong L (2016) Influence of crack surface friction on crack initiation and propagation: a numerical investigation based on extended finite element method. *Comput Geotech* 74:1–14
17. Abdulla AA (1992) Testing and constitutive modeling of cemented soils. PhD Dissertation, University of Arizona
18. Sivakumar G (2019) Crack growth analysis in rock with pre-existing flaws. PhD Dissertation, Indian Institute of Technology Madras
19. Mahabadi OK, Lisjak A, Grasselli G, Munjiza A (2012) Y-Geo: a new combined finite-discrete element numerical code for geomechanical applications. *Int J Geomech* 12(6):676–688

Chapter 5

Parametric Study on the Performance of Temporary Secant Pile Wall



V. J. Gowthaman and C. Anburaj

Introduction

With the development of metropolis and rapid increase in urbanization in growing cities is witnessed however land constraints in the urbanized cities, the construction of infrastructure is challenge task. In these cases, underground stations and underground tunnels are appropriate method to establish the connectivity across the city. Temporary and permanent retaining systems are widely used for the construction of underground metro stations. Secant pile wall is the one of the deep excavation system used in all types of deep excavation work. Secant pile wall consists of primary and secondary pile interlocking each other at desired distance. The primary piles are unreinforced PCC concrete piles which are initially bored into the soil, typically 0.8–1.0 m in diameter with minimum strength of concrete. Secondary piles are reinforced concrete piles which are bored overlapping with primary piles in the design interlocking distance. Due to overlapping, secant piles can provide watertight retention system compared to other retaining system like contiguous pile, soldier pile, etc.

Secant piles can be broadly categorized into three categories [1] as Hard/Soft secant pile in which the primary piles are generally soft pile with cement or cement with bentonite content or sand with bentonite and secondary piles are reinforced concrete piles. Hard/Firm secant pile consists of primary piles of unreinforced concrete in which the secondary piles are installed with interlock. Hard/Hard secant piles are both the primary and secondary piles that are reinforced with full-strength concrete. The detailing of primary pile reinforcement should be planned properly and

V. J. Gowthaman (✉) · C. Anburaj
L&T Construction, HCI-IC, Chennai 600089, India
e-mail: vjgowthaman@Intecc.com

C. Anburaj
e-mail: anburajc@Intecc.com

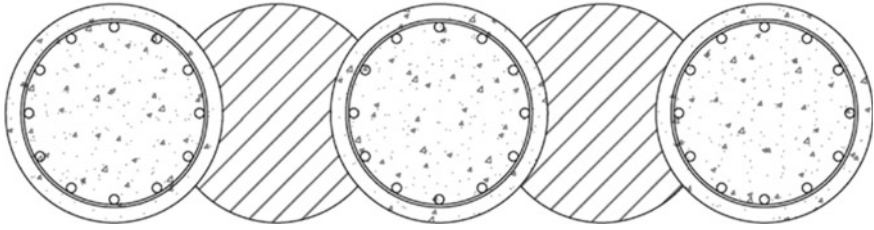


Fig. 5.1 Hard/Soft secant pile

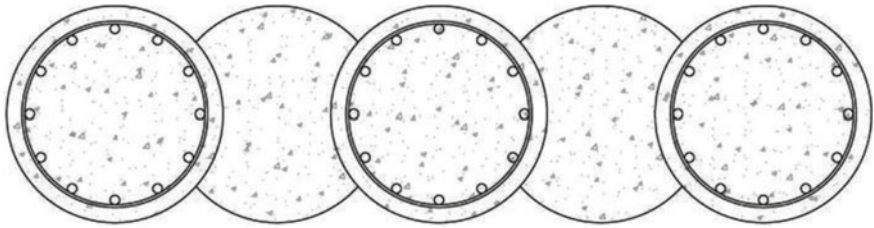


Fig. 5.2 Hard/Firm secant pile

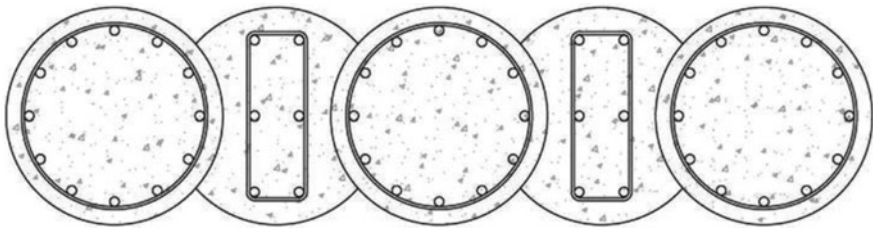


Fig. 5.3 Hard/Hard secant pile

to be placed into the ground to avoid cutting the reinforcement while execution of secondary pile (reinforced concrete pile). Figures 5.1, 5.2 and 5.3 show the different types of secant piles classified by CIRIA 760 guidelines.

Parameters Influencing the Secant Piles

The purpose of this study is to understand the behavior of secant pile by varying the parameters like diameter of piles, overlapping distance of primary and secondary pile, concrete compressive strength of piles, drained and undrained condition of soil, and support configurations. The analysis has been carried using WALLAP software, a 2-dimensional finite element model program, by changing the parameters.

Diameter of Pile

Diameter of primary and secondary piles is one of the influencing factors which changes the structural stiffness of the secant pile system. In this paper, the diameter of 800, 1000, and 1200 mm is considered for the analysis.

Overlapping Distance of Primary and Secondary Pile

The interlocking distance of primary and secondary secant piles is considered as per CIRIA. The guidelines for selection of minimum cut and spacing required for primary and secondary secant piles shall be obtained from Nomogram provided by CIRIA. Overlapping of 125, 200, and 300 mm is considered in this research study.

Material of Pile (Grade of Concrete)

Material of pile is also one of the affecting factors in terms of stability of secant pile wall. The grade of concrete mainly provides the stability to internal structural concrete. In the case of deep excavation, grade of concrete plays a vital role providing structural stiffness to the wall. Hence, grade of concrete M30, M40, and M50 is considered for the analysis.

Drained and Undrained Condition of Soil

Long-term and short-term parameters are considered for analysis which is a main factor that affects the stability of secant pile wall, two types of drainage conditions. For clay soils, long-term analysis has been done with effective stress parameters and short-term analysis with total stress parameters.

Support Configuration (Strut or Anchor)

Analysis has been done with two forms of support system—6 levels of struts (NPB Section) and 3 levels of struts with 3 levels of ground anchors (150 mm diameter). The support levels are considered at same levels; however, the construction stages are varied based on the type of supports. The typical WALLAP model with support system at final excavation stage considered in this research is shown in Fig. 5.4, and WALLAP model—finite element boundary conditions is presented in Fig. 5.5.

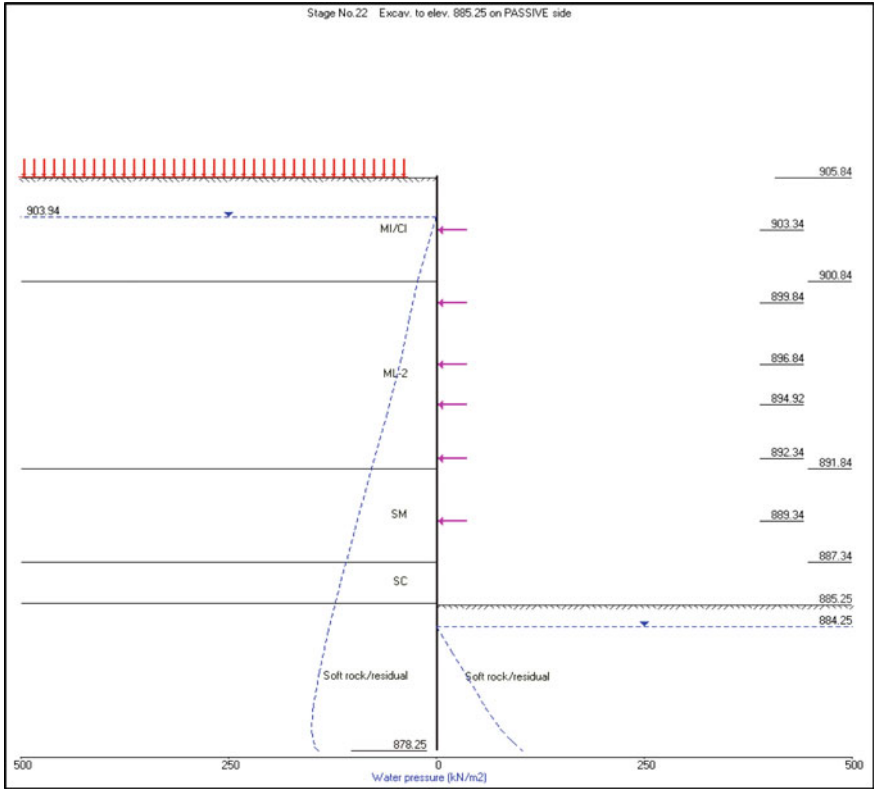


Fig. 5.4 WALLAP model at final excavation

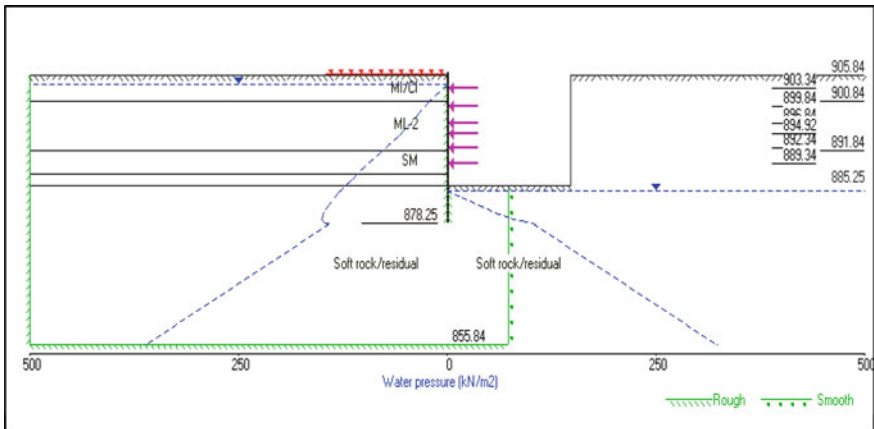


Fig. 5.5 WALLAP model—finite element boundary conditions

Soil and Wall Properties

The soil and wall properties considered for the analysis are mentioned in Tables 5.1 and 5.2.

Results and Discussion

This paper provides the analysis results of wall deflection of secant pile wall with pile length of 27.59 m with depth of excavation about 20.59 m from the ground level. The analysis has been done with variation of parameters, and the effect of temporary secant pile wall is studied.

Figure 5.6 shows wall deflection of secant pile wall with various pile diameters. The lateral displacement of the pile is higher at approximately 4–5 m above the finale excavation level. Lateral deflection of the wall decreases from 60 mm to by varying the secant pile diameter from 0.8 m to 1.2 m.

Figure 5.7 shows the comparison of results in terms of wall displacement with overlapping criteria of primary and secondary piles. As the interlocking distance increases, the stability of the secant pile also increases. However, the effect of varying the overlapping distance is not significant in the analysis, even though in terms of construction aspects, it prevents the water seepage and washing out of fines toward the excavation side.

Figures 5.8, 5.9, and 5.10 show the secant pile wall with drainage conditions as well as grade of concrete. Figure 5.10 shows the results of analysis done with different supporting systems. Support system 1 consists of 6 numbers of struts with approximately 4.5–5 m vertical spacing. Support system 2 which is a hybrid system comprises 3 struts with 3 anchors. The secant pile wall with strut support influences the maximum lateral displacement when compared with combined strut and anchor configuration since the strut support system erection and dismantling procedures are considered in the analysis. The removal stage of strut in both bottom-up and top-down construction shows the large variation in bending moment and lateral displacement. In the other side, placing the anchor in the last three rows provides the stability up to distressing of anchors even while constructing the permanent structures.

Summary

The summary of the parametric analysis on the secant pile wall using finite element analysis is mentioned below.

- (1) By increasing the diameter of secant pile from 0.8 to 1.0 m which provides the result with wall displacement is decreases by 25% decrease, and increase in the diameter from 0.8 to 1.2 m decreases the displacement by 36%. This

Table 5.1 Soil properties considered in the analysis

Depth (m)	Strata type	Density (kN/m ³)	Design/average SPT	E' (or) E_{rm} (MPa)	Type of material behavior	Cu (kPa)	Φ_u (°)	C' (kPa)	Φ' (°)
0-2.5	Fill	-	-	-	-	-	-	-	28
2.5-7.5	CL/MI/ML	18.5	6	11 + 3.8 MPa/m	Undrained	32	18	26*	24*
7.5-16.5	CL/MI/ML	18.5	19	30 + 3.8 MPa/m	Undrained	32	18	21*	25*
16.5-21	SM	18.5	43	64.2 + 3.8 MPa/m	Drained	-	-	-	38
21-26	SC	18.5	55	81.3 + 3.8 MPa/m	Drained	-	-	15	23
26-40	Soft rock	18.5	68	136 + 3.8 MPa/m	Drained	-	-	-	40

*Shear strength parameters are obtained from laboratory test results (triaxial test results—CU)

Table 5.2 Wall properties considered in the analysis

Type of structure	Pile diameter (m)	Pile length (m)	Young's modulus of wall (kN/m ²)	Moment of inertia per unit length of wall (m ⁴ /m run)	EI per unit length of wall (kN·m ² /m)
Fully embedded wall	0.8	27.59	2.7386×10^7	0.014893	407,871

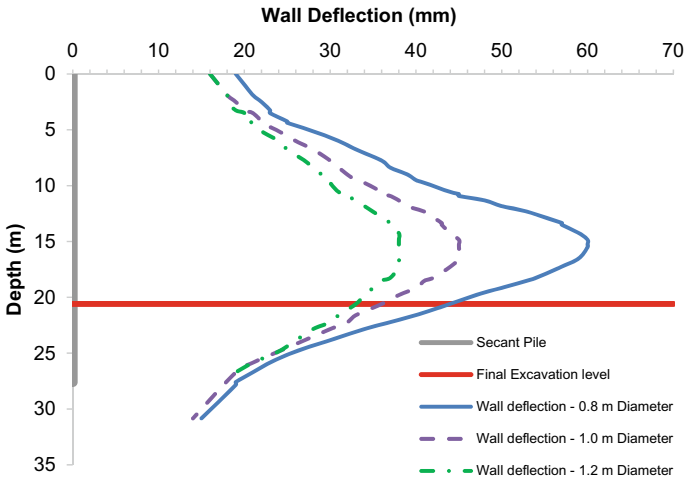


Fig. 5.6 Wall deflection with respect to variation in diameter

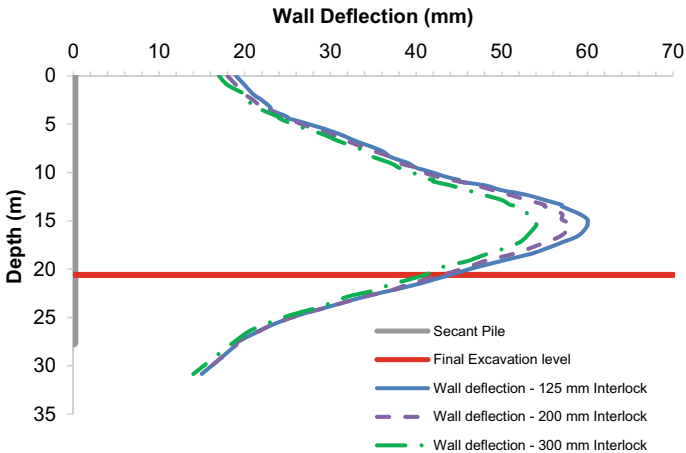


Fig. 5.7 Wall deflection with respect to variation in interlock

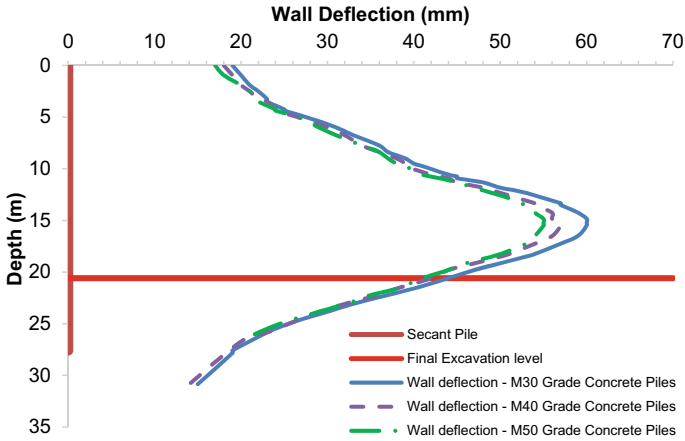


Fig. 5.8 Wall deflection with respect to variation in material of piles

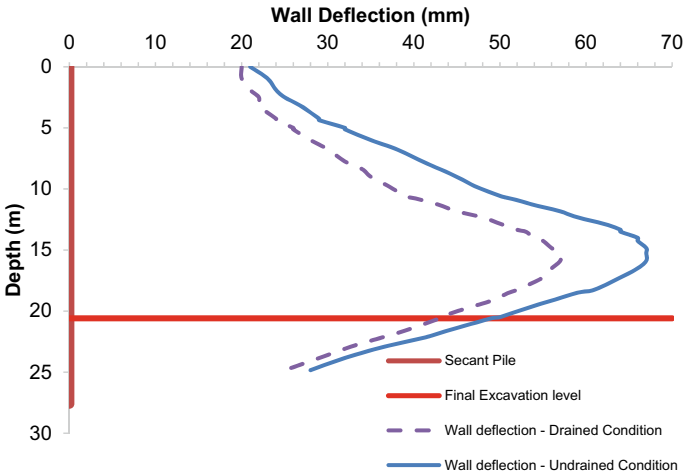


Fig. 5.9 Wall deflection with drained and undrained conditions

reduction in displacement was due to increase in the diameter which increases the stiffness modulus of the wall with larger area to act as rigid member.

- (2) Secant pile wall with composite/hybrid supporting systems, i.e., 3 levels of struts and 3 levels of anchor, is more effective than the supporting system with 6 levels of struts. Providing addition of anchors to the strut system eases the construction sequence to build the permanent structures and can afford strength to the secant pile wall up to the complete construction of permanent structure.

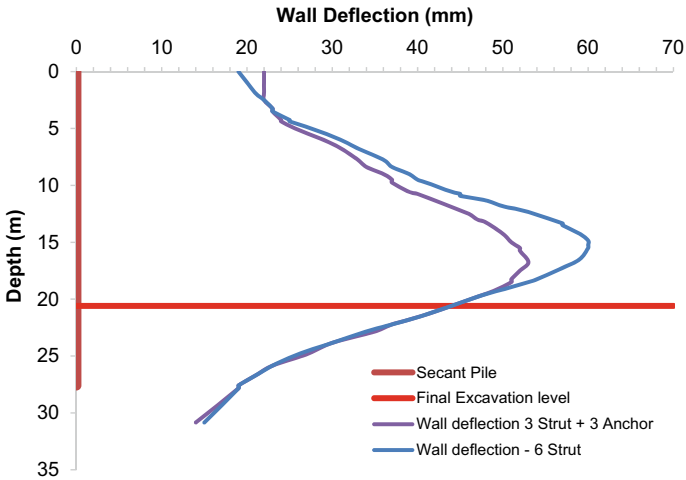


Fig. 5.10 Wall deflection with change in support configuration

- (3) Based on the analysis results, by increasing the interlock distance of primary and secondary piles, the wall deflection is decreased. However, the effect of overlapping distance is found that it is not significant in this analysis.
- (4) Casting the secant pile wall with higher grade of concrete provides more stiffness to the secant pile wall and ultimately increases internal structural stability.
- (5) The wall deflection is observed more on the undrained condition than the drained condition.

Conclusion

After doing the sensitivity analysis on the secant pile wall based on the numerical analysis with WALLAP results by changing the parameters like varying the pile diameter, interlocking distance, material of pile, subsoil condition and support system which affects the serviceability of the secant pile wall. Especially, soil drainage conditions played a vital role in restricting the wall deflections of secant pile wall. It was demonstrated that to adopt the economical retaining system for underground metro projects, a complete parametric analysis is required to limit the wall deflection.

References

1. Mahesh A, Sarath Chandra Kumar B (2019) Effect of diameter of secant pile wall in deep excavation analysis. *Int J Recent Technol Eng* 7(6C2). ISSN: 2277-3878, April 2019
2. Emuriat JE (2017) Parametric study on analysis and design of permanently anchored secant pile wall for Earthquake loading. *Int J Comput Eng Res (IJCER)* 7(5). ISSN (e): 2250-3005, May 2017
3. Brooks NJ, Spence J (1992) Design and recorded performance of a secant retaining wall in Croydon. In: *Proceedings of the conference retaining structures organized by the Institution of Civil Engineers and held at Robinson College, Cambridge on 20–23 July 1992*
4. CIRIA C760: guidance on embedded retaining wall design, London
5. CIRIA C580 (2003) *Embedded retaining walls—guidance for economic design*, London
6. CIRIA C517 (1999) *Temporary propping of deep excavations—guidance on design*, London
7. BS 8081-2015: code of practice for grouted anchors
8. WALLAP version 6—retaining wall analysis program, “WALLAP manual” GEOSOLVE, London, United Kingdom, 1985

Chapter 6

Numerical Analysis of Ground Settlement Induced by Shallow Tunnels



R. Rajaraman and Gundeti Sumanth Kumar

Introduction

Metro projects play a significant role in the present phase urbanization and increasing demand of traffic free transportation. Metro projects are normally shallow tunnel which in turn is a challenging task. Due to poor geological conditions and constrained conditions of urban environment, it is challenging to limit the settlement to ensure safety during construction activity. Settlement of ground is an important design aspect to be considered in shallow tunneling. Settlement is a form of surface disturbance caused by tunnel construction. In greenfield conditions, estimation of settlement is of least significance since there would not be any significant structures present. In urban tunneling, accurate estimation and prediction are of utmost priority to ensure safety of structures on the ground surface.

Characteristics of Ground Settlement

Settlement Causes

The main causes of ground settlement are elaborated in the present section.

R. Rajaraman (✉) · G. S. Kumar
L&T Construction, Chennai, India
e-mail: r-ramanathan@Intecc.com

G. S. Kumar
e-mail: sumanth-gundeti@Intecc.com

Groundwater Lowering

During tunnel construction, water table may get lowered. Sometimes, during construction, tunnel itself may act as a drain. This causes effective stress to be increased within ground. Ground settlement estimation needs application of theories of soil mechanics. Settlement is treated generally as an elastic phenomenon in granular soil. For fine grained soils, settlement is analyzed by the conventional consolidation theories.

Ground Losses

Ground loss is defined as additional loss of ground than the total volume of tunnel. The magnitude of ground loss depends upon the adopted methodology followed for construction.

There are 3 types of ground losses, i.e., face loss, shield loss, and tail loss. Mechanical excavation causes face losses to occur during movement of the ground toward the shield. The culmination of this happens in the form of running, flowing, caving, squeezing, etc. Shield losses are defined as losses between cutter edge of shields and tail. Similarly, the loss resulted from the space created by the tail. Tail losses are similar to shield losses, in which the losses are caused by the tail itself and the space between the tail and the support system.

Parameters or Factors Affecting Settlement Calculation

Settlement calculation in soft ground tunneling is just an estimate. The uncertainties in geotechnical conditions make settlement calculation very complicated. Ground loss of 0.5–1.0% would be achieved by an experienced contractor and a novice contractor would attain 1.0–2.0% loss. General correlation between volume loss and nature of ground is given in Table 6.1.

Table 6.1 Volume loss values for various cases of tunneling [1]

Nature of ground	V_L (%)
In firm ground, proper control of face pressure in slowly raveling or squeezing ground	0.5
Slowly raveling/squeezing ground	1.0
Raveling ground	2.0
Poor ground	3.0
Running ground	> 4.0

Analysis

Empirical Analysis

During tunneling, relationship between the volume of ground loss and predicted settlement at the ground surface is available in Peck [2]. In soft ground conditions, surface settlement volume is typically assumed equal to the volume of lost ground. Settlement trough at the ground surface is formed due to ground loss. This can potentially impact any overlying structures or buried utilities parallel to the alignment of the tunnel excavation. The shape of settlement trough is similar to shape of an inverse Gaussian curve (Fig. 6.1).

Surface settlement trough above an advancing urban tunnel is indicatively presented in Fig. 6.2.

Excavation method, depth of tunnel, diameter of tunnel, and geotechnical conditions determine shape and magnitude of the settlement trough. Ground settlement due to tunneling is generally estimated by an analytical method proposed by Attewell et al. [4] and Rankin [3]. This method is similar to the method proposed by O'Reilly and New [5]. The settlement profile at the ground surface in transverse direction well before the tunnel face is shown in Fig. 6.3.

Settlement of a point which is at a distance of 'y' is expressed as

$$S_v = S_{max} \exp\left(\frac{-y^2}{2i^2}\right)$$

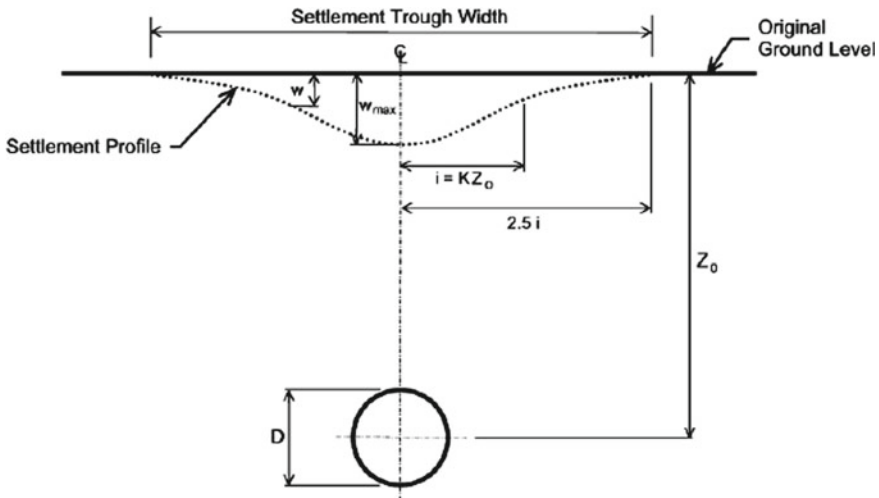


Fig. 6.1 Settlement profile due to tunneling in soft ground [3]

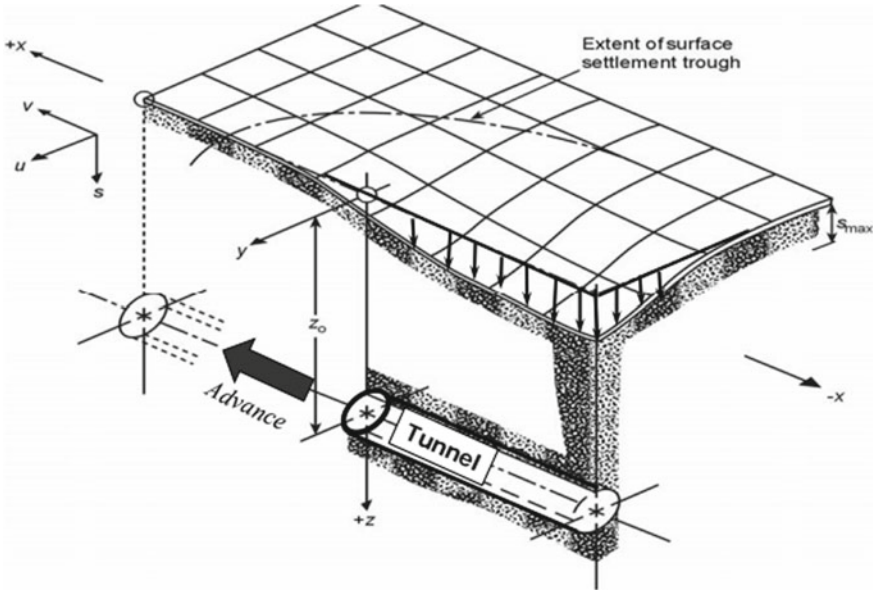


Fig. 6.2 Schematic illustration of surface settlement above an advancing urban tunnel [3]

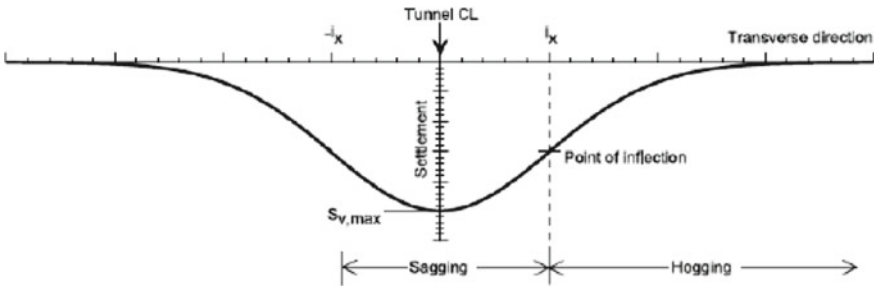


Fig. 6.3 Transverse settlement trough [2]

$$\begin{aligned}
 &= \frac{V_s}{\sqrt{2\pi} \cdot i} \exp\left(\frac{-y^2}{2i^2}\right) \\
 &= \frac{V_L \cdot A}{\sqrt{2\pi} \cdot i} \exp\left(\frac{-y^2}{2i^2}\right)
 \end{aligned}$$

where

- S_{max} is maximum settlement
- V_s —settlement trough volume/m of tunnel advance (% of theoretical volume V_L)
- i is the parameter for trough width ($i = k \cdot z_0$, 'k' a dimensionless constant)
- z_0 —depth of tunnel axis below the ground surface.

k value depends upon soil type and has been considered as 0.3–0.5 in the present analysis.

Numerical Analysis

Numerical analysis has been carried out by RS²—a finite element analysis to determine ground settlement. A plane strain analysis has been carried out by using RS² model. Infinite length has been assumed in the out-of-plane direction. This implies zero strain in the out-of-plane direction. Gaussian elimination method is used to solve the system of equations in the model.

The depth of ground cover considered in design is actual depth from the ground surface. At a depth z below the surface, ratio of average horizontal stress to vertical stress (K) is defined by the following equation.

$$\sigma_h = K\sigma_v = K\gamma z$$

where

σ_h = Horizontal stress

K = in-situ stress ratio.

In-situ stress ratio of 0.5 is considered for this analysis. Analysis has been performed corresponding to various cases of overburden height and size of tunnel. The values of settlement of ground corresponding to 0.5% volume loss have been compared with those settlements estimated by empirical methods.

This has been achieved by gradually reducing the magnitude of the internal pressure inside the tunnel. The final internal pressure corresponding to 0.5% volume loss has been used for comparative analysis. Settlement troughs for various cases have also been observed.

Typical model considered for analysis is given in Fig. 6.4.

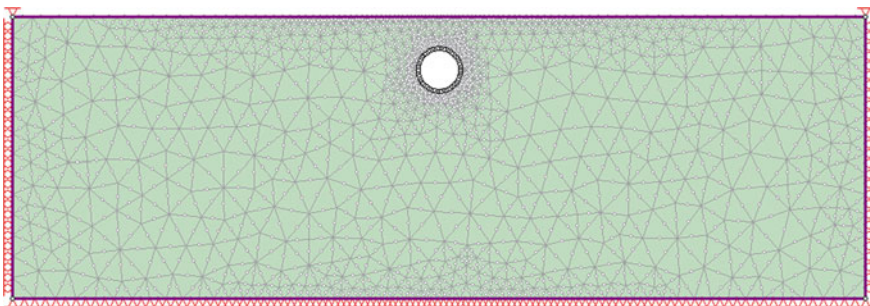


Fig. 6.4 Numerical model used for analysis

Results and Discussion

Comparative results between empirical analysis and numerical analysis are presented in Tables 6.2 and 6.3.

Maximum values for ground settlement have been obtained for k value of 0.3 (Figs. 6.5, 6.6, 6.7, 6.8, 6.9 and 6.10).

Results of numerical analysis are presented in Table 6.4.

Table 6.2 Ground settlement results using empirical analysis with $k = 0.3$

Sl. No.	Depth of cover (m)	Diameter of tunnel (m)/settlement (mm)			
		4	6	8	10
1	5	12.5	28.17	50.08	–
2	10	6.2	14.09	25.04	39.13
3	15	4	9.4	16.69	26.08

Table 6.3 Ground settlement results using empirical analysis with $k = 0.5$

S. No.	Depth of cover (m)	Diameter of tunnel (m)/settlement (mm)			
		4	6	8	10
1	5	10	22.5	40.06	–
2	10	5	11.2	20.03	31.3
3	15	3.34	7.5	13.35	20.87

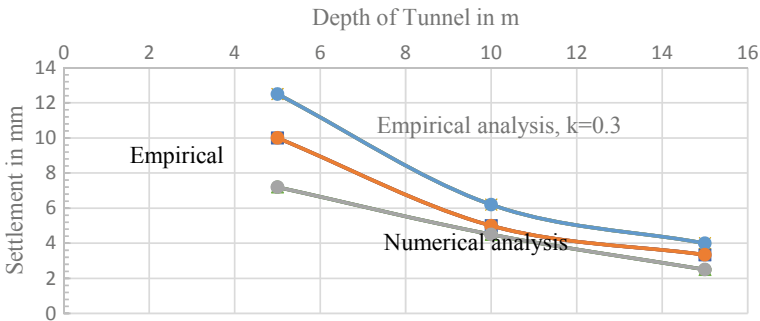


Fig. 6.5 Settlement analysis for tunnel dia = 4 m

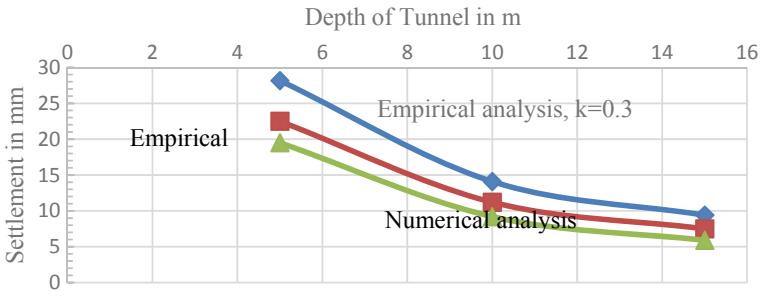


Fig. 6.6 Settlement analysis for tunnel dia = 6 m

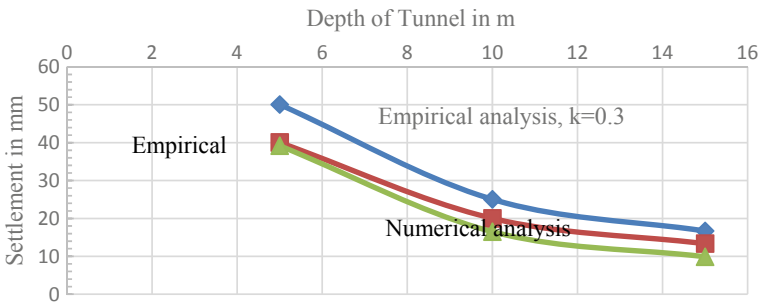


Fig. 6.7 Settlement analysis for tunnel dia = 8 m

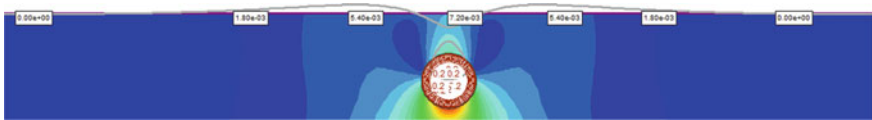


Fig. 6.8 Typical settlement trough from numerical analysis at tunnel depth = 5 m

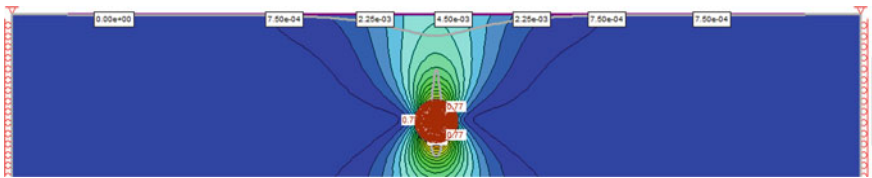


Fig. 6.9 Typical settlement trough from numerical analysis at tunnel depth = 10 m



Fig. 6.10 Typical settlement trough from numerical analysis at tunnel depth = 15 m

Table 6.4 Ground settlement results using numerical analysis

Sl. No.	Depth of cover (m)	Diameter of tunnel (m)/settlement (mm)			
		4	6	8	10
1	5	7.2	19.5	39.2	–
2	10	4.5	9.2	16.5	26.3
3	15	2.5	5.9	9.9	16.9

Table 6.5 Results of settlement analysis for a metro station

S. No.	Description	Parameter
1	Tunnel diameter	6.72 m
2	Shallowest overburden	3.36 m
3	Volume loss	1%
4	Ground settlement by empirical method	30 mm
5	Ground settlement by numerical method	26 mm

Settlement Analysis for a Metro Project

Ground settlement due to tunneling has been estimated for a metro project in south India using both empirical and numerical methods. Input parameters used for the analysis are presented in Table 6.5.

Ground settlement as determined from empirical method matches with estimated value from numerical modeling.

Conclusion

Ground settlement induced by machine tunneling for various tunnel diameters and tunnel depth below ground level has been examined. In all the cases, results obtained from numerical analysis are more or less matching with results obtained from empirical analysis. Numerical analysis predicts settlement always on the lower side compared with results from empirical analysis.

This paper only deals with tunneling through soil stratum. Trough width parameter used in empirical method (k) plays a crucial role in the determination of settlement. The values of settlement are in close conformance with derived values using numerical analysis when trough width parameter is 0.5.

Estimation of settlement trough has been estimated for various cases of tunnel diameters and tunnel depth below ground level. Shape of settlement trough obtained from numerical analysis matches with that obtained from empirical method except for the shallowest case of tunneling (depth of tunnel is 5 m below ground level). When tunnel is at 5 m below ground level, it has been found that settlement trough is also characterized by a heaving part on both sides.

References

1. Technical manual for design and construction of road tunnels—civil elements. U.S. Department of Transportation Federal Highway Administration Publication No. FHWA-NHI-10-034, 2009
2. Peck RB (1969) Deep excavation and tunneling in soft ground. In: Proceedings of the 7th international conference of soil mechanics, Mexico, State-of-art Volume, pp 225–290
3. Rankin W (1988) Ground movements resulting from urban tunneling: predictions and effects. In: Engineering geology of underground movements
4. Attewell PB, Yeates J, Selby AR (1986) Soil movements induced by tunneling and their effects on pipelines and structures
5. O'Reilly P, New M (1982) Settlement above tunnels in the United Kingdom-their magnitude and prediction. In: Proceedings of tunneling symposium, pp 173–181

Chapter 7

Seismic Assessment of Horseshoe-Shaped Tunnel Using a Pseudo-Static Approach



Ambika Srivastav and Neelima Satyam

Introduction

India is endowed with an enormous amount of hydroelectric resources and places fifth in terms of its accessible hydropotential in the world. Tunnels are the essential component of any hydropower project. Tunnels provide a way of supplying services for heavily urban areas, rail networks, and underground hydropower projects. Tunnels are perceived to perform significantly better than surface structures during earthquakes, and their seismic ability increases with an increase in depth [1, 2]. Various studies of earthquakes with an intensity greater than 0.2 g showed that significant damage has occurred in tunnels owing to devastating earthquakes [3, 4]. Underground structures in the earthquake-prone region have sustained impacts varying from mild cracking to severe collapse. Recent events (Sikkim Earthquake, 2011) challenged our understanding of the seismic design of underground structures in seismically active regions. The majority of tunnels around the world have a concrete liner. Earthquake causes the lining to collapse which can lead to subsequent disasters with major implications. Hence, it is important to understand the seismic behavior of the tunnels for the safe and reliable construction of any hydropower plant. Numerous researchers have made a significant effort to understand the internal forces of tunnel lining systems [5–7]. The literature review shows that the various studies mainly focus on the static response of tunnel lining structures but the study of the dynamic behavior is still a novel field for researchers. Zhao et al. studied the analytical bedding

A. Srivastav (✉)

Geotechnical Engineering Laboratory, Earthquake Engineering Research Centre, International Institute of Information Technology Hyderabad, Hyderabad, India
e-mail: ambika.srivastav@gmail.com

N. Satyam (✉)

Discipline of Civil Engineering, Indian Institute of Technology Indore, Simrol, Indore, India
e-mail: neelima.satyam@gmail.com

model that can predict the lining behavior of both shallow and deep tunnels reasonably. According to a study carried out by researcher [8], the percentage increases in seismic axial force developed in the liner for a different quality of rock mass. The seismic response of tunnel lining in expansive soil stratum is studied [9]. The main concern during the tunnel design is the complex and weak geological sections. Although these sections are just a few percent of the total length of the tunnel, these few percent will greatly increase the construction time. Hence, to sustain the demand for economical and sustainable underground hydropower projects, there is a critical need for seismic design and analysis for such a section of the tunnel.

The goal of this research is to use a numerical technique to examine the influence of earthquake loading on the tunnel lining during a seismic event for a hydropower tunnel in India. A standard section of a low cover (70 m) rock tunnel situated in a weak rock mass with design parameters (8.8 m diameter, horseshoe shape) was considered for evaluation. The site is located in seismic zone V, which is a highly seismic zone, according to India's seismic zoning map (IS: 1893); hence, assessment of tunnel stability under seismic conditions is essential. The rock mass within the tunnel may be described using two different methodologies for this analysis, namely the continuum and the interface continuum [10, 11]. For the static and seismic scenarios, the results derived with each of these methodologies are analyzed and compared. The pseudo-static technique is used for the analysis as it is based on empirical approaches and has been commonly used for tunnel deformation analysis [12–15]. The sum of a fixed body force that depicts earthquake movement using a static finite element analysis is known as a pseudo-static analysis. The seismic reaction of tunnel lining was inferred using a pseudo-static analytical technique owing to the difficulty of replicating seismic activity in the laboratory. This research will provide some useful references for hydropower tunnel seismic design.

Geological Details of Study Area

The Vishnugad Pipalkoti Hydroelectric Project is a river valley development initiative in Uttarakhand's Alaknanda Basin. This project would build a 65-m high diversion dam near the village of Helong ($79^{\circ} 29' 30''$ E and $30^{\circ} 30' 50''$ N), with a 2.5-km long reservoir behind it. To generate 444 MW of energy, this water will be carried over by 13.4 km tunnel.

Geological formations along the project formations comprise the formation of Helong, the formation of Gulabkoti, and the formation of Pipalkoti [16]. The Helong formation comprises low-grade metamorphic rocks like quartzite, quartz mica schist, amphibolites, etc. The Pipalkoti sequence comprises an alternating sequence of slates and dolomite limestone. The Gulabkoti formations are composed of rocks like quartzites, dolomitic limestone, mylonite, and magnesites. The rock present at the site is quartzite, dolomitic limestones, and slates.

Table 7.1 Geotechnical parameters of rock mass considered

Rock type	E_i (GPa) Intact rock modulus	GSI	m_i	σ_i (MPa)	Cohesion (MPa)	Friction
Slate	11	20	10	101.5	0.314	45.82°

Table 7.2 Geotechnical parameters of discontinuities considered

Joint details	Dip	Dip direction	Spacing
FJ	30°	N025°	30
J1	50°	N190°	20
J2	75°	N265°	80

Geotechnical Details

Geotechnical investigations have been carried out to improve the rock mass classification and facilitate the design of the support system for tunnels. The main objectives of the geotechnical investigation are to classify different rocks and discontinuity and to determine engineering properties through laboratory testing after that suitable support system can be designed for tunnels. Due to complicated Himalayan structures, the rock mass rating was modified in the study area. Intact rock properties were obtained through laboratory tests in compliance with International Society for Rock Mechanics and Rock Engineering (ISRM) requirements. Rock samples collected from the dam site and powerhouse area. Quartzite, dolomitic limestones, and slates are predominant rock types found in the region. Since tunnels constructed in poor rock mass are vulnerable to earthquakes, so numerical modeling has been considered for the properties of Slates. The Q values for the rock mass near the power tunnel location ranges from 3.44 to 6 which signifies the “poor” to “fair” quality of rock mass.

The rock mass properties used for the analysis are presented in Table 7.1. Mohr–Coulomb failure criterion was used to describe the behavior of the rock mass.

Rockmass comprises a continuous media of rock and discontinuities such as joints, faults, and bedding planes. Table 7.2 outlines the structural details observed in slates. Joint stiffness values were determined based on the analysis by Bandis et al. [17]. Representative stiffness values for three joint types are given in Table 7.3.

Methodology

The RS² was used to examine the effects of seismic stress on tunnel deformation. Phase 2 is a 2D finite element stress analysis application that may be used to analyze deep and shallow rock or soil excavations. A wide range of applications [18] include rock support design, slope stability research of finite components, and ground water seepage. In this work, the influence of seismic loading on the force created in the

Table 7.3 Representative stiffness values for three joint types

Rock type	Normal stiffness k_n (GPa/m)	Shear stiffness k_s (GPa/m)	Cohesion	Friction
Fresh to slightly weathered	3.6–22.7	0.25–2.36	0	40°
Moderately weathered	4.3–22.5	0.25–2.36	0	40°
Weathered	2.3–4.7	0.56–1.35	0	40°

liner is assessed for both static and seismic situations. The seismic axial force is the difference between the axial force during seismic loading and the axial force at the same location under static loading. The impact of earthquakes on the tunnel lining is described by this parameter.

The model's dimension should be specified so that the external boundary restrictions do not impact the area surrounding the tunnel's periphery. To reduce boundary impacts, the model's total dimension is kept 150×150 m. The grid consisted of three-noded triangles with a graded mesh. The study was performed assuming that the in situ stress was lithostatic and hydrostatic. Hydrostatic pressure is a stress condition that is characterized by the same principal stress. The depth of overburden was considered at 70 m. The peak horizontal acceleration (PHA) value of 0.36 g and the peak vertical acceleration (PVA) value of 0.24 g are the maximum credible earthquake (MCE) reported in the Site-Specific Study Report (IIT Roorkee).

The preliminary rock support analysis is carried out using a Q system support chart. The excavation support ratio (ESR) as given in the updated NMT Q system classification is considered to 1.0 [19]. The length of the bolt has been calculated using the equation suggested by Barton et al. [20].

$$L(\text{Length of the bolt}) = \frac{2 + 0.15B}{\text{ESR}}$$

where

B = span of the tunnel

ESR = excavation support ratio.

As determined from the above-mentioned equation, 4 m long rock bolts with a spacing of 2.0×2.0 m were installed for support of the excavated tunnel. M30 grade wire mesh shotcrete was used as the final tunnel support. The 150 mm thick liner was used as a final reinforcement after it had been tested for cracking and serviceability [21]. The shotcrete properties used in the study are given in Table 7.4.

Table 7.4 Shotcrete properties used in analysis

Parameters	Value
<i>E</i> modulus	30.000 MPa
Poisson’s ratio	0.2
Thickness	100 mm

Design Approaches

Approach 1: Equivalent Continuum Approach

In recent years, a numerical method has been proposed for the evaluation of rock mass with equivalent material properties to obtain the overall response. Various researchers have developed many computational methods for modeling joints in rock masses using different methodologies [5, 22]. A rock mass with no joints is known as a continuum rock mass. The rock mass is treated as a continuous series of joints in this technique, and the effect of joints is taken into account by decreasing the strength of intact rock [23]. The discontinuous rock mass is modeled using three-noded triangular elements in the equivalent continuum method. The characteristics of each element are defined in terms of certain variations of intact rock properties as well as of joints. Figure 7.1 displays the numerical model used in this analysis. The numerical model’s efficacy in calculating the displacements and forces generated in the tunnel lining for the static and seismic conditions is assessed.

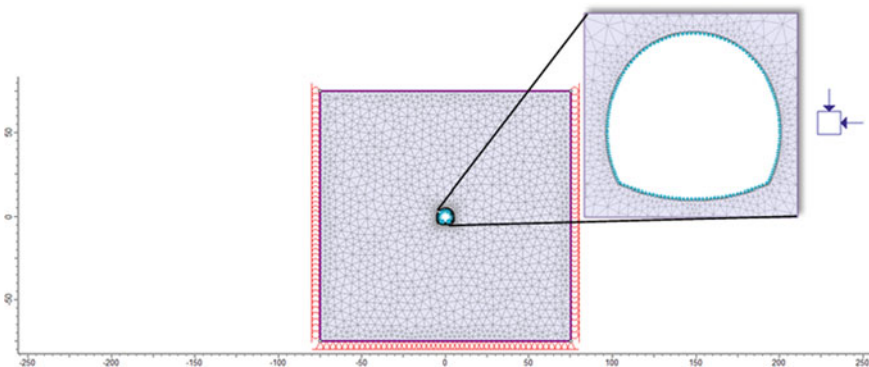


Fig. 7.1 Numerical model 8.8 m horseshoe shape tunnel for equivalent continuum approach

Approach 2: Continuum with the Interface

Seismic events greatly affect the tunnels in discontinuous jointed rock mass; hence, the interaction of seismic loads with discontinuities should be assessed. Since most of the tunnel damage recorded in the literature [5, 24] was associated with jointed rock mass, it is essential to study joint implication by proper modeling of joints in rocks. Various researchers have performed some noteworthy studies and outcomes reported in the literature dealing with the seismic response of tunnels across joints [25–27]. The tunnel is represented as an equivalent continuum with the inclusion of critical joints in the rock mass in the continuum with interface methodology. When compared to continuous methods, it is able to specify interfaces inside the rock mass as well as represent changes in anisotropy. The numerical model used for the analysis is presented in Fig. 7.2.

Results and Discussion

The goal of this work is to use a pseudo-static technique to understand the seismic response of a hydropower tunnel by modeling the rock mass using two alternative approaches: continuum rock mass and continuum with the interface. By evaluating various methodologies, the study enables us in understanding how the forces created in the liner vary. After applying a seismic load, the outcomes are examined and interpreted as major and minor primary stresses (1 and 3) and a rise in axial force in the lining. When compared to continuous approaches, it is able to specify incorporate interfaces inside the rock mass as well as represents changes in anisotropy.

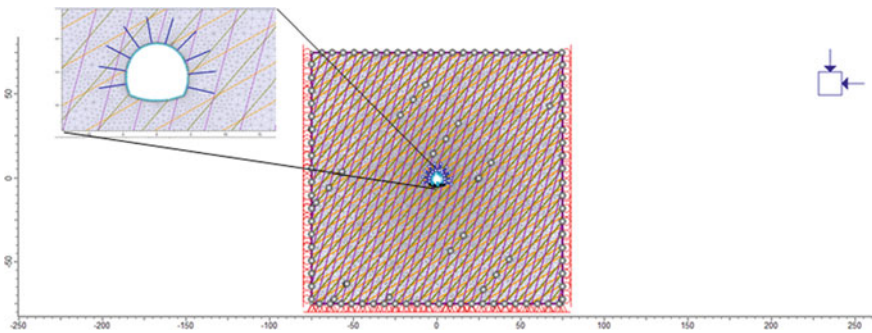


Fig. 7.2 Numerical model 8.8 m horseshoe shape tunnel for equivalent continuum with interface approach

Approach 1: Continuum Rock Mass

For the static condition, the increase in the principal stresses around the invert of the tunnel is much higher compared to other zones. With two troughs and two peaks, the axial force generated in the liner is periodic. There is an increase of 50% in the amount of seismic axial force generated in the tunnel lining for a seismic scenario when compared to a static case. Crown of the tunnel and invert shows high displacement, while points on the sidewalls of the tunnel undergo minimal displacement. Figure 7.3 demonstrates the displacement caused by the excavation boundaries for static and seismic situations. The average displacement for the static state of the tunnel is estimated to be 13 cm which increases to 22 cm after the application of seismic forces. The seismic axial forces generated in the liner are presented in Fig. 7.4.

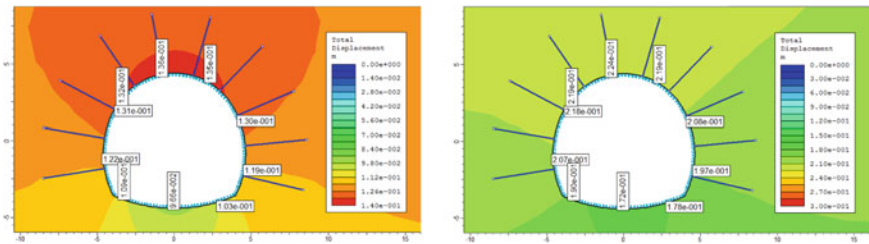


Fig. 7.3 Displacement contours around the tunnel for the first approach

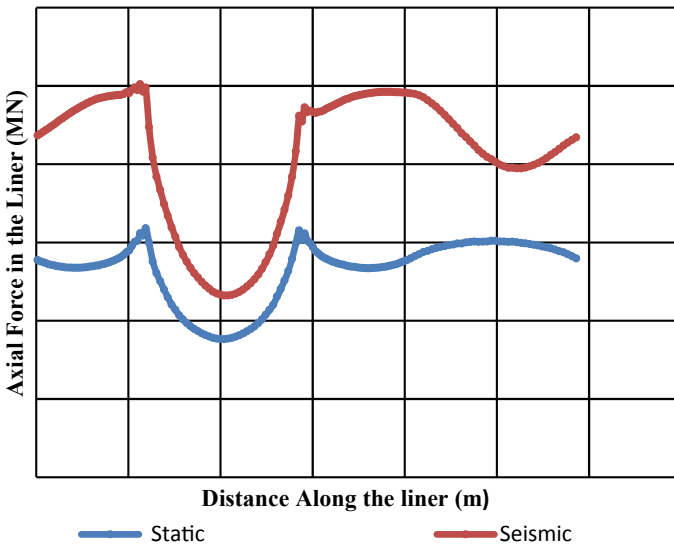


Fig. 7.4 Axial force variation in the tunnel liner for continuum approach

Approach 2: Continuum with the Interface

The rock mass is treated as an equivalent continuum with joint sets in this technique. When the rock mass around the tunnel is weakened by the joint crossing, a maximum axial force is expected to accelerate. Instead of the point of contact between the horizontal joint and the tunnel liner, the highest axial force was detected in the position of the knee and shoulder.

Figure 7.5 indicates no peaks as seen in the case of the continuum rock mass.

There is only a 20% increase in the liner forces for seismic cases when compared with the continuum approach. As it can be observed from the results that the position and magnitude of maximum axial force developed in the liner decrease because of the low strength properties of rock mass. In weak rock mass, deformation is independent of the joint intersection of the tunnel liner. There is a slight increase in the total displacement of the tunnel compared to the continuum approach as shown in Fig. 7.6.

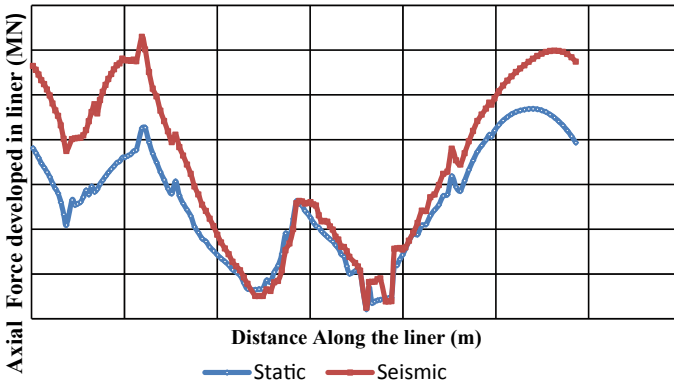


Fig. 7.5 Axial force variation in the tunnel liner for continuum-interface approach

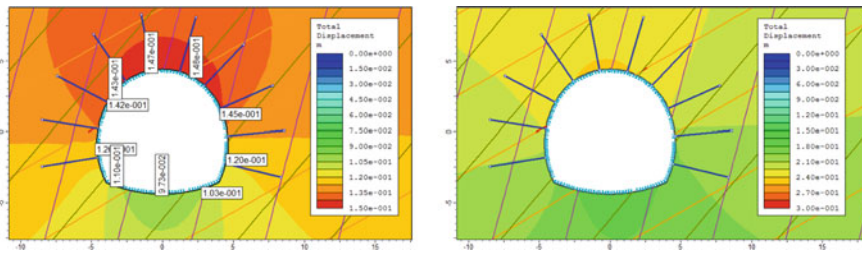


Fig. 7.6 Displacement around the tunnel for the second approach

Conclusion

The hydropower capacity of the Indian Himalayan region is still needed to be explored. Because tunnels are the main component of any power project, more tunnel construction is needed to increase the hydropower capacity. The seismic assessment of tunnels is even more significant since mountain tunnels are particularly prone to seismic activity. To evaluate the seismic performance and responses of the tunnels subjected to the earthquake, pseudo-static analysis for an 8.8 m diameter horseshoe-shaped tunnel is performed using two different modeling approaches. The observations for the axial force pattern reveal periodicity for the first approach, but no consistent pattern is seen for the second. The axial force difference on the lining for the continuum with the interface approach ranges from 15 to 20% between static and dynamic loads, whereas the increase for the continuum approach is up to 50%, indicating that the first approach overestimates the forces developed in the liner for a seismic event. The total displacement observed is almost similar for both the approaches for static (13 cm) and seismic case (22 cm). Since rock mass cannot behave as a continuum in the field; hence, it is more advantageous to use an equivalent continuum-interface method instead of an equivalent continuum method to obtain outcomes of much greater precision.

References

1. Tsinidis G et al (2016) Seismic response of box-type tunnels in soft soil: experimental and numerical investigation. *Tunnell Undergr Space Technol* 59(2016):199–214
2. Yan L et al (2020) A numerical study on the transverse seismic response of lined circular tunnels under obliquely incident asynchronous P and SV waves. *Tunnell Undergr Space Technol* 97(2020):103235
3. Wang JN, Munfakh GA (2001) *Seismic design of tunnels*, vol 57. WIT Press
4. Li J, Ma G (2010) Analysis of blast wave interaction with a rock joint. *Rock Mech Rock Eng* 43(6):777–787
5. Sitharam TG (2017) *Practical equivalent continuum analyses of jointed rockmass: experiments, numerical modeling, validation and field case studies*
6. Kampas G et al (2019) The effect of tunnel lining modelling approaches on the seismic response of sprayed concrete tunnels in coarse-grained soils. *Soil Dyn Earthq Eng* 117(2019):122–137
7. Lu C-C, Hwang J-H (2018) Damage analysis of the new Sanyi railway tunnel in the 1999 Chi-Chi earthquake: necessity of second lining reinforcement. *Tunnell Undergr Space Technol* 73(2018):48–59
8. Ttshering (2011) *The impact of earthquake on tunnels in different rockmass quality Q: Masters's thesis in Geoscience, Department of Geoscience, University of Oslo*
9. Wang YX et al (2019) Seismic response of tunnel lining structure in a thick expansive soil stratum. *Tunn Undergr Space Technol* 88:250–259
10. Tiwari G, Latha GM (2016) Design of rock slope reinforcement: an Himalayan case study. *Rock Mech Rock Eng* 49(6):2075–2097
11. Zhou Y-Y et al (2017) An enhanced equivalent continuum model for layered rock mass incorporating bedding structure and stress dependence. *Int J Rock Mech Mining Sci* 97(2017):75–98

12. Bilotta E, Lanzano G, Russo G, Santucci de Magistris F, Aiello V, Conte E, Valentino M (2007) Pseudostatic and dynamic analyses of tunnels in transversal and longitudinal direction. In: Proceeding of the fourth international conference on earthquake geotechnical engineering, Thessaloniki, Greece; Paper no 1550
13. Sedarat H et al (2009) Contact interface in seismic analysis of circular tunnels. *Tunnell Undergr Space Technol* 24(4):482–490
14. Lee T-H et al (2016) Damage analysis of cut-and-cover tunnel structures under seismic loading. *Bull Earthq Eng* 14(2):413–431
15. Pan Q, Dias D (2018) Three-dimensional static and seismic stability analysis of a tunnel face driven in weak rock masses. *Int J Geomech* 18(6):04018055
16. Thakur VC, Sriram V, Mundepi AK (2000) Seismotectonics of the great 1905 Kangra earthquake meizoseismal region in Kangra-Chamba, NW Himalaya. *Tectonophysics* 326(3–4):289–298
17. Bandis SC, Lumsden AC, Barton NR (1983) Fundamentals of rock joint deformation. *Int J Rock Mech Min Sci Geomech Abstracts* 20(6). Pergamon
18. Rocscience Inc (2011) Phase 2 program reference manual
19. NGI (2013) Using the Q-system—rock mass classification and support design. NGI Publ, Norway, p 54
20. Barton N, Loset F, Lien R, Lunde J (1980) Application of the Q-system in design decisions concerning dimensions and appropriate support for underground installations. In: International conference on sub-surface space, rock store, Stockholm, Sub-Surface Space, vol 2, pp 553–561
21. IS 456 (2000): Plain and reinforced concrete—code of practice CED 2: cement and concrete
22. Shreedharan S, Kulatilake PHSW (2016) Discontinuum–equivalent continuum analysis of the stability of tunnels in a deep coal mine using the distinct element method. *Rock Mech Rock Eng* 49(5):1903–1922
23. Srivastav A, Satyam N (2020) Understanding the impact of the earthquake on circular tunnels in different rock mass: a numerical approach. *Inno Infrastructure Solutions* 5(1):1–9
24. Shen Y, Gao B, Yang X, Shuangjiang T (2014) Seismic damage mechanism and dynamic deformation characteristic analysis of mountain tunnel after Wenchuan earthquake. *Eng Geol* 180:85–98. <https://doi.org/10.1016/j.enggeo.2014.07.017>
25. Chen Z et al (2017) Fracture evolution and energy mechanism of deep-buried carbonaceous slate. *Acta Geotechnica* 12(6):1243–1260
26. Yoo J-K et al (2018) Seismic response of circular tunnels in jointed rock. *KSCE J Civ Eng* 22(4):1121–1129
27. Varma M, Maji VB, Boominathan A (2019) Numerical modeling of a tunnel in jointed rocks subjected to seismic loading. *Undergr Space* 4(2):133–146

Chapter 8

Effects of the Shield Driving on Soil Arching Around the Tunnel



M. Vinoth  and M. S. Aswathy 

Introduction

Recently, the mechanized tunnel is mainly used in densely populated urban areas [1–4]. If face pressure and grout pressure are inadequate during tunnel driving, adjacent soils will be disturbed and the serviceability of existing adjacent structures will eventually be threatened. In cohesionless soil strata, soil arching effect is predominant due to the stress modification in the soil surrounding the mechanized tunneling. Therefore, it is necessary to understand this behaviour which threatens the functioning of adjacent structures.

Globally, studies on soil arching due to tunnel construction have been carried out by numerous researchers [5–8]. The trap door test carried out by Terzaghi [5] showed that the vertical stress increment seized and remained constant after reaching a certain depth. From previous research [6], it was noted that excavation greatly disrupts the existing earth pressure pattern. However, these research works shed light into the soil-arching phenomenon due to the disturbances caused by tunnel construction. Yet, they have their own time limits as well as costs. To overcome these limitations, recently numerical approach has been adopted to understand the development of soil arching around the tunnel as they are efficient and cost effective [9].

Of lately many, 2D numerical studies [10, 11] have been carried out to capture the evolution of soil arching around the tunnel. These numerical studies [10] revealed that the soil arching was not significant when the depth of tunnel exceeded 12 m. These 2D approaches also had limitations in understanding the soil arching effect, as they were developed under plain strain condition. Some researchers [12] performed

M. Vinoth (✉) · M. S. Aswathy (✉)
CSIR-Central Building Research Institute, Roorkee, India
e-mail: vinoth@cbri.res.in

M. S. Aswathy
e-mail: aswathy@cbri.res.in

3D analysis, but they did not perform the complete analysis to address the stress distribution. Despite several studies conducted by various researchers, the problem of the evolution of soil arching during the mechanized tunnel construction is still missing. Consequently, a 3D numerical model was developed to understand the process of evolution of soil arching in a cohesionless soil.

Input Parameters for the Numerical Analysis

The subsurface parameters were obtained from the geotechnical investigation conducted along the Grey Metro Line of Delhi Metro Rail Corporation. The water table was found at a depth of 20 m from the ground level, and same was taken into account in the analysis. Hardening soft soil (HSS) model was used for the analysis. To understand the evolution of soil arching around the tunnel, a homogenous silty sand (SM) condition was assumed in this study. The properties of the silty sand are presented in Table 8.1.

The properties of the TBM and the lining adopted in the numerical analysis are set out in Table 8.2. The tunnel was constructed using Earth Pressure Balance System (EPBS). The external diameter and internal diameter of the tunnel are 6.3 m and 5.8 m, respectively. Each segment is 1.4 m wide.

Table 8.1 Subsurface properties for HSS model

Parameter	SM	Unit
Unsaturated unit weight, γ_{unsat}	16.4	kN/m ³
Saturated unit weight, γ_{sat}	20.1	kN/m ³
Friction angle, φ	33.2	°
Dilatancy angle, ψ	3.2	°
Cohesion, c_{ref}	0.0	kPa
Initial void ratio, e_0	0.6	–
Reference secant stiffness in triaxial test, $E_{50}^{\text{ref}} [\times 10^4]$	3.13	kPa
Reference tangent stiffness for oedometer loading, $E_{\text{oad}}^{\text{ref}} [\times 10^4]$	3.13	kPa
Reference unloading/reloading Stiffness, $E_{\text{ur}}^{\text{ref}} [\times 10^4]$	9.39	kPa
Power for stress dependency of stiffness, m	0.67	–
Coefficient of permeability, $k_x = k_y [\times 10^{-2}]$	8.64	m/day
Coefficient of permeability, $k_z [\times 10^{-2}]$	2.88	m/day
Reference shear modulus at very small strains, G_0^{ref}	134,131	kPa
Shear strain, $\gamma_{0.7} [\times 10^{-5}]$	31.9	–
Reference stress, p^{ref}	100	kPa

Table 8.2 Material properties of TBM and lining (data from [11])

Parameter	TBM	Lining
Material weight, kN/m ³	76	25
Young's modulus, kPa	210×10^6	27×10^6
Poisson's ratio	0	0.15

Finite Element Model

The size of the finite element model is 100 m × 30 m × 40 m ($L \times B \times H$) as illustrated in Fig. 8.1. The dimensions have been chosen so that boundary effects are eliminated. The TBM had a total length of 12.6 m composed of nine segments. A uniform contraction of 0.5% for the tapered portion was adopted. Tunnel crown lies at a depth of 12.6 m. The numerical simulation is carried out in the same manner as it is executed in the field. Each step in the advancement of EPBS is 1.4 m. For more detail on numerical simulation, see [13]. Generally, the initial lateral stress at rest condition acting at the level tunnel centerline will be larger than the applied face pressure. In this case, face pressure was considered 30% of the initial horizontal at rest pressure (i.e., 28.05 kPa). A linear increment of 2.23 kPa over the entire depth of tunnel has been applied. The grout pressure was assumed to be 1.5 times greater than the face pressure, basically the grout pressure is higher than the face pressure.

Four spots α , β , γ , and Δ (Fig. 8.1) are taken into account in the assessment of the evolution of soil arching due to tunnel construction. Point α is located at the surface, point β is located -5 m below surface, point γ is located -8 m below surface, and point Δ is located at -12 m below surface. At the beginning, the face of the TBM is located at a distance of $2.4D$ (D diameter of tunnel) from the spots and the

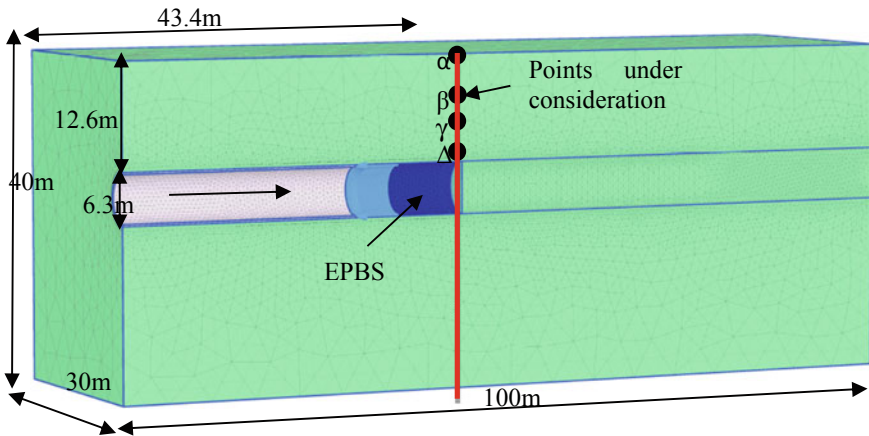


Fig. 8.1 Numerical model for assessing the evolution of soil arching around tunnel

construction stages of the tunnel have been continued until the tunnel face moves to a distance of $5D$ from the spots.

Results and Discussion

The stress variations in α , β , γ , and Δ due to the driving of shield tunnel were obtained from the numerical analysis to study the development of soil arching around the tunnel.

Stress Variation at α , β , γ , and Δ

Continuous redistribution of stress around the tunnel occurs as the tunnel is constructed. The variation of stress with depth has been shown in Figs. 8.2, 8.3 and 8.4. Changes in stress are recorded at different locations of TBM face relative to α , β , γ , and Δ .

Location I: At this stage, the TBM face is located at a distance of $2.4D$ behind the spots α , β , γ and Δ . Figures 8.2, 8.3 and 8.4 shows that the stress at all locations (α , β , γ and Δ) is unchanged. Stresses increase linearly with depth.

Location II: Now, the TBM face lies at a distance of $0.88D$ behind spots α , β , γ and Δ . Figures 8.2 and 8.3 show that σ_{zz} and σ_{xx} exceed the initial stress. Meanwhile, σ_{yy} partly changes in the lower half of the tunnel portion. This is the

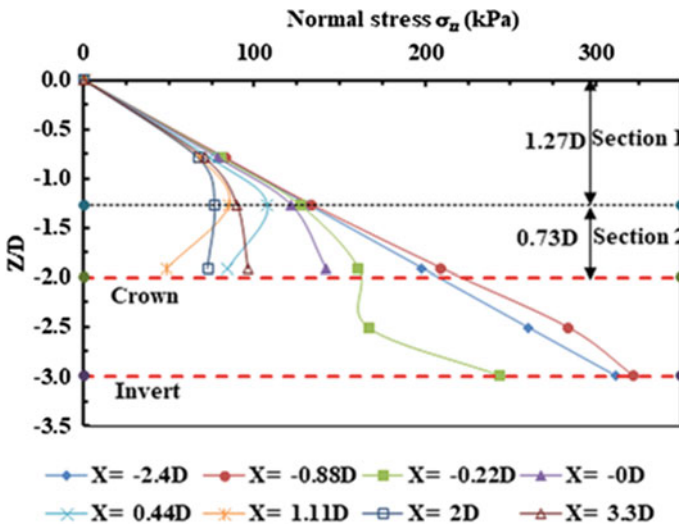


Fig. 8.2 Normal stress (σ_{zz}) variation with depth

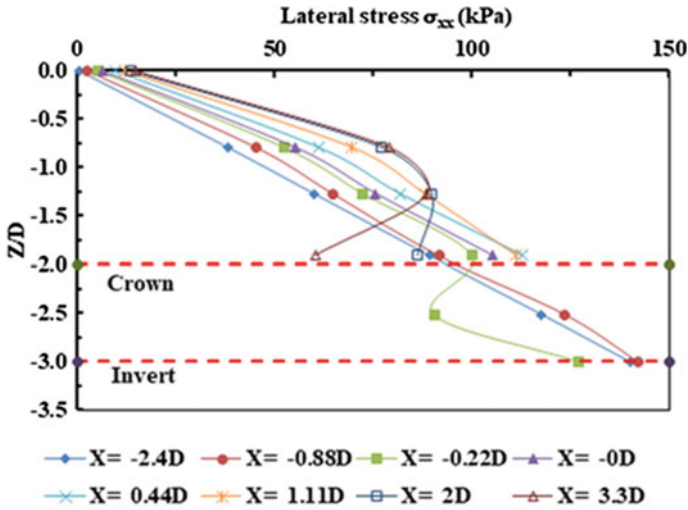


Fig. 8.3 Lateral stress (σ_{xx}) variation with depth

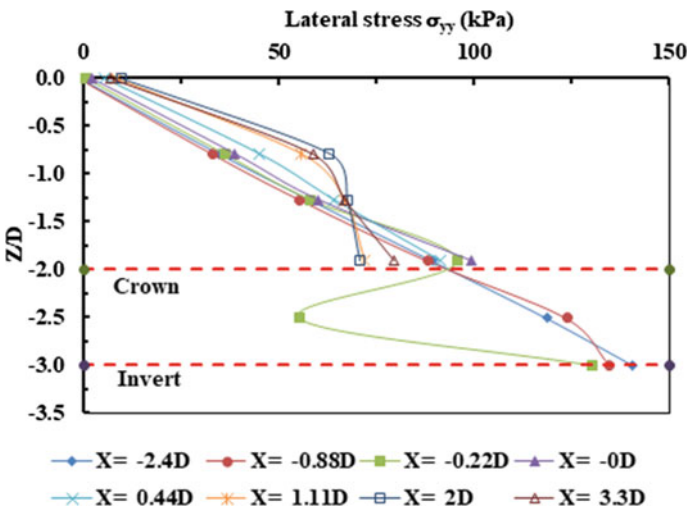


Fig. 8.4 Lateral stress (σ_{yy}) variation with depth

most obvious evidence of the formation of a loose section directly in front of the TBM face. Consequently, to stabilize this formation, soil arching takes place around this section. Due to soil arching, stress around loose section will increase. Thus, spots α , β , γ and Δ can be said to be in the stability area at location II.

Location III: The TBM face is now at a distance of $0.22D$ behind spots α , β , γ and Δ . Figure 8.2 shows that σ_{zz} decreases and no linear trend is seen. The evolution of soil arching occurs at the inflection points as indicated in Fig. 8.2 with a star symbol.

There are two inflection points in the curve (points 1 and 2). After the 1st point with an increase in depth, the σ_{zz} decreases till point 2 and beyond point 2 σ_{zz} increases in relation to the stress in the undisturbed state. This clearly represents the stress distribution to the surrounding soils. σ_{zz} decreases indicate the formation of loose section between points 1 and 2. Figures 8.3 and 8.4 shows that both σ_{xx} and σ_{yy} are increased above the crown, whereas in tunnel section both σ_{xx} and σ_{yy} are reduced, which may be due to the formation of the loose section formed by inadequate face pressure.

Location IV: Now, the TBM has passed the spots (α , β , γ and Δ) and at a $2D$ distance ahead of those points. Figures 8.2, 8.3 and 8.4 shows that σ_{zz} begins to decrease and the horizontal stress increases. Once the TBM face has passed the spots α , β , γ and Δ , the inflection points move upwards indicating the expansion of the loose section above the tunnel.

Location V: Not only does the TBM face passes the spots (α , β , γ and Δ) but also the TBM tail is passed (i.e., $> 2D$). There is not much impact in the vertical stress as the expansion of the loose section is not upwards. On the other hand, the lateral stresses undergo enormous variations at the level of the crown because of the drive of the shield, grouting and the erection of lining segments. Above tunnel crown, two distinct regions are formed one above the point of inflection ($1.27D$) and one below the point of inflection ($0.73D$).

Thus, it is understandable that the loose section above tunnel crown extends to a height of $0.73D$ and arch section has a height of $1.27D$ above the loose section.

Conclusion

A 3D finite element analysis was carried out to understand the evolution of soil arching during shield driving of tunnel in a cohesionless soil. The conclusions that can be made based on the analysis results are,

1. A clear demarcation between the soil arching and loosen section can be identified by looking into the inflection points. Inflection points also provide us with the information of how the loose section expands as the shield driving of tunnel is in progress.
2. Two sections are formed above the tunnel crown when the TBM face pressure is 30% of the initial horizontal at rest earth pressure. The height of loose section above tunnel crown extends to a height of $0.73D$. The soil arching section extends for a height of $1.27D$ above the loose section.

References

1. Cheng HZ, Chen RP, Wu HN, Meng FY (2020) A simplified method for estimating the longitudinal and circumferential behaviors of the shield-driven tunnel adjacent to a braced excavation. *Comput Geotech* 123:103595
2. Tan Y, Lu Y, Wang DL (2021) Catastrophic failure of Shanghai metro line 4 in July, 2003: occurrence, emergency response, and disaster relief. *J Perform Constr Facil* 35(1):04020125. [https://doi.org/10.1061/\(ASCE\)CF.1943-5509.0001539](https://doi.org/10.1061/(ASCE)CF.1943-5509.0001539)
3. Chang CT, Sun CW, Duann SW, Hwang RN (2001) Response of a Taipei rapid transit system (TRTS) tunnel to adjacent excavation. *Tunn Undergr Space Technol* 16:151–158
4. Sharma JS, Hefny AM, Zhao J, Chan CW (2001) Effect of large excavation on deformation of adjacent MRT tunnels. *Tunn Undergr Space Technol* 16:93–98
5. Terzaghi K (1943) *Theoretical soil mechanics*. John Wiley and Sons, New York, pp 194–197
6. Adachi T, Kimura M, Kishida K (2003) Experimental study on the distribution of earth pressure and surface settlement through three-dimensional trapdoor tests. *Tunn Undergr Space Technol* 18(2):171–183
7. Dewoolkar MM (2007) Centrifuge modeling of granular soil response over active circular trapdoors. *Soils Found* 47(5):931–945
8. Kirsch A (2010) Experimental investigation of the face stability of shallow tunnels in sand. *Acta Geotech* 5(1):43–62
9. Vermeer PA, Ruse N, Marcher T (2002) Tunnel heading stability in drained ground. *Felsbau* 20(6):8–18
10. Jiang MJ, Yin ZY (2012) Analysis of stress redistribution in soil and earth pressure on tunnel lining using the discrete element method. *Tunn Undergr Space Technol* 32(6):251–259
11. Kong XX, Liu QS, Zhang QB, Wu YX, Zhao J (2018) A method to estimate the pressure arch formation above underground excavation in rock mass. *Tunn Undergr Space Technol* 71:382–390
12. Chen RP, Tang LJ, Ling DS, Chen YM (2011) Face stability analysis of shallow shield tunnels in dry sandy ground using the discrete element method. *Comput Geotech* 38(2):187–195
13. Aswathy MS, Vinoth M, Achal M (2021) Impact of governing factors on prediction of tunneling induced surface settlement in young alluvium deposit. *Indian Geotech J*. <https://doi.org/10.1007/s40098-021-00561-4>

Chapter 9

Stability Analysis of Overburden Dump Slope—A Case Study of Marki Mangli-I Coal Mine



S. S. Geete, K. H. Singh, A. K. Verma, T. N. Singh, and P. P. Dahale

Introduction

For the extraction of coal or metal from the open cast mining, huge quantity of material is excavated called as overburden dump (OBD) material. This huge quantity of material stored in the form of the internal pit dumping and external dumping. In case of the internal pit dumping, within the pit of mine, dump material is stored, whereas in external dumping, dump material is stored outside area of mine pit. OBD slope should not be far away from the mine pit because this will increase the transportation cost of dump material. Separate place is demarcated for the storage of OBD material. Shear strength of foundation strata is less than the shear strength of the dump waste material, then stability of slope will govern by the shear strength of foundation strata [1]. Bearing capacity of the foundation soil is directly proportional to the stability of the overburden dump slope [2]. Stability of dump slope designated

S. S. Geete (✉) · P. P. Dahale
Shri Ramdeobaba College of Engineering and Management, Nagpur, India
e-mail: sumit.geete@gmail.com; geetess@rknec.edu

P. P. Dahale
e-mail: dahalepp@rknec.edu

S. S. Geete
Indian Institute of Technology, Bombay, India

K. H. Singh · T. N. Singh
Earth Science Department, Indian Institute of Technology, Bombay, India
e-mail: kumar.h.singh@iitb.ac.in

T. N. Singh
e-mail: tnsiitb@gmail.com

A. K. Verma
Department of Mining Engineering, Indian Institute of Technology, Varanasi, India
e-mail: amitvermaism@gmail.com

by a factor of safety (FOS) and generally minimum risk dump slope design for FOS 1.1 to 1.15. Fellenius method used to mark the critical failure surface of the waste dump slope. Permissible height of dumping depends on index properties of waste dump material and methods of dumping [3]. Coates proposed charts in relation to the height of dump for calculation of factor of safety based on the slope angle [3]. The failure of internal dumping is directly affecting the mine coal extraction and safety of personnel working inside the mine [4]. The relation between the height of dump and the angle of slope of dump is correlated based on various index properties of the dump material and foundation soil [5]. Relationship between FOS and height of dump also between FOS and slope angle is proposed [4]. Stability of dump slope studied for the effect of the increase of height with the inclusion of bench [2]. Overburden dump material is heterogeneous in nature so it is difficult to investigate the index properties of the OBD. Larger size particles are excluded at the time of grain size analysis of the OBD material. Total 11 mines sites dump material samples (8 Nos. per mine) were collected and tested for various geotechnical properties [6]. After dumping, physical and chemical weathering of waste dump material take place which alters the properties of dump material results in a change of shear strength and permeability [1]. Slope failed because of the failure of foundation black cotton soil or either failure of dump slope material. Once the ultimate shear strength of supporting black cotton soil is reached, failures are initiated in the soil first and then it propagates in the body of OBD [7]. Peak friction angle depends on soil index properties like soil type, relative density, unit weight, and void ratio. Peak friction angle increases with the angularity of granular soil, surface roughness, and relative density. For fine grained soil, peak friction angle depends on the plasticity index and various relationship proposed in various research articles. The relationships between grain sizes with peak friction angle for different soil types are developed. The empirical relationship effective peak friction angle and a different ratio of mix proportions by weight of coarse to fine (C/F) are developed [8]. The factor of safety of waste dump slope in the saturated condition is less than unsaturated condition. Minimum FOS for the stability of waste dump slope considers as 1.40 in most unfavorable conditions [9]. The probabilistic approach takes into account the effect of uncertainty and variation of material properties using various statistical distribution functions. Percent of coefficient of variation (%COV) is directly proportional to the probability of failure also increases. Monte Carlo method is used to evaluate the probabilistic slope stability analysis. FOS calculated by deterministic LEM and probabilistic LEM is nearly similar to each other [3, 10].

Since in mining projects, land is allotted on the basis lease; hence, OBD material should be safely stored in demarcated land. Because of land availability constraint, OBD slope should be extend vertically instead of horizontally. Hence to check the feasibility of OBD slope to extend vertically, assessment of stability of OBD slope is vital. In the present study, stability of existing and proposed vertically extended OBD slope of Marki Mangli-I coal mine is analyzed through probabilistic method.

Details of Study Site

Marki Mangli-I coal mine operated by M/s. Topworth Urja & Metals Ltd. This mine located in Jhari Jamni Tahsil in District Yavatmal of Maharashtra, India. The site is located approximately 170 km from Nagpur. Geographical location of the mine latitude (North) 19,050' 47" and longitude (East) 78,046' 41". Lease area of mine is 682.78 ha. Total extractable coal reserve is 8.35 MT. Expected life of mine is about 30 years. Production capacity of mine is 0.3 MT per annum. Effective seam thickness is 2.5–4.5 m. Average annual rainfall is 1250–1350 mm. Working depth of mine is 18–48 m. Overall stripping ratio of mine is 1:6.75. The existing dump of three benches is placed on the ground surface of black cotton soil. Dump material mainly consists of black cotton soil, sandstone, and shale. The black cotton soil is dumped separately from other OBD materials. The overall bench angle is 23°.

Mine area is comprised of Penganga group of beds consist of Gondwana, Lameta, and Deccan trap in the ascending order. The Penganga represented by limestone which are dolomitise at places and purple shales. These are overlain by Gondwana with faulted contacts. The Gondwana is overlain by Lameta consisting of clay and siliceous limestone. The Lametas are generally fringe the overlaying basaltic lava flows, i.e., Deccan trap. Within the block, surface is generally covered with black cotton soil. In the western part, exposures of Deccan trap are seen at places, while in northeast, the exposure of Pakhal/Penganga beds, talchar, barker, Lameta, and Deccan trap is present. In the major central part, Lameta beds cover under soil (Figs. 9.1 and 9.2).

Fig. 9.1 OBD at Marki Magli-I coal mine



Fig. 9.2 Sample collection of OBD material



Data Regarding Rainfall

1. Maximum rainfall in a day:250 mm
2. Maximum exposed area for direct precipitation:35 ha.
3. Max. quantity of rain water within 24 h:875,000 cum.
4. RL of HFL:230 m.
5. Annual average rainfall:1250–1350 mm.
6. Location of ground water table:3.0–5.0 m below natural ground level.

Objective

Objective of present study is to analyze the stability of

- (a) Existing (three benches) OBD slope at critical sections
- (b) Proposed vertically extended (four benches) slope at critical sections

From this stability analysis, check the feasibility of extension of one more bench of 10 m height and 20 m width over the extension OBD slope.

Methodology

Methodology of investigation of stability of slope is mentioned in the flowchart Fig. 9.3. From the site investigation, critical sections of overburden dump slope of mine are determined at chainage of 450 and 550 m. Geomechanical properties of the dump materials are evaluated in the laboratory at optimum moisture content (OMC). Shear strength parameters (cohesion (c) and internal angle of friction (ϕ)) of the OBD material are assessed by the direct shear test as per IS: 2720 (Part 13)–1986.

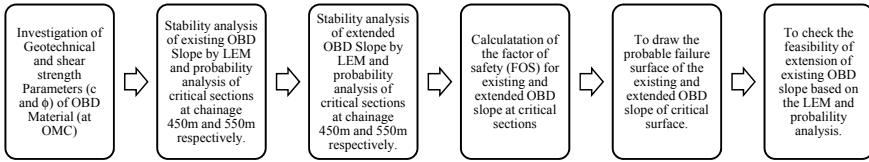


Fig. 9.3 Flowchart of methodology of dump slope stability analysis investigation

Based on the geomechanical properties, stability of the existing and vertically extended dump slope is assessed through limit equilibrium method and the probabilistic analysis. Bishop’s simplified method and Spencer-Wright method are used for stability analysis of OBD as these methods are more realistic and accurate. In probability analysis, percentage of the attainment of respective FOS is recognized. This probabilistic method elaborates the clarity of safety measured in terms of factor of safety. Extended bench height of dump is 10 m. Stability and probabilistic analyses are performed on Gelena software.

Laboratory Analysis

Laboratory investigations of dump samples are performed as per Indian standard code provisions (Figs. 9.4, 9.5 and 9.6). Various geotechnical properties are represented in Table 9.1.

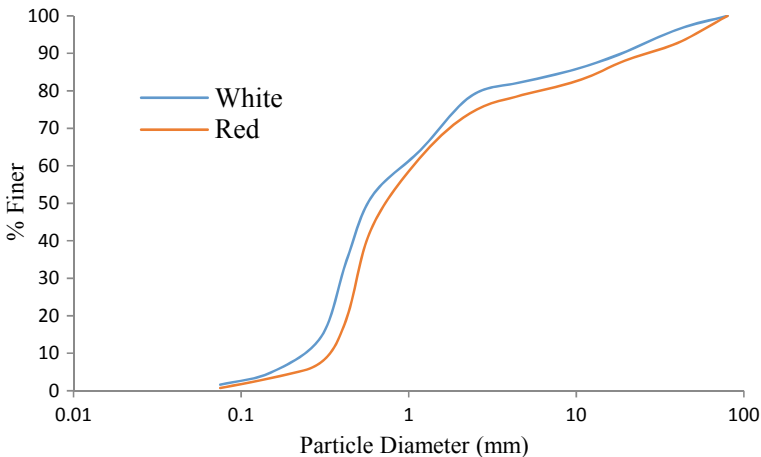


Fig. 9.4 Particle size distribution of OBD material less than 80 mm (white and red OBD material)

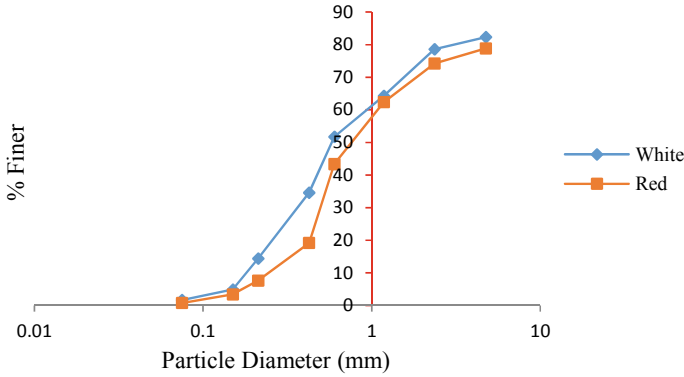


Fig. 9.5 Particle size distribution of OBD material particle size less than 4.75 mm (white and red OBD material)

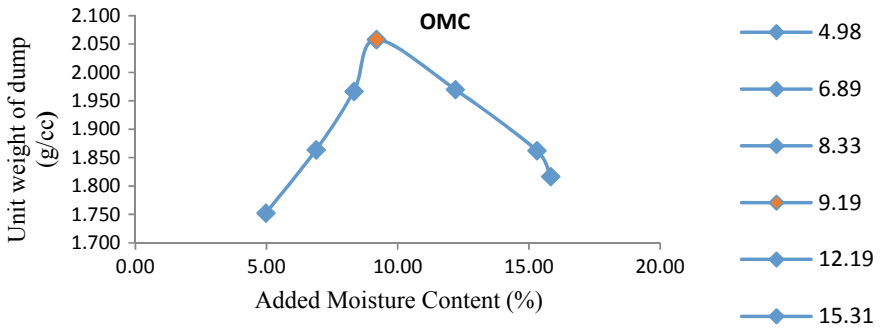


Fig. 9.6 Variation of unit weight of dump with moisture content

Table 9.1 Geotechnical properties of dump material

Moisture content (%)	Permeability (cm/s)	Specific gravity	Optimum moisture content (OMC) (%)	Maximum dry density (MDD) (g/cc)	Cohesion (kPa)	Internal angle of friction
2.04	0.00682	2.392	9.19	2.058	150	21.1°

From Fig. 9.7, cohesion and internal angle of friction (ϕ) of the OBD material are found out to be 150 kPa and 21.1°, respectively, at optimum moisture content (Fig. 9.8).

Fig. 9.7 Shear strength versus shear strain of OBD material with variation of normal stress at OMC

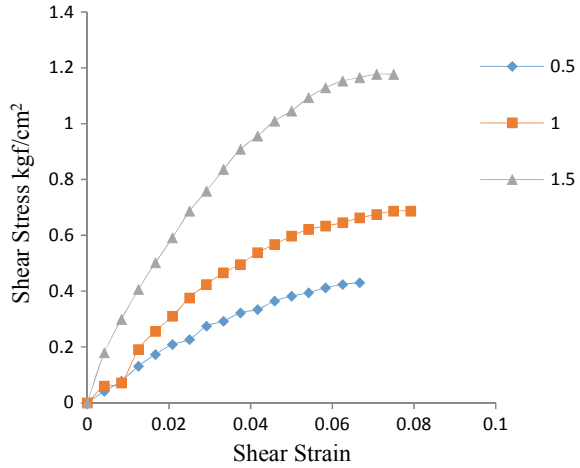
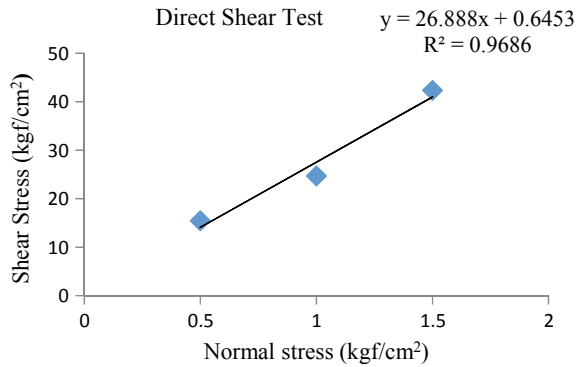


Fig. 9.8 Normal stress versus shear stress of OBD slope material at OMC



Stability Analysis of OBD Slope

Existing overburden dump consists of three benches. Height and width of each bench are 10 m and 20 m, respectively. From the site investigation, critical sections are identified at chainage 450 m and 550 m of overburden dump slope. Gelena software is used for the stability analysis through LEM and probability method of the existing and vertically extended OBD slope. Stability analysis of existing and vertically extended OBD slope at each critical sections (chainage 450 and 550 m) is evaluated.

A. Slope stability analysis existing dump slope at chainage of 450 m by LEM and probability method

See Figs. 9.9, 9.10, 9.11, 9.12 and 9.13.

B. Slope stability analysis existing dump slope at chainage of 450 m extended

See Figs. 9.14, 9.15, 9.16 and 9.17.

A. Slope stability analysis existing dump slope at chainage of 450m by LEM and probability method

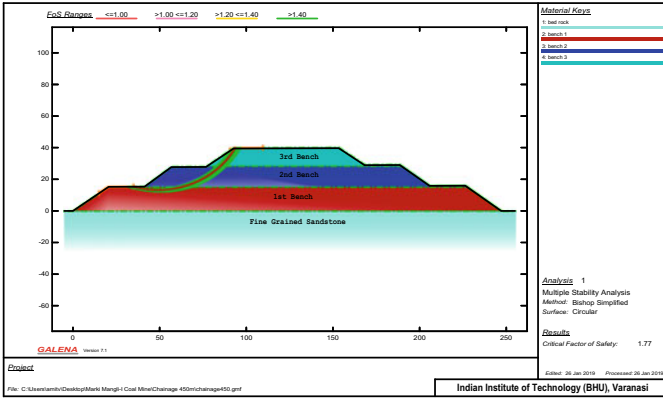


Fig. 9.9 Failure envelope of existing dump slope at chainage 450 m with critical FOS (Bishop simplified method)

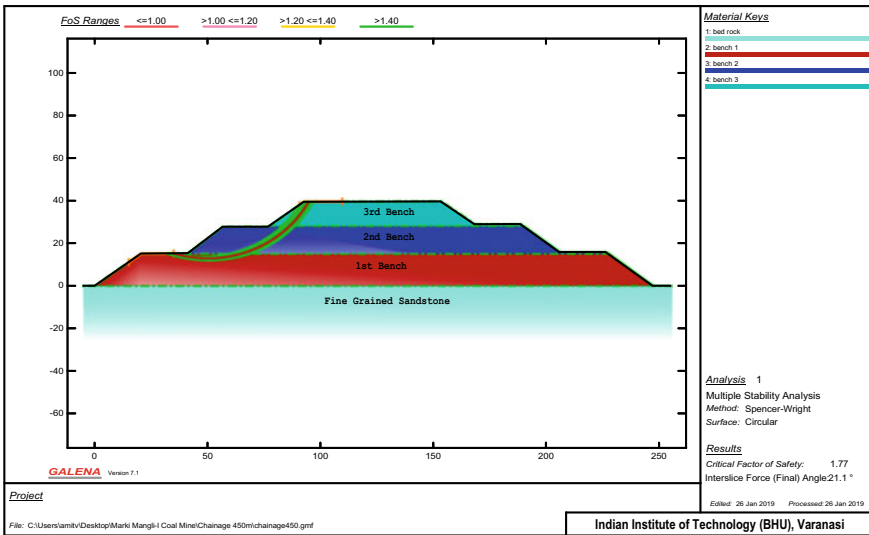


Fig. 9.10 Failure envelope of existing dump slope at chainage 450 m with critical FOS (Spencer-Wright method)

C. Slope stability analysis existing dump slope at chainage of 550 m

See Figs. 9.18, 9.19 and 9.20.

D. Slope stability analysis extended dump slope at chainage of 550 m

See Figs. 9.21, 9.22, 9.23 and 9.24.

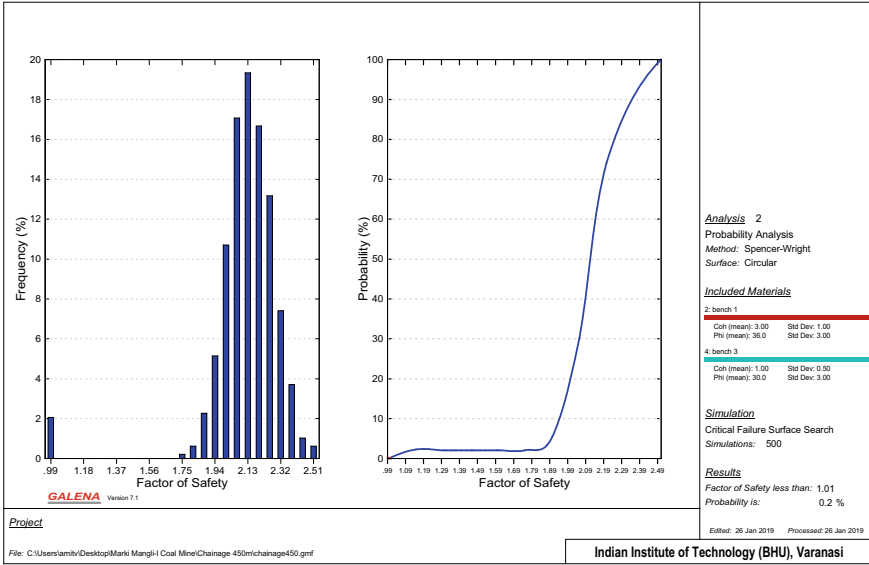


Fig. 9.11 Probability analysis of existing dump slope at section 450 m indicates FOS less than 1.01 is 0.2%

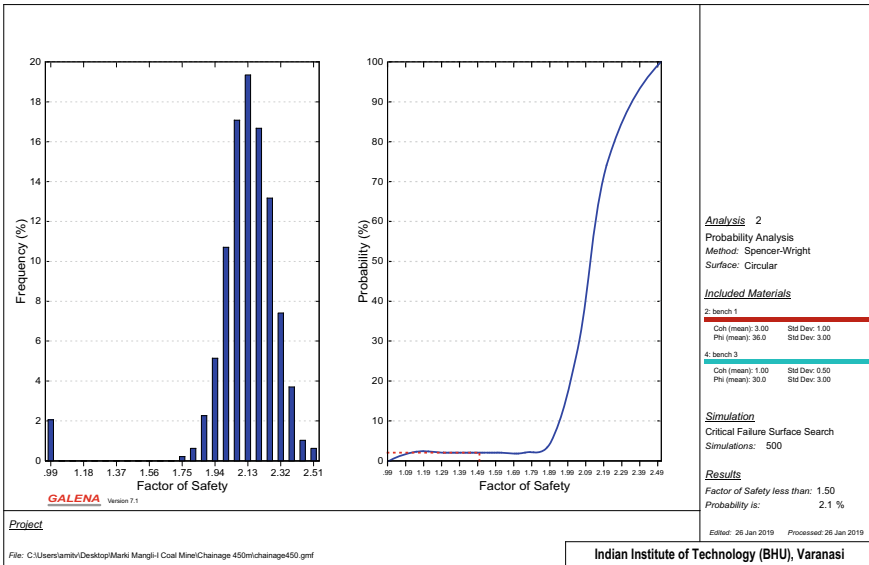


Fig. 9.12 Probability analysis of existing dump slope at section 450 m indicates FOS less than 1.50 is 2.1%

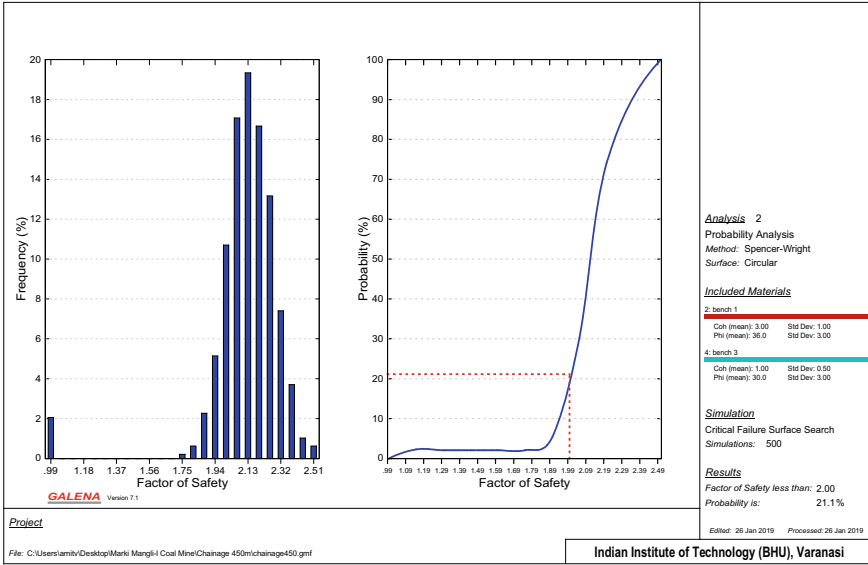


Fig. 9.13 Probability analysis of existing dump slope at chainage 450 m indicates FOS less than 2.0 is 21.1%

B. Slope stability analysis existing dump slope at chainage of 450m extended

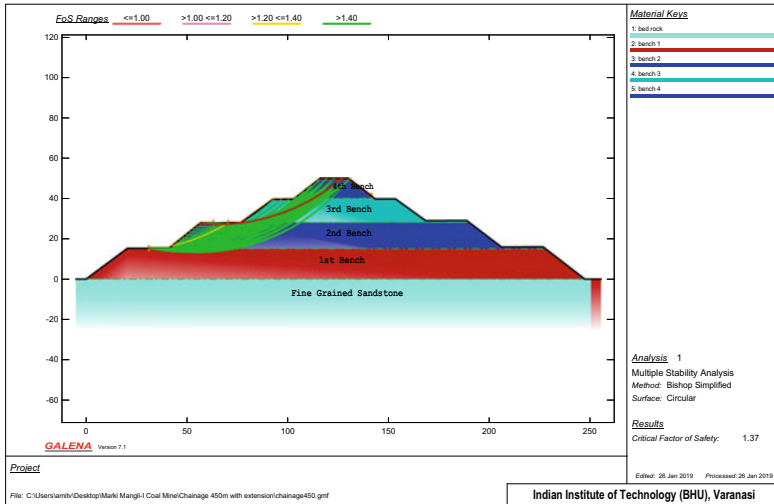


Fig. 9.14 Failure envelope of extended dump slope at chainage of 450 m with critical FOS (Bishop method) 1.37

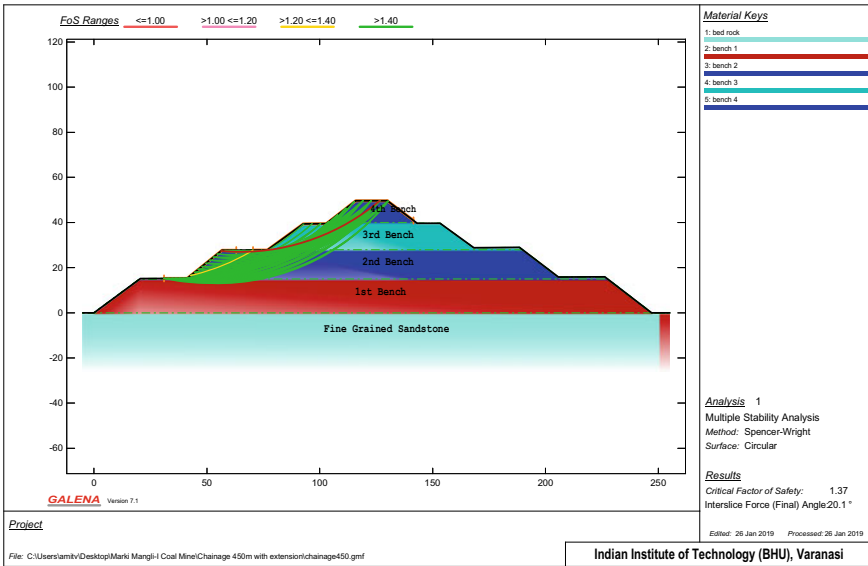


Fig. 9.15 Failure envelope of extended dump slope at chainage of 450 m with critical FOS (Spencer-Wright method) 1.37

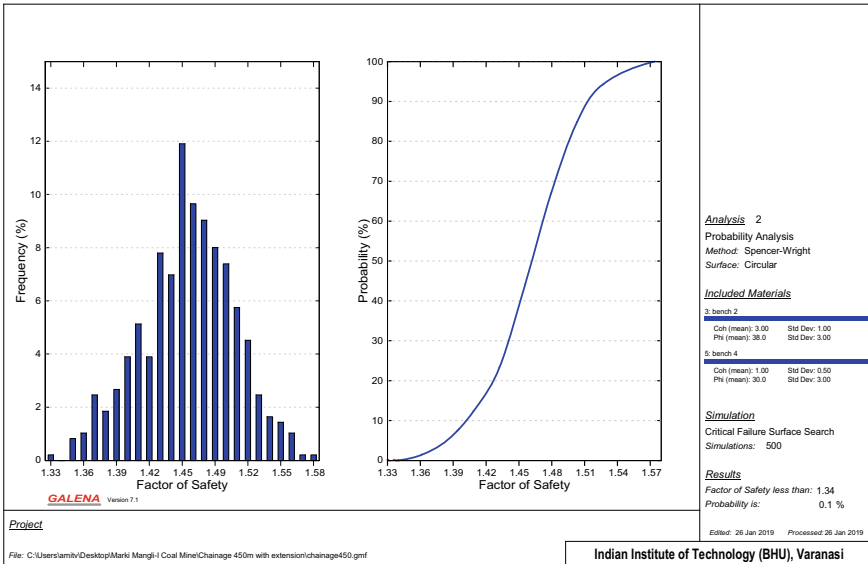


Fig. 9.16 Probability analysis of extended dump slope at chainage 450 m indicates FOS less than 1.34 is 0.1%

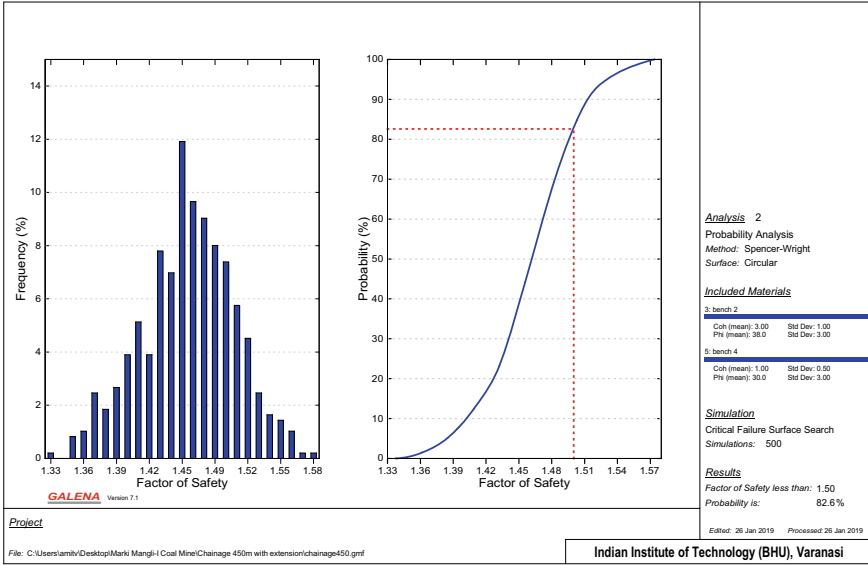


Fig. 9.17 Probability analysis of extended dump slope at chainage 450 m indicates FOS less than 1.50 is 82.6%

C. Slope stability analysis existing dump slope at chainage of 550m

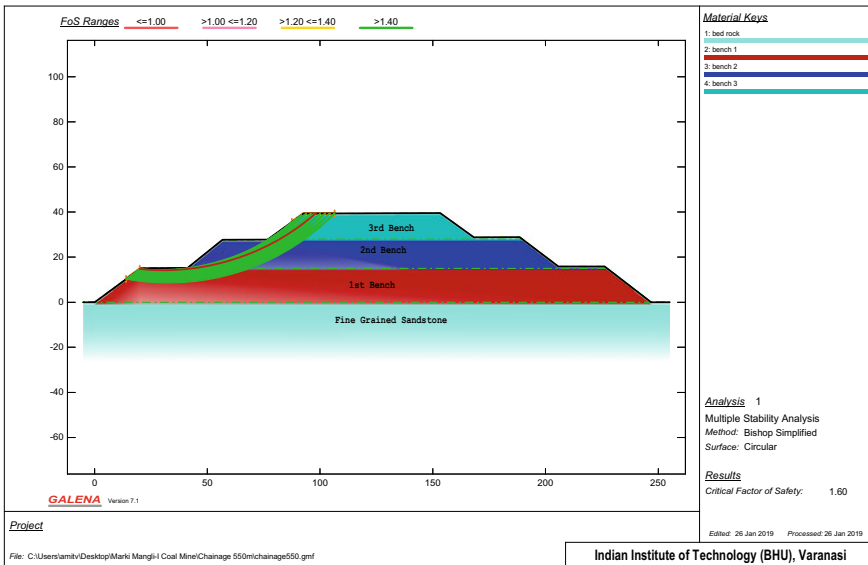


Fig. 9.18 Failure envelope of existing dump slope at chainage of chainage of 550 m with critical FOS (Bishop method) 1.60

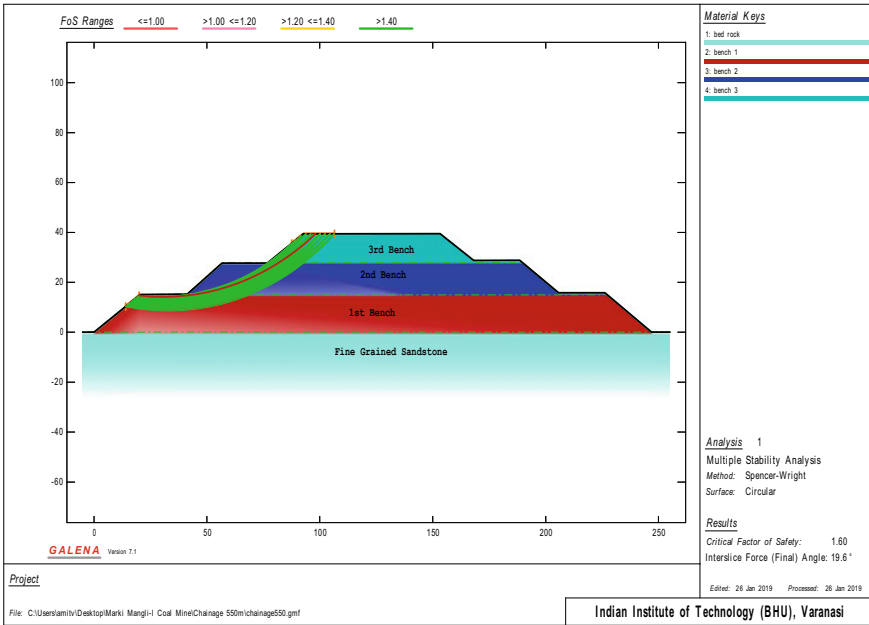


Fig. 9.19 Failure envelope of existing dump slope at chainage of chainage of 550 m with critical FOS (Spencer-Wright method) 1.60

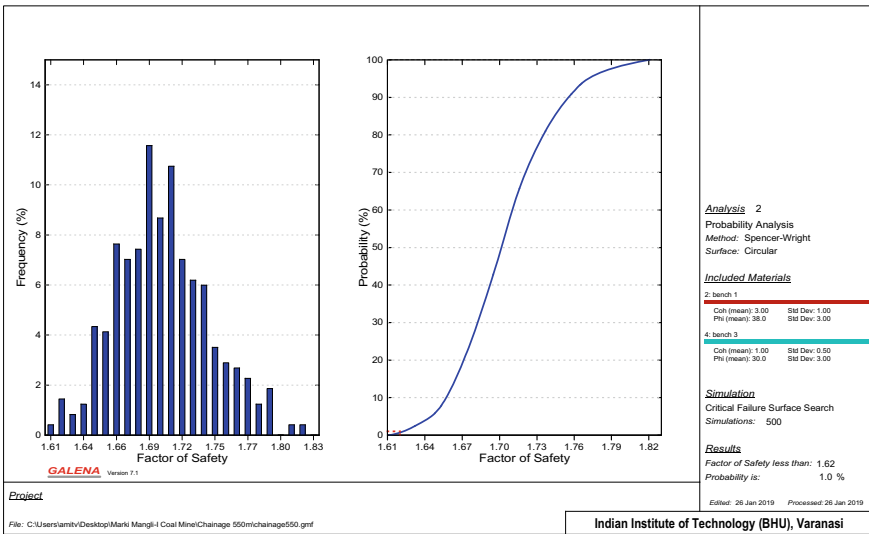


Fig. 9.20 Probability analysis of existing dump slope at chainage 550 m indicates FOS less than 1.62 is 1.0%

D. Slope stability analysis extended dump slope at chainage of 550m

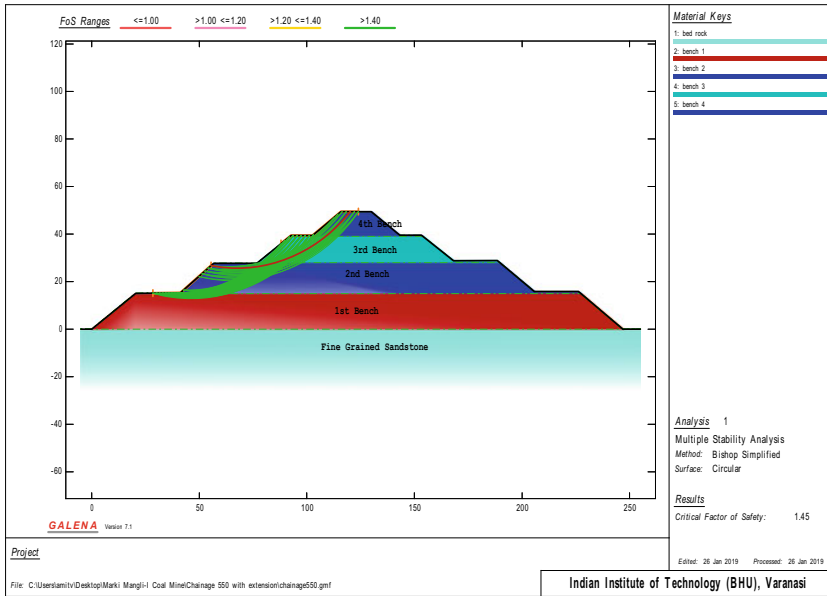


Fig. 9.21 Failure envelope of extended dump slope at chainage of chainage of 550 m with critical FOS (Bishop method) 1.45

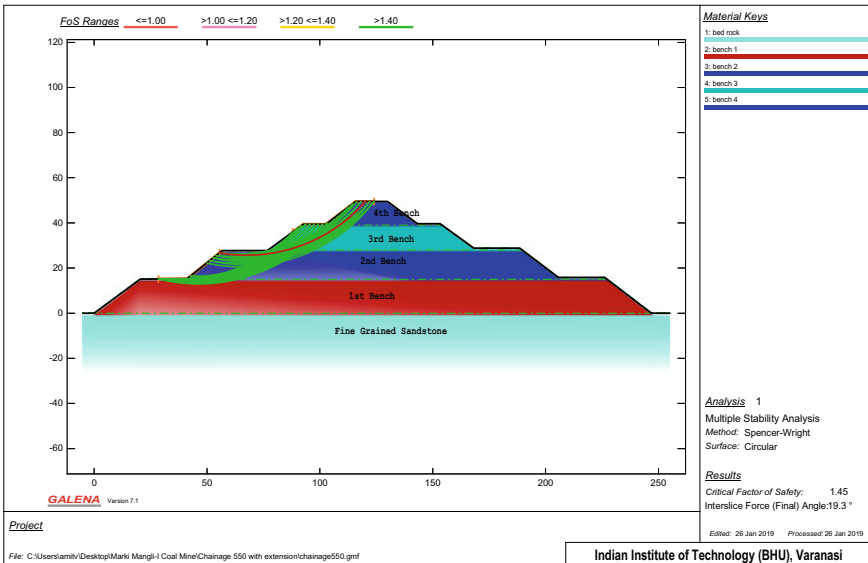


Fig. 9.22 Failure envelope of extended dump slope at chainage of chainage of 550 m with critical FOS (Spencer-Wright method) 1.45

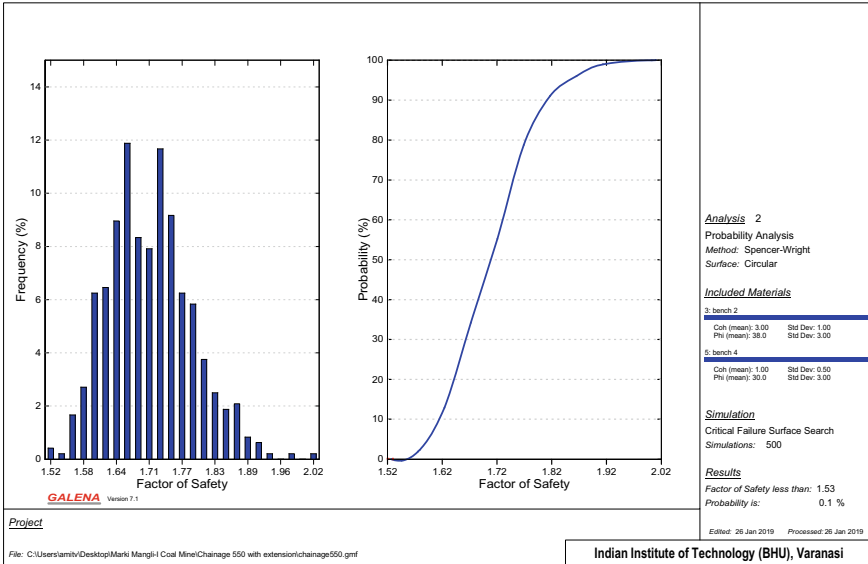


Fig. 9.23 Probability analysis of extended dump slope at chainage 550 m indicates FOS less than 1.53 is 0.1%

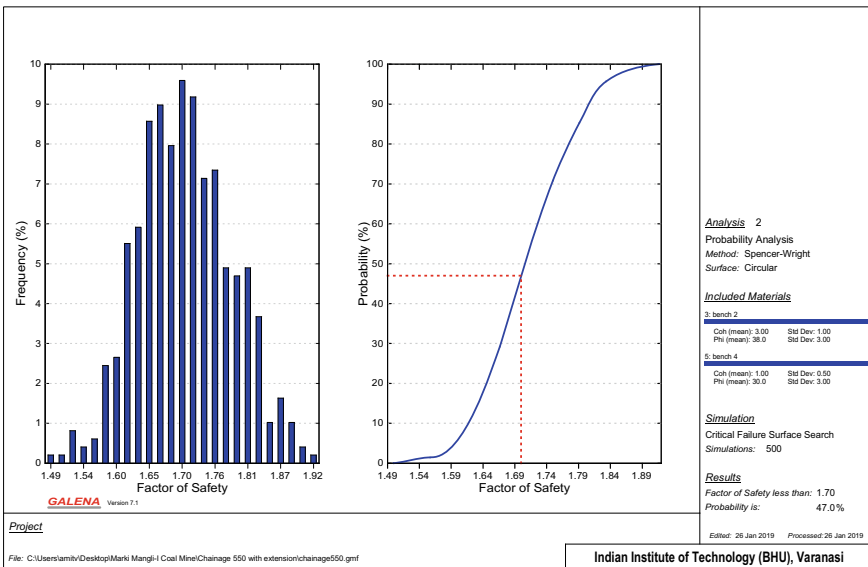


Fig. 9.24 Probability analysis of extended dump slope at chainage 550 m indicates FOS less than 1.70 is 47%

Table 9.2 Assessment of factor of safety by LEM

Method of analysis	At 450 existing	At 450 extension	At 550 existing	At 550 extension
FOS				
Bishop simplified method	1.77	1.37	1.6	1.45
Spencer–Wright method	1.77	1.37	1.6	1.45

Table 9.3 Assessment of probability by LEM

	At 450 existing			At 450 extension		At 550 existing	At 550 extension	
FOS	1.01	1.50	2.00	1.34	1.50	1.62	1.53	1.74
Probability of FOS less than	0.20%	2.10%	21.10%	0.10%	82.60%	1.00%	0.10%	47.00%

Results and Discussion

In this study, an extensive laboratory testing program has been undertaken to determine geotechnical properties of OBD material. Permeability, specific gravity, moisture content, optimum moisture, maximum dry density, particle size distribution, and direct shear strength of OBD material are investigated. Based on test results, numerical models are developed for existing dump and proposed vertically extended dump. The geometry of the slopes is kept same as that of present practiced approval from DGMS, and limit equilibrium approach has been adopted to estimate the safe dump height. Following conclusions and recommendations of are drawn from present scientific study (Tables 9.2 and 9.3).

Conclusion

From the exhaustive laboratory work, it is concluded that existing dump is safe and stable as per stability assessment through LEM for both the chainage sections (450 m and 550 m). For existing OBD slope, the probability of factor of safety less than 1.5 is only 2.1% at critical sections. Factor of safety assessed through Bishop’s method and Spencer-Wright method is same. Factor of safety of proposed vertically extended OBD slope is 1.37 as per stability assessment through LEM and probability of factor of safety less than 1.50 is less than 82.6% at critical section.

From the present stability analysis, it is concluded that proposed vertical extension of bench had factor safety less than 1.50, therefore, vertical extension is not safe. Hence, it is not permitted.

Future Scope

- 1 Stability of overburden dump slope should be analyzed at variation in moisture content of dump material.
- 2 Stability analysis of overburden dump slope should be analyzed by mixing two types of soil (white and red) with varying percentage. Because at the time of dumping of excavated percentage of mixing varies.

Acknowledgements Authors thankful to the M/s. Topworth Urja & Metals Ltd of the Marki Mangli-I coal mines for the help and cooperation extended.

References

1. Upadhyay OP, Sharma DK, Singh DP (1990) Factors affecting of stability of waste dump in mines. *Int J Surf Mining, Reclam Environ* 4(3):95–99
2. Kainthola A, Verma D, Gupte SS, Singh TN (2011) A coal mine dump stability analysis. *April*:1–13
3. Coates DR (1977) Landslide perspectives. *Rev Eng Geol* 3:3–28. <https://doi.org/10.1130/REG3-p1>
4. Koner RA, Chakravarty DE (2010) Stability study of the mine overburden dumps slope : a micromechanical approach. XXXII(1)
5. Roy I (2008) Slope stability study of external dump of Sonepur-Bazari opencast coal mine, India—a case study, 2008
6. Koner R (2015) Characterisation of overburden dump materials : a case study from the Wardha valley coal field. *Bull Eng Geol Environ*
7. Poulsen B, Khanal M, Rao AM, Adhikary D, Balusu R (2014) Mine overburden dump failure: a case study. *Geotech Geol Eng*
8. Arvanitidis C, Steiakakis E, Agioutantis Z (2018) Peak friction angle of soils as a function of grain size. *Geotech Geol Eng* 8
9. Fernando J, Nag D (2003) A study of internal overburden dump design and stability analysis for Hazelwood power mine, Latrobe Valley, Victoria, Australia. *Appl Comput Oper Res Miner Ind South African Inst Min Metall*:267–274
10. Huvaj N, Oğuz EA (2018) Probabilistic slope stability analysis : a case study. 22(5):1458–1465

Chapter 10

Living Soil Nails to Prevent Shallow Landslides in Lateritic Soil Slopes



D. Anand Praveen and P. V. Divya 

Introduction

Rainfall-induced slope failures are becoming very common nowadays in India, especially in Kerala. During the monsoon period, landslides are taking place along the residual soil slopes in Kerala. Recently, several landslides have occurred in many districts of Kerala. Kerala witnessed many rainfalls triggered landslides in the years 2018, 2019, and 2020. In 2019 and 2020, heavy rain in Wayanad, Kannur, and Idukki has caused severe slope failures and left the hilly districts completely isolated [1]. Rainfall infiltration in unsaturated soil slopes involves flow through unsaturated zone above the ground water table.

In unsaturated conditions, there are two independent stress state variables: net normal stress ($\sigma - u_a$) and matric suction ($u_a - u_w$). Here, σ is normal stress, u_a is pore air pressure, and u_w is pore water pressure which control the shear strength, volume change behavior, and permeability (seepage) of the unsaturated soil. The shear strength of the soils in unsaturated conditions can be expressed by Eq. 10.1 by Fredlund et al. [2].

$$\tau = c' + (\sigma - u_a) \tan \phi' + (u_a - u_w) \tan \phi^b \quad (10.1)$$

where c' = effective cohesion; $(\sigma - u_a)$ = net normal stress; $(u_a - u_w)$ = matric suction; ϕ' = angle of internal friction due to net normal stress; ϕ^b = an angle indicating the rate of increase in shear strength relative to soil suction. The shear strength

D. A. Praveen · P. V. Divya (✉)
Dept. of Civil Engineering (Primary), Environmental Sciences and Sustainable Engineering
Center (Secondary), Indian Institute of Technology Palakkad, Palakkad 678557, Kerala, India
e-mail: divyapv@iitpkd.ac.in

D. A. Praveen
e-mail: 102114009@smail.iitpkd.ac.in

of the soil depends upon the matric suction. Rainfall infiltration will cause reduction in matric suction. The importance of rainwater infiltration in causing slope failures is well known [3, 4]. Vibha and Divya [1] reported that the slope failures in unsaturated lateritic soil during rainfall is mainly due loss of suction due to advancement of wetting front rather than rise in ground water table. Sudden increase in pore water pressures due to establishment of perched water table leads to slope failure [5].

Several methods are available for slope stabilization including structural and non-structural elements such as retaining walls, gabion walls, geosynthetic reinforcements, and soil nailing. However, soil bioengineering techniques are gaining popularity due their economic effectiveness and environmental friendliness. Plant roots help to prevent the slope failures in two ways. It provides tensile strength to the soil and assist the soil in maintaining suction via evapotranspiration. Cardoza and Oka [6] reported that the use of vegetative stabilization increased the factor of safety in sands and silts. It was reported that the shear strength of root reinforced soil depends on the root length and root area ratio. They can be considered as “living soil nails” owing to the advantage that the roots can penetrate deep in to the soil and act like a reinforcement. This will be helpful in preventing shallow slope failures. In the present study, numerical investigations are conducted in order to investigate the performance of lateritic soil slopes during rainfall infiltration. The performance of lateritic soil slopes is compared with and without vegetation. Further, direct shear tests are conducted on residual lateritic soil with and without vegetation roots to evaluate the influence of vegetation in shear strength characteristics of lateritic soils.

Materials

The soil used in the present study was collected from a location in Kerala, where a shallow landslide had occurred in the year 2018. The soil was classified as CL as per unified soil classification system. The liquid limit and plasticity index of the soil were 27.19% and 18.6%, respectively. Percentage fines in the soil (less than 75 microns sieve size) were found to be 66%. The saturated permeability of the soil was found to be 1.58×10^{-8} m/s at a maximum dry density of 15.53 kN/m^3 and optimum moisture content of 25.5%. Cohesion intercept (c') and angle of internal friction (ϕ') are 9 kPa and 27° , respectively. The SWCC parameters are experimentally determined using filter paper technique. Van Genuchten SWCC parameters alpha (α) and pore size distribution (n) of the soil are found to be 1.06 and 1.49, respectively.

Selection of vegetation compatible with the lateritic soil is very important. The vegetation used in the study was a perennial grass named *Chrysopogon zizanioides* which is commonly known as vetiver. In order to investigate the growth rate of vetiver grass in the lateritic soil used in the present study, saplings of length of 3 cm are taken and planted in lateritic soil filled in a plastic tub of dimensions 66 cm \times 30 cm \times 33 cm as shown in Fig. 10.1a. The growth rate was observed for 45 days. Figure 10.1b, c indicates the view of the grass initially and at the end of 20 days, respectively. Figure 10.1e, f shows the status of vetiver grass G1 (as

marked in Fig. 10.1b) after 20 days and 45 days, respectively. From Fig. 10.1d–f, it can be observed that the vetiver has good compatibility with lateritic soil. Average growth rate of vetiver grass in residual lateritic soil used in the present study was found to be found to be 23 cm/month. As can be observed from Fig. 10.1f, vetiver can develop a deep, dense, and fibrous root system which will be ideal for slope stabilization in residual lateritic soil systems and also in erosion control. A literature review conducted on some common grass roots revealed that the tensile strength of *C. zizanioides* (vetiver) varies from 40 to 120 MPa [7]. Thus, the fast-growing vetiver grass can be considered as “living soil nails” in lateritic soil slopes owing to the reinforcing mechanism of deep, dense, strong, and fibrous root system in addition to its hydrological benefits.

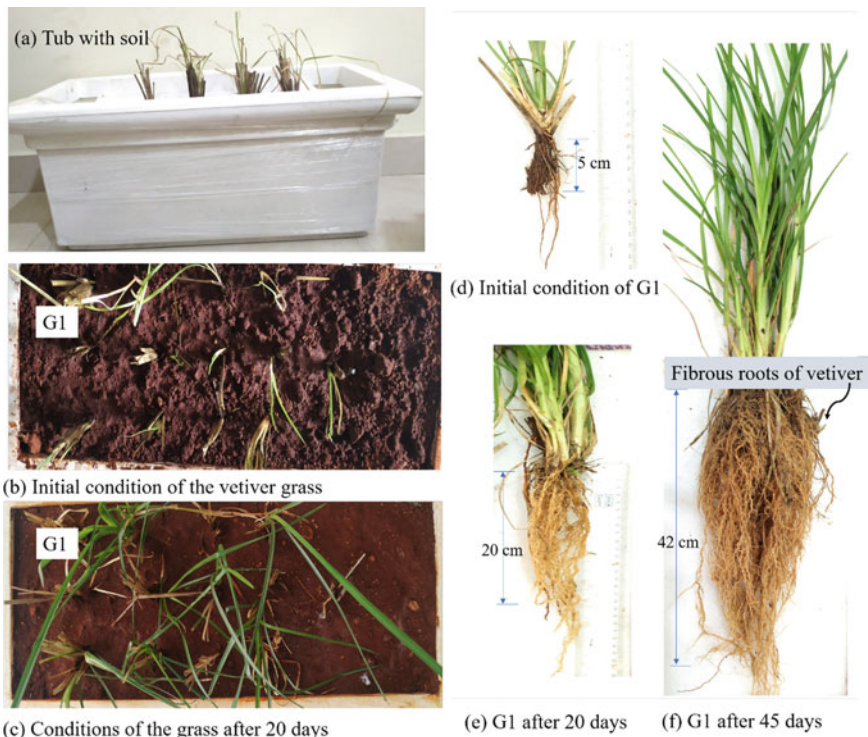


Fig. 10.1 Testing of growth rate of vetiver grass in lateritic soil

Numerical Modeling of Slopes with and Without Vegetation

Performance of lateritic soil slopes at the onset of rainfall infiltration was studied numerically using a commercially available software Hydrus. Hydrus utilizes physically based hydromechanical frameworks for simulation of the transient fields of soil moisture during rainfall infiltration. Hydrus combines variable saturation flow and stress fields to simulate the impact of rainfall on slopes. Rainfall data for the region for the month of August 2018 (Fig. 10.2) during which many landslides were occurred in Kerala were used in the present study to simulate the extreme rainfall conditions.

The landslides reported in the study area were shallow in nature. Generally, the slope height varied from 4 to 10 m and was a rolling terrain of lateritic soil along the side of a road. In the present study, a simplified geometry of slope height (H) of 8 m was modeled at an inclination (β) of 30° as shown in Fig. 10.3. Properties of the lateritic soil collected from the landslide location as explained in Sect. “Materials” were assigned to the slope. Groundwater table was considered at bottom of the slope. Top surface of the slope is subjected to atmospheric boundary conditions where rainfall infiltration and evapotranspiration take place. Sides and bottom part of the slope are subjected no flux boundary condition, where the flow is restricted (Fig. 10.3).

In order to simulate the influence of vegetation (vetiver) in the transient soil moisture fields and soil suction, root water uptake model and Feddes root water uptake parameters are used. The Feddes model parameters [8] are $PO = -10$ cm, $PO_{pt} = -25$ cm, $P2H = -300$ cm, $P2L = -1000$ cm, $P3 = -8000$ cm, $r2H = 0.50$ cm/day, and $r2L = 0.1$ cm/day. Based on potential transpiration rates (PET), root water uptake model calculates actual evapotranspiration (AET). Twelve vetiver grass of root length of 2 m with transpiration rate (PET) 15 mm/day are modeled in

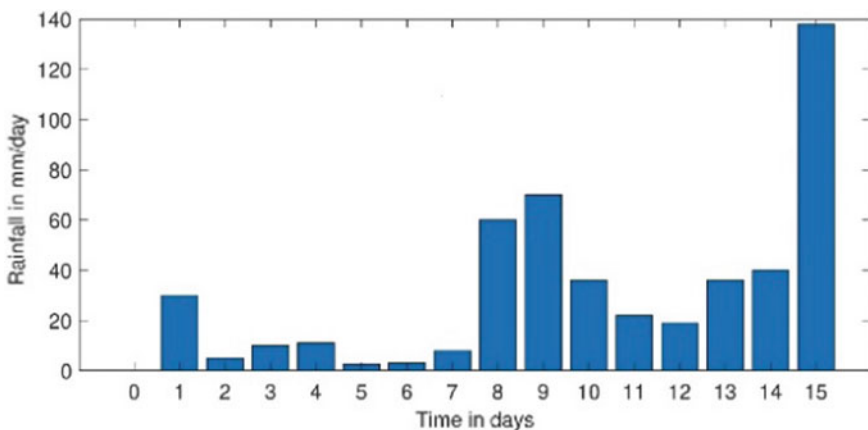


Fig. 10.2 Daily rainfall data during August 2018

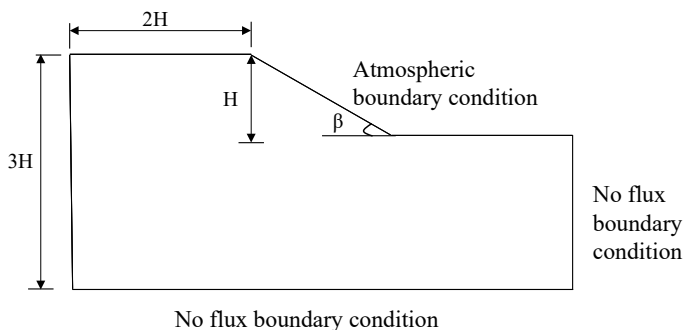


Fig. 10.3 Boundary conditions of the model adopted in the present study

the present study. Performance of slope with and without vetiver grass was compared in terms of wetting front advancement, suction distribution, and factor of safety of the slope.

Advancement of wetting front developed in the slope with and without vegetation during rainfall infiltration at different intervals of time (t) can be observed from Figs. 10.4 and 10.5. As can be seen from Fig. 10.2, the rainfall in mm/day is low in the first 7 days. As the duration of rainfall (t) increases, the wetting front advances further deep in to the slope without vegetation as shown in Fig. 10.4. The advancement of wetting front will change the saturation level and suction within the slope. In the case of slope with vegetation, the wetting front has not advanced deep in to the slope as can be seen from Fig. 10.5. The presence of vegetation and root system prevented the advancement of wetting front. Figures 10.6 and 10.7 show the variation of pressure head within the slope with and without vegetation. As can be seen from Fig. 10.6, the distribution of pressure is in accordance with the advancement of wetting front. Initially, at time $t = 0$, suction or negative pore water pressure exists above the ground water table. As the rainwater infiltrate, the suction reduces along the slope surface. As the time progress ($t = 7$ days), a zone of zero suction or zero pressure head developed near the slope surface of the slope without vegetation (Fig. 10.6). The zone of zero suction expands into the interior of slope as rainfall infiltration and advancement of wetting front further progresses ($t = 15$ days). Loss of suction can decrease the shear strength of soil and affects the stability of the slope. Whereas, in the case of slope with vetiver grass, the suction was maintained at high values due to the root water uptake as shown in Fig. 10.7. This is in accordance with the advancement of wetting front pattern observed in Fig. 10.5. Since the suction is maintained at high values in slope with vetiver grass, the shear strength and slope stability will be enhanced. This will be helpful in maintaining the integrity of the slope during rainwater infiltration. The factor of safety of the slope during rainwater infiltration with and without vetiver grass is shown in Fig. 10.8. As can be seen from Fig. 10.8, the slope without vegetation experienced failure (Factor of safety less than 1) due to rainwater infiltration. Whereas, the slope with vetiver grass maintained the integrity with higher factor of safety during the entire duration of rainfall. It is to be noted

that, only hydrological benefits are studied in the present numerical investigations. In addition to the hydrological benefits, additional strength will be contributed by means of vetiver roots. Tensile strength of the roots can further increase the factor of safety of the slope. Thus, in order to investigate the influence of vetiver root system on the shear strength characteristics of the lateritic soil, large direct shear tests were conducted on lateritic soil with and without vetiver root system.

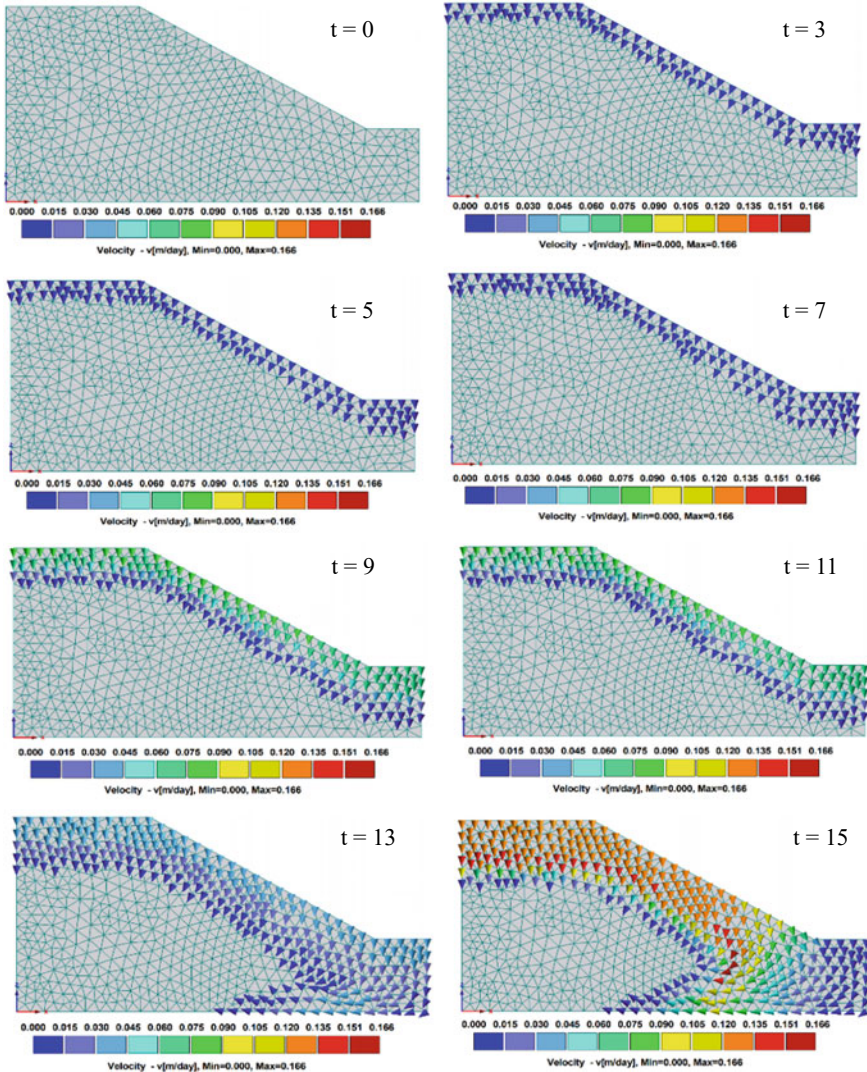


Fig. 10.4 Advancement of wetting front in slope without vegetation for different duration of rainfall (t = time in days)

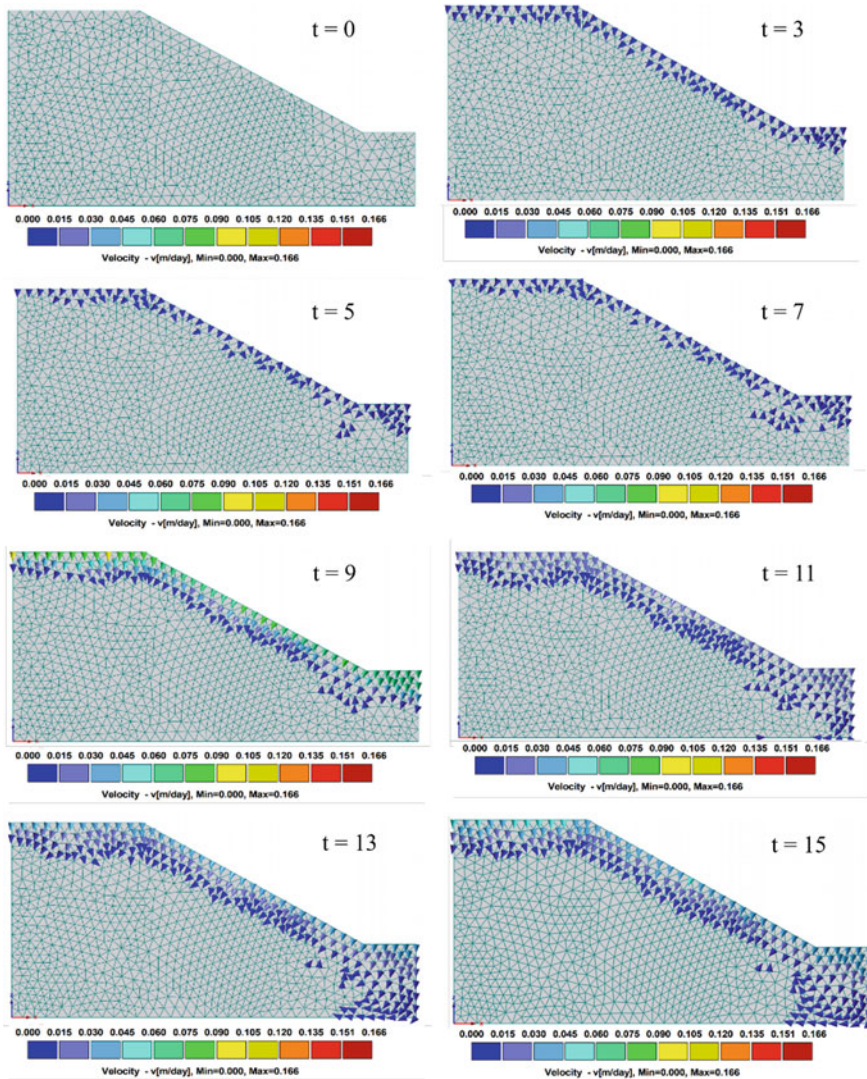


Fig. 10.5 Advancement of wetting front in slope with vegetation for different duration of rainfall ($t =$ time in days)

Experimental Investigations

In order to study the shear strength characteristics of vetiver root reinforced lateritic soil system, large direct shear testing was conducted on soil samples of dimensions $300 \text{ mm} \times 300 \text{ mm} \times 200 \text{ mm}$. In order to obtain root reinforced soil, vetiver grasses were planted at 75 mm center to center spacing and allowed to grow in a detachable

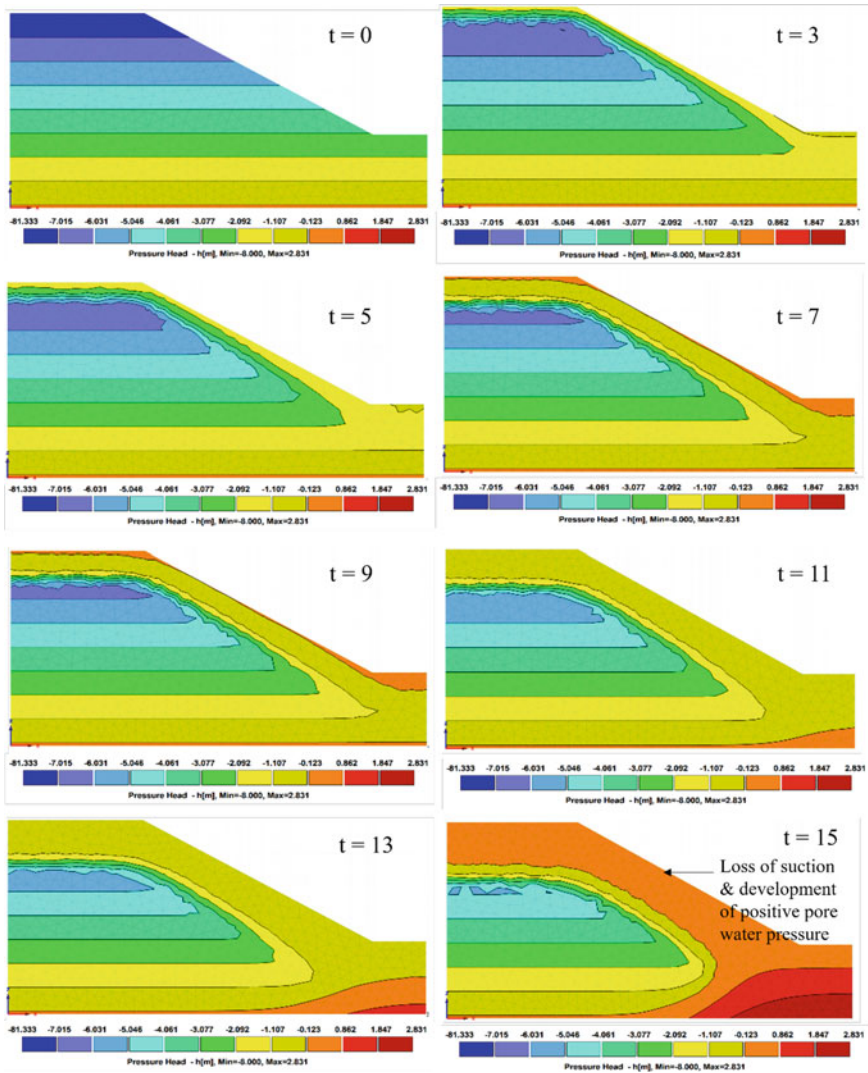


Fig. 10.6 Variation of pressure head in slope without vegetation for different duration of rainfall (t = time in days)

wooden box filled with lateritic soil at a density of 15.53 kN/m^3 and moisture content of 25.5%. Nine identical vetiver grasses as shown in Fig. 10.9a were planted in the wooden box. The inner dimensions of the wooden box are $300 \text{ mm} \times 300 \text{ mm} \times 300 \text{ mm}$ as shown in Fig. 10.9b. The growth rate of vetiver grass in the lateritic soil used in the study was promising (Fig. 10.9c) and was allowed to grow for two months. At the end of two months, the samples were extracted from the wooden box. Figure 10.9d shows the soil root system extracted from the wooden box. It can be

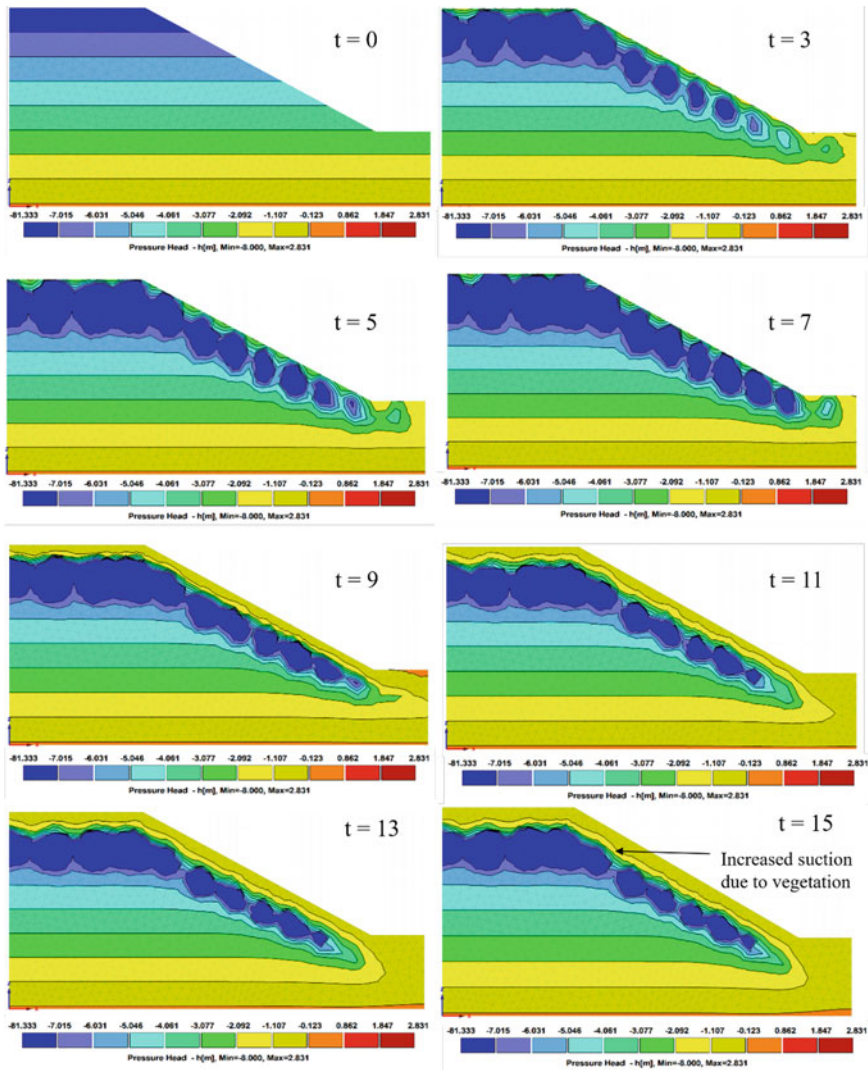


Fig. 10.7 Variation of pressure head in slope with vegetation for different duration of rainfall (t = time in days)

observed that dense fibrous roots are developed in the soil samples over two months. The trimmed sample is transferred to the direct shear test apparatus (Fig. 10.9e) and tested according to ASTM-D-3080. Tests were conducted at normal stress of 50, 75, and 100 kPa. Figure 10.9f shows the test setup. The samples with and without roots were sheared to a maximum displacement of 75 mm. Figure 10.10 shows the shear strength envelop of the soil with and without vetiver root system. As can be observed from Fig. 10.10, the cohesion intercept and angle of internal friction of the

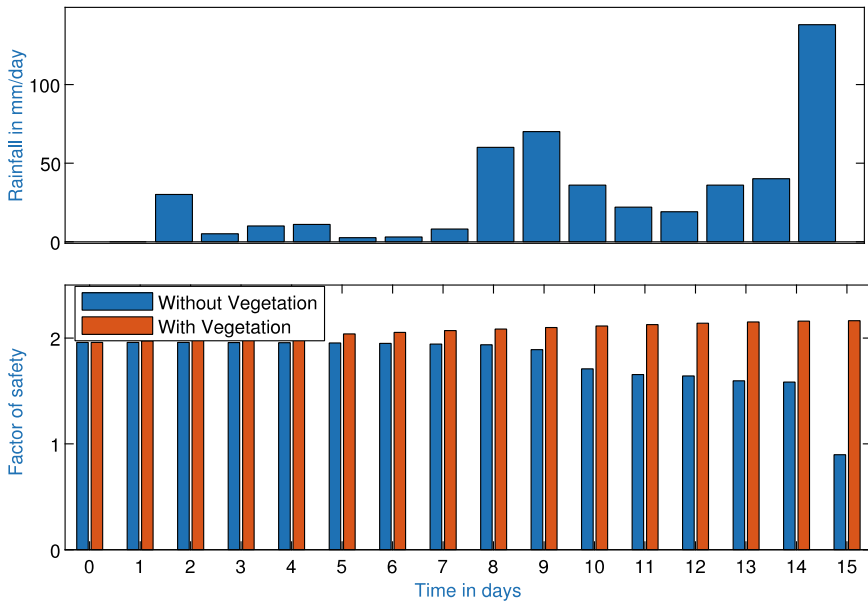


Fig. 10.8 Variation of factor of safety of the slope during rainwater infiltration with and without vetiver grass

soil were increased by 103% and 45%, respectively, when the soil was reinforced with the root system. Cohesion intercept was increased from 9 to 18.3 kPa and angle of internal friction was increased from 27° to 39°. Thus, the shear strength of the soil was increased due to the presence of vetiver root system and significantly contribute to the slope stability.

Conclusions

- Lateritic soil slope observed to lose the integrity during rainwater infiltration. Slope failure happened due to the loss of suction associated with the advancement of wetting front during rainfall. Whereas, the presence of vetiver grass helped in maintaining the suction within the soil slope and prevented the advancement of wetting front owing to the root water uptake. Lateritic soil slope with vetiver grass was able to maintain the integrity with increased factor of safety, even after subjected to a prolonged rainfall of 15 days.
- In addition to the hydrological benefits, vetiver roots helped in improving the shear strength characteristics of the lateritic soil due to the reinforcing effect of the roots. Average growth rate of vetiver grass in residual lateritic soil used in the present study was found to be found to be 23 cm/month. Deep, dense, and fibrous

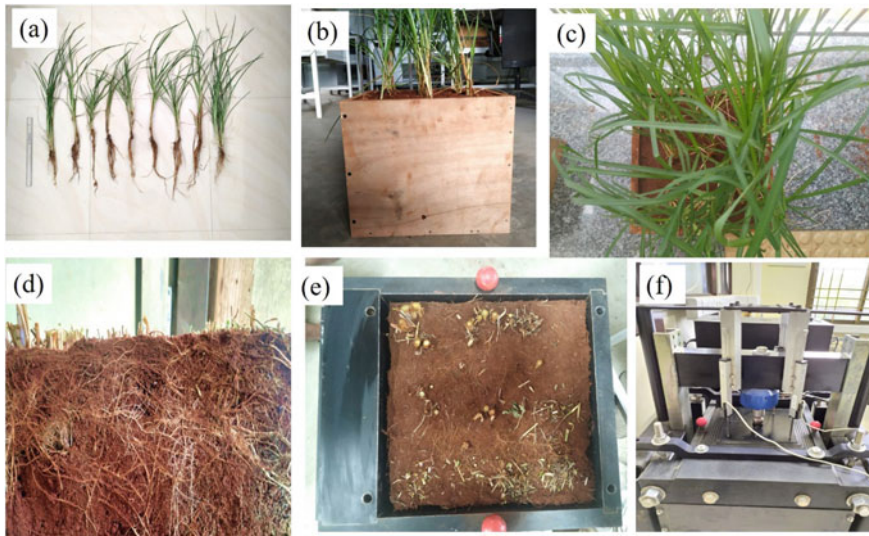


Fig. 10.9 Direct shear testing stages on soil root system (a) Nine vetiver grasses used per test specimen (b) Wooden box of 300 mm × 300 mm × 300 mm (c) Status of vetiver grass after two months (d) Dense fibrous root system developed in soil after two months (e) Trimmed sample transferred to direct shear testing apparatus (f) View of large direct shear apparatus during testing

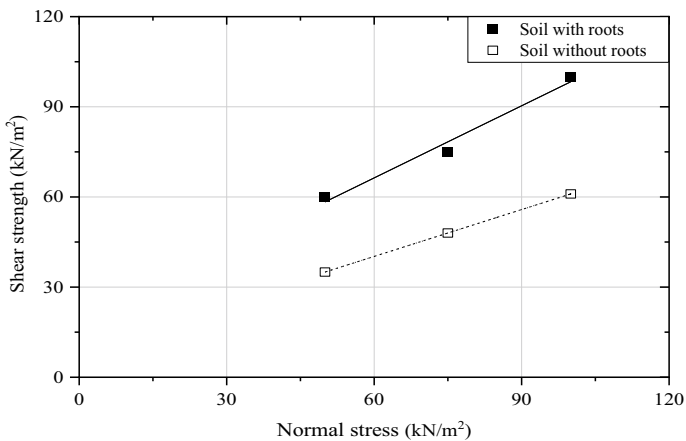


Fig. 10.10 Direct shear test results of lateritic soil with and without vetiver roots

root system was observed to develop within the lateritic soil which will be ideal for preventing shallow slope failures in lateritic soil slopes. Thus, the vetiver root system can be considered as “living soil nails.”

- Cohesion intercept and angle of internal friction of the lateritic soil were increased by 103% and 45%, respectively, when the soil was reinforced with the vetiver root

system. Cohesion intercept was increased from 9 to 18.3 kPa and angle of internal friction of the lateritic soil was increased from 27° to 39° .

References

1. Vibha S, Divya PV (2021) Performance of geosynthetic reinforced MSE walls with marginal backfills at the onset of rainfall infiltration. *Int J Geosynth Ground Eng* 7(9)
2. Fredlund DG, Morgenstern NR, Widger RA (1978) The shear strength of unsaturated soils. *Can Geotech J* 15(3):313–321
3. Rahardjo H, Ong TH, Rezaur RB, Leong EC (2007) Factors controlling instability of homogeneous soil slopes under rainfall. *J Geotech Geoenviron Eng* 133(12):1532–1543
4. Rahardjo H, Nio AS, Leong EC, Song NY (2010) Effects of groundwater table position and soil properties on stability of slope during rainfall. *J Geotech Geoenviron Eng* 136(11):1555–1564
5. Godt JW, Baum RL, Lu N (2009) Landsliding in partially saturated materials. *Geophys Res Lett* 36(2)
6. Cardoza R, Oka L (2020, Feb) Measuring the effect of grass roots on shear strength parameters of sandy soils. In: *Geo-congress 2020: biogeotechnics*. American Society of Civil Engineers, Reston, VA, pp 214–223
7. Nilaweera NS, Hengchaovanich D (1996) Assessment of strength properties of vetiver grass roots in relation to slope stabilization. In: *Vetiver: a miracle grass, Chiang Rai (Thailand)*, 4–8 Feb, 1996
8. Feddes RA, Kowalik PK, Zaradny H (1976) Simulation of field water uptake by plants using a soil water dependent root extraction function. *J Hydrol*:13–26

Chapter 11

Restoration Measures of Landslide Affected Valley Slope—A Case Study of Tindharia Area Along NH 55 in West Bengal



Avik Kumar Mandal, S. Sailesh, Pradyot Biswas, and Atanu Adhikari

Introduction on Occurrences of Landslides at Tindharia

The road, “National Highway (NH) No. 55”, starts from “Darjeeling” at “Mohanlal Chawk” (km 0 + 000) and ends at “Darjeeling More” (km 77 + 000) of “Siliguri” in the state of West Bengal. The existing road is of intermediate to two lanes. The narrow gauge railway line of “Darjeeling–Kurseong–Siliguri route of NF Railway” runs in parallel with the existing NH 55 either on its right-hand side (RHS) or left-hand side (LHS). The carriageway width between chainage km 50 + 150 (Darjeeling side) and km 53 + 475 (Siliguri side) in and around “Tindharia” area along the NH 55 was partially to severely damaged at the following three numbers of locations due to occurrence of landslide on September 18, 2011, on the valley side of the existing road.

1. Km 50 + 155 to km 50 + 187 (Tindharia I say S1)
2. Km 52 + 650 to km 52 + 750 (Tindharia II say S2)
3. Km 53 + 452 to km 53 + 485 (Tindharia III say S3)

Figure 11.1 presents the above said three locations of landslides in and around Tindharia area along NH 55.

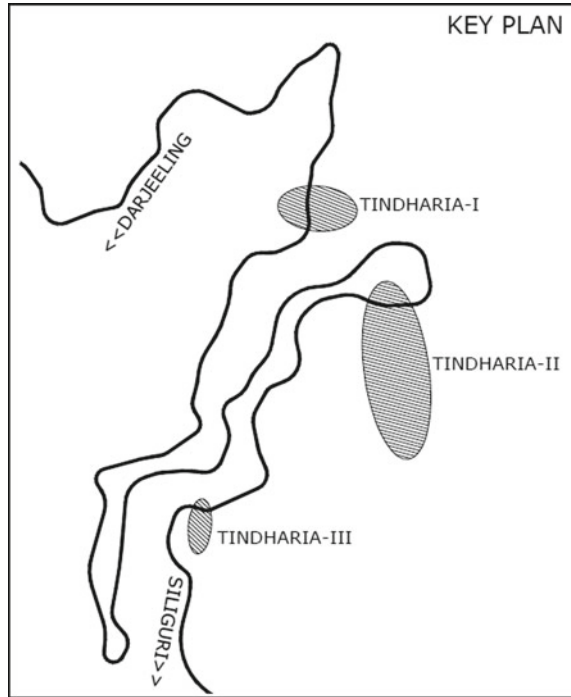
A. K. Mandal (✉) · S. Sailesh · P. Biswas
LEA Associates South Asia Pvt. Ltd., New Delhi, India
e-mail: avik@lasaindia.com

S. Sailesh
e-mail: sailesh@lasaindia.com

P. Biswas
e-mail: pradyotbiswas@lasaindia.com

A. Adhikari
Engineering and Scientific Development, Reinforced Earth India Pvt. Ltd., New Delhi, India
e-mail: atanu.adhikari@terre-armee.com

Fig. 11.1 Various Locations of Landslides in and around “Tindharia” along NH 55 in WB



The total height of valley side slope varies from 36 to 64 m from the existing road bench, and the maximum height of valley side slope affected due to landslide was around 30 m at the “Tindharia I (km 50 + 155 to km 50 + 187)” location. The angle of existing valley side slope was 56–63° with horizontal at the “Tindharia I” location. Some temporary protection work in the form of road barriers by using locally available “stone filled Gabion box” was done by the State Public Works Department (PWD) on the collapsed valley slope side. The condition of the landslide affected valley side slope at the “Tindharia I” location is shown in Fig. 11.2.



Fig. 11.2 Conditions of landslide affected valley slope at “Tindharia I”



Fig. 11.3 Conditions of landslide affected valley slope at “Tindharia II”

The maximum height of landslide affected valley slope was around 90 m out of total existing slope heights ranging from 165 to 185 m, and the angle of existing valley side slope was $55\text{--}70^\circ$ with horizontal at the “Tindharia II (km 52 + 650 to km 52 + 750)” location. The exposed highly weathered fractured rock mass can be seen on hill and valley side of slope in this road stretch. The narrow gauge railway line of “NF Railway” was in hanging condition due to occurrence of major landslide of the entire road width on valley slope side at the “Tindharia II” location where the railway department had restored the railway line by cutting and supporting the hill slope with RCC retaining wall after few months of occurrences. Figure 11.3 represent the conditions of landslide affected site at “Tindharia II”.

At the “Tindharia III (km 53 + 452 to km 53 + 485)” location, the total height of existing valley side slope is in between 39 and 49 m from the existing road bench, and the maximum height of valley side slope affected due to landslide was around 25 m. In this location, the existing valley slope angle varies from 60 to 70° with horizontal. Along this stretch, the narrow gauge railway line is at some height above the existing road level on the hill slope side. At this location, some kind of valley side slope restoration work with “stone filled Gabion box retaining walls” was done initially by state PWD, and this restoration work was destabilized in subsequent year’s heavy monsoon. The earlier condition of the valley side slope was at the “Tindharia III” location which is reflected in the Fig. 11.4.

The vegetation is present at all the above said locations of “Tindharia” area other than the slide portions of valley side slopes. The longitudinal surface drain is also present at toe of the hill slope on RHS at all the landslide affected locations in and around “Tindharia”.

The initial part of the paper presents the study comprising engineering investigations, design analysis, and restoration proposals which was made under preparation of “detailed project report (DPR)” during 2015–16 for the project client, namely “Ministry of Road Transport and Highways (MORT&H), Government of India” based on the prevailing site conditions of the landslide affected valley slope of moderate height of 30–34 m designated here as “Tindharia I”. The design confirmation work based on the latest site topographical conditions and actual rehabilitation work which

Fig. 11.4 Conditions of valley slope at “Tindharia III”



were finally undertaken by the contractor during the period from 2017 to 2020 for the landslide affected valley slope of “Tindharia I” are described here in the later part of the paper.

Probable Reasons of Occurrence of Landslide

The probable reasons of occurrence of landslide in this stretch of road at “Tindharia I (km 50 + 155 to km 50 + 187)” may be classified into following fundamental factors.

Earthquake

The main central thrust (MCT) and the main boundary thrust (MBT) are the major structural discontinuities which could be considered as the potential sources of earthquake activity in the Teesta region which is close vicinity of the project area. The areas where the transverse or oblique faults intersect the MBT or the MCT are in general the areas of high seismicity. Earthquake activities of Darjeeling Himalayas are relatively high to the north of the main boundary thrust (MBT). Activities decrease progressively southward from lesser Himalayas to the fore deep region, under the sedimentary cover.

There are tension cracks which were generated due to the repeated occurrences of seismic activities earlier to 2011 in the project area as this is located in seismic “Zone IV”. Subsequent to the earthquake of moment magnitude 6.9 (i.e., $M_w = 6.9$) in 2011 September in nearby area along the border Nepal and Indian state of Sikkim, the earlier generated tension cracks were widened and the new cracks were

also developed along this stretch of project road due to the heavy shaking caused by seismic waves.

Rainfall

The amount of rainfall plays a very important role in causing instability of slopes. A very high intensity of rainfall within a short span of time is not uncommon in Darjeeling hill areas. In respect of landslide hazards, the duration of rainfall is very important. Long duration along with heavy down pour may cause deeper infiltration and overland flow, which ultimately may result into the occurrence of landslides on weaker slopes. The records show some of the long continued down pours. Among them the most remembered ones are in 1787, 1789, 1827 (493 mm in one day), and in June 1950 (965 mm). The last such rainfall recorded during 1968 (October 2 and 5—about 1780 mm). Thereafter, 358 mm in October 1973, 382 mm in June 1983, 457 mm in September 1986, and 350 mm in 1990 were recorded.

Heavy rainfall subsequent to the occurrence of earthquake in September 2011 increased the pore water pressure and seepage force, promoted surface erosion, and reduced the shear resistance of slope forming mass which was loosened earlier due to earthquake shaking.

Poor Drainage

The landslide affected stretch of the project road was in the curve. The rainwater of this entire stretch was collected in the existing side drain and was discharged in the nearby culvert. However, due to choking of the side drain and stretch being in curve, the entire rainwater started accumulating in and around curved portion and overflowed to the valley side resulting severe surface erosion. Further, the water entered through the cracks developed during earthquake caused significant increase in hydrostatic pressures in the valley slope. These collectively increased the shear stress of the slope and resulted collapsing of slope on valley side of existing road.

Material Condition of Valley Slope

Generally, the slope is made of loose unconsolidated material and covered by thin unconsolidated scree deposits at “Tindharia” area. Weathered and fractured rock with unfavorable joints allowed rainwater to percolate inside and building up excess pore water pressure and reduced the shear strength along the joint planes. The slope geometry was quite unfavorable as the existing natural slope was steep and its height was moderately high (average height ~50 m).

Investigations of Landslide Affected Area

Following various engineering investigations were carried out to prepare the detailed restoration proposal for the landside affected location of “Tindharia I”.

Topographical Survey

A detailed topographical survey was carried out at the affected stretch of NH 55, viz. from km 50 + 155 to km 50 + 187 at “Tindharia I”. Main topographic attributes were generated based on digital terrain model (DTM) including preparation of the “contour maps”, “plan”, and “cross sections” covering hill and valley slope details at frequent intervals along the affected stretches at “Tindharia I”.

Geological Investigations

The geological and geotechnical investigations were undertaken along the landslide affected stretch at “Tindharia I”.

Regional Geology. The geology of Darjeeling and Sikkim is varied and complex than the rest of the Himalayan terrain. The intense tectonic activity experienced during Himalayan orogeny has left their impressions on rocks in the form of intricate folds, faults, and thrusts. The rocks between the foothills and Tethys Himalaya consist of several different groups, ranging in age from Pre-Cambrian to recent and include rocks of all the three genetic groups, namely igneous, sedimentary, and metamorphic. The tectonic units of Darjeeling and Sikkim Himalaya occur in a reverse order of stratigraphic superposition by Siwaliks in the south, followed by thrust sheets of Gondwana, Buxa, Dalings, and Darjeeling group, etc., toward north. The contact between different groups is marked by thrusts dipping at high angle toward north. The Daling group occupies the large area of Teesta valley and forms a dome below the Darjeeling gneiss. The most important main tectonic unit is the E–W trending north dipping thrust called main boundary thrust (MBT) which crosses the main river Teesta near “Kalijhora Township”.

Geology of Project Area. The project area is occupied by “Daling group”. The groups of rocks are represented by chlorite schists, slaty quartzite, quartzite, etc. The most important formation of Daling group of rock is observed in this area—Reyang Formation comprising graywacke type of slaty quartzite, moderately hard, and massive. Three generations of folding are discernible in this rock group. The older planar structure is bedding schistosity (S1) cofolded with quartzite interbeds into tight isoclinal fold (F1), and second generation (F2) folds are tight overturned structures of recline type. The last generation of fold is open and broad controlling

the topography. The foliation strike of rock swings from NE-SW with dip varying from 35° to 65° toward NW to north; major joint sets in rocks are given below:

- (i) N–S strike with 30° dip toward west
- (ii) NE–SW strike with 65° dip toward SE
- (iii) Foliation joint with very close spaced varies from 5 to 10 mm.

Geotechnical Investigations

A comprehensive geotechnical exploration work covering detailed field and laboratory investigation was carried out at the landslide affected stretch of “Tindharia I” in between km 50 + 155 and km 50 + 187 for doing the engineering characterization and assessment of the subsurface conditions there. Totally, three numbers of boreholes, namely BH-1A, BH-2A, and BH-3A of depth varying from 30.00 to 45.00 m, were conducted during October to November 2013 along the valley slope. The borehole “BH-1A” was close to the toe of the affected part of valley slope, and the borehole “BH-2A” was explored at some intermediate position within the slope which was around 23 m below the existing road bench. The borehole “BH-3A” was conducted at the existing road bench, i.e., at top of the landslide affected valley slope. The field investigation work consisted of soil borings and rock drillings, conducting in-situ tests, collecting and preserving soil, rock and water samples, and field records of the subsurface conditions and special phenomena including position of ground water table (if any). The laboratory testing program covered testing of samples (soil, rock, water) as collected from exploration of site to characterize the geological as well as geotechnical engineering properties. The field and laboratory testing works had been performed as per stipulations of latest version of relevant of “Bureau of Indian Standards (BIS)”.

Ground water table (GWT). The “ground water table” was not recorded in none of the boreholes drilled during the investigation along the affected valley slope at “Tindharia I”. However, for designing the restoration measures of landslide affected valley slope, the water table was considered at exposed surface of valley slope anticipating the fluctuations in the measured water levels due to seasonal variation and corresponding to the critical condition which may arise during or immediately after the monsoon in the serviceability life of the restored valley slope.

Subsurface stratifications of affected valley slope. The site-specific subsurface conditions have been characterized based on the data obtained through various field and laboratory tests which were conducted under geotechnical investigation works. The subsurface layer profile consisted of following four numbers of strata as found through the investigation at the affected stretch of “Tindharia I (km 50 + 155 to km 50 + 187)”.

- Layer I: Filled Up Soil of variable thickness, i.e., 1.95–4.55 m
- Layer II: Completely Weathered Rock of thickness 7.45 m

- Layer III: Completely Weathered Coal Band of thickness 4.95 m
- Layer IV: Completely to Highly Weathered Fractured Rock of variable thickness, 18.00–37.50 m.

The presence of various subsurface layers and its thickness including the range of engineering properties as explored, namely field SPT (N) values (blows/300 mm penetration), type of soil and rock, total core recovery (TCR), rock quality designation (RQD), rock crushing strength, rock mass rating (RMR), and the class of rock layers as per its RMR along the valley slope at “Tindharia I” is given below in Table 11.1.

From the above table of engineering properties of subsurface layers, it can be noted that there are “Filled up Soil” at top of all the boreholes with highest thickness in case of the borehole, namely “BH-1A” at the toe of affected valley slope, where the slipped materials were accumulated during landslide. The layer of “Completely Weathered Rock” which is basically the “Residual Soil” found in dense condition only at the borehole, namely “BH-1A” below the deposition of top layer of “Filled up Soil”. There is presence of 4.95-m-thick completely weathered layer of “coal” as found in between the layer of “Completely to Highly Weathered Fractured Sandstone” only in borehole, namely “BH-3A” which was explored at top of road bench affected due to landslide. The bottom most explored layer is “Completely to Highly Weathered Fractured Sandstone” which was found in all the three nos. of boreholes, and the quality of this layer is poor to very poor rock mass as per the RMR based on rock mass classification (Bieniawski 1989) [1] given in IS 13365 (Part 1):1998 (Reaffirmed 2021) [1].

Material Investigations

Material investigations were carried out to find the suitability and availability of different construction materials like “riverbed material (RBM)”, sand, aggregates, and stone dust to be used in the proposed restoration scheme. The relevant laboratory tests for various engineering parameters like grain size analysis, Atterberg’s limits (LL, PL, and PI), CBR test, compaction tests, and relative density tests were conducted for different materials as identified from the related sources. Shear strength tests parameters (i.e., cohesion, c , and angle of shearing resistance, i.e., ϕ) for “RBM” material samples are determined from “Direct Shear Test” using large-size shear box as per the relevant BIS guideline. Table 11.2 summarizes the results of various laboratory tests as conducted for the selected construction materials used for restoration work.

The “riverbed materials (RBM)” were used for the selected reinforced backfill in the rebuilding of the landslide affected valley at “Tindharia I”.

Table 11.1 Range of engineering properties of subsurface of valley slope at “Tindharia I”

Borehole no	Thickness of layer (m)		SPT (N)	Type of soil (as per IS)/rock	TCR (%)	RQD (%)	Rock crushing strength (ton/m ²)	Rock mass rating (RMR)	Class of rock as per RMR
	From	To							
Layer I: filled up soil (2.00–4.50 m)									
BH-1A	0.00	4.55	–	–	–	–	–	–	–
BH-2A	0.00	2.00	–	–	–	–	–	–	–
BH-3A	0.00	1.95	–	–	–	–	–	–	–
Layer II: completely weathered rock (7.45 m)									
BH-1A	4.55	12.00	34–40	SP-SM/ML-CL	0	0	–	–	–
Layer III: completely weathered coal band (4.95 m)									
BH-3A	21.00	25.95	18–24	SP-SW	0	0	–	–	–
Layer IV: completely to highly weathered fractured rock (18.00 to 37.50 m)									
BH-1A	12.00	30.00	> 100	Sandstone	5	0	^a 500–700	20–25	Poor to very poor rock
BH-2A	2.00	39.55	> 100		17–22	0			
BH-3A	1.95	21.00	> 100		13–20	0			
	25.95	45.00	> 100		15	0			

^aEquivalent rock crushing strength based on “point load index (PLI) strength” test results of the rock core samples

Table 11.2 Range of engineering properties of construction fill materials used at “Tindharia I”

Location	Description of material	Compaction test		Relative density test	Shear strength parameters tested at OMC and 95% MDD for “RBM” // On remolded sample compacted at 80% of “maximum dry density” for “sand”	
		MDD (t/m ³)	OMC (%)	Maximum/minimum dry density (t/m ³)	<i>c</i> (t/m ²)	ϕ (deg)
<i>Riverbed materials (RBM)</i>						
Dudhia (Mirik)	Gray non-plastic (NP) sand with gravels and little fines	2.16	6.60	–	2.3	47
Matigara (Balason river)		2.13	6.75	–	2.7	39
Champasari (Mahananda river)		2.08	7.00	–	4.3	36.5
<i>River sand</i>						
Matigara (Balason river)	Gray sand with gravels	–	–	1.885/1.566	0.0	35

Hydrological Investigations

Hydrological investigations were carried out to identify the existing streams, tributary and drainage path, to study the drainage requirement, to determine the drainage pattern and paths, and also to channelize the flow on the downstream side for the erosion protection of slope. Based on the hydrological survey, additional surface and subsurface drains and new proposed culverts (if any) along with its protection on the downstream valley slope side were suggested.

Design of Restoration for Landslide Affected Valley Slope

The detailed cross section comprising hill and valley side slopes including the intermediate road bench, properties of proposed newly added fill material as identified, and lastly the subsurface stratifications along the slopes are basic input parameters to carry out the analysis and design for assessing the behavior and performance of the proposed slope restoration during construction and service life. The subsurface

Table 11.3 Engineering properties of selected fill materials used at “Tindharia I”

Type of fill material	Description of material	Bulk unit weight, i.e., γ_b (t/m^3)	Shear strength parameters	
			c (t/m^2)	ϕ (deg)
Riverbed material (RBM)	Gray sand with gravels and fines	2.10	0	34

properties along the affected stretch at “Tindharia I” were based on the information obtained through specific boreholes in the particular location.

Proposed Slope Geometry

The geometry of the proposed slope included the finished road top width of 12.00 m at “Tindharia I” in between 50 + 155 km and 50 + 187 km. The total height of proposed restoration considered at design stage (2015) was 30.00 m for the location of “Tindharia I”. It consists of total three tiers of steep slope having angle of 65° to horizontal along with 3.00-m-wide intermediate horizontal berm at every 10.00 m intervals in between 50 + 155 km and 50 + 187 km. Considering the scarcity of suitable non-plastic frictional granular fill material in the hills, a slim section for the newly added part of the rebuilding of valley slope has been adopted there at “Tindharia I”.

Engineering Properties of Fill Material

The engineering properties for the selected reinforced fill material are furnished in the Table 11.3. All the material properties as considered are based on the test results of the collected samples from the identified nearby identified borrow area sources namely “Dudhia Lower” and “Matigara” both from “Balason River” and “Champasari” from “Mahananda River”.

Geotechnical Engineering Parameters for Subsurface Stratifications

The geotechnical engineering parameters for the subsurface stratifications of the affected valley slope at “Tindharia I” as considered in analysis and design of the proposed restoration work are indicated in Table 11.4.

Table 11.4 Geotechnical engineering parameters of subsurface stratifications along the affected valley slope at “Tindharia I”

Layer no.	Description of layers	Thickness of layers (m)	Bulk unit weight, i.e., γ_b (t/m^3)	Shear strength parameters	
				c (t/m^2)	ϕ (deg)
I	Filled up soil	2.00–4.50	1.80	0	32
II	Completely weathered rock	7.45	1.80	5	29
III	Completely weathered coal band	4.95	1.80	0	24
IV	Completely to highly weathered fractured rock	18.00–37.50	2.10	10	29

The geotechnical design parameters of the various subsurface layers of soils and rocks as mentioned above were selected based on local geology and also using the available site investigation results with an effort to simulate the site condition applying past experience and engineering judgment corresponding to critical conditions of valley slope.

Design Analysis of Restoration Works

The design of restoration works for the affected valley side slope consisted of doing the slope stability analysis by considering total height of slope including the valley as well as hill side with due satisfaction of adequate factor of safety against all possible modes of failure in static and seismic conditions. The relevant FHWA [2, 3], BS [4], and IRC codes [5, 6] and guidelines given under “Section 3100 and 3200 of MORT&H technical Specifications, Fifth Revision, 2013” [7] on “reinforced soil slope” including “soil nailing” were followed while doing the design of hybrid slope considering the provisions of steel reinforcement nailing in the existing slope portion and also by using polymeric reinforcement in the newly added multi-tiered soil mass for the valley side.

Slope stability analysis. At DPR stage, the “limit equilibrium method (LEM)” of slope stability analysis was carried out using “Bishop’s modified method” against “rotational” mode of failure along the potential slip circles in accordance with IRC-75 [5] on effective stress concept considering the maximum height of the slopes for the particular zone to assess the global stability (slope, toe, and base) of the slopes. The “translational” mode of slope failure was also analyzed by using “two wedge method of analysis” as per “simplified methods of Spencer”. The “Seismic Zone IV” was considered in design of restoration work at “Tindharia” along NH 55 in West

Table 11.5 Summary of slope stability analysis of “existing slope” at “Tindharia I”

Maximum height of valley slope (m)	Top width of existing road (m)	Mode of failure analyzed	Values of pore water pressure coefficient, i.e., r_u	Factor of safety for slope stability		Remarks
				Static	Seismic	
30	5.00	Rotational	~0.50	0.96	0.75	Unsafe

Bengal. The slope stability was checked considering pore water pressure coefficient, i.e., r_u as 0.50. The slope stability was also checked considering water table along the existing slope. As per FHWA document no FHWA-NHI-10-025 [3], the minimum “factor of safety (FOS)” was kept as 1.30 in static condition and 1.0 in seismic condition. The “limit equilibrium method (LEM)” of slope stability analysis was carried out using the software, namely “RESSA (Version 3.00)” (developed by M/s. Adama Inc., USA and recommended by FHWA, USA). The “traffic load”, i.e., “live load surcharge” over the existing intermediate road bench was considered as 2.50 ton/m². The minimum “factor of safety (FOS)” obtained from slope stability analysis for “existing slope” as it was present after the occurrence of landslide at “Tindharia I”, i.e., the stretch in between km 50 + 155 and km 50 + 187 is summarized in Table 11.5.

From the above table, it can be noted that in the stretch from km 50 + 155 to 50 + 187, the FOS in slope stability under static and seismic conditions was found as 0.96 and 0.75, respectively. So, the existing slope at the landslide affected area of “Tindharia I” was found unsafe in stability both under static and seismic conditions.

Since the existing road was proposed to be widened in stretches from 50 + 155 km to 50 + 187 km at “Tindharia I”, the stability analysis was carried out considering the proposed widening. To keep the proposed steep slope of valley side stable, multiple layers of required grade of polymeric reinforcement at designed vertical spacing were suggested inside the newly widened part of valley slope mass. The proposed reinforcement inside the added valley side fill helped in increasing the stability of new slope. The results of stability analysis of widening part of valley slope with only the layers of polymeric reinforcement and no provisions of reinforcement in existing slope are presented in Table 11.6.

The results of analysis for the steep valley slope only with polymeric reinforcement show that the FOS in slope stability (both in rotational and translational modes) for the condition of water saturation line along the existing slope and also for the condition of pore pressure coefficient ‘ r_u ’ as 0.50 was less than 1.30 in static and 1.00 in seismic conditions. Hence, the proposed section only with polymeric reinforcement was found unsafe in slope stability (both in rotational and translational modes) under static as well as seismic conditions.

To keep the new valley side slope stable, steel nailing was proposed in the existing slope along with fill soil reinforcement in the form of polymeric reinforcement inside the proposed widened part of slope. The provisions of soil nailing in the existing slope mass helped in the following ways.

Table 11.6 Summary of slope stability analysis of “proposed slope” made only with polymeric reinforcement at “Tindharia I”

Maximum height of valley slope (m)	Angle of valley slope with horizontal (deg)	Top width of finished road (m)	Mode of failure analyzed	Values of pore water pressure coefficient, i.e., r_u	Factor of safety in slope stability		Remarks
					Static	Seismic	
30	65	12.00	Rotational	~0.50	1.04	0.89	Unsafe
				Water saturation line along existing slope	0.89	0.76	
			Translational	~0.50	1.45	1.22	Marginally safe
				Water saturation line along existing slope	1.09	1.11	

- Increasing the stability within the existing slope after adding the newly proposed selected fill over existing slope
- Integrating the proposed slope with the existing slope for getting the enhanced stability of the newly added reinforced valley slope.

The results of stability analysis of widening part of valley slope with polymeric reinforcement in the newly added selected fill and also with soil nailing within the existing slope behind the newly added valley slope are presented in Table 11.7.

The results of analysis of the valley slope with proposed polymeric reinforcement and steel nails show that the FOS in rotational stability for the condition of pore pressure coefficient ' r_u ' as 0.50 was greater than 1.30 in static and 1.10 in seismic condition. Hence, the proposed model was found safe in rotational mode of slope stability both in static and seismic conditions. The slope stability was also checked considering water table along the existing slope which signifies the exceptionally worst condition; even in such scenario, the FOS was found as more than 1.20 and 1.00, respectively, under static and seismic conditions. Again, the valley slope was checked for its translational stability and FOS in that analysis was found as greater than 1.30 in static and 1.0 in seismic conditions. Hence, the proposed model was also found safe against translational mode of failure.

Design of soil nailing including its facia. The design of soil nailing and its facing as proposed for strengthening of the existing valley slope mass of landslide affected stretch at “Tindharia I” was done following the guidelines as given in FHWA publication, namely FHWA-0-IF-013-017 [2]. The following checks were done under design of proposed “drilled and grouted steel nail”.

Table 11.7 Summary of slope stability analysis of “proposed slope” made with “polymeric reinforcement” and “soil nailing” in “existing slope” at “Tindharia I”

Maximum height of valley slope (m)	Angle of valley slope with horizontal (deg)	Top width of finished road (m)	Mode of failure analyzed	Values of pore water pressure coefficient, i.e., r_u	Factor of safety in slope stability		Remarks	
					Static	Seismic		
30	65	12.00	Rotational	~0.50	1.30	1.10	Safe	
				Water saturation line along existing slope	1.21	1.00		
			Translational	~0.50	1.75	1.42		Safe
				Water saturation line along existing slope	1.57	1.35		

Tensile capacity. The maximum required tensile capacity for the steel nails as found through the “stability analysis” was 200 kN which was duly satisfied corresponding to the “factor of safety (FOS)” of 1.80 by proposing the 28 mm diameter of HYSD steel bar having minimum yield strength of 650 Mpa at the required vertical and horizontal spacing all along the exposed surface of the affected valley slope.

Pull-out capacity. The maximum tensile force of 200 kN as estimated for the steel nails through the “stability analysis” was duly satisfied corresponding to “allowable pull-out capacity” which was found by applying the “factor of safety (FOS)” of 2.0 over the “ultimate pull-out capacity” of the recommended 28 mm diameter HYSD steel reinforcement nail having the desired effective length of anchorage beyond the failure wedge.

Facia of steel nail. The facing of the steel nail was recommended to have the “metal bearing plate” of size of 200 mm × 200 mm having thickness of 20 mm, and the bearing plate was proposed to be placed over the prepared base at the projected head of the steel nail. The head of the nail was proposed to be tightened with steel nut and washer and also to have the adequate arrangement to properly connect the polymeric reinforcement proposed to be used for the newly added valley side fill.

Design Recommendations on Restoration Work as Per DPR

The proposed restoration work for the landslide affected valley slope at “Tindharia I” (km 50 + 155 to km 50 + 187) consisted of the following major items.

Reinforced slope of newly added fill. The multi-tier (three nos.) reinforced slope having angle of 65° to horizontal with 3.00 m horizontal berm at every 10.00 m intervals was proposed for the total 30-m-high newly added valley side fill at “Tindharia I”. The steep slopes of 65° at all the tiers were proposed to be constructed with suitable type of polymeric reinforcement (geogrid/geostrap/geostrip) of minimum 10.00 m length at vertical spacing of 0.500 m c/c and having minimum “long-term design strength (LTDS)” as 100 kN. The proposed polymeric reinforcements were to be satisfied the requirement given in “Clause 3103.7 under Section 3100 of MORT&H Technical Specification, Fifth Revision, 2013” [7]. The reinforcements were to be connected to steel mesh facing with mechanical/positive connector as per the guidelines given in “Clause No. 3107.4 under Section 3100 of MORT&H Technical Specification, Fifth Revision, 2013” [7]. Minimum 0.500-m-thick hard facing of boulder filling with outer protection by hard steel mesh facing was proposed. This steel mesh facing was to be protected with erosion control mat. Reinforced soil slope systems consisted of planar reinforcements arranged in nearly horizontal planes in the reinforced fill to resist outward movement of the reinforced fill mass. Facing treatments were applied to prevent unraveling and sloughing off the face. The polymeric reinforcements helped in increasing the stability of the newly added slope. The multi-tier slope was adopted to keep the newly added portion of valley restoration measure thinner by following the shape of existing slope. Since the project area falls in “Seismic Zone IV”, so flexible structure like reinforced soil slope was proposed for the valley slope restoration.

Nailing of existing valley slope. The adopted slim section resulted in less length of polymeric reinforcement than normally required for the heavier thick section. To make the slim section stable against all different modes of failures, the soil nailing was suggested to be done into the existing slope. Soil nailing consisted of the passive reinforcement (i.e., no post-tensioning) of existing ground by installing closely spaced steel bars (i.e., nails) which were subsequently encased in grout. Soil nailing helped in increasing the stability of the entire valley slope globally, and it also helped in integrating the newly built-up slope with the existing slope. The analysis of failure modes, initial design consideration, and other design considerations for the soil nailing as given under relevant clauses of “Section 3200 of MORT&H Technical Specification, Fifth Revision, 2013” [7] was followed. Minimum 28 mm diameter HYSD steel reinforcement bars having minimum yield tensile strength of 650 MPa (i.e., minimum ultimate strength 750 MPa) and length of 15 m and 20 m, respectively, for the top one tier and remaining all the bottom tiers of newly added valley slope were recommended. The steel reinforcement nails were proposed to be provided at vertical and horizontal spacing of 2.00 m and 1.00 m c/c, respectively, and at an angle of 10° with horizontal in downward direction all along the exposed surface of the weathered rock present at the affected valley slope at “Tindharia I”. The proposed steel nails for the existing slope were to be connected mechanically to the polymeric reinforcement of the newly added slope so that the tensile force generated within the fill reinforcement can be fully transferred to the steel nails during any sign of outward movement of the valley slope.

Chimney drains at interface of existing and widened valley slope. Subsurface drainage arrangement in the form of “chimney drain” was proposed for draining out of the entrapped seepage water from the existing slope at the back of newly added slope. Chimney drain was to be of 600 mm thickness and should be consisted of stone or gravels of size 20–40 mm and covered with layer of non-woven geotextile filter fabric. Finally, these chimney drains were to be connected by 160 gsm non-woven geotextile filter fabric of “Type I grade (severe installation condition)”, as mentioned in “Section 700 of MORT&H Technical Specification, Fifth Revision, 2013” [7], wrapped perforated PVC pipes to drain water toward outside of the slope. The draining out of seepage water from the existing slope mass would help in reduction of pore water pressure inside the slope which was resulted in enhanced stability of entire slope.

Erosion control measures. To prevent the erosion, the “Gabion” mattress was proposed below toe of the reinforced slope for a length of 25.00 m. Gabion mattresses were to be wire mesh boxes of 0.30 m height filled with materials of boulder size. At the end of above said 0.300-m-thick “Gabion mattress”, one “erosion control mat” was also recommended below the toe of proposed restoration work of reinforced valley slope to prevent the erosion of the slope at its bottom part. Erosion control mat was also suggested all along the outer surface of newly added reinforced slope. Erosion control mats are made up of naturally available materials like coir/jute. Natural vegetation would be encouraged on the erosion control mats with seeding of plants.

Sealing of tension cracks. Tension cracks were found present at the existing road bench level and also above of it due to the occurrences of landslides along the stretch of “Tindharia I”. These were produced due to strains caused by the incipient mass movements and were thus indicators of impending instability. Cracks had been observed with widths ranging from a few millimeters to as much as few centimeters or more. These open cracks served as a direct path for infiltration of surface runoff water, enabling it to reach deep into the slope mass, thereby further decreasing the “factor of safety (FOS)” in stability of the slope. It was, therefore, important to seal tension cracks effectively to prevent any ingress of water. As part of the remedial measures against any future instability, the tension cracks were to be sealed as per the guidelines given in “Clause No. 11.7.5 of IRC SP: 48-1998” [8].

The above stated different items of restoration work for the landslide affected valley slope at “Tindharia I” as recommended during DPR stage in 2015–16 are shown in “Fig. 11.5”.

Design Confirmation at Construction Stage

The restoration work for the landslide affected valley slope was done by the project contractor during the period 2017–2020, and the maximum design height of rehabilitations was considered as 34.023 m there along the stretch in between the 50 +

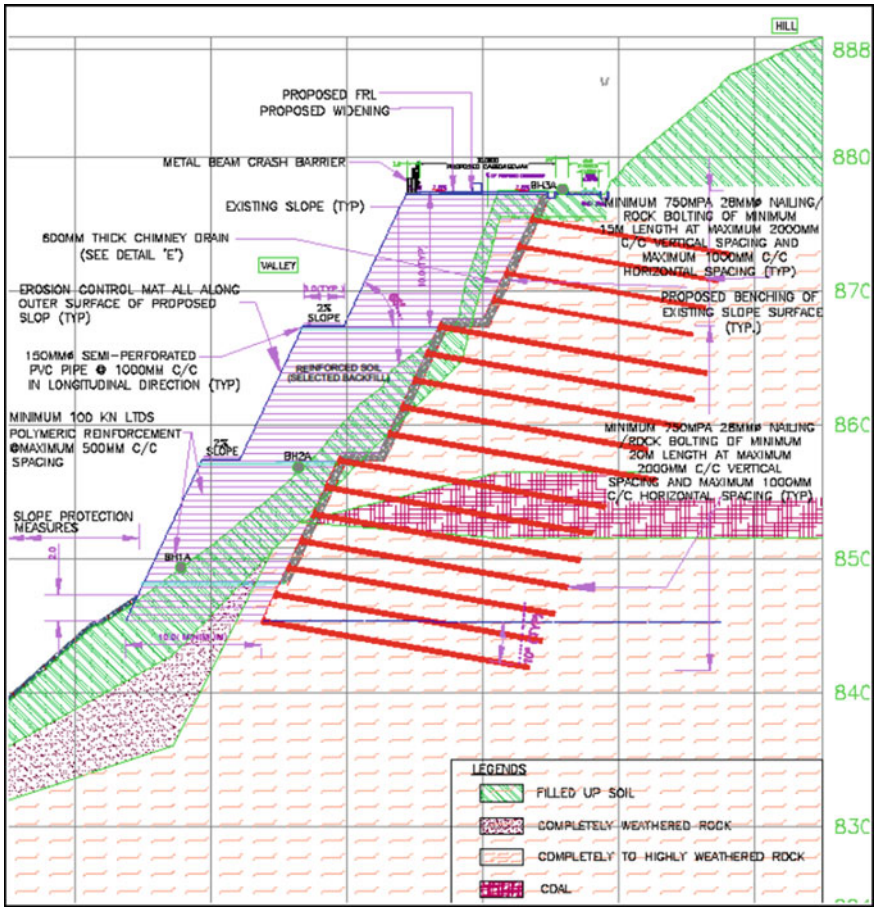


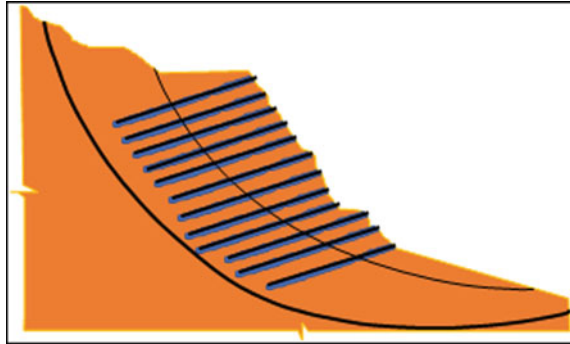
Fig. 11.5 Restoration measures for landslide affected valley slope at “Tindharia I” as per DPR

155 km and 50 + 187 km at “Tindharia I” based on the latest topography of the area. The design recommendations of restoration work for the affected valley slope as given by the consultant based on the detailed study undertaken in DPR stage during 2015–2016 were duly verified and confirmed by the specialized contractor at the time of actual execution.

Design Analysis of Existing Valley Slope Reinforced with Steel Nails

The design aim was to arrive at a soil nailing layout to ensure stability during construction. Additionally, each nail should be capable of resisting local stresses acting on

Fig. 11.6 Typical failure surface of analysis using the steel nails in existing slope.
Courtesy M/s. Reinforced Earth India Pvt. Ltd



it. The relevant mode of failure for stability analysis was rotational failure either partially or totally through the soil nail block involving breakage and/or pull-out of soil nails. The method adopted for the purpose of assessing failure mechanism was “limit equilibrium method (LEM)” of slope stability analysis using “Bishop’s modified method”. Typical failure modes are shown in Fig. 11.6. The soil nail and hot dip galvanized welded mesh (TerraNail[®]) provides complete resistance against anticipated sliding from the back of slope, offers significant contribution to global and surface stability, and hence, later transferred no retained pressure to reinforced soil (TerraLink[®]) structure. The minimum factor of safety (FOS) for the maximum restored height of 34.023 m of existing slope using the pattern of nails as proposed in DPR was found as 1.47 under “static” condition with due considerations of critical position of water table.

Design Analysis of Reinforced Earth[®] Composite Slope Structure

Since the maximum total height of valley slope restoration was 34.023 m, so total four tiers of “reinforced earth composite structure” comprised of 10 m height of first three tiers from the top of existing road bench, and then remaining 4.023 m height of bottom most tier was adopted at site. The reinforced earth composite structure had been designed in two stages, the internal checks of reinforced soil structure for calculating the required soil reinforcement including checks for the soil nails against both tension and pull-out and external checks by “rotational stability” method. The tension in the soil reinforcement had been calculated by internal stability analysis by considering the effect of inclination and the skin friction and validated by finite element modeling (FEM). The overall stability was then checked by “rotational stability method” under “limit equilibrium method (LEM)” of slope stability analysis for both static and seismic load conditions. The minimum factor of safety (FOS) in “slope stability analysis” through LEM approach for the maximum height of slope having the design recommendations of the soil reinforcement and steel nailing as

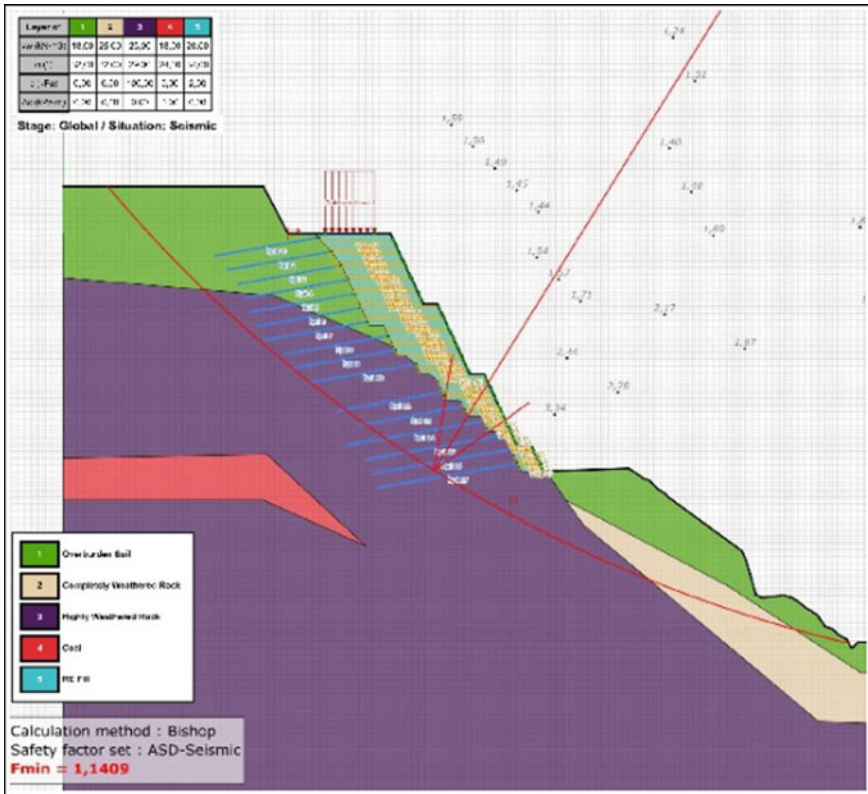


Fig. 11.7 Typical failure surface of analysis for “reinforced earth composite slope” at “Tindharia I”. *Courtesy M/s. Reinforced Earth India Pvt. Ltd*

given in DPR was found as 1.37 and 1.14 under “static” and “seismic” conditions, respectively, with due considerations of critical position of water table in the slope. The typical failure surface in the “slope stability analysis” for the “reinforced earth composite slope structure” under the “seismic condition” is shown in Fig. 11.7.

The typical detailed cross section of the maximum height of rehabilitated valley slope at “Tindharia I” is presented here in Fig. 11.8.

Sequences of Restoration Work of Valley Slope at Tindharia I

There were several challenges faced during construction stage which includes surface and subsurface drainage, safety and traffic management during construction, space constrain, absence of any access road, difficulties in drilling through challenging

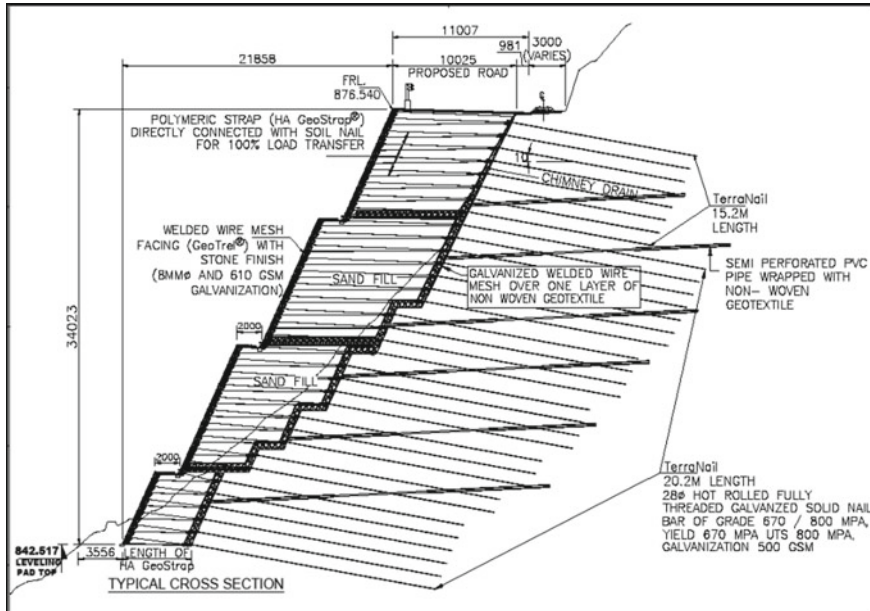


Fig. 11.8 Typical detailed cross section of maximum restored height of valley slope at “Tindharia I”. Courtesy M/s. Reinforced Earth India Pvt. Ltd

completely to highly weathered rocky strata, and presence of seasonal water table. Suitable construction method has been adopted to overcome all these challenges.

The construction sequences of the proposed restoration work as followed at site of Tindharia I” are given below.

Stabilization of Existing Slope Using Nails by Top-Down Construction

The unstable existing valley slope had been stabilized by installing “steel nails” at designed vertical and horizontal spacing. The installation of nails was done by adopting top-down drilling more specifically down the hole (DTH) method from the hanging platform keeping in mind the safety of the workers during construction and safety of the running traffic on top. Since at the start of construction, there was no approach road available, the surface cleaning was done manually by hanging from top, and then drilling activity was started at 3 m level from top. It was extremely challenging due to the presence of loose stone, boulders, and overburden fill material at top 5–10 m depth. Several methods had been adopted to overcome the challenges. The two common methods adopted were using steel casing to prevent collapsing of soil or consolidation grouting for stabilization of drill hole. The presence of water

Fig. 11.9 Activity of surface cleaning, drilling, and fixing of welded wire back mesh simultaneously with soil nailing of existing valley slope at “Tindharia I”.
Courtesy M/s. Reinforced Earth India Pvt. Ltd



Fig. 11.10 Drilling and installation of soil nail by top-down method at existing valley slope “Tindharia I”.
Courtesy M/s. Reinforced Earth India Pvt. Ltd



table and high pore pressure also made the situation worse during drilling activity. The face of the cut slope was protected by fixing galvanized welded wire mesh underlying with a layer of non-woven polypropylene geotextile filter simultaneously with soil nailing activity. This ensures stability of the slope and face during construction. Figures 11.9 and 11.10 show the above stated activities of existing slope stabilization using the steel nails.

Installation of Semi-perforated Drainage Pipes Inside of Existing Slope

The water table was stabilized by installing 75 mm diameter perforated pipes deep inside the soil (15–20 m) by drilling at different level. The perforated pipes were

Fig. 11.11 Pull-out test on the steel nailing of existing valley slope. *Courtesy M/s. Reinforced Earth India Pvt. Ltd*



installed after completion of all grouting activity for the soil nails above the respective pipe levels. This was to ensure that the pipe perforation should not get blocked during grouting activity. The installation of these perforated pipes helped in release of excess hydrostatic pressure.

Pull-Out Test of Nails

Total three pull-out tests were conducted on the sacrificial steel nails at different depth to validate the bond strength considered in design. The test was terminated after reaching the bond strength of 200 kPa as considered in the design of nail. The result was found satisfactory as no displacement noticed during the test. The typical “pull-out test” in progress for the steel nails is shown in “Fig. 11.11”.

Widening of Valley Slope by Reinforced Earth® Composite Technology (TerraLink®)

The construction of composite “Reinforced Earth®” structure was taken up after completion of soil nailing works, fixing of mesh and foundation base stabilization. The available base width at toe of the structure was less than 2.5 m (Fig. 11.12). The

Fig. 11.12 Base level of TerraLink® structure before start of filling and compaction. *Courtesy M/s. Reinforced Earth India Pvt. Ltd*



construction was a big challenge due to lack of space and difficulty in transportation of materials. By providing the true “mechanical connection system” using high adherence “Geostrap” soil reinforcement between the metal grid facing and the soil nail, it was possibly made to design and construct such large retaining structure on the limited available base width. The riverbed material (RBM) had been used as fill material which is mostly coarse sand, and fine content is less than 10% as it was selected from the nearby sources during the DPR study. The riverbed materials were stored at top and then manually dumped in hopper which slides down through the chute at the base level. The HA GeoStrap® soil reinforcement was then connected directly with the soil nail face and the welded wire mesh facing. The stones were placed behind mesh along with non-woven geotextile. The fill materials were then spread behind stone filled facing and compacted using small baby roller and/or plate compactor. This method of layer-by-layer installation of welded wire mesh, laying of soil reinforcement, placement of boulders with non-woven geotextile, filling, spreading, and compaction of fill material continued till the structure was completed up to the finish level of widened bench of the road.

Quality Control in Restoration Work of Valley Slope

All the relevant quality control laboratory tests for various engineering parameters like gradation, Atterberg’s limits (LL, PL, PI), compaction tests, relative density tests, and shear strength tests parameters (i.e., cohesion, c , and angle of shearing resistance, i.e., ϕ) for the selected borrow fill (RBM) material were conducted as per the relevant BIS guidelines and satisfying the frequency of tests as specified in the “MORT&H Technical Specification, Fifth Revision, 2013” [7]. The density of compacted reinforced fill was also checked in required frequency so that it meets the requirement as per the project specifications. The load testing of the steel nails was

conducted as per guidelines given under “Clause no 3210 of MORT&H Technical Specification, Fifth Revision, 2013” [7] after installation of the designed grade and length of nails.

Summary

This paper discusses the detailed investigation, design philosophy, and construction methodology as undertaken for the restoration of the landslide affected valley slope of moderate height of 30–34 m at “Tindharia I (km 50 + 155 to km 50 + 187)” along the project road of NH55 in the state of West Bengal. The detailed engineering investigations and design of valley slope restoration works in the form of “hybrid reinforced soil structure” by using polymeric reinforcement in the newly added steep multi-tiered valley fill and connecting the fill slope reinforcements with designed grade and length of steel nails, which were proposed to be drilled and grouted inside the existing valley slope, were carried out by following the available guidelines of FHWA [2, 3], BS [4], IRC [5, 6], and “MORT&H Technical Specifications” [7] during the DPR stage in 2015–16 which are described here at the earlier part of the paper. The restoration measures as proposed during DPR also included the provision of adequate surface and subsurface drainage measures, erosion protection measures, and sealing of the surface cracks with suitable filling material as generated due to the occurrence of landslide at the existing road bench and also on the hill slope portion. The confirmation of the DPR design recommendations and subsequent to that the construction of the restoration work as implemented in sequences during the period of 2017–2020 by the project contractor is presented in detailed manner at the later part of the paper. The detailed quality control measures as per the available BIS, IRC [5, 6], and MORT&H [7] guidelines throughout entire rehabilitation works for the landslide affected valley slope at “Tindharia I” were adopted. “Fig. 11.13” shows completed restoration works as undertaken at the landslide affected valley slope of “Tindharia I”. It is to be mentioned that a detailed recommendation on monitoring the behavior of the valley slope structure during its construction and also in post-construction say serviceability period of minimum 3 years by installing various geotechnical instrumentation, namely “slope inclinometer”, “strain gauges”, “earth pressure/load cells”, “piezometers”, and “settlement gauges”, was planned in DPR. In reality, the physical monitoring of valley slope during the restoration work and after its completion was undertaken by using the normal survey equipment at “Tindharia I”. However, till date no deformation of the restored valley slope at “Tindharia I” is observed, and the widened road bench as made in rehabilitation works is serving well for the local inhabitants and plying traffic along NH 55 in West Bengal.



Fig. 11.13 Completed restoration work for valley slope at “Tindharia I” on NH55 (Courtesy: M/s. Reinforced Earth India Pvt. Ltd)

Acknowledgements The authors thank senior managements, entire team of engineers of M/s. LEA Associates South Asia Pvt. Ltd. (LASA), New Delhi, India (A LEA Group Company, Toronto, Canada), and M/s. Reinforced Earth India Pvt. Ltd, New Delhi, India (A Terre Armée Group Company, France), for providing the support and encouragement in preparation of the paper.

References

1. IS 13365 Part 1: 1998 (Reaffirmed 2021) Indian standard quantitative classification systems of rock mass-guidelines, Part 1 Rock mass rating (RMR) for predicting engineering properties, Bureau of Indian Standards, Government of India, New Delhi
2. FHWA0-IF-03-017, Geotechnical engineering circular no. 7. Soil nail walls, Federal Highway Administration, U.S. Department of Transportation, March 2003
3. FHWA-NHI-10-025: FHWA GEC 011, Design and construction of mechanically stabilized earth walls and reinforced soil slopes, vol II, November 2009
4. BS 8006-Part 1: 2010, Code of practice for strengthened/reinforced soils and other fills
5. IRC 75: 2015, Guidelines for the design of high embankments, Indian road congress (IRC), Ministry of Road Transport and Highways (MORT&H), Government of India
6. IRC:SP:102-2014, Guidelines for design and construction of reinforced soil walls, Indian Road Congress (IRC), Ministry of Road Transport and Highways (MORT&H), Government of India
7. Specification of road and bridge works, Indian road congress (IRC), Ministry of Road Transport and Highways (MORT&H), Government of India, Fifth Revision, 2013
8. IRC:SP:48-1998, Hill road manual, Indian Road Congress (IRC), Ministry of Road Transport and Highways (MORT&H), Government of India

Chapter 12

Effect of Hysteretic SWCC on Marappalam Rainfall-Triggered Slope Failure



Nallabothula Mounika , Ammavajjala Sessa Sai Raghuram ,
B. Munwar Basha , and Arif Ali Baig Moghal 

Introduction

Rainfall-triggered slope failures are the most common natural hazards across the world and cause significant damage to the infrastructure. The main cause of these slope failures is attributed to the rapid infiltration of rainwater and an increase in positive pore water pressure (PWP) within the soil. The failure surface of these slopes may lie in the unsaturated zone. The behavior of soil in the unsaturated zones depends upon the soil water characteristics curve (SWCC). The relation between soil water content and soil suction is given by SWCC. Limit equilibrium (LE) methods are more commonly used tools for analyzing slope stability. The conventional slope stability methods assume that PWP is either positive or zero along the failure surface. The water content along critical slip surface and within a slope usually varies under rainfall conditions. Even the negative PWPs may exist. As a result, this assumption could lead to an error in the estimated shear strength value which ultimately reflects in arriving at the non-reliable factor of safety values. Therefore, when analyzing slope stability under rainfall conditions, the soil suction must be taken into account.

In general, deterministic analyses are employed to compute the stability of slopes under rainfall conditions, which does not take into account the variability of soil properties. Variability of soil properties has a considerable impact on the slope stability analysis, especially in the case of slope failure due to a decrease in soil shear strength

N. Mounika (✉) · A. S. S. Raghuram · B. M. Basha
Department of Civil Engineering, IIT Hyderabad, Kandi 502285, India
e-mail: ce18mtech11009@gmail.com

B. M. Basha
e-mail: basha@ce.iith.ac.in

A. A. B. Moghal
Department of Civil Engineering, NIT Warangal, Warangal 506004, India
e-mail: baig@nitw.ac.in

by rainfall infiltration. The SWCCs obtained by drying and wetting the soil specimen methods are not identical [1]. In addition, the suction component in wetting SWCC is always lesser than in drying SWCC at a constant value of water content. The present work aims to study the behavior of slopes to drying and wetting cycles caused by rainwater infiltration.

Several researchers investigated the influence of rainfall on the stability of slopes [2–6]. Rahardjo et al. [7] investigated the impact of hydraulic factors on homogenous slope stability and concluded that saturated hydraulic conductivity has a significant impact on slope stability under rainfall. Li et al. [8] observed that the combined effect of rainfall intensity and saturated hydraulic conductivity governs slope stability under wet conditions. In general, drying SWCC is considered for the analysis of slope failures under rainfall conditions. Moreover, the wetting SWCC fitting parameters are generally ignored for the analysis of slopes under rainfall conditions [9]. On the other hand, because the topsoil gets wetted during rainfall, ignoring the wetting SWCC may affect the stability of slopes under these conditions [10, 11].

It is observed from the literature that few studies discussed the importance of wetting SWCC in the design of slopes. The studies related to wetting-induced slope failures are limited. Hence, the present study aims to investigate the influence of drying and wetting cycles on rainfall-triggered slope failures.

Physiological Properties of the Studied Slope

Rainfall-triggered slope failures occur frequently in the Marappalam area during the rainy seasons, and the rain-induced slope failures of 1993 and 2009 here were among the most significant in Nilgiris slope failure history. The NH181 National highway that connects Mettupalayam and Udagamandalam and Marappalam is located on it. On November 10, 2009, a severe rainfall-induced slope failure occurred in Marappalam. A portion of the railway track and NH181 (approximately 100 m) was damaged as shown in Fig. 12.1.

The geometry of this failure slope is modeled as reported by Senthilkumar et al. [5], and its mesh generation is illustrated in Fig. 12.2. It can be noted from Fig. 12.2 that the slope angle varies from 18° to 29° . Further, it may be observed that the slope comprises of heterogeneous soil deposits, i.e., silty sand (varies from 0 to 6 m), dense sand (6–15 m), and soft rock (> 15 m). Due to insufficient data, the water table is assumed at the interface of the second and third layers. SLOPE/W software has been used to model the Marappalam slope. Initially, the analysis has been carried out in SLOPE/W and then coupled with SEEP/W to perform the seepage analysis.

Material Properties and Boundary Conditions

The SWCC model proposed by van Genuchten [12] is given as



Fig. 12.1 Road damage due to Marappalam slope failure (Senthilkumar et al. [5])

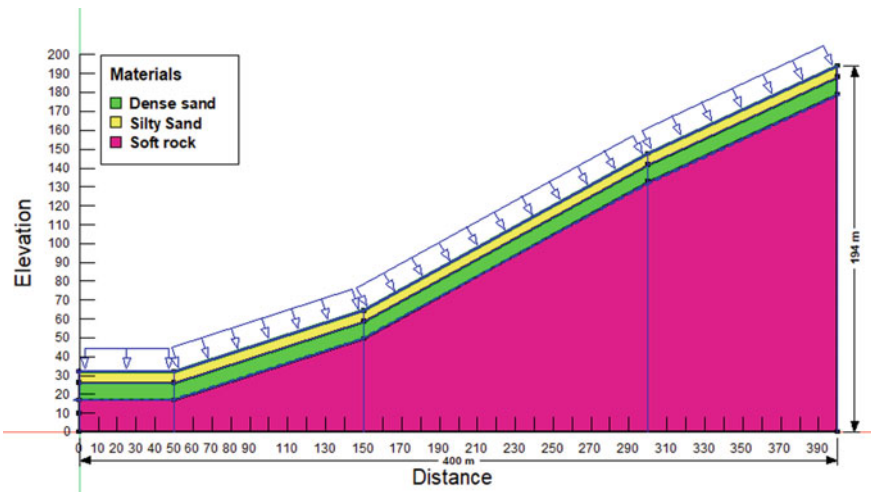


Fig. 12.2 Geometry of the Marappalam slope

Table 12.1 Engineering properties of the Marappalam soils

Properties	Silty sand	Dense sand	Soft rock
Dry unit weight (kN/m ³)	17.72	19.77	28.55
Cohesion (kPa)	15.00	0	0
Internal friction angle (°)	27.00	35.00	55
Saturated water content	0.40	0.40	0.40
Residual water content	0.04	0.04	0.04
Saturated hydraulic conductivity (k_s) (m/s)	4×10^{-6}	2.1×10^{-4}	1×10^{-12}

Table 12.2 Drying and wetting fit parameters of SWCC for silty sand and dense sand

Type of soil	Drying		Wetting	
	a (kPa)	n	a (kPa)	n
Silty sand	15.00	1.5	7.5	2.5
Dense sand	7.66	1.5	3.8	2.5

$$\theta_w = \theta_r + \frac{\theta_s - \theta_r}{\left[1 + (\psi/a)^n\right]^{(1-\frac{1}{n})}} \quad (12.1)$$

where ψ is the matric suction, a is inverse related to air entry value (AEV) and n is governs the slope of SWCC, θ_r is the residual water content, θ_w is the volumetric water content, and θ_s is the saturated water content.

Table 12.1 shows the engineering properties of the soil that are considered in the analysis (Senthilkumar et al. [5]). The wetting SWCC fitting parameters are derived from the equations proposed by Likos et al. [11]. Table 12.2 presents the drying and wetting fit parameters of SWCC. For the transient seepage analysis, the unsaturated slope model is subjected to the following boundary conditions: The water flux boundary is used to apply the rainfall intensity (q) on the ground surface. The rainfall was then simulated using these boundary conditions. A high-intensity rainfall recorded from 1st to 10th November 2009 has been considered [5]. No boundary conditions are applied along the sides and the bottom of the slope.

Monte Carle Simulations

The number of successful and failed simulations is counted using an indicator function. The failure probability (p_{f_MP}) is given by

$$p_{f_MP} = \frac{\sum_{i=1}^N I(\text{FS}_{MP} < 1.0)}{N} \quad (12.2)$$

where N = the number of randomly generated samples. The number of failure events is counted by the indicator function $I(g(x)) < 0$. The value of $I(FS_{MP} < 1.0)$ can be taken as 1.0 when $FS_{MP} < 1$ occurs and 0 when $FS_{MP} \geq 1.0$ occurs. The reliability indices can be estimated from Eq. (12.3).

$$\beta = \Phi^{-1}(1 - p_{f_MP}) \quad (12.3)$$

where Φ is the standard normal distribution function.

Results and Discussion

Figure 12.3 depicts the hysteresis of SWCC. The drying curve is a portion of SWCC from initial saturation to residual saturation, as shown in Fig. 12.3. A wetting curve is a curve that starts from a residual condition and progresses to a saturated state during wetting. It is observed that suction in wetting is always lesser than drying due to the contact angle effect [1]. Figure 12.4a, b show the effect of drying and wetting cycles on the stability of the Marappalam slope in unsaturated conditions, respectively (without rainfall). Further, Fig. 12.4a, b reveal that the difference in factor of safety (FS_{MP}) computed using drying and wetting cycles is negligible. It is attributed to low matric suction associated with sand. Therefore, the contribution of matric suction to shear strength is marginal and has less influence on the hysteretic SWCC for this slope. As an illustration, the FS_{MP} estimated using drying and wetting SWCCs for this slope are 1.85 and 1.83, respectively.

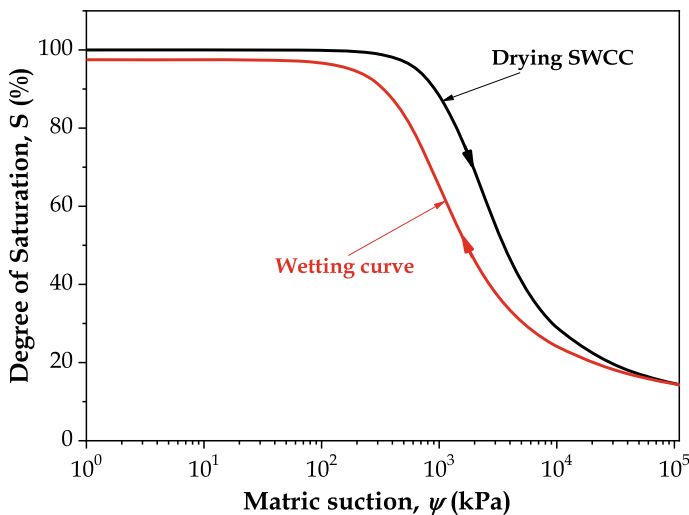


Fig. 12.3 Hysteretic soil water characteristic curve

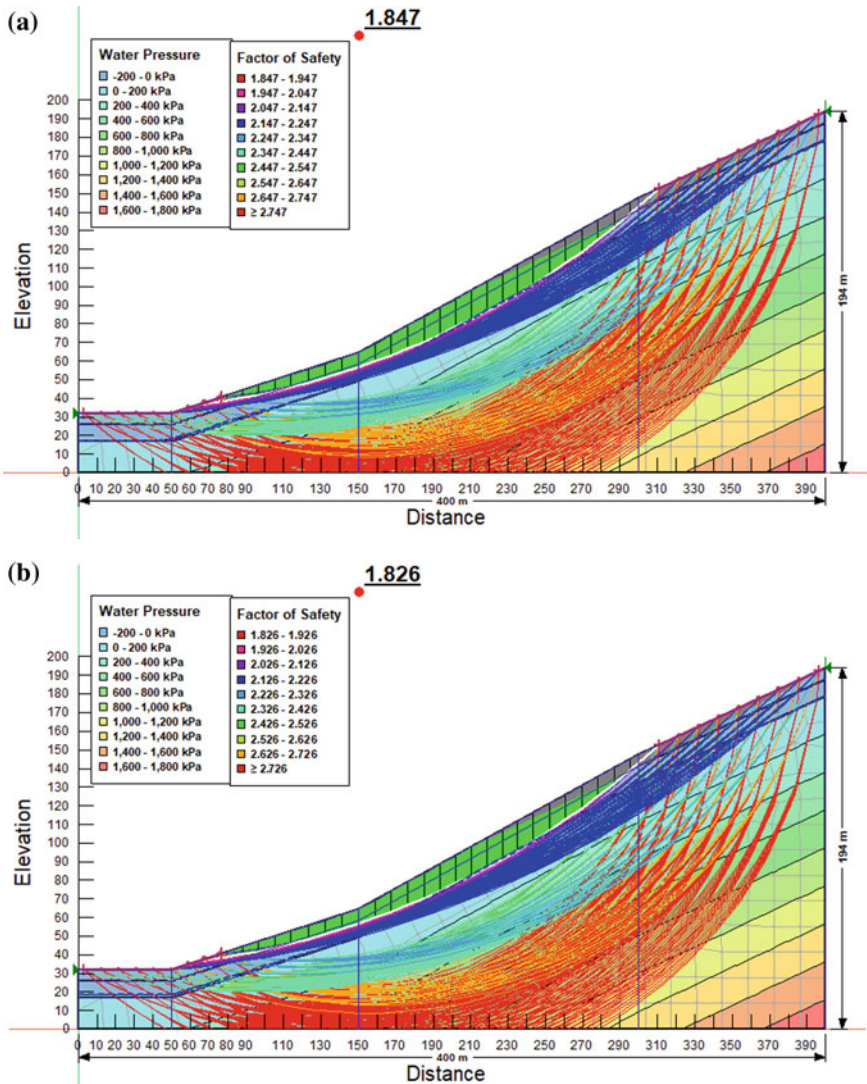


Fig. 12.4 a Critical factor of safety of Marappalam slope computed using drying SWCC. b Critical factor of safety of Marappalam slope computed using wetting SWCC

Influence of Hysteretic Cycles on Factor of Safety

Transient seepage analysis has been performed on the Marappalam slope. The rainfall data from 1st to 10th November 2009 as presented in Table 12.3 [5] are considered for the stability analysis. Table 12.4 demonstrates the statistics of the parameters used in this study. The effect of hysteretic SWCCs on the FS_{MP} of this slope under

Table 12.3 Recorded rainfall in from 1st to 10th of November 2009

Number of days	Rainfall (mm/day)
0	5.5
1	5.5
2	5.5
3	5.5
4	12
5	35
6	30
7	15
8	55
9	175
10	405

rainfall conditions is demonstrated in Fig. 12.5. Results presented in Fig. 12.5 depict that there is a considerable difference in the FS_{MP} values estimated from drying and wetting SWCCs under rainfall conditions. It may be observed from Fig. 12.5 that the FS_{MP} reduced from 1.82 to 0.94 in the drying case and 1.81 to 0.93 in the wetting case.

Additionally, it may be noted that there is an insignificant change in FS_{MP} for the first three days, and thereby, FS_{MP} reduced significantly with the hysteretic cycles which is attributed to the low-intensity rainfall.

The difference in FS_{MP} obtained from drying and wetting SWCCs increased significantly from 5 to 8th day as illustrated in Fig. 12.5, as low-intensity rainfall increased the suction stress in the soil. Hence, due to the contact angle effect, the suction in the wetting case is found to be less than the suction in the drying case. Hence, a substantial difference in the FS_{MP} computed from hysteretic cycles is noted. On the contrary, most of the soil pores get filled with water at high rainfall intensity

Table 12.4 Statistics of the parameters used in the analysis

Type of soil	Parameters	Mean	COV (%)	Distribution
Silty sand	Dry unit weight (kN/m^3)	17.72	5	Normal
	cohesion (kPa)	15.00	20	
	Internal friction angle ($^\circ$)	27.00	20	
Dense sand	Dry unit weight (kN/m^3)	19.77	5	
	cohesion (kPa)	0.00	20	
	Internal friction angle ($^\circ$)	35.00	20	
Soft rock	Dry unit weight (kN/m^3)	28.55	5	
	cohesion (kPa)	0.00	20	
	Internal friction angle ($^\circ$)	55.00	20	

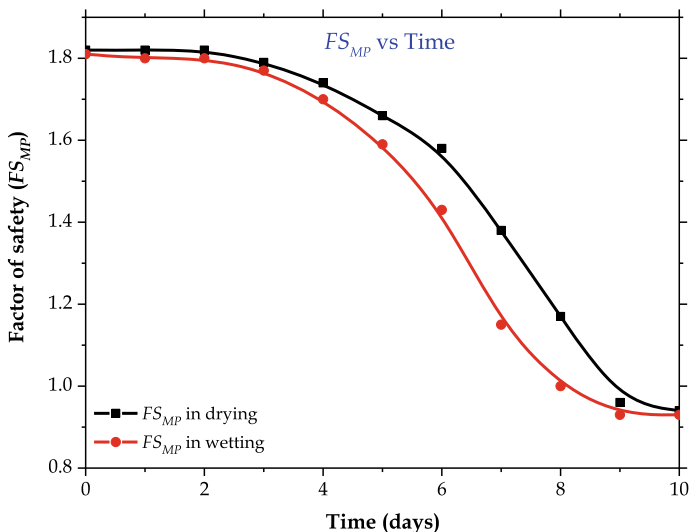


Fig. 12.5 Influence of hysteretic cycles on the factor of safety of Marappalam slope

(observed on 10th day) resulting in a negligible difference in the estimated FS_{MP} using drying and wetting SWCCs.

Influence of Hysteretic Cycles on Reliability Index

Figure 12.6 depicts the effect of hysteretic cycles on the reliability index. The results shown in Fig. 12.6 demonstrate that the reliability index values are negative during high-intensity rainfall (i.e., 10th day, at the time of slope failure) which classified the slope under the hazardous category as per the United States Army Corps of Engineers (USACE) classification [13]. The negative reliability index values may be attributed to the consideration of the variability associated with the shear strength parameters. Furthermore, negative reliability indices may also signifies that the driving forces are more when compared to resisting forces. Similar, observation was made by Huzefa and Hegde [14].

Conclusion

This study emphasizes the significance of considering wetting SWCC and variability associated with the shear strength parameters when analyzing slope stability under rainfall conditions. The following conclusions are drawn:

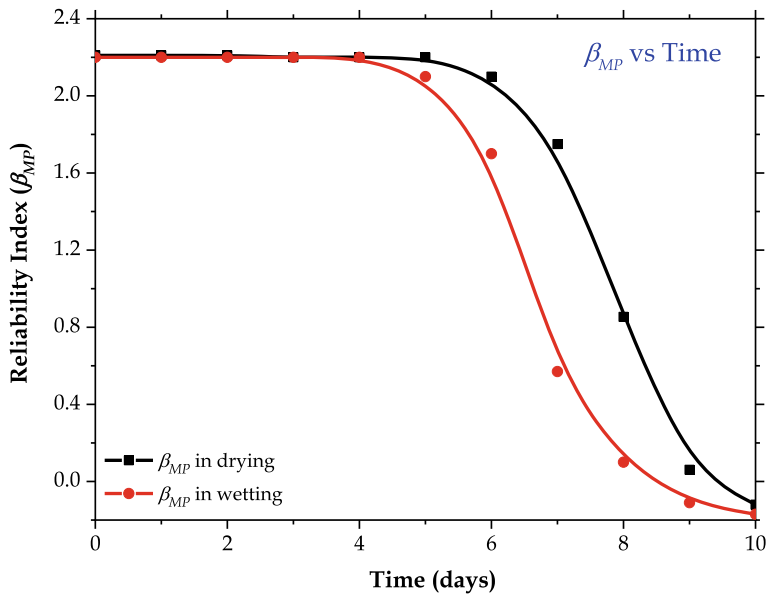


Fig. 12.6 Influence of hysteretic cycles on the reliability index of Marappalam slope

- A considerable difference in the factor of safety (FS_{MP}) is observed when FS_{MP} is computed using drying and wetting cycles during 5th November to 8th November in 2009.
- The factor of safety during the time of failure in drying and wetting cases is 0.94 and 0.93, respectively.
- The Marappalam slope is prone to failure as per factor of safety approach and probabilistic approach.
- At the time of failure, the reliability index values are negative which categorize the slope performance as ‘hazardous’ as per USACE criteria.

The results have revealed the fact that due consideration must be given to wetting SWCC and the variability of the shear strength parameters while designing the slopes under rainfall conditions.

References

1. Raghuram ASS, Basha BM, Moghal AAB (2020) Effect of fines content on the hysteretic behavior of water-retention characteristic curves of reconstituted soils. *J Mat Civil Eng* 32(4):04020057
2. Muntohar AS, Ikshan J, Soebowo E (2013) Mechanism of rainfall triggering landslides in Kulonprogo, Indonesia. In: *Proceedings, geo-congress 2013*. ASCE, Reston, VA, pp 452–461
3. Ering P, Babu GLS (2016) Probabilistic back analysis of rainfall induced landslide—a case study of Malin landslide, India. *Eng Geol* 208:154–164

4. Yang KH, Uzuoka R, Thuo JN, Lin GL, Nakai Y (2017) Coupled hydro-mechanical analysis of two unstable unsaturated slopes subject to rainfall infiltration. *Eng Geol* 216:13–30
5. Senthilkumar V, Chandrasekaran SS, Maji VB (2018) Rainfall-induced landslides: case study of the Marappalam landslide, Nilgiris district, Tamil Nadu, India. *Int J Geomech* 18(9):05018006
6. Raghuram ASS, Basha BM (2021) Analysis of rainfall-induced slope failure using Monte Carlo simulations: a case study. In: *Geohazards*. Springer, Singapore, pp 111–127
7. Rahardjo H, Ong TH, Rezaur RB (2007) Factors controlling instability of homogeneous soil slopes under rainfall. *J Geotech Geoenviron Eng* 133:1532–1543
8. Li WC, Lee LM, Cai H, Li HJ, Dai FC, Wang ML (2013) Combined roles of saturated permeability and rainfall characteristics on surficial failure of homogeneous soil slope. *Eng Geol* 153:105–113
9. Iverson RM (2000) Landslide triggering by rain infiltration. *Water Resour Res* 36:1897–1910
10. Tsai TL (2010) Influences of soil water characteristic curve on rainfall-induced shallow landslides. *Environ Earth Sci* 64(2):449–459
11. Likos WJ, Lu N, Godt JW (2013) Hysteresis and uncertainty in soil-water retention curve parameters. *J Geotech Geoenviron Eng*. 140(4):04013050
12. van Genuchten MT (1980) A closed-form equation for predicting the hydraulic conductivity of unsaturated soil. *Soil Sci Soc Am J* 44(5):892–898
13. USACE (United States Army Corps of Engineers) (1999) Risk-based analysis in geotechnical engineering for support of planning studies, engineering and design. Report No. 20314-1000. Department of Army, USACE, Washington, DC
14. Huzefa HS, Hegde RA (2010) Reliability analysis for the stability of slope in Mumbai region. In: *Proceedings of Indian geotechnical conference, GEOTrendz, IIT Bombay, Mumbai*, pp 1073–1076

Chapter 13

Effect of Antecedent Uniform Rainfall Pattern on the Stability of a Typical Northeastern Slope



Sreeram Shruthija  and Sudheer Kumar Yamsani 

Introduction

The Indian Himalayan region is greatly affected by the frequent occurrence of landslides, particularly rain-induced landslides. Out of all the landslides that happen around the world, 30% of them occur in the Himalayan region (GSI Report, 2016) leading to a loss of one billion USD, and there is a human life lost every year which is about 200 people per year. According to the NDMA report (2011), it is estimated that there is land loss of 120 m/km/yr, leading to a loss of 2500 tons/km² per year because of landslides. 0.49 million km² is affected by landslides which are around 15% of India's land area. Most of the landslides are because of rainfall and earthquakes.

Rain-induced landslides are seen in many parts of the world particularly in the tropical regions having hot and humid climates [4]. Rain-induced slope failures are seen in natural slopes, cut slopes, and embankments. Most of the rain-induced slope failures are shallow with the depth of failure less than 3 m, and the orientation of the slip surface is parallel to the surface of the slope. Tropical climatic conditions lead to the formation of residual soils which are usually in partially saturated conditions [5]. In tropical regions, depth of the water table is greater and hence will have greater suction. It is observed by many researchers that matric suction has a greater role in rain-induced slope failures [6]. Most of the rain-induced slope failures occur due to the wetting front and decrease in matric suction rather than an increase in the ground water table. Variation of matric suction is affected by climatic conditions like the intensity of rainfall, duration of rainfall, rainfall pattern, evaporation, and evapotranspiration.

S. Shruthija (✉) · S. K. Yamsani
National Institute of Technology, Warangal 506004, India
e-mail: srrmshruthi@gmail.com

S. K. Yamsani
e-mail: skyamsani@nitw.ac.in

As the rainfall infiltrates into the unsaturated soil, the matric suction or the negative pore water pressure starts decreasing; as a result, the shear strength of the soil is reduced leading to the failure of the slope. Northeast India has residual soils with their ground water levels at very greater depths and hence will have large initial suction values. The shear strength contributed by matric suction is also greater. Pore water pressures in the soil start changing as the rainfall gets infiltrated; this leads to variation in the ground water table, variation in pore pressures, and thereby, the strength contributed by matric suction is also lost. Loss of strength contributed by suction will result in failure of slope, and hence, the landslides occur. A lot of research has been done by the researchers in the area of various factors affecting rain-induced landslides like pore water pressures, properties of soil, the intensity of rainfall, duration of rainfall, antecedent rainfall (rainfall that occurs before the failure or it is the rainfall that is experienced by the slope in before), lithology, ground water table position, hysteresis, matric suction, land use and land cover, improper road constructions, drainage characteristics, the inclination of slope (angle), the elevation of slope (height of the slope), and the morphology of the area. There is limited work that is done in the area of antecedent rainfall and its patterns. The work that is presented in this paper focuses on one of the identified patterns from northeastern rainfall data (rainfall of Guwahati in the year 2018 is taken), and its impact on the stability of slope with varying soil properties and slope angle is discussed.

Background

Lim et al. [8] studied the effect of matric suction on the stability of residual soil slope and observed that canvas covered section shows less effect when compared with grassed covered and bare land slope sections with change in matric suction. Rahardjo et al. [11] studied the significance of antecedent rainfall on the distribution of pore water pressure in slopes with residual soils and concluded that antecedent rainfall, initial pore water pressures before the occurrence of significant rainfall, and magnitude of antecedent rainfall play a major role in developing the worst pore-water conditions. The significance of this antecedent rainfall is observed to be greater in low-conductivity soils when compared with high-conductivity soils. Once the slope reaches the highest pore water pressure profile, its contribution to subsequent rainfall is observed to be nil.

Rahardjo et al. [10] studied the significance of ground water table location, soil properties on slope stability during rainfall and observed that the slopes with the ground water table at greater depth at driest period will have a rapid reduction in factor of safety (FoS) of the slope. And also, that the soils which have a higher % of fine particles will have a high air entry value of the soil–water characteristic curve (SWCC), the permeability function will be gentle, and the saturated permeability will be less. Minimum FoS may not occur immediately after the rainfall ends, but few hours after rainfall ends.

Rahimi et al. [12] studied the significance of antecedent rainfall patterns on slope stability and found that the rate of decrease in FoS, the time corresponding to the occurrence of minimum FoS, and its value are controlled by antecedent rainfall patterns. The significance of the antecedent rainfall pattern is observed to be more on low-permeable soil slopes when compared with high-permeable soil slopes. Kim et al. [7] worked on the instability of unsaturated soil slopes with variation in rainfall and concluded that climate change influences shallow landslides.

Wu et al. [14] experimentally analyzed rain-induced slope failures and found that lesser rainfall intensity for a longer duration leads to a larger scale landslide. Failure patterns are observed to be related to the intensity of rainfall, slope gradient, and the initial conditions of matric suction. Zhang et al. [15] studied the delay phenomenon in slope instability due to rainfall and observed that the soils with a low water entry value and a lesser rate of rainwater infiltration had a greater probability of generating a delayed phenomenon. The influence of initial ground water table depth on the delay phenomenon is observed to be related to soil properties. The most obvious delay phenomenon is seen for soils with an anisotropic ratio $k_y/k_x = 0.5$ and also when saturated hydraulic conductivity is the same as the intensity of rainfall.

Bhardwaj et al. [1] did a case study on rain-induced landslides in the Indian Himalayan region. It is observed that slopes having slope angles 20–30° and elevation from 1000 to 2000 m are more susceptible to rain-induced landslides (R.I.L), and the landslides are found to be more susceptible in places having garnet ferrous gneiss, schist, migmatite rock. Dikshit et al. [3] wrote a review paper on RIL in the Himalayan region in which hazard monitoring, forecasting, and susceptibility analysis are focused.

The numerous factors that are used to analyze landslides are also studied. The study admits that there are numerous fields in which research work is required like including climatic change or the use of high-quality primary data as input data for computational models.

Soil Properties

Guwahati is a city in Assam, having hill slopes with residual soils of varied stratification. These are formed due to residual weathering. After geological investigation, it is identified that these soils comprise weathered basal rock, decomposed granite, core stones, lateritic and saprolitic residual soils. Isovolumetric weathering of bedrock leads to the formation of a residual soil layer called saprolite. These are dense and resemble parent rock fabric and structure. These are found to be very compact although being porous due to the leaching of fine particles. Once they are disturbed, they lead to landslides. Most of the landslides in Guwahati are found to be RIL, so it is very much essential to have the data of soil properties both physical and engineering properties for the analysis of slopes. Physical and engineering properties are collected from Sarma et al. [13] (See Fig. 13.1).

Fig. 13.1 Picture showing soils of a slope in Guwahati (site: cut slope in IIT Guwahati, Sarma et al. [13])



Table 13.1 Properties of soils in slopes of Guwahati

Property	Silty sand	Silty clay
Specific gravity	2.44	2.7
Liquid limit (%)	39	41.5
Plastic limit (%)	Non-plastic	23.2
USCS classification	SM	CL
γ (KN/m ³)	16.8	19
c^l (Kpa)	0	25
ϕ^l (degrees)	36	18
ϕ^b (degrees)	36	18
Saturated permeability (m/s)	6.6×10^{-5}	8.3×10^{-7}

USCS: Unified soil classification system

c^l : Effective cohesion

ϕ^l : Effective angle of internal friction

γ : Unit weight

ϕ^b : Angle of internal friction with respect to matric suction

SM: Silty sand; CL: Low compressible clay

Soils in Guwahati have two layers of soil; top layer is silty clay, and the bottom layer is silty sand. It is found that Guwahati slopes have unsaturated soils with the ground water table at greater depths, so it is very much important to have SWCC of these soils which are taken from literature review [2, 9] (See Table 13.1).

SWCC of the two soils is collected from a literature review [2] (See Figs. 13.2 and 13.3).

Fig. 13.2 SWCC for silty clay

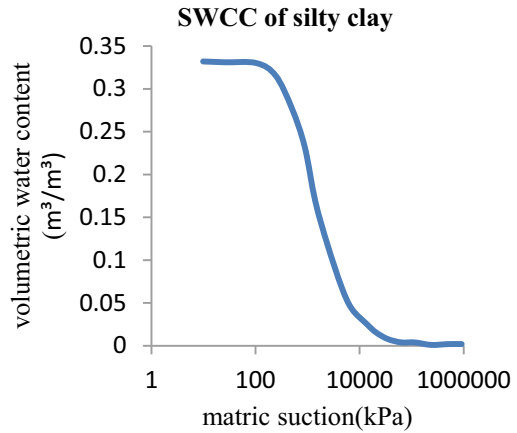
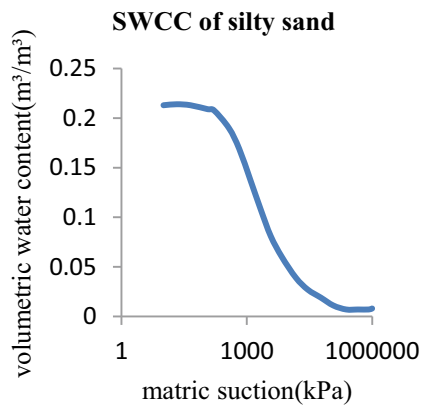


Fig. 13.3 SWCC for silty sand



The SWCCs are given as input in Geostudio software as volumetric data point functions. From the defined volumetric data point function, the hydraulic conductivity of soils is further estimated using the van Genuchten model. This defined SWCC and hydraulic conductivity function is assigned for the slope to perform seepage analysis.

Slope Geometry

See Fig. 13.4.

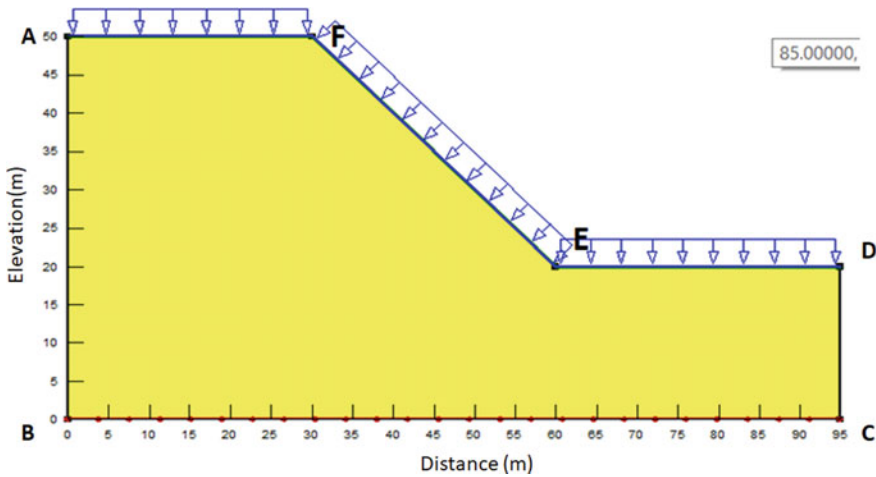


Fig. 13.4 Slope geometry

Boundary Conditions

AB, DC: No flow condition is assigned.

BC: Zero pressure line or datum line (free drainage).

AF, FE, ED: Rainfall is given; it is also the potential seepage face (Excess rainfall flows as runoff).

The slope angle is 45° , and the slope height is 50 m.

Methodology

The seepage analysis is performed using seep/w (module in Geostudio 2012). Pore water pressure data from seepage analysis are taken for slope stability analysis using slope/w (module in Geostudio 2012). Slope stability analysis is done by using the Mohr–Coulomb material model, and the suction contribution from shear strength is taken based on defined volumetric water content data point function.

Morgenstern price limit equilibrium method is used to find the FoS of slope using slope/w. This method is used because it satisfies all the conditions of equilibrium like moment equilibrium, force equilibrium, and can also be used for both circular and non-circular failure surfaces. This method also considers normal and shear forces acting on the sides of slices. Limit equilibrium method is used in the analysis because it is more conventional. One can also perform finite element analysis for slope stability using Geostudio by coupling with sigma/w analysis.

Designing Rainfall Patterns

Rainfall patterns are designed based on the methodology given by Rahimi et al. [12]. Rainfall data of Guwahati in the year 2018 are taken for evaluating most repeated patterns. Five patterns are identified as the most repeated patterns. Out of five patterns, a uniform rainfall pattern is considered and analyzed in this study. Maximum rainfall of 350 mm is taken in the present study. The maximum daily rainfall from the collected data is 71 mm. The maximum rainfall intensity calculated is $8.11E-7$ m/s. The analysis is carried out for 10 days with 5 days of uniform rainfall, and after five days, rainfall is kept zero till the 10th day. Now, another analysis is carried out with initial 5 days uniform rainfall pattern followed by a major rainfall for 8 h (i.e., on the 6th day). The results are checked for 10 days keeping the rainfall as zero after 8 h of rainfall on 6th day till 10th day. This analysis is done to know how the antecedent rainfall is making the slope's initial condition worst. The major rainfall intensity given is the calculated maximum rainfall intensity. Gradually, the intensity of major rainfall is increased and observed.

Rainfall is assigned as a boundary condition in seep/ w . Rainfall intensity and its duration values are given as boundary conditions by defining a new boundary condition. Rainfall intensity values are given as a step data point function.

Results and Discussions

Pore water pressure variations and infiltration values for uniform rainfall patterns are taken from results of seep/ w . FoS variations with time are taken from slope/ w results. Normalized FoS is the ratio of the FoS at a particular instant of time to the initial FoS. Normalized FoS is used for comparing results of uniform rainfall patterns because initial FoS for different soil types will be different as they have a wide range of pore water pressure distributions (Fig. 13.5).

It is observed that there is a 20% reduction of normalized FoS for low-conductive soil (silty clay) and a reduction of 10% for high-conductive soil (silty sand). To

Fig. 13.5 Effect of antecedent uniform rainfall for 5 days with varying soil types

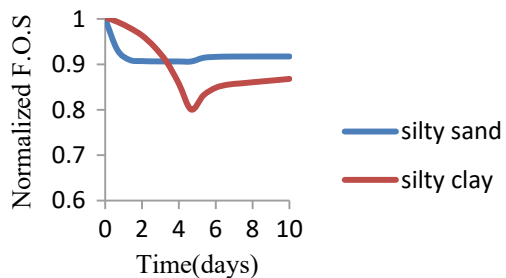


Fig. 13.6 Pore water pressure variation at depth 2 m below the toe of the slope

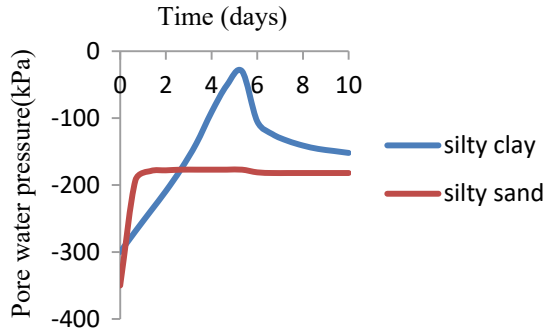
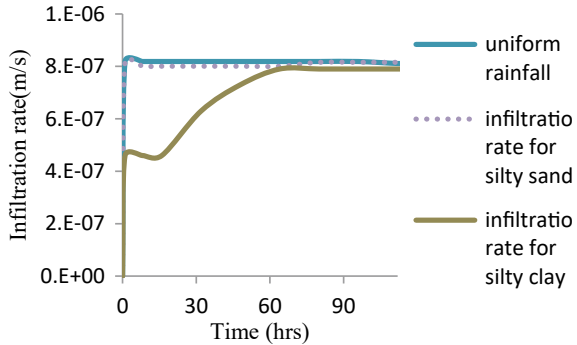


Fig. 13.7 Infiltration rate with varying soil type under 5 days antecedent uniform rainfall pattern



understand the above results, pore water pressure variations and also the infiltration rates are observed for slopes with both the soil types.

From Fig. 13.6, it is clear that the pore water pressure variations are greater for slope with low-conductive soil than high-conductive soil, and also that the trend in which the pore water pressures are varying is the same as the trend in which the normalized FoS is varying with time.

From Fig. 13.7, it is seen that the rainfall intensity and the infiltration rate are the same for slope with silty sand. This can be because of greater permeability all the rainwater infiltrates into the slope. For a slope with silty clay initially, the rainfall intensity and infiltration rate are not the same. This can be because for a low-conductive soil, the permeability will be less thereby the amount of water that gets infiltrated is very less. The unsaturated pores will saturate gradually with time, and hence, with time, as the saturated permeability is greater than the unsaturated permeability of the soil, the infiltration rate also gets increased (Fig. 13.8).

It is observed that a slope that experienced antecedent rainfall for 5 days when subjected to a major rainfall of intensity $8.11E-7$ m/s for 8 h has undergone a reduction of normalized FoS of 26% for a slope with silty clay and a reduction of approximately close to 10% for a slope with silty sand. Without antecedent rainfall, the slope with major rainfall for 8 h has a reduction in normalized FoS of 1% for

Fig. 13.8 Effect of major rainfall with and without antecedent rainfall

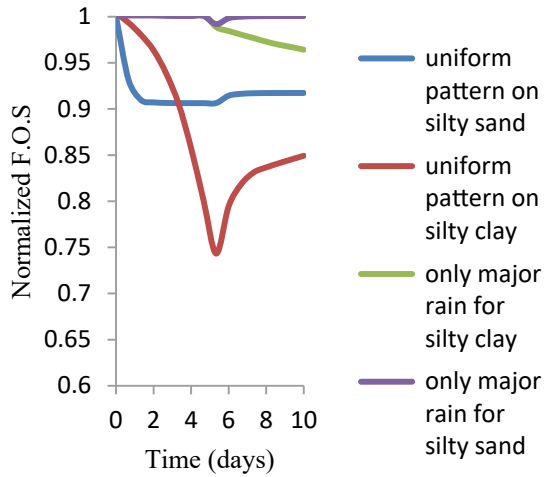
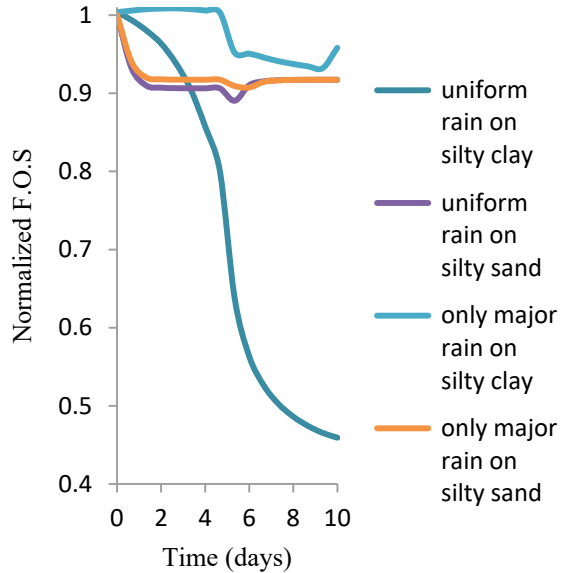


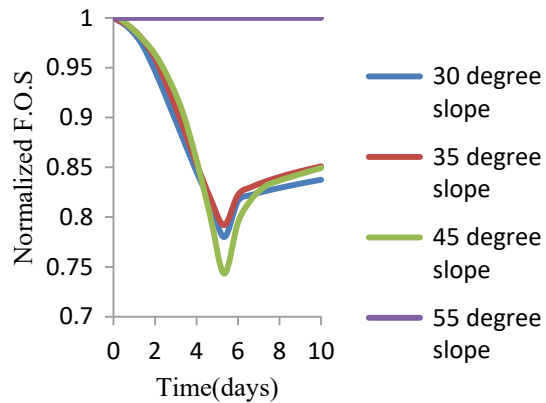
Fig. 13.9 Effect of increased major rainfall with and without antecedent rainfall



silty sand and 4% for silty clay. This clearly shows the significance of antecedent rainfall. Antecedent rainfall affected both slopes with silty sand and silty clay, but its significance is greater for low-conductive soil slope similar to findings of Rahardjo et al. [10] (Fig. 13.9).

When the magnitude of major rainfall is tripled, the low-conductive soil slope with antecedent rainfall followed by major rainfall has failed. This clearly indicates the significance of antecedent rainfall which is creating the worst initial conditions for low-conductive soil slopes (Fig. 13.10).

Fig. 13.10 Effect of antecedent rainfall with varying slope angle on low-conductive soil slope



Slope angle is changed for low-conductive soil slope. It is observed that the shallow slopes are significantly affected than the steep slopes. This is contradicting to our general understanding in soil mechanics that shallow slopes are more stable than steep slopes. This is because shallow slopes have more infiltration of rainwater, whereas in steep slopes infiltration is very less (more of the rainwater goes in runoff). In Fig. 13.8, it is observed that 45 degree slope is affected greatly because of the effect of both geometry and infiltration.

Conclusion

From this limited study, the following understandings are made.

Antecedent rainfall before the occurrence of major rainfall affected both low-conductive and high-conductive soil slopes, and the effect is more significant in low-conductive soil slope.

Pore water pressure variations are greater for low-conductive soil slope.

The trend in which the pore water pressure is changing is the same as the trend in which the normalized factor of safety is changing.

The infiltration rate and rainfall rate are the same for high-conductive soil slope.

For low-conductive soil slope, the infiltration rate is less than the rainfall rate.

The value of the minimum FoS is governed by the amount of infiltrated water.

The time at which the minimum FoS occurs is the time at which the pore water pressure is minimum.

Shallow slopes with low-conductive soils are more significantly affected by antecedent rainfall because the possibility for infiltration is more in the case of shallow slopes.

References

1. Bhardwaj A, Wasson RJ, Ziegler AD, Chow WT, Sundriyal YP (2019) Characteristics of rain-induced landslides in the Indian Himalaya: a case study of the Mandakini catchment during the 2013 flood. *Geomorphology* 330:100–115
2. Chatterjee D, Krishna AM (2019) Effect of slope angle on the stability of a slope under rainfall infiltration. *Indian Geotech J* 49(6):708–717
3. Dikshit A, Sarkar R, Pradhan B, Segoni S, Alamri AM (2020) Rainfall induced landslide studies in Indian Himalayan region: a critical review. *Appl Sci* 10(7):2466
4. Frattini P, Crosta G, Soso R (2009) Approaches for defining thresholds and return periods for rainfall-triggered shallow landslides. *Hydrol Process: Int J* 23(10):1444–1460
5. Han KK, Rahardjo H, Broms BB (1995). Effect of hysteresis on the shear strength of a residual soil. In: proceedings of the first international conference on unsaturated Soils/unsat'95/paris/france/6-8 september 1995. Vol. 2
6. Indrawan IGB, Rahardjo H, Leong EC (2006) Effects of coarse-grained materials on properties of Residual soil. *Eng Geol* 82(3):154–164
7. Kim J, Jeong S, Regueiro RA (2012) Instability of partially saturated soil slopes due to alteration of rainfall pattern. *Eng Geol* 147:28–36
8. Lim TT, Rahardjo H, Chang MF, Fredlund DG (1996) Effect of rainfall on matric suctions in a residual soil slope. *Can Geotech J* 33:618–628
9. Malaya C, Sreedeeep S (2013) A study on unsaturated hydraulic conductivity of hill soil of north-east India. *ISH J Hydraulic Eng* 19(3):276–281
10. Rahardjo H, Nio AS, Leong EC, Song NY (2010) Effects of groundwater table position and soil properties on stability of slope during rainfall. *J Geotech Geoenviron Eng* 136(11):1555–1564
11. Rahardjo H, Ong TH, Rezaur RB, Leong EC (2007) Factors controlling instability of homogeneous soil slopes under rainfall. *J Geotech Geoenviron Eng* 133(12):1532–1543
12. Rahimi A, Rahardjo H, Leong EC (2011) Effect of antecedent rainfall patterns on rainfall-induced slope failure. *J Geotech Geoenviron Eng* 137(5):483–491
13. Sarma CP, Krishna AM, Dey A (2019) Geotechnical characterization of hillslope soils of Guwahati region. In: *Geotechnical characterisation and geoenvironmental engineering*. Springer, Singapore, pp 103–110
14. Wu LZ, Huang RQ, Xu Q, Zhang LM, Li HL (2015) Analysis of physical testing of rainfall-induced soil slope failures. *Environ Earth Sci* 73(12):8519–8531
15. Zhang J, Li J, Lin H (2018) Models and influencing factors of the delay phenomenon for rainfall on slope stability. *Eur J Environ Civ Eng* 22(1):122–136

Chapter 14

Response of Isolated Shallow Footing on Sloping Ground with Dynamic Loading



Saumitro Mandal, Aniket Chanda, and Arghadeep Biswas 

Introduction

Slope stability can be referred to as the ability of the inclined soil body to withstand excessive outward movement of soil. Analysis of slope aims to understand the potential causes of ‘failure’. It can be defined in terms of factor of safety as the ratio between resisting shear mobilization and driving shear stress. The factor of safety of a ‘stable’ slope can be disturbed either by increasing driving force and/or decreasing the resistance of the soil. Either of the issues can be intensified cause of instability in presence of dynamic forces like earthquakes. Slope movement can lead to several problems including structural damage and/or fatal accidents causing loss of lives. Irrespective of its triggering agency, whether natural or artificially, guaranteeing slope safety is difficult as well as challenging and thus has been a topic of interest for many geotechnical practitioners.

As the result of growing problems and uncertainty in estimating the behavior, the slope-stability issue is investigated by several researchers, and many alternatives are developed to encounter the situation. Terzhagi (1950), the father of soil mechanics, has introduced the pseudo-static method for analyzing the seismic stability of a slope [1]. In this approach, earthquake force was applied in terms of equivalent earthquake acceleration. The analysis method was simple and provided a fairly satisfactory result [2, 3]. Seed [4] calibrated the pseudo-static method for seismic stability analysis of earth dams with soils that do not suffer significant strength loss. Regarding the pseudo-static analysis, many researchers have concluded it as

S. Mandal · A. Chanda
Department of Civil Engineering, Jalpaiguri Government Engineering College, Jalpaiguri, West Bengal 735102, India

A. Biswas (✉)
Department of Civil Engineering, Jadavpur University, Kolkata, West Bengal 700032, India
e-mail: arghadeep.biswas@gmail.com

a simple and time-saving method depending on convergence and comparative end-results concerning actual and/or other methods [5–7]. Clough and Chopra [8] have shown slope behavior can be effectively well simulated through the finite element method (FEM). Leshchinsky and Baker [9] reported a mathematical approach based on the limiting equilibrium method to analyze slope stability. It has been concluded that the factor of safety is independent of normal stress distribution over the critical slip surface. This analysis provided a nonlinear first-order partial differential equation that enables the development of numerical procedures to determine the minimum factor of safety. Duncan [10] compared the slope-stability issue through limit equilibrium and finite element analysis.

The present study investigated the effect of an earthquake on the stability of shallow-isolated footing constructed on and away from the slope with varying configurations. The commercially available finite element software package, Plaxis^{3D}, is used for this purpose. The Plaxis^{3D} is capable of and offers both time history analysis and pseudo-static analysis; however, due to time constraints and simplicity, the pseudo-static analysis is adopted. The stability of slopes for different configurations is compared and analyzed based on the factor of safety.

Materials and Modeling

A c - ϕ soil is considered for constructing the slope for this study. Reinforced concrete is assumed to be the material constructing the footing (width, $b = 2$ m) which will transfer the super-structural load into the soil. In the finite element program, the soil is modeled as Mohr–Coulomb material, while the reinforced concrete is considered as a linear elastic material. The material properties are summarized in Table 14.1.

In general, earthquake load can be analyzed in two ways, such as time-domain analysis and pseudo-static loading. In the pseudo-static method, seismic force is applied as a statically applied inertia force, the magnitude of which is a product of a seismic coefficient k and weight of the corresponding mass. These are approximately constants body forces with magnitude proportional to the horizontal and/or vertical accelerations imposed by the dynamic loading and can be generalized as $F_i = k_i W$, where ‘ i ’ denotes the force direction in X , Y , and Z directions, respectively. Hence,

Table 14.1 Material properties

Parameters	Soil	Concrete
Material model	Mohr–Coulomb	Linear elastic
Angle of internal friction ($^\circ$)	30	–
Cohesion (kN/m^2)	20	–
Poisson’s ratio	0.4	0.15
Unit weight (kN/m^2)	18	25
Modulus of elasticity (kN/m^2)	1.2×10^4	2.5×10^7

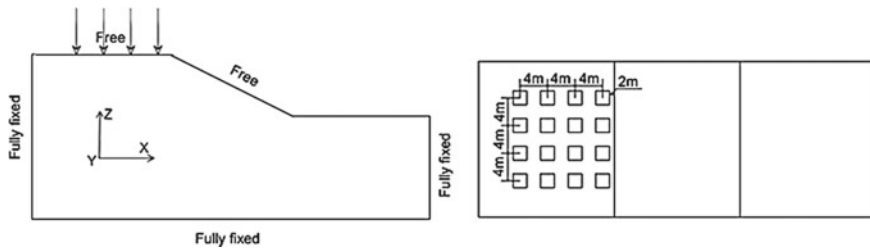


Fig. 14.1 Geometry of the problem statement in elevation and plan with boundary fixities

the F_i represents the body forces, and k_i is the pseudo-static acceleration in the corresponding directions; while 'W' represents the corresponding mass.

In this study, the performance of slopes having a set of 16 isolated square footings ($b = 2$ m) embedded (u) 1.5 m below the ground surface and positioned at the upper side of sloping surfaces is investigated using Plaxis^{3D}. The foundation system is considered to be constructed at variable distances from the sloping face. The variables considered in this study are the distance (d) of the extreme footing from the sloping surface, slope angle and height (h), and the dynamic forces. In Fig. 14.1, a schematic of the problem statement and boundary fixities for the model are presented. It may be noticed that boundaries, such as x_{\min} , x_{\max} , z_{\min} , are kept fully fixed, while the y_{\min} and y_{\max} are normally fixed. The ground and slope surface (z_{\max}) is considered free to allow possible deformations. In all the investigations, the ground water effect is avoided by putting the water table deep into the soil and far below the footing bottom.

Results and Discussions

This study addressed the slope stability issues under a foundation system consisted of 16 nos. square isolated footings subjected to different parametric variations including dynamic loads. In the study, load calculation for each footing is done as per Indian standards, and a load of 500 kN is assigned for every footing. The footings were embedded at a depth of 1.5 m (u) on the upper side of the slope with variable distances (d) from the sloping surface. Different slopes and slope heights (h) are considered to compare the performance. The dynamic loading was applied as pseudo-static acceleration, in the range 0.1–0.6 g. An analysis for the static condition is also performed, indicated as '0 g' (in Table 14.2) to compare the dynamic effects. In Table 14.2, the factor safety against the stability of slopes for different parametric variations and combinations considered for the study is summarized.

The factor of safety (FOS) is the parameter to compare the performance of slopes of varying configurations. The variation of FOS with the d from slope edge for different pseudo-static accelerations, with a slope angle 2H:1V and $h = 6$ m, is presented in Fig. 14.2. It is noticed that the performance of footings is more sensitive

Table 14.2 Summary of the factor of safety for different slope configurations

Slope	h	d	Factor of safety				
			0 g	0.2 g	0.4 g	0.5 g	0.6 g
2H:1V	3	2	4.822	2.946	1.733	1.398	1.17
		4	5.377	3.007	1.732	1.399	1.154
		6	5.727	3.033	1.732	1.4	1.172
	6	2	3.432	2.219	1.558	1.295	1.08
		4	3.632	2.271	1.565	1.297	1.1
		6	3.791	2.304	1.567	1.299	1.099
	9	2	2.894	1.883	1.346	1.159	F
		4	2.944	1.891	1.354	1.156	F
		6	3.012	1.911	1.348	1.157	F
1.5H:1V	3	2	4.334	2.945	1.728	1.393	1.169
		4	5.223	2.996	1.728	1.339	1.173
		6	5.49	2.998	1.734	1.398	1.151
	6	2	3.005	2.075	1.515	1.304	1.096
		4	3.23	2.149	1.535	1.288	1.097
		6	3.31	2.193	1.542	1.295	1.08
	9	2	2.478	1.71	1.246	1.076	F
		4	2.548	1.727	1.244	1.071	F
		6	2.628	1.77	1.267	1.09	F
1H:1V	3	2	4.106	2.869	1.723	1.4	1.172
		4	4.495	2.93	1.731	1.4	1.139
		6	4.693	2.976	1.728	1.393	1.169
	6	2	2.437	1.8	1.366	1.193	1.039
		4	2.671	1.883	1.38	1.196	1.036
		6	2.738	1.946	1.405	1.207	1.039
	9	2	2	1.466	1.103	F	F
		4	2.078	1.494	1.113	F	F
		6	2.105	1.507	1.113	F	F
0.5H:1V	3	2	3.244	2.39	1.725	1.398	1.171
		4	3.693	2.67	1.729	1.399	1.172
		6	3.705	2.705	1.73	1.397	1.17
	6	2	1.89	1.462	1.112	F	F
		4	2.057	1.538	1.125	F	F
		6	2.11	1.568	1.131	F	F
	9	2	1.465	1.133	F	F	F
		4	1.52	1.155	F	F	F
		6	1.57	1.175	F	F	F

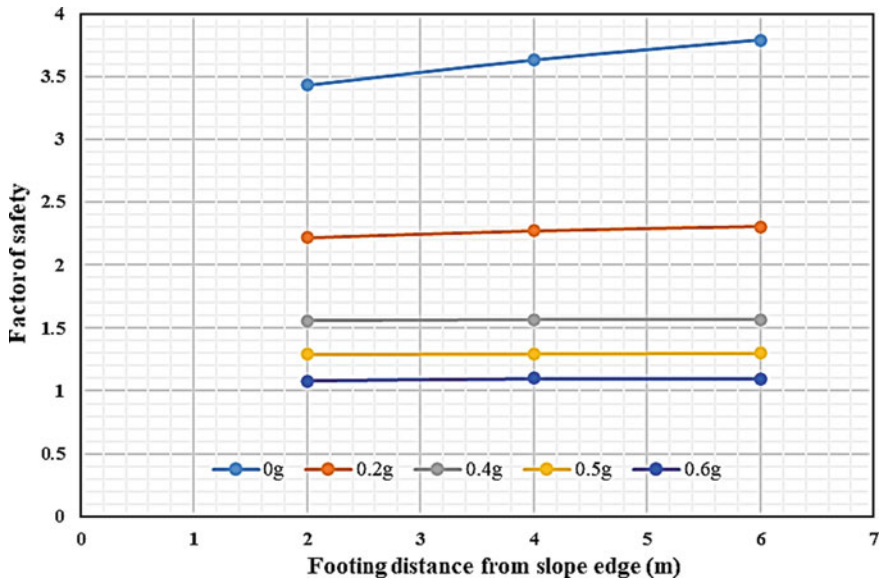


Fig. 14.2 Variation of FOS with d for different k_x (slope angle = 2H:1V; $h = 6$ m)

nearer to the slope under dynamic forces. Observations indicated that as the footings move toward the slope the stability of slopes reduces. The behavior is reflected in terms of reducing FOS. However, the stability of slopes remains unaffected (concerning d) for an acceleration intensity of 0.2 g.

The slope performance with d for different slope angles is compared in Fig. 14.3 (for $h = 6$ m and $k_x = 0.2$ g). The comparison indicated the increasing vulnerability of slopes, though decreasing FOS, with the increase in slope steepness (2H:1V being the least and 0.5H:1V being the steepest slope).

The variation of FOS with k_x/g ratio for different d for 1H:1V slope and $h = 3$ m is presented in Fig. 14.4. It is noticed that the FOS has decreased with the increase of pseudo-static acceleration. Footing placed at a distance more than 4 m (i.e., 2 times the footing width, $2b$) has depicted less influence on the stability; however, it has indicated that the increase in pseudo-static acceleration can destabilize the slope, and the rate of such instability is considerably high.

In Fig. 14.5, the factor of safety analysis for different slope heights for earthquake accelerations of variable intensities is presented. A slope with an angle of 1.5H:1V is considered for the purpose. It is observed that the stability, in terms of FOS, has decreased with the increase in horizontal acceleration.

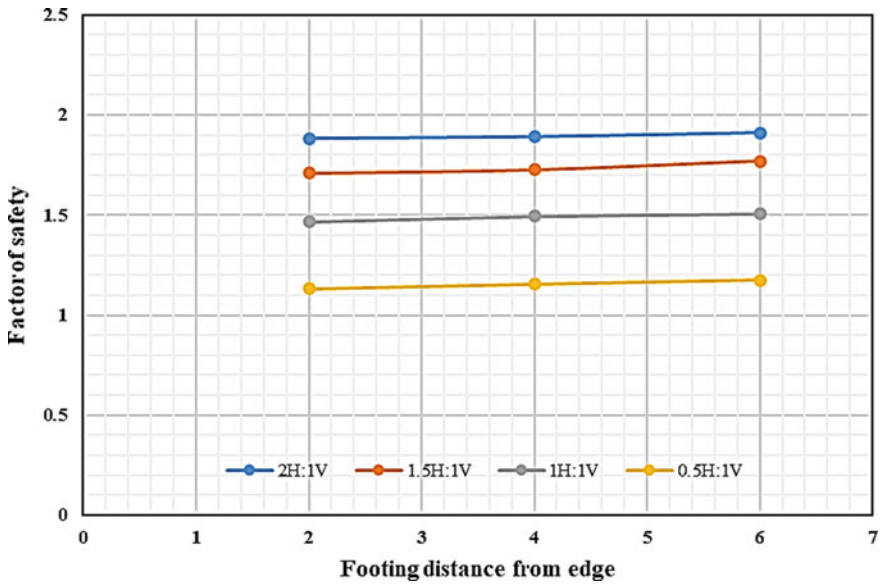


Fig. 14.3 Variation of FOS with d for different slope angles ($h = 6$ m and $k_v = 0.2$ g)

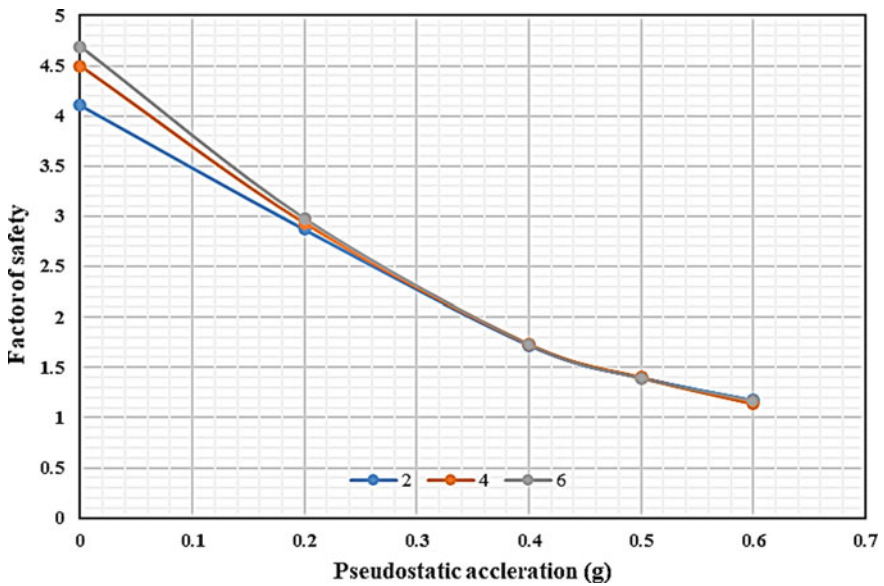


Fig. 14.4 Variation of FOS with acceleration/ g for different d (slope angle = 1H:1V; $h = 3$ m)

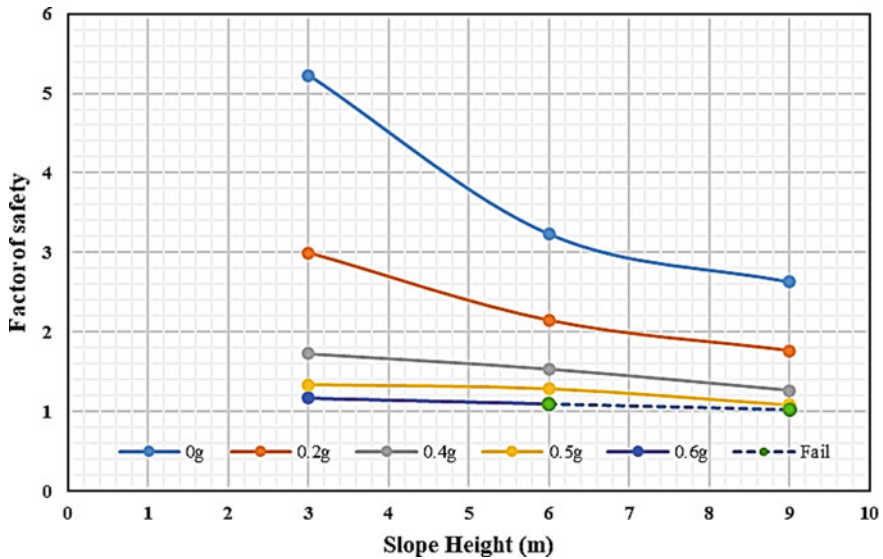


Fig. 14.5 Variation of FOS with h for different k_x (slope angle = 1.5H:1V; $d = 4$ m)

Conclusion

The study has reported the performance of slopes subjected to a foundation system consisted of a set of 16 isolated square footings founded nearby a slope of varying configurations. The parametric variations considered the distance of footing from the sloping edge, the slope height and angle, and the horizontal accelerations. As per the observation, the following conclusions can be drawn.

It is observed that with the increase of pseudo-static acceleration, the factor of safety decreases. However, beyond the acceleration magnitude of 0.2 g, the effect of footing distance on stability is very found to be negligible.

The 2H:1V slope is found to be most sable, and the 0.5H:1V slope showed minimum stability. This indicated the increase in steepness of slope decreases its stability.

The slope angle of 0.5H:1V is very much unstable when the depth is 9 m and the horizontal acceleration is greater than 0.2 g.

Further analysis indicated that despite the steepness of the slope, the smaller the slope height is, the safer it will be. For example, a relatively (compared to 9-m slope height) smaller depth of 6 m slopes, with a similar angle, are more stable than the slope with 9 m height.

References

1. Terzhagi K (2012) Mechanism of landslides. In: Paige S (ed) Application of geology to engineering practice (Berkey Volume). Geological Society of America, New York, pp 83–123
2. Kontoe S, Pelecanos L, Potts D (2013) An important pitfall of pseudo-static finite element analysis. *Comput Geotech* 48:41–50
3. Maula BH, Zhang L (2011) Assessment of embankment factor safety using two commercially available programs in slope stability analysis. *Procedia Eng* 14:559–566
4. Seed HB (1979) Considerations in the earthquake-resistant design of earth and rockfill dams. *Geotechnique* 29:215–263
5. Tabesh A, Poulos HG (2000) A simple method for the seismic analysis of piles and its comparison with the results of centrifuge tests. In: 12th World conference on earthquake engineering, Paper no.1203 Auckland, New Zealand
6. Tabesh A, Poulos HG (2001) Pseudostatic approach for seismic analysis of single piles. *J Geotech Geoenviron Eng* 127(9):757–765
7. Tabesh A, Poulos HG (2001) The effect of soil yielding on seismic analysis of single piles. *Soils Found* 41(3):1–16
8. Clough RW, Chopra AK (1966) Earthquake stress analysis in earth dams. *ASCE J Eng Mech Div* 92:197–211
9. Leshchinsky D, Baker R (1985) Three dimensional analysis of slope stability. *Int J Num Analy Method Geo-Mech* 9:199–223
10. Duncan JM (1996) State of the art: limit equilibrium and finite element analysis of slopes. *J Geotech Eng* 122(7):577–596

Chapter 15

Detection, Monitoring, and Early Warning of Landslides Using In-Situ Ground-Based Monitoring Techniques: A Review



Shreya Maheshwari and Riya Bhowmik

Introduction

Landslide or ‘mass wasting’ refers to any downslope movement of rock and soil which rapidly transforms into a destructive natural disaster. The union territory of Jammu and Kashmir in India is located in the Northwest Himalayan range and encompasses significant landslide-prone regions. The frequency of occurrence of landslides has further increased due to global climate change. Thus, monitoring of susceptible and vulnerable slopes and early warning of landslide occurrences are essential in reducing the loss of lives and property.

This paper briefly reviews the essential components of real-time ground-based monitoring techniques of landslides. It further presents the details of the wireless sensor network, which integrates the ground-based sensor data with early warning systems. Since the early warning algorithms employ predefined thresholds for the monitored triggering parameters, this paper also presents some of the reported threshold models reported in the literature.

Sensors Desirable for Landslides Monitoring

In-situ ground-based monitoring techniques are a vital part of landslide monitoring. It comprises an arrangement of sensors for real-time data capturing in hilly areas. Table 15.1 lists the sensors used in reported studies on landslide monitoring by various researchers. This includes: (a) capacitance-type dielectric soil moisture sensor, which evaluates the volumetric moisture content of the soil by comparing the dielectric

S. Maheshwari (✉) · R. Bhowmik
Indian Institute of Technology Jammu, Jammu, India
e-mail: shreyamahe777@gmail.com

constant of the buried soil with the dielectric constant of water, (b) strain gauge-type or vibrating wire-type pore water pressure sensor to measure the change in pore water pressures resulting from precipitation, (c) tilt sensors/MEMS inclinometer for measuring any change in slope or tilt angle, (d) geophones to measure any vibrations which may occur at the onset of landslides, and (e) rain gauge to measure the amount of precipitation. Together, these sensors form an arrangement that measures the precipitation, change in soil moisture, pore water pressures (indicates the reduction in shear strength of soil), linear and angular displacements, and ground vibrations, and thus, together form the basis for landslide early warning system.

Wireless Sensor Network

The wireless sensor network [16, 23] is one of the best-suited technologies with great progressions that can rapidly respond to quick data variations and transfer the sensed data to a data management center. The sensors, which are either placed inside a sensor column [20, 26] or deep earth probe [21, 22] in the landslide-prone region, sense the magnitude of deformation and its respective location in real-time with minimum maintenance and provide reliable and efficient real-time information of the landslide parameters.

In a WSN, all the sensors interface with a data acquisition board (DAQ) through signal conditioning circuitry. The DAQ board then connects the various sensors to a mote, resulting in a wireless sensor node. The data collected by the sensor nodes are routed to the gateway or network coordinator via a network of relay nodes. The gateway serves as a link between two different networks and is capable of data collection, data processing using the available algorithm, and data transfer. Figure 15.1 depicts the architecture of wireless sensor networks (WSNs) for monitoring and detecting landslides.

Landslides Detection Algorithms

As the network starts working, each wireless sensor node samples the sensors such as moisture sensors, rainfall sensors, pore pressure sensors, and so on. The information collected by all the installed wireless sensor nodes in the field is transformed into data packets containing the various information. This information is analyzed by performing the peak transmission analysis by identifying the peak data value among all the sensors installed in the field. For deciding whether the landslide will happen or not, a threshold-based approach is commonly followed. The analysis outcomes are compared with a predefined threshold previously set to the wireless node of the network. These predefined threshold values are generally determined from statistical analysis of the field or lab-based data for the concerned parameter.

Table 15.1 Sensors employed for landslides monitoring

Author	Sensors	Parameters observed	Specification (if any)
Ramesh [20]	Pore pressure transducer	Soil pore pressure	
	Dielectric moisture sensor	Volumetric water content of the soil	
	Strain gauge	Soil movement	
	Geophones	Ground vibrations	
	Rain gauge—tipping bucket	Monitoring of rainfall	
	Tilt meters	Slope inclination angle	
Mishra et al. [19]	MEMS inclinometer	Slope angle	Linear range $\pm 5^\circ$
Wang et al. [27]	Soil moisture sensor	Water content of the soil	
	Soil temperature	Temperature variation	
	Distance sensor	Displacement of land	Range 1–15 m, precision 1 mm
	Tilt sensor	Tilting angle	Range $\pm 90^\circ$, precision 0.025°
	Rainfall sensor	Rainfall	Resolution 0.1 mm, range 0.1–7 mm/min
Shukla et al. [24]	Piezometer	Pour water pressure	Range $0 \pm 5 \text{ kg/cm}^2$
	Tilt meter	Vertical angle of strata	Range $\pm 5^\circ$
	In-place inclinometer	Horizontal angle of strata	Range $\pm 10^\circ$
	Crack meter	Displacement of strata	Range $0 \pm 500 \text{ mm}$
	Rain gauge	Rainfall intensity	Range 0–99 mm
Giorgetti et al. [9]	Air thermometer	Temperature of air	Range -20° to $+80^\circ \text{ C}$, acc. $\pm 0.2\%$
	Rain gauge	Rainfall	Resolution 0.2 mm
	Air hygrometer	Amount of water vapor in air	Range 5–95%, acc. $\pm 2\%$
	Anemometer	Wind speed and direction	Speed acc. $\pm 5\%$, dir. acc. $\pm 4^\circ$
	Soil hygrometer	Moisture content in soil	Range 5–95%, acc. $\pm 3\%$
	Extensometer (wire and bar)	Movement or displacement of land	Range 250 mm, acc. 130 μm (wire) and range 150 mm, acc. 0.08 mm (bar)

(continued)

Table 15.1 (continued)

Author	Sensors	Parameters observed	Specification (if any)
	Tilt meter	Slope inclination angle	Range $\pm 15^\circ\text{C}$, acc. $\pm 0.02^\circ$
Giri et al. [10]	3-axis accelerometer	Gravity and linear acceleration—tilting and movement rate of slope	
	3-axis gyroscope	Angular speeds of soil or rock masses	
Joshi et al. [13]	Soil moisture sensor	Moisture content	
	Pore pressure sensor	Soil pore pressure	
	Displacement sensor	Position and movement of soil	
	Rain gauge	Rainfall quantity	
Sruthy et al. [25]	Soil moisture sensor	Soil water content	
	Accelerometer ADXL335	Land movement	Range $\pm 3\text{ g}$
Abraham et al. [1]	MEMS tilt sensors	Tilting angles	Resolution 0.003°
	Volumetric water content sensors	Moisture content at shallow depths	Resolution $0.002\text{ m}^3/\text{m}^3$

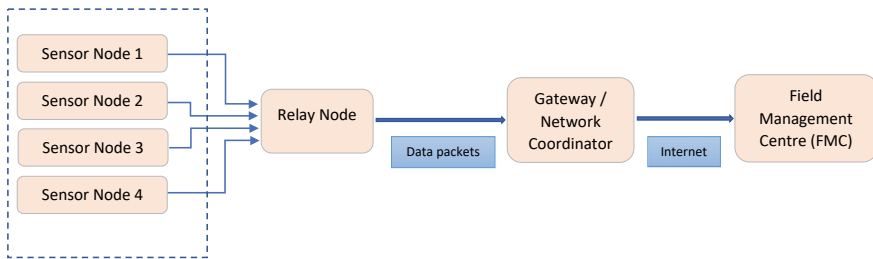


Fig. 15.1 Architecture of wireless sensor networks (WSNs) for monitoring and detecting landslides

The rainfall-based threshold model is mostly used for the early warning system. This threshold uses the previously recorded minimum rainfall values responsible for triggering the landslides under similar hydro-geological conditions [11]. The most extensively used rainfall threshold model expresses the thresholds using the power law relationship between the intensity of rainfall (I) and its duration (D) [3].

$$I = c + \alpha \cdot D^\beta \tag{15.1}$$

where I is the intensity of rainfall in mm/h, D is the rainfall duration in hours, c is a constant ≥ 0 , and α and β are scale and shape parameters obtained empirically. The rainfall thresholds are identified as local, regional, and global thresholds based on

Table 15.2 I – D -based rainfall thresholds for the occurrence of landslides

Author	Area	Expression	Range	Threshold
Caine [3]	World	$I = 14.82D^{-0.39}$	$0.167 < D < 500$	Global threshold
Cancelli and Nova [4]	Valtellina, northern Italy	$I = 44.67D^{-0.78}$	$1 < D < 1000$	Local threshold
Larsen and Simon [17]	Porte Rico, Caribbean Sea	$I = 91.46D^{-0.82}$	$2 < D < 312$	Regional threshold
Crosta and Frattini [6]	World	$I = 0.48 + 7.2D^{-1}$	$0.1 < D < 1000$	Global threshold
Aleotti [2]	Piedmont region, Italy	$I = 19.0D^{-0.50}$	$4 < D < 150$	Regional threshold
Cannon and Gartner [5]	World	$I = 7.0D^{-0.6}$	$0.1 < D < 3$	Global threshold
Dahal and Hasegawa [7]	Himalaya, Nepal	$I = 73.9D^{-0.79}$	$5 < D < 720$	Regional threshold
Guzzetti et al. [11]	World	$I = 2.2D^{-0.44}$	$0.1 < D < 1000$	Global threshold
Mathew et al. [18]	Garhwal Himalaya, India	$I = 58.7D^{-1.12}$	$5 < D < 100$	Regional threshold
Kanungo and Sharma [14]	Chamoli-Joshimath, Garhwal Himalayas	$I = 1.82D^{-0.23}$	$24 < D < 336$	Local threshold
Dikshit and Satyam [8]	Kalimpong, Darjeeling, India	$I = 3.52D^{-0.41}$	$24 < D < 120$	Regional threshold
Harilal et al. [12] ^a	Sikkim	$I = 43.26D^{-0.78}$	$1 < D < 30$	Regional threshold
	Gangtok	$I = 100D^{-0.92}$	$1 < D < 30$	Local threshold

^a D , rainfall duration in days; I , the intensity of rainfall in mm/days

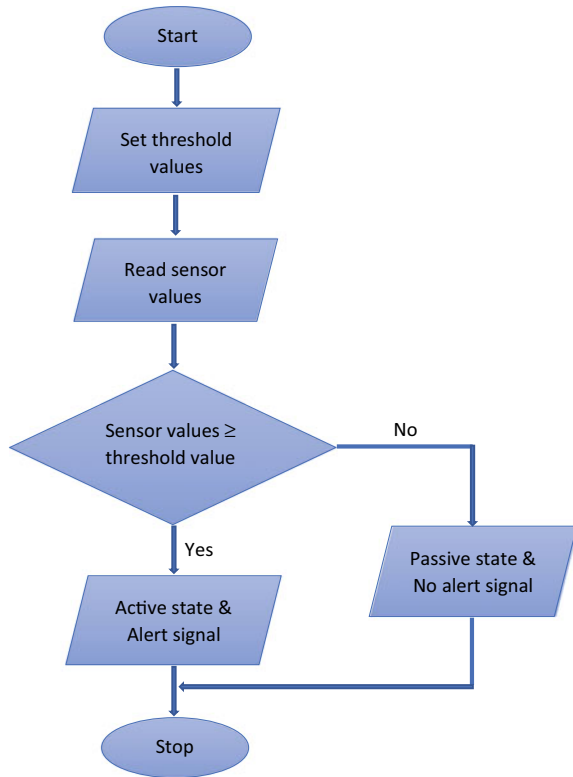
the geographical area. Table 15.2 lists the various I – D relationships and thresholds reported in the literature.

The pore pressure and moisture thresholds are only activated once the rainfall data crossed its respective threshold [22]. If data analysis outcomes provide a triggering parameter value more than the predefined threshold value, then the node is changed to an active state and generates the alert signal. Otherwise, it drops the data packet and stays in a passive state, and no alert signal occurs, as shown in Fig. 15.2.

Limitations

The main limitation of IoT-based networks is that it requires a continuous power supply for real-time monitoring of sensed data which is very difficult when the

Fig. 15.2 Flowchart for early warning of landslides based on threshold model



monitored sites are in remote locations. This complexity becomes further aggravated due to rough weather conditions [16]. Deployment of IoT-based systems requires comprehensive field investigations, which is not always feasible in hilly terrains with extensive vegetative index. Also, WSN for landslide monitoring of vast regions involves a large number of wireless nodes, which not only increases the size of the network and its complexity, but also compromises the accuracy of the detection system [15].

Summary

The present study reviews the essential components of real-time ground-based monitoring techniques of landslides. The study shows that the WSN-based early warning system is one of the best-suited effective technologies for real-time monitoring of regions prone to landslides by using various sensors capable of functioning in real-time and continuous monitoring of landslides-triggering parameters. The network integrates wireless sensor nodes for effective data collection, data processing, data

transfer, and a threshold-based early warning system. The three primary components of this system are as follows: (a) An arrangement of sensors installed at landslide-prone region to monitor the critical parameters like rainfall, soil moisture, pore water pressure, displacement and tilt, (b) Wireless sensor networks (WSNs) connecting the network of sensors with a data management center, and (c) Landslide detection algorithms which continuously analyze the sensed data and compare with a predefined threshold value for triggering parameters like rainfall and soil moisture and activate an alert signal if any of the sensed data exceeds the corresponding threshold value. Thus, this system detects all the environmental changes that trigger landslides, generates an early alert signal, and reduces the loss of lives and property.

References

1. Abraham MT et al (2020) IoT-based geotechnical monitoring of unstable slopes for landslide early warning in the Darjeeling Himalayas. *Sensors* (Switzerland) 20(9). <https://doi.org/10.3390/s20092611>
2. Aleotti P (2004) A warning system for rainfall-induced shallow failures. *Eng Geol* 73:3–4. <https://doi.org/10.1016/j.enggeo.2004.01.007>
3. Caine N (1980) The rainfall intensity-duration control of shallow landslides and debris flows. *Geogr Ann Ser A* 62:1–2. <https://doi.org/10.1080/04353676.1980.11879996>
4. Cancelli A, Nova R (1985) Landslides in soil debris cover triggered by rainstorms in Valtellina (Central Alps—Italy). In: *Proceedings of the 4th international conference and field workshop on landslides*. The Japan Geological Society, Tokyo, pp 267–272
5. Cannon SH, Gartner JE (2007) Wildfire-related debris flow from a hazards perspective. In: *Debris-flow hazards and related phenomena*. https://doi.org/10.1007/3-540-27129-5_15
6. Crosta G, Frattini P (2001) Rainfall thresholds for triggering soil slips and debris flow. In: *Proceeding of 2nd EGS Plinius conference on Mediterranean storms*, Siena, pp 463–487
7. Dahal RK, Hasegawa S (2008) Representative rainfall thresholds for landslides in the Nepal Himalaya. *Geomorphology* 100:3–4. <https://doi.org/10.1016/j.geomorph.2008.01.014>
8. Dikshit A, Satyam DN (2018) Estimation of rainfall thresholds for landslide occurrences in Kalimpong, India. *Innov Infrastruct Solut* 3:1. <https://doi.org/10.1007/s41062-018-0132-9>
9. Giorgetti A et al (2016) A robust wireless sensor network for landslide risk analysis: system design, deployment, and field testing. *IEEE Sens J* 16:16. <https://doi.org/10.1109/JSEN.2016.2579263>
10. Giri P et al (2019) Wireless sensor network system for landslide monitoring and warning. *IEEE Trans Instrum Meas* 68:4. <https://doi.org/10.1109/TIM.2018.2861999>
11. Guzzetti F et al (2008) The rainfall intensity-duration control of shallow landslides and debris flows: an update. *Landslides* 5:1. <https://doi.org/10.1007/s10346-007-0112-1>
12. Harilal GT et al (2019) Towards establishing rainfall thresholds for a real-time landslide early warning system in Sikkim, India. *Landslides* 16:12. <https://doi.org/10.1007/s10346-019-01244-1>
13. Joshi A et al (2020) Real-time landslide monitoring, detection and early warning system for Tangni landslide. *SSRN Electron J*. <https://doi.org/10.2139/ssrn.3511001>
14. Kanungo DP, Sharma S (2014) Rainfall thresholds for prediction of shallow landslides around Chamoli-Joshimath region, Garhwal Himalayas, India. *Landslides* 11:4. <https://doi.org/10.1007/s10346-013-0438-9>
15. Khan R et al (2021) Exploring a design of landslide monitoring system. *Complexity*. <https://doi.org/10.1155/2021/5552417>

16. Kumar S et al (2020) Reliable network connectivity in wireless sensor networks for remote monitoring of landslides. *Wirel Netw* 26:3. <https://doi.org/10.1007/s11276-019-02059-7>
17. Larsen MC, Simon A (1993) A rainfall intensity-duration threshold for landslides in a humid-tropical environment, Puerto Rico. *Geogr Ann Ser A, Phys Geogr* 75(1/2). <https://doi.org/10.2307/521049>
18. Mathew J et al (2014) Integrating intensity-duration-based rainfall threshold and antecedent rainfall-based probability estimate towards generating early warning for rainfall-induced landslides in parts of the Garhwal Himalaya, India. *Landslides* 11:4. <https://doi.org/10.1007/s10346-013-0408-2>
19. Mishra P et al (2011) Detection of landslide using wireless sensor networks. *IEEE*
20. Ramesh MV (2009) Real-time wireless sensor network for landslide detection. In: *Proceedings—2009 3rd international conference on sensor technologies and applications, SENSORCOMM 2009*. <https://doi.org/10.1109/SENSORCOMM.2009.67>
21. Ramesh MV, Vasudevan N (2012) The deployment of deep-earth sensor probes for landslide detection. *Landslides* 9:4. <https://doi.org/10.1007/s10346-011-0300-x>
22. Ramesh MV (2014): Design, development, and deployment of a wireless sensor network for detection of landslides. *Ad Hoc Netw* 13 Part A. <https://doi.org/10.1016/j.adhoc.2012.09.002>
23. Romdhane RF et al (2017) Wireless sensors network for landslides prevention. In: *2017 IEEE international conference on computational intelligence and virtual environments for measurement systems and applications, CIVEMSA 2017—Proceedings*. <https://doi.org/10.1109/CIVEMSA.2017.7995330>
24. Shukla SK et al (2014) Real-time monitoring system for landslide prediction using wireless sensor networks. *Int J Mod Commun Technol Res* 2:12
25. Sruthy MR et al (2020) IoT based landslide detection and monitoring system. *Int J Res Eng Sci Manag* 3(4):596–599
26. Terzis A et al (2006) Slip surface localization in wireless sensor networks for landslide prediction. In: *Proceedings of the fifth international conference on information processing in sensor networks, IPSN'06*. <https://doi.org/10.1145/1127777.1127797>
27. Wang H et al (2011) Research on one ZICM2410-based wireless sensor network for landslide monitoring. In: *7th International conference on wireless communications, networking and mobile computing, WiCOM 2011*. <https://doi.org/10.1109/wicom.2011.6040373>

Chapter 16

A Comprehensive Review on Rainfall-Induced Slope Failures: Mechanism, Models, and Influencing Factors



Vineet Gajamer and Abhishek Kumar

Introduction

‘Landslide’ refers to any outward and downward movement of materials forming the slope, due to various artificial and natural causes. It is a general term that incorporates all possible material and mass movement behavior [1]. Rainfall-induced landslides are one of the most common problems faced by sub-tropical and tropical countries. Not only slopes but other geotechnical structures such as fills and embankments are also seriously affected by the rainfall. Hong Kong, Singapore, and India are some of the countries where landslides are predominantly rainfall induced [2–4].

Conventionally, rainfall is incorporated into slope stability analysis by increasing the pressure head at the boundary by raising the ground water table. Such an approach does not always represent the actual field condition as in the case of a shallow slope failure [5]. These are caused due to reduction in the shear strength of the soil caused by the loss of matric suction due to seepage of wetting front [6]. Numerous works have been done to model water flow in soil for a better understanding of seepage and infiltration in a slope. This study initially presents a concise review of the mechanism of rainfall-induced slope failure, followed by numerical modeling of a typical failed slope to understand the mechanism of failure.

V. Gajamer (✉) · A. Kumar

Department of Civil Engineering, Indian Institute of Technology Guwahati, Guwahati 781039,
India

e-mail: vineetgajamer@gmail.com

Mechanism of Rainfall-Triggered Landslides

For an unsaturated soil slope, the stability condition can generally be understood based on the degree of saturation and matric suction. A single rainfall event can adversely affect the matric suction at shallower depths, but seasonal trends and prolonged rainfall can affect the slope at greater depths [7]. Collins and Znidarcic [8] explained three different mechanisms of failure due to infiltration. The first mechanism highlights the rise in pore water pressure (PWP) at deeper depths of a slope or along a soil–rock interface. This can induce capillary barrier effect. Small displacements along such zones with high degree of saturation can cause rapid movements with large runout distances and ultimately static liquefaction [9]. In the second mechanism, Collins and Znidarcic [8] discussed slope failures due to loss in shear strength because of reduction in soil suction in an unsaturated soil slope. In this failure mechanism, there is no development of seepage force as the PWP is not positive. The third failure mechanism is for coarse-grained soil slopes, where the conventional mechanism is not considered. If slope is composed of coarse-grained soil, failure usually occurs in zones of positive PWP regimes, triggered by seepage forces acting downward from the top of the slope [8].

Cascini et al. [10] highlighted the role played by the flux conditions along the underlying bedrock interface in affecting the PWP regime. Failure due to generation of spring water in bedrock has been identified from field monitoring studies in San Francisco Bay [11] and the Oregon Coast range [12]. Cascini et al. [10] state that a possible combination of rainfall infiltration from the surface and spring from bedrock serves as a possible triggering mechanism. Hydrogeological and geomorphological analyses done for shallow landslides in pyroclastic deposits in Italy showed the same triggering mechanism [13].

In another work, McSaveney and Griffiths [14] highlight the critical role that temperature plays in aggravating rainfall-induced landslides. In the year 1978, a landslide was reactivated in Waipara, New Zealand after a rainy winter. The study by McSaveney and Griffiths [14] suggested that dry summer-initiated desiccation cracking makes it possible for water to percolate into impermeable regolith. As a result, the movement started when the water accumulation was at its peak at the end of the winter. The infiltration of rainwater through desiccation cracks caused leaching and dilation of over-compacted mudstone leading to displacement of a block by 155 m.

Though numerous studies were done in due course of time where rainfall-triggered landslides were explained in terms of soil weight, PWP variations, seepage forces, etc., the mechanism of some landslides still could not be explained. Liu et al. [15] performed water–air (two phase) flow numerical simulations and experimentation to confirm the reduction in effective stress in the soil due to increase in pore gas pressure. The numerical study results exhibit that when shallower depths of a slope are saturated, pore gas within the slope gets compressed. The study highlighted that the decrease in the factor of safety with the consideration of water–air coupling

is twice the decrease in the factor of safety without the consideration of water–air coupling. It was emphasized that the pressure generated at the toe may induce a landslide. It has to be highlighted here that this failure mechanism may not be prevalent in all types of slopes as it depends on the sealing conditions of the slope, which is influenced by factors such as soil type, topography, and rainfall intensity. Such a failure mechanism is mostly observed in slopes having gases within, e.g., a waste landfill.

Infiltration Models

Infiltration can be defined as “the entry of water into the soil surface and its subsequent vertical motion through the soil profile” [16]. The soil system is a complex system with spatially varying properties and complex boundary conditions. The most robust and exact representation of infiltration can be given by combining Darcy’s law with the equation of continuity. In such a case, the solution to the partial differential equations is complex and it requires time and expertise to solve. To avoid such complexities, conceptual models were developed where a reasonable representation of physical reality compensates for the simplification of the physical conditions. Examples of some conceptual models are: *Green-Ampt*, *Lumb*, *Sun et al.*, *Gavin and Xue*, *Chen and Young* infiltration models [17–20].

However, the conceptual models had some major assumptions and limitations when applied to sloping surface. Factors such as the slope of the surface and the downward flow along the slope were not considered in most conceptual models. Further, consideration of a distinct wetting front separating saturated and unsaturated zones of soil is not something that always occurs in the field [21]. The dependency of hydraulic properties of soil on the degree of saturation is also not generally taken into account in conceptual models [21]. A more accurate representation of PWP distribution of complex cases can be generated by solving the governing equation of water flow. Solutions to the governing equation can be obtained either analytically or numerically.

The governing equation of water flow in unsaturated soil was formulated by Richard [22] based on Darcy’s law and mass conservation law, given by:

$$\frac{\partial}{\partial x} \left(k_x \frac{\partial h}{\partial x} \right) + \frac{\partial}{\partial y} \left(k_y \frac{\partial h}{\partial y} \right) + \frac{\partial}{\partial z} \left(k_z \frac{\partial h}{\partial z} \right) = - \frac{\partial \theta_w}{\partial t} \quad (16.1)$$

Here, ‘ θ_w ’ is the volumetric water content (VWC); (x, y, z) define the co-ordinate system, and ‘ t ’ is time. The hydraulic conductivity ‘ k ’ is a function of soil suction, which is in turn a function of VWC. ‘ h ’ denotes the total head. Equation 16.1 is a second-order partial differential equation, and obtaining a solution to the equation is a complex procedure.

Basha [23] applied Green’s function to develop a general analytical model for a multi-dimensional non-steady infiltration for a shallow water table. Arbitrary

initial and boundary conditions were used in the model. Hydraulic conductivity was assumed to be varying exponentially with water pressure and linearly with moisture content. Infiltration models for various simple geometry were developed. Most of the solutions were a product of two functions: a function of depth and a function of time and lateral co-ordinates. The effect of water table and soil type on two-dimensional moisture movement could be observed from a strip source. Chen et al. [24] introduced a new method of applying Fourier integral to obtain multi-dimensional linearized Richard's equation. Both hydraulic conductivity and VWC are considered to vary exponentially with soil suction. The analytical solutions can be used to estimate ponding time and obtain the temporal and spatial distribution of VWC. Yuan and Lu [25] derived analytical solutions to Richard's equation describing the variation of pressure head, VWC, and fluid flow for rooted, homogeneous soils. Kirchhoff transformation was used to linearize Richard's equation. Solution to the equation for steady-state condition is a closed-form solution, while the solution for transient conditions is an infinite series. The assumptions are the model's limitations, but the model is flexible and can be modified according to one's interest of application.

The advent of numerical modeling happened to address the limitations of analytical modeling. The high nonlinearity of soil hydraulic properties in transient conditions could not be incorporated in the analytical models. Moreover, assumptions had to be made assuming some initial and boundary conditions [26]. Attempts were made by researchers to study slope subjected to rainfall by numerical modeling by researchers such as Ng and Shi [21] and Gasmo et al. [27]. Cai and Ugai [28] successfully modeled a slope numerically and studied the effects of initial degree of saturation, hydraulic characteristics, boundary conditions, rainfall intensity and duration. The results were in good comparison with results obtained from existing methods. Huang and Jia [29] extended the finite element modeling to shear strength reduction technique (FEMSSR) considering unsaturated transient seepage. FEMSSR technique has been widely used hereafter considering the accurate results given by the study. Numerous computer software have been developed to numerically model seepage of water into unsaturated slopes such as *Seep/W*, *RS2*, *SVflux*, and *Hydrus*.

Other Factors

Numerous researchers have studied the influencing factors by segregating different parameters and performing a parametric study as highlighted below:

Cai and Ugai [28], conducted finite element-based analysis and investigated the effects of hydraulic characteristics, initial degree of saturation, boundary condition, and rainfall pattern and intensity on PWP developed in slopes. As per the work, soils with low permeability exhibited sudden rise in PWP when the unsaturated zone got fully saturated. Further, the rate of increase in PWP was higher for soils with comparatively higher degree of saturation. In addition, the effect of a different boundary condition was more in the case of slopes composed of high-permeable soil.

For slopes with low permeability, it was observed that the slope failed only if the rainfall lasted a threshold duration even when the rainfall intensity was high.

Rahardjo et al. [30] attempted to understand rainfall-induced landslides in residual soil slopes of tropical regions. The major aim of the study was to quantify flux boundary conditions. The study concluded that runoff was generated when the rainfall exceeded an intensity of 10 mm/hr. It was also found out that the residual slope was affected more by a number of rainfall events of less intensity than a single event of higher intensity. It was also observed that the matric suction is recovered during drier periods due to redistribution.

Rahardjo et al. [3] instrumented four slopes of majorly two geological formation types in Singapore to depict the PWP variation due to various rainfall events, which directly controls the flux boundary condition. The study's key finding was that for residual slopes, antecedent rainfall plays a more critical role in creating the worst PWP pressure conditions in less-permeable slopes composed of higher fines than more permeable slopes composed of lesser fines. The factor of safety for residual slopes with high cohesion was not affected by PWP variation due to rainfall. In addition, antecedent rainfall and initial PWP conditions play a crucial role in the behavior of slopes when it undergoes a major rainfall event.

Ali et al. [31] investigated the general assumption that failure of slopes occurs at an impermeable boundary that exists at a certain depth. Three boundary conditions (fully drained, partially drained, and undrained) at the soil–rock interface were considered for the analysis.

It was found that for more permeable boundaries, only, shallow slope failure occurred, and for less permeable boundary condition, deep failure occurred. The depth of failure decreases nonlinearly with the increase in rainfall intensity. Further, the effect of boundary conditions becomes more prominent when the rainfall intensity falls below the critical value, with failure occurring only at the boundary.

Case Study

Study Area and Material Parameters

A slope on the southeastern face of 'Kurseong' Hill in West Bengal has been in constant discussion due to recurring landslides, mainly during the monsoon period. The geolocation of the slope under study is N 26.52° to N 26.53° and longitude E 88.17° to E 88.19°. The slope has a varying profile with a maximum slope angle of 84° [32]. The geology of the area majorly comprises four different lithology types [1], which directly implies the presence of structural discontinuities. In combination with structural discontinuities, the geological formations are mostly meta-sedimentary rocks comprising schists, phyllites, and quartzites. Such a geological setup causes tectonic denudation, making slopes highly susceptible to slope failure. This is a common cause of slope failures in the Eastern Himalayas [33].



Fig. 16.1 Failed slope face (2021)

Temperate climatic condition is prevalent in the study region with most of the rainfall occurring in July. The mass movement was initiated due to toe erosion at a very high rate, which happened because of the artificial manipulation of stream paths in 2005 [34]. Though slope stabilization works had been carried out, the slope has experienced repeated failure, most of it occurring during monsoon due to heavy rainfall (Fig. 16.1).

Samanta and Majumdar [32] showed that at a particular section, the slope has no strong geomaterial at least up to a depth of 18 m by means of electrical resistivity survey. This section has been chosen for the finite element-based analysis. The slope profile was developed using ArcGIS. Since the presence of soil was confirmed only up to a depth of 18 m, analysis was done for two soil thicknesses, i.e., 20 and 30 m. The results of the model with 20-m soil thickness matched well with the field observation; hence, the analysis for 30-m soil thickness was discarded. Figure 16.2 shows the 2D model considered for analysis.

The input parameters for the soil have been adopted from [35], and for the weathered bedrock, Geological Strength Index value of 25 has been adopted from field observations of scarp faces. Subsequently, the values of various parameters for quartzo feldspathic bedrock have been adopted from the literature [36–39] considering Generalized Hoek–Brown Failure Criterion.

Analysis and Results

A finite element analysis was done on a software package developed by Rocscience, namely RS2. A fully coupled transient seepage analysis was performed governed by

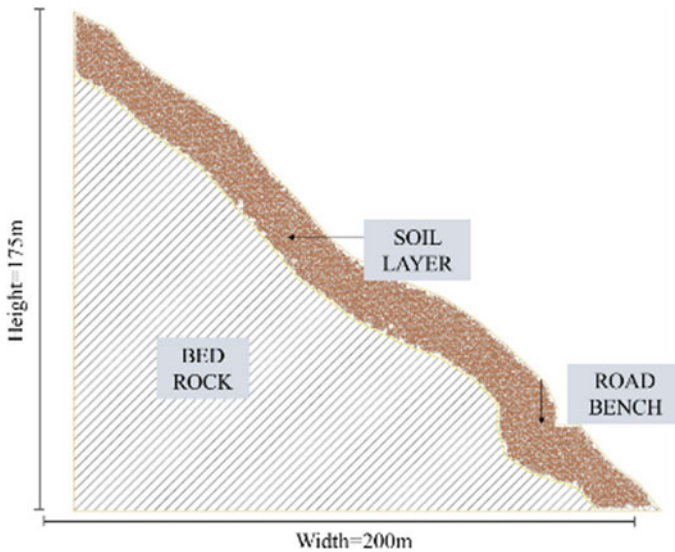


Fig. 16.2 Model considered for analysis

Biot's consolidation equation. Six-noded triangular elements were used to discretize the model, and an optimum mesh resolution was attained using h-convergence method. Further, to make the analysis more realistic, real-life rainfall data were obtained from a nearby weather station. It is imperative to incorporate matric suction because of its vital role in imparting stability, as discussed in the earlier sections. Hence, unsaturated soil parameters were estimated using available data for a similar soil type [40] with the help of the software package RETC.

The analysis has been instrumental in uncovering the critical aspects of the failure of the slope. The matric suction was relatively high before rainfall which decreased drastically when high-intensity rainfall was applied to the model. Subsequently, the strength reduction factor is also reduced, indicating reduced stability of the slope. In addition to the reduced stability due to the decrease in matric suction, water accumulates in the soil-rock interface, completely saturating it (Fig. 16.3), due to capillary barrier effect. The matric suction was quickly recovered even when the slope was subjected to a nominal rainfall intensity.

The total displacement contour (Fig. 16.4) exhibits translational movement at the mid-section of the slope whereas, at the toe region the slip surface formed is circular.

The top scarp position obtained in the analysis is in accordance with the scarp position in the field. Also, the sagging of road in the field is an indication of formation of a similar slip surface below the road bench, as obtained in the analysis.

The study shows that a slope's stability can be highly compromised due to rainfall as seepage can saturate critical locations within a slope, triggering mass movement. Such slopes should be identified, and proper drainage arrangements should be made to stop hazards.

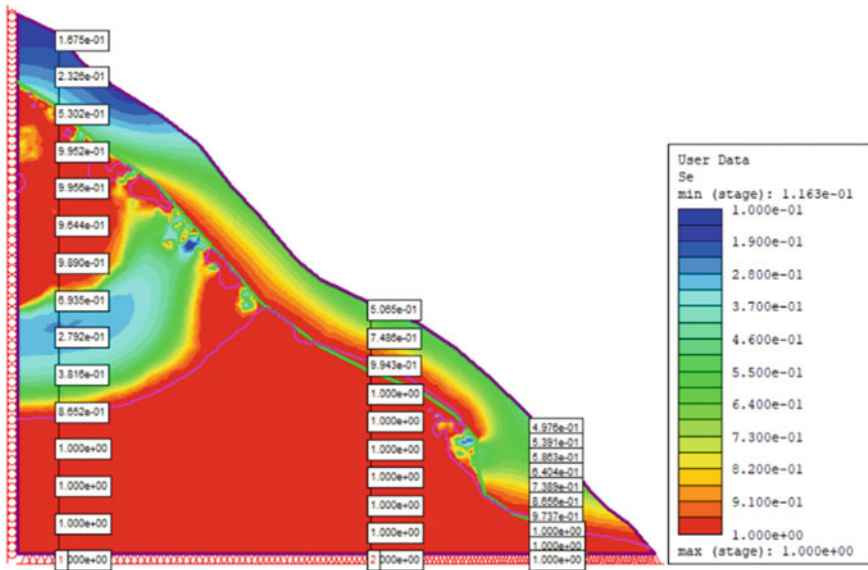


Fig. 16.3 Degree of saturation

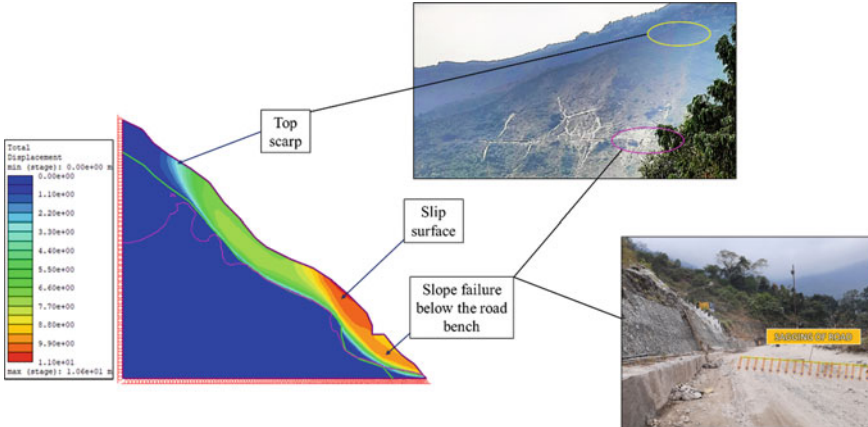


Fig. 16.4 Displacement profile of the slope

Conclusion

This paper summarizes the literature on mechanism, models, and influencing factors pertaining to rainfall-induced landslides. Further, more studies toward understanding the infiltration with surface vegetation, transition in movement type of slope-forming materials, role of fracture and macropores in preferential flows and anisotropy are

required. In addition, a case study of slope failure has been analyzed in RS2 platform using in-situ information. Based on the analysis, it is concluded that seepage due to prolonged rainfall caused full saturation of critical locations within the slope, leading to mass movement in the form of slope failure.

References

1. Varnes DJ (1958) Landslide types and processes. Highw Res Board. Spec Rep no 29
2. Lumb P (1962) The properties of decomposed granite. *Géotechnique* 12(3):226–243. <https://doi.org/10.1680/geot.1962.12.3.226>
3. Rahardjo H, Leong EC, Rezaur RB (2008) Effect of antecedent rainfall on pore-water pressure distribution characteristics in residual soil slopes under tropical rainfall. *Hydrol Process* 22(4):506–523. <https://doi.org/10.1002/hyp.6880>
4. Senthilkumar V, Chandrasekaran SS, Maji VB (2018) Rainfall-induced landslides: case study of the Marappalam landslide, Nilgiris district, Tamil Nadu, India. *Int J Geomech* 18(9):5018006. [https://doi.org/10.1061/\(ASCE\)GM.1943-5622.0001218](https://doi.org/10.1061/(ASCE)GM.1943-5622.0001218)
5. Fourie AB (1996) Predicting rainfall-induced slope instability. *Proc Inst Civ Eng Geotech Eng* 119(4):211–218. <https://doi.org/10.1680/igeng.1996.28757>
6. Rezaur RB, Rahardjo H, Leong EC, Lee TT (2003) Hydrologic behavior of residual soil slopes in Singapore. *J Hydrol Eng* 8(3):133–144. [https://doi.org/10.1061/\(ASCE\)1084-0699\(2003\)8:3\(133\)](https://doi.org/10.1061/(ASCE)1084-0699(2003)8:3(133))
7. Alsubal S, bin Sapari N, Harahap ISH, Al-Bared MAM (2019) A review on mechanism of rainwater in triggering landslide. *IOP Conf Ser Mater Sci Eng* 513(1):012009. <https://doi.org/10.1088/1757-899X/513/1/012009>
8. Collins BD, Znidarcic D (2004) Stability analyses of rainfall induced landslides. *J Geotech Geoenviron Eng* 130(4):362–372. [https://doi.org/10.1061/\(ASCE\)1090-0241\(2004\)130:4\(362\)](https://doi.org/10.1061/(ASCE)1090-0241(2004)130:4(362))
9. Wang G, Sassa K (2001) Factors affecting rainfall-induced flowslides in laboratory flume tests. *Géotechnique* 51:587–599. <https://doi.org/10.1680/geot.51.7.587.51386>
10. Cascini L, Cuomo S, Manuel, Sorbino G (2010) Modeling of rainfall-induced shallow landslides of the flow-type. *J Geotech Geoenviron Eng* 136(1):85–98. <https://doi.org/10.1061/ASCEGT.1943-5606.0000182>
11. Johnson KA, Sitar N (1990) Hydrologic conditions leading to debris-flow initiation. *Can Geotech J* 27(6):789–801. <https://doi.org/10.1139/T90-092>
12. Montgomery DR, Dietrich WE, Heffner JT (2002) Piezometric response in shallow bedrock at CB1: implications for runoff generation and landsliding. *Water Resour Res* 38(12):10–11. <https://doi.org/10.1029/2002WR001429>
13. Cascini L, Guida D, Nocera N, Romanzi G, Sorbino G (2000) A preliminary model for the landslides of May 1998 in Campania region. In: Evangelista A, Picarelli L (eds) *Proc 2nd Int symp on the geotechnics of hard soils-soft rocks*, Napoli: 1623–1649
14. McSaveney MJ, Griffiths GA (1987) Drought, rain, and movement of a recurrent earthflow complex in New Zealand. *Geology* 15(7):643–646. [https://doi.org/10.1130/0091-7613\(1987\)15%3c643:DRAMOA%3e2.0.CO;2](https://doi.org/10.1130/0091-7613(1987)15%3c643:DRAMOA%3e2.0.CO;2)
15. Liu G, Tong F, Zhao Y, Tian B (2018) A force transfer mechanism for triggering landslides during rainfall infiltration. *J Mt Sci* 15(11):2480–2491. <https://doi.org/10.1007/S11629-018-5043-X>
16. Assouline S (2013) Infiltration into soils: conceptual approaches and solutions. *Water Resour Res* 49(4):1755–1772. <https://doi.org/10.1002/WRCR.20155>
17. Heber Green W, Ampt GA (1911) Studies on soil Physics. *J Agric Sci* 4(1):1–24. <https://doi.org/10.1017/S0021859600001441>

18. Lumb P (1975) Slope failures in Hong Kong. *Q J Eng Geol* 8(1):31–65. <https://doi.org/10.1144/GSL.QJEG.1975.008.01.02>
19. Gavin K, Xue J (2008) A simple method to analyze infiltration into unsaturated soil slopes. *Comput Geotech* 35(2):223–230. <https://doi.org/10.1016/J.COMPGEO.2007.04.002>
20. Chen MYL (2006) Green-Ampt infiltration model for sloping surface. *Water Resour Res* 42:1–9
21. Ng CWW, Shi Q (1998) A numerical investigation of the stability of unsaturated soil slopes subjected to transient seepage. *Comput Geotech* 22(1):1–28. [https://doi.org/10.1016/S0266-352X\(97\)00036-0](https://doi.org/10.1016/S0266-352X(97)00036-0)
22. Richards LA (1931) Capillary conduction of liquids through porous mediums. *Physics* 1:318–333. <https://doi.org/10.1063/1.1745010>
23. Basha HA (2000) Multidimensional linearized nonsteady infiltration toward a shallow water table. *Water Resour Res* 36(9):2567–2573. <https://doi.org/10.1029/2000WR900150>
24. Chen J-M, Tan Y-C, Chen C-H (2001) Multidimensional infiltration with arbitrary surface fluxes. *J Irrig Drain Eng* 127(6):370–377. [https://doi.org/10.1061/\(ASCE\)0733-9437\(2001\)127:6\(370\)](https://doi.org/10.1061/(ASCE)0733-9437(2001)127:6(370))
25. Yuan F, Lu Z (2005) Analytical solutions for vertical flow in unsaturated, rooted soils with variable surface fluxes. *Vadose Zo J* 4(4):1210–1218. <https://doi.org/10.2136/VZJ2005.0043>
26. Zhang LL, Zhang J, Zhang LM, Tang WH (2011) Stability analysis of rainfall induced slope failure: a review. *Proc Inst Civ Eng Geotech Eng* 164(5):299–316. <https://doi.org/10.1680/jeng.2011.164.5.299>
27. Gasmoo JM, Rahardjo H, Leong E (2000) Infiltration effects on stability of a residual soil slope. *Comput Geotech* 26:145–165. [https://doi.org/10.1016/S0266-352X\(99\)00035-X](https://doi.org/10.1016/S0266-352X(99)00035-X)
28. Cai F, Ugai K (2004) Numerical analysis of rainfall effects on slope stability. *Int J Geomech* 4(2):69–78. [https://doi.org/10.1061/\(ASCE\)1532-3641\(2004\)4:2\(69\)](https://doi.org/10.1061/(ASCE)1532-3641(2004)4:2(69))
29. Huang M, Jia C-Q (2009) Strength reduction FEM in stability analysis of soil slopes subjected to transient unsaturated seepage. *Comput Geotech* 36(1–2):93–101. <https://doi.org/10.1016/j.compgeo.2008.03.006>
30. Rahardjo H, Lee TT, Leong EC, Rezaur RB (2005) Response of a residual soil slope to rainfall. *Can Geotech J* 42(2):340–351. <https://doi.org/10.1139/t04-101>
31. Ali A, Huang J, Lyamin AV, Sloan SW, Cassidy M (2014) Boundary effects of rainfall-induced landslides. *Comput Geotech* 61:341–354. <https://doi.org/10.1016/j.compgeo.2014.05.019>
32. Samanta SK, Majumdar RK (2020) Identification of landslide-prone slopes at Paglajhora area, Darjeeling Himalaya, India. *Landslides* 17(11):2643–2657. <https://doi.org/10.1007/s10346-020-01472-w>
33. Petley DN et al (2007) Trends in landslide occurrence in Nepal. *Nat Hazards* 43(1):23–44. <https://doi.org/10.1007/s11069-006-9100-3>
34. Desai M (2005) Geological survey for suggesting remedial measures in respect of rehabilitation of NH-55 and Giddha Pahar area at Km 34 of NH-55 in the district of Darjeeling, West Bengal. Netaji Institute for Asian Sciences
35. Mandal S (2015) A comprehensive review on Paglajhora sinking zone landslide in the Shivkhola watershed of Darjeeling Himalaya. *Int J Geol Earth Environ Sci* 5(2):156–170
36. Özbek A, Gül M, Karacan E, Alca Ö (2018) Anisotropy effect on strengths of metamorphic rocks. *J Rock Mech Geotech Eng* 10(1):164–175. <https://doi.org/10.1016/j.jrmge.2017.09.006>
37. Hoek E, Carranza C, Corkum B (2002) Hoek-brown failure criterion—2002 edition. *Proc NARMS-TAC Conf, Toronto* 1:267–273
38. Zhang L (2008) A generalized three-dimensional Hoek-Brown strength criterion. *Rock Mech Rock Eng* 41(6):893–915. <https://doi.org/10.1007/s00603-008-0169-8>
39. Dev H (2017) Deformability characteristics of Garnetiferous Quartzo-Feldspathic Gneiss rock mass—a case study. *Int J Innov Res Sci Technol* 3(9):64–68
40. Das UK, Saikia BD (2011) Evaluation of a prediction model for shear strength of unsaturated soils. *Proc Indian Geotech Conf, Kochi*:643–646

Chapter 17

Optimum Thickness of Veneer Cover Soil of MSW Landfill for Stability Against Uplifted-Floating Failure



Dabbiru Soujanya and B. Munwar Basha

Introduction

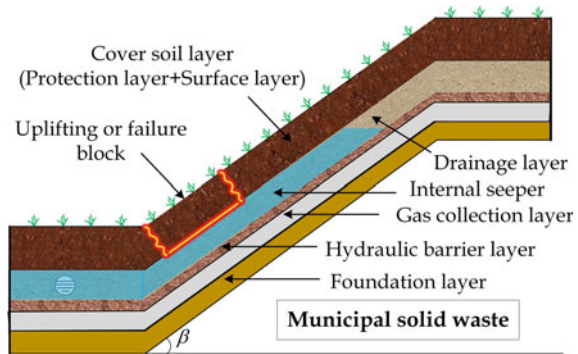
Veneer cover is a multi-layered system that is constructed as a final closure of municipal solid waste (MSW) landfill to prevent the entry of stormwater into it. The veneer cover system also controls the toxic emissions of landfills and protects the surrounding environment and human health. The components of the veneer cover system which include the foundation layer, gas collection layer, hydraulic barrier layer, drainage layer, a protection layer, and surface layer are schematically shown in Fig. 17.1. The stability and durability of the landfill cover system depend on the functioning of each of its individual components. However, the occurrence of cover system failures has been noticed in recent times due to the improper design of individual layers [1].

A well-designed drainage layer of the cover system plays a key role in maintaining stability during heavy rainfall conditions by draining the stormwater. A poorly designed drainage layer may not successfully drain the water. It leads to the clogging of water in the drainage layer. The combination of rainfall-induced seepage build-up and inadequate internal drainage is the major factor to cause instability of cover soil slope [2]. Chen et al. [3] defined the accumulated water in the drainage layer as internal seep. The excess pore water pressure exerted by the internal seep influences the overlying layers of the drainage layer in losing their stability. Most of the past studies discussed the sliding failure of the cover system caused due to the seepage forces produced in the drainage layer. Apart from direct-slip failure,

D. Soujanya (✉) · B. M. Basha
Indian Institute of Technology Hyderabad, Kandi, Sangareddy, Telangana 502205, India
e-mail: soujanyacivil@gmail.com

B. M. Basha
e-mail: basha@ce.iith.ac.in

Fig. 17.1 Veneer cover system of MSW landfill showing internal seeper in the drainage layer



uplifted-floating (*uf*) failure is proposed by Chen et al. [3] which might occur due to the uplifting forces produced by the internal seeper formed in the drainage layer.

The present study results are helpful in providing optimum, economical, and safe design of veneer cover system. The present study aims at developing design charts to provide the optimum design thickness of the cover soil layer. These design charts assure the safety of veneer cover against uplifted-floating failure mode. The study considers the influence of retained water (i.e., internal seeper) in the drainage layer of the cover system which is subjected to static loading.

Literature Review

Most of the cover soil slope failures reported in the past research are involved with the seepage accumulation in the drainage layer. Seven out of eleven cover soil failures reported by Boschuk [4] were seepage-induced slope failures. Seepage accumulation in the drainage layer is the foremost cause for the long-term failures in slopes [5]. The dreadful impact of such failures has brought out awareness to the designers to consider the seepage effect on the stability of cover soil in recent times.

Nadukuru et al. [2], Feng et al. [6], Khoshand et al. [1], Chen et al. [3], and Soujanya and Basha [7] have reported the effect of seepage build-up in the drainage layer on the sliding stability of the cover system. Nadukuru et al. [2] performed a combined seepage and slope stability analysis to assess the impact of varying drainage conditions on veneer cover stability of landfills. Chen et al. [3] evaluated the veneer cover system stability against direct-slip (*ds*) and uplifted-floating (*uf*) failure modes with the presence of clogged water in the drainage layer. Soujanya and Basha [7] compared the sliding stability of the cover system with and without an internal seeper. Authors reported that there is a significant reduction in the factor of safety against sliding stability in the presence of internal seeper as compared to no seeper condition.

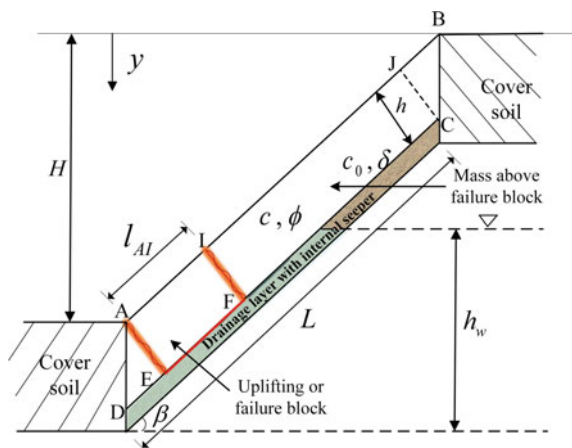
Objectives of the Present Study

It can be noted from the literature that very few studies have discussed the uplifted-floating failure mode of the veneer cover system. The studies pertaining to the determination of the optimum thickness of landfill cover systems with internal seeper are scarce. Therefore, the current study has carried out the analysis of uplifted-floating (*uf*) failure mode that may occur due to the internal seeper formed in the drainage layer of the cover system. This study aims at provides the design charts to recommend the optimum thickness of the cover soil layer in order to ensure stability against uplifted-floating (*uf*) failure. The results are provided for varying immersion-level conditions for different values of stability number and friction angle of cover soil. A design example is illustrated at the end to understand the feasibility and usage of the design charts.

Analysis of Uplifted-Floating (*uf*) Failure

An analytical model is presented for uplifted-floating (*uf*) failure mode as shown in Fig. 17.2. The wedge ‘AEFI’ is the uplifted of failure block, and wedge ‘IFCJ’ is the mass above the failure block as shown in Fig. 17.2. The symbolic notations used in the present analysis are defined as H = height of landfill, h = thickness of cover soil layer above the drainage layer, L = slope length of cover soil, h_w = vertical height of accumulated seepage level, β = slope angle of cover soil, c = cohesion of cover soil layer, ϕ = angle of internal friction of cover soil layer, c_0 = interface cohesion between the drainage layer and the overlying cover soil, δ = interface friction angle between the drainage layer and the overlying cover soil.

Fig. 17.2 Failure blocks and mass above failure blocks for uplifted-floating failure of MSW landfill cover system



As shown in Fig. 17.2, AE and IF are the lower and upper shearing planes, respectively. The location of the upper shearing plane (IF) reflects the size of the uplifted block (AEFI). The size of uplifted or failure block can be assessed by the term failure ratio (Ω) which defines the failure degree of cover soil expressed by Eq. (17.1). Chen et al. [3] carried out the failure ratio analysis to determine the most endangered position of uplifted-floating (*uf*) failure.

$$\Omega = \frac{l_{AI}}{L} \quad (17.1)$$

where l_{AI} is the length of the uplifted failure block as shown in Fig. 17.2. The expressions for the areas of failure blocks and mass above failure blocks (A_f and A_{af}) are given by Eqs. (17.2) and (17.3).

$$A_f = \Omega Lh \quad (17.2)$$

$$A_{af} = \left(1 - \Omega - \frac{h \tan \beta}{L} \right) Lh \quad (17.3)$$

Immersion ratio (I_r) is the term that defines the level of accumulated seep in the drainage layer of the cover system, which is expressed as follows:

$$I_r = \frac{h_w}{L \sin \beta} \quad (17.4)$$

Force Analysis and Factor of Safety Against Uplifted-Floating Failure, FS_{uf}

The forces acting on the failure block (AEFI) and mass above the failure block (IFCJ) are shown in Figs. 17.5 and 17.6. These forces acting on the blocks are described as follows (Figs. 17.3 and 17.4).

The hydraulic pressures acting on the faces AE, EF, and IF for eight different cases of immersion conditions as shown in Figs. 17.3 and 17.4 are derived following the method adopted by Chen et al. [3].

$W_f = \gamma_{sat} A_f$ is the weight of failure block; $W_{af} = \gamma_{sat} A_{af}$ is the weight of mass above failure block; γ_{sat} is the saturated unit weight of cover soil; R_{AE} , R_{EF} , R_{IF} are soil pressures acting on the faces AE, EF, and IF in failure block, respectively; R'_{IF} and R_{FC} are soil pressures acting on the faces IF and FC in the mass above failure block; S_{AE} and S_{IF} are shear resisting forces acting on the faces AE and IF in failure block; S'_{IF} is the shear resisting force acting on the face IF in mass above failure block; U_{AE}^z , U_{EF}^z , U_{IF}^z are hydrostatic pressures acting on the faces AE, EF, and IF

Fig. 17.3 Different cases of immersion levels for the calculation of hydraulic pressures in uplifted-floating failure mode when $\Omega > h/L \tan \beta$, i.e., $l_{AI} > l_{FG}$

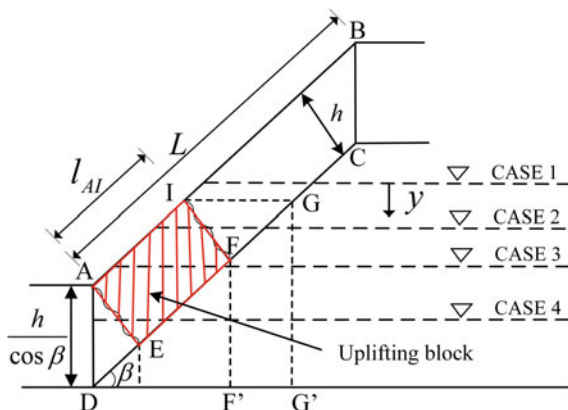


Fig. 17.4 Different cases of immersion level for the calculation of hydraulic pressures in uplifted-floating failure mode when $\Omega < h/L \tan \beta$, i.e., $l_{AI} < l_{FG}$

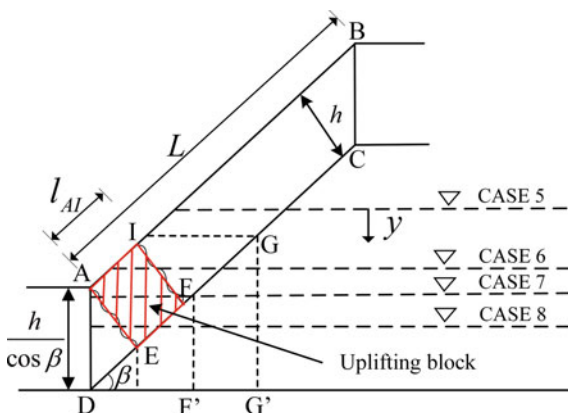
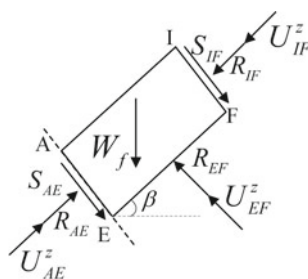


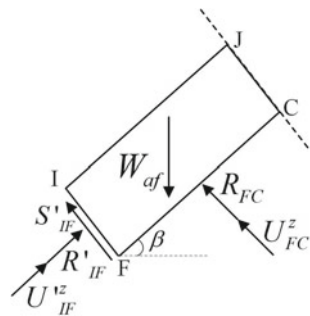
Fig. 17.5 Forces acting on failure block 'AEFI' when there is an internal seep



in failure block; U_{IF}^z, U_{FC}^z are hydrostatic pressures acting on the faces IF and FC in mass above failure block. The 'z' is the case number shown in Figs. 17.3 and 17.4. The present study assumes the horizontal seepage build-up condition in the analysis.

The factor of safety against uplifted-floating (*uf*) failure (FS_{uf}) can be obtained using the force equilibrium approach and is given by Eq. (17.5).

Fig. 17.6 Forces acting on mass above the failure block 'IFCJ' when there is an internal seep



$$F S_{uf} = \frac{2ch + pW_f + qW_{af} - (U_{AE}^z + U_{IF}^z) \tan \phi}{U_{AE}^z} \tag{17.5}$$

where $p = (\sin \beta \tan \phi + \cos \beta)$ and $q = 2 \sin \beta \tan \phi$.

Results and Discussion

Koerner and Soong [8] recommended the use of the minimum factor of safety of 1.5 for the design of veneer cover soil against sliding failure. However, there were no recommendations available in the literature on the allowable factor of safety against uplift floating failure available. Therefore, the minimum factor of safety of 1.5 is chosen for the design of veneer cover soil against uplift floating failure. The allowable thickness of cover soil layer (h) corresponding to the target factor of safety ($FS_{uf} \geq 1.50$) against uplifted-floating failure is computed. The present study considers the following range of design parameters: slope angle of veneer cover (β) = 10° – 60° , length of slope of veneer cover, (L) = 5–80 m, height of the landfill (H) = 5–70 m, thickness of cover soil layer (h) = 0.1–1.5 m, stability number ($c/\gamma_{sat}H$) = 0.02, 0.04, and 0.06, angle of internal friction of cover soil (ϕ) = 20° , 25° , 30° , and 35° , and immersion ratio (I_r) = 0, 0.1 to 0.7. Figures 17.7a–d, 17.8a–d, and 17.9a–d are the design charts developed for $c/\gamma_{sat}H = 0.02$, 0.04, and 0.06, respectively, for different values of friction angle (ϕ) under different immersion ratio (I_r) conditions.

Effect of Immersion Ratio (I_r)

It can be noted from Figs. 17.7a–d, 17.8a–d, and 17.9a–d that the optimum cover soil thickness (h) required to stabilize the cover soil increases with the increase in immersion ratio (I_r). This is because of the increase in uplifting forces caused by the increase of seepage forces with immersion level.

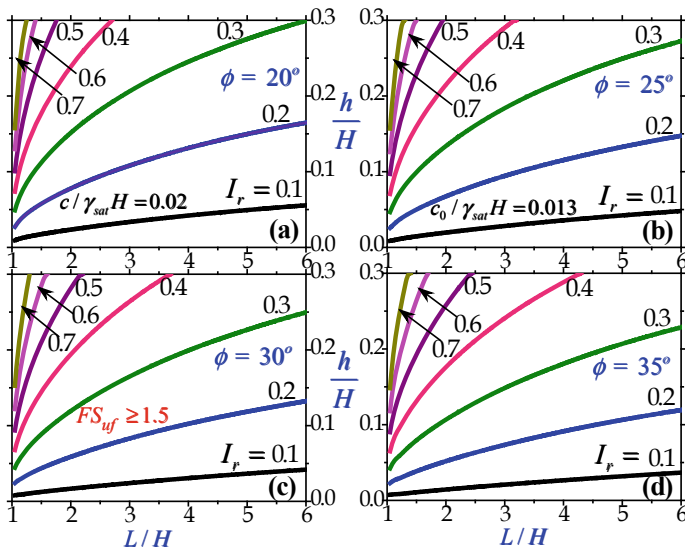


Fig. 17.7 Optimum thickness of cover soil layer (h/H) for $c/\gamma_{sat}H = 0.02$, $c_0/\gamma_{sat}H = 0.013$ for different values of immersion ratio (I_r) and friction angles

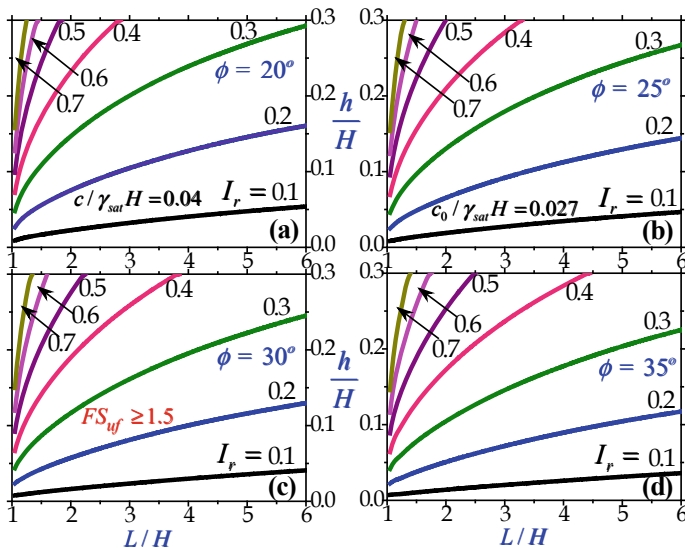


Fig. 17.8 Optimum thickness of cover soil layer (h/H) for $c/\gamma_{sat}H = 0.04$, $c_0/\gamma_{sat}H = 0.027$ for different values of immersion ratio (I_r) and friction angles

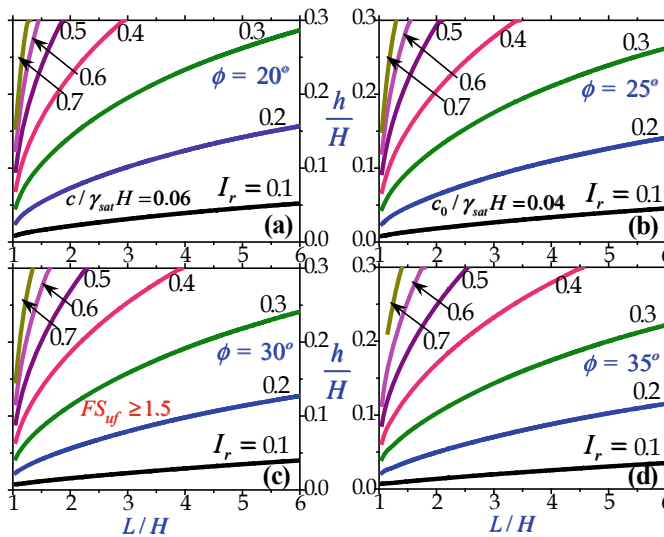


Fig. 17.9 Optimum thickness of cover soil layer (h/H) for $c/\gamma_{sat}H = 0.06$, $c_0/\gamma_{sat}H = 0.04$ for different values of immersion ratio (I_r) and friction angles

Effect of ϕ and $c/\gamma_{sat}H$

Figures 17.7a–d, 17.8a–d, and 17.9a–d show that the optimum cover soil thickness (h) reduces with the increase in values of ϕ and $c/\gamma_{sat}H$. This is due to the increase of shear resistance within the cover soil layer with the increase of shear strength parameters (c and ϕ) as per Mohr–Coulomb law. This indicates that improving the cohesion and friction angle of cover soil can stop the occurrence of uplifted-floating failure for a designed thickness of cover soil.

Effect of L/H Ratio

It can be observed from Figs. 17.7a–d, 17.8a–d, and 17.9a–d that the optimum cover soil thickness (h) increases as the L/H ratio increases for all the immersion ratios (I_r). This is owing to the fact that failure ratio (Ω) reduces with the increase in length of the slope of cover soil (L) resulting in the reduction of anti-uplifting forces. Therefore, an increase in cover soil thickness (h) brings forth the required anti-uplifting forces for the veneer cover system to attain stability against uplifted-floating failure.

Design Example

Assume an MSW landfill of height (H) of 10 m and slope angle (β) of 30° . The parameters considered for the design of the veneer cover system are as follows: stability number ($c/\gamma_{\text{sat}}H$) = 0.04 and angle of internal friction of cover soil (ϕ) = 25° . The drainage layer of the veneer cover system is assumed to be accumulated with internal seeper with an immersion ratio (I_r) of 0.3. For the above given specifications, the optimum thickness of cover soil layer (h) required to resist uplifted-floating failure for the factor of safety (FS_{uf}) ≥ 1.50 can be computed as follows: For the design conditions of the veneer cover system mentioned above, Fig. 17.8b needs to be used to determine the value of h . The computed length of the slope (L) = $H/\sin \beta$ is 20 m, and therefore, the L/H ratio becomes 2.0. The corresponding h/H ratio of 0.13 is obtained for $I_r = 0.3$ and $L/H = 2.0$ from Fig. 17.8b. Therefore, the optimum cover soil-layer thickness (h) is obtained as 1.3 m using the relation, $h = (h/H) * H$.

Conclusion

The present study recommends the optimum veneer cover thickness (h) to resist the uplifted-floating (uf) failure of the veneer cover system of MSW landfill. Limit equilibrium approach is used to obtain the expression of a factor of safety (FS_{uf}) against uplifted-floating failure. This study targets the factor of safety against uplifted-floating failure (FS_{uf}) ≥ 1.50 for the successful and durable performance of the veneer cover system. The optimum length of cover soil slope (L) can also be estimated for a given h/H ratio.

The conclusions drawn from the study are as follows:

- The immersion ratio (I_r), friction angle of cover soil (ϕ), and stability number of cover soil ($c/\gamma_{\text{sat}}H$) influence the optimum thickness (h) of the veneer cover soil layer.
- The optimum thickness (h) of the veneer cover soil layer obtained from the design charts is the minimum permissible thickness required for the target value of the factor of safety, $FS_{uf} \geq 1.50$.
- The optimum thickness (h) of the veneer cover soil layer may be increased with the increase of immersion ratio (I_r).
- The optimum thickness (h) of veneer cover soil layer may be reduced with the increase in values of ϕ and $c/\gamma_{\text{sat}}H$.
- The optimum cover soil-layer thickness (h) increases with the increase in value of L/H for the constant values of I_r , ϕ , and $c/\gamma_{\text{sat}}H$.

References

1. Khoshand A, Fathi A, Zoghi M, Kamalan H (2018) Seismic stability analyses of the reinforced tapered landfill cover systems considering seepage forces. *Waste Manag Res* 36(4):361–372
2. Nadukuru S, Zhu M, Gokmen C, Bonaparte R (2017) Combined seepage and slope stability analysis of a landfill cover system. In: *Geo-frontiers: waste containment, barriers, remediation, and sustainable geoengineering*. ASCE, Florida, Reston, VA, pp 170–179
3. Chen Y, Xue Q, He X, Zhang S, Wang P, Song C (2019) Stability analysis on veneer cover system for landfill considering the effect of internal seep. *Eng Geol* 252:99–109
4. Boschuk JJ (1991) Landfill covers: an engineering perspective. *Geotech Fabrics Report* 9:23–34
5. Soong TY, Koerner RM (1996) Seepage induced slope instability. *Geotext Geomembr* 14(7–8):425–445
6. Feng SJ, Chen ZW, Chen HX, Zheng QT, Liu R (2018) Slope stability of landfills considering leachate recirculation using vertical wells. *Eng Geol* 241:76–85
7. Soujanya D, Basha BM (2020) Analysis and design of veneer cover soils with internal seep. In: *Proceedings of Indian geotechnical conference, Visakhapatnam, India*
8. Koerner RM, Soong TY (2005) Analysis and design of veneer cover soils. *Geosynth Int* 12(1):28–49

Chapter 18

A Concise Review of State-of-the-Art on Landslide Monitoring and Warning System in India



Shikha Sharma , Naresh Mali , and Venkata Uday Kala 

Introduction

Landslides are a major problem in hilly areas due to the sloped terrain [22, 52, 66]. When the driving forces increase or the resisting forces decrease, the slopes tend to destabilize. Landslides are caused by an imbalance of forces in slip planes in geological substrata. Gravity is constantly at work pushing the soil and rock mass down the slope. As a result, landslides are unpredictable because substrata can be resistant to slippage for centuries before experiencing instability, disrupting the balance between driving and resisting forces. This imbalance of forces can be caused by both natural and anthropogenic factors [36, 37]. Natural causes include non-site-specific geological, morphological, and hydrogeological aspects. While the anthropogenic causes of this disaster in the hills include encroachment, deforestation, unplanned drainage, and construction activities. As a result, it is necessary to assess the risk associated with the landslide hazard by developing control measures in both structural and non-structural forms. Avoidances, removal, and stabilization of the unstable slope are structural measures for hazard control. These measures, however, are effective but impractical. Mitigating the unstable slopes from imminent failure for the entire hilly terrain is uneconomical. As a result, real-time early warning systems can be used to deploy an alternative and non-structural measure for consequential risk assessment and control.

Time-based monitoring methods are used to predict impending hazards and, as a result, to develop early warning system schemes. These early warning systems (EWS) are designed to detect significant changes in the environment by using thresholds to generate necessary alarms in the form of alerts and warnings. Landslide monitoring is typically sensor-based, with data collected in real-time transferred and analyzed,

S. Sharma · N. Mali · V. U. Kala (✉)

Indian Institute of Technology Mandi, Kamand Campus, Mandi, Himachal Pradesh 175075, India
e-mail: uday@iitmandi.ac.in

and slope failure alarms developed after validation with thresholds. These alarms are then forecasted in order for local authorities to generate susceptibility maps [29, 30, 51, 54–57, 61, 62, 64] for preparedness and evacuation in order to avoid casualties. The monitoring scheme is carried out at different scales to reduce false alarms in order to increase the confidence of the prediction. As a result, the monitoring scale is divided into regional, zonal, and local scales based on the spatial distribution of hazards.

Regional Scale Monitoring

Regional scale monitoring focuses on specific regions with similar geological, hydrogeological, and morphological characteristics, as well as the same environmental conditions. As a result, a physical and empirically based model for generating landslide thresholds can be developed. Rainfall is a major contributor to landslides. In India, 77% of all landslides occurred during the monsoon season in sloped geographical areas. Daily rainfall, preceding rainfall, and storms alter the hydrogeological condition of the soil by altering its water content. As water seeps into the subsurface layers, it raises pore water pressure and thus reduces effective normal stresses, resulting in a decrease in soil shear strength. The factor of safety decreases as the shear strength of the soil, which is the resisting force, decreases. As a result of these changes in geotechnical characteristics, soil instability occurs. Furthermore, rainfall increases the destabilizing force due to soil saturation and decreases the resisting forces by reducing shear strength, resulting in the majority of slope failures during the monsoon. As a result, rainfall becomes an imminent triggering factor of slope instability, which leads to landslides when it equals or exceeds the threshold value.

The rainfall thresholds are defined as the amount of rainfall a slope can withstand before triggering a landslide and are calculated using past cumulative rainfall, antecedent rainfall, and daily rainfall data combined with landslide susceptibility data [1–10, 17, 18, 27, 28, 33–35, 38, 49, 50, 59, 63, 65]. Thresholds are not representative and are subject to change as the topographical, geological, and hydrological characteristics of a location change. The same intensity and duration of rainfall that causes severe damage in one location may not cause even a landslide in another. Various studies of these thresholds are carried out using various physical and empirical models, taking into account the variability and randomness of the phenomenon. Due to non-uniformity, various factors such as lithology, morphology, and soil characteristics are not considered when conducting such statistical analyses using rainfall thresholds.

The indirect impact of rainfall on the soil is studied directly using physically based models by combining rainfall patterns with geotechnical and geometrical properties of soil to predict soil instability. Empirical models or statistical analyses of rainfall data are used to derive empirical thresholds for a regional, zonal, and local level for quantitative prediction of landslides [4, 10, 24, 26, 29–31, 57, 60]. The empirical analysis is useful for aggregating rainfall for specific landslides, defining thresholds for

antecedent rainfall, and incorporating hydrogeological conditions. Furthermore, for quantitative prediction, data-driven analysis between locations of landslides caused by rainfall and rainfall parameters in the form of cumulative rainfall, antecedent rainfall, intensity–duration data, and event duration analysis are evaluated. The intensity–duration (I – D) thresholds [5, 18, 32, 50], rainfall event–duration (E – D) thresholds [34], and rainfall event–intensity (E – I) thresholds are the three types of precipitation parameters. This type of statistical analysis of conditioning factors based on geographical factors is investigated at three different scales: regional, local, and zonal. Also regardless of geographical variation, the global threshold provides the minimum level above which landslides are likely to occur. This global threshold was empirically defined using a power-law model that took into account the intensity and duration of rainfall regardless of geomorphological, hydrological, or lithological conditions. However, over time, by defining local conditions and soil types, various regional specific thresholds are defined using intensity–duration models with probability density of the residual using kernel density estimation, a nonparametric technique for estimating the probability density function of random variables.

Mathematical Relationships Were Developed for Historical Rainfall Data in India

In general, intensity–duration threshold equations [15, 18, 23, 24, 32, 38, 50] connect the mean rainfall intensity (I) with the rainfall event duration (D), as shown in Eq. 18.1:

$$I = \alpha D^{-\beta} + c \quad (18.1)$$

where α and β are empirical parameters, and c are constants. In general, $c = 0$. The intercept and slope of the graph are then calculated from the log–log plot of duration and intensity. As a result of the nature of the intensity–duration threshold equation, an intense rainfall event with a short duration can cause slope failure; a small intensity rainfall event with a slightly longer duration can cause a landslide. However, the rainfall thresholds are not accurate due to a gap in acquiring rainfall data, which causes the estimation of intensity–duration profiles to be inconsistent.

To overcome this ambiguity, data from local rain gauges, increasing the availability of satellite-driven precipitation to derive regional-scale data, or using the stochastic dis-aggregation technique to allow rain rate fields collected by radar and numerically simulating the statistical pattern can be used. A significant amount of research has been conducted in the Indian Himalayan region [30–34] to investigate rainfall thresholds in the Gharwal region by deriving a relationship between intensity and duration on a log–log plot. Also, the intensity–duration plot for the Kalimpong region was established using a probabilistic approach. Several researchers developed event duration relationships to better understand the cumulative effect (Table 18.1).

Table 18.1 Developed intensity–duration relationships for different areas in India

Literature	I – D relationships	Region
Mathew et al. [50]	$I = 58.7 D^{-1.12}$	Gharwal region
Kanungo and Sharma [38]	$I = 1.82 D^{-0.23}$	Chamoli-Joshimath region
Dahal and Hasewaga [23]	$I = 73 D^{-0.79}$	Gharwal region
Dikshit and Satyam [24]	$I = 3.72 D^{-0.48}$	Kalimpong region
Harilal et al. [33]	$I = 43.26 D^{-0.78}$	Sikkim region

Zonal Scale of Monitoring

Data-driven models are used to calculate the likelihood of a landslide occurring in a given location by taking into account the precipitating factors and analyzing the spatial distribution of the cause–effect relationship for the given zone.

The statistical and machine learning techniques are used in data-driven models. The statistical relationships between various triggering factors at a given landslide location were evaluated, and quantitative predictions for landslide-free areas under similar conditions were made. The relative importance of the factors that can cause landslides is determined by this practice. The problem can be treated as binary classification for these data-driven approaches, and the data were obtained from various sources. The researchers were assisted in producing the landslide hazard mapping by using geographical information systems (GIS) in conjunction with machine learning algorithms. The susceptibility analysis took into account geological and geomorphological characteristics, as well as historical rainfall data [11–16, 18–20, 28, 34–49, 54, 55].

Prior research studies showed that the application of machine learning techniques and the GIS was used to develop hazard mapping [21, 53]; however, locating the individual locations where failures are likely to occur in the future is difficult. As a result, the loop with the highest probability of occurrence yields the most prone landslide zones. Several machine learning techniques were also used to prepare the landslide susceptibility mapping. The landslide susceptibility mapping was developed for the Indian Himalayan region, taking into account the causal factors extracted from geological and geomorphological characteristics and treating the problem as a binary classifier [34–49]. Several studies found that land cover, slope aspect, and other factors were the most influential in the occurrence of landslides, and the resulting influential parameters were obtained using feature selection machine learning techniques. Furthermore, various machine learning techniques such as random forest, artificial neural network (ANN), and AdaBoost outperformed the other models used [11–16, 18–20, 28, 34–49, 54–56].

Stochastic disintegration techniques are currently being developed in order to generate many different outcomes from a single input field in order to determine the vulnerable area to the given triggering factor. Because it accounts for uncertainties in the available data, this probabilistic analysis has the highest predictive capacity. The results obtained through data-driven models are reliable because they uncover the relationships between various triggering factors and landslide locations.

In place of the various available technologies, as mentioned in the literature, the real-time predictions were modified by taking into account local topographical, rainfall data, geotechnical, and hydrological characteristics. Physical-based methods combined with field study results help to reduce the false predictive capability when combined with data-driven models.

Site-Specific Monitoring

Various triggering factors govern different types of slope failures, depending on soil characteristics, hydrogeological conditions, topography, lithology, and slope geometry. Sensors are installed at the local level to monitor local geographical indicators such as displacements, tilt, suction, capillary action, gully formation, and soil erosion, which can be potential causes of landslides.

To monitor these in-situ slope failure conditions, a flexible and customizable system that can adapt to different contexts based on relevant parameters is required for generating necessary alerts. The implementation of remediation work to reduce risk comes at a high cost, but site-specific monitoring using sensing technology, and IoTs is not only less expensive but also more reliable and accurate [3, 14–18, 21–24, 42, 50–53, 57, 58]. Different sensors can be installed to govern these failures depending on the various triggering factors, such as for rockfall, and crack-o-meter can give alerts about the displacement criteria, tensiometers for soil suction, and accelerometer about slope sliding. Prior research studies have included the creation of a landslide monitoring and early warning system that is susceptible to rainfall. Several researchers proposed that the concept of rainfall-induced slope failure prediction methodology could be achieved by observing moisture content responses at different levels within the soil slopes.

Furthermore, numerical and physical-based studies were used for early warning system against slope failure hazards [3, 7, 19, 24, 25, 33, 47, 49, 50, 59]. It was suggested that the increase of moisture levels against rainfall events from the field, numerical and physical-based studies were used for early warning system against slope failure hazards. According to Wang et al. 2018 [67], triggering thresholds for robust early warning systems were defined, such as displacement detection using a microelectro-mechanical system (MEMS), accelerometer sensors, temperature measurements, and a tensiometer to measure the suction capacity of the soil. The most commonly used sensors are rain gauges, which are calibrated to measure the amount of rainfall in a given area, and sensors used for landslide monitoring, which should be calibrated and then installed [3, 19, 25, 42, 47]. Thus, sensors contribute

Table 18.2 Depolymnt of the sensing technologies used in India

Literature	Sensors used for deployment	Region
Aggarwal et al. [11]	Vedio camera	India
Dikshit et al. [25]	MEMS (Tilt and moisture sensors)	Kalimpong, India
Chaturvedi et al. [20]	MEMS (Accelerometer and moisture sensors)	Mandi, India

to long-term risk management by monitoring triggering thresholds and cataloging signals that typically cause different types of landslides.

Aside from traditional monitoring systems, new technologies such as UAV photogrammetry, remote sensing (RS) technology, InSAR, and digital close-up photogrammetry are some visual sensors that can perceive more information and contain a network capable of handling higher level visual tasks. Aside from sensors, one of the most significant technological advancements that has emerged is the development of IoTs, which is an effective early warning tool. Integration of various field processes with the Internet and improved connectivity between different components result in automated innovative monitoring tools. This automated monitoring system theory operates on three levels: (1) Perception layer: for gathering and transmitting site-specific information. (2) Data layer: data from sensors is gathered and elaborated to produce the desired output. (3) Presentation layer: the results for providing the required forecast. The resulting study of risk reduction using sensors in vulnerable areas is site specific and is zeroed in on after the stochastic disintegration technique. Following statistical analysis at the zonal and regional levels, landscape models are created to demarcate threshold values in order to identify precursors of triggering factors. The focus on the threshold cannot be predicted globally, but only locally, which requires iterative and intense temporal data. Sensors can only monitor the indirect factors that contribute to slope failure, such as soil moisture content and water table level, but not the actual cause of failure. Sensor design technology and architecture are deterministic in the absence of other uncertainties (Table 18.2).

Sensing technologies were used all over the world. For the field, laboratory, and physical-based studies, the soil movement data and rainfall data obtained from sensing technology combined with IoT were used to predict future slope failure events. Prior research looked into several approaches to reduce false alarms using historical rainfall data, field monitoring data, results from data-driven models, and physical-based approaches. The rainfall thresholds were calculated using probabilistic, statistical, and physical methods [1–10, 17–34]. Real-time sensor data were combined with machine learning techniques to predict future events based on rainfall threshold equations.

Conclusion

Landslide losses can be mitigated through structural measures that can redeem from future occurrences of sliding events, or through non-structural measures that reduce the consequences of the risk involved. In either case, the risk of a landslide hazard can be reduced while adhering to the cost-effectiveness and longevity of the method proposed to address the underlying cause. Non-structural methods include mapping, hazard zonation, and landslide monitoring, and a warning system aids in the generation of alerts for impending threats. These methods are highly predictive and have saved numerous lives. Several advanced technologies used in the Indian Himalayan region were discussed in the current paper. The quantitative method of early warning, on the other hand, is deterministic and does not take into account the temporal variation of triggering factors. Furthermore, it focuses on simple thresholds locally and is not a representative method for measuring triggering aspects. As a result, precise thresholds can be determined through efficient data collection and analysis in order to develop robust technology for early warning systems.

References

1. Abraham MT, Pothuraju D, Satyam N (2019) Rainfall thresholds for prediction of landslides in Idukki, India: an empirical approach. *Water* 11:2113
2. Abraham MT, Satyam N, Bulzinetti MA, Pradhan B, Pham BT, Segoni S (2020) Using field-based monitoring to enhance the performance of rainfall thresholds for landslide warning. *Water* 12:3453
3. Abraham MT, Satyam N, Pradhan B, Alamri AM (2020) IoT-based geotechnical monitoring of unstable slopes for landslide early warning in the Darjeeling Himalayas. *Sensors* 20:2611
4. Abraham MT, Satyam N, Kushal S, Rosi A, Pradhan B, Segoni S (2020) Rainfall threshold estimation and landslide forecasting for Kalimpong, India using SIGMA model. *Water* 12:1195
5. Abraham MT, Satyam N, Rosi A, Pradhan B, Segoni S (2020) The selection of rain gauges and rainfall parameters in estimating intensity-duration thresholds for landslide occurrence: case study from Wayanad (India). *Water* 12:1000
6. Abraham MT, Satyam N, Pradhan B, Alamri AM (2020) Forecasting of landslides using rainfall severity and soil wetness: a probabilistic approach for Darjeeling Himalayas. *Water* 12:804
7. Abraham MT, Satyam N, Rosi A, Pradhan B, Segoni S (2021) Usage of antecedent soil moisture for improving the performance of rainfall thresholds for landslide early warning. *CATENA* 200:105147
8. Abraham MT, Satyam N, Pradhan B (2021) Forecasting landslides using mobility functions: a case study from Idukki district, India. *Indian Geotech J*
9. Abraham MT, Satyam N, Pradhan B (2021) Potential use of antecedent soil moisture in the forecasting of rainfall-induced landslides. In: NSF convergence workshop on bringing land, ocean, atmosphere and ionosphere data to the community for hazards alerts
10. Abraham MT, Satyam N, Shreyas N, Pradhan B, Segoni S, Maulud KNA, Alamri AM (2021) Forecasting landslides using SIGMA model: a case study from Idukki, India. *Geomatics, Nat Haz Risk* 12(1):540–559
11. Aggarwal S, Mishra PK, Sumakar KVS, Chaturvedi P (2018) Landslide monitoring system implementing IOT using video camera. In: 3rd International conference for convergence in technology (I2CT), pp 1–4

12. Agrawal K et al (2017) Minute-scale prediction of soil movement using machine-learning techniques. In: Indian landslide congress 2017, Indian Institute of Technology Bombay, Mumbai
13. Agrawal K et al (2017) A comparison of class imbalance techniques for real-world landslide predictions. In: 2017 International conference on machine learning and data science (MLDS), pp 1–8
14. Arabameri A et al (2020) Comparison of machine learning models for gully erosion susceptibility mapping. *Geosci Front* 11(5):1609–1620
15. Askarinejad A, Akca D, Springman SM (2018) Precursors of instability in a natural slope due to rainfall: a full-scale experiment. *Landslides* 15:3–10
16. Bell R, Glade T (2004) Quantitative risk analysis for landslides—examples from Bıldudalur, NW-Iceland. *Nat Hazards Earth Syst Sci* 4:117–131
17. Bulzineti MA, Abraham MT, Satyam N, Pradhan B, Segoni S (2020) Combining rainfall thresholds and field monitoring data for the development of LEWS. EGU General Assembly
18. Caine N (1980) The rainfall intensity: duration control of shallow landslides and debris flows. *Geografiska Annaler. Ser A, Phys Geogr* 62(1/2):23–27
19. Chae BG, Park HJ, Catani F et al (2017) Landslide prediction, monitoring and early warning: a concise review of the state-of-the-art. *Geosci J* 21:1033–1070
20. Chaturvedi P, Thakur K, Mali N, Yadav S, Kumar S, Uday KV, Dutt V (2018) A low-cost IoT framework for landslide prediction and risk communication. In: *Internet of Things A to Z: technologies and applications*, ch 21. Wiley-IEEE Press
21. Chen W, Reza H, Pourghasemi, Naghibi SA (2018) Prioritization of landslide conditioning factors and its spatial modelling in Shanganan Country, China using GIS-based data mining algorithms. *Bull Eng Geol Environ* 77:611–629
22. Cruden DM (1991) A simple definition of a landslide. *Bull Eng Geol Environ* 43:27–29
23. Dahal RK, Hasegawa S (2008) Representative rainfall thresholds for landslides in the Nepal Himalaya. *Geomorphology* 100(3–4):429–443
24. Dikshit A, Satyam N (2017) Application of FLIR model for early warning system in Chibo Pashyor, Kalimpong, India for rainfall-induced landslides. *Nat Hazard* 295:1–18
25. Dikshit A, Satyam DN, Towhata I (2018) Early warning system using tilt sensors in Chibo, Kalimpong, Darjeeling Himalayas, India. *Nat Hazards* 94:727–741
26. Dikshit A, Satyam N, Pradhan B (2019) Estimation of rainfall-induced landslides using the TRIGRS model. *Earth Syst Environ* 3:575–584
27. Dikshit A, Satyam N (2019) Probabilistic rainfall thresholds in Chibo, India: estimation and validation using a monitoring system. *J Mt Sci* 16:870–883
28. Dikshit A, Satyam N, Pradhan B et al (2020) Estimating rainfall threshold and temporal probability for landslide occurrences in Darjeeling Himalayas. *Geosci J* 24:225–233
29. Formetta G, Capparelli G, Versace P (2016) Evaluating performance of simplified physically-based models for shallow landslide susceptibility. *Hydrol Earth Syst Sci* 20:4585–4603
30. Gupta SK, Shukla DP, Thakur M (2018) Selection of weightages for causative factors used in the preparation of landslide susceptibility zonation. *Geomatics, Nat Haz Risk* 9(1):471–487
31. Guzzetti F, Carrara A, Cardinali M, Reichenbach P (1999) Landslide hazard evaluation: a review of current techniques and their application in a multi-scale study, Central Italy. *Geomorphology* 31(1–4):181–216
32. Guzzetti F, Peruccacci S, Rossi M et al (2008) The rainfall intensity–duration control of shallow landslides and debris flows: an update. *Landslides* 5:3–17
33. Harilal GT, Madhu D, Ramesh MV et al (2019) Towards establishing rainfall thresholds for a real-time landslide early warning system in Sikkim, India. *Landslides* 16:2395–2408
34. He S, Wang J, Liu S (2020) Rainfall event-duration thresholds for landslide occurrences in China. *Water* 12:494
35. Jakob M, Weatherly H (2003) A hydroclimatic threshold for landslide initiation on the North shore mountains of Vancouver, British Columbia. *Geomorphology* 54(3–4):137–156
36. Jha CS, Dutt CBS, Bawa KS (1995) Deforestation and land use changes in Western Ghats, India. *Curr Sci* 79(1):231–238

37. Jones S, Kasthurba AK, Bhagyanathan A et al (2021) Impact of anthropogenic activities on landslide occurrences in southwest India: an investigation using spatial models. *J Earth Syst Sci* 130:70
38. Kanungo DP, Sharma S (2014) Rainfall thresholds for prediction of shallow landslides around Chamoli-Joshimath region, Garhwal Himalayas, India. *Landslides* 11:629–638
39. Kumar P, Priyanka, Pathania A, Agarwal S, Mali N, Singh R, Chaturvedi P, Uday KV, Dutt V (2019) Predictions of weekly slope movements using moving-average and neural network methods: a case study in Chamoli, India. In: 9th International conference on soft computing for problem solving—SocProS 2019, Liverpool, UK
40. Kumar P et al (2020) Predictions of weekly soil movements using moving-average and support-vector methods: a case-study in Chamoli, India. In: Correia A, Tinoco J, Cortez P, Lamas L (eds) *Information technology in geo-engineering. ICITG 2019. Springer series in geomechanics and geoengineering*. Springer, Cham
41. Kumar P et al (2020) Predictions of weekly slope movements using moving-average and neural network methods: a case study in Chamoli, India. In: Nagar A, Deep K, Bansal J, Das K (eds) *Soft computing for problem solving 2019. Advances in intelligent systems and computing*, vol 1139. Springer, Singapore
42. Kumar P, Sihag P, Sharma A et al (2021) Prediction of real-world slope movements via recurrent and non-recurrent neural network algorithms: a case study of the Tangni landslide. *Indian Geotech J*
43. Kumar P, Sihag P, Chaturvedi P, Uday KV, Dutt V (2021) BS-LSTM: an ensemble recurrent approach to forecasting soil movements in the real world. *Front Earth Sci*
44. Kuradusenge M, Kumaran S, Zennaro M (2020) Rainfall-induced landslide prediction using machine learning models: the case of Ngororero district, Rwanda. *Int J Environ Res Public Health* 17:4147
45. Ma Z, Mei G, Piccialli F (2020) Machine learning for landslides prevention: a survey. *Neural Comput Appl*
46. Madawala CN, Kumara BTGS, Indrathilaka L (2019) Novel machine learning ensemble approach for landslide prediction. In: *International research conference on smart computing and systems engineering (SCSE)*, Colombo, Sri Lanka, pp 78–84
47. Mali N, Chaturvedi P, Dutt V, Uday KV (2019) Training of sensors for early warning system of rainfall-induced landslides. In: *1st Arabian journal of geosciences*, Hammamet, Tunisia, recent advances in geo-environmental engineering, geomechanics and geotechnics, and geohazards
48. Mali N, Dutt V, Uday KV (2021) Determining the geotechnical slope failure factors via ensemble and individual machine learning techniques: a case study in Mandi, India. *Front Earth Sci* 9:701837
49. Mandal P, Sarkar S (2021) Estimation of rainfall threshold for the early warning of shallow landslides along National Highway-10 in Darjeeling Himalayas. *Nat Hazards* 105:2455–2480
50. Mathew J, Babu DG, Kundu S, Kumar KV, Pant CC (2014) Integrating intensity–duration based rainfall threshold and antecedent rainfall-based probability estimate towards generating early warning for rainfall-induced landslides in parts of the Garhwal Himalaya, India. *Landslides* 11(4):575–588
51. Nhu VH et al (2020) Landslide susceptibility mapping using machine learning algorithms and remote sensing data in a tropical environment. *Int J Environ Res Public Health*:174933
52. Prakash S (2011) Historical records of socio-economically significant landslides in India. *South Asia Disaster Stud* 4:177–204
53. Pham BT, Bui DT, Prakash I, Dholakia M (2016) Evaluation of predictive ability of support vector machines and Naïve Bayes methods for spatial prediction of landslides in Uttarkhand state (India) using GIS. *J Geomatics* 10(1):71–79
54. Pham BT, Pradhan B, Bui DT, Prakash I, Dholakia MB (2016) A comparative study of different machine learning methods for landslide susceptibility assessment: a case study of Uttarkhand area (India). *Environ Model Softw* 84:240–250
55. Pham BT, Khosravi K, Prakash I (2017) Application and comparison of decision tree-based machine learning methods in landslide susceptibility assessment at Pauri Garhwal area, Uttarakhand, India. *Environ Processes* 4:711–730

56. Pham BT, Shirzadi A, Shahabi H, Omidvar E, Singh SK, Sahana M, Talebpour AD, Bin Ahmad B, Kim Quoc N, Lee S (2019) Landslide susceptibility assessment by novel hybrid machine learning algorithms. *Sustainability* 11:4386
57. Sorbino G, Sica C, Cascini L (2010) Susceptibility analysis of shallow landslides source areas using physically based models. *Nat Hazards* 53:313–332
58. Springman SM, Jommi C, Teyssie P (2003) Instabilities on moraine slopes induced by loss of suction: a case history. *Geotechnique* 53(1):177–204
59. Satyam N, Abraham MT (2021) Development of landslide early warning using rainfall thresholds and field monitoring: a case study from Kalimpong. In Garg A, Solanki CH, Bogireddy C, Liu J (eds) *Proceedings of the 1st Indo-China research series in geotechnical and geoenvironmental engineering*. Lecture Notes in Civil Engineering, vol 123. Springer, Singapore. https://doi.org/10.1007/978-981-33-4324-5_11
60. Segoni S, Abraham MT, Satyam N, Rosi A, Pradhan B (2021) Application of SIGMA model for landslide forecasting in Darjeeling Himalayas. EGU General Assembly
61. Shahri AA, Spross J, Johansson F, Larsson S (2019) Landslide susceptibility hazard map in southwest Sweden using artificial neural network. *CATENA* 183:104225
62. Shahri AA, Maghsoudi MF (2021) Landslide susceptibility mapping using hybridized block modular intelligence model. *Bull Eng Geol Environ* 80:267–284
63. Teja TS, Dikshit A, Satyam N (2019) Determination of rainfall thresholds for landslide prediction using an algorithm-based approach: case study in the Darjeeling Himalayas, India. *Geosciences* 9:302
64. Tien BD, Pradhan B, Lofman O, Revhaug I (2012) Landslide susceptibility assessment in Vietnam using support vector machines, decision tree, and Naïve Bayes models. *Math Probl Eng*:1–26
65. Tohari A, Nishigaki M, Komatsu M (2007) Laboratory rainfall-induced slope failure with moisture content measurement. *J Geotech Geoenviron Eng* 133(5):575
66. Varnes DJ (1978) Slope movement types and processes. In: Schuster RL, Krizek RJ (eds) *Landslides, analysis and control*. Transportation Research Board, Special Report 176; National Research Council, Washington, DC, USA, pp 12–33
67. Wang CC, Chang WJ, Huang AB, Chou SH, Chien YC (2018) A simplified monitoring and warning system against shallow rainfall-induced slope failures. *Can Geotech J* 55(10):1421–1432

Chapter 19

Probabilistic Slope Stability Analysis of Bioreactor Landfills



Ankit Goel, Subhadeep Metya , and Gautam Bhattacharya

Introduction

A landfill forms one of the most popular waste disposal methods all around the globe. In recent times, it has become the dominant method of removing municipal solid wastes because it is the most convenient and cost-effective method of storing this type of waste, particularly in developing countries. India, for instance, produces more than 55 million tons of MSW each year, with a yearly increase of roughly 5% according to the Energy Alternatives India (EAI) report. Solid waste production in India's small, medium, and large cities is estimated to be between 0.1 and 0.3 kg per capita per day, and the annual growth in per capita waste production is nearly 1.33 percent per year. The volume of municipal solid trash is continually increasing and its composition is changing as a consequence of rising urbanization, shift in lifestyle and eating habits, etc. Waste accumulation has never been a threat in the past, but due to globalization and industrialization, a more effective waste disposal system is now needed. Accordingly, for the design of conventional landfills, moisture infiltration is kept to a minimum [23]. Due to the absence of moisture, the waste mass degrades at suboptimal rates for years and centuries. Pohland [15] proposed the idea of enhancing the waste degradation by the inclusion of extra water. Based on his proposed methodology, a new dumping technology known as bioreactor landfill has emerged [8]. Recent advancements in sanitary landfill studies have shown that use of landfills as bioreactors is a more sustainable method of waste management. In a traditional landfill, waste is deposited to delay the biodegradation process by reducing moisture entry. Bioreactor technology, on the other hand, speeds up the

A. Goel · S. Metya (✉)

Department of Civil Engineering, National Institute of Technology, Jamshedpur, India
e-mail: smetya.ce@nitjsr.ac.in

G. Bhattacharya

Department of Civil Engineering, IEST, Shibpur, India

biodegradation process in landfills by regulating moisture input (leachate migration) and increasing nutrients and bacterial populations. Due to the slower generation and atmospheric release of methane-rich landfill gas, as well as resource depletion, operating ordinary landfills only for the purpose of limiting ground water pollution is not economical in respect of material and space and may be counterproductive. Faster biodegradation means quicker waste stabilization which allows landfill owners to utilize space. While a traditional landfill can take 50–100 years to stabilize waste, a bioreactor landfill may do so in 5–10 years [24]. Improved biodegradation increases the output of landfill gas (LFG), making it possible for landfill operators to recover methane at a profit. The faster breakdown of waste in bioreactor landfills also has a significant impact on the geotechnical properties of the trash. With all these benefits, bioreactor landfills have a few demerits such as the increase in leachate leaks, odors, likelihood of standing water, and fire, especially in aerobic systems [21]. Side slope stability, perched liquid inside the landfill, differential settling, and watering out from gas collection lines are some of the potential issues to be concerned about.

With greater understanding of landfill behavior and MSW breakdown, there has been a significant progress to update the existing landfill process from a storage or confinement strategy to a process-based system such as a bioreactor landfill. However, due to the early decomposition of MSW, there are several stability challenges associated with the bioreactor landfills. Lot of effort, both analytical and experimental, has been put in to handle these concerns. It has been found the stability of these landfills decreases with decomposition [8], and hence, it should be designed according to advance stages.

In finite element platform, Varga [22] has discovered that as the degradation process advances, the factor of safety (FS) decreases, and stressed the importance of stability considerations in deposition process design to avoid unexpected failure. Hiroshan and Louis [7] have used PLAXIS to conduct stability analyses of unreinforced and geogrid reinforced MSW slopes and demonstrated how geogrids might help in enhancing stability of bioreactor landfills. Rajesh et al. [16] demonstrated the significance of MSW property variability in stability analysis. Ismail et al. [9] have also used PLAXIS to study the slope stability of conventional and bioreactor landfills which have revealed a significant decrease in FS for bioreactor landfill as compared to the conventional landfill.

The ambiguity associated with the municipal waste properties due to wide variability of deposited waste, time-dependent behavior, challenges in collecting and testing typical samples. Strain inconsistency amidst the MSW and underneath material has prompted the researchers to study the stability of MSW landfill within a probabilistic framework. Researchers including Srivastav et al. [20], Sivakumar Babu et al. [18], Datta and Sivakumar Babu [2], Rajesh et al. [16], Reddy et al. [17], Mehdizadeh et al. [10] have highlighted the importance of all these aspects and studied the simulation-based probabilistic slope stability analysis. But none of these studies has applied the first-order reliability method (FORM) [4] as a reliability model to measure the slope stability, more so in relation to the bioreactor landfill.

Keeping the above in consideration, the study in this paper presents a reliability-based assessment of a bioreactor landfill having 1V:3H slope [5] using the FORM.

The limit equilibrium methods, namely the Bishop's simplified method [1] and the Spencer's method [19] have been employed to re-analysis the slopes in identifying the critical slip surface and the associated minimum factor of safety. The following parts are given with salient aspects and key observations from the investigation.

Analysis Methods and Illustrative Example

Limit Equilibrium Based Deterministic Stability Analysis

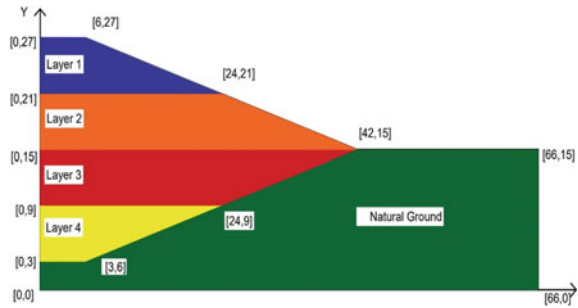
Slope stability analysis is a statically indeterminate problem and engineers use a variety of methods for its solution. The conventional slope stability analysis methods can be categorized as the limit equilibrium, the limit analysis, and the finite element analysis. The bulk of computer techniques for stability analysis for a two- or three-dimensional model are based on the concept of limit equilibrium. Under plane strain conditions, two-dimensional sections are analyzed. Simple analytical approaches to stability analysis of two-dimensional slope geometries usually provide useful insights into slope design and associated risk management.

The simplified Bishop approach and the Spencer's method were employed in this work, based on the multiple slice limit equilibrium methods available for slope stability analysis. The Bishop's method considers a slip surface of circular shape and satisfies overall moment equilibrium of the sliding mass. In this method, it is assumed that the side forces of any slice have zero resultant in the vertical direction. An iterative method has to be used to solve for the factor of safety. The Spencer's method also considers a circular slip surface but satisfies both force and moment equilibrium conditions.

In this paper, a 27-m-high MSW landfill with side slope of 1 vertical: 3 horizontal, as shown in Fig. 19.1, has been selected as an illustrative example. Four layers of solid waste have been considered for the bioreactor landfill. The configuration has been adopted from Haque [5]. The layers 1 to 4 represent the stage of landfilling. Each layer is originally assumed to be decomposed at different stages. The assumption is that layer 1 is in the initial decomposition stage immediately after landfill closure and, at the same time, layers 2, 3, and 4 are in, respectively, the second, third, and last stages of decomposition. With the passage of time, the MSW layers are predicted to approach to next stages of decomposition and eventually after the complete stabilization, the MSW layers will be at the last stage of decomposition of bioreactor landfill.

As already stated, the above two methods are selected for determination of safety factor and for evaluating the performance function for the reliability analysis. The solution method for FS of a particular slip surface is formulated as a mathematical programming problem, which is solved using the sequential quadratic programming (SQP) methodology in MATLAB [11–14]. SQP method is one of the most promising methods for numerically solving constrained nonlinear optimization problems [3]. It has a strong theoretical basis and efficient algorithmic methods for solving large-scale

Fig. 19.1 Cross-section of the MSW landfill slope model (after Haque [5])



technologically related problems. The job of determining the critical slip surface is similarly described as a mathematical programming problem which is handled again using the sequential quadratic programming (SQP) technique. The coordinates of the initial slip surface were chosen judiciously and with the help of this, the coordinates of several trial slip surfaces for a particular stage were generated, and slip circle having the minimum factor of safety (FS_{min}) is accepted as the critical slip surface.

Probabilistic Stability Analysis

Among the family of first-order second moment (FOSM) reliability techniques, the FORM has established itself as the most versatile method, and is used in this study [4]. The fundamental feature of this method is that it calculates the design point in the reduced coordinate system which is the shortest distance from the origin to the limit state surface. This minimum distance is called the reliability index symbolized as β [6]. Reliability index determination is framed as an optimization problem and answered using MATLAB environment with the SQP. The solution produces the design point on the failure surface and associated reliability index β . The reliability index can be determined using the coordinates of the deterministic slip surface. In terms of reliability index (β), the probability of failure (P_F) has been determined as $P_F = \Phi(-\beta) = 1 - \Phi(\beta)$, where $\Phi(\cdot)$ signifies the cumulative standard normal distribution function.

Results and Discussion

Results of the Limit Equilibrium Based Slope Stability Analysis

Table 19.1 presents the solid waste parameters used in this study, and as reported in [5], these parameters were determined based on extensive laboratory experimentations on MSW samples collected from a transfer station in Burlington, Texas. At first

Table 19.1 Solid waste parameters used in the study (after Haque [5])

Material set	Unit weight γ_{moist} , kN/m ³	Cohesion c' , kN/m ²	Friction angle ϕ'
Phase 1	9.01	11.2	26.7°
Phase 2	9.44	20.5	21.5°
Phase 3	10.22	5.3	20.6°
Phase 4	11.02	2.4	19.0°
Natural ground	15.90	9.60	30.0°

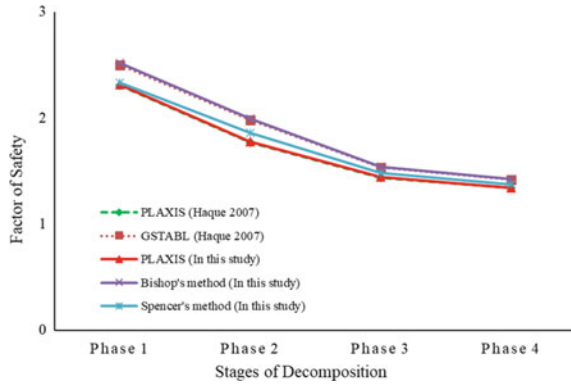
Table 19.2 Summary of factor of safety values from different studies

Stage of decomposition	Haque [5]	Present study (FS _{min})		
	PLAXIS	PLAXIS	Bishop's simplified method	Spencer's method
1	2.31	2.313	2.520	2.335
2	1.77	1.774	1.994	1.862
3	1.44	1.442	1.540	1.483
4	1.34	1.339	1.427	1.375

for the purpose of validation, the landfill model has been re-analyzed in PLAXIS to compare the outcomes reported by [5]. The closeness of entries in the two “PLAXIS” columns (Table 19.2) serve to validate developed model used. As already stated, two limit equilibrium methods, namely the Bishop’s simplified method and the Spencer method have been adopted for calculation of factor of safety (FS). Further, the factor of safety of a candidate slip surface is designed as a mathematical programming problem which is solved in the MATLAB setting using the SQP technique. The coordinates of the initial slip surface have been selected judiciously and the intermediate slip surface coordinates during the optimization run have been obtained. The slip circle with the least FS is then designated as the critical slip surface. The results of the limit equilibrium analyses are presented in Table 19.2.

The factor of safety values obtained by using the FEM and LEM-based assessments at various phases of decomposition are plotted in Fig. 19.2. With time needed for decomposition of MSW, the factor of safety values gradually decrease in the case of bioreactor landfills. The factor of safety decreased from 2.313 in phase 1, i.e., immediately after closure to 1.339 in phase 4, i.e., after complete decomposition. As the solid waste progresses to the subsequent stages of decomposition, the strength qualities of refuse decreases which is attributed to the decrease in factor of safety values. It may be noted that in general, the FS values obtained using the limit equilibrium analysis are slightly on the higher side with maximum difference of 12.40% in the Bishop’s method and 4.96% in case of Spencer’s method as compared to that obtained using the FEM-based analysis at different phases of decompositions. This is as per expectation due to the relatively rigorous nature of analysis carried out in the Spencer’s method.

Fig. 19.2 Factor of safety from FEM and limit equilibrium analysis



Results of the Probabilistic Slope Stability Analysis

As already mentioned, the FORM has been adopted to determine the reliability index and the allied probability of failure. The statistical parameters used for reliability analysis are given in Table 19.3. Using the developed computer program, the values of reliability indices and their associated probabilities of failure have been determined and presented in Table 19.4.

Sensitivity Analysis

Sensitivity analysis has also been performed using the FORM to identify the input parameters that played a dominating role on the reliability study. The aim of the sensitivity analysis is also to classify irrelevant random variables so that they can be handled deterministically to minimize the problem’s complexity. Figure 19.3 presents the sensitivity analysis of phase 1 of decomposition of MSW in which cohesion in layer 3 has been found out to be the most dominating random variable followed by the unit weight in layer 2. As the waste proceeds to the second phase of decomposition, the unit weight dominates the cohesion and friction angle (Fig. 19.4) but when the waste is in phase 3, the cohesion dominated the other two (Fig. 19.5), and finally at the phase 4 of decomposition (Fig. 19.6), friction angle is found out to be the most dominating random parameter. Thus, it is observed that there is no such general trend among the random variables considered, and hence, all the parameters should be considered for reliability analysis.

Effect of Coefficient of Variation

So far, a special set of coefficients of variation (COV) of the elementary random variables, as indicated in Table 19.3, has been concentrated for reliability studies.

Table 19.3 Statistical parameter for reliability analysis

Material set	Cohesion c' , kN/m ²		Friction angle ϕ'		Unit weight γ_{moist} , kN/m ³	
	Mean	COV (%)	Mean	COV (%)	Mean	COV (%)
Phase 1	11.2	35	26.7	15	9.01	5
Phase 2	20.5	35	21.5	15	9.44	5
Phase 3	5.3	35	20.6	15	10.22	5
Phase 4	2.4	35	19	15	11.02	5
Natural ground	9.6	–	30.0	–	15.90	–

Range of COV (%)

1–10

1–10

1–10

1–10

–

Table 19.4 Results from the reliability analysis for the particular set of COV

Stages	β	P_F
Phase 1	8.63	3.20×10^{-18}
Phase 2	6.29	1.61×10^{-10}
Phase 3	3.13	8.72×10^{-04}
Phase 4	2.19	1.42×10^{-02}

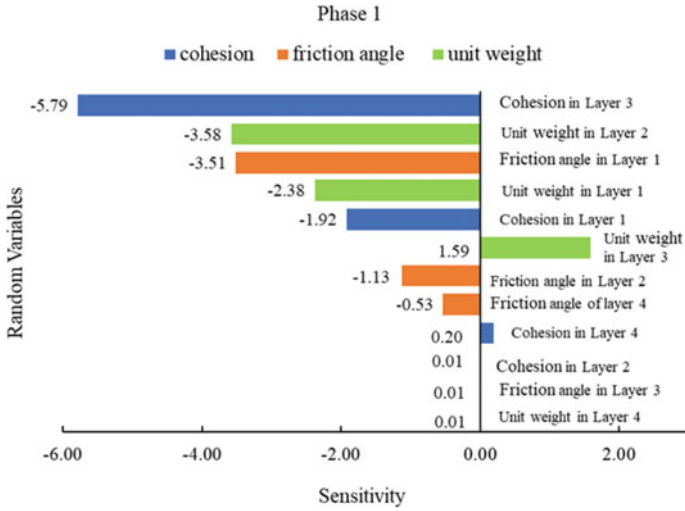


Fig. 19.3 Sensitivity analysis based on FORM method for phase 1

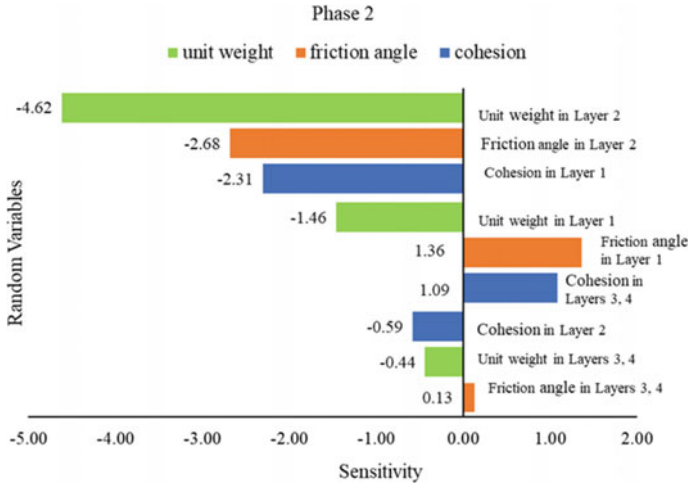


Fig. 19.4 Sensitivity analysis using FORM method for phase 2

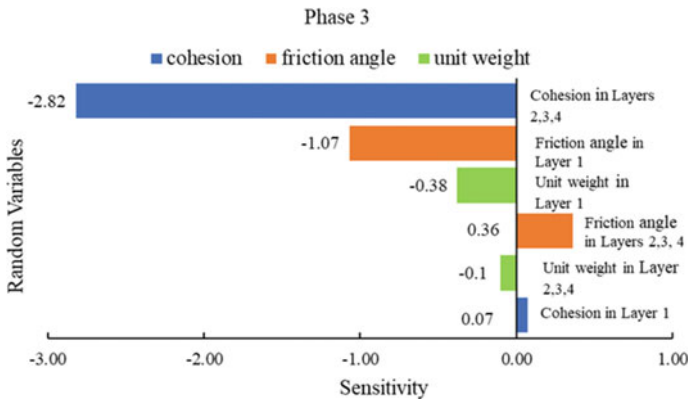


Fig. 19.5 Sensitivity analysis using FORM method for phase 3

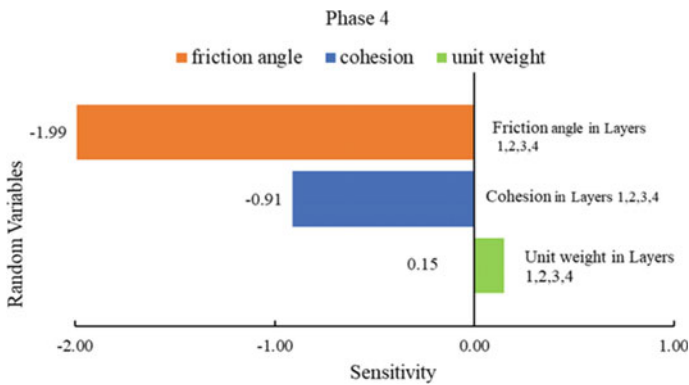


Fig. 19.6 Sensitivity analysis using FORM method for phase 4

The dependability results change when the COV values of the fundamental random variable vary throughout the range of values in Table 19.3 are intriguing to watch.

In examining this consequence, the COV values of c , $\tan\phi$, γ are moved from their corresponding lower bounds to their upper bounds according to $COV_c = 0.2 + 0.3\eta$, $COV_{\tan\phi} = 0.1 + 0.1\eta$, and $COV_\gamma = 0.01 + 0.09\eta$ for η ranging from 0 to 1 [11]. The reliability index values have been calculated for individual set of COV values conforming to a specific value of η and plotted in Fig. 19.7. From Fig. 19.7, it is observed that as COVs are enhanced from their lower bound ($\eta = 0$), and the reliability index decreased for all the phases of decomposition. But the rate of decrease has been observed to be very fast in phase 1, and it is slowly decreasing with increasing degree of decomposition.

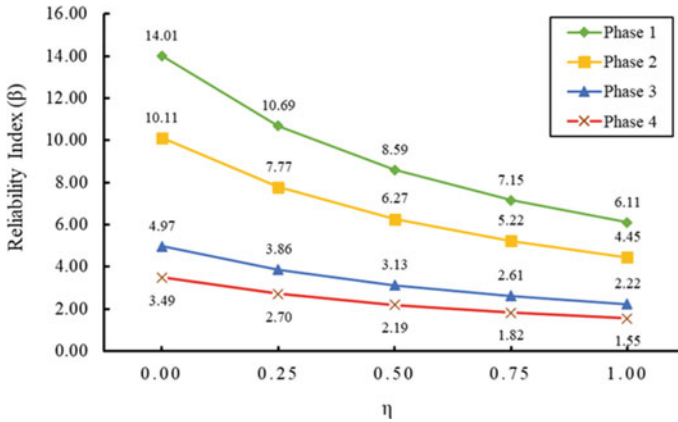


Fig. 19.7 Variation of reliability index (β) with η

Conclusion

In this study, a numerical simulation of a bioreactor landfill model under various key design parameters in combination with a probabilistic slope stability analysis has been presented. Based on the results of different analyses, the following concluding remarks can be drawn:

1. The numerical study based on PLAXIS revealed that the factor of safety (FS) associated with the stability analysis severely dropped as the decomposition stages progressed, reaching a minimum at the final stages of decomposition.
2. From the two limit equilibrium methods used for the analysis of stability of the bioreactor landfill model, it is also observed that the factor of safety decreases as the stages of decomposition increases but the values of FS are found out to be on the non-conservative side compared to those obtained from PLAXIS; the margin of non-conservatism is, however, much smaller with the Spencer method.
3. From the sensitivity analysis using the FORM, the angle of internal friction of the MSW is found out to be the most dominating parameter among all the three random variables considered in the analysis in the final decomposition stage. However, there is no such general trend observed in the other stages of decomposition.
4. The values of the reliability indices associated with the MSW slope decreases as the waste progressed toward the final stage of decomposition. Thus, it is observed that the probability of failure of MSW slope is found out to be maximum at the most advanced stages of decomposition, and hence, the final stage of decomposition should be taken into account as design criteria while designing the bioreactor landfill.
5. The effect of coefficient of variation associated with the random variables on reliability results has also been investigated. It is observed that as the COVs are

enhanced in their range from lower bound to upper bound, the reliability index significantly decreases. The maximum difference is found in stage 1 (56.39%) and the lowest difference in stage 3 and stage 4 (both are nearly identical at 55%) while varying η from 0 to 1.

References

1. Bishop AW (1955) The use of the slip circle in the stability analysis of slopes. *Géotechnique* 5(1):7–17
2. Datta S, Sivakumar Babu GL (2016) Prediction of the slope stability of municipal solid waste landfills using the reliability analysis. In: *Geo-Chicago 2016, Proceedings*, pp 668–677
3. Fletcher R (2010) The sequential quadratic programming method BT—Nonlinear optimization. In: Bomze IM, Demyanov VF, Fletcher R, Terlaky T, Di Pillo G, Schoen F (eds) *Lectures given at the C.I.M.E. Summer school held in Cetraro, Italy, July 1–7, 2007*. Springer Berlin Heidelberg, Berlin, Heidelberg, pp 165–214
4. Haldar A, Mahadevan S (2000) *Probability, reliability and statistical methods in engineering design*. Wiley, New York
5. Haque MA (2007) Dynamic characteristics and stability analysis of municipal solid waste in bioreactor landfills. The University of Texas at Arlington
6. Hasofer AM, Lind NC (1974) Exact and invariant second-moment code format. *J Eng Mech Div* 100(1):111–121
7. Hiroshan H, Louis G (2009) Use of geogrids to enhance stability of slope in bioreactor landfills: a conceptual method. In: *Contemporary topics in ground modification, problem soils, and geo-support*, GSP 187, Proceedings
8. Hossain MS, Haque MA (2009) Stability analyses of municipal solid waste landfills with decomposition. *Geotech Geol Eng* 27(6):659
9. Ismail S, Taib AM, Rahman NA, Hasbollah DZA, Ramli AB (2019) Slope stability of landfill with waste degradation. *Int J Inno Technol Explor Eng* 9(1):393–398
10. Mehdizadeh MJ, Shariatmadari N, Karimpour-Fard M (2020) Probabilistic slope stability analysis in Kahrizak landfill: effect of spatial variation of MSW's geotechnical properties. *Bull Eng Geol Env* 79(5):2679–2695
11. Metya S, Bhattacharya G (2014) Probabilistic critical slip surface for earth slopes based on the first order reliability method. *Indian Geotech J* 44(3)
12. Metya S, Bhattacharya G (2016) Probabilistic stability analysis of the Bois Brule Levee considering the effect of spatial variability of soil properties based on a new discretization model. *Indian Geotech J* 46(2)
13. Metya S, Bhattacharya G (2016) Reliability analysis of earth slopes considering spatial variability. *Geotech Geol Eng* 34(1)
14. Metya S, Bhattacharya G (2020) Accounting for 2D spatial variation in slope reliability analysis. *Int J Geomech* 20(3)
15. Pohland FG (1994) *Landfill bioreactors: historical, perspective, fundamental principles, and new horizons in design and operation*
16. Rajesh S, Babel K, Mishra SK (2017) Reliability-based assessment of municipal solid waste landfill slope. *J Hazard Toxic Radioactive Waste* 21(2):4016016
17. Reddy KR, Kumar G, Giri RK, Basha BM (2018) Reliability assessment of bioreactor landfills using Monte Carlo simulation and coupled hydro-bio-mechanical model. *Waste Manage* 72:329–338
18. Sivakumar Babu GL, Reddy KR, Srivastava A (2014) Influence of spatially variable geotechnical properties of MSW on stability of landfill slopes. *J Hazard Toxic Radioactive Waste* 18(1):27–37

19. Spencer E (1967) A method of analysis of the stability of the embankments assuming parallel interslice forces. *Geotechnique* 17(1):11–26
20. Srivastava A, Sivakumar Babu GL, Haldar S (2010) Influence of spatial variability of permeability property on steady state seepage flow and slope stability analysis. *Eng Geol* 110(3):93–101
21. Tolaymat TM (2005) Bioreactor landfills, theoretical advantages and research challenges. Presented at EPA region 5 bioreactor landfill work; Chicago, IL, September 27, 2005
22. Varga G (2011) Some geotechnical aspects of bioreactor landfills. *Periodica Polytechnica Civ Eng* 55(1 SE-Research Article):39–44
23. Warith M (2002) Bioreactor landfills: experimental and field results. *Waste Manage* 22(1):7–17
24. Warith M, Li X, Jin H (2005) Bioreactor landfills: state-of-the-art review. *Emirates J Eng Res* 10(1):1–14

Chapter 20

Experimental Investigation of Pull-Out Resistance of Grouted Soil Nails—A Critical Review



Ruchita Salvi and Ashish Juneja

Introduction

Design standards are fixed by various countries with some design issues still unclear amid some engineers and academicians. Pull-out resistance is a significant parameter in the design of nails leading to an accurate design. Factors influencing it include method of installation, overburden pressure, grout pressure, surface roughness of nail, in-situ water content of soil, soil dilation, and nail bending. This study examines the evolution of the nail and provides a brief overview of the factors that influence soil nailing, as well as current design guidelines. The main focus of this study is to review thoroughly on the factors affecting the pull-out capacity of soil nail like overburden pressure, change in in-situ moisture content at the grout–soil interface, grouting pressure, variation in bond strength at the soil–grout interface, and its effect on pull-out resistance.

Pull-Out Box Tests

Pull-out testing in the lab is a simple and effective way to examine many characteristics of soil nailing in a controlled operated conditions. The capacity to simulate diverse ground and loading conditions encountered in actual field circumstances is a benefit of laboratory testing. Several researchers have investigated the behavior of soil nails, particularly keeping in mind, grout and steel tendons for laboratory pull-out testing on small-scale and large-scale models. Tei [18], Milligan and Tei [17], Chu and Yin [2], Pradhan et al. [14], Junaideen et al. [11], Chu [2], Su [16], Su et al.

R. Salvi (✉) · A. Juneja
Civil Engineering Department, Indian Institute of Technology, Bombay, India
e-mail: ruchitassalvi456@gmail.com

Table 20.1 Experimental pull-out tests

Author	Test box (m)	Test nail (mm)	Type of nail	Inclination of the nail (°)	Soil type
Milligan et al. (1997)	0.6 × 0.6 × 0.6	100	Grouted	0	Clay and Sand
Tei et al. [17]	0.25 * 0.25 * 0.2	70	Grouted (stiff and extensible)	0	Sand
Chu and Yin [2], Yin and Zhou [20]	0.7 * 0.7 * 0.610	100	Grouted	0	Granitic soil
Junaideen et al. [11], Pradhan et al. [14]	2 * 1.6 * 1.4	100	Grouted	0	Completely decomposed granitic soil
Fonzo et al. (2008)	1.6 * 0.8 * 0.8	75	Grouted	0	Pyroclastic silty sand
Su et al. (2006, 2010) [15]	1 * 0.6 * 0.8	100	Grouted	0	Granitic soil
Gurpersaud et al. [5]	1.5 * 1.2 * 1.10	100	Grouted	15	Poorly graded sand
Tokhi et al. [19]	1.5 * 1.0 * 1.0	37.7	Helical nail	0	Clay
Ghosh et al. [4]	0.69 * 0.34 * 0.45	60	Grouted	0	Powai soil

[15], Zhou [21], and Gurpersaud et al. [5] are some of the most well-known investigators who have conducted pull-out lbox studies models at a large scale. Yin and Su [16] implemented pull-out studies in an innovative fully instrumented pull-out box to explore the soil nail pull-out behavior under suitable planned overburden pressures, degree of saturation, and grout pressures Su [15]; Zhou [21]. In Table 20.1, the main features of pull-out box studies are presented.

Interface Shear Tests

The behavior of the soil nail interface received good amount of attention using various sizes of shear boxes. In most cases, the nail/grout is filled in the lower half portion of the shear box, while the soil is placed in the upper portion. Load and shear is applied in a similar way as direct shear testing for determining soil shear strength. As a result, the direct shear test provides a convenient way to examine the response of a soil nail under pull-out forces at a small scale. Although the results obtained from

direct shear tests cannot be correlated directly with field pull-out test, the behavior of soil at interface can be understood.

In the tests conducted with different type of sand and for medium and large shear testing apparatus, Pedley [13] noticed that the surface roughness and orientation of the reinforcement significantly impacted the tensile stresses along the nail, restricting the shear stress applied. Furthermore, reinforcing stiffness was revealed to have a considerable impact on soil shear strength, causing a rise in parameters for strength, and the strength has the effect on reinforcing stiffness. Davies and Le Masurier [3] used a large shear box to conduct direct shear testing to investigate the soil nail contact process. To understand the stiffness of the nail and soil, 100 and 200 kPa confining pressures were applied to the nails with 2 different materials like steel and aluminum (40 mm dia. and having length of 2.8 m) buried in medium dense and dense sand; as well as compacted cohesive soil. In direct shear testing using degraded granitic soil, Hossain and Yin [9] looked at the effect of dilatancy and shear strength on the interfacial behavior of grout–soil. The hardening or softening of the soil–cement grout interface, as well as its dilatancy, was influenced significantly by normal stress.

Chu and Yin [2] performed tests on a (0.31 * 0.31, top and 0.41 * 0.31 bottom sections) shear box and experimental pull-out studies in a box with dimensions of 0.69 m * 0.56 m * 0.61 m high. Laboratory pull-out studies were compared to the findings of interface shear testing in the shear box with different rough surfaces textured at angles. The findings of the shear tests and pull-out tests were compared, and it was discovered that the direct shear box may be used to determine the interface strength properties which are essential for the design and installation of nails.

Morris [12] executed 7 tests in clay to understand the effect of the interface friction between grout and soil. The test was performed in the standard direct shear box at different displacement rates as well as at different vertical stresses. The grout was prepared same as used in the soil nail pull-out test. The shear rate applied was 0.3, 1.2, and 0.01 mm/min, and surcharge was changed in the range of 50–200 kN/m². The interface friction test was compared with pull-out test to predict the bond strength of soil nails. The behavior of the effective stress of soil is unknown in either case of interface and pull-out test, because these were predicted as undrained or partially drained. The development of shear zone is pretty narrow in case of pull-out test as it is less confined. As a result, the shear strain is greater for the interface friction test, and the strain rate is greater than that of pull-out test at the same displacement. Another reason is in interface friction test, the vertical stress is acting throughout the test where in case of pull-out test the average of vertical and horizontal stress acting on the grout surface. So it is practically impossible to create the horizontal stress quickly in interface friction test, although the shearing rate is kept same for both the pull-out test and interface test. Finally, the interface friction basically depends on the roughness of the grouting material, frictional angle, and dilatancy of soil. Pradhan et al. [14] found that the peak pull-out shear stress increased linearly with the applied displacement, and after attaining the peak pull-out force, the shear stress decreases afterward. But in case of the direct shear test result, due to constraining of displacement, the soil sample reaches to peak shear stress gradually remain constant. Due to larger displacement obtained in pull-out box, it shows higher cohesion relative

to that of direct shear box result. When the soil sample is sheared at a displacement similar to pull-out container it shows almost same cohesion and angle of internal friction because the soil sample now sheared up to the critical condition state. The effect of degree of saturation was also observed in the testing. The degree of saturation changed over the testing procedure to 70, 74, 78, and 86%. It has been found that with the rise in value of S_r of the soil, the maximum shear stress decreases because due to saturation, the interlocking friction of soil sample decreases. The surface roughness of nail also an important parameter as the interface friction angle increases about 9.3% more than in smooth nail surface.

Effect of In-Situ Moisture Content Variation

For large box test, Gurbarsaud et al. [5] conducted pull-out research with the setup, allowing soil nail pull-out testing in inclination, vertical, and horizontal orientations. The study's goal was to see how the variation in matric suction is found to affect the pull-out load of nails in saturated, partly saturated, and unsaturated soil conditions in sands. It was found that the matric suction and pull-out capacity, and a semi-empirical approach for predicting the pull-out load of soil nails in saturated soil was presented based on this finding. It was stated, the drop in pull-out force is because of the SWCC of the soil under test, which showed that matric suction decreased as the moisture content increased, rather than the decrease in apparent friction coefficient, as previously claimed by Pradhan et al. [14], Chu and Yin [2], and Su et al. [15]. The S_r of the tested soil varied frequently due to the change in the level of ground water, environment conditions, and rainfall. Due to change in saturation water level of the soil, the matric suction changes. As shown in Fig. 20.1, the SWCC for every type of soil is different and according to the existing moisture content in soil while installation, the response of soil to the nailing can be anticipated. The pull-out resistance of a nail may go down below acceptable limits in case of severe rainfalls due to the reduction in matric suction of the soil in the vicinity of the nail. There were just a few research that looked at the consequence of soil saturation on soil nail pull-out load. The maximum pull-out load was found reduced by almost 50% when the water content was increased to the saturation limit of the soil, as reported in the FNRPC (1991). Pradhan et al. [14] reported the nail soil interface adhesive reaction strength was decreased because of the increase S_r in the laboratory pull-out tests which was conducted on grouted nails installed in loose CDG fill performed at NMC and saturated soil. The friction angle at interface remained unaltered. Tests performed on soil nails at S_r ranging from 38 to 98% as reported by Su [16]; Su et al. [15]; Zhou [22]. After testing the soil samples, it was found that at a high level of saturation (98%) had been attained.

Shear plane shift was observed in the soil as the in-situ water content changes were observed with the change in S_r . The displacements observed at peak shear stress for saturated soil tests were found to be less at saturated state than for partially saturated soil, and the post-peak pull-out shear stress decreased at a faster pace as the water

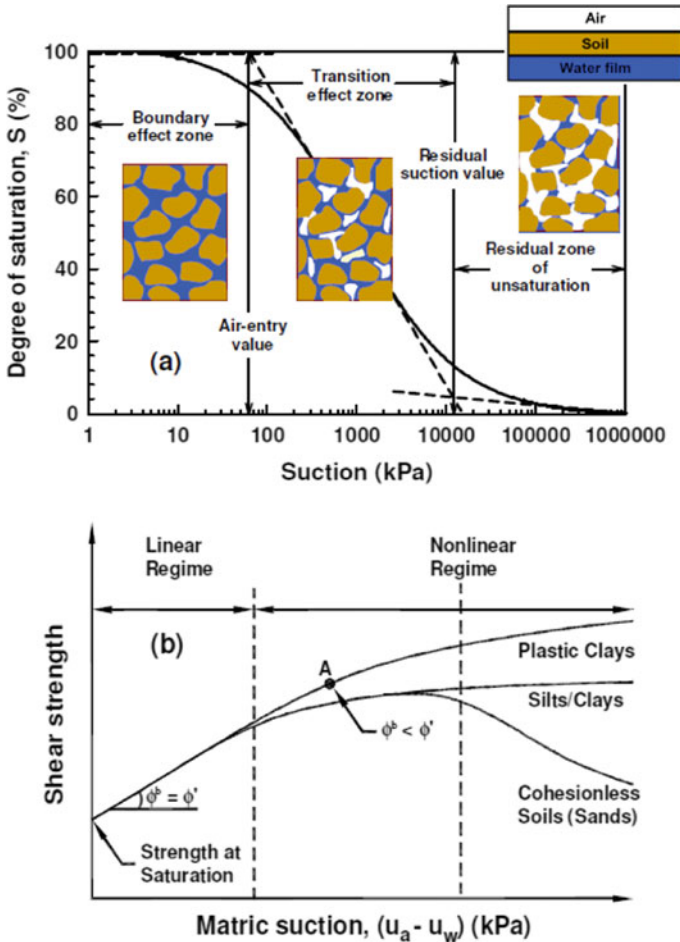
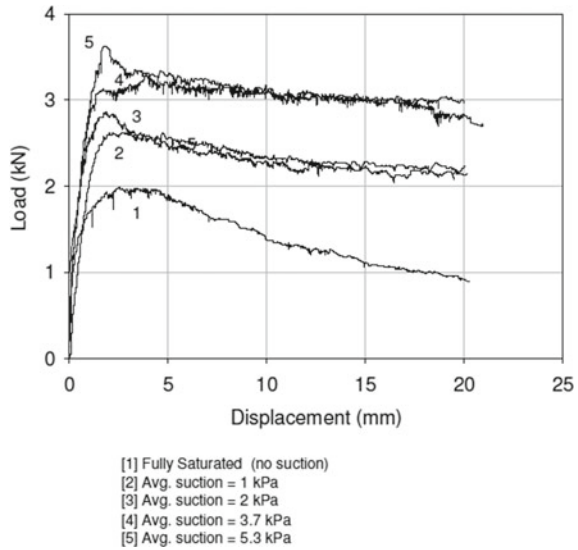


Fig. 20.1 a Soil water characteristic curve (SWCC) and b shear strength versus matric suction; Gurbarsad et al. [5]

content in the soil increased. The maximum value of pull-out load was observed at 50–75% and least values are noticed at 38 and 98% which is indicating there is a contraction of cement grout and decreased water content at soil nail interface giving lesser bond strength. It is believed that if the existing moisture content of soil is less, water is more quickly absorbed because of the high matric suction in the soil. The binding strength developed at the interface between soil and grout affects because of the shrinkage in grout. This also can be attributed to the existing water content at which soil nail is installed. In experiments with soil at 38% saturation, an instantaneous fall in earth pressure around the drill hole was noted after grouting, the earth pressure was not retrieved after the grout has achieved its strength and cured, presumably indicating a variance that occurred during the cement curing process.

Fig. 20.2 Load versus displacement at different soil suction; Gurbarsaud et al. [5]



This suggests that the influence of moisture on pull-out response of nail is important and should be considered wisely when designing a soil nailing system (Fig. 20.2).

Ghosh et al. [4] carried out total pull-out tests at a time period after 7, 14, and 21 days of curing period. Change in moisture content was measured at surrounding soil radially at distances of 45, 60, and 90 mm. The decrease in pull-out resistance was observed in 7–14 days but after 14 days became constant. Till a radial distance of 60 mm from the center of the nail, moisture content loss occurs closer to the soil nails. As demonstrated in Fig. 20.3, shrinkage and creation of gap at the interface of the soils near the soil nail contact is caused by a decrease in moisture content. Contact change is the possible reason for the gradual deterioration of pull-out strength.

Hong et al. [6] concluded that water content of soil sample was affected at a proximity of grouting soil compared to the soil sample observed at a distance. To validate the result, a field test was conducted on a slope where the height of the slope is 12 m and the length of the slope in prototype was 26.5 m along with 15° to 48° slope angle. Eight soil nails were inserted, and the soil nail was 2.5 m long and grouted diameter 100 mm with 1.2 m grouted nail. The pull-out was done after seven days of grouting in the field where the increment of pull-out force was kept 5 kN. After achieving the maximum pull-out, it was kept pulling out so that water content could be measured at grouting interface. The more the water content, the lesser will be the pull-out resistance. A new term water content ratio was introduced as:

$$\delta_w = W_s / W_o \quad (20.1)$$

Here W_s surrounding water content and W_o is the water content value to the radial distance of grouting soil water content after the pull-out test had been completely done. The water content ratio fluctuates between 0.15 and just about 1. The picture

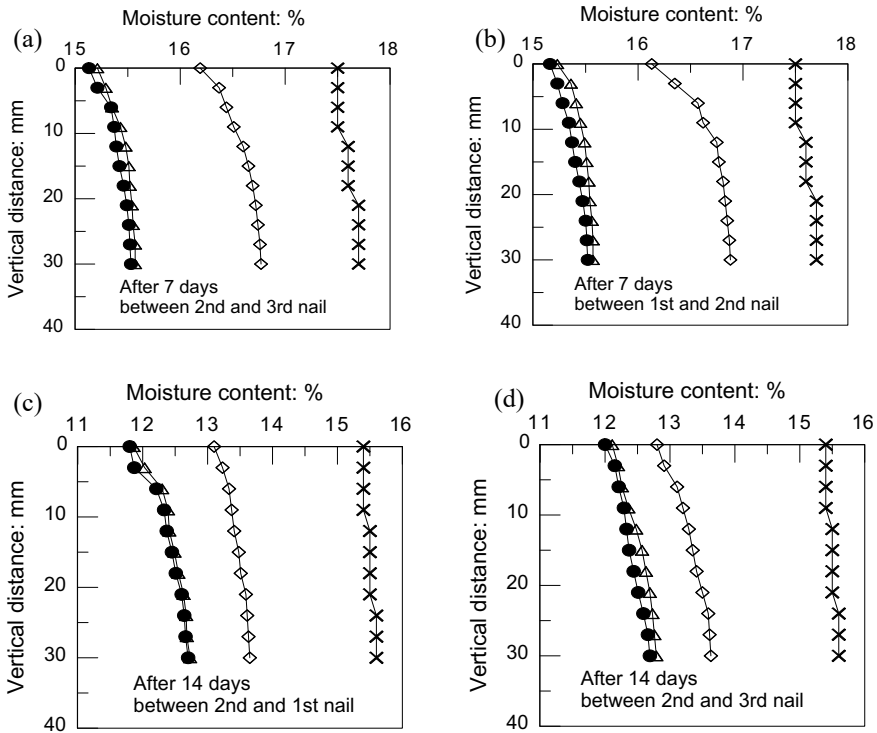


Fig. 20.3 Variation in moisture content with vertical distance from nails; Ghosh et al. [4]

depicts the results of the laboratory pull-out tests conducted by various researchers, with the water content ratio changing during the test., Zhou [21], Chu [2], Chai [1].

The reason for changing the water content ratio is due to the strength achieved because of the heat of hydration effect of cement grout which absorbs the water from the soil radially extending from the nail. The field test result shows a pretty much scattering plot because of the unpredictability of soil sample in the field.

Ghosh et al. observed water-cement ratio to prepare the grout which is also an important parameter to achieve the required strength of soil nail. In grouted nails, the water to cement ratio is kept to be 0.4–0.5. The compressive strength of grout mixture decreases as the water-cement ratio increases. In grouted soil nail procedure, hydration of cement starts as soon as the cement comes in contact with the moisture in the soil and due to the hydration effect may lead to bond breakage of soil and hence the pull-out load of the nail will reduce.

Hydrated cement can absorb up to 20% of its own weight in water from the earth around it. Inadequate moisture present in the soil will eventually impact the soil’s complete strength. Furthermore, the grout interface was found to be the most influential component in a soil nail’s pull-out resistance, causing a substantial increase in pull-out force by forming a strong link between nail and the soil. Grout injection

into the soil causes spaces in the surrounding soil to fill and solidify, enhancing the nail’s bonding to the soil, and resulting in increased pull-out resistances.

Effect of Overburden Pressure

Investigators including Su et al. [15], Yin et al. [20], Zhou et al. [21], Su et al. [16] studied the impact of pressure exerted due to the existing overburden on the pull-out load response of soil nails installed in compacted fill material including CDG soil. The numerical simulations exhibited that dilatancy due to constrained soil was linked with overburden pressure, but a direct relationship was not observed to affect the load response of the soil nail. However, the studies performed by Yin and Zhou [20] reported that at low pressures applied to the grout the pull-out resistance is barely reliant on the pressure exerted by the overburden. The effect was found to be increased for higher grout pressures (Fig. 20.4).

In parametric studies carried out by Su et al. [15] using FEM analysis to investigate the effect of overburden, which did not show much variation as compared with the variation spotted in laboratory testing.

Zhou et al. [21] reported from the FEM analysis that pull-out load showed increment as either the overburden or the grout pressure is increased. This was addressed by Isaka et al. [10] conducted pull-out studies in lateritic soils under different overburden load and at different saturation of soil. The influence of the grout interface on pull-out resistance was also assessed in this study. The pull-out force increases with increasing overburden pressure, hence the fill height up to the nail interface and the externally applied surcharge must be correlated in the design of nails and constructions, according to the test results.

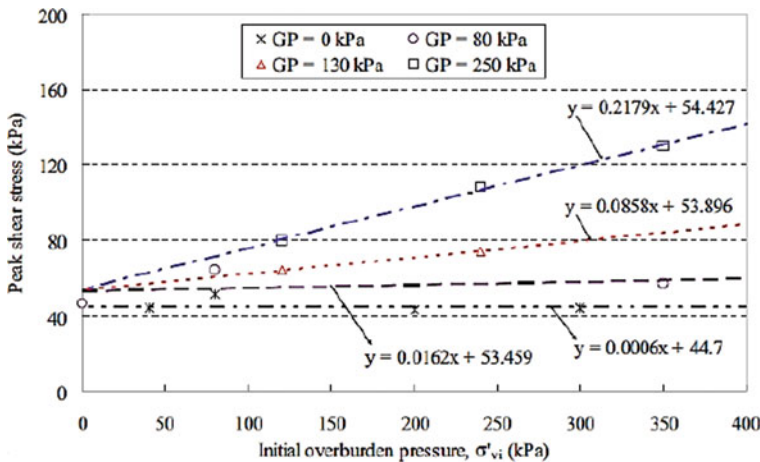


Fig. 20.4 Peak shear stress versus initial overburden pressure at various grouting pressure

The results of all tests conducted by Yin and Zhou [20] were combined and analyzed to look at the impact of grout pressure and overburden at the soil-grout interface and its shear strength. Due to collapse of surrounding soil arching action, vertical tension around the soil nail rises to some amount during saturation, but remain well below the original vertical overburden stress. The bigger the rise in tension found, the higher the grouting pressure applied. Mutually, overburden stress and grout pressure both have an impact on nail pull-out response. When the grout pressure is low, the soil nail pull-out resistance is barely or marginally affected by the overburden stress, but once the grout pressure is comparatively large, the overburden stress increases.

Effect of Grout Pressure

On field, the grouting of the drilled hole is done by gravity and mostly no external pressure is applied. As a result, pull-out capacity is likely to be altered, soil gets remolded and the strength achieved due to compaction at the soil-grout interface are thought to be highly reliant. The mechanical condition of the soil is modified and the strains are eased with a quick decrease in tensions as a result of borehole drilling for inserting soil nails. Because of the binding between soil and grout, if the gravity grouting is done under pressure regulated at a certain value, the re-compaction because of the grout entering into voids of the soil have a tendency to improve the pull-out load significantly. Furthermore, in clays or silts soils, the interface is even, and when water comes in contact, the interface performs as if it is lubricated, resulting in a much reduced pull-out capacity. Several studies have explored the impacts of grout pressure on the behavior of reinforced soil using field studies through sacrificial nails, laboratory studies, or finite element modeling, singly or combined. Some of the investigators include, Yin and Zhou [20], Hong et al. [6], Zhou [20], Hossain and Yin [9], Hong et al. [6], Hong et al. [7]. The association between grout pressures and shear resistance was observed to perform linearly between the grout pressures applied at a range from 0 to 130 kPa, according to the findings of multiple soil nail pull-out experiments. Hong et al. [6] performed in-situ pull-out study to examine the connection between the apparent coefficient of friction, the grout, and overburden pressure. It is noticed that as the grout pressure is increased, a linear trend is observed in the coefficient of friction. As the overburden stress grows, the curve is translated upwards, resulting in larger apparent coefficients of friction. Su et al. [15] found that gravity and pressure grouted tested in the field with 2 and 3 m nails in length, respectively. In Busan, South Korea, the nails were put in granitic soil. The study's main findings were that pressure grouting had a 36% higher pull-out capacity and had rougher surfaces. The surrounding attached soil around the nails was compacted as a result of the pressure applied while grouting.

Conclusion

From the thorough review, following conclusions were made in the present study.

1. At higher grouting pressure like 250 kPa, the overburden pressure significantly affects and at lower grout pressure, the overburden pressure is not found to be significantly affecting pull-out resistance.
2. For drilled-grouted nails, overburden pressure does not much affects the change in pull-out values of soil nail.
3. Increase in pull-out load is observed with rise in overburden pressure at saturated and at natural moisture content.
4. The pull-out resistance is found to vary with the variation in the in-situ moisture content of the soil because of the variation in bond strength at the interface.
5. Decrease in pull-out resistance for certain moisture content can be attributed to the creation of gap during hydration of cement due to which interface properties change.
6. Emphasis must be given on understanding the behavior of grout–soil interface for different soils considering the effect of soil water characteristic curve which is responsible for achieving the desired design bond strength.

References

1. Chai XJ, Hayashi S (2005) Effect of constrained dilatancy on pull-out resistance of nails in sandy clay. *Proc Inst Civ Eng Ground Improvement* 9(3):127–135
2. Chu L, Yin J (2005) Comparison of interface shear strength of soil nails measured by both direct shear box tests and pull-out tests. *J Geotech Geo-environ Eng* 131(9):1097–1107
3. Davies MCR, Le Masurier JW (1997) Soil-nail interaction mechanisms from large direct shear tests, *Ground improvement geosystems: densification and reinforcement*. In: *Proceedings of the third international conference on ground improvement geosystems*, London 3–5 June 1997, pp 492–499
4. Ghosh A, Chakraborty S, Juneja A (2020) Effect of variation of in situ moisture content on pullout capacity of grouted soil nail. In: *Construction in geotechnical engineering proceedings of IGC 2018*, pp 27–39
5. Gursaud N, Vanapalli S, Sivathayalan S (2013) Semiempirical method for estimation of pull-out capacity of grouted soil nails in saturated and unsaturated soil environments. *J Geotech Geoenviron Eng* 139(11):1934–1943
6. Hong CY, Yin JH, Pei HF (2013) Comparative study on pull-out behaviour of pressure grouted soil nails from field and laboratory tests. *J Central South University* 20:2285–2292
7. Hong C-Y, Yin J-H, Pei H-F, Zhou W-H (2013) Experimental study on the pull-out resistance of pressure-grouted soil nails in the field. *Can Geotech J* 50(7):693–704
8. Hossain M, Yin J (2012) Influence of grouting pressure on the behavior of an unsaturated soil-cement interface. *J Geotech Geo-environ Eng* 138(2):193, 202–245
9. Hossain M, Yin J (2014) Dilatancy and strength of an unsaturated soil-cement interface in direct shear tests. *Int J Geomech*:04014081
10. Isaka A, Madushanka B, Priyankara N (2016) Analysis of pullout resistance of soil-nailing in lateritic soil

11. Junaideen SM, Tham LG, Law KT, Lee CF, Yue ZQ (2004) Laboratory study of soil–nail interaction in loose, completely decomposed granite. *Can Geotech J* 41(2):274–286
12. Morris JD (1999) Physical and numerical modelling of grouted nails in clay. Magdalen College, University of Oxford, pp 1–242
13. Pedley MJ (1990) The performance of soil reinforcement in bending and shear, University of Oxford
14. Pradhan B, Lee CF, Tham LG, Yue QZQ (2003) Laboratory study of soil nail pull-out strength in loosely compacted silty and gravelly sand fills. In: 12th Pan American conference on soil mechanics and geotechnical engineering, 39th U.S. rock mechanics symposium
15. Su L, Chan T, Yin J, Shiu Y, Chiu S (2008) Influence of overburden pressure on soil-nail pull-out resistance in a compacted fill. *J Geotech Geo-environ Eng* 134(9):1339–1347
16. Su L-J, Chan TCF, Shiu YK, Cheung T, Yin J-H (2007) Influence of degree of saturation on soil nail pull-out resistance in compacted completely decomposed granite fill. *Can Geotech J* 44(11):1314–1328
17. Tei K, Taylor RN, Milligan GWE (1998) Centrifuge model tests of nailed soil slopes. *Soils Found* 38(2):165–177
18. Tei K (1993) A study of soil nailing in sand, University of Oxford
19. Tokhi H, Ren G, Li J (2016) Laboratory pull-out resistance of a new screw soil nail in residual soil. In: *Geotechnical and Geological Engineering*
20. Yin J, Zhou W (2009) Influence of grouting pressure and overburden stress on the interface resistance of a soil nail. *J Geotech Geo-environ Eng* 135(9):1198–1208
21. Zhou W (2008) Experimental and theoretical study on pull-out resistance of grouted soil nails. PhD Thesis, The Hong Kong Polytechnic University
22. Zhou W-H (2015) Chapter 20—Pull-out resistance of grouted soil nails. In: *Ground improvement case histories*, pp 533–571

Chapter 21

Reduction of Surface Erosion of Soil Slopes Using Alkali Activated Binder Treated Jute Fibers



Gunde Sachin Chakravarthy  and Anasua GuhaRay 

Introduction

Soil erosion has been a major issue for society since the beginning of civilization. Soil erosion is a constant loss of top layer or displacement of soil from one location to another, resulting in soil collapse, ecological degradation, slope failure, and other issues. Soil erosion is mostly caused by heavy rainfall, floods, and wind forces, among other things. Erosion mostly affects soils without cohesion in nature. Soil erosion can take several forms, including splash, sheet, rill, and gully erosion. This type of erosion is more likely to happen on highly inclined slopes than on flat ground. Mostly occurring type of soil erosion in India is due to loss of top soil because of rainfall. Splash erosion is a complex process in which raindrop collisions on the soil surface generate soil particle detachment, followed by short-distance movement of the detached particles. At around 53.34 million hectares of soil is being eroded annually due to rainwater as per Indian Council of Agricultural Research [1]. Understanding soil erosion processes is essential for developing and implementing soil management approaches that reduce and control the risk of soil erosion.

Geotechnical experts, scientists, and research personalities are attempting to understand the erosion of soil slopes in a variety of ways. Using of coir geotextiles in the form of nettings for stabilization of hilly areas along with vegetation showed positive result in controlling soil erosion [2]. In earlier studies, geosynthetics made of synthetic materials like polyolefins and polyesters received the considerable attention. Despite its potential, the utilization of naturally occurring fiber materials for similar applications has received little attention till date [3]. A wide range of temporarily degradable and long-term non-degradable materials have been fabricated into rolls to help with reduction of soil erosion and vegetation growth [4].

G. Sachin Chakravarthy · A. GuhaRay (✉)
BITS-Pilani Hyderabad Campus, Secunderabad 500078, India
e-mail: guharay@hyderabad.bits-pilani.ac.in

Geotextiles made of synthetic fibers pollute the soil and pollute the ecosystem, and their manufacturing process pollutes the environment as well [5]. Rain splash detachment is well controlled by natural geotextiles such as jute and coir. Process of runoff after precipitation which leads to soil erosion can be reduced by applying jute geotextile as cover [6]. Natural geotextiles, such as jute, have the ability to mitigate soil erosion but they are biodegradable within the duration of 180–365 days [7]. Chemical techniques such as alkali treatment, acetylation, and bleaching can improve the durability of natural geotextiles [8]. The use of vegetation and geojute for erosion control on slopes in a subtropical climate resulted in soil erosion reduction, particle displacement, and mulching of the topsoil for enhanced vetiver growth. Vegetable roots grow and take over the role of geojute as it degrades over time. When the side slope was protected with vetiver and geojute, there was no difficulty of erosion [9]. Application of jute geotextile on the shoulder and slope surface leads to retaining of soil particles and prevented its detachment from constructed slope. Soil stability and erosion were improved as a result of the introduction of plants on slopes [10]. The hydraulic prerequisites of landslides were studied by Park and Song [11] by applying artificial rainfall to a homogenous sandy laboratory slope model. Dey and Sengupta conducted a series of centrifuge experiments and numerical calculations on a 55° inclined unsaturated sandy slope with a less permeable, stronger silty-sand layer included inside it [12]. The authors concluded that the factor of safety decreased due to the low porous layer's effect. The writers also computed the slope's factor of safety by modeling seepage into the slope caused by rainfall infiltration [13]. During rainstorms, the effect of geocomposite layers on slope stability was explored by Bhattacharjee and Viswanadham [14] on a model silty-sand slope. The geocomposite reinforced slope was found to be stable under rainfall conditions, with negligible deformation as the rainfall progressed.

A comprehensive study on the research works carried out on modeling of slope erosion showed that a number of studies are available on prototype model scale slopes without any geosynthetic reinforcement. However, limited studies are available to measure the erosion rate of soil slopes protected with natural geotextiles. In the present study, the durability of natural jute geotextiles was improved by using alkali activated binder treatment method [15]. The jute was treated with varied water to solid ratios of alkali activated binder (0.35, 0.40, 0.45). An aluminosilicate precursor (fly ash/slag) reacts with an alkaline activator solution including sodium silicate and sodium hydroxide to form AAB. An artificial rainfall arrangement was framed, as splash type soil erosion with two different flow rates of 500 and 900 lit/hr. The soil erosion due to the impact of raindrops was measured for both unreinforced slope and slope reinforced with untreated and AAB treated jute geotextiles.

Table 21.1 Properties of untreated jute

Parameters	Values
Aperture opening dimension (μm^2)	4.7×10^7
Thickness (μm)	0.64
Mass per unit area (gm/cm^2)	0.0225
Elongation at break (%)	66.38
Tensile strength (kN/m^2)	10,440
Young's Modulus (kN/m^2)	2.28×10^7

Materials

Jute

In this study, natural jute geotextile bundles having a width of 0.91 m and a length of 30 m were used. The woven type *Corchorus olitorius* Tossa jute material was manufactured using newly available raw jute. Jute fibers were removed by retting the stem and outer skin of the jute plant, and then the non-fibrous debris was peeled away. After that, the fibers were spun into yarns. It was guaranteed that the jute fiber had not been scoured or bleached. The jute was found to contain 58% cellulose, 22% hemicellulose, and 14% lignin. The basic parameters of jute, including mass per unit area, aperture opening dimension, and thickness, were determined using the Indian Standard Code IS 15868 (Parts 1–6): 2008 and were tabulated in Table 21.1.

Alkali Activated Binder

The alkali activated binder solution was produced by mixing an alkali activator solution with an alum inosilicate precursor (Class F fly ash). Sodium silicate comprised of (55.9% water, 29.4% silica, and 14.7% sodium oxide) and sodium hydroxide (99% pure pellets) were combined to make an alkali activator solution. The mass percentages of fly ash, sodium hydroxide, and sodium hydroxide in the AAB mix were estimated as 74.07:1.96:2.97 [15].

AAB solutions were made using three distinct water to solid (w/s) ratios of 0.35, 0.40, and 0.45. The alkali activator solution is exothermic for the initial 24 h after mixing the ingredients. Fly ash and water are added to the cooled alkali activator solution. Throughout the application process of AAB on jute sheets with paint brushes, the required uniformity was maintained. To gain strength, painted jute sheets were exposed to 40 °C for 24 h. After curing for seven days at 27 °C, AAB treated jute sheets were ready for use. Table 21.2 summarized the quantities of fly ash, sodium silicate, sodium hydroxide, and water required to coat 1 m² of jute geotextile.

Table 21.2 Quantities of raw materials required for preparation 1 m² AAB jute

w/s ratios	AAB (kg/m ²)	Fly ash (kg/m ²)	NaOH (kg/m ²)	Na ₂ SiO ₃ (kg/m ²)	Water (kg/m ²)
0.35	3.45	2.20	0.060	0.71	0.50
0.40	3.10	1.90	0.050	0.61	0.54
0.45	2.75	1.70	0.045	0.53	0.56

Soil

In the present study, red soil, consisting of 2.36% gravel, 55.47% sand, and 42.17% fines (silt and clay), was used. The soil was taken from a depth of 30 cm below the ground surface to ensure that it was free of undesired things such as debris, plant roots, and other waste material. According to the Unified Soil Classification System (USCS), it was classed as silty sand (SM). The maximum dry unit weight and optimum moisture content of the soil was reported to be 17.9 kN/m³ and 16%, respectively. The soil has an angle of internal friction of 24.5° and a cohesion of 3.4 kN/m².

Laboratory Scale Slope Model Setup

Artificial Rainfall Setup

The effects of rain on soil erosion were explored in this study. When a raindrop hits the ground, soil particles get detached which leads to erosion. The following approach was used to create an artificial rainstorm arrangement in the laboratory to allow for this type of erosion. In the first phase, a large open container with dimensions of 2.7 × 2.7 m² and a height of 0.17 m was placed on a flat surface.

Non-recording type rain gauge is the most common type of rain gauge used by the meteorological department. In the present approach, it consisted of a cylindrical vessel 127 mm in diameter. At its top section, a funnel was provided with a circular brass rim which was 127 mm exactly so that it can fit into the vessel well. According to grid iron system methodology, a total of 12 pipes with a spacing of 7.5 cm were arranged. Drippers were fitted to pipe with a 5 cm space between them. Based on the discharge, the rainfall simulator arrangement was designed to have 2.97 mm diameter holes with center to center spacing of 5 cm. This grid pipe network was constructed prior to connecting the main water line, and it was subsequently attached to the wooden rods system. To supply water, a container with a volume of 1 × 1 × 1 m³ was filled with water, and a water pump motor with a capacity of 0.5 Hp was utilized for water supply. The motor pump's outlet was connected to the grid pipe's

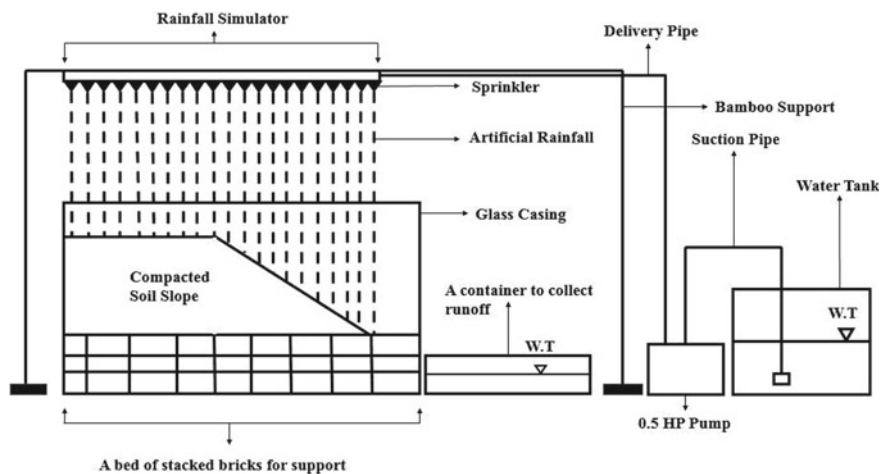


Fig. 21.1 Schematic diagram of experimental setup for surface erosion

input via an L shape connector. After this setup, water flow through pump and drip system was checked to avoid operational errors.

The water flow was controlled by a rotameter, and after multiple trials, two flow settings were established: a low flow rate of 500 L per hour and a high flow rate of 900 L per hour. The rainfall intensities obtained for low and high flow rates are 5.68 mm/min and 17.76 mm/min, respectively. Figure 21.1 showed the schematic diagram of the experimental setup.

To preserve uniformity, all trials were carried out in the same position relative to the rainfall simulators. The runoff was collected at 5-min intervals from the start of the simulated rainstorm to the end of the hour, for a total of 12 time periods. The amount of runoff was determined, and the samples were oven-dried for 48 h at 105 °C to determine the sediment production. The average of at least 10 cycles was considered to calculate the average value of precipitation. Figure 21.2 showed the images of eroded soil with water and the dried soil.

Laboratory Scale Slope Model

In this research laboratory, soil slope model was set up to calculate the soil erosion. Based on following procedure, slope model setup was arranged. An acrylic container of size $1.8 \times 1.8 \text{ m}^2$ and height 30 cm was made. It was taken care that no leakage of water through it while rainfall hits on soil slope and one opening of $0.15 \times 0.15 \text{ m}^2$ was made to collect the eroded soil and runoff water. The soil was compacted to 90–95% of maximum dry density value to achieve field compaction value. The soil slope model was in right angle trapezoidal shape with long base of 90 cm and short base of 45 cm and angle between long base to slope side is maintained at 45°. The soil

Fig. 21.2 Eroded soil with water and dried soil



was tamped in three layers to achieve the desired compaction. After compaction, the soil surface was smoothed using a wooden trowel, which helped to reduce the number of voids or cracked paths created in it. Figure 21.3 showed the soil slope model.

A total of 5 sets of experiments were carried out on the slope without any reinforcement, and reinforced slope with untreated and 0.35, 0.40, and 0.45 AAB treated jute geotextiles. The jute geotextiles were spaced 5 cm apart, with each sheet measuring 0.25 m in width and 0.9 m in length. To avoid movement, all of the reinforcement sheets were nailed to the soil. Figure 21.4 showed pictures of a slope model with reinforcement.

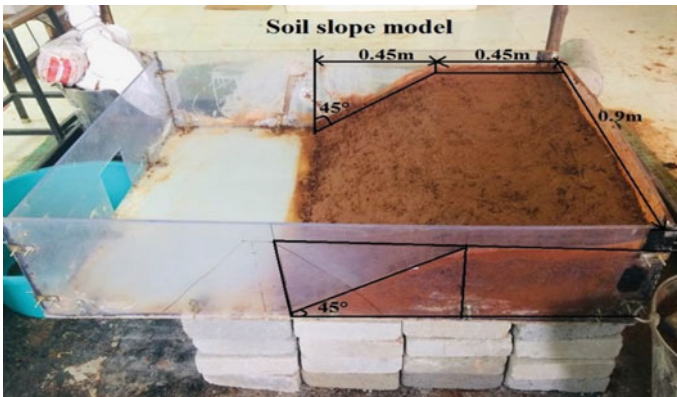


Fig. 21.3 Soil slope model setup with opening at one end

Fig. 21.4 Soil slope reinforced with jute and



Analysis of Erosion Rate

The soil erosion was computed in $\text{gm/m}^2/\text{hr}$ as per the following equation.

$$\text{Soil erosion rate } (\text{gm m}^{-2}\text{hr}^{-1}) = \frac{\text{Average weight of eroded soil}}{\text{Area of rainfall} \times \text{Duration of rain fall}} \quad (21.1)$$

The percentage reduction in surface erosion of soil slope for various reinforcements when exposed to rainfall was shown in Fig. 21.5. When a rain drop fell from certain height, it hit the soil and detached the soil particles which lead to displacement of soil particles along with runoff water. After separating the water from soil particles, they were dried to calculate the weight of eroded soil. Considering unreinforced slope, around 965.9 gm of soil was eroded with effect of low rainfall, whereas the same increased to 5482.3 gms for high rainfall. However, the amount of soil eroded after reinforcement with untreated jute was 90.7 gm for low rainfall and 305.8 gm for high rainfall effect. For 0.35 AAB treated jute reinforced soil slope, 65.9 gm and 191.1 gm of soil was eroded at low and high rainfall intensities, respectively. With increase in w/s ratio, the amount of erosion increased to a small extent. For 0.40 AAB treated jute reinforced soil slope, 73.3 and 212.2 gm of soil were eroded for low and high rainfall intensities. In a similar line, for 0.45 AAB treated jute reinforced soil slope, 84.6 gm and 245.1 gm of soil were eroded for low and high rainfall, respectively. To compare the variation, the corresponding soil erosion for all of these forms of reinforcement is computed based on a particular duration of rainfall, i.e., 5 min.

From these results, it could be observed that comparatively 0.35 AAB treated jute geotextile reduced surface erosion to a maximum extent of around 93.1% for low intensity rainfall and 96.5% for high intensity rainfall. From the figure, it was noteworthy to mention that there is only 6.5% difference in reduction of surface erosion between untreated and AAB treated jute geotextiles. This might be attributed to the fact that 0.35 AAB treated jute has the highest consistency and the number

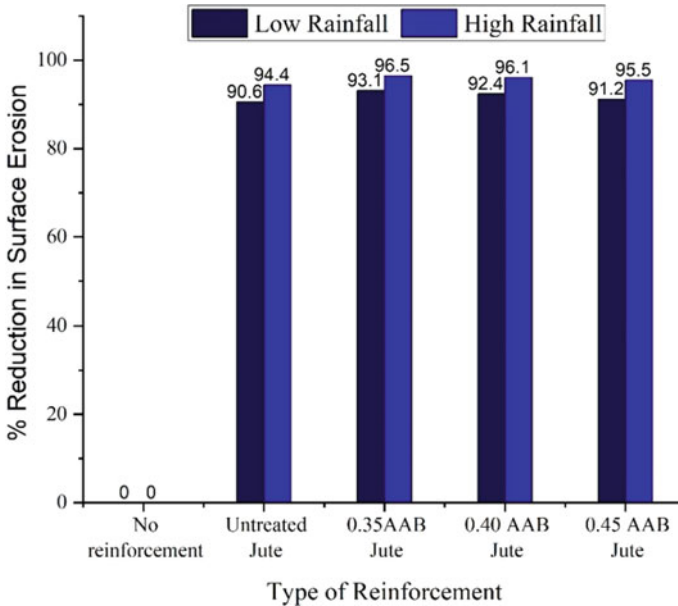


Fig. 21.5 Percentage reduction in surface erosion when exposed to rainfall

of micropores developed in this treatment was less compared to others, which led to maximum protection against erosion. However, it must be noted that untreated jute geotextile had a high susceptibility to biodegradation, while the AAB treated jute helped to increase the durability of the natural geotextiles [15]. After 90 days of soil burial exposure, it was noticeable that jute geotextiles treated with 0.35 AAB had the highest tensile strength, 63.04%, when compared to untreated jute geotextiles. The results from the study can be utilized as an economic and eco-friendly solution for reduction of surface erosion (Fig. 21.6).

Conclusions

Rainfall-induced slope failure is a major geotechnical disaster that has occurred in many parts of the world. The present study aims to analyze the effectiveness of treated natural fibers to reduce of surface erosion of soil slopes. This experimental study presents a novel approach of reducing surface erosion of soil slopes due to rainfall effect by employing alkali activated binder treatment to jute geotextiles. Two flow rates are considered to simulate low and high intensity rainfall. According to the findings of the study, 0.35 AAB treated jute geotextile reduced surface erosion to a maximum degree of roughly 93.1% for low intensity rainfall and 96.5% for high intensity rainfall. Although treatment of naturally available jute geotextile with

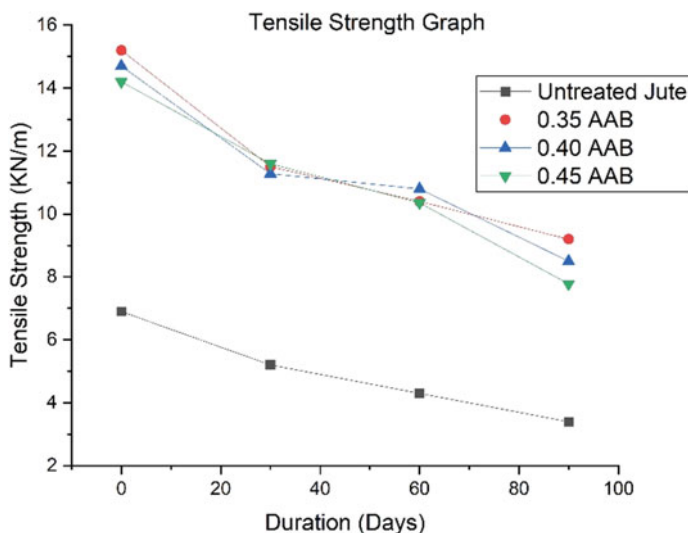


Fig. 21.6 Tensile strength of various jute geotextiles after exposure to soil burial

AAB having different w/s ratio improved the rate of reduction of surface erosion by a marginal extent, however, the AAB treated jute contributed to the natural geotextiles' increased durability. The study's findings can be used to reduce surface erosion in a cost-effective and environmentally responsible manner.

Acknowledgements We would like to appreciate Auto Traders in Secunderabad for contributing the jute.

Funding This work is supported by Department of Science and Technology (DST), International Bilateral Cooperation Division, Govt. of India through Indo-Austria bilateral grant (Project ID: INT/AUSTRIA/BMWF/P-22/2018).

References

- Reddy LR, Arumairaj PD, Janaki Raman S, Nancy DS (2019) A study on erosion of soil in slopes using laboratory slope model. *Int J Eng Adv Technol* 8(2):356–359
- Lekha KR (2004) Field instrumentation and monitoring of soil erosion in coir geotextile stabilised slopes—a case study. *Geotext Geomembranes* 22(5):399–413. <https://doi.org/10.1016/j.geotexmem.2003.12.003>
- Ogbobe O, Essien KS, Adebayo A (1998) A study of biodegradable geotextiles used for erosion control. *Geosynth Int* 5(5):545–553. <https://doi.org/10.1680/gein.5.0131>
- Allen SR (1996) Evaluation and standardization of rolled erosion control products. *Geotext Geomembranes* 14(3–4 SPEC):207–221. [https://doi.org/10.1016/0266-1144\(96\)00011-8](https://doi.org/10.1016/0266-1144(96)00011-8)
- Bhattacharyya R, Smets T, Fullen MA, Poesen J, Booth CA (2010) Effectiveness of geotextiles in reducing runoff and soil loss: a synthesis. *CATENA* 81(3):184–195. <https://doi.org/10.1016/j.catena.2010.03.003>

6. Kalibová J, Jačka L, Petru J (2016) The effectiveness of jute and coir blankets for erosion control in different field and laboratory conditions. *Solid Earth* 7(2):469–479. <https://doi.org/10.5194/se-7-469-2016>
7. Sanyal T (2017) Jute geotextiles and their applications in civil engineering
8. Rosa MF et al (2009) Effect of fiber treatments on tensile and thermal properties of starch/ethylene vinyl alcohol copolymers/coir biocomposites. *Bioresour Technol* 100(21):5196–5202. <https://doi.org/10.1016/j.biortech.2009.03.085>
9. Islam MS, Nasrin S, Islam MS, Moury FR (2013) Use of vegetation and geo-jute in erosion control of slopes in a sub-tropical climate. *World Acad Sci Eng Technol* 73:1162–11
10. Choudhury PK, Sanyal T (2010) Embankment slope stabilization with jute geotextiles—a case study in NH-2 Allahabad by-pass. In: *Proceedings of Indian geotechnical conference—2010*
11. Park JY, Song YS (2020) Laboratory experiment and numerical analysis on the precursory hydraulic process of rainfall-induced slope failure. *Adv Civil Eng* 2717356. <https://doi.org/10.1155/2020/2717356>
12. Dey N, Sengupta A (2020) Effect of a less permeable stronger soil layer on the stability of non-homogeneous unsaturated slopes. *Front Struct Civ Eng* 14(6):1462–1475. <https://doi.org/10.1007/s11709-020-0674-8>
13. Dey N, Sengupta A (2018) Effect of rainfall on the triggering of the devastating slope failure at Malin, India. *Natural Hazards* 94:1391–1413. <https://doi.org/10.1007/s11069-018-3483-9>
14. Bhattacharjee D, Viswanadham BVS (2018) Effect of geocomposite layers on slope stability under rainfall condition. *Indian Geotech J* 48(2):316–326. <https://doi.org/10.1007/s40098-017-0280-4>
15. Sachin Chakravarthy G, Anasua GuhaRay, Arkamitra Kar (2021) Effect of soil burial exposure on durability of alkali activated binder treated jute geotextile. *Innov Infrac Solut* 6(62) <https://doi.org/10.1007/s41062-020-00441-5>

Chapter 22

Parametric and Stability Analysis of Landslide Near Somwarpet, Coorg District, Karnataka



Anand. M. Hulagabali, V. Shilpa, N. C. Shobharani, G. S. Vasundhara, and M. L. Prashanth

Introduction

A landslide is a sort of “mass wasting” that refers to any downward movement of soil and rock caused by gravity. When forces pressing downslope surpass the strength of the earth components that make up the slope, the slope moves. Those that enhance the effects of shear stress, as well as factors that lead to low or reduced strength (shear strength), change the condition of the material from stable to unstable, are among the causes. Rainfall, snowmelt, changes in water level, stream erosion, changes in groundwater, earthquakes, volcanic activity, disturbance by human activities, or any combination of these variables can cause landslides in slopes already on the edge of moving. The analytical approaches are based on the idea of limit equilibrium, which is dictated by the safety factor (FOS). This is the ratio of active (tangential) forces to passive-resistant forces, which is expressed as soil cohesion. For theoretical and practical importance, a comprehensive study of stability analysis is required.

Literature Review

In the current state of practice, there are numerous slope stability analysis methods available. However, the scope of this report is limited to a discussion on the limit equilibrium methods.

Anand. M. Hulagabali · V. Shilpa (✉) · N. C. Shobharani · G. S. Vasundhara · M. L. Prashanth
Department of Civil Engineering, The National Institute of Engineering, Mysuru 570008, India
e-mail: shilpavkote7@gmail.com

Anand. M. Hulagabali
e-mail: anandmh@nie.ac.in

Preji and Longhinos [1] carried out a case study about the landslide susceptibility in Sastha valley of Periyar river basin, Idukki district, Kerala. The author concludes that analyzing and preparing a landslide zonation map is one of the important directions toward avoiding the impacts of landslides on human life and properties. By analyzing the impact of rainfall, it was found that antecedent rainfall has more influence on pore water pressure compared with daily rainfall. Moreover, a relatively high factor of safety results was obtained from the GIS-TISSA model. The zonation map based on the field investigation and GIS method can be used to identify the locations that are vulnerable to landslide. The stratigraphy of soil and its properties is the other direction of the investigation. It can give a better idea of the failure mechanism and nature of the slip surface of the landslides.

Ahmad et al. [2] explained that landslide may occur due to excavation or undercutting of its foot or due to gradual disintegration of the structure of the soil. The author found the result by comparing slope stability factors and by using GOES-LOPE software, the contribution of soil shear strength was considered. However, the influence of the unsaturated soil on shear strength was lessened by the presence of high groundwater tables. The software package slope/W, with its advanced numerical modeling techniques, is emerging as a better way to undertake routine geotechnical analysis.

Chen Huan [3] carried out work based on the geological environment and the actual situation of reservoir wading landslide, which take the typical wading landslide and Outang landslide. The landslide stability is evaluated by calculating the field of seepage flow and landslide stability by the two modules of SEEP/W, SLOPE/W in GeoStudio two-dimensional numerical simulation analysis software. In this paper, the stability of the calculation method using Morgenstern–Prince method, introducing seep/w calculated in different conditions of landslides saturation line. The calculated results into slope/w, in order to calculate the stability. Slope stability analysis model based on previous seep/w model performs the quantitative calculation.

Methodology

The present study deals with the parametric study and stability analysis of the slope using the limit equilibrium method using GeoStudio (SLOPE/W) software. The study is carried out in two parts. The first part deals with the analysis of a general homogeneous slope by varying different soil parameters and the second part includes the analysis of a case study with slope failure. Suitable remedial measures are also recommended and demonstrated for the slope. The analysis gives a single value of the factor of safety (FOS). In the case of an infinite slope, the factor of safety with respect to strength is given by the equation.

For granular soils, $c' = 0$ and factor of safety F_s becomes equal to $(\tan \phi') / (\tan \beta)$. This indicates that in an infinite slope in the sand, the value of F_s is independent of height H , and the slope is stable as long as $\beta < \phi'$.

$$F_s = \frac{c'}{\gamma H \cos 2\beta \tan \beta} + \frac{\tan \phi'}{\tan \beta} \tag{1}$$

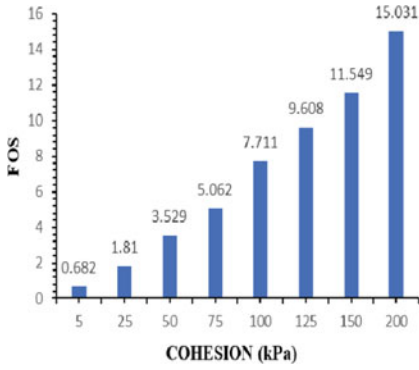
Parametric Study

A parametric study has been carried out to know the effect of the different soil parameters on the landslide. For analysis of slope stability, the Morgenstern–Price method has been adopted. There are three general classes of parameters that decide the strength or instability of a slope based on soil mechanics concepts, such as soil geometry, soil strength, and pore water pressure, which includes seepage forces. Our methodology in this analysis is to keep some of the parameters stable when investigating the effects of the remaining parameters on slope stability, such as slope geometry, cohesion, friction, unit weight, and groundwater table variation. Thus comprehends the influence of different parameters on slope stability.

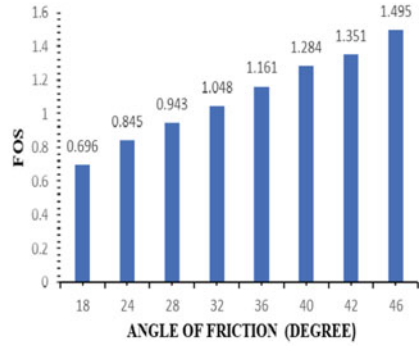
For the parameter cohesion, cohesion is being increased, while other parameters such as angle of friction (18°), unit weight (19 kN/m³), slope height (10 m), and slope angle (50°) are kept constant. Similarly, the change in FOS is observed with the change in other parameters as given in Table 22.1 and Fig. 22.1.

Table 22.1 FOS of different parameters

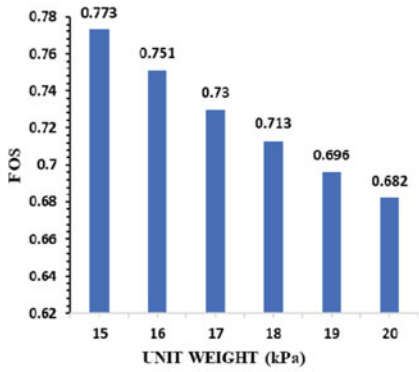
Cohesion		Angle of friction			
C in (kPa)	FOS	Ø in (Degrees)		FOS	
5	0.682	18		0.696	
25	1.810	24		0.845	
50	3.529	28		0.943	
75	5.062	32		1.048	
100	7.711	36		1.161	
125	9.608	40		1.284	
150	11.549	42		1.351	
200	15.031	46		1.495	
Unit weight		Slope angle		Slope height	
γ in (kN/m ³)	FOS	β in (Degrees)	FOS	H in (meter)	FOS
15	0.773	40	0.813	5	1.412
16	0.751	50	0.696	10	0.696
17	0.730	60	0.575	15	0.559
18	0.713	70	0.48	20	0.496
19	0.696	80	0.38	25	0.460
20	0.682			30	0.447



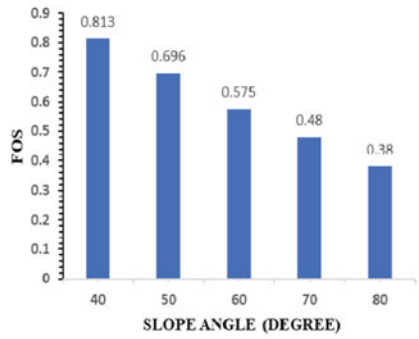
(a) Variation of FOS with respect to Cohesion



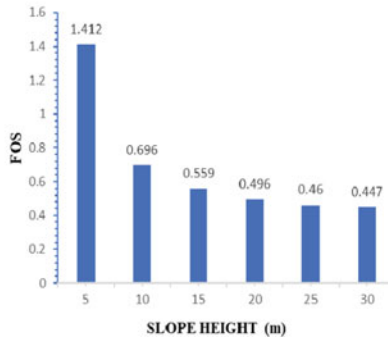
(b) Variation of FOS with respect to Angle of Friction



(c) Variation of FOS with respect to Unit Weight



(d) Variation of FOS with respect to Slope Angle



(e) Variation of FOS with respect to Slope Height

Fig. 22.1 Variation of FOS with different soil parameters

A series of experiments are carried out on a slope with simple homogenous geometry. The variations of FOS values with different soil parameters are shown in Fig. 22.1.

The parametric study shows that as the cohesion and angle of internal friction increases, FOS increases. But for slope height and slope angle, as these factor increases the FOS decreases. From Fig. 22.1c, it has been found that FOS decreases with increases in unit weight of soil. This can be justified using the Eq. (1), it is understood that, FOS is indirectly proportional to unit weight of soil.

Therefore, $FOS \propto \frac{1}{\gamma}$.

Case Study at Kundalli, Somwarpet Taluk

Study Area

In this study, Kundalli is selected where the landslide occurred in 2018. Kundalli area is an agricultural area situated in Somwarpet taluk, Coorg district, Karnataka. The site is located at an altitude of latitude of N 12° 40' 21.3" and longitude of E 75° 45' 03.9". The failure area comprised a toe width of 60 m with an elevation of 55 m. At an elevation of 128 m subsidence occurred. Due to landslide crops, road and other materials which are locally connected are washed away. Fortunately, no loss of life. The area consists of dry deciduous. The hill has a slope of 34° with a height of 152 m from the mean sea level (MSL). Laterite has orange to red color and clay of white color. Soils exhibited medium to fine-grained texture (Fig. 22.2).



Fig. 22.2 Kundalli, Somwarpet taluk, Coorg district, Karnataka

Experimental Investigations

Geotechnical investigations are carried out to determine the nature and strength characteristics of the material comprising the slope. Disturbed and undisturbed samples of soil are collected from the three different locations identified in the study area. Disturbed samples are used for determining the index properties and grain size analysis. Undisturbed samples are collected from the open pits using an appropriate type of sampling cores. Good quality undisturbed samples are a basic requirement for the reliable evaluation of shear strength parameters.

The main objective of the experimental study is to determine the density and shear strength parameters of the soil samples. The soil samples are subjected to various tests in the laboratory to determine the soil properties. A direct shear test is carried out for undisturbed samples. For disturbed soil sample, grain size analysis (targeted at unraveling the particle size distribution, coefficient of uniformity (Cu), the coefficient of curvature (Cc)), and specific gravity test is carried out.

Samples have been taken in three different locations left, center, and right of the site. The slope height, height of inclination, and slope angle for left, center, and right locations have been shown in Fig. 22.3.

The test results for the sample at field and laboratory conditions are reported in Tables 22.2, 22.3, and 22.4.

Fig. 22.3 Details of slope geometry for three different locations

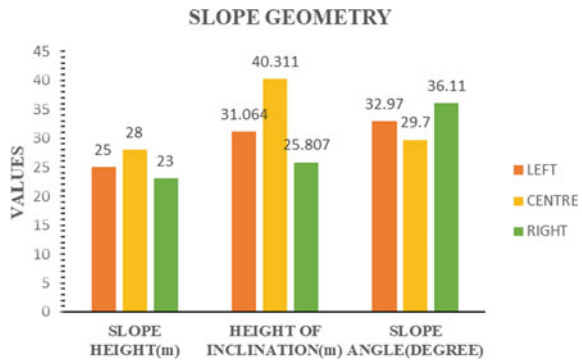


Table 22.2 Direct shear test for an undisturbed sample

S No.	Position	Cohesion (C) (kPa)	Angle of friction (ϕ) (degrees)
1	Left	0	27
2	Centre	0	25
3	Right	0	27

Table 22.3 Grain size analysis for disturbed samples

S No.	Position	Silt + Clay (%)	Sand (%)	Gravel (%)	Coefficient of uniformity	Coefficient of curvature	Type of soil
1	Left	4.8	74.2	21.0	10.63	1.15	SW
2	Centre	2.4	79.8	17.8	9.20	2.9	SW
3	Right	3.4	63.8	32.8	11.25	1.76	SW

Table 22.4 Soil Properties

S No.	Position	Bulk unit weight (kN/m ³)	Water content (%)	Dry unit weight (kN/m ³)	Specific gravity of soil
1	Left	15.4	36.21	11.30	2.46
2	Centre	16.0	30.79	12.20	2.52
3	Right	14.1	14.22	12.34	2.48

Numerical Analysis of Kundalli Landslide

Slope stability analysis is carried out using the SLOPE/W tool. The data required to facilitate this area's study is collected from the results as mentioned in Sect. [Experimental Investigations](#), which is then computed in the SLOPE/W to determine the factor of safety based on the Morgenstern–Price approach of limit equilibrium. The geometric models of the three locations where the samples are collected are analyzed using GeoStudio software, by taking the actual measurements of the location at the site. The three geoslopes of the site have base width 50 m, 59 m, and 45 m at left, center, and right, respectively. The selected location has height of 25 m at the left, 28 m at the center, and 23 m at the right. The depth of the slope is considered as 8 m for all the models. The area has homogeneous soil and the bund width of 14 m and 10 m is considered for all the models. For a considerable height of the slope, no ground water table has been observed. The models have been analyzed for base failure (Fig. [22.4](#)).

The typical model of the study site has been analyzed in GeoStudio software to obtain respective FOS and it is shown in the below Fig. [22.5](#). The left section is showing a FOS of 1.109, whereas the center section showing FOS of 1.105 and a right section showing FOS of 1.068. The FOS obtained is less than 1.5 hence the slope is not stable. Hence, it is observed that the landslide occurred at the site 4 years back due to this reason.

Conclusion

Kundalli is an important location for landslide investigation, and the landslide susceptibility of this area is analyzed in this study. These slopes are studied for stability

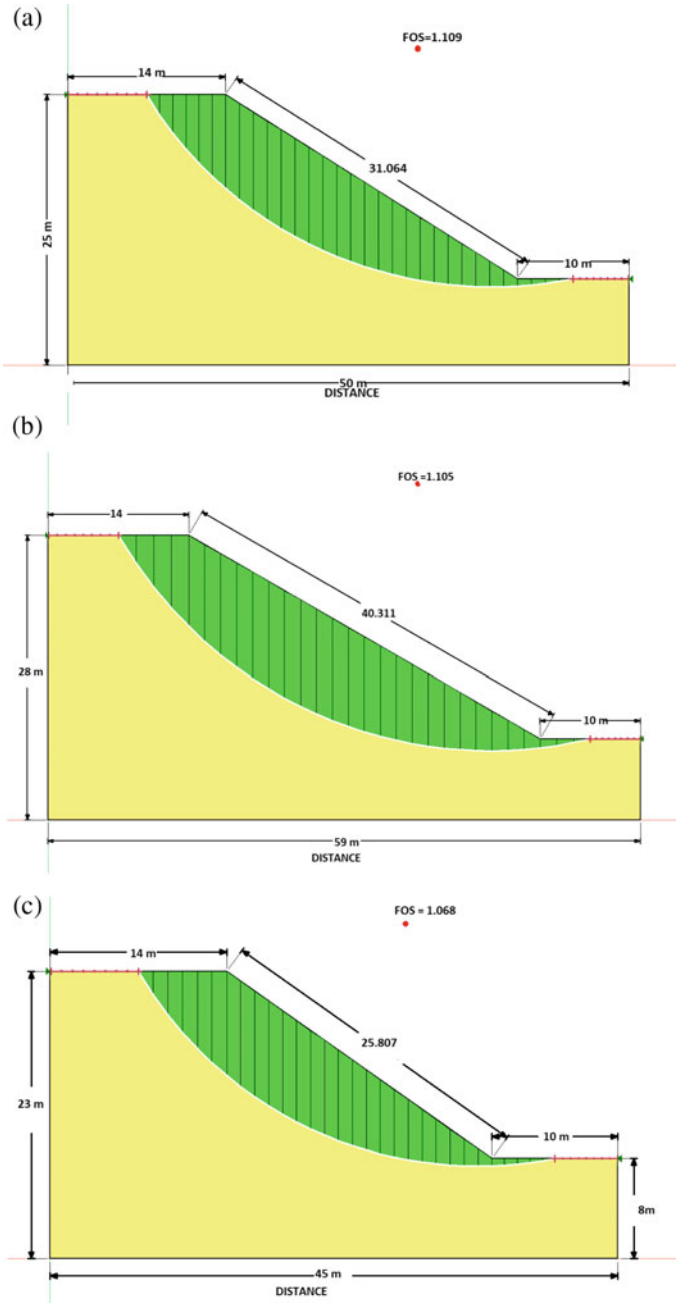
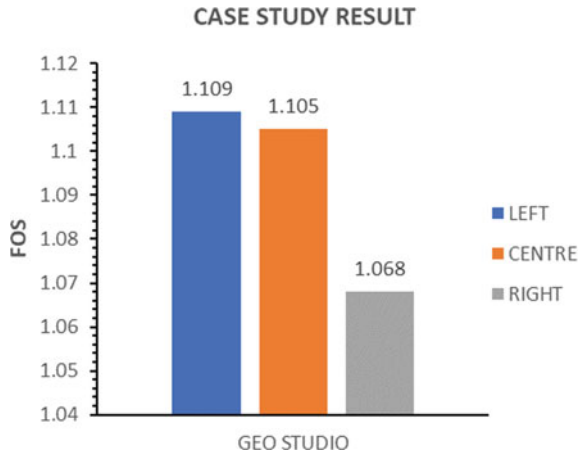


Fig. 22.4 a Left, b center and, c right model

Fig. 22.5 FOS for case study models



using SLOPE/W analysis. The slopes undergo a circular failure mechanism with high shear strain rates at the failure zones. The three selected locations are found to be critical having the factor of safety less than 1.5 after the stability analysis. Since the slope angle is greater than the angle of internal friction, there is less stability in the slope. It is also observed that the absence of cohesion in the soil ($C = 0$) leads to less adhesive property in between the particles. The occurrence of the landslide at the study site can also be due to the heavy rainfall in that area. From the present slope stability analysis, it is observed that the slope is unstable. With the consideration of the importance of landslide prevention, it is suggested that the installation of the drainage system, soil nails, retaining walls, and vegetation and flexible barriers can be used at the landslide site.

References

1. Preji P, Longhinos B (2018) Landslide susceptibility analysis and mapping in Sastha valley of Periyar river basin. IGC Indian Institute of science, Bengaluru
2. Ahmad R, Mardhanie AB, Suroso P, Sutarto TE, Alfajri R (2019) Effect of groundwater table on slope stability and design of retaining wall. IOP Publishing
3. Huan C (2016) Analysis of numerical simulation of wading landslide in Three Gorges Reservoir area based on Outang Landslide. *Math Model Eng Probl* 3(2):71–74. <https://doi.org/10.18280/mmep.030205>

Chapter 23

Dynamic Stability and Landslide Simulations in Hilly Regions of Kerala



Geethu Maria Joseph and K. Ranga Swamy

Introduction

The recently occurred landslides in the hillside regions of Kerala cause severe damages to civil infrastructures and the death of human beings. The intensity of landslides kept rising when humankind activities of unscientific quarrying, road expansion, and big infrastructure projects are carried out in these regions. The change in the rhythm of the monsoon is also an added factor. High intense rainfall leads to the most disastrous fluidized landslides, which usually occur very unexpectedly. Landslides become severe with dynamic activities of continuous vibrations due to constant heavy traffic movements, mining activities, and industrial machine operations in addition to excess rainfall intensity. Kerala is known for its low seismic history. But, the effects of excavation of building stones through blasting with explosives are high on landslide movement in the hilly regions. Since the natural formations and boulders in these locations are prone to rockfall and landslides, it is essential to study the dynamic stability of the slopes. The present paper aims to model landslide movement triggered by rainfall intensity and minor seismic amplitude at a few existing soil slopes of Kerala using integrated landslide simulation model LS Rapid software. Since the average pore pressure ratio represents the rainfall intensity, the pore pressure ratios are varied from 0.1 to 0.9 to study the effect of rainfall intensity on landslide stability. Further, the slopes are subjected to low seismic amplitude to represent the influence of minor dynamic loading conditions. It also examined the effect of soil properties on landslide stability.

G. M. Joseph (✉) · K. Ranga Swamy
National Institute of Technology, Calicut 673601, India
e-mail: geethumariajoseph94@gmail.com

Characterization of Soil Slopes

Integrated Landslide Simulation Model—LS Rapid

LS Rapid is computer simulation model software that integrates the initiation process to the rapid landslide motion triggered by rainfall and earthquake. It may be due to strength reduction and the entrainment of deposits in the run-out path [1]. The available stability analysis methods based on LEM used to analyze the soil slopes assume that the sliding mass fails only once. But, in actual landslides, the regions subjected to high pore pressures fail first, followed by expansion of the failure area around the initial failure zone. Eventually, the whole landslide mass will start to move. LS Rapid software simulations can reproduce such progressive failure phenomenon. The basic concept of the LS Rapid model is rooted in establishing an imaginary vertical column within the moving landslide mass. The forces acting on the soil column shown in Fig. 23.1 are including self-weight of the soil column (W), horizontal seismic forces in X and Y directions (F_x and F_y), vertical seismic force (F_v), and lateral earth pressure acting on the walls (P), shear resistance acting on the bottom of the column (R), normal stress acting at the bottom (N) and pore pressure acting on the bottom (U). The component of self-weight parallel to the slope, shear resistance, and sum of the balance of lateral earth pressures in X and Y directions can cause the landslide mass to slide downward.

The landslide mass (m) is accelerated by acceleration (a) generated by the total forces acting on the vertical soil column. It is denoted as:

$$am = (W + F_v + F_x + F_y) + \left(\frac{\partial P_x}{\partial x} \Delta x + \frac{\partial P_y}{\partial y} \Delta y \right) + R \quad (23.1)$$

where R includes the effect of normal stress and pore pressure acting on the bottom of the soil column. All the stresses and displacements are calculated by projecting into a horizontal plane.

Fig. 23.1 Soil column element within a moving landslide mass

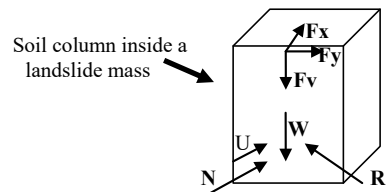


Table 23.1 Location and geometrical details of the soil slopes

Location	Slope angle (°)	Slope height (m)	Latitude	Longitude
Aadit, Idukki	41.96	950	N10°1'15"	E77°2'48.8"
Kallar, Idukki	44.23	1140	N10°02'25.3"	E77°00'19.9"
Mavadi, Idukki	44.6	1058	N9°52'09.1"	E77°07'46.5"
Kakkattuppara, Wayanad	45	490	N11°25'42.3"	E76°20'45.7"
Kavalappara, Wayanad	35	275	N11°24'43.2"	E76°14'13.92"
Mananthavadi, Wayanad	52	924	N11°50'36"	E75°58'51"
Puvaramthodu, Wayanad	41	1281	N11°22'47.5"	E76°18'44.5"

Geometrical Features of the Slopes

For the present study, three slopes from the Idukki district and four from the Wayanad district of Kerala have opted. All the slopes selected are located near to previously occurred landslides. The slope angles of the chosen locations are found to be greater than 30°. Table 23.1 gives the site of the place and geometrical features of the slopes.

Creation of Topography

ArcGIS software and LS Rapid software of version 2.1 have been used to create the topographies of the soil slopes. The digital elevation model (DEM) of the regions was created using ArcGIS software. The DEM file is incorporated into LS Rapid software to get the topographies. The present study assumed that the failure begins in the steeper portion of a slope, and the failure surface was created using an ellipsoidal sliding surface setting in the steepest part of the hill slope.

Soil Properties

The soil properties required for the simulation are including steady-state shear strength (τ_{ss}), lateral earth pressure ratio (k), peak friction angle (ϕ_p), peak cohesion (c), friction angle during motion (ϕ_m), shear displacement at the start of strength reduction, shear displacement at the beginning of steady-state, pore pressure generation rate, and unit weight of the soil (γ). In this study, the residual shear strength of the soil determined from the undrained triaxial shear test is considered to be steady-state shear strength. The properties of soils collected from the soil slopes of different locations are given in Table 23.2.

Table 23.2 Soil properties of slopes located at different sites (Geotechnical lab, NIT Calicut)

Location of soil sample	Unit weight (kN/m ³)	Shear strength parameters		Lateral earth pressure coefficient (k)	Shear strength of the soil (kPa)
		c (kPa)	ϕ (°)		
<i>Aadit</i>					
Top	17	4	35	0.426	74
Middle	17.2	4	32.2	0.467	66.5
Bottom	18.2	5	35.2	0.423	75
<i>Kallar</i>					
Top	13	5	24.8	0.58	51
Middle	13.4	5	27.1	0.54	56.1
Bottom	17	5	28	0.53	58.2
<i>Mavadi</i>					
Top	12.8	1	14.3	0.753	26.5
Middle	15.8	5	15.3	0.736	32.3
Bottom	14.6	5	25.8	0.56	53.3
<i>Kakkattuppara</i>					
Top	15.9	20	18.3	0.68	35
Middle	13.8	25	19.3	0.66	60
Bottom	15.9	15	17.8	0.7	47.3
<i>Kavalappara</i>					
Top	14.4	0	30	0.33	25
Middle	14.5	0	30	0.33	25
Bottom	14.3	0	30	0.33	25
<i>Mananthavadi</i>					
Top	13.5	12	34.7	0.43	81.24
Middle	13.7	12	33	0.45	76
Bottom	15.8	25	34.6	0.43	83
<i>Puvaramthodu</i>					
Top	13.5	10	32	0.47	72
Middle	14	10	33	0.45	74.9
Bottom	18	12	31	0.48	72

Numerical Simulation of Rainfall Induced Landslides

Average pore pressure ratios (PPRs) build in the soil slopes during rainfall are used to vary to study the effect of rainfall intensity on landslide stability. An increase in rainfall increases the saturation level of the soil that leads to building the pore pressures. In turn, it increases the average pore water pressure of the soil. At higher rainfall intensity, the soil slope becomes fully saturated with a PPR of 1, and it becomes

unsaturated with PPR of 0.7, 0.5, and 0.1 at moderate to low rainfall intensities. The present study used to vary the pore pressure ratios from 0.1 to 0.9 to analyze the failure of the soil slopes under various rainfall intensities. Table 23.3 presents the detailing on the instability of soil slopes at different locations, including the maximum vertical depth and the volume distribution of sliding mass and the rainfall intensity, i.e., PPR at which the landslide is initiated. From the simulation test results, the slopes located at Mavadi (Idukki) and Kakkattuppara (Wayanad) regions fail at a low pore pressure ratio of 0.1 with very low rainfall intensity. It also found that the soil slope located at Kakkattuppara has an enormous volume of landslide mass and can be considered critical.

It observed that the soil slopes located at Puvaramthodu, Kallar, and Mananthavadi areas are initiated to fails at low rainfall intensity with a PPR of 0.3–0.5 onward. However, the slopes at Kavalppara and Aadit are initiated to fail at high rainfall intensities with a PPR of 0.7 onward. The typical results on the simulation of progressive failure of soli slope located at Kakkattuppara subjected to a pore pressure ratio of 0.7 are shown in Fig. 23.2. Similar kinds of progressive failures are also produced in other cases of soil slopes. Figure 23.3 shows the sliding mass surface details in longitudinal section of soil slope located at Kakkattuppara subjected to a pore pressure ratio of 0.7. It finds that the green color boundary shows the original slope surface before failure; dense red color indicates the sliding surface, and the pink color boundary shows the surface of landslide mass after sliding failure. It shows the stable and unstable parts of the slope and the deposition region of the landslide mass.

Table 23.3 Failure details of the soil slopes tested in the present study

Location	Maximum vertical depth of the landslide body (m)	Volume of landslide body (m ³)	Pore pressure ratio to initiate slope failure
Aadit, Idukki	19.1	123.1×10^3	0.7
Kallar, Idukki	37.51	448.6×10^3	0.4
Mavadi, Idukki	53.78	513.3×10^3	0.1
Kakattuppara, Wayanad	68.05	1178×10^3	0.1
Kavalappara, Wayanad	24.91	341.3×10^3	0.7
Mananthavadi, Wayanad	34.1	327.5×10^3	0.5
Puvaramthodu, Wayanad	48.65	949.3×10^3	0.3

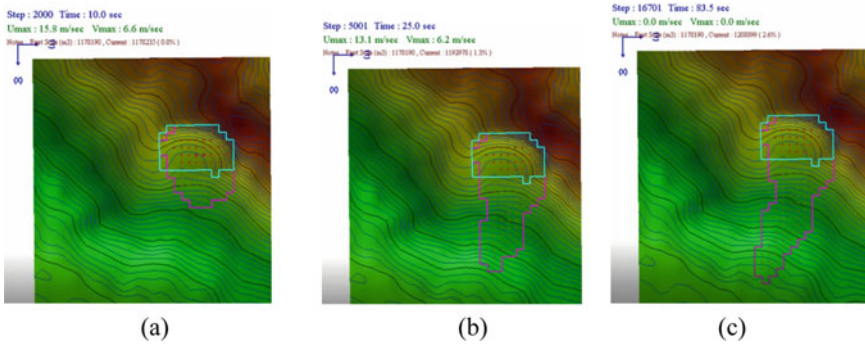


Fig. 23.2 Progressive failure of soil slope located at Kakkattuppara subjected to high rainfall intensity with PPR of 0.7: Land slide at **a** initiation; **b** distribution; and **c** deposition stages



Fig. 23.3 Sliding surface in longitudinal section of soil slope situated at Kakkattuppara region subjected rainfall intensity with PPR of 0.7

Numerical Simulation of Seismically Induced Landslides

The slopes were subjected to low seismic amplitude of 0.009 g to study the influence of minor dynamic loading on the failure of soil slopes. The details of the seismic time history used to perform the simulations are given in Table 23.4. Numerical simulations were performed on the dynamic stability of landslides at no rainfall intensity, i.e., PPR = 0 and moderate rainfall intensity with PPR of 0.5 conditions. Table 23.5 summarizes the influence of seismic load alone and combined seismic load with moderate rainfall intensity on the susceptibility of soil slopes failure. From the simulation results, it has been found that the soil slopes located at Aadit (Idukki) and Puvaranthodu (Wayanad) were safe under seismic load alone at no rainfall intensity. However, it caused local deformation in soil slopes located at Kallar (Idukki), Mavadi (Idukki), and Kavalappara (Wayanad) regions. It is also seen that the soil slopes located at Kakkattuppara and Mananthavadi (Wayanad) areas are failed under seismic load alone at no rainfall intensity. All the soil slopes situated at different places are

Table 23.4 Details of the seismic time history used for the simulations

Location	Phek-Nagaland
Latitude	25.7 N
Longitude	94.6 E
Origin time	01-07-2012 04:13
PGA	0.009 g
Record duration	65.000 s

Table 23.5 Failure conditions of soil slopes subjected to seismic load and rainfall intensity

Location	Seismic load alone (PPR = 0)	Seismic load with moderate rainfall intensity (PPR = 0.5)
Aadit, Idukki	No failure	Failed
Kallar, Idukki	Local deformation	Failed
Mavadi, Idukki	Local deformation	Failed
Kakattupara, Wayanad	Failed	Failed
Kavalappara, Wayanad	Local deformation	Failed
Mananthavadi, Wayanad	Failed	Failed
Puvaramthodu, Wayanad	No failure	Failed

failed under the influence of combined action of seismic load with moderate rainfall intensity, i.e., PPR of 0.5.

Parametric Study

The present study is extended to study the effect of rainfall intensity, dynamic loading amplitude, and soil properties on landslide stability of soil slopes located at different places. The simulation results provide the maximum velocities of soil flow and volume of sliding soil mass in the lateral and vertical directions of soil slopes.

Effect of Rainfall Intensity, i.e., Average Pore Pressure Ratio

Initially, the study focuses on the effect of rainfall intensity on the maximum velocity of soil slope deformation at the failure stage. Table 23.6 summarizes the variation of maximum flow velocities of the soil slopes in a lateral direction with different pore pressure ratios representing the rainfall intensity. Results indicate that the maximum flow velocities of soil slope deformations increase with increased rainfall intensities with pore pressure ratios in the range of 0.1–0.9. Similar results are also produced in the vertical direction but less significant when compared in the lateral movement. It

suggests that the effect of rainfall intensity is more significant on soil flow velocities at failure state. The increase of soil flow velocity with rainfall intensity is due to a reduction in the effective strength of soil with built-up of pore pressure. The present study also focuses on the effect of rainfall intensity on the variation of volumetric landslide soil mass distribution at the failure stage. The slopes become unstable with large volumetric soil displacements as the rainfall intensity increases, i.e., pore pressure ratios. Results indicate that the soil slopes at Mavadi (Idukki) and Kakkattuppara (Wayanad) are inconsistent, and others are stable at low rainfall intensity with a PPR of 0.1. It may be due to the high slope angle and low shear strength for Mavadi and Kakkattuppara soil slopes. The volumetric landslide soil mass distribution is increased with an increase in rainfall intensities. Table 23.7 shows the variation of volumetric landslide soil deformations of the soil slopes with different pore pressure ratios representing the rainfall intensity.

Table 23.6 Summary on variation of maximum flow velocities of the soil slopes in lateral direction with rainfall intensity, i.e., different pore pressure ratios

Location of soil slope	Maximum velocities of soil mass movement in lateral direction (u_{max}), m/s, with rainfall intensity, i.e., PPR of			
	0.1	0.5	0.7	0.9
Aadit, Idukki	0	0	18.5	19.8
Kallar, Idukki	0	20	20.5	31.7
Mavadi, Idukki	14	14.7	26.8	28.9
Kakattuppara, Wayanad	10	15.3	17.4	52.5
Kavalappara, Wayanad	0	0	52.2	73
Mananthavadi, Wayanad	0	21	26.6	30.9
Puvaramthodu, Wayanad	0	25.2	26.2	38.3

Table 23.7 Summary on variation of volumetric landslide soil deformations of the soil slopes with rainfall intensity, i.e., different pore pressure ratios

Location of soil slope	Volumetric landslide soil deformations of the soil slopes, $\times 10^3 \text{ m}^3$, with rainfall intensity, i.e., PPR of		
	0.5	0.7	0.9
Aadit, Idukki	129	135	136
Kallar, Idukki	484	489	493
Mavadi, Idukki	565	565	565
Kakattuppara, Wayanad	1179	1209	1246
Kavalappara, Wayanad	0	366	376
Mananthavadi, Wayanad	125	141	142
Puvaramthodu, Wayanad	945	945	945

Table 23.8 Effect of seismic loading on volumetric flow of soil mass of landslides

Location of soil slope	Volumetric flow of soil mass, $\times 10^3 \text{ m}^3$		
	Seismic load alone with no rainfall (PPR = 0)	Rainfall intensity alone (PPR = 0.5)	Seismic load + moderate rainfall intensity (PPR = 0.5)
Aadit, Idukki	Stable	Stable	135.5
Kallar, Idukki	Local deformation	484.6	486.0
Mavadi, Idukki	545.2	564.6	570.7
Kakattupara, Wayanad	1237.5	1179.4	1295.6
Kavalappara, Wayanad	Local deformation	Stable	375.5
Mananthavadi, Wayanad	256.2	124.6	270.4
Puvaramthodu, Wayanad	Stable	945.2	980.9

Effect of Dynamic Loading

The effect of seismic loading with low amplitude is studied on the stability of landslides in dry conditions and partially saturated with moderate rainfall intensity, i.e., PPR of 0.5. Table 23.8 summarizes the effect of seismic loading combined with moderate rainfall intensity on landslide volumetric flow of soil mass. It is found that the seismic load, along with moderate rainfall intensity, causes a significant effect on landslide occurrence with high maximum flow velocities of soil movements and also the volume of sliding of soil mass.

Effect of Cohesion

The cohesion strength of soil located at the Kakkattupara soil slope has been varied to study the effect of cohesion on landslide mass. The cohesive strength of the soil slope was varied as 30, 40, and 50 kPa to study the effect of cohesive strength on landslide. The triggering factor considered was seismic load with moderate rainfall intensity. The maximum soil flow velocities in lateral and vertical directions and the percentage variation in volumetric soil flow of landslide under different cohesion values are shown in Fig. 23.4. It can be noted that when the cohesion of the soil increased from 30 to 50 kPa, the maximum velocities of sliding mass in the horizontal direction decreased from 15.5 to 6.8 m/s. Similarly, the flow velocities in the vertical direction decreased from 10.2 to 4.8 m/s. Also, the percentage variation in the volume of sliding soil mass decreased from 5.6 to 2.1%. Hence, it is proved that soil cohesion strength greatly helps mitigate the occurrence of landslides.

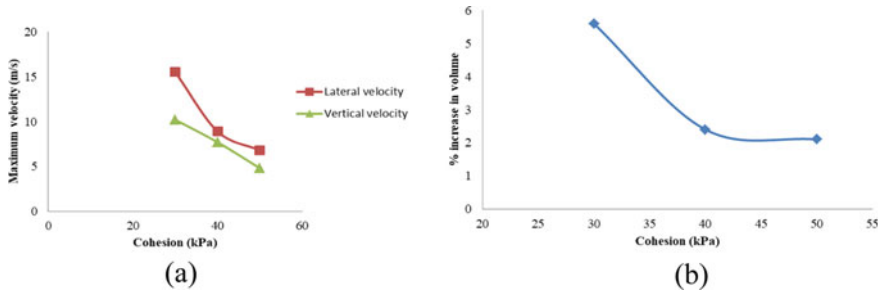


Fig. 23.4 Variation of **a** maximum velocity of soil flow, and **b** volume of sliding soil mass with cohesion strength of soil on Kakkattuppara soil slope under seismic load with moderate rainfall intensity

Table 23.9 Effect steady-state shear strength on volume of sliding soil mass during landslide

Location of soil slope	Slope (°)	Steady-state shear strength (kPa)	% Variation in volume of sliding soil mass (%)
Mavadi, Idukki	44.6	37.3	15.4
Kakkattuppara, Wayanad	45	47.4	10
Kallar, Idukki	44.2	55.1	6.6

Effect of Steady-State Shear Strength of Soil

The present study uses the steady-state shear strengths of three soil slopes located at Mavadi, Kakkattuppara, and Kallar sites to study the influence of steady-state shear strength on the volume of sliding soil mass. These soil slopes are having a similar slope angle of about 44–45°. The effect of steady shear strength is examined on the volume of sliding soil mass of landslides that occurred due to 90% rainfall intensity. Table 23.9 shows that the sliding area covered by a landslide decreases with an increase of steady-state shear strength of the soil. As the steady-state shear strength of the soil increases from 37.3 to 55.1 kPa, the percentage variation in the volume of sliding soil mass decreases from 15.4 to 6.6%. Thus, the steady-state shear strength of soil mass affects the area covered by the landslide mass.

Conclusions

The present study has performed numerical simulations of landslides that occurred in seven soil slopes of Idukki and Wayanad districts in Kerala state. The major conclusions drawn from the current study are given below.

- Soil slopes located at Mavadi and Kakattuppara are initiated to fails at even very low rainfall intensity with a PPR of 0.1 onward. It also found that the soil slopes

located at Puvaramthodu, Kallar, and Mananthavadi are initiated to fails at low rainfall intensity with a PPR of 0.3–0.5 onward. However, the slopes at Kavalppara and Adit are initiated to fail at high rainfall intensities with a PPR of 0.7 onward. It indicates that soil slopes located at Mavadi and Kakattupara causing severe landslide mass distribution compared with other soil slopes.

- All the soil slopes tested except two hill slopes located at Aadit and Puvaramthodu areas are failed under dynamic loading alone with no rainfall condition. Soil slopes that are stable under moderate rainfall intensity failed when they were subjected to a combination of dynamic loading with moderate rainfall intensity. Thus, dynamic loading can increase the instability of landslides occurred at average rainfall intensities.
- An increase in cohesion strength of the soil causes a decrease in the maximum velocities of soil flow and volume of soil mass distribution. Improving the steady-state shear strength of the soil can reduce the occurrence of landslides.

References

1. Sassa K, Nagai O, Solidum R, Yamazaki Y, Ohta H (2010) An integrated model simulating the initiation and motion of earthquake and rain induced rapid landslides and its application to the 2006 Leyte landslide
2. He B, Sassa K, Ostric M, Takara K, Yamashiki Y (2013). Effects of parameters in landslide simulation model LS-RAPID on the dynamic behaviour of earthquake-induced rapid landslides
3. Keefer DK (2000) Statistical analysis of an earthquake-induced landslide distribution—the 1989 Loma Prieta, California event
4. Wang F, Sassa K (2009) Landslide simulation by a geotechnical model combined with a model for apparent friction change
5. Wang G, Suemine A, Hata Y, Kamai T (2013) On the initiation and movement of Hanokidaira landslide from the 2011 Tohoku Earthquake, Japan
6. Wang G, Sassa K (2002) Pore-pressure generation and movement of rainfall-induced landslides: effects of grain size and fine-particle content

Chapter 24

Historical Development of Landslide Early Warning System (LEWS): A Review



Prashant Sudani , K. A. Patil, and Y. A. Kolekar

Introduction

Landslide is one of the most significant hazards in terms of socio-economic costs, threatening infrastructures, and human settlement. A landslide is a geological event consisting of mass movement of the earth under gravity triggered by natural or man-made factors. Petley reported more than 4600 fatalities due to non-seismic landslides in a year [1]. India, China, Italy, Japan, and United States have economical losses of more than 1 billion \$ each due to landslide hazards [2, 3]. Landslides are found as frequently accruing natural hazards in the monsoon in the history of India and the rest of the world. A total of twenty-two states and two union territories of the country are affected by the landslide. The landslide is affected by the 0.49 million square kilometers of country area, approximately 15% of the total country area [4]. The landslide hazard map of India indicating landslide affected state is as shown in Fig. 24.1. It is ranked third in terms of the number of death due to natural disasters. It found that only Himalayan landslides kill 1 person per 100 km² area every year; estimated average losses due to landslides in Himalaya costs more than 550 crores and more than 200 deaths [4].

Historical trends reveal the growing impact of the landslide hazard on society as it can destroy both precious human lives, live stakes, and infrastructure of the country by both direct and indirect means. Few of them which were found more disastrous impacted in the history of Indian landslides are as given in Table 24.1.

P. Sudani (✉)
College of Engineering Pune, SPPU, Pune, India
e-mail: sudaniprashant93@gmail.com

K. A. Patil · Y. A. Kolekar
College of Engineering Pune, Pune, Maharashtra, India

Fig. 24.1 Country map (India) of landslide affected areas. *Source* geological survey of INDIA

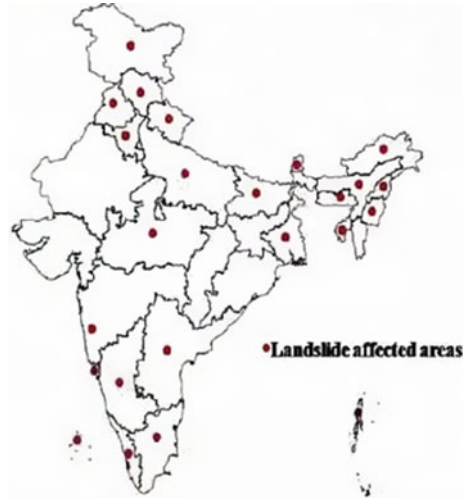


Table 24.1 Disastrous incidences in the history of Indian landslides

Sr. No.	Landslide name	Live losses	State affected	Year	References
1	Nainital	150	Uttarakhand	1880	[5]
2	Chamoli	55	Uttarakhand	1970	[6]
3	Luggarbhati	65	Himachal	1995	[7]
4	Malpa	380	Uttarakhand	1998	[7]
5	Dharla	62	Himachal	2007	[7]
6	Chamoli	70	Uttarakhand	2010	[6]
7	Malin	162	Maharashtra	2014	[8]

Further, as Schuster and Fleming noted in 1971–74, on average, 600 lives were lost due to landslide hazards [3]. Globally, in terms of the fatal landslide, South Asia, East Asia, and Southeast Asia face 44, 30, and 26% fatal landslides.

To minimize the impact of the landslide on livelihood, we need to equip efficient solutions. We can prevent the hazard by restricting the development on the hilly region or stabilizing the hill slope with different engineering solutions, but this would not be possible on existing infrastructure; sometimes, even after providing a proper engineering solution, it may be failed. In such a place, monitoring of landslide followed by instrumenting landslide early warning system holds the excellent output. An early warning system (EWS) can help the affected people leave before it begins to slide.

Definition of the early warning system founds differs from researcher to researcher and available in the literature. One can define it as the “designed device that can monitor to completely prevent or at least diminish the hazard on livelihood, costly properties of the country, and the environment” [9]. EWS, as define by United Nations

International Strategy for Disaster Reduction-2019 (UNISDR), is “the set of aspects needed to produce and issue timely and significant risk threatening information to public, societies, and government organizations who were vulnerable by a hazard so that they can be prepared and to act appropriately with the strategic plan and in a sufficient time to reduce the possibility of injury or damage.” After all, whatsoever the definition of the EWS, it is a monitoring and forecasting tool that functioned as a risk retarder by issuing a timely warning of the hazard. In the current work, we exposed a bunch of historically developed landslide early warning systems (LEWS).

Historical Advancement of Landslide Early Warning System

From the end of the twentieth century to date, many researchers were made an effort to establish an EWS for the landslide. Different methods, statistical, and physical, and model-based approaches were used to reach a conclusion and give the threshold-based or FOS-based warning. Also, from the history of developing LSEWS, we can see the instrumentation variation used with time for field and off fieldwork. An extensive effort was made in literature survey to prepare a detailed historical development in a landslide early warning system, and here, it is displayed with taking some of the well-known author’s work into consideration so it can be helpful to researcher in the future for getting an idea about what was being used till date and what should still need to improve. Total 50 numbers of the work were well explored, and insight into monitoring and warning of the landslide were extracted from the landslide’s historical developing monitoring and warning system as shown in Table 24.2.

Table 24.2 shows a wide range of the methodology and instrumentation used in the historical development of the monitoring and warning of the landslide early warning system. A majorly two types of warning threshold are used in the warning system: rainfall-based threshold and displacement-based warning threshold. As shown in Fig. 24.2a, it is found that 56% of the considered warning system was used rainfall as a threshold, while the rest, 44% of the warning system adopts the displacement threshold. As shown in Fig. 24.2b, based on the geometrical presence of the considered warning systems, it is found 14% in the USA, 6% in Canada, 10% in China, 30% in Italy, 4% in California, 12% in India, and 24% in other countries.

Various warning systems present in Table 24.2 were found unique in their methodology and instrumentation and various analysis software. It also shows the variety of instrumentation used in the warning system, and it is found interesting that we can look at a wide range of the different instruments that can monitor the landslide from various angles. As shown in Fig. 24.3a, it is found that 24% of warning systems were used remote sensing techniques to assess the landslide remotely, 10% were used pore pressure devices, 22% used displacement monitoring devices, 6% used the various geotechnical testing methodology, 6% used various geophysical methods, 20% used the rainfall data from various sources, and 12% found which were used a combination of these all instrumentation in the warning system. From

Table 24.2 Historical advancement of landslide early warning system

Sr. No.	Country/year	Method of monitoring	Instrument used	Triggering event	References
1	1971/USA	Displacement		Rainfall	[10]
2	1977/Canada	Model study	Piezometer	Rainfall	[11]
3	1980/Nevada	Displacement	Inclinometer	Rainfall	[12]
4	1985/Utah	Graphical plots	Extensometer	Rainfall	[13]
5	1987/Colorado	Displacement	Aquatic emission	Rainfall	[14]
6	1987/California	Empirical	Rain gauge	Rainfall	[15]
7	1990/California	Pore pressure	Piezometer	Rainfall	[16]
8	1990/Budapest	Moisture effect	Triaxial	Rainfall	[17]
9	1990/Netherland	Non-invasive	Geophysical	Rainfall	[18]
10	1993/Italy	Displacement	Extensometer	Rainfall	[19]
11	1994/China	Creep monitoring	Soil strainmeter	Rainfall	[20]
12	1995/Canada	Hazard assessment	Radar technology	Rainfall	[21]
13	1997/Hongkong	Probability	Rain gauge	Rainfall	[22]
14	1998/USA	Displacement	Remote sensing	Rainfall	[23]
15	1999/Netherland	Surface monitoring	Hyperspectral imagery	Rainfall	[24]
16	2001/Malasia	Modeling	Rain gauge + Geotech	Rainfall	[25]
17	2001/Malasia	Displacement	Soil strainmeter	Rainfall	[26]
18	2002/France	Displacement	GPS sensor	Rainfall	[27]
19	2002/Germany	Displacement	GPS sensor	Rainfall	[28]
20	2002/Italy	Displacement	Inclinometer	Rainfall	[29]
21	2003/Italy	Displacement	Radar technology	Rainfall	[30]
22	2004/Italy	Rain data analysis	Rain gauge	Rainfall	[31]
23	2005/Italy	Field monitoring	Piezometer, GPS, inclinometer, extensometer	Rainfall	[32]
24	2006/Italy	Displacement	Radar technology	Rainfall	[33]
25	2007/USA	Rain analysis	Rain gauge	Rain/EQ	[34]
26	2008/Newzeland	Modeling	Laboratory testing	Rainfall	[35]
27	2008/USA	Rain analysis	Satellite survey	Rainfall	[36]
28	2008/Italy	Displacement	Radar data and GPS	Rainfall	[37]
29	2009/China	Data analysis	Field and laboratory testing	Rainfall	[38]

(continued)

Table 24.2 (continued)

Sr. No.	Country/year	Method of monitoring	Instrument used	Triggering event	References
30	2010/India	Vibration	Geophone, pore pr. transducer	Rainfall	[39]
31	2010/Italy	Displacement	Radar technology	Rainfall	[40]
32	2011/Italy	Modeling	Rain gauge	Rainfall	[41]
33	2012/Italy	Displacement	Extensometer, rain gauge	Rainfall	[42]
34	2012/China	Displacement	GIS and GPS sensor	Rainfall	[43]
35	2013/Germany	Modeling	Field test, electrical resistivity	Rainfall	[44]
36	2013/India	Modeling	Rain gauge and total station	Rainfall	[45]
37	2013/China	Modeling	Rain gauge	Rainfall	[46]
38	2013/Italy	Empirical	Rain gauge	Rainfall	[47]
39	2014/India	Modeling	Pore pr sensor, inclinometer, moisture sensors, laboratory testing	Rainfall	[48]
40	2014/Italy	Modeling	Laboratory testing, rain data	Rainfall	[49]
41	2014/Italy	Geophysical	Electrical resistivity	Rainfall	[50]
42	2015/Japan	Empirical	Tiltmeter, moisture	Rainfall	[51]
43	2015/Italy	Artificial neural	Rain and soil data	Rainfall	[52]
44	2016/Canada	Displacement	GPS sensor, piezometer, extensometer	Rainfall	[53]
45	2016/UK	Displacement	GPS sensor, piezometer, extensometer	Rainfall	[54]
46	2017/Vietnam	Modeling	Field and laboratory testing	Rainfall	[55]
47	2017/Italy	Displacement	Satellite radar	Rainfall	[56]
48	2017/India	Modeling	Piezometer, laboratory testing	Rainfall	[4]
49	2019/India	Displacement	Inclinometer, piezometer	Rainfall	[57]
50	Switzerland/2020	Modeling	Moisture sensors	Rainfall	[58]

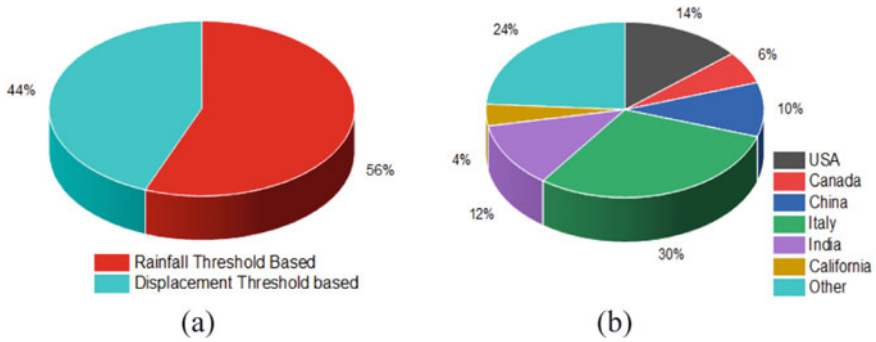


Fig. 24.2 Distribution of warning system based on a threshold (a) and Geometry of Earth (b)

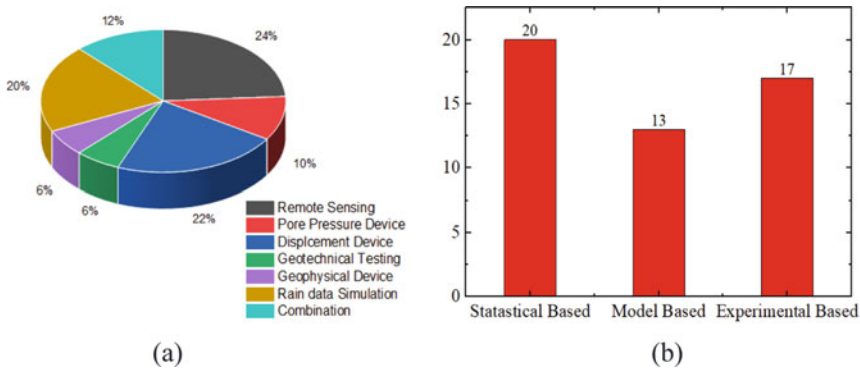


Fig. 24.3 Distribution of warning system based on Instrumentation (a) and methodology used (b)

the insight of the various warning system, it is found three methodological approaches on which warning system used to design, (i) Statistical-based warning, which used various empirical methods to correlate the threshold with monitoring parameter, (ii) Model based which used modeling which can provide stability-based warning, and (iii) Experimental based which used the field and experimental laboratory setups for monitoring and warning. As shown in Fig. 24.3b, it is found that 40% of considered warnings are based on statistical based, 26% were model based, and 34% are experimental based.

Historical Trend

The foundation stone of understanding the evolution of the landslide warning system was founded in the early nineteenth century. In that era of the nineteenth century, several theories of slope stability based on the geotechnical approach were presented,

such as Taylor's method, Bishops' method of stability, Jambu's method, and many more. These methods provide the information of stability of any slope based on their geometrical and geotechnical parameters, which was purely based on the balancing principle. During the mid-nineteenth century, the sharp growth of population and urbanization led to building new infrastructures in hilly regions, and people especially liked to habit on such place as it can have a peaceful, natural environment. This activity leads to come up with several landslide incidences, which caused several live losses. The Nainital landslide of Utrakkhand in 1880 is one of such a type of failure observed in the nineteenth century. This type of incidence then seems more often rounds the world and becomes a critical issue that attracts researchers during the late nineteenth century.

Based on the literature available, most of the studies from 1975 to 2000 were based on statistical approaches based on the past incidence of the landslide and corresponding failure conditions. Warning systems of this era are not found accurate to the mark as it was based on a purely statistical approach; the rate of false alarming was higher, which breaks the end-users trust and makes them unusable. The central constituent geotechnical interpretation is much essential in the analysis of the failure of the landslide. In 1996, Glawe and Lotter presented the importance of geotechnical knowledge and movement monitoring in landslide research [59]. In the same year, 1996, Cornforth covers several geotechnical parameters in their list of ideal features of landslide monitoring, which impacted a significant part of the instability [60]. Along with geotechnical laboratory testing and their interpretation field, investigation along with boreholes is found a more accurate method for landslide investigation as it can provide a bunch of the information regarding soil strata, their mechanical properties, their geotechnical properties, hydraulic properties, and probable slip surface of the slope [61].

The importance of the geotechnical knowledge and their effectiveness on the efficiency of the landslide analysis was mainly started to see in research which was implemented after 2000. The main constituent affected landslide from the geotechnical side is pore water pressure, suction effect, water content, density of the soil, shear parameter cohesion, and angle of the internal friction. Recently, monitoring and analysis of landslides can carry out by invasive methods such as geophysical methods and remote sensing.

In very recent modeling of the slope for stability analysis is in trend. Several limit equilibrium modeling software is available in the market, analyzing the slope effectively and error-free in less time. A few examples of such modeling are Slope/W, Geo-5, Midas, CHASM, and Plaxis. Collins, in 2004 states that it is possible to develop the landslide warning system based on safety (FoS). The innovation in the modeling reaches to analyze the hydrological analysis in the slope along with slope stability analysis bring the revolution in the monitoring and warning research of landslide. One such procedure for combining hydrological and limit equilibrium analysis of landslide was presented by Rahimi [62] in two steps, as shown in Fig. 24.4.

Rahimi in 2010 suggested two steps for the landslide analysis using finite element analysis modeling procedure are (I) conducting finite element seepage analysis providing knowledge of the pore water pressure and soil water curve followed by

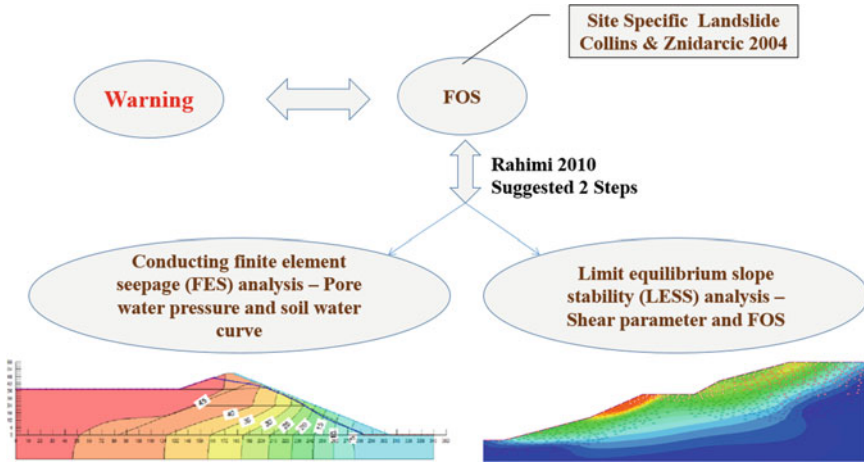


Fig. 24.4 Two-step procedure suggested by Rahimi for combining hydrological and limit equilibrium analysis of the landslide

(II) limiting equilibrium slope stability analysis considering shear parameter and yielding the factor of safety of the slope [62].

Currently Available Different Methods of Monitoring and Early Warning System

In the first instance, viewers feel a landslide is a surprising event as they proceed without warning. However, in this connection, Terzaghi says that it is more accurate to say the observer failed to detect the phenomenon behind the failure of the landslide [63]. Therefore, the mechanics of the failure needed to be understood is crucial, and this can be achieved by following the landslide by monitoring it for a long time.

Several researchers implemented numerous approaches for finding the phenomenon of the landslide occurrence, such as analysis of the soil mass and movement analysis [64]. A wide range of landslide analysis approaches was presented to understand the basic phenomenon behind the landslide, including displacement monitoring both surface and subsurface, pore pressure influence, suction effect, hydrological and geotechnical implementation, along with model simulations [44, 46, 48, 51, 65, 66].

One of the immersing warning systems was developed in Utah, USA, in 1984 [67]. The system generated thresholds based on rainfall, movement, and temperature changes as snow melting are needed. The system was statistical based and yielding good results as snow melting, and their effect on the stability is considered by temperature monitoring [68]. Another such warning system was implemented for San Francisco Bay provenance and run for ten years from 1986 to 95. The warning

was made based on the previous landslide incidence and corresponding rainfall data, which was compared to forecasted rainfall data, and in case of exceedance warnings, were used to issue [69]. In 1992, warning system uses the radar interpretation for effective rainfall resolution to provide an efficient warning threshold.

Schuster, in 2007, states one of the most effective landslide early warning systems, which was implemented in the Hong Kong region of China [70]. 70% of the total area of this region has terrain steeply rising hills, only 30% area covers the medium slope angle [71]. After two hazardous landslide incidents in 1972 and 1976, which caused more than 100 fatalities, a geotechnical control center was formed [72]. After 1972 disaster, warning thresholds were implemented based on rainfall by Lumb (1975) in Hongkong, which was several times then revised to get a reliable threshold value of rainfall. After 1976 disaster, authority initiated the installing and operation of the landslide warning system based on the rainfall data. The technical concept behind the warning threshold is to derive the rainfall data from 100 rain gauges and by using appropriate statistical methods [73]. Initially, the warning was made based on 20 h rainfall, then redesigned to 4 h rainfall period for better results [74]. After 1980, it was again redesigned for hourly precipitation for efficient and accurate results. However, the advancement of geotechnical in landslide research since the 1980s transformed attention toward warning conversation.

In 1980, Daniel presented a displacement-based warning system that was experiment based [12]. He used an inclinometer and sensor for recording the displacement with an accuracy of 0.001 inches. The author used to place such a sensor on the 600 m long side of the slope. The deformation displacement relationship evolves the threshold of 0.250 inches, showing that a slide can be expected if displacement more than the threshold is observed.

In 1990, Harp presented one more such experimental-based warning system based on pore pressure analysis [16]. He used two different sites for the experimental work and analyzed the effect of the pore pressure by artificially added water in the field until failure. He found that pore pressure was observed to sudden decrease before 5–50 min of failure. The result of the study has been used for warning. In 1990, Farkas developed a correlation-based warning [17]. He used combine laboratory and field investigation. The author measured pore pressure and rainfall data from the field and other geotechnical parameters from the laboratory. He used to correlate parameters responsible for instability with the water content for moisture-based threshold.

Pochini, in 1993, presented the real-time-based warning system [19]. He used to monitor the slope in real time by continuously monitoring the slope in a country named Italy. He used an inclinometer, extensometer, and geophones for data collection from the site. They presented a displacement Vs. time graph indicating the proper threshold for warning. Singhroy, in 1995, comes up with synthetic aperture radar (SAR) to measure the movement with millimetric accuracy [21]. Finlay (1997) developed one statistical-based warning in 1997 based on the relationship between precipitation and the possibility of the slide based on the record of the landslide and corresponding rainfall [22]. The mathematical model was developed for data analysis which used the linear, quadratic, and cubic correlation. The accuracy of the warning

threshold was not found accurate due to the lack of essential data in the system, such as geology, geometry, and drainage.

In 2002, Lauterbach derived the landslide warning system for the country name Germany [28]. The author used a GPS network for monitoring the movement with five measuring points having 1 mm accuracy. Two alarm was operated, one for station damage and another when the movement got exceeded the pre-defined threshold. To reduce the false alarming rate in case of a warning, it is used to send threshold to expert for validation if further action could be made.

In 2008, Schmidt developed the physically based live integration model for landslide warning [35]. The probability of the landslide was used to determine based on a physically based model using weather forecast. The model got considerable uncertainty in prediction, and hence, it got discontinued. Emanuele Intriери [42] implement the warning system in Italy in 2012. The research covers all the needful aspects, such as the geology of slides, displacement analysis, hydrological simulation, monitoring system, and choice of instrumentation. The system consists of a wire extensometer for displacement monitoring, thermometer for snow melting, a rain gauge for rainfall data collection, and cameras for continuous monitoring. Thresholds were generated using empirical means.

In 2013, Benni Thiebes implemented the physically based model for early warning of the landslide [44]. He used combine hydrological and stability analysis using FEM-based CHASM model. Rainfall threshold was used for the warning, which was estimated based on model simulation. Model runs both analyses hydrological and stability simultaneously. Rain forecasting was used for warning purposes. In 2014, Shio presented the importance of the antecedent rainfall on the landslide using an antecedent soil water status (ASWS) model [46]. Thresholds were derived from both antecedent and hourly rainfall effects on the slope. Results show that the presence of highly antecedent rainfall required less hourly rainfall for failure and vice versa.

In India, during 2014, Manisha designed and implemented an efficient wireless early warning system [48]. She used the various sensor for retrieving the data from the field for same she designed multi-sensor probe which can measure pore pressure, moisture, strain, and rain at the same time. The three-level warning was adopted, including early, intermediate, and imminent warnings. In early stage, moisture monitoring was adopted, and in intermediate and imminent, one pore pressure was incorporated. The software directly issued the warning in case of exceeding the pre-defined limit of the threshold. In 2019, Kanungo designed the rainfall intensity-based warning system for the shallow landslide [57]. The set of instrumentation used includes an inclinometer, extensometer, weather station, and pore water pressure sensor for time-dependent monitoring of the rainfall and displacement. Interpretation of the monitoring shows the positive correlation between rainfall and displacement, which shows a possibility of the defining threshold based on rainfall displacement analysis.

Concluding Remark

Landslide research is a complex task as it cannot be affected by only a few parameters that can effectively be measured. It has needed multidisciplinary knowledge to solve the problem. Further, monitoring and warning of the landslide can be divided into two categories; first, regional landslides monitoring and second, local landslide monitoring. Regional is those that covers the entire region, and local is limited to one site only. Regional landslide is analyzed based on the statistical analysis, which depends on the records of the landslide and corresponding rainfall and other conditions, and it is found cheapest compared to the local landslide, which is analyzed by experimental and modeling means. Regarding the effectiveness, regional landslides were found less effective than the local landslide due to not adopting a detailed investigation of the slide into the analysis.

Several kinds of research are presented in connection with the landslide warning in the present hour, but we still did not get an effective and globally excepted warning system. Most of the warnings depended on the records of the landslide and rainfall intensity analysis, which resulted in a higher rate of false alarm as it does not cover other important aspects of the analysis. Every landslide warning should be designed by keeping the focus on the requirement of the end-user. However, the available landslide warning system only monitors a few parameters such as warning based on movement analysis or based on rainfall records, or based on the pore pressure analysis, which does not yield efficient results and not fulfill the requirement of the end user. Warning should be real-time based which can able the end-user to observe moment to moment update on their screen so they can live without fear of the hazard.

Further, alarm communication has excellent importance in warning systems, and it should be required to well-performed during warning issuance, which is rarely seen in the present warning system. Some of the recent landslide warning systems are well developed using the wireless network. Such a system stored the required data on the server, and from the control office, it got automatically analyzed using appropriate stability software, and in case of excess threshold, it can generate the warning. Such a warning system seems to provide real-time warning, but its cost of operation and implementation are too high. Also, the data interpretation on a real-time basis is too complicated. In the current hour, we need more focus of researchers on developing the real-time-based cost-effective landslide warning system without compromising the system's requirement of user and efficiency.

References

1. Petley D (2012) Global patterns of loss of life from landslides. *Geology* 40(10):927–930
2. Wieczorek (1996) Landslide triggering mechanisms in Turner. *Landslides*
3. Schuster RL, Fleming RW (1986) Economic losses and fatalities due to landslides. *Bull Assoc Eng Geol* 23(1):11–28. <https://doi.org/10.2113/gseegeosci.xxiii.1.11>

4. Chaturvedi PB, Srivastava P, Kaur S, Landslide early warning system development using statistical analysis of sensors' data at Tangni landslide, Uttarakhand, India. In: Proceedings of sixth international conference on soft computing for problem solving
5. Clay JM (1928) *Nainital: a historical and descriptive amount*. Government Press, United Provinces, Allahabad
6. Chauhan S, Sharma M, Arora MK (2010) Landslide susceptibility zonation of the Chamoli region, Garhwal Himalayas, using logistic regression model. *Landslides* 7(4):411–423. <https://doi.org/10.1007/s10346-010-0202-3>
7. Rautela P, Pande RK (2005) Traditional inputs in disaster management: the case of Amparav, North India. *Int J Environ Stud* 62(5):505–515. <https://doi.org/10.1080/00207230500034586>
8. Ering P, Babu GLS (2016) Probabilistic back analysis of rainfall induced landslide—a case study of Malin landslide, India. *Eng Geol* 208:154–164. <https://doi.org/10.1016/j.enggeo.2016.05.002>
9. Medina-Cetina Z, Nadim F (2008) Stochastic design of an early warning system. *Georisk* 2(4):223–236. <https://doi.org/10.1080/17499510802086777>
10. Ingmire TJ, Patri T (1971) An early warning system for regional planning. *J Am Plan Assoc* 37(6):403–410. <https://doi.org/10.1080/01944367108977390>
11. Sterrett RJ, Edil TB (1982) Ground-water flow systems and stability of a slope. *Groundwater* 20(1):5–11. <https://doi.org/10.1111/j.1745-6584.1982.tb01324.x>
12. Bailey DJ (1980) Land movement monitoring system. *Bull Assoc Eng Geol* 17(4):213–221
13. Butler DK, Llopis JL, Dobecki TL, Wilt MJ, Corwin RF, Olhoef G (1990) Comprehensive geophysics investigation of an existing dam foundation: engineering geophysics research and development, Part 2. *Geophysics* 9(9):44–53. <https://doi.org/10.1190/1.1439782>
14. Jurich DM, Miller RJ (1987) Acoustic monitoring of landslides. *Transp Res Rec* 1:30–38
15. Keefer DK et al (1987) During heavy rainfall
16. Harp EL, Wells WG, Sarmiento JG (1990) Pore pressure response during failure in soils. *Bull Geol Soc Am* 102(4):428–438. [https://doi.org/10.1130/0016-7606\(1990\)102%3c0428:PPRDFI%3e2.3.CO;2](https://doi.org/10.1130/0016-7606(1990)102%3c0428:PPRDFI%3e2.3.CO;2)
17. Farkas J (1990) Action of rainfall and moisture increase to develop landslides. *Period Polytech Civ Eng* 34(3–4):201–213
18. McCann DM, Forster A (1990) Reconnaissance geophysical methods in landslide investigations. *Eng Geol* 29(1):59–78. [https://doi.org/10.1016/0013-7952\(90\)90082-C](https://doi.org/10.1016/0013-7952(90)90082-C)
19. Pochini M, Allagosta A (1993) Monitoring sample landslides in seismic areas: Camporaghenia in Lunigiana
20. Guifang LU (1994) Formation and monitoring and forecast of Jimingsi landslide. *Chinese J Geol Hazard Control* 5:376–383
21. Singhroy V (1995) Sar integrated techniques for geohazard assessment. *Adv Sp Res* 15(11):67–78. [https://doi.org/10.1016/0273-1177\(95\)00076-Q](https://doi.org/10.1016/0273-1177(95)00076-Q)
22. Finlay PJ, Fell R, Maguire PK (1997) The relationship between the probability of landslide occurrence and rainfall. *Can Geotech J* 34(6):811–824. <https://doi.org/10.1139/t97-047>
23. Girard JM, McHugh E (2000) Detecting problems with mine slope stability. National Institute for Occupational Safety and Health, Spokane Research Laboratory
24. Carrara A, Guzzetti F, Cardinali M, Reichenbach P (1999) Use of GIS technology in the prediction and monitoring of landslide hazard. *Nat Hazards* 20(2–3):117–135. <https://doi.org/10.1023/A:1008097111310>
25. Lloyd DM, Othman A, Wilkinson PL (2001) Predicting landslides: assessment of an automated rainfall based landslide warning system
26. Husaini O, Ratnasamy M (2001) An early warning system for active landslides. *Q J Eng Geol Hydrogeol* 34(3):299–305. <https://doi.org/10.1144/qjegh.34.3.299>
27. Malet JP, Maquaire O, Calais E (2002) The use of global positioning system techniques for the continuous monitoring of landslides: application to the Super-Sauze earthflow (Alpes-de-Haute-Provence, France). *Geomorphology* 43(1–2):33–54. [https://doi.org/10.1016/S0169-555X\(01\)00098-8](https://doi.org/10.1016/S0169-555X(01)00098-8)

28. Lauterbach M, Krauter E, Feuerbach J (2002) Satellitengestuetztes monitoring einer Grossrutschung im Bereich eines Autobahndamms bei Landstuhl/Pfalz. *Geotechnik* 25(2)
29. Lollino G, Arattano M, Cuccureddu M (2002) The use of the automatic inclinometric system for landslide early warning: the case of Cabella Ligure (North-Western Italy). *Phys Chem Earth* 27(36):1545–1550. [https://doi.org/10.1016/S1474-7065\(02\)00175-4](https://doi.org/10.1016/S1474-7065(02)00175-4)
30. Tarchi D et al (2003) Landslide monitoring by using ground-based SAR interferometry an example of application to the Tessina landsli 68:15–30
31. Aleotti P (2004) A warning system for rainfall-induced shallow failures. *Eng Geol* 73(3–4):247–265. <https://doi.org/10.1016/j.enggeo.2004.01.007>
32. Corsini A, Pasuto A, Soldati M, Zannoni A (2005) Field monitoring of the Corvara landslide (Dolomites, Italy) and its relevance for hazard assessment. *Geomorphology* 66(1–4):149–165. <https://doi.org/10.1016/j.geomorph.2004.09.012>
33. Casagli N, Farina P, Leva D, Tarchi D (2006) Application of ground-based radar interferometry to monitor an active rockslide and implications for emergency management. *Landslides* 49:157–173. https://doi.org/10.1007/978-1-4020-4037-5_9
34. Hong Y, Adler RF (2007) Towards an early-warning system for global landslides triggered by rainfall and earthquake. *Int J Remote Sens* 28(16):3713–3719. <https://doi.org/10.1080/01431160701311242>
35. Schmidt J, Turek G, Clark MP, Uddstrom M, Dymond JT (2008) Probabilistic forecasting of shallow, rainfall-triggered landslides using real-time numerical weather predictions
36. Hong Y, Adler RF (2008) Predicting global landslide spatiotemporal distribution: integrating landslide susceptibility zoning techniques and real-time satellite rainfall estimates. *Int J Sediment Res* 23(3):249–257. [https://doi.org/10.1016/S1001-6279\(08\)60022-0](https://doi.org/10.1016/S1001-6279(08)60022-0)
37. Noferini L et al (2007) Using GB-SAR technique to monitor slow moving landslide. *Eng Geol* 95(3–4):88–98. <https://doi.org/10.1016/j.enggeo.2007.09.002>
38. Liao Z et al (2010) Prototyping an experimental early warning system for rainfall-induced landslides in Indonesia using satellite remote sensing and geospatial datasets. *Landslides* 7(3):317–324. <https://doi.org/10.1007/s10346-010-0219-7>
39. Kunnath AT, Ramesh MV (2010) Integrating geophone network to real-time wireless sensor network system for landslide detection, 167–171. <https://doi.org/10.1109/sensordevices.2010.38>
40. Casagli N, Catani F, Del Ventisette C, Luzi G (2010) Monitoring, prediction, and early warning using ground-based radar interferometry. *Landslides* 7(3):291–301. <https://doi.org/10.1007/s10346-010-0215-y>
41. Capparelli G, Versace P (2011) FLAIR and SUSHI: two mathematical models for early warning of landslides induced by rainfall. *Landslides* 8(1):67–79. <https://doi.org/10.1007/s10346-010-0228-6>
42. Intriери E, Gigli G, Mugnai F, Fanti R, Casagli N (2012) Design and implementation of a landslide early warning system. *Eng Geol* 147–148:124–136. <https://doi.org/10.1016/j.enggeo.2012.07.017>
43. Li T, Zhao J, Li P, Xing, Wang F (2012) Failure and motion mechanisms of a rapid loess flowslide triggered by irrigation in the Guanzhong irrigation area, Shaanxi, China
44. Thiebes B, Bell R, Glade T, Jäger S, Anderson M, Holcombe L (2013) A WebGIS decision-support system for slope stability based on limit-equilibrium modelling. *Eng Geol* 158:109–118. <https://doi.org/10.1016/j.enggeo.2013.03.004>
45. Shan C, Bastani M, Malehmir A, Persson L, Engdahl M (2013) Integrated 2D modeling and interpretation of geophysical and geotechnical data to delineate quick clays at a landslide site in southwest Sweden. *Geophysics* 79(4):EN61–EN75. <https://doi.org/10.1190/GEO2013-0201.1>
46. Bai S, Wang J, Thiebes B, Cheng C, Yang Y (2014) Analysis of the relationship of landslide occurrence with rainfall: a case study of Wudu County, China. *Arab J Geosci* 7(4):1277–1285. <https://doi.org/10.1007/s12517-013-0939-9>
47. Greco R, Giorgio M, Capparelli G, Versace P (2013) Early warning of rainfall-induced landslides based on empirical mobility function predictor. *Eng Geol* 153:68–79. <https://doi.org/10.1016/j.enggeo.2012.11.009>

48. Ramesh MV (2014) Ad Hoc Networks Design, development, and deployment of a wireless sensor network for detection of landslides. *Ad Hoc Netw* 13:2–18. <https://doi.org/10.1016/j.adhoc.2012.09.002>
49. Formetta G, Rago V, Capparelli G, Rigon R, Muto F, Versace P (2014) Integrated physically based system for modeling landslide susceptibility. *Procedia Earth Planet Sci* 9:74–82. <https://doi.org/10.1016/j.proeps.2014.06.006>
50. Supper R et al (2014) Geoelectrical monitoring: an innovative method to supplement landslide surveillance and early warning. *Near Surf Geophys* 12(1):133–150. <https://doi.org/10.3997/1873-0604.2013060>
51. Uchimura T et al (2015) Precaution and early warning of surface failure of slopes using tilt sensors. *Soils Found* 55(5):1086–1099. <https://doi.org/10.1016/j.sandf.2015.09.010>
52. Pumo D et al (2016) The SESAMO early warning system for rainfall-triggered landslides. *J Hydroinformatics* 18(2):256–276. <https://doi.org/10.2166/hydro.2015.060>
53. Macciotta R, Hendry M, Martin CD (2016) Developing an early warning system for a very slow landslide based on displacement monitoring. *Nat Hazards* 81(2):887–907. <https://doi.org/10.1007/s11069-015-2110-2>
54. Uhlemann S et al (2016) Assessment of ground-based monitoring techniques applied to landslide investigations. *Geomorphology* 253:438–451. <https://doi.org/10.1016/j.geomorph.2015.10.027>
55. Gian QA, Tran DT, Nguyen DC, Nhu VH, Tien Bui D (2017) Design and implementation of site-specific rainfall-induced landslide early warning and monitoring system: a case study at Nam Dan landslide (Vietnam). *Geomatics, Nat. Hazards Risk* 8(2):1978–1996. <https://doi.org/10.1080/19475705.2017.1401561>
56. Bovenga F, Pasquariello G, Pellicani R, Refice A, Spilotro G (2017) Landslide monitoring for risk mitigation by using corner reflector and satellite SAR interferometry: the large landslide of Carlantino (Italy). *CATENA* 151:49–62. <https://doi.org/10.1016/j.catena.2016.12.006>
57. Falae PO, Kanungo DP, Chauhan PKS, Dash RK (2019) Electrical resistivity tomography (ERT) based subsurface characterisation of Pakhi Landslide, Garhwal Himalayas, India. *Environ Earth Sci* 78(14):1–18. <https://doi.org/10.1007/s12665-019-8430-x>
58. Wicki A, Lehmann P, Hauck C, Seneviratne SI, Waldner P, Stähli M (2020) Assessing the potential of soil moisture measurements for regional landslide early warning. *Landslides* 17(8):1881–1896. <https://doi.org/10.1007/s10346-020-01400-y>
59. Glawe M, Lotter U (1996) Time prediction of rock slope failures based on monitoring results. In: *In Landslides*, pp 1551–1555
60. Cornforth PE, Mikkelsen DH (1996) Continuous monitoring of the slope above an excavation within a marginally stable landslide. In: *In Landslides*, pp 1539–1544
61. Nakamura H (2004) Field instrumentation and laboratory investigation. In: *In Landslides: evaluation and stabilization*, pp 541–548
62. Rahimi A, Rahardjo H, Leong EC (2010) Effect of hydraulic properties of soil on rainfall-induced slope failure. *Eng Geol* 114(3–4):135–143. <https://doi.org/10.1016/j.enggeo.2010.04.010>
63. Terzaghi K (1950) Geologic aspects of soft-ground tunneling
64. Glade MJ, Crozier T (2005) Landslide hazard and risk: concluding comment and perspectives. *Landslide hazard and risk*. Wiley, pp 493–516
65. Chan RKS (2007) Challenges in slope engineering in Hong Kong. *Geotech Eng* 38(3):255
66. Falae PO, Kanungo DP, Chauhan PKS, Dash RK (2019) Renewable energy and its innovative technologies. Springer Singapore
67. Baum RL, Godt JW (2010) Early warning of rainfall-induced shallow landslides and debris flows in the USA. *Landslides* 7(3):259–272. <https://doi.org/10.1007/s10346-009-0177-0>
68. Baum RL et al (2005) Regional landslide-hazard assessment for Seattle, Washington, USA. *Landslides* 2(4):266–279. <https://doi.org/10.1007/s10346-005-0023-y>
69. Campbell RH (1975) Soil slips, debris flows, and rainstorms in the Santa Monica Mountains and vicinity, southern California, vol 851. US Government Printing Office

70. Schuster RL, Highland LM (2007) The third Hans Cloos lecture. Urban landslides: socio-economic impacts and overview of mitigative strategies. *Bull Eng Geol Environ* 66(1):1–27. <https://doi.org/10.1007/s10064-006-0080-z>
71. Brand EW (1984) Landslides in Southeast Asia, a state-of the art report. In: In Proceedings of 4th international symposium landslides
72. Malon AW (1997) Risk management and slope safety in Hong Kong. *HKIE Trans Hong Kong Inst Eng* 4(2–3):12–21. <https://doi.org/10.1080/1023697X.1997.10667719>
73. Brand EW (1984) Landslides in Southeast Asia, a state-of the art report. In: In Proceeding of 4th international symposium landslides
74. Chan RKS, Pun WK (2004) Landslip warning system in Hong Kong. *Geotech. News* 22(4):33–35

Chapter 25

Study on Design of Reinforced Earth Retaining Wall with Copper Slag as Fill Material



C. N. V. Satyanarayana Reddy, R. Dhanunjay Kumar Reddy,
and M. Nagalakshmi

Introduction

The construction of reinforced earth retaining wall involves the use of fill material, reinforcement and facing. River sand and moorum are the most commonly used fill materials in the construction of reinforced earth retaining walls due to their ability to mobilize high angle of shearing resistance. Due to rapid construction activity, the demand for conventional fill materials has been widely increased and several developing nations have encountered difficulties in meeting the demand of these conventional materials. To overcome this scenario, alternate materials have to be explored for use as fill material in reinforced earth retaining walls.

Very huge amounts of wastes are being generated from industries in the recent times and their disposal has become a big problem. In this scenario, the successful utilization of some granular non-hazardous industrial waste materials as fill materials in reinforced soil constructions not only reduces the construction cost but also helps in their disposal. Hence in the present study, an attempt has been made to evaluate the potential of copper slag as fill material in reinforced earth retaining wall of varying backfill heights (4–10 m) with geotextile reinforcement. The design requirement obtained from BS 8006–1:2010 is compared with reinforced earth retaining walls with conventional fill material in non-seismic and seismic conditions.

C. N. V. Satyanarayana Reddy · R. Dhanunjay Kumar Reddy · M. Nagalakshmi (✉)
Department of Civil Engineering, Andhra University College of Engineering, Visakhapatnam,
Andhra Pradesh 530040, India
e-mail: nagalakshmi20.bec@gmail.com

C. N. V. Satyanarayana Reddy
e-mail: prof.cnvsreddy@andhrauniversity.edu.in

Literature Review

The scarcity and cost of conventional fill materials made the researchers to carry out studies for exploring new alternative fill materials. Various studies recommended the use of some industrial waste materials such as fly ash, rock flour, pond ash, bottom ash, blast furnace slag, in reinforced soil structures. The interaction between fill and the reinforcement lays crucial role in the stability of the reinforced soil structures [1–5]. The degree of interaction mainly depends on the gradation and plasticity characteristics of the fill material and it should satisfy the criteria stated by Jones [6].

Copper slag is a non-hazardous industrial waste material obtained during smelting and refining of copper. Copper slag consists of sand sized angular particles and mobilize higher angle of shearing resistance of about 35° – 49° . Based on its frictional characteristics and strength parameters, copper slag can be used as potential fill material in reinforced earth walls [7–9]. Copper slag is found to have good drainage and can be used as substitute for sand in sand drains [10]. Even though copper has high density, it reduces the dynamic earth pressure and lateral movements when used as a fill material in retaining walls due to its high shear strength [11]. The addition of Copper slag in conjunction with other materials such as cement, lime, silica fume improves the shear strength, UCC, CBR of soil and reduces swelling and shrinkage of expansive soils [12–14]. It can also be used in landfill applications.

Material Properties

Copper slag required for the present study is procured from Sterlite Copper, Thoothukudi, Tamil Nadu. The Engineering properties of copper slag are evaluated by conducting extensive laboratory investigation. Copper slag is non-plastic and is classified as equivalent to poorly graded sand based on gradation characteristics. It is found to have a maximum dry density of 2.35 g/cc, which about is 15% higher in comparison to moorum fill.

Based on gradation characteristics, conventional fill material is classified as Silty Gravel. The engineering properties of conventional fill material and Copper slag are presented in Table 25.1. Andhra University campus soil is used as backfill material in the study which is a silty sand possessing density of 1.94 g/cc and angle of internal friction of 31° .

Polypropylene woven geotextile is used as reinforcement for reinforced earth retaining walls with copper slag and conventional fill material. It is procured from M/s Garware Wall Ropes, Pune.

Table 25.1 Engineering properties of fill materials under study

Property	Moorum	Copper slag
Specific gravity	2.66	3.34
Grain size analysis		
(a) Gravel size (%)	48	1
(b) Sand size (%)	38	99
(c) Fines (%)	14	9
(d) Coefficient of uniformity	–	1.746
(e) Coefficient of curvature	–	0.707
Plasticity characteristics		
Liquid limit (%)	NP	NP
Plastic limit (%)	NP	NP
IS classification	GM	SP
Compaction characteristics		
(a) Optimum moisture content (%)	9	7
(b) Maximum dry density (g/cc)	2.05	2.35
Shear strength parameters		
(a) OMC and MDD condition		
(i) Cohesion (kN/m ²)	0	0
(ii) Angle of internal friction	35°	41°
(b) Saturated condition		
(i) Cohesion (kN/m ²)	0	0
(ii) Angle of internal friction	33°	38°
Interfacial shear parameters		
Saturated condition		
(i) Cohesion (kN/m ²)	0	0
(ii) Angle of internal friction (ϕ)	35°	41°

Design of Reinforced Earth Retaining Walls

In this study, Reinforced earth retaining walls (RERW) for retaining backfill heights of 4, 6, 8, and 10 m are designed using moorum and copper slag as fill materials and woven geotextile as reinforcement. A live uniform surcharge of 24 kN/m² is considered to be acting on the reinforced wall. The Stability analysis of these walls is carried out as per BS 8006–1:2010.

BS 8006 recommends a minimum reinforcement length of 0.7 times the total height of retaining wall and embedment depth of 1/20 to 1/10th of the height of retaining wall. The external stability of these walls is similar to that of the concrete retaining walls except that the BS code uses different partial safety factors and load combinations in the design. External stability and internal stability of reinforced soil walls is as explained below.

External Stability

Bearing and tilt failure

The bearing pressure imposed by soil retaining structure is based on Meyerhof distribution and should satisfy the following condition.

$$q_r \leq \frac{q_{ult}}{f_{ms}} + \gamma D_m \quad (25.1)$$

where,

- q_r = Factored bearing pressure acting on the base of the wall = $\frac{R_v}{L-2e}$
- R_v = Resultant of all factored vertical load components
- L = Reinforcement length at the base of the wall
- e = Eccentricity of resultant load R_v about the center line of the base width L
- γ = Foundation soil density
- D_m = Embedment depth and
- f_{ms} = Partial material factor applied to q_{ult} .

Sliding along the base

The reinforced earth wall should be safe against forward sliding. The properties of either foundation soil or reinforced soil whichever is weaker are considered in computing the resistance to sliding. For stability against sliding.

When there is soil-to-soil contact at the base of the structure

$$f_s R_h \leq R_v \frac{\tan \phi'_p}{f_{ms}} + \frac{C'L}{f_{ms}} \quad (25.2)$$

When there is reinforcement-to-soil contact at the base of the structure.

$$f_s R_h \leq R_v \frac{a' \tan \phi'_p}{f_{ms}} + \frac{a'_{bc} C'L}{f_{ms}} \quad (25.3)$$

where,

- R_h = horizontal factored disturbing force
- ϕ'_p = peak angle of shearing resistance under effective stress condition
- C' = cohesion of the soil under effective stress condition
- L = effective base width for sliding
- f_{ms} = partial material factors applied to $\tan \phi'_p$ and C'
- f_s = partial factors against base sliding
- a' = interaction coefficient relating soil/reinforcement bond angle with $\tan \phi'_p$
- and
- a'_{bc} = adhesion coefficient relating soil cohesion to soil/ reinforcement bond.

Internal Stability

In the present study, the internal stability of the reinforced wall is checked by adopting Tie back wedge method.

The maximum tensile force induced in a reinforcement layer at a depth of h_j is

$$T_j = T_{pj} + T_{sj} + T_{fj} \quad \text{for frictional fill} \tag{25.4}$$

$$T_j = T_{pj} + T_{sj} + T_{fj} - T_{cj} \quad \text{for cohesive frictional fill} \tag{25.5}$$

where,

T_{pj} is tensile force due to self-weight of fill and surcharge

T_{sj} , T_{fj} , and T_{cj} are the tensile forces developed due to the effect of strip loading, shear, and cohesion.

$$T_{pj} = \frac{K_{a1} (f_{fs} \gamma_1 h_j + f_{qs}) S_{vj}}{\left(1 - \frac{K_{a2} (f_{fs} \gamma_2 h_j + 3 f_{qs}) \left(\frac{h_j}{L}\right)^2}{3 (f_{fs} \gamma_1 h_j + f_{qs})} \right)} \tag{25.6}$$

where f_{fs} and f_q are partial load factors taken for the appropriate load combination from Table 12 and Table 13 of BS8006-1:2010.

K_{a1} and K_{a2} are the active earth pressure coefficients of the reinforced zone and the fill behind respectively, w_s is surcharge and $S_{vj} =$ vertical spacing of reinforcement.

Effect of cohesion on the force in the reinforcement

$$T_{cj} = 2S_{vj} \frac{C'}{f_{ms}} \sqrt{K_a} \tag{25.7}$$

f_{ms} is the partial material factor applied to C' as per Table 11 of BS8006-1:2010.

Local stability check

The reinforcing elements are designed to satisfy rupture as well as adherence criteria detailed below.

Rupture

The tensile force at each layer of reinforcement should be less than the design tensile strength.

$$\frac{T_D}{f_n} \geq T_j \tag{25.8}$$

where,

T_D is the design strength of the reinforcement, and f_n is the partial factor for economic ramifications of failure.

A factor of safety of 2.5 as a whole is considered for obtaining tensile strength of reinforcement which includes the reduction factors for creep, internal damage, and chemical or environmental effects including economic ramifications of failure.

Adherence

The perimeter each layer of reinforcing elements required to satisfy local stability considerations is

$$P_j \geq \frac{T_j}{\mu L_{ej} \left(\frac{f_{fs} \gamma 1h_j + f_f w_s}{f_p f_n} \right) + \frac{a'_{bc} c' L_{ej}}{f_{ms} f_p f_n}} \tag{25.9}$$

where,

- P_j = is the total horizontal width of the top and bottom faces of the reinforcing element at the j th layer
- f_{fs} and f_f are the partial load factors applied to soil self-weight and surcharge dead loads taken from the same load combination as T_j
- μ = coefficient friction between fill and reinforcing element = $a' \tan \phi'_p / f_{ms}$ (a' = the interaction coefficient relating soil/reinforcement bond angle with $\tan \phi'_p$ and f_{ms} = is the partial material factor applied to $\tan \phi'_p$)
- L_{ej} = length of reinforcement in the resistant zone
- w_s = the surcharge due to dead loads
- f_p = the partial factor for reinforcement pull-out resistance.

Wedge Stability Check

Wedges are assumed to behave as rigid bodies and may be of any size and shape. Stability of any wedge may be maintained when friction forces acting on the potential failure plane in conjunction with the tensile resistance of reinforcements embedded in the fill beyond the failure plane is able to resist the applied loads.

With uniform surcharge, the inclination of potential failure plane is taken as $\beta = 45 - (\phi/2)$. Various potential failure wedges are checked for stability at different heights of the wall.

The reinforcement design is done to satisfy the following requirements within the considered wedge to avoid tension and pull-out failures. The lesser of the values from Eqs. (25.10) and (25.11) for each layer is used in the summation.

$$\sum \frac{T D_j}{f_n} \geq T \tag{25.10}$$

or

$$\sum \left[\frac{P_j L_{ej}}{f_p f_n} \left(\mu f_{fs} \gamma 1 h_j + \mu f_f w_s + \frac{a'_{bc} c'}{f_{ms}} \right) \right] \geq T \tag{25.11}$$

Seismic Design Considerations

External Stability

In seismic conditions, the retaining wall should be able to resist the inertial force (P_{ir}) acting simultaneously with 50% of dynamic thrust (P_{ae}) in addition to the static earth pressure force (AASTHO MSE Bulletin 9).

The total lateral force in seismic loading is

$$R_h(\text{seismic}) = R_h(\text{static}) + P_{ir} + 0.5 P_{ae} \tag{25.12}$$

where,

$$P_{ir} = \text{inertia force developed in reinforcing layers} = 0.5 \gamma H^2 \alpha_m \tag{25.13}$$

$$\alpha_m = (1.45 - \alpha_h) \alpha_h \tag{25.14}$$

$$P_{ae} = \frac{1}{2} (K_{ae} - K_a) \gamma H^2 \tag{25.15}$$

$$K_{ae} = \frac{\cos^2(\emptyset - \theta)}{\cos^2 \theta \left[1 + \sqrt{\frac{\sin \emptyset \sin(\emptyset - \theta)}{\cos \theta}} \right]^2} \tag{25.16}$$

$$\theta = \tan^{-1} \alpha_h / 1 - \alpha_v$$

α_h and α_v are calculated as per IS 1893:1984. The retaining wall should satisfy the external stability criteria stated in the non-seismic case by considering R_h (seismic) in place of R_h .

Internal Stability

The induced tensile forces will be increased during seismic conditions due to development of internal dynamic thrust. The total inertial force (T_{md}) is divided among the layers of the reinforcement based on the length of reinforcement beyond the failure lane.

The total tensile force $T_{\text{total}} = T_{\text{max}}(\text{static}) + \Delta T_{md}$

$$T_{md} = \alpha_{h(m)} W_a \tag{25.17}$$

Inertial force in each layer

$$\Delta T_{md} = \frac{T_{md}}{\sum L_{ej}} L_{ej} \tag{25.18}$$

where,

W_a = weight of the fill in Active zone and
 L_{ej} length of reinforcement beyond failure plane at j th layer.

The pull-out resistance of reinforcement in seismic case is considered as 0.8 times the pull-out resistance in static case. 75% of static factors of safety are sufficient to check the stability in seismic case.

Design Results

The design details of reinforced earth walls for retaining backfill heights ranging from 4 to 10 m carrying a surcharge of 24k N/m² with Moorum and Copper Slag as Fill Materials in non-seismic condition are presented in Table 25.2. Seismic design of these walls is also carried out for seismic zone II as Visakhapatnam is located in zone II and the results are presented in Table 25.3.

Typical calculations of detailed internal stability analysis of reinforced earth wall retaining a 4 m high backfill and a surcharge of 24 kN/m² with copper slag as fill material in non-seismic condition is performed as stated in Sect. Internal Stability

Table 25.2 Design results of reinforced earth retaining wall using moorum and copper slag as fill materials in non-seismic case

Fill material	Moorum				Copper slag			
	4 m	6 m	8 m	10 m	4 m	6 m	8 m	10 m
Height of backfill	4 m	6 m	8 m	10 m	4 m	6 m	8 m	10 m
Depth of foundation (m)	0.5	0.6	1.0	1.0	0.5	0.6	1.0	1.0
Height of retaining wall (m)	4.5	6.6	9.0	11.0	4.5	6.6	9.0	11.0
Width of retaining wall (m)	3.2	4.8	6.3	7.70	3.2	4.8	6.3	7.70
Sliding force (kN/m)	175	335	577	828	175	335	577	828
Frictional forces resisting sliding (kN/m)	362	745	1280	1871	487	1007	1738	2549
Factor of safety against over turning	3.4	3.9	3.88	4.0	3.86	4.4	4.4	4.5
Induced bearing pressure (kN/m ²)	245	320	421	498	262	347	458	543
Safe bearing pressure (kN/m ²)*	360	508	712	822	360	508	712	822
Spacing (m)	0.5	0.5	0.5	0.5	0.5	0.5	0.5	0.5
Maximum induced tensile force (kN/m)	30	41	52	63	27	37	47	57
Tensile strength of reinforcement (kN/m)	80	120	140	160	80	100	120	150

* Safe bearing pressure is computed as $\frac{q_{ult}}{f_{ms}} + \gamma D_m$ considering f_{ms} as 1.35

Table 25.3 Design results of reinforced earth retaining wall using moorum and copper slag as fill materials in seismic case

Fill material	Moorum				Copper slag			
	4 m	6 m	8 m	10 m	4 m	6 m	8 m	10 m
Height of backfill	4 m	6 m	8 m	10 m	4 m	6 m	8 m	10 m
Depth of foundation (m)	0.5	0.6	1.0	1.0	0.5	0.6	1.0	1.0
Height of retaining wall (m)	4.5	6.6	9.0	11.0	4.5	6.6	9.0	11.0
Width of retaining wall (m)	3.2	4.8	6.3	7.70	3.2	4.8	6.3	7.70
Sliding force (kN/m)	190	366	635	914	190	366	635	914
Frictional forces resisting sliding (kN/m)	362	745	1280	1871	487	1007	1738	2549
Factor of safety against over turning	3.0	3.3	3.2	3.3	3.3	3.7	3.6	3.7
Induced bearing pressure (kN/m ²)	263	342	454	538	278	367	488	579
Safe bearing pressure* (kN/m ²)	360	508	712	822	360	508	712	822
Spacing (m)	0.5	0.5	0.5	0.5	0.5	0.5	0.5	0.5
Maximum induced tensile force (kN/m)	33	44	55	68	29	39	49	60

* Safe bearing pressure is computed as $\frac{q_{ult}}{f_{ms}} + \gamma D_m$ considering f_{ms} as 1.35

and are presented in Tables 25.4, 25.5, 25.6 and 25.7. Similar computations are done for other heights of backfill also in non-seismic as well as seismic condition and are in good agreement with stability conditions.

$$T_{pj} = \frac{Ka1(f_{fs}\gamma h_j + f_{qws})S_{vj}}{\left(1 - \frac{Ka2(f_{fs}\gamma 2h_j + 3f_{qws})\left(\frac{h_j}{L}\right)^2}{3(f_{fs}\gamma h_j + f_{qws})}\right)}$$

K_{a1} = coefficient of active earth pressure of fill material

K_{a2} = coefficient of active earth pressure of backfill material

f_{fs} = partial load factor for soil mass = 1.5 (from Table 12 of BS 8006–2010)

Table 25.4 Induced tensile forces of 4 m height retaining wall with copper slag in non-seismic condition

Depth of reinforcement h_j (m)	Induced tensile force T_j (kN/m)
0.5	6.47
1.0	8.73
1.5	11.10
2.0	13.67
2.5	16.46
3.0	19.53
3.5	22.99
4.0	26.93

Table 25.5 Adherence capacity of reinforcing fabric in RERW of 4 m height with copper slag in non-seismic condition

h_j (m)	L_{ej} (m)	Required bond length (m)	P_j
0.5	1.25	0.54	2
1.0	1.49	0.30	2
1.5	1.74	0.22	2
2.0	1.98	0.18	2
2.5	2.22	0.15	2
3.0	2.47	0.14	2
3.5	2.71	0.13	2
4.0	2.96	0.12	2

Table 25.6 Induced tension in wedge of RERW of 4 m height with copper slag in non-seismic condition

h_j (m)	T	No. of layers of reinforcement	T_D/f_n (kN/m)	$\sum T_D/f_n$ (kN/m)
1.0	12.76	2	32	64
2.0	33.90	4	32	128
3.0	63.43	6	32	192
4.0	101.34	8	32	256

Table 25.7 Adherence capacity of wedge of RERW of 4 m height with copper slag in non-seismic condition

h_j (m)	L_{ej} (m)	Pull-out resistance (kN/m)	Tension (kN/m)
1.0	1.49	371.95	12.76
2.0	1.98	737	33.90
3.0	2.47	1223	63.43
4.0	2.96	1298	101.34

f_q = partial load factor for surcharge = 1.5 (from Table 12 of BS 8006–2010)

γ_1 = unit weight of copper slag = 23.5 kN/m³

γ_2 = unit weight of backfill material = 19.4 kN/m³

h_j = depth of reinforcing layer below the top of the structure.

Required tensile strength of reinforcing fabric (woven geotextile) is determined as $T_{required} = \text{Factor of safety} \times (T_j)_{max} = 2.5 \times 27 = 66 \text{ kN/m}$.

Considering woven geotextile of tensile strength of 80 kN/m,

$$\frac{T_D}{f_n} = T/FOS = 80/2.5 = 32$$

$\frac{T_D}{f_n} > T_j$. Hence the section is safe against rupture.

b. Adherence

The perimeter P_j of the j th layer of reinforcing elements needed to satisfy local stability considerations is

$$P_j > \frac{T_j}{\mu L_{ej} \left(\frac{f_{js} \gamma^1 h_j + f_f w_s}{f_p f_n} \right) + \frac{a'_{bc} c' L_{ej}}{f_{ms} f_p f_n}}$$

P_j = is the total horizontal width of the top and bottom faces of the reinforcing element at the j th layer = 1 + 1 = 2 m.

Adherence capacity of woven geotextile with fill material at different depths is checked and presented in table.

$$P_j > \frac{T_j}{\mu L_{ej} \left(\frac{f_{js} \gamma^1 h_j + f_f w_s}{f_p f_n} \right) + \frac{a'_{bc} c' L_{ej}}{f_{ms} f_p f_n}}, \text{ hence the section is safe against adherence failure.}$$

$\sum T_D / f_n > T$. Hence wedge stability consideration is satisfied.

Conclusions

- (i) The gradation characteristics of copper slag in compacted state are satisfying the requirements of frictional fill material.
- (ii) Copper slag has higher pull-out resistance in comparison moorum which is attributed due to more roughness of copper slag particles.
- (iii) Copper slag induces bearing pressures of about 5–9% more than that of moorum due to its higher density.
- (iv) The increase in bearing pressures during seismic loading for copper slag is relatively lower in comparison to moorum.
- (v) Due to its greater angle of shearing resistance, copper slag can resist seismic movements in a better way and induces lower tensile forces when compared to moorum.
- (vi) Non- seismic designs of reinforced soil retaining walls under study are adequate to withstand seismic loading of Zone-II.
- (vii) The induced tensile forces in retaining earth walls with copper slag are observed to reduce by about 10–13% when compared reinforced earth walls with conventional fill material moorum in both non-seismic and seismic conditions
- (viii) Copper slag can be used as cost effective alternative to conventional fill material in reinforced soil retaining walls.

References

1. Koerner RM (1990) Designing with geosynthetics, New York. Graw Hill publishers, Mc

2. Reddy CNVS, Moorthy NVR (2002) Potential of rock flour for use in reinforced soil construction. *J Geotechn Eng SEAGS* 149–152
3. Srikanth Reddy S, Satyanarayana Reddy CNV (2015) A study on seismic design of reinforced soil retaining walls with sand and crusher dust as fill materials. Indian geotechnical conference IGC 2015, Pune
4. Lim TT, Chu J (2006) Assessment of the use of spent copper slag for land reclamation. *Waste Manage Res* 24(1):67–73
5. Vidal H (1969) The principle of reinforced earth. *Highway Res Record* 282:1–16
6. Jones CJFA (1985) Earth reinforcement and soil structures, *Advanced Series in Soil Engineering*. Adv Series Soil Eng Butterworth, London
7. Das BM, Tarquin AJ, Jones AD (1982) Geotechnical properties of copper slag. *Trans Res Record* 941
8. Prasad PS, Ramana GV (2016) Feasibility study of copper slag as a structural fill in reinforced soil structures. *Geotext Geomembr* 44:623–640
9. Satyanarayana Reddy CNV, Dhanunjay Kumar Reddy R, Copper slag potential for use as a backfill/fill material in conventional and reinforced earth retaining walls. *Indian J Geosynthetics Ground Improvement* 9(1):46–51
10. Nawagamuwa UP, Senanayake A, Rathnaweera T (2013) Utilization of waste copper slag as a substitute for sand in vertical sand drains and sand piles. In: *Proceedings of the 18th international conference on soil mechanics and geotechnical engineering, Paris*
11. Sathya M, Shanmugavalli B (2014) Effect of using copper slag as a backfill in retaining wall. *Mater Sci Int J Res Eng Technol* 3(9):364–369
12. Sharma K, Kumar A (2020) Geotechnical behaviour of copper slag mixed with different proportions of soil, lime, fly ash and cement—a review. *Sustain Environ Infrastr Proc EGRWSE* 2019, pp103–116
13. Saranya K, Rohini K, Naveena A (2017) A review on utilization of copper slag and silica fume in geotechnical engineering. *Int Res J Eng Technol* 04(02)
14. Sree Rama Rao A, Lavanya C (2017) Study of swelling potential of copper slag cushion laid over expansive soil bed. *Indian Geotechn J* 47(6)

Chapter 26

Multi-Approach Global Stability Assessment of Soil Nail Walls



Vikas Pratap Singh 

Introduction

Soil nailing is an in-situ earth retaining technique in which construction proceeds from the top to bottom by installing closely spaced passive inclusions/reinforcement in the form of steel bars (i.e., nails or tendons). These steel bars may or may not be encased in grout cover. Soil nail walls are most suitable to support in-situ excavation/slope faces that bears an inclination close to 90° (i.e., almost vertical face) with respect to the horizontal particularly encountered in applications such as approaches to the underpass and basement for multistoried buildings [1–3].

For the given in-situ soil and geometric conditions, the conventional design of soil nail walls is based on assuming a configuration of design parameters including nail spacing in horizontal and vertical directions, diameter, length and inclination of nails, etc. such that it satisfies the safety criteria against various failure modes. According to FHWA [4], the broad categories of various modes of failure for a typical soil nail wall are external failure modes (e.g., global stability, sliding stability, basal heave), internal failure modes (e.g., nail pullout failure, nail tensile failure) and facing failure modes (e.g., facing punching shear failure, facing flexure failure). Among various failure modes of soil nail walls, global stability is one of the prominent failure modes representing the overall stability of the reinforced soil mass. Global stability analysis plays a significant role in the long-term stability and overall performance of the soil nail wall.

Further, a soil nail wall is typically a three-dimensional problem of a composite material including components such as in-situ soil, steel bars (i.e., nails), and facing elements (i.e., cast in-situ concrete or pre-cast panels). Thus, global stability of soil nail walls is a function of the complex soil–structure interaction among these

V. P. Singh (✉)

National Institute of Technology Uttarakhand, Srinagar, Garhwal, Uttarakhand 246174, India
e-mail: vpsingh@nituk.ac.in

components. Also, it largely depends on the in-situ soil parameters such as cohesion c , angle of internal friction φ , and unit weight γ . In conventional design, typically a representative value of these soil parameters is adopted which fails to account for the uncertainties involved in the determination of soil parameters through field and/or laboratory experiments [5, 6].

Another important aspect in the design of soil nail walls is the consideration of the seismic loading. It has been reported in the literature that soil nail walls have performed relatively better to the other conventional gravity earth retaining structures under seismic loading [7–13]. Global stability analysis of soil nail walls subjected to the seismicity could be performed using pseudo-static limit equilibrium method [14] and/or by simulating time-history data with the help of a suitable computational tool. In the available literature, limited studies exist on the detailed analysis of the performance and stability of soil nail walls subjected to the seismic loading, and therefore, deserves further investigation.

In the present study, a typical soil nail wall of 8 m height is considered, and specifically global stability of the wall is studied under the following conditions: (a) static loading, (b) seismic loading, and (c) uncertainty in the determination of the in-situ soil parameters based on reliability concept. Study is conducted using the allowable stress design approach [4], performing numerical simulations using a two-dimensional finite element-based computational tool [15], and by Hasofer-Lind reliability method [16] for reliability analysis.

Deterministic Global Stability Analysis

As stated earlier, for deterministic global stability analysis of soil nail wall, limit equilibrium-based methodology is adopted. A planar failure surface leading to a triangular failure wedge is considered for studying the global stability under static and seismic conditions [4, 17]. Inclination of the failure surface is assumed at an angle $\psi = 45 + (\varphi/2)$ (in degrees) with respect to horizontal. Table 26.1 summarizes the design parameters and the geometric configuration of the soil nail wall considered in the study, and Fig. 26.1 shows its schematic layout along with the various forces required in the computation of the global stability.

The global stability is expressed in terms of the factor of safety FS_G which can be determined using Eqs. (26.1) and (26.2) obtained by considering the equilibrium of the resisting forces ΣR and driving forces ΣD acting tangentially to the potential failure plane.

$$FS_G = \frac{\sum R}{\sum D} \quad (26.1)$$

$$FS_G = \frac{cL_F + T_{eq} \cos(\psi - i) + [(W + Q_T - F_v) \cos \psi + T_{eq} \sin(\psi - i) - F_h \sin \psi] \tan \varphi}{(W + Q_T - F_v) \sin \psi + F_h \cos \psi} \quad (26.2)$$

Table 26.1 Details of the soil nail wall design parameters and geometric configuration

Parameter	Value
Vertical height of wall H (m)	8.0
Nailing type	grouted
Surcharge load q_s (kPa)	0.0
Diameter of reinforcing element, i.e., nail tendon d (mm)	16.0
Drill hole diameter D_{DH} (mm)	100.0
Length of nail L (m)	4.7
Nail inclination with respect to horizontal i (degrees)	15.0
Horizontal nail spacing S_h (mm)	1.0
Vertical nail spacing S_v (mm)	1.0
Modulus of elasticity of soil, E_s , MPa	20.0
Poisson's ratio of soil, μ	0.35
Yield strength of nail, f_y , MPa	415
Modulus of elasticity of nail, E_n , GPa	200.0
Allowable bond strength, q_a (kPa)	50.0

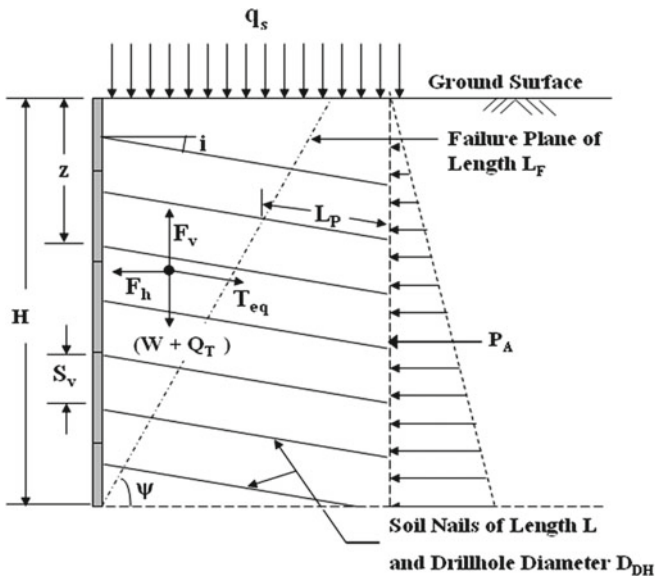


Fig. 26.1 A Schematic layout of a typical soil nail wall

where L_F (m) = length of the failure plane equal to ($= H/\sin \psi$); W (kN/m) = weight of failure wedge ($= 0.5\gamma H^2 \cot \psi$); Q_T (kN/m) = total surcharge load ($= q_s H \cot \psi$); q_s (kPa) = distributed surcharge loading; T_{eq} (kN/m) = equivalent nail force [4, 18], and F_h and F_v (kN/m) = horizontal and vertical inertia forces due seismic loading considered in the pseudo-static approach, respectively, and can be computed using Eqs. (26.3a, 26.3b).

$$F_h = k_h(W + Q_T) \quad (26.3a)$$

$$F_v = k_v(W + Q_T) \quad (26.3b)$$

It is to be noted that the seismic inertial forces F_h and F_v should be directed such that the resultant seismic force shall cause critical loading condition for global stability, and therefore, as shown in Fig. 26.1, the direction of the horizontal inertia force F_h is taken away from the slope and the vertical inertia force F_v is considered acting vertically upwards [4]. In the present study the earthquake data from Bhuj earthquake [19] dated January 26th, 2001 recorded at Ahmedabad station is used. Figure 26.2 shows the time-history plot of the horizontal acceleration component of the said earthquake, which is also used for the dynamic analyses using a computational tool in the subsequent sections. From the time-history plot, horizontal seismic coefficient k_h is determined equal to 0.106, and is used to compute the horizontal inertia force for the pseudo-static analysis. The vertical seismic coefficient k_v is disregarded in the present study as it results in the conservatism in the computation of global stability by reducing the self-weight component vis-à-vis shear strength along failure plane. According to FHWA [4], the typical factor of safety for global stability for soil nail walls is in between 1.35 and 1.50 for static conditions and 1.10 under seismic conditions.

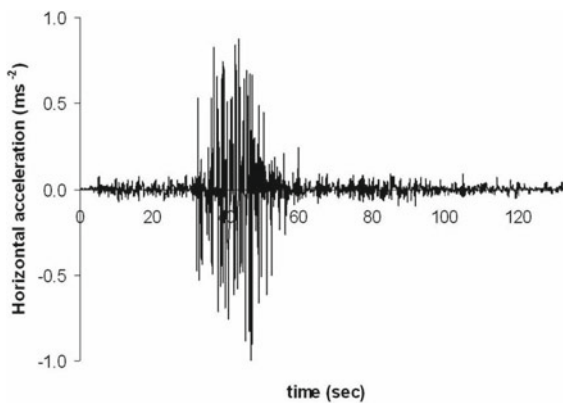


Fig. 26.2 Time-history data for Bhuj earthquake [19]

Reliability-Based Global Stability Analysis

Hasofer-Lind reliability indices [16] are determined for the global stability failure mode of the soil nail wall considered in the present study. Built-in optimization program Solver available in Microsoft Excel Program [20, 21] is used to perform the reliability analysis.

The Hasofer-Lind reliability index β can be represented in the matrix form as given by Eq. (26.4).

$$\beta = \min_{x \in F} \sqrt{\left[\frac{x_i - \mu_i^N}{\sigma_i^N} \right]^T [R]^{-1} \left[\frac{x_i - \mu_i^N}{\sigma_i^N} \right]} \tag{26.4}$$

where x_i , μ_i^N , R , and σ_i^N represent vectors/matrices of random variables, equivalent normal mean values, correlation among random variables, and equivalent normal standard deviation, respectively. F corresponds to the failure domain. For reliability analysis, three non-correlated random variables are considered, namely, in-situ soil unit weight γ and shear strength parameters (i.e., cohesion c and angle of internal friction φ). The random variables are assumed to follow the lognormal probability distribution function. Table 26.2 summarizes the statistical properties of the variables.

The limit state function (or performance function) for the global stability, $perfn(1)$, of soil nail wall is given by Eq. (26.5). Various terms in Eq. (26.5) have same meaning as mentioned earlier.

$$\begin{aligned} perfn(1) = & cL_F + T_{eq} \cos(\psi - i) - \{(W + Q_T - F_v) \sin \psi + F_h \cos \psi\} \\ & + [(W + Q_T - F_v) \cos \psi + T_{eq} \sin(\psi - i) - F_h \sin \psi] \tan \phi = 0 \end{aligned} \tag{26.5}$$

Table 26.2 Statistical properties of random variables (i.e., in-situ soil parameters)

Parameter	Probability distribution	Mean value μ	#Coefficient of variation COV %		
			Minimum	Average	Maximum
Cohesion c	Lognormal	5 kPa	10	20	30
Angle of internal friction φ	Lognormal	30 ⁰	02	06	10
Unit weight γ	Lognormal	16 kN/m ³	03	05	07

#—Phoon and Kulhawy [5], Duncan [6]

Computational Global Stability Analysis

For the typical soil nail wall considered in the study, numerical simulations are performed using a commercially available finite element-based computational tool Plaxis 2D [15]. Global stability is assessed by determining factors of safety under static, pseudo-static, and dynamic conditions. Figure 26.3 shows the simulated model of the soil nail wall.

Plaxis uses strength reduction technique [22] for the computation of factor of safety. Strength reduction technique has the advantage that the critical failure mechanism is automatically identified. A plane strain state of stress using 15–node triangular elements with medium mesh density is assumed for numerical simulations. Soil nails and wall facing are simulated using plate elements behaving as linear elastic materials, and interfaces are considered rigid. The in-situ soil stress–strain behavior is simulated using Mohr–Coulomb material model. For dynamic analysis (i.e., time-history analysis), shear wave (V_S) and compression wave (V_p) velocities computed using elastic properties of soil E_S and μ are given as additional input parameters. The earthquake is modeled by imposing prescribed displacement at the bottom boundary and inputting the earthquake data corresponding to the time-history shown in the Fig. 26.2 as dynamic multiplier.

Further, simulation of construction stages is also performed. Soil nail wall is constructed in four stages represented as E1, E2, E3, and E4 in the Fig. 26.3. In each construction stage, installation of soil nails and facing elements is done after simulating an in-situ soil excavation of 2 m depth. For both static and dynamic analyses, standard simulation procedures with reference to the software manual [15] and details given in Singh and Sivakumar Babu [23] specifically on 2D numerical simulations of soil nails walls using Plaxis 2D software are followed.

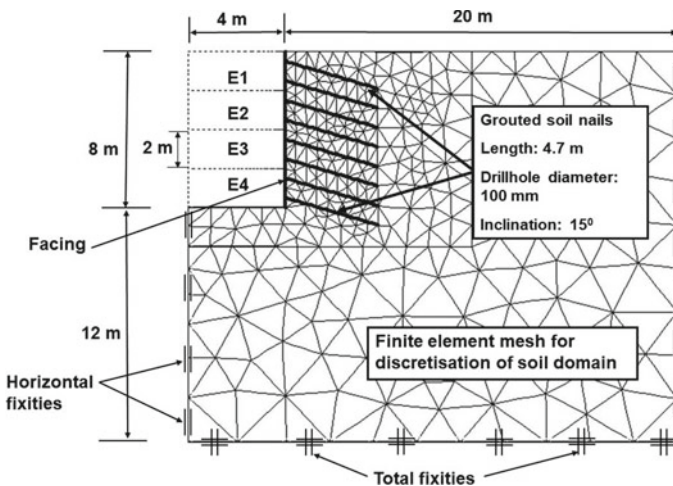


Fig. 26.3 Simulated model of soil nail wall

Results and Discussion

For the typical soil nail wall considered in the study, Plaxis is used for the numerical simulations. Further, using the deterministic expression given by Eq. (26.2), factor of safety values for global stability of the soil nail wall considered in the study are obtained as 1.81 and 1.65 for static and pseudo-static (for $k_h = 0.106$ and $k_v = 0.0$) conditions, respectively. Since these values of factor of safety are much more than the minimum desirable, the soil nail wall is safe against global failure. However, it is to be noted that these factors of safety values are computed corresponding to the mean values of in-situ soil parameters (i.e., cohesion, friction angle, and unit weight) given in Table 26.2. These mean values presume that both the resisting and driving components of the Eq. (26.1) have a probability of occurrence equal to unity, i.e., no uncertainty is involved in their determination. Thus, assessment of global stability merely based on deterministic approach is subjective and depends on the failure definition and the representative material parameters adopted. Also, the deterministic approach fails to provide any information about the associated probability of the failure.

To overcome the above-mentioned limitations of the deterministic approach, reliability-based evaluation of the global stability of the soil nail walls is expected to provide a better insight into the stability assessment. As stated earlier, the reliability indices are determined by Hasofer-Lind method using Eqs. (26.4) and (26.5), considering in-situ soil parameters (i.e., cohesion, friction angle, and unit weight) as uncorrelated lognormal random variables. According to Phoon [24], a reliability index β value equal to 3.0 signifies “above average” stability of the geotechnical structures, and the corresponding probability of failure P_f is approximately of the order of 1×10^{-3} . For high stability of geotechnical structures, minimum β is equal to 5.0 with $P_f \approx 3 \times 10^{-7}$.

Hasofer-Lind reliability index values for global stability β_{GL} were computed for both static and pseudo-static conditions. Further, to study the influence of uncertainty involved in determination of a given soil parameter, coefficient of variation (COV) of one parameter is varied at a time from its minimum to the maximum COV values mentioned in Table 26.2 and keeping COV s of other two parameters constant at their respective average values. Figure 26.4a–c shows variation in the reliability indices for global stability determined by considering the influence of uncertainty in the determination of in-situ soil parameters (i.e., c , ϕ , and γ). From Fig. 26.4a–c, it is evident that the uncertainty in the determination of in-situ soil friction angle has significant influence on the stability of soil nail wall. The trend is then followed by the unit weight and in-situ soil cohesion, respectively. Another observation from Fig. 26.4a–c is that for the soil nail wall under consideration, reliability index for global stability is more than 5.0 both in static as well as pseudo-static conditions. Thus, it is highly stable against global failure with probability of failure as low as 3×10^{-7} .

From the above discussion, it is apparent that reliability-based analysis provided much better insight into the global stability of soil nail wall in comparison to the

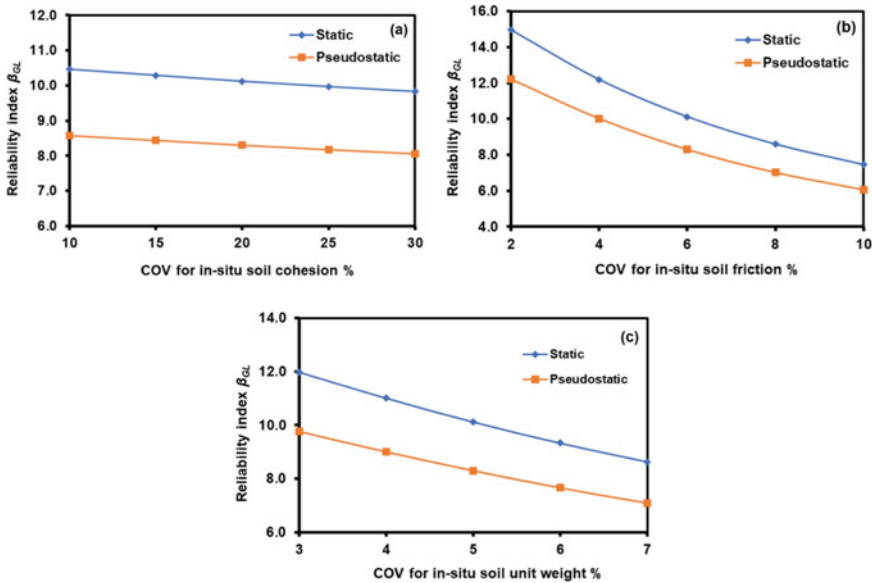


Fig. 26.4 Variation in reliability indices for global stability due the uncertainty in the determination of in-situ soil parameters: **a** cohesion, **b** friction angle, φ , **c** unit weight, γ

deterministic analysis. But, as stated earlier, factors such as composite structural behavior, complex soil–structure interaction, construction stages, 3D state of stresses, etc. greatly influences the long-term global stability of a soil nail wall. Both the above discussed deterministic and reliability-based approaches fail to address these aspects due to the complexity involved in their analytical modeling. Thus, for a holistic analysis of global stability of soil nail walls, computational modeling is an inevitable choice. Accordingly, factors of safety for global stability of the soil nail wall were computed using numerical simulations [15] for static, pseudo-static, and time-history (dynamic) analyses at its various construction stages E1, E2, E3, and E4. Table 26.3 summarizes the construction stage-wise factors of safety for global stability computed using numerical simulations. Construction stage is expressed as percentage of height of wall constructed upto the given excavation lift (in present case, each excavation lift is of 2 m) with respect to the full height of wall, i.e., 8 m.

From Table 26.3, it is evident that for 100% construction stage, i.e., fully constructed 8 m high wall, factors of safety are more than the minimum desirable factors of safety in static (i.e., 1.35–1.50) and seismic (i.e., 1.10) conditions, therefore, the given soil nail wall is stable against global failure. It is can also be noted from Table 26.3 that factors of safety against global stability have shown decreasing trend with construction stage. Further, Table 26.3 shows that the factor of safety value for dynamic analysis using time-history data for any given construction stage is relatively higher than the corresponding value using pseudo-static analysis. This observation may be attributed to the fact that in pseudo-static analysis seismic inertia forces are

Table 26.3 Summary of globality stability analyses using numerical simulations

Construction stage %	Legend (see Fig. 26.3)	Factor of safety, FS_G		
		Static analysis	Pseudo-static analysis	Time-history (dynamic) analysis
25	E1	2.40	1.80	1.90
50	E2	1.95	1.56	1.68
75	E3	1.75	1.42	1.55
100	E4	1.55	1.28	1.35

Table 26.4 Global stability assessment using different approaches

Analysis type	Deterministic approach	Reliability approach			Computational approach
		At minimum $COVs$	At average $COVs$	At maximum $COVs$	
Static	$FS_G = 1.81$	$\beta_{GL} = 21.97$	$\beta_{GL} = 10.12$	$\beta_{GL} = 6.52$	$FS_G = 1.55$
Pseudo-static	$FS_G = 1.65$	$\beta_{GL} = 18.04$	$\beta_{GL} = 8.30$	$\beta_{GL} = 5.33$	$FS_G = 1.28$
Time-history	–	–	–	–	$FS_G = 1.35$

Note All analyses performed using the mean values of soil parameters given in Table 26.2

considered to be continuously applied in the critical direction of loading, whereas in time-history analyses direction of loading keep changing with time resulting in both critical and non-critical loading combinations.

Table 26.4 presents a summary of global stability assessment of the soil nail wall of 8 m vertical height considered in the present study using different approaches, namely, deterministic, reliability based, and computational simulations.

From Table 26.4, it can be observed that for the same soil nail wall, global stability can be assessed and quantified differently depending upon the approach adopted for analysis. The factor of safety values obtained using computational approach are relatively less than the corresponding values using deterministic approach. Owing to the merits of computational analysis over conventional deterministic approach, global stability assessment using computational simulation can be considered as more realistic and accurate. Further, only a computational analysis can facilitate simulation of actual time-history data for seismic loading, which is certainly better than pseudo-static approach. Table 26.4 also highlights the importance of accurate determination of the representative mean soil parameters to be used for global stability analysis. It can be seen from Table 26.4 that the reliability indices corresponding to minimum $COVs$ values are much higher than those corresponding to the maximum $COVs$. For example, for static analysis $\beta_{GL} = 21.97$ for the more accurate determination of soil parameters (i.e., minimum $COVs$) and $\beta_{GL} = 6.52$ for the less accurate determination of soil parameters (i.e., maximum $COVs$). As stated earlier, β_{GL} is directly linked to the probability of failure which in turn is a function of construction cost and anticipated risk.

Concluding Remarks

The present study highlighted the significance of multi-approach global stability analyses for soil nail walls. For illustration, a soil nail wall of vertical height 8 m was analyzed for global stability using conventional deterministic approach, reliability-based approach, and computational approach using a finite element-based software. Based on the results and discussions presented in the study, it can be concluded that the global stability analysis using computational approach is more realistic, and uncertainty involved in the determination of representative soil parameters should be addressed by the reliability-based approach. Therefore, it is recommended that for a more holistic global stability analyses, computational approach shall be invariably coupled with the reliability approach. Deterministic methods shall only be used for a preliminary study. Further, it is also recommended that time-history (dynamic) analyses shall be preferred over pseudo-static approach for studying the seismic stability of the soil nail wall.

References

1. Murthy BRS, Sivakumar Babu GL, Srinivas A (2002) Analysis of prototype soil nailed retaining wall. *Ground Improvement* 6(3):129–136
2. Sivakumar Babu GL, Murthy BRS, Srinivas A (2002) Analysis of construction factors influencing the behavior of soil nailed earth retaining walls. *Ground Improvement* 6(3):37–143
3. Sivakumar Babu GL, Rao RS, Dasaka SM (2007) Stabilisation of vertical cut supporting a retaining wall using soil nailing: a case study. *Ground Improvement* 11(3):157–162
4. FHWA0-IF-03-017 (2003) Geotechnical engineering circular no. 7 soil nail walls. Federal Highway Administration (FHWA), Washington D.C.
5. Phoon KK, Kulhawy FH (1999) Characterization of geotechnical variability. *Can Geotech J* 36(4):612–624
6. Duncan JM (2000) Factors of safety and reliability in geotechnical engineering. *J Geotech Geo-Environ Eng* 126(4):307–316
7. Felio GY, Vucetic M, Hudson M, Barar O, Chapman R (1990) Performance of soil nailed walls during the October 17, 1989 Loma Prieta earthquake. In: *Proceedings of the 43rd Canadian geotechnical conference, Quebec*, pp. 165–173
8. Vucetic M, Tufenkjian M, Doroudian M (1993) Dynamic centrifuge testing of soil-nailed excavations. *ASTM Geotech Testing J* 16(2):172–187
9. Tatsuoka F, Koseki J, Tateyama M (1997) Performance of reinforced soil structures during the 1995 Hyogo-ken Nanbu earthquake. In: *Proceedings of the international symposium on earth reinforcement (IS Kyushu '96)*, Balkema, pp 973–1008
10. Tufenkjian MR, Vucetic M (2000) Dynamic failure mechanism of soil-nailed excavation models in centrifuge. *J Geotech Geo-Environ Eng* 126(3):227–235
11. Sivakumar Babu GL, Singh VP (2008) Numerical analysis of performance of soil nail walls in seismic conditions. *ISET J Earthq Technol* 45(1–2):31–40
12. Mokhtari M, Barkhordari K, Karafshani SA (2020) A comparative study of the seismic response of soil-nailed walls under the effect of near-fault and far-fault ground motions. *J Eng Geol* 13(5):121–146
13. Muthukumar S, Kolathayar S, Valli A, Sathyan D (2020) Pseudostatic analysis of soil nailed vertical wall for composite failure. *Geomech Geoeng Int J*. <https://doi.org/10.1080/17486025.2020.1827163>

14. Kramer SL (2003) Geotechnical earthquake engineering, 1st edn. Pearson Education, India
15. Plaxis: User manual, Plaxis bv, Bentley Systems Inc., The Netherlands (2020)
16. Hasofer AM, Lind NC (1974) Exact and invariant second moment code format. *J Eng Mech* 100(1):111–121
17. Sheahan TC, Ho CL (2003) Simplified trial wedge method for soil nailed walls analysis. *J Geotech Geo-Environ Eng* 129(2):117–124
18. Sivakumar Babu GL, Singh VP (2009) Reliability analysis of soil nail walls. *Georisk: Assess Manage Risk Eng Syst Geohazards* 3(1):44–54
19. Shrikhande M (2201) Atlas of Indian strong motion records. Department of Earthquake Engineering, Indian Institute of Technology, Roorkee
20. Low BK, Tang WH (1997) Efficient reliability evaluation using spreadsheet. *J Eng Mech* 123(7):749–752
21. Low BK (2005) Reliability-based design applied to retaining walls. *Geotechnique* 55(1):63–75
22. Matsui T, San KC (1992) Finite element slope stability analysis by shear strength reduction technique. *Soils Found* 32(1):59–70
23. Singh VP, Sivakumar Babu GL (2010) 2D numerical simulations of soil nail walls. *Geotech Geol Eng* 28(4):299–309
24. Phoon KK (2004) Towards reliability-based design for geotechnical engineering. Special Lecture for Korean Geotechnical Society, Seoul, pp 1–23

Chapter 27

Finite Element Analysis of Back-To-Back Mechanically Stabilized Earth Wall



K. A. Aboorvaraj , P. V. Premalatha , and A. Karthikeyan

Introduction

A Mechanically stabilized earth retaining wall (MSEW) is a retaining structure consisting of alternating layers of compacted backfill and geosynthetic reinforcement elements, which are fastened to a wall facing. The stability of the wall system completely depends on the interaction between the backfill and soil reinforcements. The function of the wall facing is to preventing erosion of the structural backfill. MSEW is a flexible retaining wall which can carry heavy loads and can tolerate large settlements.

Back-To-Back MSEW

Mechanically stabilized earth walls (MSEW) are commonly found in highways, used as ramps and embankments. In cases where width is restricted for ramps or embankments, it results in the construction of parallel MSE walls at immediate vicinity, in few cases the backfill of MSE walls overlaps over each other. Such walls are referred to as back-to-back MSE walls.

K. A. Aboorvaraj (✉)
Department of Civil Engineering, Anna University Regional Campus Coimbatore,
Coimbatore 641046, India
e-mail: aboorvaraj.k.a@gmail.com

P. V. Premalatha
Professor, Department of Civil Engineering, M.I.E.T. Engineering College,
Tiruchirappalli 620007, Tamil Nadu, India

A. Karthikeyan
M/S Karthikeyan Associates, Arumbakkam, Chennai 600106, India

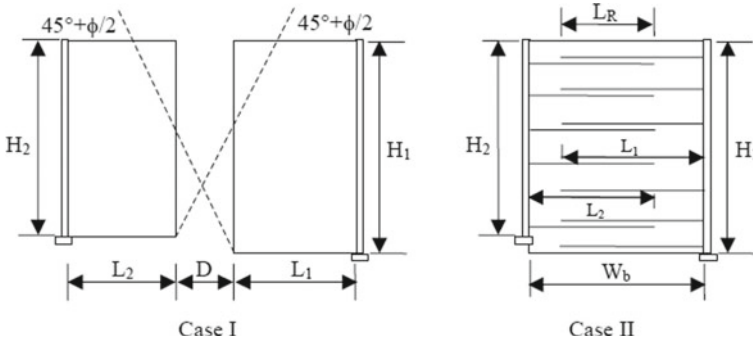


Fig. 27.1 Classification of BBMSEW

However, the available design guidelines are limited in which w/h ratio determines the analysis methods. For design two extreme cases are identified as in Fig. 27.1: (Case I) the walls are far apart, independent of each other, and (Case II) reinforcements of parallel wall meet in the middle [1, 2].

In both cases, the active region is kept separate by maintaining a w/h ratio > 1.1 [2, 3]. BBMSEW stays stable by the use of interaction between the reinforcement and the fill which is supported by reinforcement extending into the dormant/stable fill away from the active region. This interaction is difficult to predict thus in Federal Highway Administration (FHWA) Guidelines. Back-to-back MSE design methodology opted for numerical analysis and structure instrumentation, utilizing which current codes and guidelines are created.

BBMSEW are extensively used in highways, due to its flexible nature and resist high deformation which allows construction of narrow cross-sections even in high seismic regions.

Current Study

The study focuses on the use of a tall back-to-back mechanically stabilized earthen wall with a w/h ratio < 1.1 and using a single layer reinforcement. It is important to study this particular case because people tend to go with single layer reinforcement for such a slender cross-section. It is logical to save material by reducing the cross-sections and replacing overlapping reinforcement with single layer reinforcement, but the effects of overlapping active regions and the lack of contact area of the reinforcement make it difficult to comprehend the stability of the structure. Thus, numerical analysis is adopted to arrive at a fair conclusion over the use of single layer reinforced slender BBMSEW and its failure mechanism.

For this purpose, the following wall sections as given in Table 27.1 are considered for analysis of the proposed structure.

Table 27.1 Summary of sections considered for analysis

Sl. No.	Description	W/H	Height (m)	Width (m)
1	Section A'	0.353	17	6
2	Section B'	0.5	12	6
3	Section C'	0.857	7	6
4	FHWA standard. ratio	1.1	5.5	6

Literature Review

Past research on back-to-back mechanically stabilized walls, provides insights on influencing factors such as distance between back-to-back, W/H ratio, reinforcement length, critical failure plane which helps in determining the stability of BBMSEW. Studies show that when the walls are far apart, perform independently and when they are close, they interact with each other [4]. Wall behaves independently when the wall's w/h ratio is above 1, but when the ratio is less than one of the walls interact with each other. The interaction between walls is less significant greater when D is greater than 0.5 H and more pronounced below 0.5H [5]. Highway lanes are constructed based on the existing median, because if that many back-to-back structures have small w/h ratios, walls often less than 0.7. There are no FHWA design guidelines for back-to-back walls closer than 1.2 times the wall height. Under seismic loads narrow structures do not suffer significantly greater movements compare to that of MSE wall of the same height and W/h ratio greater than 1.2 [6]. The numerical and limit equilibrium methods support the statement that two back-to-back walls perform independently when they are far apart and interact with each other when they are close. When walls are close to each other the interaction will change the location and shape of the critical failure surface. The FHWA design guideline underestimates the interaction distance [7]. Studies also show that there is an increase in geometry involved a decrease in Factor of safety and an increase in wall displacement occurs [5]. The effect of adopting various W/H ratios 3–0.8 results agree with the results of the FHWA design guideline. The results also show that the FHWA design guideline underestimates the lateral earth pressure when back-to-back walls interact with each other. When D, width of the inert fill between BBMSE wall approaches to zero Rankine lateral thrust (active lateral earth pressure) decreases to 77% [8].

The overlapping of reinforcement reduces the length of reinforcement and also an increase in height requires an increase in overlapping length, overlapping of reinforcement from 0.6 to 2.4 m decreases displacement by 20% and increase in Factor of safety by 50%. The overlapping is pronoun only when the ratio of overlapping length to height is higher than 0.3 m [9]. The use of continuous reinforcement develops a large tension load than overlapping. The maximum tension occurred at the mid-height. Overall safety factor increases for both overlapping and (single layer) continuous reinforcement [5]. Maximum tension in geosynthetic reinforcements were nearly independent of the distance between the back-to-back walls and the FHWA assumption gives very conservative results [4, 10]. The width to height

ratio of the back-to-back wall has a slight effect on the distribution of the maximum tension in the reinforcement at height [7, 11].

Few studies collected data on existing structures which helps to comprehend the standards over BBMSEW. Usually, BBWMSE is constructed with a Narrow footprint ratio of $0.5 \leq W/H \leq 1.0$, which says that FHWA has conservatively considered $W/H \leq 1.1$ [12–14]. The back-to-back design methodology is compared confirmed by numerical and structured instrumentation. The use of the Coherent gravity method is recommended for the design of BBWMSE. The studies confirm that the design of the BBMSE wall can be done separately and benefited not only by the elimination of horizontal earth pressure, normally resisted by single-faced retaining structures but also form the overlap of reinforcement. The study also suggests avoiding single reinforcement. The reinforcement density in back-to-back MSE walls with overlap reinforcement is much higher than the single-faced wall [12].

Numerical Model

The study is carried out to understand the effect of using single layer continuous reinforcement in a tall BBMSEW with $W/H < 1.1$ using the Finite element method. A plane strain condition is considered for analysis and a 2-dimensional model representing the BBMSEW is modeled using finite element software, PLAXIS 2D. Many researchers [4, 14–16] have given general guidelines on using various soil models and arriving parameters for structural components like walls. The properties of the finite element model used for analysis is as given in Fig. 27.2.

Four different cross-sections are considered for analysis with the same material and geometrical property. The soil used in the analysis is modeled based on the Mohr–Coulomb model given in Table 27.2. The soil parameters for a typical case is taken from Djabri and Benmebark [4].

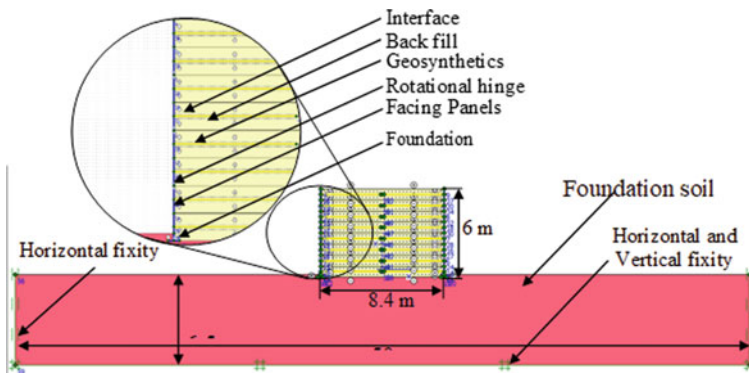


Fig. 27.2 BBMSEW finite element model

Table 27.2 Soil index properties of investigated model [4]

Properties	Foundation soil Mohr–Coulomb	Backfill soil (reinforced and natural backfill) Mohr–Coulomb
Unit weight (γ dry) [kN/m ³]	22	18
Elasticity modulus (E) [kN/m ²]	200,000	30,000
Poisson ratio (ν)	0.1	0.3
Internal friction angle (ϕ) °	30	35
Cohesion (C) [kN/m ²]	100	5
Dilatancy angle (ψ) °	0	0
Shear modulus (G) [kN/m ²]	90.909	11.540

Concrete facing panels are modeled using plates of 1.50 m of width and height, a panel thickness of 0.15 m is widely used which is adopted for modeling. A foundation of 0.5 m thick and 1 m width is used.

Foundation: M-35

$$E = 5000 \sqrt{f_{ck}} = 5000\sqrt{35} = 29.58 \times 103 \text{ N/mm}^2$$

$$EA = E \times b \times d = 29.58 \times 109 \times 0.5 \times 1 = 14.79 \times 109 \text{ kN/m}$$

$$EI = \frac{E \times b \times d^3}{12} = 29.58 \times 109 \times 1 \times 0.53/12 = 30.8125 \times 107 \text{ kNm}^2/\text{m}$$

$$D_{\text{eff}} = \sqrt{\left(12 \frac{EI}{EA}\right)} = 0.5 \text{ m}$$

$$W = \gamma \times d = 24 \times 0.5 = 12 \text{ kN/m}^2/\text{m}.$$

Facing: M35

$$EA = E \times b \times d = 4.51 \times 106 \text{ kN/m}$$

$$EI = \frac{E \times b \times d^3}{12} = 8437.5 \text{ kNm}^2/\text{m}$$

$$D_{\text{eff}} = \sqrt{\left(12 \frac{EI}{EA}\right)} = 0.15 \text{ m}$$

$$W = \gamma \times d = 24 \times 0.15 = 3.6 \text{ kN/m}^2/\text{m}.$$

The connection between facing panels is modeled by some researchers by simple hinges and the compressibility that develops between them due to the presence of pads is neglected, boundaries were varied and the appropriate boundaries were adopted. The boundary was determined to be provided at a ratio of 6 times the width of the structure in the horizontal direction 2 times of the height of the structure in the vertical direction after a series of trial analysis ran to reduce the boundary effect.

For this project, a medium size mesh is used for analysis which generates roughly 250 elements, a plastic analysis is undertaken and as the construction is a staged construction, the load input is carried out as staged construction.

Results

A validation study is carried out for the model simulation comparing the results. The model is validated, using Djabri and Benmebrk [4] the results were approximate due to the parameters like depth of foundation, rotational tolerance which were not mentioned. The failure pattern and the curve trend prove that the model is of similar behavior (Fig. 27.3).

The objective of the analysis is to identify the feasibility of providing a single layer reinforcement in a BBMSEW and to check the stability of the proposed slender section. Parameters like tensile force on reinforcement, horizontal earth pressure, and horizontal wall displacement were analyzed and compared.

The required tensile strength for different sections considered for analysis is given in Fig. 27.4. There is a gradual increase in the reinforcement tension at the bottom of the retaining wall, this is predominantly due to the height. At the joints where rotational hinges are provided experiences a hike in tensile strength due to the horizontal flexibility.

As the height of the wall is increased there is a backward rotation observed in the wall this is due to the tie bin behavior of the geosynthetic reinforcement. Due to this tied behavior, there is a spike in displacement at the midspan of the retaining

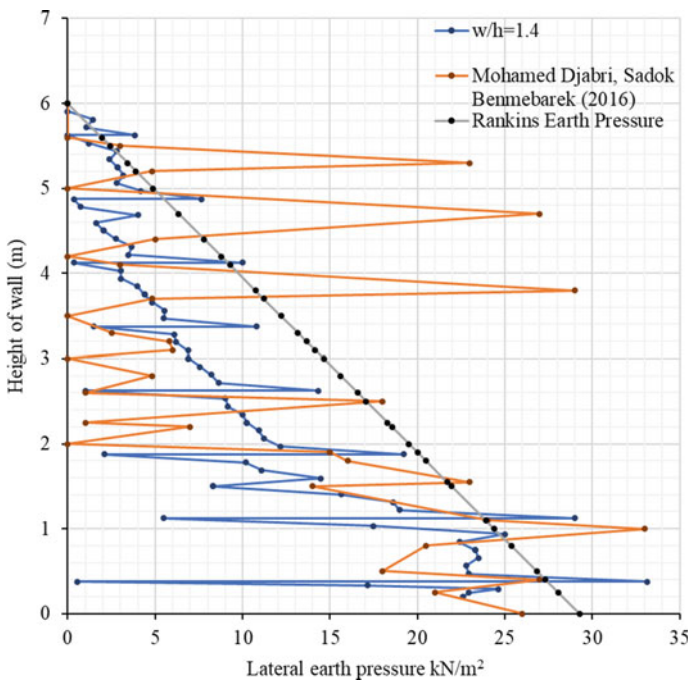


Fig. 27.3 Validation graph lateral pressure versus height

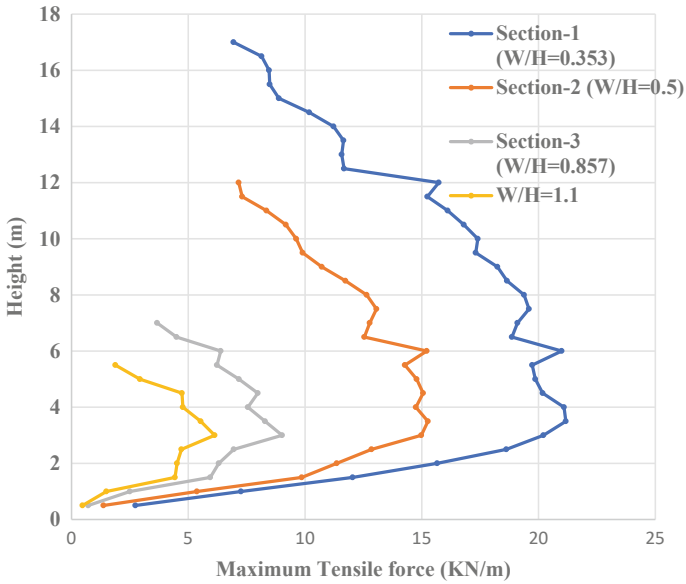


Fig. 27.4 Height versus tensile force

wall. Displacement of facing panel is nearly zero near the footing panel. Even for the section at $W/H = 1.1$ experiences a backward rotation (Fig. 27.5).

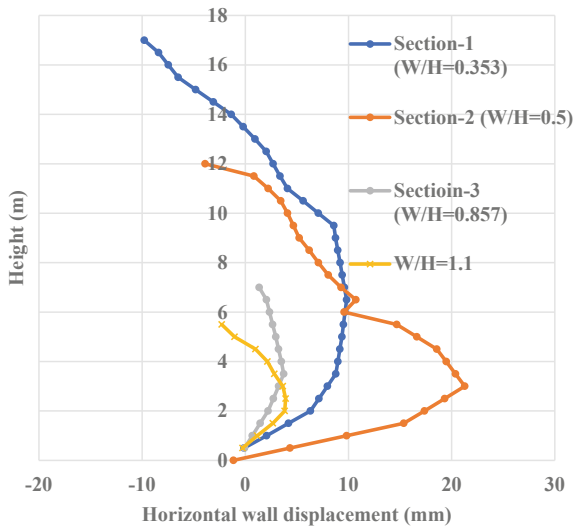


Fig. 27.5 Height versus horizontal wall displacement

When $D = 0$, FHWA suggest neglecting the lateral earth pressure when there is no inert backfill. The result shows that there is an active thrust exit behind the retaining wall which must be considered for external stability. At the reinforced nodes the active earth pressure drops to zero, this proves that the reinforcement reduces the active earth pressure, Fig. 27.6 shows the lateral earth pressure along the face of the wall panel, the spike in the lateral earth pressure represents the reduction of earth pressure at the point where the panels are tied to the soil reinforcement and increase in pressure where reinforcements not present.

The location of the critical failure surface of a Back-to-back MSE is predicted based on the shear strain rate. For all W/H ratios the critical failure surface occurs at the joint, there is excessive stress created at the connections, causing it to fail at the joints, analysis shows the critical failure plane in each section, predominantly there is a high strain rate at the connection, which will cause the failure of connection.

The deformed mesh after analysis for the various section. It shows that there is an excessive displacement of walls at the center and backwards rotation at the crest. In $W/H = 0.35$ vertical settlement is observed at the top, this is due to the displacement of the soil. When height is reduced, the vertical settlement also reduces, this shows that there is a rotation due to lateral earth pressure.

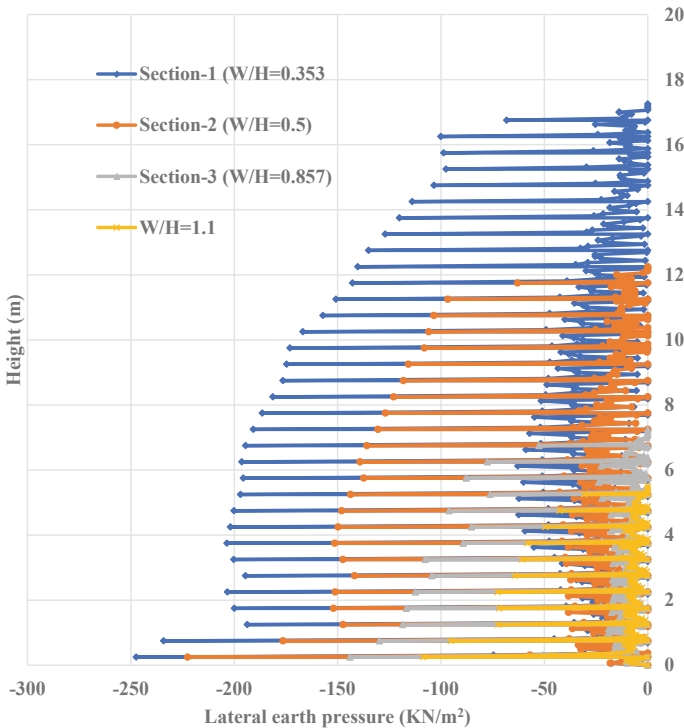


Fig. 27.6 Height versus lateral earth pressure

Conclusion

- The present study is carried out to find the effect of using single layer reinforcement, in a back-to-back mechanically stabilized earth wall (BBMSEW). Former research work did not provide a clear picture of the criticality of using single layer reinforcement. In FHWA standards, there is no suggestion to use single layer reinforcement. The study carried out revealed that a single layer can be provided to the BBMSEW but the behavior is more similar to that of a tied bin wall. The results on the critical failure surface provide the fact that there will be excessive deformation and stresses at the connection of reinforcement and the wall.
- The W/H ratio adopted in this structure is very slender, previous studies on reducing the width of the BBMSEW showed a reduction in maximum tensile force on reinforcement, which is observed, in the study. There is a gradual increase in the tensile force on the reinforcement as the height increases.
- On the other hand, constructing for such a huge height causes high vertical settlement due to the displacement of soil.
- Federal Highway Administration (FHWA) guidelines clause 6.4 ($p-6-18$) have conservatively considered the external stability calculation for Case 2 ($D = 0$). A study over lateral earth pressure revealed that there is a presence of active earth pressure which must be considered while designing. There is a backward rotation of walls observed during analysis.
- The analysis is carried out to understand critical issues involved in construction of a BBMSEW with w/h ratio < 1.1 with single layer reinforcement. It revealed that there is a predominant tied Crib bin behavior and constructing a BBMSEW with single layer reinforcement is not advisable. If constructed extreme care must be taken to avoid deformation at the reinforcement panel joint. Neglecting such conditions will cause sudden failure at the connection and can lead to the sudden collapse of the structure.

References

1. AASHTO (2014) LRFD bridge design specifications, 7th edn. American Association of State Highway and Transportation Officials, Washington, DC
2. National Highway Institute (2009) Design and construction of mechanically stabilized earth walls and reinforced soil slopes. FHWA-NHI-10-024 and 025, vol I and II, NHI Course Nos. 132042 and 132043
3. IRC SP 102-2014, Guidelines for design and construction of reinforced soil wall. Indian Road Congress
4. Djabri M, Benmebarek S (2016) FEM analysis of back-to-back geosynthetic-reinforced soil retaining walls. Int J Geosynth Ground Eng 2(3). <https://doi.org/10.1007/s40891-016-0067-1>
5. El-Sherbiny R, Ibrahim E, Salem A (2013) Stability of back-to-back mechanically stabilized earth walls. Geo-Congress. <https://doi.org/10.1061/9780784412787.058>
6. Hardianto FS, Truong KM (2010) Seismic deformation of back-to-back mechanically stabilized earth (MSE) walls. Earth Retention Conference 3. [https://doi.org/10.1061/41128\(384\)70](https://doi.org/10.1061/41128(384)70)

7. Han J, Leshchinsky D (2010) Analysis of back-to-back mechanically stabilized earth walls. *Geotext Geomembr* 28(3):262–267. <https://doi.org/10.1016/j.geotextmem.2009.09.012>
8. Benmebarek S, Attallaoui S, Benmebarek N (2016) Interaction analysis of back-to-back mechanically stabilized earth walls. *J Rock Mech Geotech Eng* 8(5):697–702. <https://doi.org/10.1016/j.jrmge.2016.05.005>
9. Benmebarek S, Djabri M (2017) FEM to investigate the effect of overlapping-reinforcement on the performance of back-to-back embankment bridge approaches under self-weight. *Transport Geotech* 11:17–26. <https://doi.org/10.1016/j.trgeo.2017.03.002>
10. Mirmoradi SH, Ehrlich M (2018) Numerical simulation of compaction-induced stress for the analysis of RS walls under working conditions. *Geotext Geomembr* 46(3):354–365. <https://doi.org/10.1016/j.geotextmem.2018.01.006>
11. Onur MI, Tuncan M, Evirgen B, Ozdemir B, Tuncan A (2016) Behavior of soil reinforcements in slopes. *Procedia Eng* 143:483–489. <https://doi.org/10.1016/j.proeng.2016.06.061>
12. Anderson PL, Gladstone RA, Brabant K, Sankey J (2018) Back-to-back MSE walls—a comprehensive understanding. *Innovat Geotech Eng*. <https://doi.org/10.1061/9780784481639.029>
13. Dodson MD (2010) Lessons learned from settlement of three highway embankment MSE walls. *Earth Retention Conference* 3. [https://doi.org/10.1061/41128\(384\)60](https://doi.org/10.1061/41128(384)60)
14. Koerner RM, Koerner GR (2018) An extended data base and recommendations regarding 320 failed geosynthetic reinforced mechanically stabilized earth (MSE) walls. *Geotext Geomembr* 46(6):904–912. <https://doi.org/10.1016/j.geotextmem.2018.07.013>
15. Premalatha P, Muthukumar K, Jayabalan P (2021) Effect of tie rod anchor on the behaviour of berthing structures. *Proc Instit Civil Eng Maritime Eng* 1–35. <https://doi.org/10.1680/jmaen.2017.28>
16. Premalatha P, Muthukumar K, Jayabalan P (2015) Experimental study on behaviour of piles in berthing structure. *Proc Instit Civil Eng Maritime Eng* 168(4):182–193. <https://doi.org/10.1680/jmaen.13.00012>

Chapter 28

Behavior of Diaphragm Wall in Semi Top-Down Construction Method: A Case Study



C. Vimala, P. V. S. R. Prasad, and Madan Kumar Annam

Introduction

The demand of deep excavation for the basement construction is increased widely in the fast-developing cities. The underground commuter amenity center with two level basement is proposed in the middle of the city which is consisting of parking area and retail shops. A park facility is planned to be developed for public usage on the surface. The total excavation depth is 9 m below existing ground level (EGL) and perimeter of wall is around 900 m.

In general, two types of construction methods are used in the construction industry for the basement construction (i) Top-down method (ii) Bottom-up method. In top-down method, appropriate retaining wall will be installed and the basement floor slabs shall be used a lateral support for retaining wall. In this method, excavation will be difficult and takes more time due to limited height and space. Whereas in bottom-up method, the retaining wall with lateral supports like steel struts or anchors will be installed to facilitate the excavation. In order to optimize the project cost by reducing excavation duration and eliminating lateral supports, hybrid construction method, i.e., semi top-down excavation was adopted as a stable and safe retention system in this project. Advantages of semi top-down method are (1) passive berm in front of wall provides lateral support to wall and minimizes cost of steel struts or ground anchors according to Tuan et al., (2) excavation process can be done faster when compare to full top-down method.

C. Vimala (✉) · P. V. S. R. Prasad · M. K. Annam
Keller Ground Engineering India Pvt Ltd., Chennai, Tamilnadu, India
e-mail: vimala@kellerindia.com

P. V. S. R. Prasad
e-mail: prasad@kellerindia.com

M. K. Annam
e-mail: madankumar@kellerindia.com

Table 28.1 Subsoil layers (layer thickness and SPT N)

Depth in RL, m (from)	Depth in RL, m (to)	Layer thickness, m	Soil description	SPT N values	Cu, kPa	Φ , deg	E_s , kPa
+7.1	+2.0	5.1	Stiff silty clay	10	50	–	12,500
+2.0	–2.0	4.0	Medium dense silty sand	17	–	31	25,500
–2.0	–5.0	3.0	Medium dense silty sand	25	–	33	37,500
–5.0	–9.0	4.0	Dense silty sand	50	–	36	75,000
–9.0	–21.0	12.0	Hard silty clay	35	175	–	61,250
–21.0	–23.0	2.0	Weathered rock	100	700	–	1,50,000

Subsoil Stratigraphy

The subsoil investigation was carried out through boreholes up to 30 m below EGL. The subsoil conditions reveal stiff silty clay at top 5 m depth followed by medium dense to dense silty sand. This layer is underlain by hard silty clay of 12 m thick followed by a completely weathered rock layer. The ground water table was encountered from 2.1 to 4.3 m below EGL at the time of investigation. The existing ground surface varies from RL + 6.5 m to RL + 8.1 m and the average ground level considered as RL + 7.1 m for analysis purpose. The subsoil layers are indicated in Table 28.1.

Analysis of Retaining Wall

The proposed site is in the congested place surrounded by busy roads, residential buildings and sensitive underground metro line. The safe and stable retention system shall be designed to avoid disturbance to the surrounding structures. WALLAP software is used to predict behavior of diaphragm wall in terms of bending moment, shear force and wall deflections during temporary condition (excavation stage).

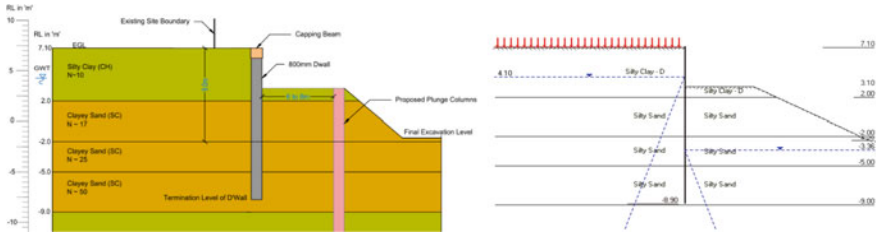


Fig. 28.1 Typical cross section and WALLAP model

Subsoil and Ground Water Table

The subsoil parameters play an important role in the retaining wall design and are derived based on the subsoil information illustrated in Table 28.1. Since ground water table (GWT) is varying, it is decided to consider GWT at 3.0 m below EGL and the same is considered at EGL during permanent condition.

Surcharge

To simulate the loads due to construction activity within the site boundary and vehicular load on the roads, a surcharge of 20 kPa is considered. This surcharge load is applied throughout the construction duration and in all construction stages.

Analysis and Design

Retention system using Diaphragm wall with passive berm and surrounding features were modeled using WALLAP software. The analyses were carried out for varying wall thicknesses by considering different dimensions of passive berm to arrive an optimized stable solution.

An 800 mm thick D' wall with passive berm of 6–8 m top width, 17–19 m bottom width, and 5 m height was arrived as stable solution to support 9 m deep excavation. Figure 28.1 shows typical retention system and WALLAP model.

Construction Sequence Modeled in WALLAP

The following construction sequence were considered in the design and same was adopted at site during execution. Detailed construction sequence is illustrated in Fig. 28.2.

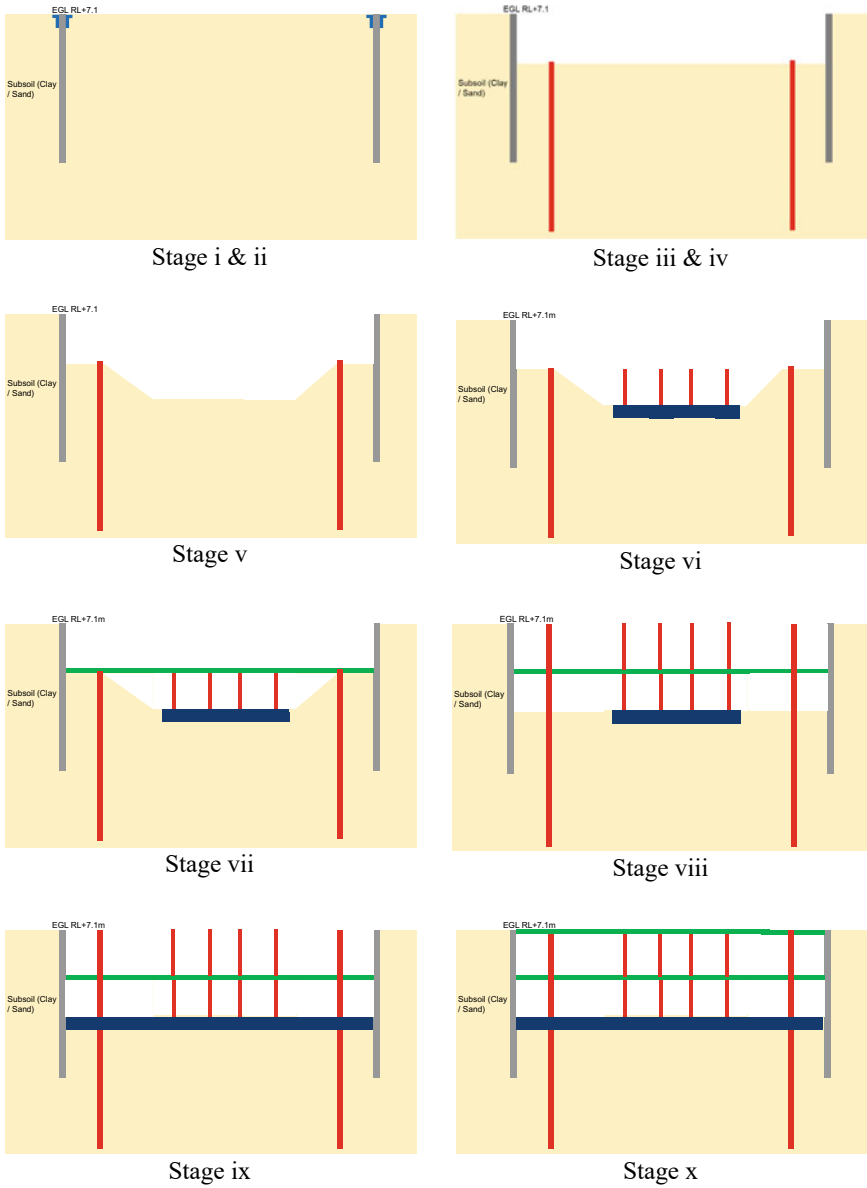


Fig. 28.2 Typical construction sequence

- (i) Construction of Guide wall as per the approved design
- (ii) Installation of 800 mm thick diaphragm wall to required termination level
- (iii) Installation of plunge columns along the periphery as per the design requirements to support intermittent slabs
- (iv) Excavation up to first level slab/parking slab up to 4.0 m below EGL
- (v) Excavation up to 9.0 m depth by forming the passive berm in front of D'wall after maintaining top width of 6–8 m
- (vi) Construction of raft in the middle portion of the site and extending structural columns
- (vii) Construction of first level slab (end to end connection)
- (viii) Removal of soil in the passive berm portion
- (ix) Construction of raft in the berm portion and connecting to D'wall
- (x) Construction of roof slab.

The typical site photo showing passive berm and raft construction is indicated in Fig. 28.5.

Analysis Results

Temporary condition:

Based on the finalized D'wall thickness and passive berm dimensions, the analysis were completed and the results, i.e., bending moment, shear force, and wall deflection arrived from WALLAP is considered for the structural design of diaphragm wall. Results of analysis is presented in Fig. 28.3.

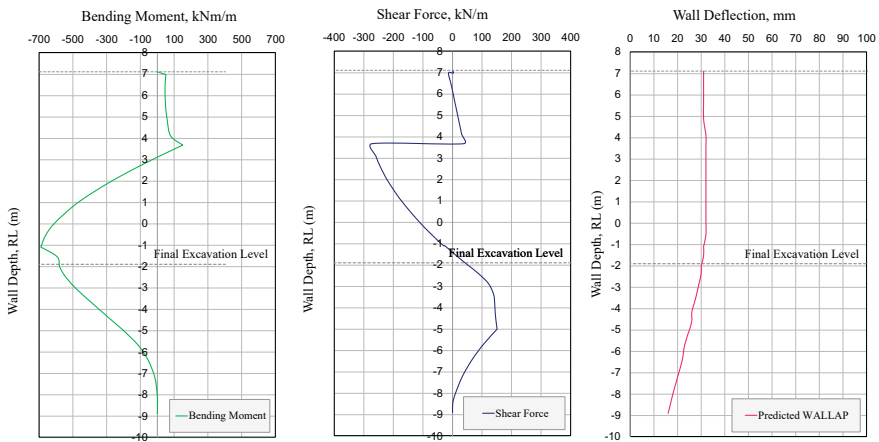


Fig. 28.3 Analysis results; bending moment, shear force, and deflection

Permanent condition (overall stability):

The overall stability of underground structure was carried out using ETABS software. A 3D finite element model of the proposed structure was established to obtain the forces developed in each element, i.e., D'wall, raft, floor slabs and columns and is shown in Fig. 28.4. The structural design of element was carried out based on the analysis results. The structural design of D'wall in permanent condition was carried based on the results obtained from ETABS.

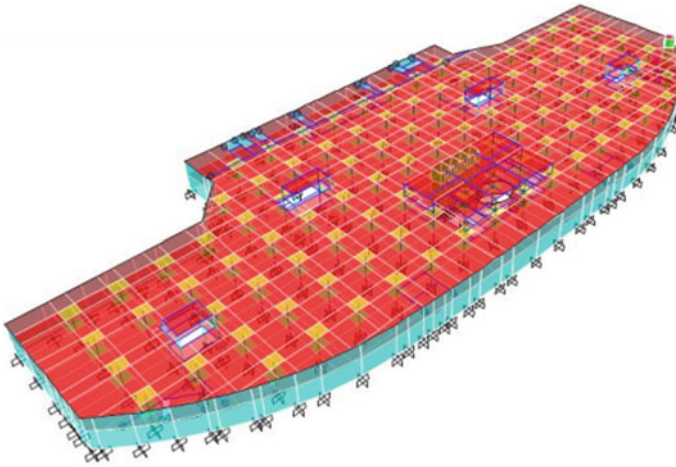


Fig. 28.4 3D finite element model using ETABS



Fig. 28.5 Site view showing passive berm and raft construction

Construction Sequence Adopted at Site

The construction sequence assumed in the analysis (illustrated in Sect. [Construction Sequence Modeled in WALLAP](#)) were meticulously adopted with regular supervision of design engineer at site. After installation of diaphragm wall, one row of 600 mm diameter BCIS piles were installed along the periphery to support the intermittent slab as plunge columns and later these piles have been converted as structural columns with appropriate modifications. Then the center portion of the site was excavated up to the depth of 9 m and the passive berm was formed to provide lateral support to the diaphragm wall. The intermittent slab/parking slab was constructed along the peripheral area parallelly during the excavation process. After reaching 9 m depth, the raft of designed thickness was installed in the center portion and the structural columns are extended up to the intermittent slab level to support the slab. Then the complete parking slab was constructed (end to end connection) prior to removal of soil in the passive berm portion. Raft was connected to the diaphragm wall along the periphery and roof slab was constructed parallelly. The typical site picture showing passive berm and raft construction is illustrated in Fig. [28.5](#)

Monitoring of Retention System

In general, the retention system design is carried out with assumptions like design soil parameters, ground water table, and other loads. Monitoring of installed retaining wall with appropriate instruments will help to prove design assumptions (Bin-Chen Benson Hsiung et al.,). In this project, total 16 inclinometers and 4 piezometers were installed at site to monitor the wall behavior during excavation and basement construction process. Layout of inclinometers and piezometers is indicated in Fig. [28.6](#).

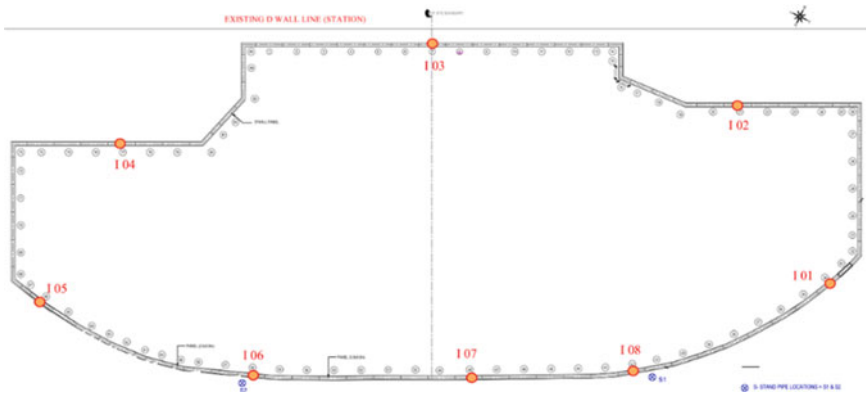
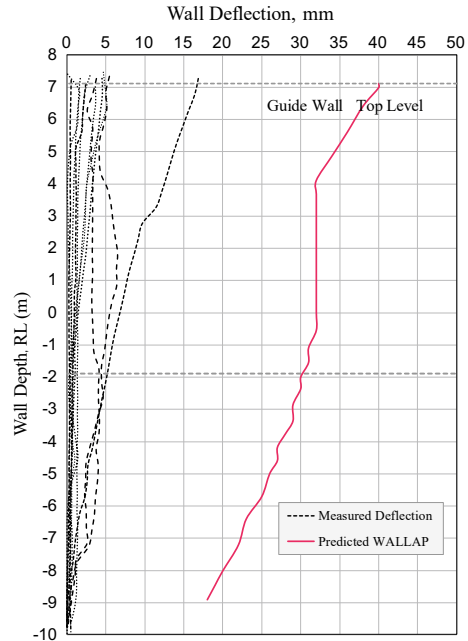


Fig. 28.6 Typical layout indicating location of monitoring instruments

Fig. 28.7 Predicted and measured wall deflections



The observed wall deflection is less than the predicted deflection and the maximum deflection measured at site is ~ 18 mm at top whereas the predicted deflection was around 40 mm at top. The deflection patterns of observed and predicted wall deflections are similar in trend. The monitoring results indicates that the measured wall deflections are well within the permissible design limits. Comparison of measured and predicted wall deflections are indicated in Fig. 28.7.

Conclusions

This paper discussed about the design and construction of retention system using diaphragm wall with semi top-down method to support 9.0 m deep excavation. The semi top-down method with passive berm helps to resist the wall deflection and the stability of wall for optimized berm dimensions. Semi top-down method is a cost-effective solution which uses permanent slab as a lateral support and helps for faster excavation than top-down method. The construction stages assumed in the design assumptions confirms satisfactory performance of wall. The diaphragm wall behavior was observed by installing inclinometers and adopting systematic monitoring schedule from start of excavation to completion of basement construction. The measured wall deflection is well within the predicted wall deflections. This proves design assumptions are reasonable and represents the condition of real ground.

Acknowledgements The authors acknowledge with gratitude to Keller management for their continuous support and encouragement in finalization of theme of this paper. Appreciations to other colleagues who have helped the authors in compilation of the paper. Thanks also to Keller India site management for providing photographs, execution, and monitoring data.

Chapter 29

Review of Use of Asphaltic Concrete Core in Earthen/Rock Fill Embankment Dam



Satyajit Roy, V. K. Jain, Manish Gupta, and R. Chitra

Introduction

Introduction

The first embankment dam with a compacted asphalt concrete core was built in Germany in 1961–1962. Since then, asphaltic concrete core earthen dam have been constructed worldwide. More than 130 asphalt core embankment dams have been built so far [1]. Most asphalt-core dams have been built in Europe, but China has also built and is currently building several dams of this type, among them the 170 m high Quxue Dam that will be the highest so far. The Yele Dam is also an example of asphalt core rock fill dam constructed on the Nanya River along the border of Mianning County and Shimian County, Sichuan Province, China. It is 124.5 m high and 411 m long [2].

Advantage of Asphaltic Concrete Core

The main advantage for application of asphaltic cores in dams is an elasto-plastic behavior of the asphaltic concrete as building material. This elasto-plastic behavior helps to prevent cracks in the core subsequent to deformations of the embankment, thus ensuring the imperviousness of the core. The main specification to be complied with in the placing of a bituminous core is the maintenance of water impermeability under all conceivable deformation conditions. The prerequisite for achieving this aim is the workability, i.e., the placibility and compactibility of the asphaltic mix [3]. The

S. Roy (✉) · V. K. Jain · M. Gupta · R. Chitra
Central Soil and Materials Research Station, New Delhi 110016, India
e-mail: satyajitcmrs@gmail.com



Fig. 29.1 Asphaltic core in dam (Styggevatn Dam, Norway, [4])

asphaltic concrete core helps in providing the highest protection against mechanical defects caused by acts of violence or earthquake which it is possible to attain for a dam structure. Asphaltic concrete cores are non-erosive, crack free and thus water impermeability is ensured by the plastic deformability which conforms to all deformations of the dam body which cannot be accurately determined in advance during the design and calculation stages [3]. Impounding during construction is possible in asphaltic concrete core, as a result potential seasonal rainwater can be collected prior to full completion of the works. In case of occurrence of minor seepage in the core wall, the asphaltic concrete has a good possibility for self-healing due to subsequent creep and migration of fine particles from the upstream face transition zone into fissures or other small deficiencies of the core. The choice of an asphaltic concrete core allows continuous earth and rock fill operations for the dams' shells during and after a rainy period. These works are not sensitive to water but they are dependent on the progress of the core placing operation, which in the case of clay core is highly sensitive to rain and has not only to be interrupted during rainfall but can only be continued after a certain drying period. Figure 29.1 depicts the asphaltic core in Dam.

The asphaltic construction materials are insoluble in water, environmentally compatible and have been proven to be non-harmful to drinking water sources. The dams have been found suitable for construction under various climatic and foundation conditions.

Characteristics of Asphaltic Concrete Core

An asphalt concrete core, or each layer of an asphalt concrete facing, has a unique mixture of asphalt, aggregate and filler, designed to provide the intended function(s) of that element [5].

- (a) The core, or the impervious layers of a facing system, the asphalt content varies from 6 to 8% in asphalt mix, compacted to about a 3% air voids content [3].
- (b) For prime coat on the embankment, the tack coat between layers, the seal coat (SL) on the impervious layer, and the protective coating or layer (PT) special grades of asphalt or asphaltic emulsion, varying in penetration from 100 to 40 are used [5].

Table 29.1 Critical temperature related to asphaltic concrete [6]

Field Activity	Asphalt viscosity (Poises)	Temperature Low Viscosity Asphalt °C	Temperature High Viscosity Asphalt °C (°F)
Mixing	1	165	178
Start rolling	10	155 110	170 125
Stop rolling	100	80	95

- (c) The density of aggregate in the impervious layer, should ranges from 2.1 to 2.5 tones/m³ [1].
- (d) Permeability’s of the various layers vary from impervious (10⁻⁷–10⁻⁹ cm/sec, and lower) for the core [1].
- (e) The compaction of the mix generally should take place when the viscosity of asphalt in the mix ranges between 1 and 10 poise [1].
- (f) The critical temperatures depend on the viscosity of the asphalt. The Table 29.1 given below shows critical temperature related to asphaltic concrete [6]:

The temperature of the binder at the time of mixing should be in the range of 150–165 °C and of aggregates in the range of 150–170 °C, provided that at no time the difference in temperature between aggregate and binder should exceed 14 °C.

Design Principle

The thin asphaltic concrete core has to adjust to the deformations in the embankment and to differential displacements in the dam foundation [4]. Displacements accumulate during embankment construction, filling of reservoir, time-dependent consolidation and creep, fluctuations in reservoir level and any earthquake shaking or fault movements. The essential function of the core is to remain impervious without any significant increase in permeability due to shear dilatancy or cracking. ICOLD has given following guidelines in the field of design principles:

- (a) The asphaltic concrete core is constructed at simultaneous levels with the dam fill [1].
- (b) Dams’ height over 30 m in height, the core thickness should be between 60 and 100 cm, depending on dam height [3].
- (c) Grain sizes from filler, sand and chipping/gravel should lie between 0 and 16 mm [5].
- (d) The bitumen (asphalt) content of mix should be 6% approx. (by weight), the mix is easy to place and compact to a void’s percentage of below 3% (by volume) [3]. With this void content, the asphaltic concrete is impervious even under high water pressure. However, from other studies in design of asphalt concrete of embankment dams using the highest amount of bitumen for reaching the

flexibility against seismic load, allowed that amount of bitumen should be 5.5–7% in water barrier asphaltic concrete. Also, the amount of bitumen to reach flexibility during the earthquake and after that suggested 6.5–7% [4, 7].

- (e) The transition zones installed on the upstream and downstream sides of the asphaltic concrete core should be 1–2 m and comprise graded hard rock material with a maximum grain size of 100 mm, although dams with well graded transition material have been built with a max aggregate size of 200 mm [3]. For implementing the self-healing of possible leakage points in the core, the upstream transition zones can receive an appropriate fine grain admix, which also helps in considerable reduction in the volume of water inflow at a defect. The upstream transition zone should also be designed in such a way that it is possible to introduce pipes into it to allow supplementary sealing at a later date by injecting bentonite or clay if any leakage occurs [1].
- (f) The compaction of the transition zone and hot plastic asphaltic concrete core should be intensive for close interlocking of both construction material. As a result of which asphaltic concrete core will not deform differentially from the transition zone [1].
- (g) For a dam with a height of up to 60 m, the core is usually carried out as vertical throughout. For higher dam and in order to increase the statically effective cross-section of the dam, core can be arranged nearer to upstream side or can be slightly inclined toward the downstream side in the upper side. This reduces the danger of the upstream embankment becoming detached from the core in the detached area [3].
- (h) For hydraulic structures, asphaltic concrete is taken as water tight as long as its void content **does not exceed 3% (by volume)** [3]. However, this threshold value must be maintained not only after installation but also under all possible stress/strain and deformation states during operation of the dam.

Typical cross-section of Storglomvatn, Norway dam are shown in Fig. 29.2.

Construction Methods

Production

In design of asphaltic cores, it must be remembered that pure bitumen behaves like a liquid in the long-term, and will flow out of the core unless prevented by certain measures. For this reason, bitumen is mixed with various sized aggregate in different proportions to give a combined skeleton with sufficient capacity to avoid being over-filled with bitumen. Adhesion forces between the bitumen and the aggregate prevent the binder flowing out, and it can be proved by calculations that for a well-graded bituminous concrete the possible rate at which the binder can extrude is 1 cm per million years [1].

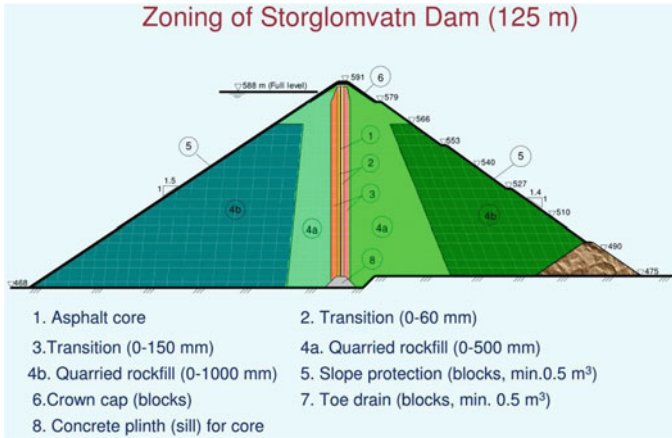


Fig. 29.2 Typical cross-section of Storglomvatn Dam (125 m), Norway [4]



Fig. 29.3 Modern asphalt concrete plant [8]

Asphaltic Concrete Plant

A reliable batch plant with a capacity of 50–60 tons an hour is normally sufficient having a minimum of 4 hot aggregate storage bins, and a data printout of all weights per batch [8]. An arrangement for adding filler in the mix is also attached in the plant. Figure 29.3 depicts the images of different asphalt concrete plant;

Spreading

The paving equipment shown in Fig. 29.4 places asphaltic concrete and filter simultaneously in 20 cm horizontal layers. The machine is a hydraulically driven crawler paver, and the widths of the core and filter screeds are adjusted according to the design specifications. The speed of the paver should be 1 m/min [4].



Fig. 29.4 Asphalt core placing machine (paver) [4]



Fig. 29.5 Simultaneous compaction of core and filter [4]

Compaction

Asphaltic concrete and filter are compacted by three vibrating rollers of 1.5–2.5 tons working in parallel as depicts in Fig. 29.5.

Joint Treatment

Treatment of joint is one of the vital activities for water tightness of the facing. The main challenge which comes during execution is to cut the uncompacted a layer on edges or before laying adjacent layer as it is mandatory for water tight joints.

Test Methods

Tests on Mixes

Marshall test for the mix is one of the main tests for finding suitability of mix. Marshall test includes (i) stability, (ii) flow, (iii) percent air voids, (iv) percent void in mineral aggregate, and (v) percent voids filled with bitumen. The other tests are density, permeability, unconfined compressive test at various temperature, triaxial

test, flow test on slope, frost and temperature change resistance, aging, flexibility, creep etc.

Triaxial Test

For higher dams it is recommended that in every case the core and supporting shells material should also be given triaxial tests [1]. Stress–strain–strength tests were performed on 100 mm diameter samples drilled out of the asphalt core during construction. The results from strain-controlled compression triaxial tests, keeping the lateral confining stress constant during each test, as shown in Fig. 29.6. The stress–strain curves show a very ductile asphalt concrete behavior with insignificant strain-softening even for tests with very low confining stress [2].

Apart from the stability and deformability of the bituminous concrete core, placing of core material in clean surface, sufficient and uniform compaction must be ensured.

Figure 29.7 depicts typical image of asphaltic core concrete.

Fig. 29.6 Triaxial compression test, 100 mm diameter Yele Dam core [2]

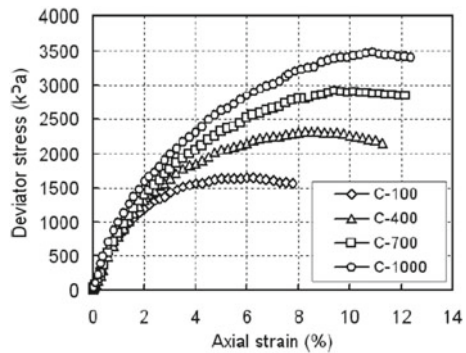


Fig. 29.7 Typical image of asphaltic core concrete [8]

Asphalt Concrete Core Versus Clay Core

Relative Performance Evaluation

Nuresa Merga Bayisa, [9] tells that use of asphaltic concrete core in rock fill embankment dam gives satisfactory results from safety, seepage control and monitoring induced deformation point of view and used Plaxis 8.5, finite element-based software was employed for analysis of the dam as well as Geostudio 2012 for seepage analysis. The following comparison have been made in above study:

Seepage Analysis: Seepage records higher percentage of dam failure in embankment dam [9]. Figure 29.8 depicts flux reading through asphalt core:

The result of flux reading shown in the above figure (0 m³/sec) is obtained in the core section of the dam and this is justifying the fact that asphalt concrete core is impervious. Many researchers Alicescu, Wang and Hoeg, Veidekke, and Hoeg [7, 8, 10] also confirmed zero seepage in asphaltic concrete core. Further, stability analysis of dam during different loading conditions analyzed by Nuresa Merga Bayisa [9] are presented in Table 29.2:

Again, Zomorodian et al. [11] has given following comparisons and are shown in Table 29.3:

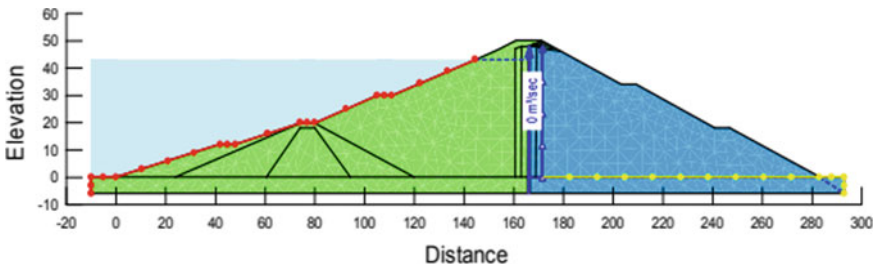


Fig. 29.8 Flux reading through asphalt core. Source Geostudio 2012 [9]

Table 29.2 Stability analysis during different loading conditions [9]

SL	Loading conditions/displacement	Asphaltic concrete core dam	Clay core dam
1	During construction factor of safety	1.638	1.618
2	Steady state factor of safety	1.661	1.446
3	End of construction	No Pore water pressure development in core	Pore water pressure developed in core
4	Vertical displacement	0.59562 m	0.59562 m
5	Horizontal displacement	87.20×10^{-3} m	385.98×10^{-3} m

Table 29.3 Stability analysis during different loading conditions [11]:

SL	Loading conditions/displacement	Asphaltic concrete core dam	Clay core dam
1	Seepage qty	26 L/sec	42 L/sec
2	During construction factor of safety	1.41	1.16
3	Steady state during full reservoir factor of safety	1.5	1.26
4	Rapid drawdown/earthquake factor of safety	1.5	1.26

Therefore, from stability point of view, the result of analysis obtained from the two dam shows that due to flexible and visco-elastic nature of the asphalt core, use of asphalt concrete core is better alternative.

Field Values of Seepage as Well as Displacement Values of Dams

The Result of seepage analysis of some of the earthen/rock fill embankment dam are given in Table 29.4 [3]:

Again, Table 29.5 reflects the performance in terms of vertical and horizontal displacement for some of the earthen/rock fill asphaltic core dam [1]

Table 29.4 Seepage analysis of some of the asphaltic concrete core dam [3]

SL	Description of dam	Seepage	Remarks
1	Yele Dam, China Max. height = 124.5 m Crest length = 411.0 m Total vol. = 6,200,000 m ³	277 L/sec, at full supply level	Anticipated design seepage at full supply level = 500 L/sec
2	Storvatn Dam, Norway Max. height = 90.0 m, Crest length = 1472 m Total vol. = 9.5 mill. m ³	At maximum reservoir level = 10 l/s	However, part of this comes from under seepage and from the abutments, so the leakage through the core is even smaller
3	Megget Dam, Scotland Max. height = 56.0 m, Crest length = 568.0 m Core wall = 20,000 m ²	1.61 l/s	Largest earthen dam in Scotland

Table 29.5 Performance in terms of vertical and horizontal displacement for some of the earthen/rock fill asphaltic core dam are given [1]

SL No	Description of Dam	Displacement	Remarks
1	Storvatn Dam, Norway Max. Height = 90.0 m, Crest Length = 1472 m	= 165 mm at center of core or 0.18% of dam height Maximum embankment displacement (inside downstream shell at mid height) = 580 mm (520 mm vertically and 206 mm horizontally)	Maximum settlement of core 5 years after end of construction
2	Berdalsvatn Dam, Norway Max. Height = 65.0 m, Crest Length = 465 m Total Vol. = 1.0 mill. m ³	= 70 mm at center of core or 0.1% of dam height	Maximum settlement of core 3 years after end of construction
3	Styggevatn Dam, Norway Max. Height = 52.0 m, Crest Length = 880.0 m Total Vol. = 2.5 mill. m ³ Core wall = 79,000 m ²	= 35 mm at center of core The maximum displacements are 67 mm vertically and 68 mm horizontally at about Mid height of the downstream slope	Maximum settlement of core 1 year after end of construction

(continued)

Table 29.5 (continued)

SL No	Description of Dam	Displacement	Remarks
4	Riskallvatn Dam, Norway Max. Height = 45.0 m, Crest Length = 600.0 m Total Vol. = 1.1 mill. m ³	The maximum vertical settlement recorded at the top of the core = 45 mm or 0.1% of the dam height	6 years after end of construction

Conclusion

- (a) In terms of safety, seepage control and monitoring induced deformation, it has been seen worldwide that using asphaltic concrete core in rock fill embankment gives good result in comparison with clay core.
- (b) From the above review, it is understood that the optimum binder content for reaching flexibility during the earthquake and after that is 6.5–7%.
- (c) The air void content should not exceed 3% (by volume) for asphaltic concrete to be water tight.
- (d) Use of asphaltic concrete core reduces piping and internal erosion in core significantly, as a result probability for earthen dam failure also reduces.
- (e) Under significant loading condition of steady state, upstream water pressure and its distribution in embankment material highly reduces the safety factor of clay core dam. By introducing asphalt concrete core in the dam, a reasonable minimum safety factor requirement has been attained, which satisfy the USACE recommendation. It also gives good result of safety factor for other loading condition [6].
- (f) Use of asphaltic concrete core improve factor of safety for all the condition of stability analysis of earthen/rock fill dam, i.e., end of construction, steady state seepage, and rapid draw down.
- (g) Self-healing and flexible nature of asphaltic concrete core reduces piping phenomenon in core, as a result settlement and induced deformation of core also reduces.
- (h) In the high temperature region, the asphalt concrete core as water barrier has more concern. However, polymer modified bitumen may be used in in-lieu of normal bitumen as it increases softening point of bitumen.
- (i) From the above review it is found that Marshall Stability test is one of the most important tests for evaluating stability and deformation of asphaltic core of earthen/rock fill embankment dam. For **higher dams** it is recommended that in every case the core and supporting shells material should also be given **triaxial tests**.

Figure 29.9 depicts **Storglomvatn Dam (125 m), Norway**.



Fig. 29.9 Storglomvatn Dam (125 m), Norway [8]

References

1. ICOLD 42: Bituminous cores for Earth and Rockfill Dam
2. Wang W, Höeg K, Zhang Y (2010) Design and performance of the Yele asphalt-core rockfill dam. *Can Geotech J* 47:1365–1381
3. ICOLD 84: Bituminous cores for fill dams
4. Höeg K (1993) Asphaltic concrete cores for embankment dams. Experience and practice. Norwegian Geotechnical Institute
5. ICOLD 32 a: Bituminous concrete facings for earth and Rockfill dams
6. United States Society on Dams Materials for Embankment Dams January 2011, Prepared by the USSD Committee on Materials for Embankment Dams
7. Veidekke (n.d) Asphalt core dams. NGI, Oslo
8. Wang W, Höeg K (2009) The asphalt core embankment dam: a very competitive alternative. Norwegian Geotechnical Institute NGI. Norwegian Geotechnical Institute (NGI), Chengdu, China, p 1
9. NM Bayisa (2019) Relative performance evaluation of asphaltic concrete core embankment dam and clay core embankment dam: by plaxis software application, *Am J Sci Eng Technol* 4(1):18–29. Department of Hydraulic and Water Resources Engineering, College of Engineering and Technology, Bule Hora University, Bule Hora, Ethiopia
10. Alicescu V (2010) Design and construction of Nemiscau-1 Dam. Canadian Dam Association, Ottawa
11. Zomorodian SMA, Charrakh M, Heidarpour M (2005) A comparison of asphaltic concrete core dams and asphaltic lining dams with clay core dams. *EJGE*

Chapter 30

Construction of Diaphragm Wall for Seawater Intake Pump House



B. Govind Raj, Madan Kumar Annam, and Bairagi Kondapalli

Introduction

The embedded retention wall systems offer constructive solutions for underground structures in crowded areas or at complex locations where deep excavation is required. Of all the embedded retaining walls, diaphragm walls are the most widely used technique when it comes to the water tightness. Diaphragm wall can be designed into a single foundation unit to address temporary shoring, permanent basement walls, hydraulic contained structures, and vertical support elements. They are proven to be an economical alternative in many circumstances because of multipurpose application [1].

A 18.5 m deep excavation below existing ground was necessitated in West Coast of India for building sea water intake structure. The intake structure is located about 200 m away from the coastline on shore. The presence of high-water table, variations in tides and deep excavation demands usage of diaphragm wall construction.

This paper illustrates various considerations of design and execution phases of construction of diaphragm wall. Also, impact of various analysis methods, influence of water table, over dig and drained and undrained behavior of soil on performance of the retention system is covered.

B. Govind Raj (✉)

Keller Ground Engineering India Pvt. Ltd., Mumbai 400059, India

e-mail: govind@kellerindia.com

M. K. Annam

Keller Ground Engineering India Pvt. Ltd., Chennai 600024, India

B. Kondapalli

L&T Construction, Chennai 600089, India

Site Conditions

A desalination plant was proposed to cater growing water requirement of the region. Project specifications demands watertight condition for the Sump of Pump House.

Subsoil Environment

Two boreholes were explored to 40 m deep below the existing ground level (EGL). The average ground elevation of site was around + 9.50 RL. The subsoil consists of stiff to very stiff clay of varying consistency up to -12.50 RL followed by very dense sand or sand with presence of fines having low plasticity. Ground water table was observed to be 2–3 m below EGL at the time of soil investigation (Fig. 30.1).

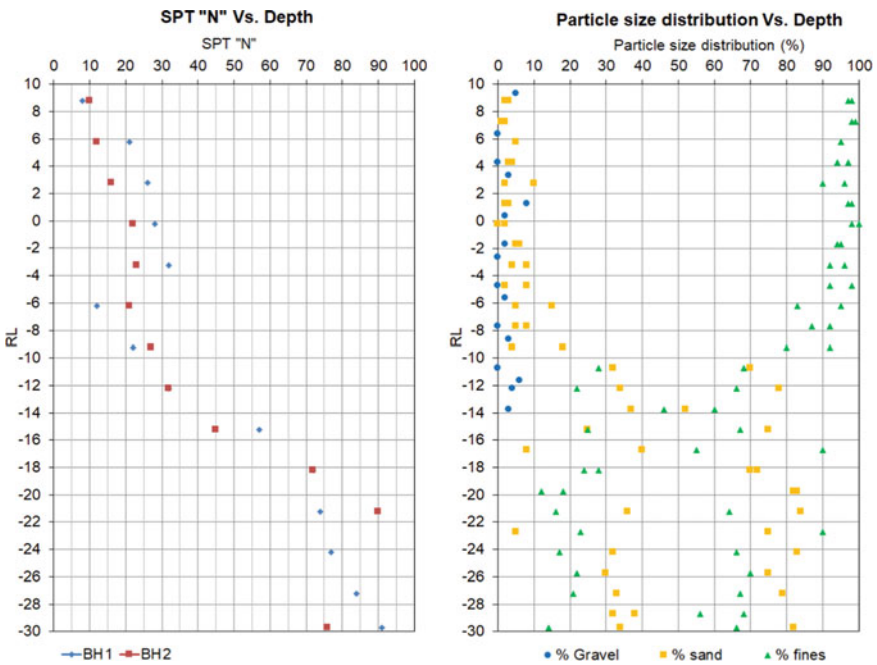


Fig. 30.1 Plot showing SPT-N, grain size distribution versus depth

Numerical Analysis

Retention system of optimized diaphragm wall thickness of 1.20 m supported by 4 levels of intermediate supports, raft at excavation level and an RCC beam on top was considered for analysis (Ref Fig. 30.2).

Effect of Analysis Method

Common analyses methods such as Limit Equilibrium Method, Subgrade Reaction Method, and Finite Element Method were used to estimate forces on wall, deflections, and prop forces [2]. They relied on the limiting earth pressure coefficients, beam and spring approach and breaking of the structure into the finite elements, respectively. Results of analyses are presented in Table 30.1 (Fig. 30.3).

Results of analyses suggest that use of limit equilibrium methods shall be made with caution as it ignores the soil structure interaction and consider struts/anchors as support point only. At the same time, the Subgrade Reaction Methods and the Finite Element Methods shows reasonable agreement between the values [3].

Fig. 30.2 Typical retaining wall section

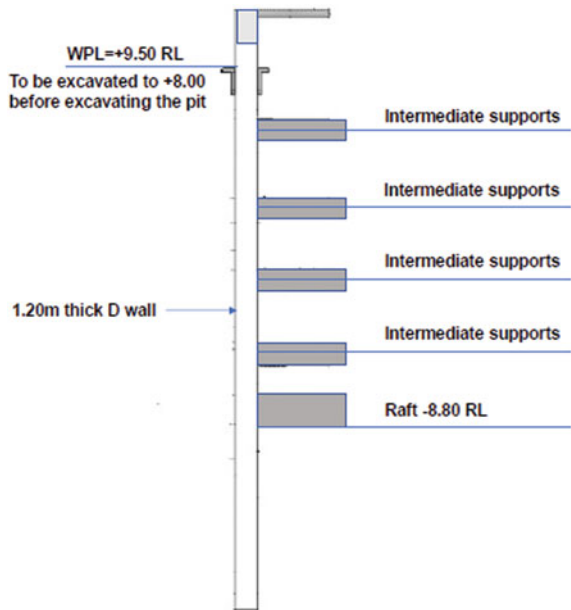


Table 30.1 Comparison of results of various methods of analyses

Item	Equilibrium method	Subgrade reaction method	Finite element method
SLS bending moment kNm/m	1652	2486	2270
SLS shear force (kN/m)	677	738	686
SLS prop force (kN/m)	990	806	726
Deflection (mm)	–	43	54

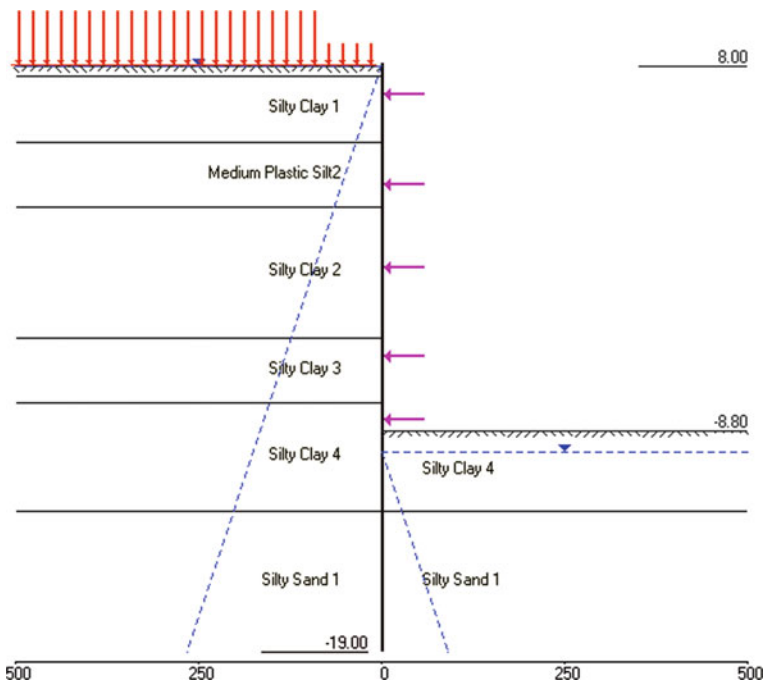


Fig. 30.3 Typical wallap model (subgrade reaction approach)

Effect of Water Table

There is seasonal variation in water table observed across the project site. Ground water table at + 8.00 m RL was considered for analysis. An exercise was carried out to assess influence of varying water table over bending moment. It is found that

Table 30.2 Comparison of results, drained versus undrained cases

Item	Drained analysis	Undrained analysis
SLS bending moment (kNm/m)	2486	1780
SLS shear force (kN/m)	738	603
Deflection (mm)	43	30

water table levels are playing major impact on the behavior of the retention wall. About 3 m raise in water table resulted in 12% increase in bending moment.

Effect of Over Dig

Over dig due to improper construction practices can play a major role in the performance of wall. Parametric study considering an over excavation of 1.0 m suggests an increase of 6% in wall bending moment.

Effect of Drained/Undrained Analysis

The distinction between drained/undrained analysis is very important in a retaining wall design. Exposure of pit for long time will eventually lead to the instability of wall, if it is designed only for undrained cases. Effect of drained and undrained conditions are presented in Table 30.2.

Embedment Depth of Multi Propped Walls

Multi propped walls are statically indeterminate structures. Often, the embedment checks are ignored considering the stability offered by multiple supports. Toe movements indicates a good prediction of the stability of a wall. Toe movements are calculated in both service conditions and under the Ultimate ULS DA1 (combination of Eurocode 7) and are observed to be 20 mm and 119 mm, respectively. The toe movement in ULS stage is found to be lower than Wall Height/200 criteria (allowable deflection considered for the service limits).

Execution Challenges

Working Platform Stability

The ground conditions necessitated a stable platform for the safe maneuver of construction equipment. A maximum load intensity of 15–18 t/m² was considered on the ground due to construction machinery movement. A granular layer of 750 mm thick was proposed as working platform considering weak nature the subsurface soil and varying ground water conditions. Stability calculations were in accordance with “BRE470: Working platforms for tracked plant” guidelines [4]. In addition, usage of steel plates was suggested during the monsoon, for additional safety.

Working Platform Level

Average ground level of the site is about + 9.50 m RL. Calculations showed that the panels are subjected to high stresses/bending moments when excavation is done from the existing ground level. In order to optimize bending moment and depth of wall, pre-excavation to + 8.00 m RL is proposed. This resulted in cost saving of 10%. However, pre-excavation to + 8.00 m RL create concerns for the working platform stability and for the movement of vehicles during the panel construction stage. To avoid this, the panel construction was initiated from + 9.50 m RL, however before starting pit excavation, ground levels outside the pit are brought down to + 8.00 m RL.

Cage Stability

The maximum cage weight for a single panel was estimated to be 35 tons and it was decided to lift in single cage which was fabricated on ground. Cage lifting plan for the “critical lift” was worked out satisfying safe lifting practices. Two cranes were used during cage lifting operations (see Fig. 30.4). Steel plates were also used under the crawlers for more stability.

Conclusions

Results from analyses of diaphragm wall is compared by focusing various methods. It is observed that the Subgrade and Finite Element Analysis shows similar results for deeper multi anchored/strutted walls. However, Limit Equilibrium Method indicated considerable difference in bending moments and prop loads. The negligence

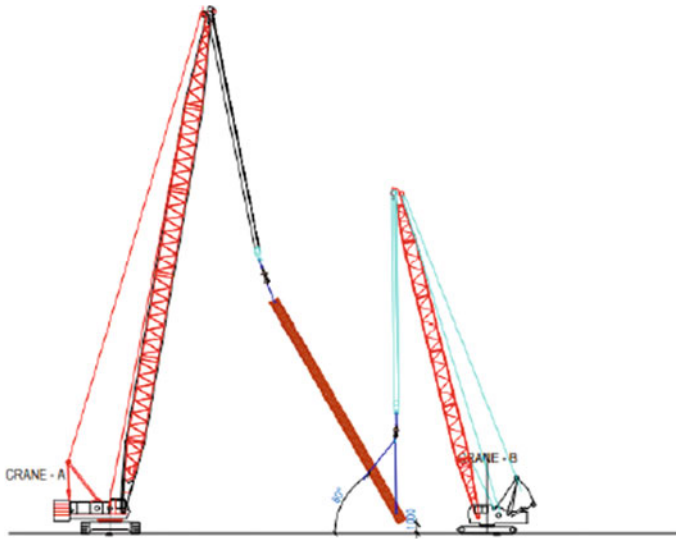


Fig. 30.4 Lifting of reinforcement cage in single lift

of soil structure interaction grossly underestimated the structural loads in the Limit Equilibrium method.

It is observed that drained/undrained nature of the soil plays a major role in the performance of the wall. The bending moments showed considerable increase when the analysis shifted from undrained to drained. Hence, behavior of the wall shall be analyzed for both drained and undrained conditions especially when clayey soils are encountered.

Multi propped walls are statically indeterminate, and the embedment requirements are often under looked by considering it as a stable configuration. The present study suggests that the toe movements can be effectively used as a tool to decide the embedment of the multi propped walls. The toe movements in both service and ultimate load cases (Ultimate ULS DA1 combination of Eurocode 7 in the present case) need to be assessed and compared with the movements required for the mobilization of passive resistance.

References

1. Pearlman SL, Walker MP, Boscardin MD (2004) Deep underground basements for major urban building construction. ASCE Geo-Support
2. CIRIA C760 (2017) Guidance on embedded retaining wall design
3. Raj G, Kumar K (2020) Embedded retention wall design practices, consequences and measures. In: Indian geotechnical conference
4. BRE470: Working platforms for tracked plant guidelines

Chapter 31

Seismic Stability of Reinforced Soil Wall Using Horizontal Slice Method: Effect of Surcharge on Cohesive-Frictional Soils



M. C. Venkatasubbaiah and G. V. Narasimhareddy

Introduction

The fundamental theories for the design of RE walls depended on rankine's/coulomb. Further, the coulomb's hypothesis was extended and elaborated the seismic acceleration for cohesionless soil using the pseudo-static methodology [1, 2]. The Mononobe-Okabe theory was incorporates soil having a combined effect of cohesion and friction [3]. The conventional method of slope stability was to verify slope failure is a vertical slice procedure. Shahgholi et al. [4] introduced the horizontal slice approach, and the seismic stability was elaborated [5]. Nouri et al. [6] estimated the tensile force required to maintain the stability of the reinforced wall. The geosynthetic vertical wall is analyzed, followed by pseudo-static and pseudo-dynamic solution subjected to transverse pull [7].

The cohesive-frictional soils are adopted in various locations over the universe for monetary motive, and few kinds of literatures are available in static solution. The value of cohesion and surcharge under seismic loading for the reinforced soil was analyzed using HSM [8]. Ghose and Debnath [9] examine the horizontal (H_i) and vertical (V_i) magnitude of the forces, and the reliable relation is assumed as under [10]:

$$H_i = \lambda \cdot f_i \cdot V_i \quad (31.1)$$

M. C. Venkatasubbaiah (✉) · G. V. Narasimhareddy
Department of Civil Engineering, JNTUH, Kukatpally, Hyderabad 500085, Telangana, India

G. V. Narasimhareddy
e-mail: gvnreddy@jntuh.ac.in

As indicated by [11] is an improvement over the above study, and the yield strength is a constant value of shear (H_i) is a constant fraction of the shear strength, and this coefficient for each slice is average shear stress along with each slice. This coefficient (λ_i) is always less than unity, written as

$$H_i = [V_i \tan \phi + C] \lambda_i \quad (31.2)$$

The utilization of poor backfill ($\phi < 30^\circ$) and higher ranges of seismic coefficients ($k_h > 0.20$) require the higher resistive forces and reinforcement length for the stability [12]. Soil friction angle is an important parameter on the strength of inextensible sheet; with the increase of friction angle, the normalized reinforcement strength decreases with the different horizontal seismic coefficients for inclined a vertical earth structures. The influence of ϕ is bigger for greater values of K_h [13]. The use of cohesive soils with $\phi < 30^\circ$ and the values of $K_h > 0.2$ necessitate the increase of reinforcement length and higher factor of safety to maintain the stability of soil structure [5].

The current investigation focused on vertical reinforced soil with c - ϕ backfill, the horizontal slice concept proposed by [6] adopted, and the limit equilibrium strategy utilized to the pseudo-static approach with sheet reinforcement undergoes transverse pull under kinematics of failure. In any case, no investigation is available on the impact of cohesion and surcharge. The proposed technique depends on the extension of the strategy [7] and linear backfill response due to transverse pull. On this observation, the solution is analyzed in MATLAB Program to evaluate the variation in wall geometry, angle of internal friction, cohesion, seismic coefficients, and q on backfill.

Methodology

Figure 31.1 shows the wall supporting horizontal cohesive backfill of height, H , embedded with of length (L) reinforcement with unit weight (γ). The angle of internal friction (ϕ) and the interface friction between the sheet–soil (ϕ_r). The backfill is reinforced with ‘ n ’ no. of reinforcements and the vertical spacing in top and bottom most layers of $S_v/2$ and have equal spacing of S_v .

Figure 31.2 portrays the slice of horizontal reinforcement undergoing pull-out and the moving soil oblique to the aligned reinforcement. This oblique component gives extra normal stress, which gives additional stresses and relatively more pull-out.

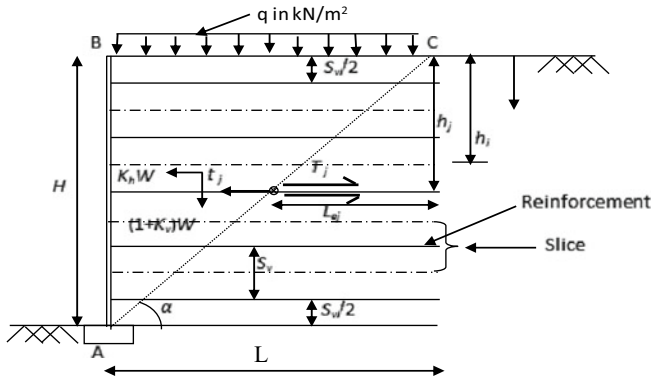


Fig. 31.1 Geometrical characteristics of RE Wall

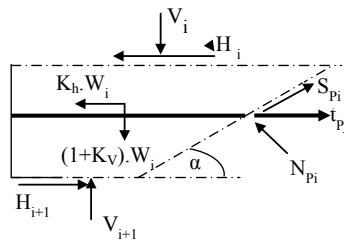


Fig. 31.2 Single slice with central reinforcement subjected to transverse pull

Assumption

- Vertical stress acting on a horizontal slice is assumed to be overburden pressure, $V_i = q \cdot L_a + \gamma \cdot h_i$ (for the vertical wall). Where L_a is the active length of reinforcement.
- The method is applies to homogeneous cohesive-frictional soils.
- The F.O.S (FS_r) is assumed to be equal to individual slices.
- The Shear force between each horizontal slice is considered to be $H_i = (V_i \tan \phi + C) \lambda_i$
- The surcharge load acting above the wall must be $q \cdot L_a$
- The length of failure i th slice is $b_i = \frac{H_i}{n \cdot \sin \alpha}$

Proposed Formulation

Tensile Force Due to Oblique Pull

The precise solution shows satisfying $\sum F_x, \sum F_y, \sum M$ equilibrium equations. The vertical equilibrium of the forces are;

$$\sum F_y = 0$$

$$V_{i+1} - V_i - [1 + K_v]W_i + S_i \sin \alpha + N_i \cos \alpha = 0 \tag{31.3}$$

where the interslice forces (V_i and V_{i+1}), weight (W_i), K_v is a vertical seismic coefficient, the failure angle (α). The shear force (S_i) is

$$S_i = \frac{Cb_i + N_i \tan \phi}{FS_{sr}} \tag{31.4}$$

where FS_{sr} is unity, $b_i = \frac{H_i}{n \cdot \sin \alpha}$ is the length of the base of the slice. Sub. For S_i from Eq. (31.4) into Eq. (31.3) and solving for normal force (N_i)

$$\bar{N}_i = \frac{V_i - V_{i+1} + (1 + k_v)W_i - \frac{C \cdot b_i \cdot \sin \alpha}{FS_{sr}}}{\frac{\tan \phi}{FS_{sr}} \cdot \sin \alpha + \cos \alpha} \tag{31.5}$$

$$\sum F_x = 0$$

$$\sum_{j=1}^m \bar{T}_j = \sum_{i=1}^n \bar{N}_i \sin \alpha - \sum_{i=1}^n \bar{S}_i \cos \alpha + \sum_{i=1}^n \bar{W}_i K_h + \bar{H}_i - \bar{H}_{i+1} \tag{31.6}$$

Sum of the tensile forces generated in the reinforcement considering mobilized transverse force determined by the Eq. (31.6), we get

$$\begin{aligned} \bar{N}_i \sin \alpha = & \left[\frac{\sin \alpha \cdot FS_{sr}}{\tan \phi \cdot \sin \alpha + FS_{sr} \cdot \cos \alpha} \right] [1 + K_v] \gamma h_i l_i - [1 + K_v] \gamma h_{i+1} l_{i+1} \\ & + [1 + K_v] \frac{\gamma H}{2n} [l_i + l_{i+1}] - \frac{CH}{n} \end{aligned}$$

$$\begin{aligned} \bar{S}_i \cos \alpha = & \left[\frac{\tan \phi \cdot \cos \alpha}{\tan \phi \cdot \sin \alpha + FS_{sr} \cdot \cos \alpha} \right] [1 + K_v] \gamma h_i l_i - [1 + K_v] \gamma h_{i+1} l_{i+1} \\ & + [1 + K_v] \frac{\gamma H}{2n} [l_i + l_{i+1}] - \frac{CH}{n \sin \alpha} \cdot \cot \phi \cdot \cos \alpha \end{aligned}$$

$$\begin{aligned} \bar{W}_i K_h &= \frac{\gamma H}{n} \left[\frac{l_i + l_{i+1}}{2} \right] K_h \\ \sum_{j=1}^m \bar{T}_{Tj} &= \left[\frac{\tan \theta_r}{n} \left[\frac{L}{H} \right] - \frac{\tan \theta_r}{n} \tan[90 - \alpha] \right] \sum_{j=1}^m [2 + P_j^*] \left[j - \frac{1}{2} \right] \\ &+ \left[\frac{2 \tan \theta_r}{n^2} \tan[90 - \alpha] \right] \sum_{j=1}^m [2 + P_j^*] \left[j - \frac{1}{2} \right]^2 \end{aligned} \quad (31.7)$$

$$\begin{aligned} \sum_{j=1}^m \bar{P}_j &= \left[\frac{1}{n} \left[\frac{L}{H} \right] - \frac{1}{n} \tan[90 - \alpha] \right] \sum_{j=1}^m P_j^* \left[j - \frac{1}{2} \right] \\ &+ \left[\frac{1}{n^2} \tan[90 - \alpha] \right] \sum_{j=1}^m P_j^* \left[j - \frac{1}{2} \right]^2 \end{aligned} \quad (31.8)$$

$$P^* = \mu_j \frac{W_L}{L_{ej}} \frac{1}{n_e} \left[\frac{W_{i+1}}{2} + \sum_{k=2}^n W_k \right] \quad (31.9)$$

$$W_k = \frac{T_i^* n_e^2 [W_{k-1} + W_{k+1}]}{\left[2n_e^2 T_k^* + \frac{\mu_j}{2 \tan \theta_r} \right]} \quad (31.10)$$

$$T_{k+1}^* = \frac{1}{2n_e} \left[\mu_j W_k \frac{W_L}{L_{ej}} + 2 \right] + T_k^* \quad (31.11)$$

The inextensible reinforcements are divided into sub elements (n_e), the normalized displacement, and tension at node k (W_k and T_k^*). Based on Eq. (31.9), the normalized transverse force (P^*) for a single reinforcement assuming linear backfill response utilizing local factors μ_j and W_L/L_{ej} expressed as follows. The inextensible reinforcement normalized to a parameter K [dimensionless], which is equivalent to the earth pressure coefficient [8]

$$K = \frac{\sum_{i=1}^n \bar{t}_{pj}}{0.5\gamma H^2} \quad (31.12)$$

Incorporating the local normalized displacements & relative stiffness factors and from Eqs. (31.12) and (31.13), the normalized transverse force is determined from Eq. (31.7) considering linear backfill response. The factor of safety due to transverse pull [component of oblique] from Eq. (31.15) is as follows (Table 31.1);

$$\mu_j = \mu \frac{\left[\frac{L_{ej}}{L} \right]}{\left[\frac{h_j}{H} \right]} \quad (31.13)$$

Table 31.1 Backfill properties of the wall

Parameters	Description	Values
γ	Backfill unit weight (kN/m ³)	18
H	Vertical reinforced wall (m)	5
L/H	Normalized length of reinforcement	0.5
m	Reinforcement layers	5
n	No. of horizontal slices	5
μ	Stiffness of backfill	50, 200, 2000, 5000, 10,000
W_L	Normalized displacement	0.001,0.0025,0.0005,0.0075,0.01
ϕ	Angle of shearing resistance	20°, 25°, 30°, 35°, 40° and 45°
ϕ_r/ϕ	Normalized angle of interface friction	2/3
K_h	Horizontal seismic acceleration	0, 0.2, 0.4, 0.6, 0.8 and 1.0
K_v/K_h	Normalized seismic coefficient	0.5
C	Cohesion (kN/m ²)	0, 5, 10, 15
q	Surcharge load (kN/m ²)	0, 25, 50

$$\frac{w_L}{L_{ej}} = \frac{w_l}{L} \frac{1}{\left[L_{ej}/L \right]} \tag{31.14}$$

$$FS_T = \frac{\sum_{j=1}^m \bar{T}_{Tj}}{\sum_{j=1}^m \bar{t}_j} \tag{31.15}$$

Results and Discussion

Variation in FOS (FS_T) with an Angle of Friction of Soil (Φ)

The F.O.S (FS_T) on angle of internal friction $\phi = 30^\circ, 35^\circ, 40^\circ, 45^\circ$ with $K_h = 0, 0.2, 0.4, 0.6, 0.8, 1.0$ shown in Fig. 31.3. In the present analysis, as ϕ increase from 30° to 45° , the angle of the failure plane with horizontal increases due to the reduction in soil pressure on the wall. The reinforcement strength to maintain the stability of the wall is the same as earth pressure. The factor of safety due to oblique pull-out (FS_T from 2 to 3.51) increases with an increase of ϕ for $K_h = 0$.

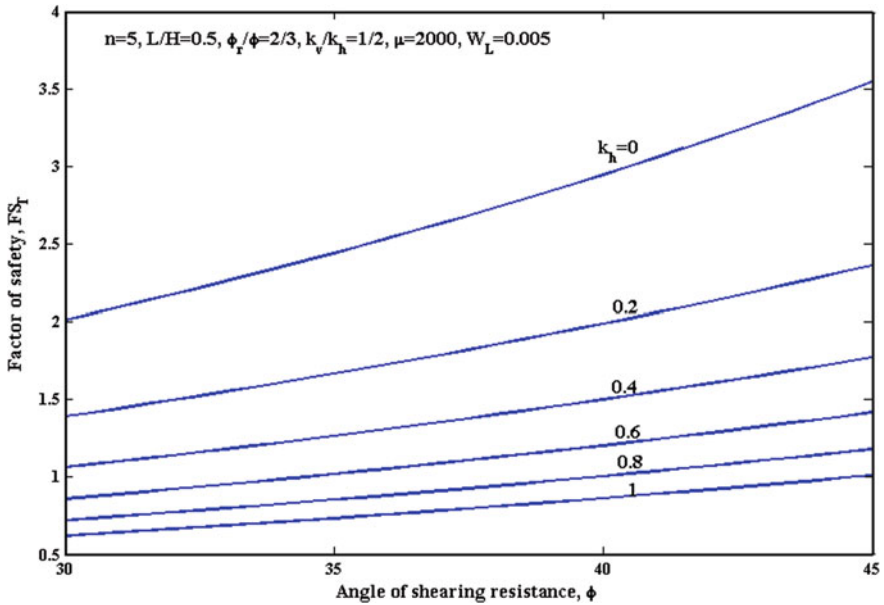


Fig. 31.3 Variation of FS_T w.r.t ϕ

Effect of Stiffness of Backfill

The transverse displacement to the soil stiffness for various seismic coefficients (K_h), shown in Fig. 31.4. For $n = 5$, $L/H = 0.5$, $\phi = 30^\circ$, $\phi_r/\phi = 2/3$, $K_v/k_h = 0.5$, $W_L = 0.005$, and $q = 50 \text{ kN/m}^2$. Due to the backfill surcharge and cohesion, the factor of safety due to transverse displacement and increases with an increase in soil stiffness for low values of seismic coefficients. According to Motlagh et al. [12], for $K_h > 0.2$, provide the higher length of reinforcement and shear resistance to increase the factor of safety due to normalized displacement. FS_T increases by 116% for $K_h = 0$, $q = 50 \text{ kN/m}^2$, $c = 0$ with an increase in subgrade stiffness from 50 to 10,000. The increases in FS_T is 60% for $K_h = 0$, $q = 50 \text{ kN/m}^2$, $c = 5 \text{ kN/m}^2$ for corresponding values of μ . The Cohesion of backfill increases from $c = 0$ to 5 kN/m^2 with an increase in FS_T from 1.2 to 5.0 due to surcharge conditions. Hence, the scope for increased in tension of the reinforcement with the stiffness of C- ϕ soil is more.

Variation in FS_T with K_h

The effect of L/H ratio on safety considering transverse pull on K_h is shown in Fig. 31.5. Due to transverse pull, the F.O.S decreases with K_h increases ($L/H = 0.3, 0.4, 0.5, 0.6$). The rise in FS_T with an increase in length due to additional shear with

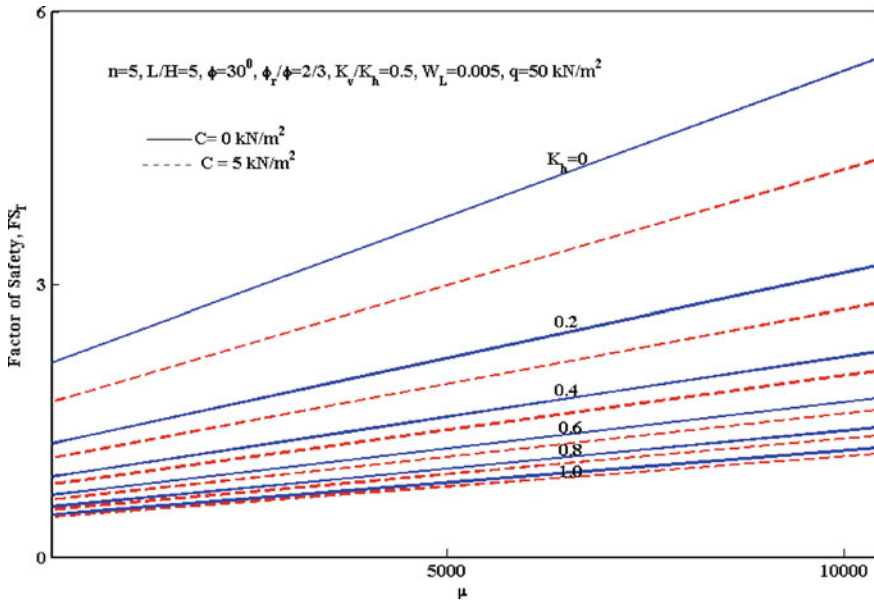


Fig. 31.4 Variation of backfill stiffness (μ) with F.O.S (FS_T)

transverse pull. Hence, the influence of additional transverse pull is very effective for a larger range of K_h .

Effect of No. Of Reinforcements (N) on FS_T

Figure 31.6 elaborates on F.O.S with the transverse force (FS_T) increase in no. of layers for $K_h = 0-1.0$. FS_T decreases nonlinearly with the increase in k_h ($= 0-1.0$) and no. of reinforcement layers in the $c-\phi$ soil. The difference between cohesion $C = 0$ and 15 kN/m^2 increases inversely proportionately w.r.t number of reinforcement layers from 3 to 9 because of additional shear resistance increase with the transverse pull; hence reinforcement opposes the failure within FS_T . Therefore, the mobilized transverse pull is more significant for static case ($K_h = 0$) as compared to dynamic seismic coefficient ($K_h > 0$) with no. of reinforcement layers.

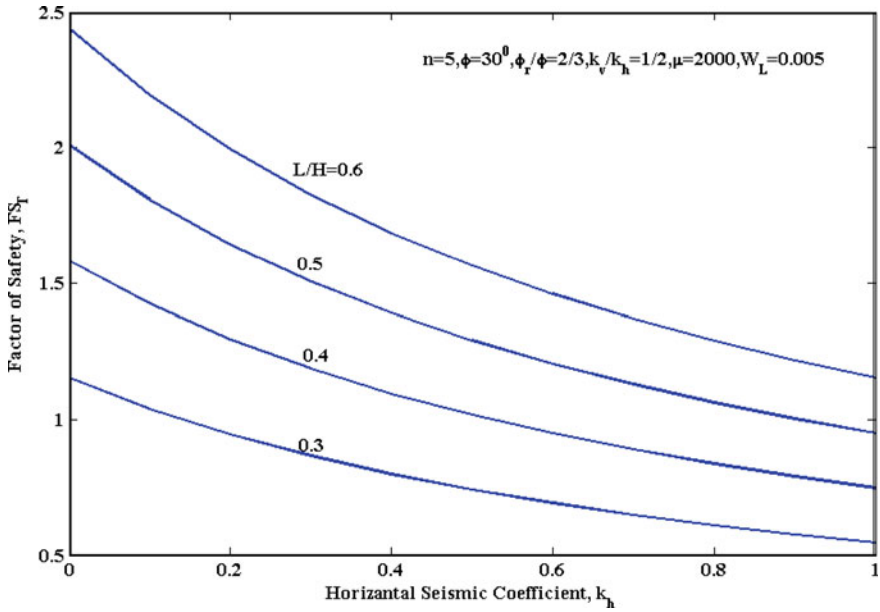


Fig. 31.5 Variation in K_h w.r.t F.O.S (FS_T)

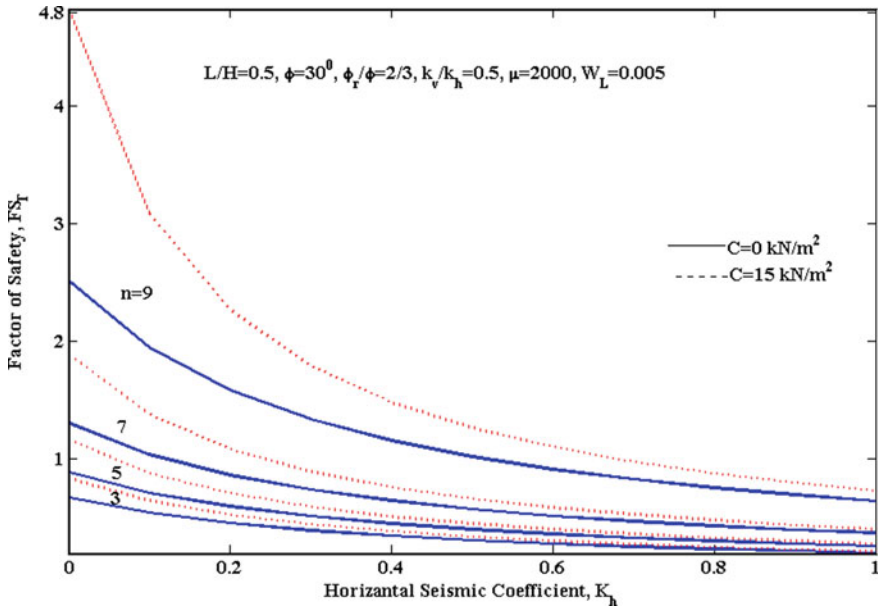


Fig. 31.6 Variation in K_h with F.O.S (FS_T)

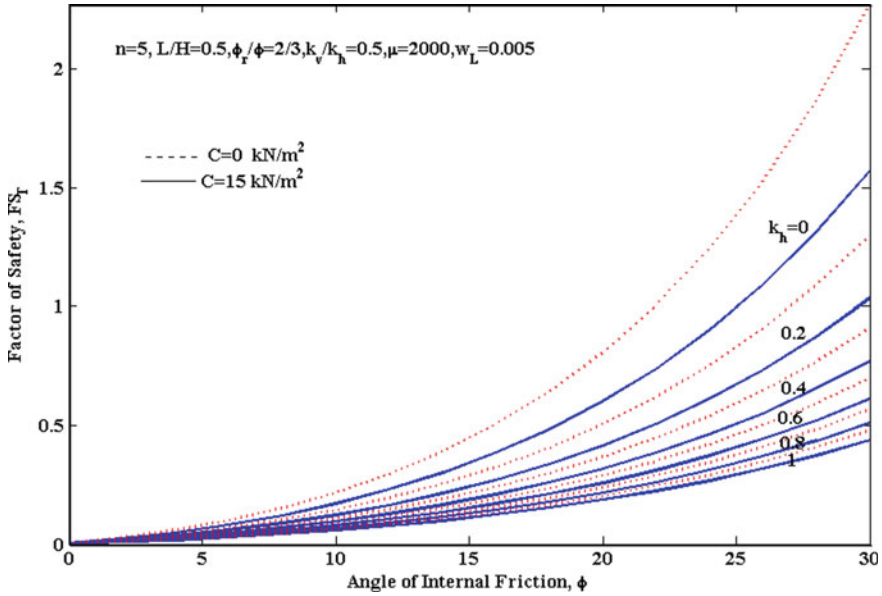


Fig. 31.7 Variation of the angle of internal friction with the factor of safety

Effect of K_h with Cohesion on Various Horizontal Seismic Coefficients

The effect of friction on the transverse pull, the cohesion of soil under seismic coefficient is shown in Fig. 31.7. The influence of FS_T with cohesion C on various horizontal seismic coefficients. As the value of cohesion increases (0–15 kN/m²), the required value of K (equivalent earth pressure coefficient) increases to maintain the wall’s stability. For a vertical wall with $K_h > 0.2$, the value of FS_T reduces when C improves from 0 to 15 kN/m². The effect of surcharge loading on the backfill is a negligible effect of the factor of safety. Hence the impact of the increase of cohesion is critical, with a decrease of ϕ .

Conclusion

The present evaluation shows the vertical reinforced wall with cohesive-frictional soil carrying uniform surcharge made the following conclusions:

1. The tensile force required to maintain the stability of the reinforcement is a function of seismic coefficients. Also, the increase in cohesion (0–15 kN/m²) and internal friction decrease in FS_T due to a reduction in force in reinforcement.

2. The failure wedge angle in cohesive-frictional soils is linear. Due to the backfill surcharge and cohesion, the safety factor due to transverse displacement increases with an increase in soil stiffness for low values of seismic coefficients.
3. The no. of reinforcement layers increase with the increase in factor of safety is due to shear resistance opposing the failure.
4. The FOS (FS_T) increases with the L/H ratio for the normalized displacement of 0.005 for about 1.2 ($L/H = 0.3$) to about 2.4 (For $L/H = 0.6$).

References

1. Okabe S (1926) General theory of earth pressure. J Jpn Soc Civ Eng 12(1):1277–1323
2. Mononobe N, Matuso H (1929) The determination of earth pressures during earthquakes. Proc World Eng Congr Tokyo Jpn 9:177–185
3. Shukla SK (2013) Seismic active earth pressure from the sloping $c-\phi$ soil backfills. Indian Geotech J 43(3):274–279
4. Shahgholi M, Fakher A, Jones CJFP (2001) Horizontal slice method of analysis. Geotechnique 51(10):881–885
5. Nouri H, Fakher A (2007) The effect of earthquake on the seismic stability of reinforced slopes using horizontal slice method. In: 4th international conference on earthquake geotechnical engineering, Thessaloniki, Greece
6. Nouri H, Fakher A, Jones CJFP (2008) Evaluating the effects of the magnitude and amplification of pseudo-static acceleration on reinforced soil slopes and walls using the limit equilibrium horizontal slices method. Geotext Geomembr 26(3):263–278
7. Reddy GVN, Madhav MR, Reddy ES (2008) Pseudo-static seismic analysis of reinforced soil wall—effect of oblique displacement. Geotext Geomembr 26(5):393–403
8. Chandaluri VK, Sawant VA, Shukla SK (2015) Seismic stability analysis of reinforced soil wall using horizontal slice method. Int J Geosynthe Ground Eng 23(1):1–10
9. Ghose S, Debnath C (2013) Pseudo-static analysis of reinforced earth retaining wall considering non-linear failure surface. Geotech Geo Eng 34:981–990
10. Morgenstern NR, Prince V (1965) The analysis stability of general slip surfaces. Geotechnique 15(1):79–93
11. Ahmadabadi M, Ghanbari A (2009) New procedure for active earth pressure calculation in retaining walls with reinforced cohesive frictional backfill. Geotext Geomembr 27(6):456–463
12. Motlagh AT, Ghanbari A, Maedeh PA, Wu W (2018) A new analytical approach to estimate the seismic tensile force of geosynthetic reinforcement respect to the uniform surcharge of slopes. Earthquakes and Structures 15(6):687–699
13. Chehade HA (2020) Seismic analysis of geosynthetic-reinforced retaining wall in cohesive soils. Geotext Geomembr 47:315–326
14. Shekarian S, Ghanbari A (2008) A pseudo-dynamic method to analyze retaining wall with reinforced and unreinforced backfill. JSSE 10(1):41–47
15. Abd AH, Utili S (2017) Design of geosynthetic-reinforced slopes in cohesive backfills. Geotext Geomembranes 45:627–641

Chapter 32

A Comparative Study on the Stability Analysis of Tailings Pond Embankments Under Transient and Steady-State Seepage Conditions



Surender Singh, Abhishek Kumar, and T. G. Sitharam

Introduction

A huge quantity of liquid waste (commonly termed tailings) is released by the mining industries during the extractions of minerals from their respective ores. Tailings due to its toxic nature have an adverse effect on the environment as well as to the human and therefore must be properly disposed of. In most cases, mining waste is disposed of by impounding the tailings slurry behind the embankments resulting in the formation of TP. The height of TP is raised in stages where the new embankments are constructed once the storage limit of the previously built embankment is surpassed. This can be achieved by following three widely accepted construction techniques, i.e., U/S, D/S, and centerline technique [5, 18]. Frequent failures of these TP have raised a deep concern regarding their design and construction. Seepage-induced slope instability has been identified as one of the key factors contributing to the failure of TP, particularly in the case of U/S type TP [8]. Therefore, in most cases, seepage analysis in conjunction with slope stability analysis is performed while evaluating the overall stability of TP. Traditionally, steady seepage analysis has been typically utilized by the engineers to define the seepage flow field within the TP [3, 12, 20]. However, [14] in their study pointed out the inappropriateness of steady-state analysis in describing the hydromechanical behavior of TP during its staged construction. Furthermore, classical seepage analysis does not take into account the transient condition, which is induced due to the self-weight consolidation of both tailings and embankment material during the construction and operation of TP [14]. As previously stated, TP is built in stages, with new embankments being built over the existing ones, resulting in the build-up of EPWP, effect of which is not taken into account in the steady-state seepage analysis. A high build-up of EPWP due to an excessive rate of embankment

S. Singh (✉) · A. Kumar · T. G. Sitharam
Department of Civil Engineering, IIT, Guwahati 781039, Assam, India
e-mail: surendersingh@iitg.ac.in

raise (defined as height raised in m per year) can even lead to the collapse of EoTP, particularly in the case of U/S type TPs [4, 13]. Therefore, to analyze the realistic hydromechanical response of TP including the influence of EPWP developed while increasing the height of EoTP in phases, a transient coupled stress-pore pressure study is required [9, 11].

This article presents a stability analysis of TP, the height of which is planned to be increased by 24 m to enhance its storage capacity. The D/S construction technique is employed to raise the height of EoTP, where the new embankments are built toward the D/S portion of the TP. Initially, the stability of TP is evaluated under steady seepage flow conditions. Thereafter, the hydromechanical behavior of TP during its staged construction is then investigated by performing a transient fully coupled stress-pore pressure analysis using the FEM-based code RS2. Consequently, the build-up of EPWP within the TP during various phases of construction is analyzed. Finally, the results obtained from both analyses are compared in terms of critical SRF, EPWP, etc., that substantiate the importance of the transient analysis approach in evaluating the stability of TP.

Site Description and Geometry of Existing EoTP

The concerned TP is situated at Rampura Agucha Mine (RAM) in the Bhilwara district of Rajasthan, India. At RAM, Zn is being produced as a primary product along with Cd as secondary. Extraction of these metals results in the generation of a huge quantity of liquid waste, which is disposed into the TP. The present height of TP is 51 m, and it was built in two phases, each with four lifts. The D/S method of construction was used to construct the EoTP in phase 1, which resulted in a total height of 27 m. The height of EoTP was further increased by 24 m in phase 2 construction, using both the U/S and D/S construction styles, achieving a total height of 51 m. The N-E segment of TP was built using the D/S approach, whereas the S-W section was constructed following the U/S technique (see Fig. 32.1). It is important to note that in the U/S technique, the height of TP is increased by building new embankments on the U/S side, whereas in the D/S method, the new embankments are added toward the D/S side of existing embankments [18]. The detailed geometry of the existing EoTP is shown in Fig. 32.2.

Geometry of Embankments for Height Raising

The storage capacity of the present TP is likely to reach its maximum limit within a few years due to the ongoing generation of Zn tailings from the RAM [16]. As a result, the present TP's height must be raised in order to increase its storage capacity. The concerned authority decided to raise the TP by another 24 m, bringing its overall height to 75 m. Both U/S and D/S construction techniques are employed to raise the

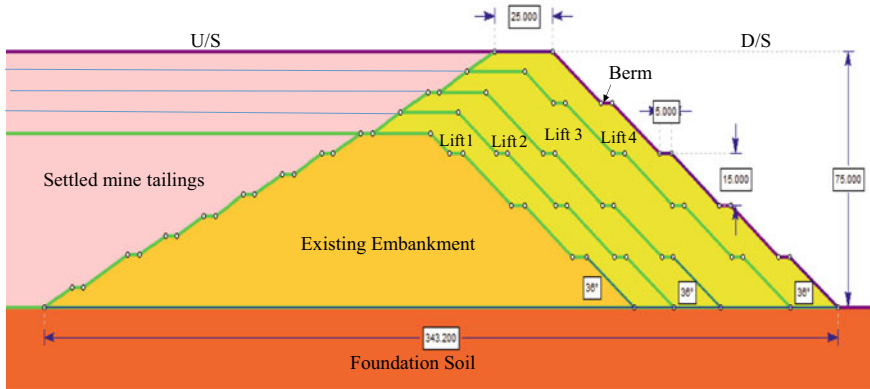


Fig. 32.1 Typical cross-section of TP embankments constructed by D/S method

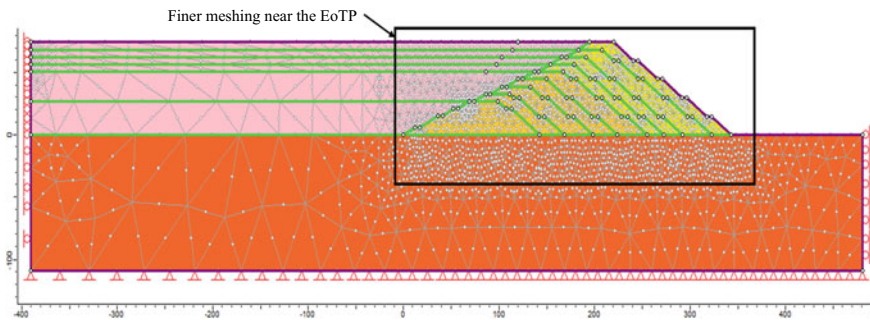


Fig. 32.2 Finite element meshed geometry of TP at the end of construction

height of the existing TP due to space constraints. However, stability in this article is assessed only for the D/S section.

The height of TP’s embankments is raised in four stages by providing 4 lifts of 6 m each. To begin with, a berm of width 5 m is provided on the U/S slope at the beginning of the first and third lift (see Fig. 32.2). Similarly, a berm of 5 m is provided on the D/S slope at every 15 m rise (measured from the foundation level). In addition, a slope of 1V:2H (identical to that provided in the U/S case) is provided at the U/S slope of the embankment (built in each lift). On the other hand, a slope angle 36° is maintained for the D/S slope of embankments, which is similar to that provided in the existing EoTP. Further, the crest width of 25 m is provided for the embankments at the end of each lift. Figure 32.2 shows the cross-section of TP embankments at the end of final construction following the D/S technique.

Methodology

As highlighted earlier, steady-state seepage analysis overlooks the effect of self-weight consolidation of tailings during staged construction of TP's embankments. However, consolidation of tailings due to its self-weight plays a vital role in defining the flow of fluid within the TP system [2]. Therefore, to account for the self-weight consolidation and thereby the transient response of TP during its staged construction, [2] consolidation theory is used in this work. A fully coupled stress-pore pressure analysis is carried out in FEM-based program RS2, which incorporates Biot's consolidation theory to model the soil-fluid interaction. Furthermore, the shear strength reduction (SSR) technique is utilized to determine the critical SRF, which is generally used in FEM-based analysis to quantify the stability of slopes. In the SSR technique, cohesion (c) and angle of internal friction (ϕ') of a material are reduced by a factor (i.e., by SRF) in each step until the mobilized shear stresses equal the shear strength of the soil. It is worth noting that the significance of SRF in FEM is analogous to the factor of safety used in the limit equilibrium methods (LEM).

Finite Element Modeling in RS2

Simulation of Staged Construction

The entire geometry of TP has three components, i.e., (a) EoTP, (b) settled mine tailings, and (c) foundation system. The various components of TP are drawn in the RS2 modeler as per the specifics given in the preceding section (for both D/S and U/S scenarios). The bedrock at the TP site is present at a depth of 10 m. However, the foundation and side boundaries of TP system are extended sufficiently in the vertical and horizontal direction to avoid any edge errors. Further, to simulate the raising of embankment in each lift, five stages are created in RS2. To represent the initial condition of existing TP, an extra stage, i.e., stage 0, is defined before the construction of new embankments (height = 51 m), which is characterized by a steady-state seepage analysis. The construction in each lift (defined in RS2 as stages 1, 2, 3, and 4) comprises two steps, i.e., (a) height raising phase (R, which includes the construction of new embankment and filling of pond) and (b) consolidation phase (C, which represents the self-weight consolidation of stored mine tailings). An embankment-raising rate of 6 m/year is assumed in the analysis with a raising phase of 30 days (for each lift) and a consolidation phase of 335 days (for each lift). To evaluate the hydromechanical behavior of the TP facility during each lift, a consolidation analysis is performed for each stage. For each stage, a new set of mechanical and hydraulic boundary conditions is applied. The hydraulic and mechanical boundary conditions given throughout construction stages are explored in greater detail in the following sections. The seepage field within the TP is not only affected by the hydraulic characteristics of materials (tailings and embankment soil) but also by the

beach formed behind the EoTP [18]. Beach is a section within the TP, which consists of an exposed surface of the dry tailings between the point of discharge and the decant pond. The width of the beach behind the EoTP determines the location of the phreatic surface within TP, which can affect the overall stability of TP especially in the case of the U/S method. Keeping this in view, beach width equal to the height of TP is provided at the end of each lift. Furthermore, tailings are expected to be stored up to the embankment crest level (i.e., zero freeboard) at the end of each stage, which is a worst-case scenario for the TP’s stability.

Materials and Constitutive Laws

Material properties: Construction of EoTP is done by utilizing the mine spoils (crushed waste rocks) extracted during the extraction of Zn at mine. The existing TP was constructed over a very low permeable soil layer (permeability coefficient, $K_x = 10^{-8}$ m/s) followed by a rocky strata. The geotechnical properties of foundation soil, embankment material, and the tailings used in the analysis are taken from the work carried out by one of the coauthors [16], which are tabulated in Table 32.1. Additionally, hydraulic characteristics of mine spoil and settled mine tailings are referred from the work done by [11]. Due to its layered nature, settled mine tailings deposits display anisotropy, which is taken into account by using the vertical to horizontal permeability ratios (K_y/K_x) of 0.3 and 0.8 for mine tailings and mine spoil, respectively [11, 18].

Constitutive laws used: Failure of various materials (i.e., mine spoil, mine tailings, and foundation soil) is defined by the Bishop’s (1959) effective stress approach, which takes into account the effect of matric suction (force of attraction between unsaturated soil grains developed due to surface tension of water). In order to define the shear strength of partially saturated soils, Bishop (1959) extended the Mohr–Coulomb failure criterion as follows:

$$\tau = c' + [(\sigma - u_a) + \chi(u_a - u_w)]\tan\phi' \tag{32.1}$$

Table 32.1 Geotechnical properties of various materials used in the numerical simulation

Material type	c' (kPa)	ϕ' (Degree)	Bulk unit weight (kPa)	E (kPa)	K_x (m/s)	α (m^{-1})	n
Mine spoil	2	39	20.7	25,700	1×10^{-2}	15.10	7.35
Foundation soil	20	38	22.0	51,428	1×10^{-8}	0.80	1.80
Settled mine tailings	1	35	20.0	12,800	1×10^{-5}	1.60	1.37

where τ = soil's shear strength (kPa), c' = effective cohesion (kPa), σ' = effective normal stress (kPa), ϕ' = effective soil's internal friction (degree), u_a = air pressure, and χ = matric suction coefficient.

In addition, the hydraulic conductivity function (HCF) of settled mine tailings and the mine spoil is defined in the current study using the Van Genuchten-Mualem [10, 17] model. The constitutive law followed for HCF in Van Genuchten-Mualem [10, 17] model is given as follows:

$$K = K_s (\sqrt{S_e} [1 - (1 - S_e^{1/m})^m]^2) \quad (32.2)$$

where S_e = effective degree of saturation

$$S_e = \frac{1}{[1 + (\alpha h)^n]^m} \quad (32.3)$$

K_s = saturated hydraulic conductivity, h = suction head, and m, n = curve fitting parameters.

The values of $\alpha, n,$ and m for settled tailings (corresponding to fine silt) and mine spoil (corresponding to coarse sand) are taken from the default values (see Table 32.1) given in RS2 [19].

Loading and Boundary Conditions

EoTP are generally exposed to three types of loading, i.e., (a) load due to self-weight, (b) load from settled mine tailings, and (c) load from ponded water expressed in term of hydrostatic pressure. Moreover, the TP is situated in seismic zone II, which as per IS: 1893 [6] is leveled as a zone of low seismicity. Therefore, the effect of seismic loading is considered by using pseudo-static approach where the seismic force is considered as an equivalent inertial force, which is determined by using suitable seismic coefficients [15]. Accordingly, a horizontal seismic coefficient of 0.06 g is considered in the present work [16].

Mechanical boundaries: Bottom boundary of model is provided with the fixed supports to restrain both horizontal and vertical displacements. However, the side boundaries are provided with the pinned roller support, which restricts the deformations in horizontal direction only (as soil mass extends to infinity in horizontal direction).

Hydraulic boundaries: To define the hydrostatic pressure exerted by the ponded water, total head boundary condition given in RS2 is utilized. A different set of total head value is provided on the U/S side (within the TP) depending upon the height of embankment achieved at the end of each lift. In addition, the location of phreatic surface within the TP facility is searched by invoking, pressure, $p = 0$ boundary condition at the D/S slope of the EoTP.

To obtain the optimum meshing parameters required for the model discretization, mesh convergence study is performed to check the sensitivity of meshing parameters with regard to total head (critical parameter in stability analysis). Four sets of trial analysis are performed with 1020, 1660, 2440, and 3420 number of 6-noded triangular elements. Based on the sensitivity analysis, the entire TP's geometry (at the end of 4th lift) is discretized into 2440 number of 6-noded triangular elements as negligible change in results (in terms of total head) are obtained with higher (>2440) number of elements. In addition, to increase the accuracy of the analysis, finer meshing is provided toward (see Fig. 32.2) the EoTP.

Once the set of input parameters and the boundary conditions are defined, first set of stability analysis is carried out under steady-state condition. Subsequently, transient coupled stress-pore pressure analysis is carried out to examine the evolution of EPWP during various stages of construction. Results from both the analysis are compared in the terms of critical SRF, total displacements, and maximum plastic shear strain observed at the end of construction of final stage, which are discussed in the following section.

Results and Discussion

Evolution of EPWP and Critical SRF During Different Phases of Construction

Results from the fully coupled transient stress-pore pressure analysis, performed during each phase of raising (i.e., R1, R2, R3, and R4) and consolidation (i.e., C1, C2, C3, and C4), are expressed in terms of critical SRF and EPWP developed. EPWP during each phase of raising is observed to be increasing due to the application of additional loads from the newly constructed embankments. However, the EPWP is found to be decreasing during the consolidation phases as the EPWP gets dissipated during the process of consolidation. Figures 32.3 and 32.4 show the evolution of EPWP during R4 and C4 phases. It can be observed from Fig. 32.3 that a high EPWP zone is developed within the foundation soil beneath the newly constructed embankments during R4 phase, a part of which gets dissipated during the C4 phase (see Fig. 32.4). Further, a minimal amount of EPWP is observed to be developed within the existing EoTP due to higher hydraulic conductivity (i.e., 10^{-2} m/s) of mine spoil.

The values of critical SRF for EoTP during various phases of construction depend upon the build-up of EPWP. It can be seen from Fig. 32.5 that critical SRF decreases during the raising phase (due to development of EPWP), whereas it increases during the consolidation phase (due to dissipation of EPWP). Furthermore, the variation in SRF is found to be more substantial for first two phases of construction (i.e., R1, C1, R2, and C2). However, a minimal change in SRF is observed during the last phase of raising and consolidation (i.e., R4, C4). The above observations with respect to the

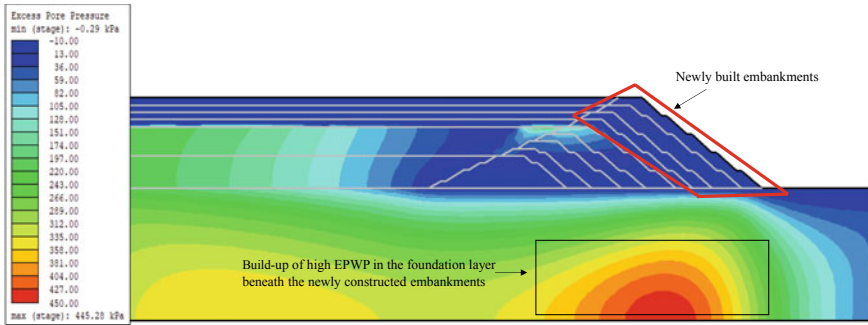


Fig. 32.3 Evolution of EPWP during R4 phase ($t = 1125$ days)

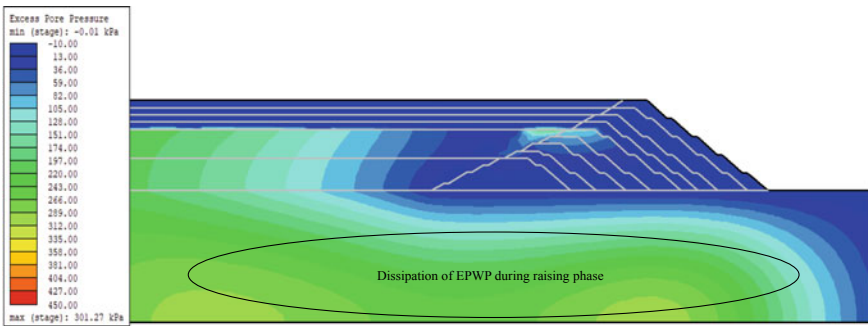


Fig. 32.4 Evolution of EPWP during C4 phase ($t = 1460$ days)

decrease in SRF during raising and increase in SRF during consolidation cannot be examined from the steady-state analysis. Overall, the critical SRF (during different phases of construction) is found to be acceptable as per [1] (FOS > 1.5) and IS 7894:1975 (reaffirmed 1997) (FOS > 1) recommendations.

Comparison of Transient and Steady-State Analysis

In order to substantiate the need of transient analysis in assessing the stability of TP, the results obtained from transient fully coupled analysis are compared with that obtained from steady-state analysis. Steady-state analysis is performed at the end of construction of each stage maintaining a L/H of 1 during each phase. It can be observed from Fig. 32.6 that critical SRF decreases for transient analysis for each stage of construction as compared to the steady-state analysis. For example, the critical SRF obtained from the transient analysis for the last phase (i.e., lift 4) of construction drops from a value of 2.30 to 2.01. This is due to the reason that transient analysis takes into account the effect of EPWP (developed due to raising

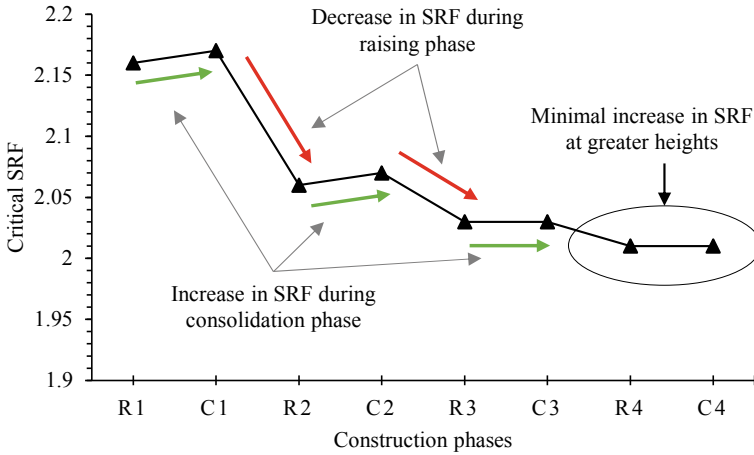


Fig. 32.5 Variation of critical SRF obtained during different phases of construction

of embankments) which reduces the effective stresses and hence the reduction in SRF values. Steady-state analysis, on the other hand, does not consider the effect of staged construction (i.e., the effect of EPWP), thereby providing more conservative SRF values than the transient analysis.

In addition, the zone of maximum horizontal displacements is observed to be different in transient and steady-state analysis. Maximum horizontal displacements in the transient analysis are observed within the previously existing EoTP (see Fig. 32.7), which is understandable as additional construction loads (coming from the subsequent stages) are imposed on the embankments during various phases of construction. Maximum horizontal displacements from the steady-state analysis, on

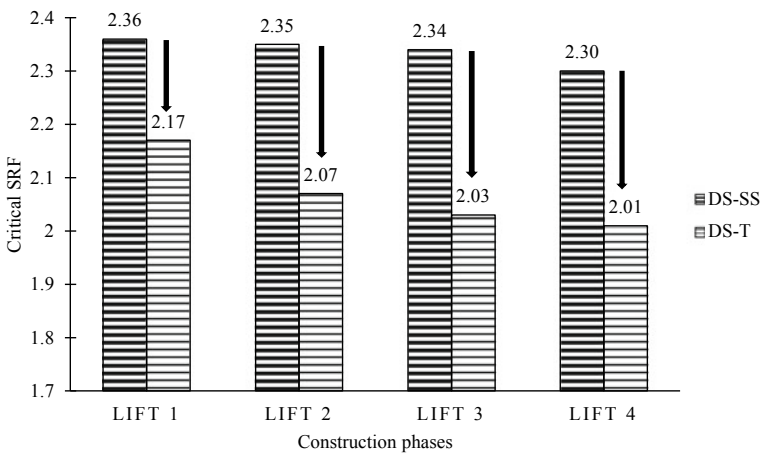


Fig. 32.6 Critical SRF obtained considering steady-state (SS) and transient (T) analysis

the other hand, are observed near the toe portion of the embankment built in the last stage (see Fig. 32.8). However, the failure pattern obtained in both the analysis (at the end of final construction) is found to be quite similar with failure surface initiating from the toe portion (signifying the toe failure) of embankment (see Figs. 32.9 and 32.10).

Considering the observations from the both analyses, it can be said that steady-state analysis fails to incorporate the build-up of EPWP occurring during various stages of construction. Transient analysis, on the other hand, takes into account

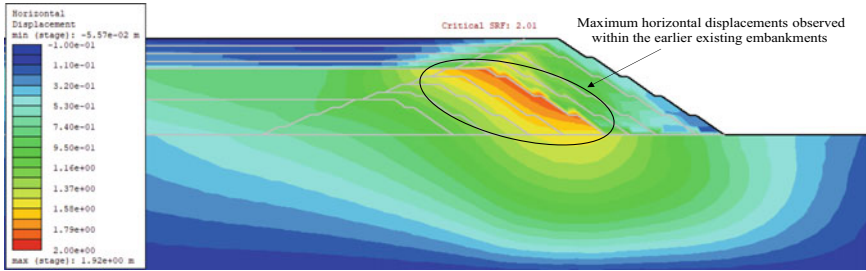


Fig. 32.7 Contours of horizontal displacements obtained using transient analysis ($t = 1460$ days)

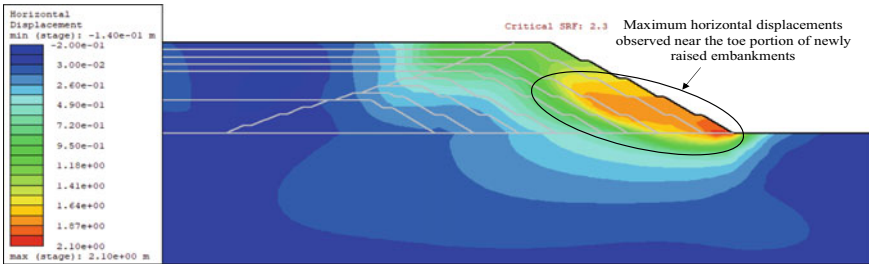


Fig. 32.8 Contours of horizontal displacements obtained from the steady-state analysis

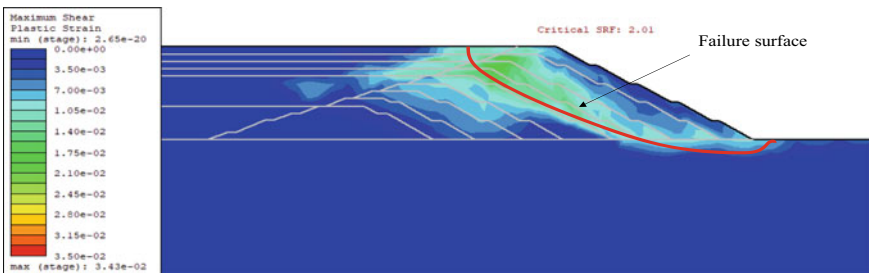


Fig. 32.9 Contours of maximum shear strain obtained from the transient analysis at $t = 1460$ days

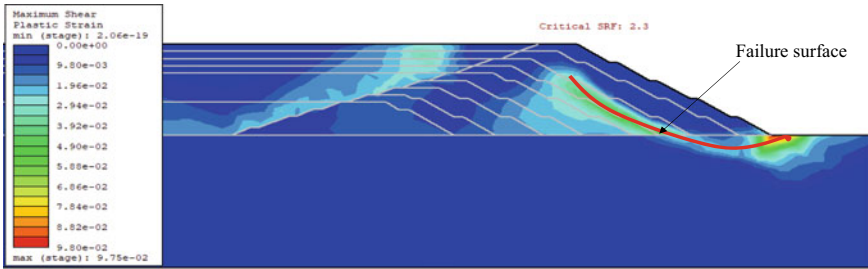


Fig. 32.10 Contours of maximum shear strain obtained using steady-state analysis

the realistic hydromechanical behavior of TP by incorporating the effect of EPWP developed during various phases of construction.

Conclusions

In this article, the stability of a TP was investigated while raising the height of existing EoTP from 51 to 75 m. The height of EoTP was raised in four phases (6 m lift in each stage) by utilizing the D/S construction technique. Two sets of numerical analyses were conducted in FEM-based software RS2. In the first analysis, the stability of TP was assessed by conducting the steady-state stress-seepage analysis at the end of each stage. Subsequently, in the second set, a transient fully coupled stress-pore pressure analysis was done to simulate the realistic hydromechanical behavior of TP during its staged construction. Following four conclusions are drawn from both the analysis:

1. Due to the application of construction loads from the subsequent stages, a build-up of high EPWP (thus a decrease in overall SRF) was observed within the foundation soil and the tailings deposit during each phase of raising. However, a reduction in EPWP (thus an increase in SRF) was observed within the TP system due to the dissipation of pore water pressure during the consolidation phases.
2. During each phase of construction, a zone of high EPWP was noticed within the foundation soil and tailings deposit (due to low hydraulic conductivities). However, due to the higher hydraulic conductivity of mine spoil, which causes EPWP to dissipate quickly, a minimal EPWP was developed within the EoTP (during various stages of construction).
3. A lower value of critical SRF was observed in the transient analysis during each phase of construction (due to the inclusion of the EPWP effect) as comparison to steady-state analysis. However, critical SRF observed at the end of final construction of TP, from both transient (SRF = 2.01) and steady-state (SRF = 2.30) analysis, was found to be within the safe values as per the guidelines given by [1] (FOS > 1.5) and IS 7894 [7] (reaffirmed 1997) (FOS > 1).

References

1. ANCOLD (2012) Guidelines on tailings dam design, construction and operation. Australian National Committee on Large Dam
2. Biot MA (1941) General theory of three-dimensional consolidation. *J Appl Phys* 12(2):155–164
3. Coulibaly Y, Belem T, Cheng L (2017) Numerical analysis and geophysical monitoring for stability assessment of the Northwest tailings dam at Westwood Mine. *Int J Min Sci Technol* 27(4):701–710
4. Davies MP (2001) Impounded mine tailings: what are the failures telling us? *CIM Bulletin* 53–59
5. EPA (1994) Design and evaluation of tailings dam. United State Environmental Protection Agency, office of solid waste, Washington, DC
6. IS 1893-part 1 (2016) Indian standard criteria for earthquake resistant design of structures. General provisions and buildings. Bureau of Indian Standards, New Delhi
7. IS 7894 (1975) Code of practice for the stability analysis of the earth dams. Bureau of Indian Standards, New Delhi
8. Lyu Z, Chai J, Xu Z, Qin Y, Cao J (2019) A comprehensive review on reasons for tailings dam failures based on case history. *Advances in Civil Engineering* 1–18 (2019)
9. Naeini M, Akhtarpour A (2018) Numerical analysis of seismic stability of a high centreline tailings dam. *Soil Dyn Earthq Eng* 107:179–194
10. Mualem Y (1976) A new model for predicting the hydraulic conductivity of unsaturated porous media. *Water Resour Res* 12(3):513–522
11. Ormann L, Zardari MA, Mattsson H, Bjelkevik A, Knutsson S (2013) Numerical analysis of strengthening by rockfill embankments on an upstream tailings dam. *Can Geotech J* 50(4):391–399
12. Pak A, Nabipour M (2017) Numerical study of the effects of drainage systems on saturated/unsaturated seepage and stability of tailings dams. *Mine Water Environ* 36(3):341–355
13. Rico M, Benito G, Salgueiro AR, Díez-Herrero A, Pereira HG (2008) Reported tailings dam failures: a review of the European incidents in the worldwide context. *J Hazard Mater* 152(2):846–852
14. Saad B, Mitri H (2011) Hydromechanical analysis of upstream tailings disposal facilities. *J Geotech Geoenviron Eng* 137(1):27–42
15. Singh S, Kumar A (2021) Methodologies available for the determination of seismic active thrust acting on retaining walls: a critical review. *Indian Geotechnical Journal* 1–13
16. Sitharam TG, Hegde A (2017) Stability analysis of rock-fill tailing dam: an Indian case study. *Int J Geotech Eng* 11(4):332–342
17. van Genuchten MT (1980) A closed-form equation for predicting the hydraulic conductivity of unsaturated soils. *Soil Sci Soc Am J* 44(5):892–898
18. Vick SG (1990) Planning, design, and analysis of tailings dams. BiTech, Richmond, BC, Canada
19. Vogel T, Van Genuchten MT, Cislerova M (2000) Effect of the shape of the soil hydraulic functions near saturation on variably-saturated flow predictions. *Adv Water Resour* 24(2):133–144
20. Zhang C, Chai J, Cao J, Xu Z, Qin Y, Lv Z (2020) Numerical simulation of seepage and stability of tailings dams: a case study in Lixi, China. *Water* 12(3):742

Chapter 33

Structural Behavior of Partial Seepage Barriers for Variations in Depth of Pervious Stratum



S. Sivakumar , P. V. Premalatha , and N. Almas Begum 

Introduction

Hydraulic structures like barrages, dams, and anicuts are normally founded in pervious soil foundations. This pervious foundation allows the water stored in the upstream side to seep into downstream side through the pores of soil matrix due to the differential pressure head. This seeping water, due to its seepage velocity, induces some destabilizing forces which require significant attention to ensure the safety of structures.

The destabilizing forces can be managed with the concepts of uplift pressure and exit gradient. The seeping water creates pore pressure which in turn acts at bottom of the structure against the gravity. This uplift force is required to be counterbalanced by the weight of the overlaid structure to ensure safety of the whole structure. Safety of structure from exit gradient is the safety of structure from piping failure. The seepage water passing through the soil pores loses its pressure head due to friction between soil and water molecules. Therefore, the water emerges out at the downstream side with residual pressure head after the losses. The residual pressure head with which the water emerges out at the downstream bed is called exit gradient. If the residual pressure head is higher enough to carry away the soil particles at the downstream bed, a backward progressive piping phenomenon will occur and leads to total structural failure.

S. Sivakumar (✉)
Planning and Design Division, TN WRD, Thanjavur 613001, India
e-mail: sivahare2002@gmail.com

P. V. Premalatha
Professor, Department of Civil Engineering, M.I.E.T Engineering College,
Tiruchirappalli 620007, Tamil Nadu, India

N. A. Begum
Building C&M (Medical Works) Division, TN PWD, Trichy 620001, India

By altering the configurations of floor length and cut-off walls, the effects due to exit gradient and uplift pressure can be controlled. There are numerous studies on the configuration of the cut-off wall and their hydraulic behaviors to conquer the exit gradient and uplift pressure.

Kenney et al. [3] observed that seepage force of seeping water depends on seepage velocity of the water. Khairy et al. [4], on analyzing the subsurface concrete dam, observed that increased thickness of wall improves mobilized passive pressure that acts on the opposite face of wall. Neshaei et al. [8] studied that placing the wall at upstream floor end reduces both uplift pore pressure and hydraulic gradient, but, placing the wall at downstream floor end increases the uplift pore pressure and reduces exit gradient. Sedghi-Asl et al. [16] prove that the conjunctive use of sheet pile and impermeable blanket could effectively control the seepage and piping failure.

Tung et al. [23] studied that the exit gradient reduces on increase in length of pile. On shifting the pile away from the downstream end, increases exit gradient and reduces probability of piping failure. Mansuri and Salmasi [6] observed that by providing the cut-off at middle of foundation, the rate of seepage got reduced and the piping danger also got reduced. They observed that as depth of cut-off for any locations increases, the seepage discharge reduces. Moharamiet al. [7] found that lowest uplift pore pressure and highest exit gradient are observed while positioning the cut-off at dam's upstream end and the reverse happens, while positioning the cut-off at dam's downstream end. It was also reported that the maximum seepage flux occurs while placing the cut-off at center than that of placing at the ends of dam.

Shayan and Tokaldany [18] concluded that to have the reduced seepage, best position of cut-off wall is downstream floor end and for reduced uplift pore pressure is upstream floor end. They also found that cut-off wall is more effective than the upstream blanket in reducing the exit gradient. Tunget al. [24] concluded that on increasing the length of pile, the exit gradient reduces. They observed that on shifting the position of sheet pile toward the upstream end, the factor of safety against piping failure decreases.

Rice and Duncan [14] indicated that pore pressure regime change could be a mechanism causing deformation and cracking in rigid seepage barriers. Rice and Duncan [15] observed that seepage barriers are subjected to deformation due to the differential pressure head and pressure gradient between both faces of hydraulic barriers. Javanmard et al. [2] observed that tension cracks are likely to occur in cut-off wall as the plastic concrete is under tension due to the stress produced by bending moment and axial force. Shakouri and Mohammadi [17] observed that the penetration depth is the major influencing factor of seepage rate, hydraulic gradient, stress, and displacement in cut-off wall. Norouzi et al. [9] found that in cut-off walls, the maximum hydraulic gradient is experienced on their faces. The minimum value of hydraulic gradient is experienced when it is positioned at center of clay core. Premalatha et al. [12] and [13] reported the soil-structure interaction under lateral loads.

All above studies are mostly oriented toward the hydraulic properties of cut-off wall. No studies were carried out to determine their structural behaviors under varying configurations. However, Sivakumar et al. [19] conducted studies to assess

structural deformation in partial seepage barrier or cut-off wall under different soil and structural configurations.

Sivakumar et al. [20] proved that the seepage force plays a more predominant role in deforming the partial seepage barriers than the pore pressure variations. Sivakumar et al. [21] reported deformation of partial seepage barriers under seepage forces for various parametric changes. They reported that for all cases, the downstream cut-off experiences higher displacement and bending moment than the upstream cut-off experiences. On increase of soil modulus or relative density of soil, there is a reduction in deformation in partial seepage barriers. Sivakumar et al. [22] reported that deformation in the partial seepage barrier is minimum when it is placed at upstream floor end and maximum when it is placed at the center of diversion dam.

This study is devoted to determine the structural behavior of cut-off wall for various depth ratios (the ratio between depth of cut-off wall and depth of pervious stratum).

Problem Description and Modeling

It is proposed to study the effects of variations in depth of cut-off wall with respect to the depth of pervious stratum. By varying the depth of cut-off walls and depth of pervious stratum, 12 numbers of models with various depth ratios (ratio between the depth of cut-off wall and depth of pervious stratum) of 0.20, 0.40, 0.60, and 0.80 are obtained as shown in Table 33.1.

A typical model of the diversion structure is placed in Fig. 33.1. After conducting the conversion study, model width of 100 m is chosen to avoid boundary effects. The differential or net pressure of 5 m water head is applied for this study. 12 models

Table 33.1 Models with varying depth ratios

SL. No.	Depth of cut-off walls in m	Depth of pervious status in m	Depth ratio	Model No
1	4.0	20.0	0.20	0.20 A
2	5.0	25.0	0.20	0.20 B
3	6.0	30.0	0.20	0.20 C
4	8.0	20.0	0.40	0.40 A
5	10.0	25.0	0.40	0.40 B
6	12.0	30.0	0.40	0.40 C
7	12.0	20.0	0.60	0.60 A
8	15.0	25.0	0.60	0.60 B
9	18.0	30.0	0.60	0.60 C
10	16.0	20.0	0.80	0.80 A
11	20.0	25.0	0.80	0.80 B
12	24.0	30.0	0.80	0.80 C

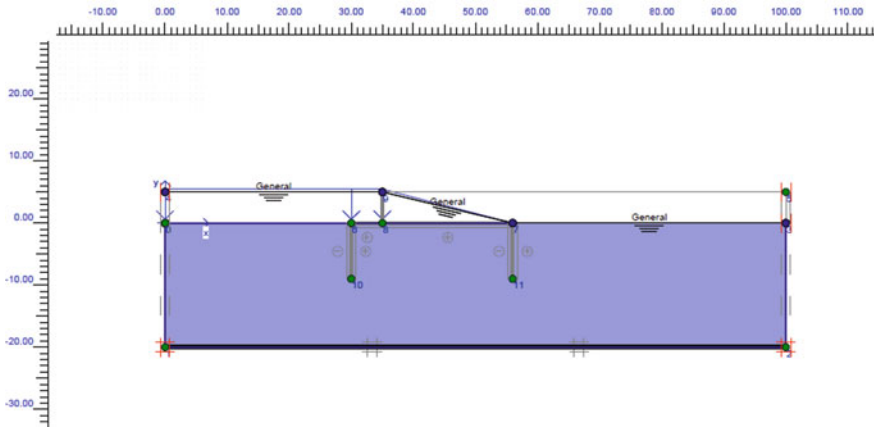


Fig. 33.1 Typical model of the diversion structure

comprising various combinations of depth of cut-off wall and depth of pervious stratum are studied.

Numerical study using Plaxis 2D software is conducted. Plaxis 2D software is versatile and user-friendly geotechnical software available in the market. This software has various soil models to suit the field conditions. In this study, Mohr–Coulomb model is adopted as this model requires very few soil parameters resulting in lesser chances for error.

The soil and structural properties adopted in this model are given in Tables 33.2 and 33.3, respectively. These soil parameters are derived from SPT correlations as prescribed by [1, 11], and [10]. Soil and structural parameters considered for this study (presented in Tables 33.2 and 33.3) have also been used by the authors for a different study.

Study and Discussion

Models having varying depth of cut-off walls and pervious layers are considered. All other structural configurations and soil parameter are kept constant except the depth of cut-off walls and depth of pervious stratum. Numerical studies with these selected models are conducted at constant differential or net pressure head. The displacements and bending moments in upstream wall from all 12 models are plotted. Likewise, the displacements and bending moments in the downstream cut-off are also plotted. The deformation plots of both these cut-off walls are analyzed for their behavioral pattern.

Table 33.2 Properties of soil [21]

Relative density of soil in % D_r	Saturated unit weight of soil in kN/m^3 γ_{sat}	Soil modulus in kN/m^2 E_{ref}	Unsaturated unit weight of soil in kN/m^3 γ_{unsat}	Angle of internal friction in degree φ	Angle of dilatancy in degree ψ	Soil cohesion in kN/m^2 C_{ref}	Poisson's ratio ν	Permeability of soil m/day K
70	21.0	22,500	17.2	37	13	1.0	0.3	6.5

Table 33.3 Properties of structural elements [19]

Structure	EA—axial rigidity in kN	EI—flexural rigidity in kNm ²	Width in m	ν	w—Weight in kN/m	Depth d in m
Upstream wall	1.50 E+07	4.50 E+05	0.6	0.0	8.3	9.0
Downstream wall	1.50 E+07	4.50 E+05	0.6	0.0	8.3	9.0
Floor or apron	2.90 E+10	5.45 E+06	1.5	0.15	10.5	—
Crest or body wall	4.84 E+07	2.52 E+07	2.4	0.15	17.5	5.0

Displacement Study in Upstream Cut-Off

The deformation in upstream cut-off obtained from 12 models is plotted in Fig. 2a. From the displacement plot of upstream cut-off, it is observed that with lower depth ratio, the maximum displacement occurs at lower end of the cut-off. On increasing depth ratio, point of occurrence of maximum displacement shifts upwards. Beyond 0.4 depth ratio, the point of occurrence of maximum displacement shifts to top end of cut-off and remains there. The normalized displacements of upstream cut-off are plotted in Fig. 2b. On observing the normalized displacement plot, it can be established that the displacement pattern of upstream cut-off for a particular depth ratio is similar irrespective of the actual depth of cut-off.

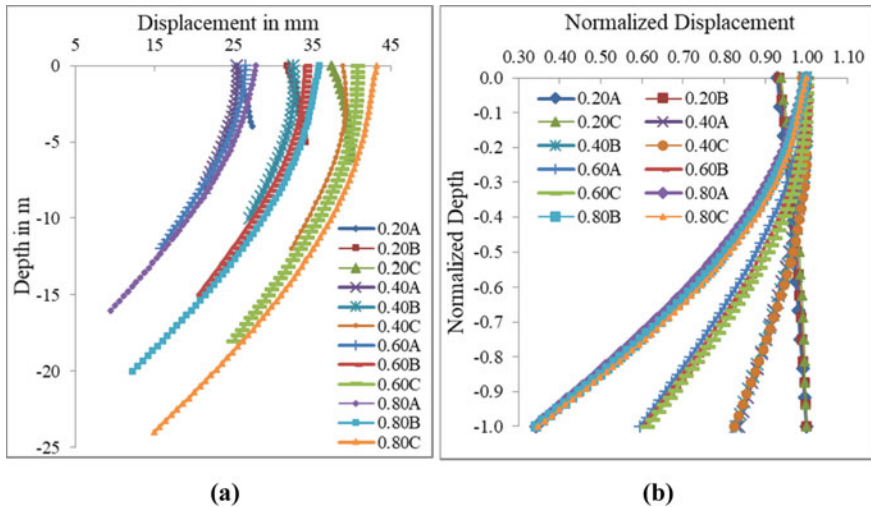


Fig. 33.2 Displacement and normalized displacement in upstream cut-off

Take the case of model No. 0.40 C and 0.60 A wherein the depth of cut-off in both models is 12 m. However, the depth of pervious stratum in model No. 0.40 C and 060 A is 30 m and 20 m, respectively. Even though the depths of cut-off walls are similar, the variation in depth of pervious stratum influences the behaviors of cut-off walls. Hence, the deformation is different for different depth of pervious stratum, while the depth of cut-off wall is being constant.

Bending Moment Study in Upstream Cut-Off

The selected numerical models are studied for bending moment in their upstream cut-off and are depicted in Fig. 3a. Normalized plot of upstream cut-off is plotted in Fig. 3b. On observing this plot, it is understood that, on increasing depth ratios, the point of occurrence maximum bending moment shifts downward from the top end of the cut-off wall. However, at 0.8 depth ratio, apart from shifting the maximum BM downward, negative bending moment occurs at upper end of cut-off.

It is understood that the bending moment profile is the function of length/depth of cut-off wall. Therefore, on higher depth ratios, due to higher depth of cut-off wall, there is a point of rotation on the wall inducing both positive and negative bending moments. If the depth of cut-off wall is less, i.e., in the case of lower depth ratio, there will not be any fixity or point of rotation resulting in either positive or negative moments.

The normalized bending moment diaphragm for depth ratio of 0.2, 0.4, 0.6, and 0.8 is shown, respectively, from Fig. 4a to d, to have clear comparisons. It is observed

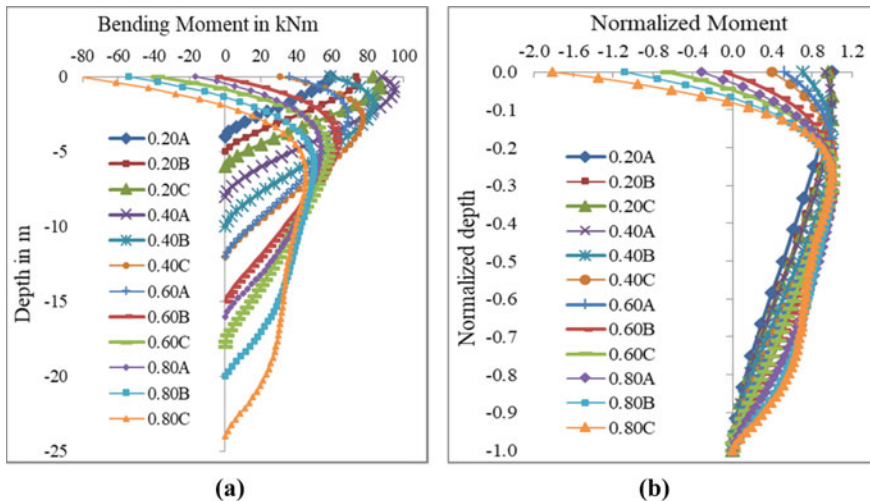


Fig. 33.3 Bending moment and normalized bending moment in US cut-off

that at 0.2 depth ratio, the bending moment pattern is almost identical. However, for remaining depth ratios, beyond the depth of $0.2d$ (where d is the depth of cut-off wall) from top end, all bending moment patterns are almost similar with very little variations. However, up to the depth of $0.2d$ from top end, the variation in the bending moment pattern increases at an increasing rate from 0.4 to 0.8 depth ratios.

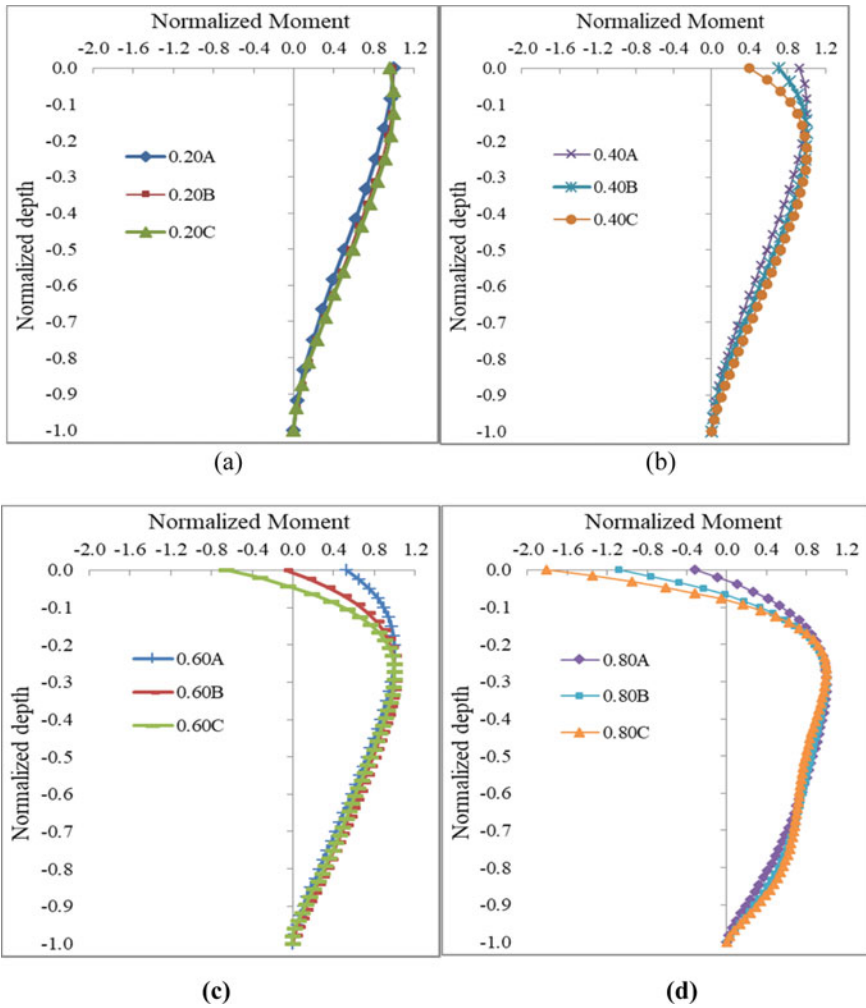


Fig. 33.4 Normalized BM diaphragm for depth ratio of 0.2, 0.4, 0.6, and 0.8 of upstream cut-off

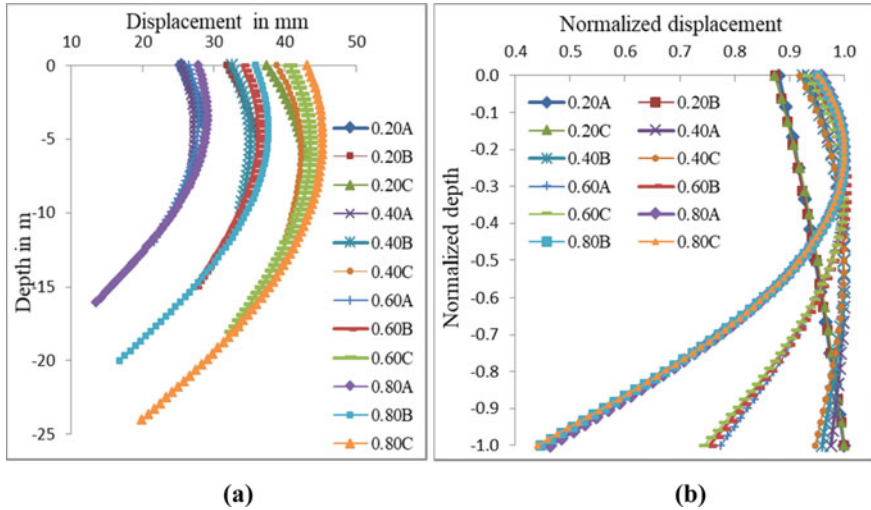


Fig. 33.5 Displacement and normalized displacement in downstream cut-off

Displacement Study in Downstream Cut-Off Wall

The displacements obtained from 12 models in respect of downstream cut-off wall are plotted in Fig. 5a and are studied for their behavior. In downstream cut-off wall, when the depth ratio is less than 0.2, the maximum displacement occurs at bottom end. The normalized displacement pattern of downstream cut-off is plotted in Fig. 5b.

This normalized displacement diagram shows that cut-off wall with similar depth ratios behaves similarly as observed in upstream cut-off wall, with disregard to its actual depth. As observed, with depth ratio 0.20, the maximum deflection occurs at bottom end of downstream cut-off. On increasing the depth ratio, the location of maximum deformation shifts upwards and locates near $0.2d$ of cut-off, where d is depth of cut-off. For a given depth ratio, the longer cut-off wall undergoes maximum displacement in absolute term.

Bending Moments in Downstream Cut-Off

Bending moment in downstream cut-off obtained from 12 models is plotted in Fig. 6a. The normalized pattern of bending moment is plotted in Fig. 6b. For better understanding and comparison, normalized bending moment plots are prepared for each depth ratios separately and placed from Fig. 7a to d. On studying these plots, it is observed that at 0.2 depth ratio, the bending moment pattern for all models is identical. However, on increasing the depth ratio further, the bending moment pattern starts varying.

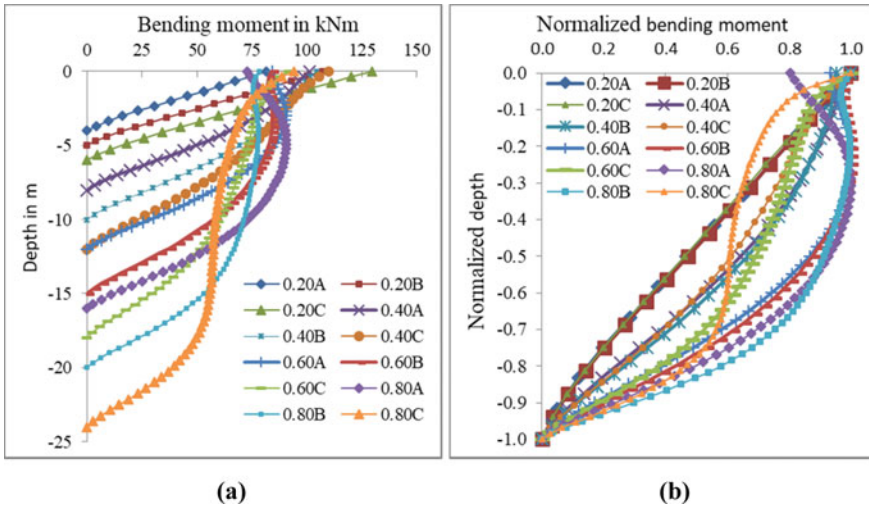


Fig. 33.6 Bending moment and normalized bending moment in downstream cut-off

Maximum Bending Moment in Cut-Off Walls

The maximum bending moment observed in both cut-off walls for different depth ratios is plotted in Fig. 33.8. This plot shows that the downstream cut-off is experiencing higher deformation than the upstream cut-off. Lesser deformation is experienced in upstream cut-off, despite it being positioned at higher pressure gradient zone. This phenomenon can better be understood with [5] seepage theory.

Khosla et al. [5] state that seepage force acts at every point on the streamlines and tangential to the seepage flow path. So, when the seepage flow is downward at upstream end, seepage force acts downward on soil particles, thereby increasing the effective stress on the soil. When the streamline flow path turns upward beyond downstream cut-off, this seepage force acts in upward direction. Due to this upward seepage force, saturated weight of the soil particles on the downstream side of the diversion dam reduces partially, thereby, reduced effective stress acts on downstream side of the downstream cut-off. Due to both, lower pressure gradient and reduced effective stress on downstream side of structure, result in increasing the net or differential force acts on downstream cut-off, thereby higher deformation is experienced in the downstream cut-off wall.

Ideal Depth Ratios in Cut-Off Walls

The effects of depth ratio on deformation of cut-off can be studied to find an ideal depth ratio in terms of its structural requirements. Maximum displacement and

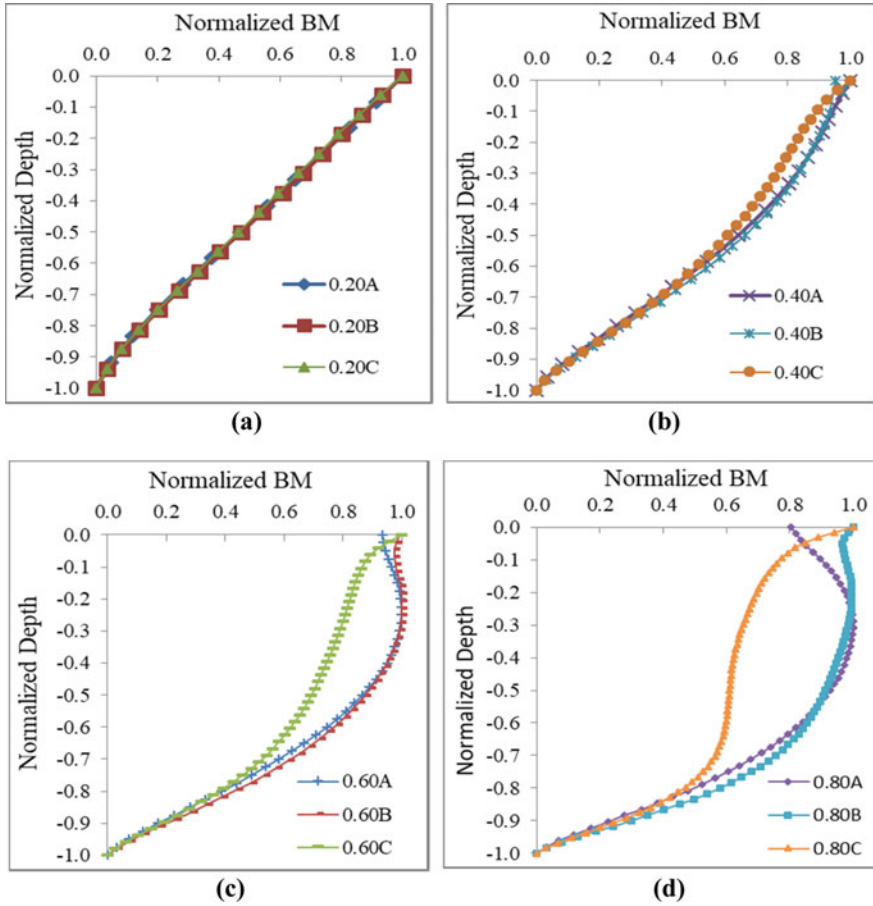
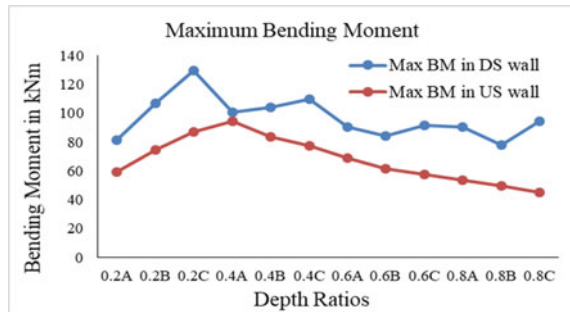


Fig. 33.7 Normalized BM diaphragm for depth ratio of 0.2, 0.4, 0.6, and 0.8 of downstream cut-off

Fig. 33.8 Maximum BM in both cut-off walls



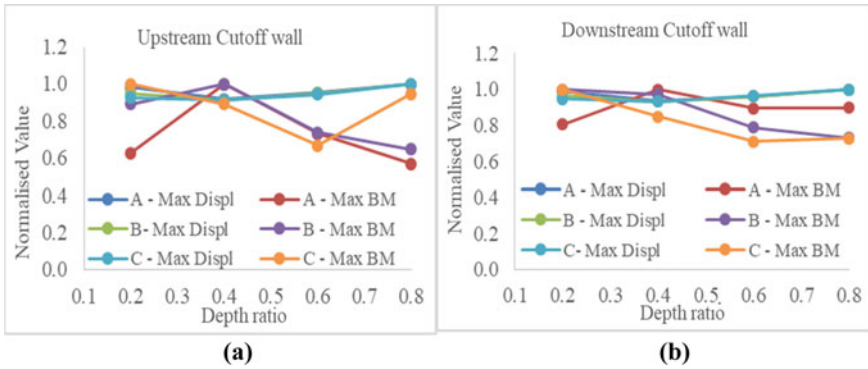


Fig. 33.9 Max displacement and BM for upstream and downstream cut-off wall for varying depth ratio

maximum bending moment for both cut-off walls on varying depth ratio are studied and plotted in Fig. 9a, b. On observing these plots, it can be construed that the ideal depth ratio in terms of reduced structural requirement for both upstream and downstream cut-off is 0.60.

Conclusion

Numerical study is conducted to ascertain the structural behavior of suspended type cut-off walls for variations in depth of pervious soil stratum with relation to depth of cut-off wall. Numerical models with different depth ratio 0.20 A, 0.20 B, 0.20 C, 0.40 A, 0.40 B, 0.40 C, 0.60 A, 0.60 B, 0.60 C, 0.80 A, 0.80 B, and 0.80 C are selected. Under constant differential pressure head, their deformation patterns are studied. The displacement and bending moments in both upstream and downstream cut-off walls from all 12 models are plotted. The normalized plot of displacement and bending moment for both cut-off walls is also plotted.

1. In upstream cut-off wall, it is observed that with lower depth ratio, the maximum deformation occurs at lower end of cut-off wall. However, increase in depth ratio results in shifting the location of maximum deformation toward top end.
2. In downstream cut-off wall, at lower depth ratio, the maximum deflection occurs at lower end of cut-off wall. On increase in depth ratio, the location of maximum deformation shifts upwards and locates near $0.2d$ from upper end of cut-off wall.
3. On observing normalized displacement plots, it can be established that pattern of displacement and bending moment of both cut-off walls at a particular depth ratio is similar irrespective of the depth of cut-off walls. With clear disregard to their actual depth, cut-off walls with similar depth ratio behave similarly.

4. The deformation in downstream cut-off wall is always higher than the deformation in upstream cut-off wall, even though it is located at higher pressure gradient zone than that of downstream cut-off wall located.
5. It is also observed that the ideal depth ratio in terms of reduced structural requirements for both cut-off walls is 0.60.

References



1. Bowles JE (1997) Foundation analysis and design, 5th edn. The McGraw-Hill Companies, Inc., England. ISBN-0-07-118844-4
2. Javanmard M, Mottaghi R, Hosseini SMM (2018) Investigating the influence of penetration length of cut-off wall on its dynamic interaction with core and foundation of earth dam. *Civ Eng J* 4(12):3019–3026
3. Kenney TC, Chiu CE, Ofoegbu GI, Omange GN, Ume CA (1985) Controlling constriction sizes of granular filters. *Can Geotech J* 22(1):32–43
4. Khairy AT, Al-Ghamdi AS, Gutub SA (2010) Analysis and design of a deep subsurface dam. *International Journal of Civil and Environmental Engineering* 10(03):27–35
5. Khosla AN, Bose NK, Mckenzie ET (1936) Design of weirs on pervious foundation. Publication number 12 of the central Board of Irrigation, Simla, India
6. Mansuri B, Salmasi F (2013) Effect of horizontal drain length and cut-off wall on seepage and uplift pressure in heterogeneous earth dam with numerical simulations. *Journal of Civil engineering and Urbanization* 3(3):114–121
7. Moharami A, Moradi G, Bonab MH, Katebi J, Moharami G (2014) Performance of cut-off walls under hydraulic structures against uplift pressure and piping phenomenon. *Geotech Geol Eng*. <https://doi.org/10.1007/s10706-014-9827-7>
8. Neshaei SAL, Mehrdad MA, Mahzoon NA (2010) Optimum design of cut-off walls located in the foundation of diversion dam using boundary element method. *WIT Transactions on Modeling and Simulations* 15
9. Norouzi R, Salmasi F, Arvanaghi H (2020) Uplift pressure and hydraulic gradient in Sabalan dam. *Appl Water Sci* 10:111. <https://doi.org/10.1007/s13201-020-01195-2>
10. Obrzud R, Truty A (2012) The hardening soil model - a practical guidebook. Z Soil. PC 100701 report. Revised 31 Jan 2012
11. Peck RB, Hanson WE, Thornburn TH (1974) Foundation engineering. Wiley, New York
12. Premalatha PV, Muthukkumaran K, Jayabalan P (2021) Effect of tie rod anchor on the behavior of berthing structures. In: Proceedings of the institutions of civil engineers, maritime engineering. ICE Publications, UK. Published online on 12 Feb 2021. <https://doi.org/10.1680/jmaen.2017.28>
13. Premalatha PV, Senthil Kumar S, Baskar K (2017) Influence of change in pile diameter at various locations of a pile group in a berthing structure. *Indian Journal of Geo-Marine Sciences* 46(06):1198–1209
14. Rice JD, Duncan JM (2010) Findings of case histories on the long-term performance of seepage barriers in dams. *J Geotech Geoenviron Eng* 136(1):2–15. [https://doi.org/10.1061/\(ASCE\)GT.1943-5606.0000175](https://doi.org/10.1061/(ASCE)GT.1943-5606.0000175)
15. Rice JD, Duncan JM (2010) Deformation and cracking of seepage barriers in dams due to changes in the pore pressure regime. *J Geotech Geoenviron Eng* 136(1):16–25. [https://doi.org/10.1061/\(ASCE\)GT.1943-5606.0000241](https://doi.org/10.1061/(ASCE)GT.1943-5606.0000241)
16. Sedghi-Asl M, Rehim H, Khaleghi M (2011) Laboratory investigation of the seepage control measures under coastal dikes. *Exp Tech* 36(1):61–71
17. Shakouri B, Mohammadi M (2019) Evaluation of penetration depth for cut-off walls in the core of earth dams. *Geotech Geol Eng*. <https://doi.org/10.1007/s10706-019-01004-x>

18. Shayan HK, Tokaldany EA (2015) Effects of blanket, drains and cut-off wall on reducing uplift pressure, seepage and exist gradient under hydraulic structure. *International Journal of Civil Engineering* 13(4)
19. Sivakumar S, Almas Begum N, Premalatha PV (2018) Behavior of partial seepage barrier in highly permeable soils. *International Journal of Civil Engineering and Technology* 9(02):286–298. ISSN Print: 0976-6308, ISSN Online: 0976-6316
20. Sivakumar S, Almas Begum N, Premalatha PV (2018) Numerical study on deformation of diaphragm cut off walls under seepage forces in permeable soils. *Computers and Geotechnics* 102:155–163. ISSN 0266-352X
21. Sivakumar S, Almas Begum N, Premalatha PV (2018) Effects of depth variations in deformation of cut-off walls. *International Journal of Civil Engineering and Technology* 9(5):634–643. ISSN Print: 0976-6308. ISSN Online: 0976-6316
22. Sivakumar S, Almas Begum N, Premalatha PV (2019) Deformation analysis of suspended type cut off wall of diversion structures. *Heliyon* 5:e02213. ISSN 2405-8440
23. Tung S, Bhandari GN, Mukherjee SP, Deb K (2013) Effect of sheet pile on seepage below earthen dam. *Indian Geotechnical Conference December, Roorkee* 3(10)
24. Tung S, Bhandari GN, Mukharjee SP (2015) Effect of seepage cut-off below earthen dam under rapid drawdown. In: *50th Indian geotechnical conference, Pune, India*

Chapter 34

Performance Evaluation of Scrap Rubber-Sand Mixture Reinforced with Geogrids as a Backfill Material in Retaining Walls



K. P. Anjali  and Renjitha Mary Varghese 

Introduction

The waste tire rubber has many applications in construction and geotechnical fields like replacement material for bitumen and asphalt in roadways, replacement for railway sub-ballast layers, soil stabilization, seismic isolation of buildings, lightweight backfill material for retaining walls, etc. [1]. These effective incorporations of waste tire rubbers in various works can reduce the disposal problem of tires in an environmentally and economically beneficial way. Some previous studies showed that waste tires can be used as lightweight backfill alternative in retaining structures [2]. It is also evident that the use of tire mixed with soil in various proportions potentially enhances the foundation stability and also reduces settlements problems. Also some studies proved that the use of tire rubber-sand mixture mixed at various proportions can effectively improve the backfill stability by increasing its shear strength properties [3].

In this study, a series of large-size direct shear tests are done to understand the shear strength variation with varying rubber content in sand, size of rubber granules, and applied normal stresses.

Materials

The locally available sand was used in the present study (see Fig. 34.1). Table 34.1 represents the sand properties. According to IS.1498-1970, sand is classified as SP (poorly graded).

K. P. Anjali (✉) · R. M. Varghese
National Institute of Technology, Calicut, Kozhikode, India
e-mail: kpanjali.sg@gmail.com



Fig. 34.1 Sand and rubber samples, R1 and R2

Table 34.1 Properties of sand

Property	Value
Specific gravity, G	2.62
D_{10}	0.21 mm
D_{30}	0.33 mm
D_{60}	0.5 mm
Coefficient of uniformity, C_u	2.381
Coefficient of curvature, C_c	1.037
Maximum unit weight, γ_{dmax}	14.61 kN/m ³
Minimum unit weight, γ_{dmin}	13.24 kN/m ³
Maximum void ratio, e_{max}	0.94
Minimum void ratio, e_{min}	0.758

As per ASTM D6270-12, the shredded tire can be classified as different groups according to their sizes. The rubber tire products are usually referred as tire shreds if size is between 50 and 305 mm, similarly tire chips for size 12 and 50 mm, granulated rubber for size 0.425 and 12 mm, and ground rubber for size <0.425 and 2 mm. Two sets of granulated rubber (R1 and R2) have been used in this study (see Fig. 34.1) with different size specifications shown in Table 34.2.

Specific gravity of both the sets of rubber samples was found according to ASTM D854-02 as 1.023 and 1.061 for R1 and R2, respectively, which is within the range of 0.88–1.27 as mentioned in the previous literature [4].

Other preliminary properties such as grain size distribution, coefficient of curvature, and uniformity coefficient for sand and two sets of rubber were also determined. The particle size distribution of R1 and R2 compared to pure sand is shown in Fig. 34.2. R1 is found to be poorly graded as compared to R2.

Table 34.2 Size of granulated rubber

Sample name	Size of granulated rubber
R1	<4.75 mm
R2	<12 mm

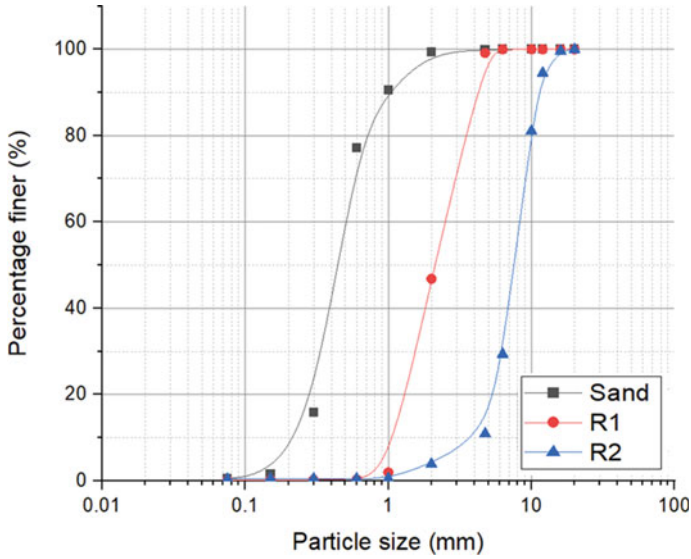


Fig. 34.2 Particle size distribution for sand, R1, and R2

Reinforcing Material

Commercially available geogrids made of high-density polyethylene (HDPE) were used as the planar reinforcement (see Fig. 34.3). Uniaxial physical and mechanical properties of the geogrid material used for the experiment are listed in Table 34.3.

Fig. 34.3 Geogrid sample

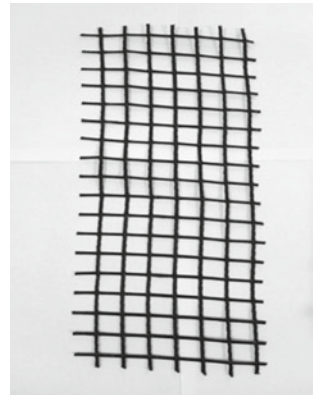


Table 34.3 Properties of geogrid used for this study

Property	Value
Opening size	20 mm × 20 mm
Rib thickness	0.1 mm
Mass per unit area	68 g/m ²
Ultimate tensile strength	40 kN/m
Axial tensile strain at failure	11%

Experimental Program

The stress–strain behavior and interfacial friction angle of the rubber-sand mixture reinforced with geogrids were found from large-size direct shear test results. The length, breadth, and height of the test box were of dimension 300 mm × 300 mm and 150 mm, respectively. The influence of rubber size, rubber percentage, and normal stress on shear behavior of rubber-sand mixture was also studied. Altogether 81 large-scale direct shear tests were conducted. Table 34.4 represents the experiment details of this study. RxSy in Table 34.4 represents rubber-sand mixture with *x*% of rubber mixed with *y*% of sand by volume.

The rubber-sand mixtures have been prepared at ratios 0:100, 10:90, 30:70, and 50:50 by volume. The volume of particles in the rubber-sand mixture, $V_p(\chi)$, is calculated as per Eq. (34.1)

$$V_p(\chi) = \frac{m_S(\chi)}{G_{sS}} \left(\frac{g}{\gamma_w} \right) + \frac{m_R(\chi)}{G_{sR}} \left(\frac{g}{\gamma_w} \right) \tag{34.1}$$

where m_S and m_R are masses of sand and rubber, respectively. G_{sR} and G_{sS} are the specific gravities of rubber and sand, respectively. ‘*g*’ and ‘ γ_w ’ represent the acceleration due to gravity and unit weight of water, respectively [4]. The quantity of rubber and sand required for achieving a relative density of 70% for each percentage

Table 34.4 List of experiments

Un reinforced			Geogrid reinforced		
Test code (R _x S _y)	Normal stress (kPa)	No of tests	Test code (R _x S _y)	Normal stress (kPa)	No of tests
R ₀ S ₁₀₀	50,100,150	9	–	–	–
R ₁ –R ₁₀ S ₉₀	50,100,150	9	–	–	–
R ₁ –R ₃₀ S ₇₀	50,100,150	9	R ₁ –R ₃₀ S ₇₀	50, 100, 150	9
R ₁ –R ₅₀ S ₅₀	50,100,150	9	–	–	–
R ₂ –R ₁₀ S ₉₀	50,100,150	9	–	–	–
R ₂ –R ₃₀ S ₇₀	50,100,150	9	R ₂ –R ₃₀ S ₇₀	50, 100, 150	9
R ₂ –R ₅₀ S ₅₀	50,100,150	9	–	–	–

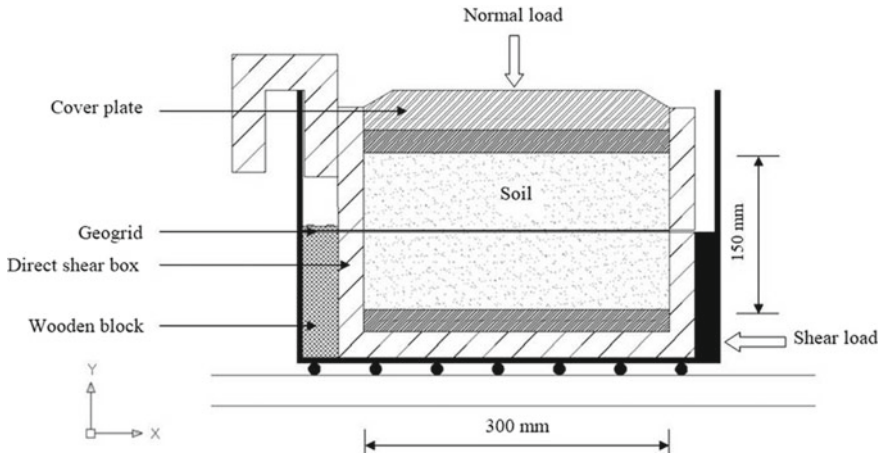


Fig. 34.4 Schematic diagram of direct shear test box

composition for both the R1 and R2 was estimated. The rubber-sand mixtures were thoroughly mixed by hand and transferred to the shear box in different layers for getting uniformity. The prepared specimen was filled in the box in four different layers, and proper compaction was given to obtain the prescribed related density.

Geogrid samples of length 300 mm and breadth 250 mm were taken and placed in between the two halves of direct shear test box with rubber-sand mixtures for obtaining the interface shear properties. They were placed in shear box by clamping one end to the wooden clamping block using bolts and cover plates.

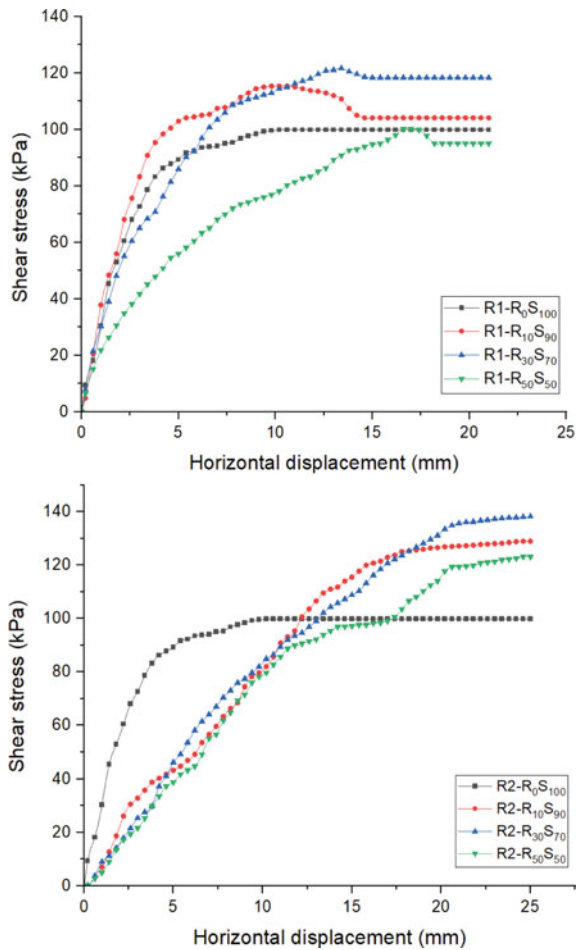
The tests were conducted for three different normal stresses of 50, 100, and 150 kPa to cover the stress range of lightweight fill in field embankment applications, [5] and the constant shear strain of 1.25 mm/min was applied. A schematic diagram of direct shear test box is shown in Fig. 34.4. References [2, 6] pointed out there is no visible definite failure point for the rubber-sand mixtures; thus, a failure point at 25 mm horizontal displacement was adopted for a direct shear box of 305 mm dimension. Hence, the experiments are conducted for a maximum horizontal displacement of 25 mm.

Results and Discussions

The behavior of rubber-sand mixture shear strength parameters was obtained from the large-size direct shear test results for both geogrid reinforced and unreinforced cases. The interface shear parameters between the geogrid reinforcement and rubber-sand mixtures such as adhesion (ca) and angle of interface friction between rubber-sand mixture and geogrid (δ) were also determined.

Effect of rubber percentage on shear-strain behavior: Study on stress–strain behavior of rubber-sand mixtures for various percentages of rubber content was conducted. Figure 34.5 shows the stress–strain behavior at different rubber content for R1 and R2 under 150 kPa normal stress. Initially, shear stress was found to increase as the rubber percentage increases from 0 to 30%, and after that, it starts to decrease. The initial increase is contributed by the filling of voids with rubber but after reaching specific rubber content, segregation occurs, and thus, the rubber-sand mixture behaves like a rubber mass with sand inclusions rather than a reinforced soil mass. This is similar to the results obtained in [7], and when different normal stresses are applied, the shear resistance of rubber-sand mixture was found to be higher than that of sand alone case, but this increasing trend was observed only up to 30% of rubber, and beyond this value, the shear resistance starts to show a decreasing trend.

Fig. 34.5 Shear stress versus horizontal displacement curve for R1-sand mixture and R2-sand mixture at 150 kPa normal stress



It is also observed that addition of rubber in the mixture increased the axial strain at which the maximum stress was observed. When the percentage of rubber content is 50%, the maximum stress which is equal to the maximum shear stress of normal sand was obtained at higher strain levels. The peak shear strength of pure sand reaches at an axial strain of 1.3–1.7%, whereas for R₅₀S₅₀ mixture, it reaches at axial strain of 5–8.4%. This indicates the additional flexibility obtained by sand by introducing rubber content. Similar observations were reported in [8–10]. The experimental results showed that R₃₀S₇₀ mixture has the highest shear strength values.

The variation of the internal friction angle of rubber-sand mixtures with varying rubber contents for R1 and R2 rubber types shows that the internal friction angle increases with increase in the rubber content and reaches a peak value when the rubber content is 30% and then decreases for rubber contents beyond this value (see Fig. 34.6). A similar trend was observed in [11]. The decrease in friction angle at higher rubber contents is because of the presence of more rubber in failure plane which increases rubber-to-rubber interaction and reduces rubber-sand and sand-sand interactions [7].

Effect of rubber size on shear strength: The variation of peak stress for both R1 and R2 mixtures at 30% rubber content shows that with increasing rubber size from R1 to R2, the peak shear strength is found to increase (see Fig. 34.7). Similar pattern is observed for other rubber-sand mixtures of various proportions. These results are similar to those obtained in [7].

More interlocking capacity of bigger particles than the smaller particles can be reason for this variation in shear strength with the size of rubber particles. In case of R1, the average percentage increase peak shear stress is 31.2%, and for R2, it is 45%. The comparison of axial strain indicates that 30% of R2 sized rubber provides 12% more maximum peak. It is found that with the increase in size of the rubber the shear strength and flexibility for all percentages of rubber content are increased which enable in reducing the cost of shredding by using bigger tire shreds.

Fig. 34.6 Variation of internal friction angle, ϕ with rubber content

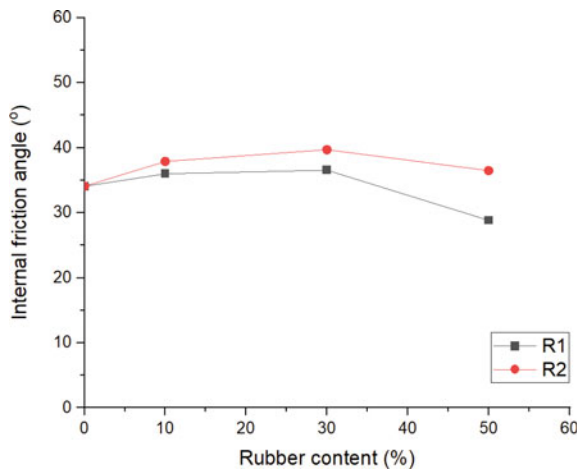
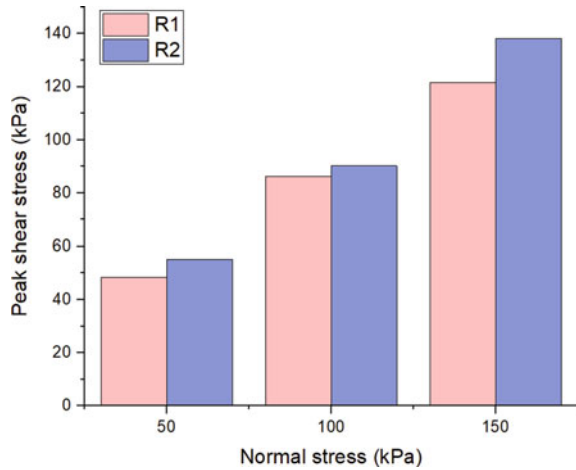


Fig. 34.7 Variation of peak shear stress for two different sizes of rubber, R1 and R2 mixtures at 30% rubber content



It is observed that the friction angle for bigger sized R2 is higher at all rubber contents compared to smaller sized R1 (see Fig. 34.6). This increase can be the result of the more interlocking capacity of larger rubber particles with sand, thus giving rise to higher internal friction in the shearing zone.

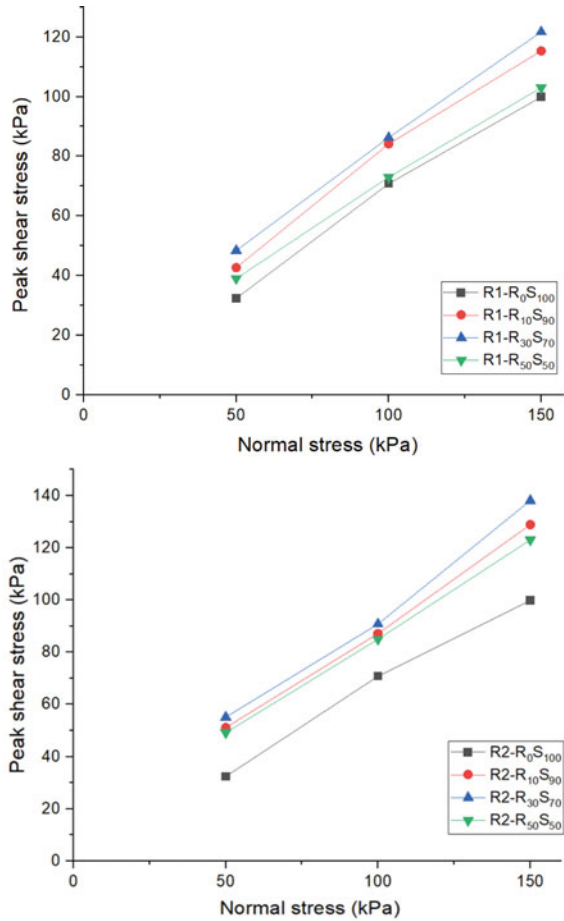
Influence of normal stress: The peak shear stress versus normal stress characteristics at different rubber contents for R1 and R2 mixtures in sand at normal stresses of 50, 100, and 150 kPa show that the shear parameters for all rubber-sand mixtures were higher when compared to sand only case (R_0S_{100}) (see Fig. 34.8).

Also, at all normal stresses, the peak value of shear strength was obtained for $R_{30}S_{70}$ combination. At $R_{50}S_{50}$, the peak strength reduction is found higher. The increasing trend of shear strength with increasing normal stress occurs due to reduction in the voids when overburden pressure is increased. This ultimately increases the interlocking capacity between the rubber and sand granules [12]. The peak stress is found decreased at higher rubber contents due to the presence of more voids compared to lesser rubber content cases.

Interfacial shear strength coefficient: The interfacial shear properties between the rubber-sand mixture and the geogrids were studied for two sets of rubber sizes at varying normal stress at 30:70 by volume mixture ratio of sample for which the maximum shear stress was observed. The interfacial shear parameters between geogrid reinforcement and rubber-sand mixtures such as adhesion (c_a) and interface friction angle between rubber-sand mixture and geogrid (δ) were also determined from large direct shear tests. For the comparison of the interface shear strength of soil against any geosynthetic material, the shear strength values can be normalized using a non-dimensional parameter called interface shear strength coefficient (α). Interfacial friction strength coefficient can be calculated by using the formula given in [13],

$$\alpha = \tau_{\text{sand - geosynthetic}} / \tau_{\text{sand}} \quad (34.2)$$

Fig. 34.8 Peak shear stress versus normal stress characteristics at varying rubber contents for R1 and R2



where $\tau_{\text{sand-geosynthetic}}$ denotes the peak shear stress at sand-geosynthetic interface and τ_{sand} denotes the peak shear stress of unreinforced sand.

Using Eq. (34.2), shear strength coefficient for the rubber-sand mixture with geogrid reinforcement can be determined. Table 34.5 shows the values obtained from the tests for shear strength parameters for two sets of rubber types mixed at various proportions. The shear parameters were found to be higher at R₃₀S₇₀ proportion in both R1 and R2 cases. The interface friction angle between rubber-sand mixture and geogrid (δ) was found to be 36.5 and 40.0 for R1 and R2 cases, respectively, which is found to be slightly greater than the unreinforced case. The shear strength variation of geogrid reinforced case with varying rubber size is similar to that of unreinforced case.

Table 34.5 Shear parameters for geogrid reinforced and unreinforced rubber-sand mixtures

Rubber set	Unreinforced case		Geogrid reinforced case		
	φ	c	δ	ca	α
R1-R ₁₀ S ₉₀	35.9	8.0			
R1-R ₃₀ S ₇₀	36.2	12.3	36.5	13.3	1.0191
R1-R ₅₀ S ₅₀	28.8	6.7			
R2-R ₁₀ S ₉₀	37.8	11.2			
R2-R ₃₀ S ₇₀	39.6	12.6	40.0	13.6	1.0277
R2-R ₅₀ S ₅₀	36.4	10.5			

The peak shear strength for R1-sand geogrid combination was found to be 124.2 kPa and R2-sand geogrid combination was found to be 141.6 kPa. Consequently, the interfacial shear strength coefficient values for R1 and R2 combination were found to be 1.0191 and 1.0277, respectively; i.e., it provides only 2 and 2.8% interface shear strength improvement compared to sand without reinforcement. Hence, the interfacial shear strength responses of the rubber-sand mixture and geogrid showed that there is no significant difference in the interfacial frictional strength when rubber-sand mixture is reinforced with geogrids and it is independent of granular rubber size in mixture which enhances the usage of bigger rubber shreds. The findings from the experimental studies lead to a sustainable as well as cost-effective design of retaining structures.

Conclusions

The shear strength properties of different percentages of rubber-sand mixtures (0:100, 10:90, 30:70, 50:50 by volume) were studied from large-size direct shear tests. The interaction between rubber-sand mixtures with geogrid reinforcement was also studied. It has been found that the shear strength of the mixtures is influenced by rubber content, rubber granule size, and normal stresses.

The conclusions that can be drawn from the results are as follows:

- The inclusion of tire rubber shreds into the sand increases the shear strength of the sand in both unreinforced and geogrid reinforced case.
- With increase in proportion of rubber content, the shear stress has increased initially up to 30% and then decreases beyond this value. This explains the sand-like and rubber-like behavior shown at different rubber percentages.
- As granular rubber size increases, the shear strength and flexibility are increased for all percentages of rubber content. This reduces cost of shredding by using bigger tire shreds.
- The normal stress is also a dominant factor that affects the improvement in strength of rubber-sand mixtures. With the increase in the normal stress, shear strength of

mixture is found to increase for both R1 and R2 combinations at all percentage contents.

- The shear strength parameters also begin to increase initially with increasing percentage of rubber content initially followed by a decrease later.
- The interface friction strength coefficient for R1-sand combination was found to be 1.0191 and R2-sand mixture was found to be 1.0277. This shows an interface shear strength improvement of 2 and 2.8%, respectively, in comparison with unreinforced sand. Also, it is independent of size of the rubber particles in the mixture which enhances the usage of bigger rubber shreds.
- The findings from experimental studies lead to a sustainable as well as cost-effective design of retaining structures.

References

1. Mohajerani A, Burnett L, Smith JV, Markovski S, Rodwell G (2020) Resources, conservation & recycling recycling waste rubber tyres in construction materials and associated environmental considerations: a review. *Resour Conserv Recycl* 155:104679. <https://doi.org/10.1016/j.resconrec.2020.104679>
2. Pincus H, Edil T, Bosscher P (1994) Engineering properties of tire chips and soil mixtures. *Geotech Test J* 17(4):453. <https://doi.org/10.1520/gtj10306j>
3. Tanchaisawat T, Bergado DT, Voottipruex P, Shehzad K (2010) Geotextiles and geomembranes Interaction between geogrid reinforcement and tire chip—sand lightweight backfill. *Geotext Geomembranes* 28(1):119–127. <https://doi.org/10.1016/j.geotexmem.2009.07.002>
4. Sheikh MN, Mashiri MS, Vinod JS, Tsang H, Asce M (2014) Shear and compressibility behavior of sand—tire crumb mixtures. *J Mater Civ Eng* 25(10):1366–1374. [https://doi.org/10.1061/\(ASCE\)MT.1943-5533.0000696](https://doi.org/10.1061/(ASCE)MT.1943-5533.0000696)
5. Youwai S, Bergado DT (2003) Strength and deformation characteristics of shredded rubber tire—sand mixtures. *Can Geotech J* 40(2):254–264. <https://doi.org/10.1139/02-104s>
6. Foose GJ, Benson CH, Bosscher PJ (1996) Sand reinforced with shredded waste tires. *J Geotech Eng* 122(9):760–767. [https://doi.org/10.1061/\(asce\)0733-9410\(1996\)122:9\(760\)](https://doi.org/10.1061/(asce)0733-9410(1996)122:9(760))
7. Anbazhagan P, Manohar DR, Rohit D (2017) Influence of size of granulated rubber and tyre chips on the shear strength characteristics of sand—rubber mix. *Geomechanics and Geoengineering* 12(4):266–278. <https://doi.org/10.1080/17486025.2016.1222454>
8. Masad E, Taha R, Ho C, Papagiannakis T (1996) Engineering properties of tire/soil mixtures as a lightweight fill material. *Geotech Test J* 19(3):297–304. <https://doi.org/10.1520/gtj10355j>
9. Liu C, Zornberg JG, Asce M, Chen T, Ho Y, Lin B (2010) Behavior of geogrid-sand interface in direct shear mode. *J Geotech Geoenviron Eng* 135(12):1863–1871. [https://doi.org/10.1061/\(ASCE\)GT.1943-5606.0000150](https://doi.org/10.1061/(ASCE)GT.1943-5606.0000150)
10. Rao GV, Dutta RK (2006) Compressibility and strength behaviour of sand: tyre chip mixtures. *Geotech Geol Eng* 24:711–724. <https://doi.org/10.1007/s10706-004-4006-x>
11. Ghazavi M (2011) Experimental determination of waste tire chip-sand-geogrid interface parameters using large direct shear tests experimental determination of waste tire chip-sand-geogrid interface parameters using large direct shear tests, Dec 2015
12. Marto A, Latifi N, Moradi R, Oghabi M, Zolfeghari SY (2013) Shear properties of sand-tire chips mixtures. *Electron J Geotech Eng* 18:325–334
13. Makkar FM (2017) Performance of 3-D geogrid-reinforced sand under direct shear mode. *Int J Geotech Eng* 6362:1–9

Chapter 35

Behavior of Cantilever Concrete Diaphragm Wall Under Sequential Excavation of Front-Fill Soil: A Numerical Study



Abhijit Debnath and Sujit Kumar Pal

Introduction

Due to the rapid growth of construction activities in urban areas, deep excavation is often practice for engineers close to existing structures. Deep excavations are often used in high-rise buildings, basements, underground mass transport systems, water distribution networks, etc. [5, 7]. Diaphragm walls are widely used as temporary as well as permanent retaining structures to support soils during deep excavations on congested sites [4]. Bose and Som [2] carried out a study using FEM; a parametric analysis was done on a 13.6 m deep excavation using lateral bracing [2]. The influence of soil elastic modulus, creep, and wall–soil interface was studied by Hsiung [7] by numerical modeling and the numerical model results compared with a case study of sand excavation. Over the last few decades, much research has been done on deep excavation, but a more comprehensive analysis needs to be done. The construction procedures involved sequential soil excavation in front of a wall or soil backfilling behind the wall generating different types of loading conditions in the ground, leading to change in wall behavior [1]. So, in the present study, sequential soil excavation in front of the diaphragm wall was considered. In this paper, a numerical model study by a finite element program of ABAQUS was done on stratified sand deposits under natural and modified front-fill soil conditions to investigate the effects of different magnitudes of surcharge strip loadings on the wall by varying loading positions. Wall deflections, bending moments, ground settlements, and horizontal earth pressures were investigated under natural and modified soil conditions.

A. Debnath (✉) · S. K. Pal
Department of Civil Engineering, NIT, Agartala 799046, India
e-mail: abhijit.nita2020@gmail.com

Wall and Soil Profiles

The diaphragm wall chosen in the present study comprises 30 m in height (H) and 0.8 m thick (t_{wall}). The properties of the concrete diaphragm wall are given in Table 35.1. To represent the elastic strain component of the soil behavior, the parameters required for the Mohr–Coulomb model are Modula’s of elasticity, E , and Poisson’s ratio, ν . To represent the plastic strain component of the soil behavior, the effective strength parameters are cohesion, \acute{c} , and angle of friction, $\acute{\phi}$, along with the dilation angle, ψ , which are required. Dilation angle, ψ , is calculated using the equation $\psi = \acute{\phi} - 30^\circ$ [10]. The soil–wall interface is represented by the parameter interface friction angle (δ). The friction coefficient (μ) value between soil–wall interfaces is taken as $\tan\delta$ for different soil profiles. As described by Chowdhury et al., the properties of soil were used in the current model [5]. The parameters of soil used in the present analysis are shown in Tables 35.2 and 35.3. The load is applied into three steps: Geostatic step is used to generate the initial conditions, to keep the model in equilibrium; in the second step, self-weight is applied in the whole model; and finally, the surcharge loading is applied at the top of the soil using a footing. In this study, a surcharge strip load of varying magnitude of 50 kPa, 100 kPa, and 150 kPa was imposed, the surcharge positions were varied from the edge of the wall. The width of the surcharge was taken as 0.5 times the height of the wall ($0.5 \times H = 7.5$ m) [6].

In the current study, Poisson’s ratio of soil was set at 0.30 for the case of natural soil condition and 0.32 in modified soil condition. The value of Modula’s of elasticity (E_{wall}) and Poisson’s ratio (ν_{wall}) of the diaphragm wall was collected from Bose and Som [2], shown in Table 35.1.

Table 35.1 Description of wall considered in this analysis (data from Bose and Som [2])

Material type	Unit weight (KN/m ³)	Poisson’s ratio, μ_{wall}	E_{wall} (KN/m ²)	Moment of inertia I_{wall} (m ⁴ /m)
Concrete	24	0.15	2.5×10^7	0.0427

Table 35.2 Description of soil parameters used in this study (data from Chowdhury et al. [5])

Depth of soil below ground level (m)	Layer serial numbers	Bulk unit weight (KN/m ³)	Soil cohesion, \acute{c} (KN/m ²)	Angle of friction, $\acute{\phi}$ (°)	Poisson’s ratio, μ	Modula’s of elasticity E (KN/m ²)
0.0–5.0	1	18.8	0	30	0.3	11,500
5.0–15.0	2	19.0	0	32	0.3	15,500
15.0–30.0	3	19.5	0	33	0.3	19,500
30.0–90.0	4	19.8	0	34	0.3	31,500

Table 35.3 Description of modified soil parameters in the front-fill zone used in this study

Depth of soil below ground level (m)	Layer serial number	Bulk unit weight (KN/m ³)	Soil cohesion, \acute{c} (KN/m ²)	Angle of friction, $\acute{\phi}$ (degree)	Poisson's ratio, μ	Modula's of elasticity, E (KN/m ²)
15.0–30.0	3	20	0	42	0.32	75,000

Numerical Modeling

The finite element software ABAQUS was used to carry out the present study. The 2D mesh and boundary conditions adopted in the present analysis are shown in Fig. 35.1. The wall and soil were modeled by a four-nodded bilinear quadrilateral plane strain element (CPE4R). The vertical boundaries of the model are free to move in the vertical direction, and its movement is restricted in the horizontal direction. The movements of the bottom boundary are restricted in horizontal as well as in vertical directions [2–5, 9]. The Mohr–Coulomb constitutive soil model has been frequently used [3–5, 8–10]. In the present study, Mohr–Coulomb constitutive model was taken. Hence, the soil is modeled as an elastic–perfectly plastic Mohr–Coulomb model by a non-associated flow rule with an angle of dilation of zero (0). The boundaries of the model geometry are selected to avoid disturbance during numerical operation on the response of the soil movements during the excavation process [3]. The horizontal boundary was taken as six times the total height of the wall ($6 \times H = 180$ m) to avoid the numerical disturbance, and the wall was placed in the center of the width of the model. The vertical boundary was three times the total height of the wall ($3 \times H = 90$ m). A finer mesh was used in and around the diaphragm wall where the stress concentration is high, and the coarser mesh was used in the regions away from the diaphragm wall. The ratio of interface friction angle to the angle of internal friction, $\delta/\acute{\phi}$, ranges from 0.5 to 0.9 for the steel and sand interface [11]. Here, δ is interface friction angle, and $\acute{\phi}$ is the angle of internal friction. In this study, the average range, $\delta/\acute{\phi} = 0.7$, was taken, and the interface friction angle used for the four soil layers was calculated based on that ratio [1]. The construction method was simulated by the excavation of front-fill soil in lifts. The total depth of soil removed was done in six steps; each lift had a thickness of 2.50 m. In the present analysis, the effective cohesion for the soil (\acute{c}) was fixed at zero. The lateral pressure coefficient at rest (K_0) was collected from Jaky's equation which is $K_0 = 1 - \sin \acute{\phi}$.

Numerical Model Validation

To verify the present numerical model, the results obtained from the model test were compared with the values (based on numerical model study) as reported in Hsiung [7]. The numerical analysis performed by Hsiung [7] was based on the excavation at the

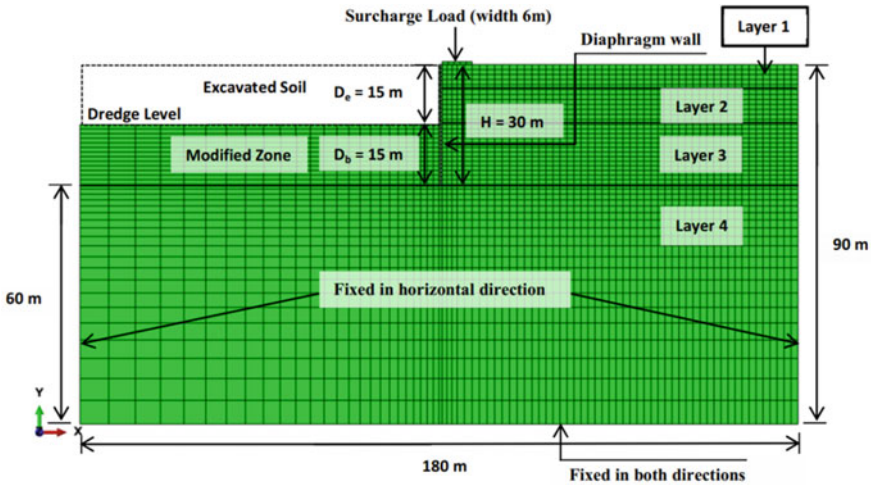


Fig. 35.1 Cantilever concrete diaphragm wall–soil model considered in the present analysis in ABAQUS 2D

O6 station on the orange line in the Kaohsiung rapid transport system. The present diaphragm wall was supported by struts at five different levels without surcharge for the model validation purpose. Considering the similar ground condition as used by Hsiung [7], it can be seen in Fig. 35.2 that there are very small differences in settlement values in the present model and results obtained by Hsiung [7]. Hence, good agreement is observed between the current numerical analysis and Hsiung [7] analysis.

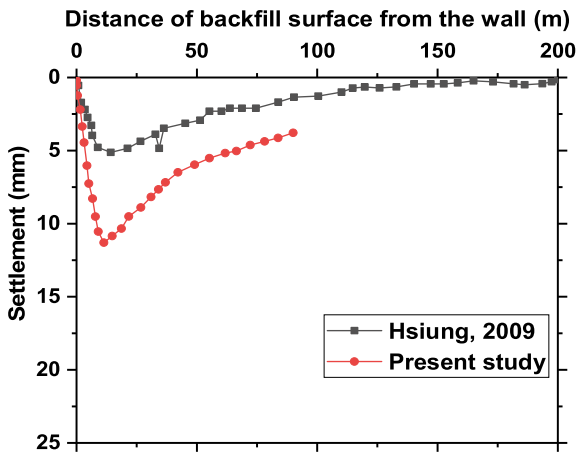


Fig. 35.2 Comparison of the current numerical model results with numerical observation by Hsiung [7]

Results and Discussion

Lateral earth pressures, deformations of wall, bending moments of wall, and ground settlements were studied for natural and modified front-fill soil conditions. In all the cases, a surcharge pressure of 50 KN/m², 100 KN/m², and 150 KN/m² was positioned at a distance of 0.00, 3.75, 7.50, 11.25, and 15.00 m from the wall. The results of the two cases are presented in detail to assess the effect of modified soil on concrete diaphragm wall behavior constructed by the sequential excavation of front-fill soil.

Lateral Earth Pressures

Lateral pressures (active and passive pressure) behind the 30 m high wall for natural and modified soil conditions with different surcharge magnitude placed at various locations over the backfill soil are shown in Figs. 35.3 and 35.4.

From Fig. 3a, b, and c, it was seen that the maximum total active earth pressure was reduced by 40%, 45%, and 50%, respectively, for 50 kPa, 100 kPa, and 150 kPa surcharge in modified soil conditions. But passive earth pressure is higher for modified soil conditions. Figures 3a and 4a show that varying the surcharge position has very little effect on total active and passive earth pressure distribution. But Figs. 3b, c and 4b, c show that varying the surcharge position significantly affects total active and passive earth pressure. The magnitude of active earth pressure change was relatively considerable below the dredge line.

It was seen from Fig. 4a, b, and c that the magnitude of passive earth pressure was significantly changed for a depth of 3.46 m beneath the dredge line for natural soil condition and 2.30 m beneath the dredge line for modified soil condition. Both active and passive pressure variations are found very little at the toe of the wall.

Displacements of Wall

Lateral displacements behind the 30 m high wall for natural and modified soil conditions are as shown in Fig. 35.5. Figure 35.5 indicates that wall deflection is maximum at the top for all the cases, as expected.

From Fig. 5a, b, and c, it is found that soil modification in front-fill foundation soil will reduce the deflection. The results indicated that as the amount of surcharge increases, the deflection of the wall also increases. In all the cases, the position of surcharge pressure also greatly affected the lateral wall deformations.

Figure 5a, b, and c indicate that closer the surcharge to the wall gives a higher value of wall deflection. The deflections are less when the surcharge is placed far away from the wall. So, here the position 0.00 m gives higher wall deflection, and 15.00 m shows lower deflection values.

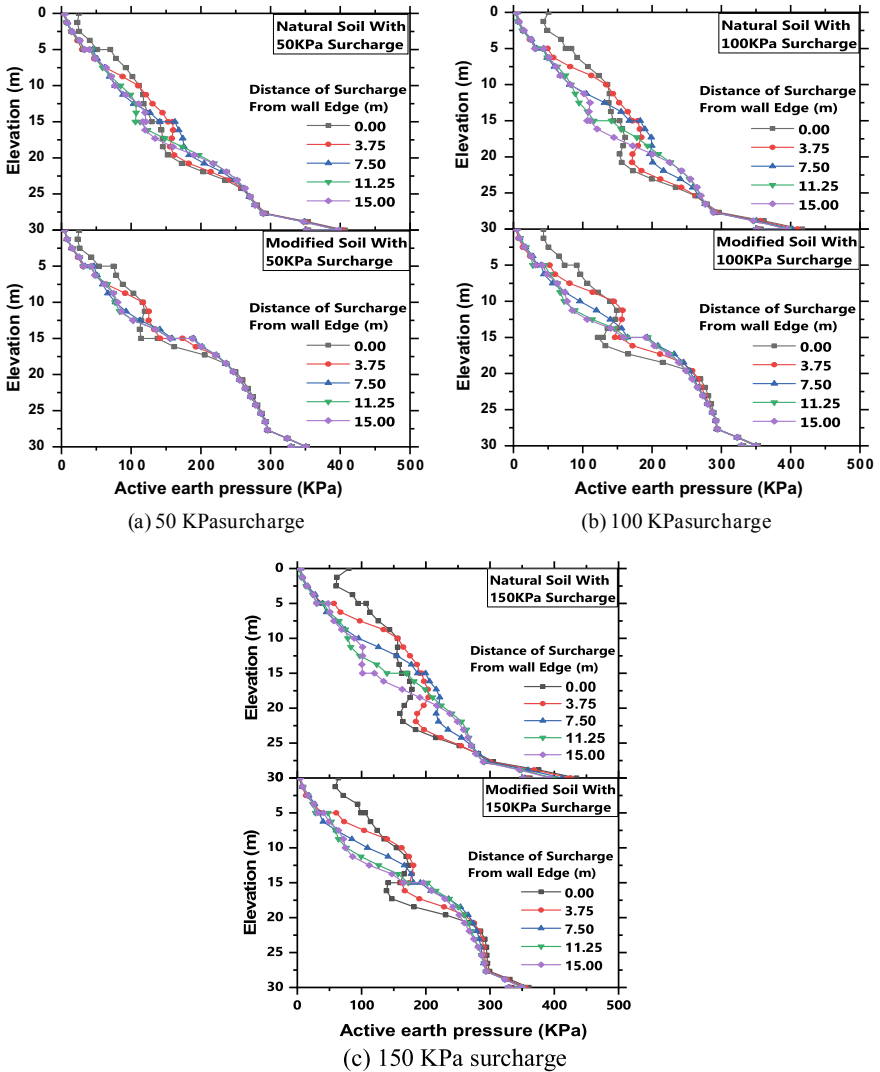


Fig. 35.3 Lateral earth pressures (active earth pressure) for 30 m high wall

Due to the modification of front-fill foundation soil, the maximum deflection of the wall reduces by an average value of 0.55 times the deflection obtained in natural soil. This reduction is independent of the magnitude of the surcharge load and its position.

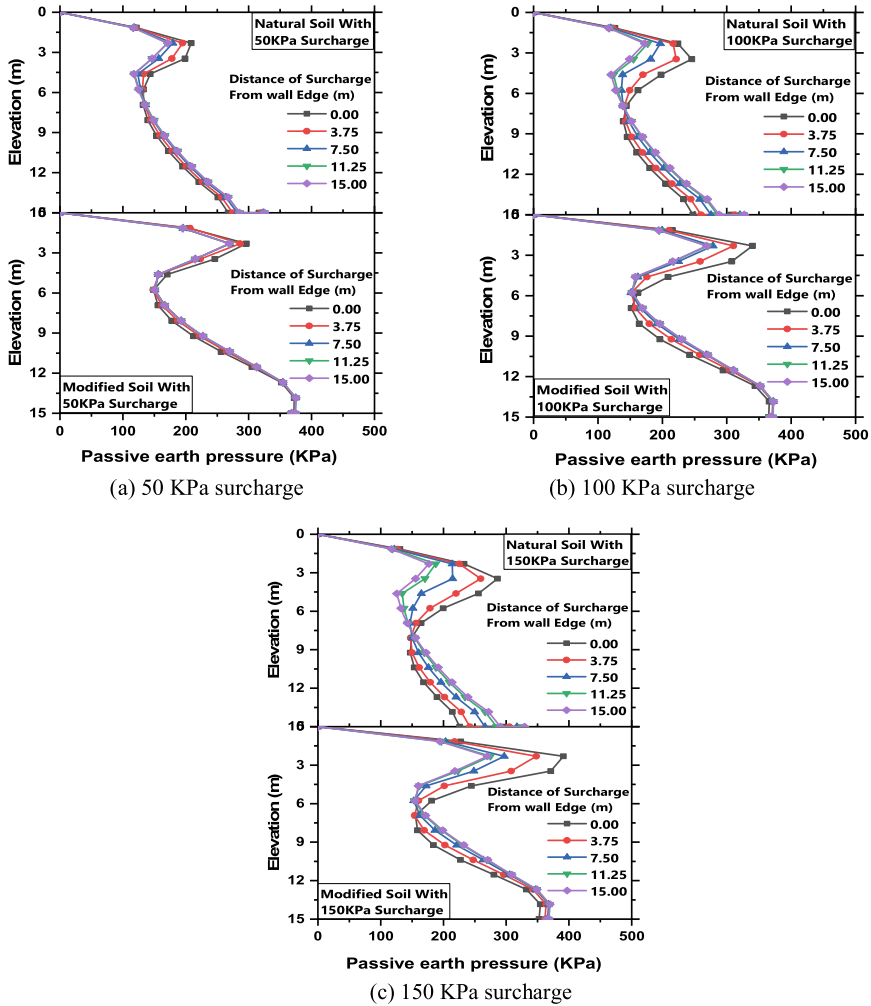


Fig. 35.4 Lateral earth pressures (passive earth pressure) for 30 m high wall

Bending Moments

Bending moments in the diaphragm wall for natural and modified soil conditions are shown in Fig. 35.6. The analysis results show a significant difference in bending moments between the natural and modified conditions. The magnitude of surcharge and position also affects the bending moment magnitude and its shape. The analysis results show significant changes in positive and negative bending moments between natural and modified front-fill soil conditions. Figure 6a, b, and c indicate that the soil modification in front-fill soil results in the reduction of maximum bending moment.

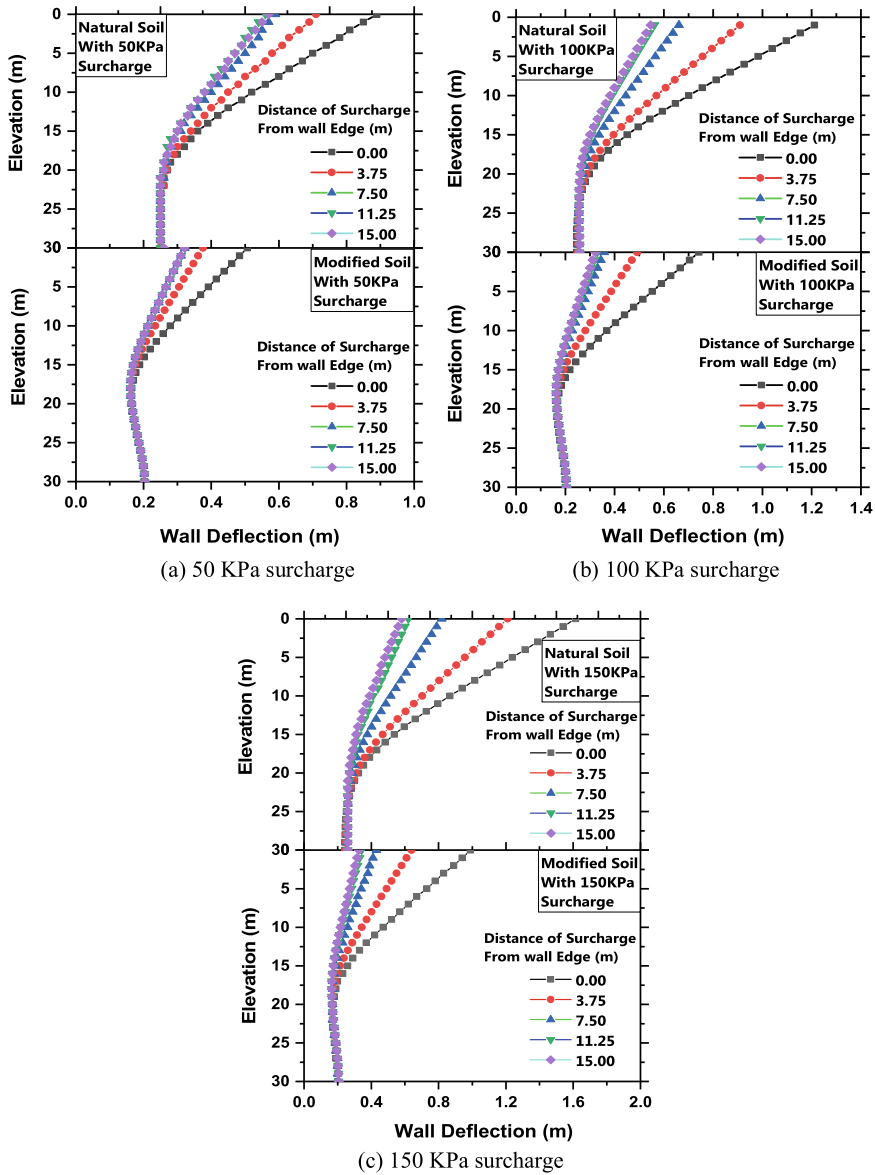


Fig. 35.5 Lateral deformations of 30 m high wall

The use of modified front-fill soil results in the increase of negative bending moment at the toe of the wall. For all magnitude of surcharge loads, the maximum positive moment was found at a depth of 18 m beneath the top of the diaphragm wall for natural front-fill soil conditions. For the modified condition, the corresponding depth was 17 m beneath the top of the diaphragm wall. Similarly, the maximum negative moment was at a depth of 28 m beneath the top of the diaphragm wall for the natural front-fill soil condition. For the modified condition, the corresponding depth was 29 m beneath the top of the diaphragm wall.

Increase in the magnitude of surcharge results in a significant increase in bending moments in both natural and modified front-fill soil conditions. The position of surcharge also results in a difference in the magnitude of bending moments. From Fig. 6a, b, and c, it is observed that closer the surcharge to the wall gives a higher value of bending moment. The bending moment is significantly reduced if the surcharge is far away from the wall. It was found from the graphs that modification of front-fill soil reduces the maximum bending moment about 8% for 50 kPa surcharge; similarly for 100 kPa surcharge, the reduction was 6%; and for 150 kPa surcharge, the reduction was 2.2%, for surcharge position of 0.00 m.

Deformation of the Ground Surface After Final Excavation

Figure 7a and b show the ground deformation profile of 15 m excavation for a surcharge placed at 0 and 15 m from the wall edge. Figure 7a and b show that the vertical deformation was reduced for the modified case. The vertical deformation was found maximum under the surcharge, irrespective of its magnitude and position; a similar pattern was observed for 3.75, 7.5, and 11.25 m.

Figure 8a, b, and c show the variation of maximum ground deformation after the final excavation of 15 m with varying surcharge positions for 50 kPa, 100 kPa, and 150 kPa surcharge magnitude, respectively, for natural and modified soil conditions. Figure 8a, b, and c show that modified front-fill soil effectively reduced the maximum ground deformation. Higher the magnitude of surcharge produces a higher value of maximum vertical ground deformation.

Conclusions

Numerical analysis by finite element method was performed to study the influence of sequential excavation on the concrete diaphragm wall behavior in cohesionless soils. The following conclusions are made:

- Soil modification will decrease the magnitude of total active earth pressure and increase the magnitude of total passive earth pressure.

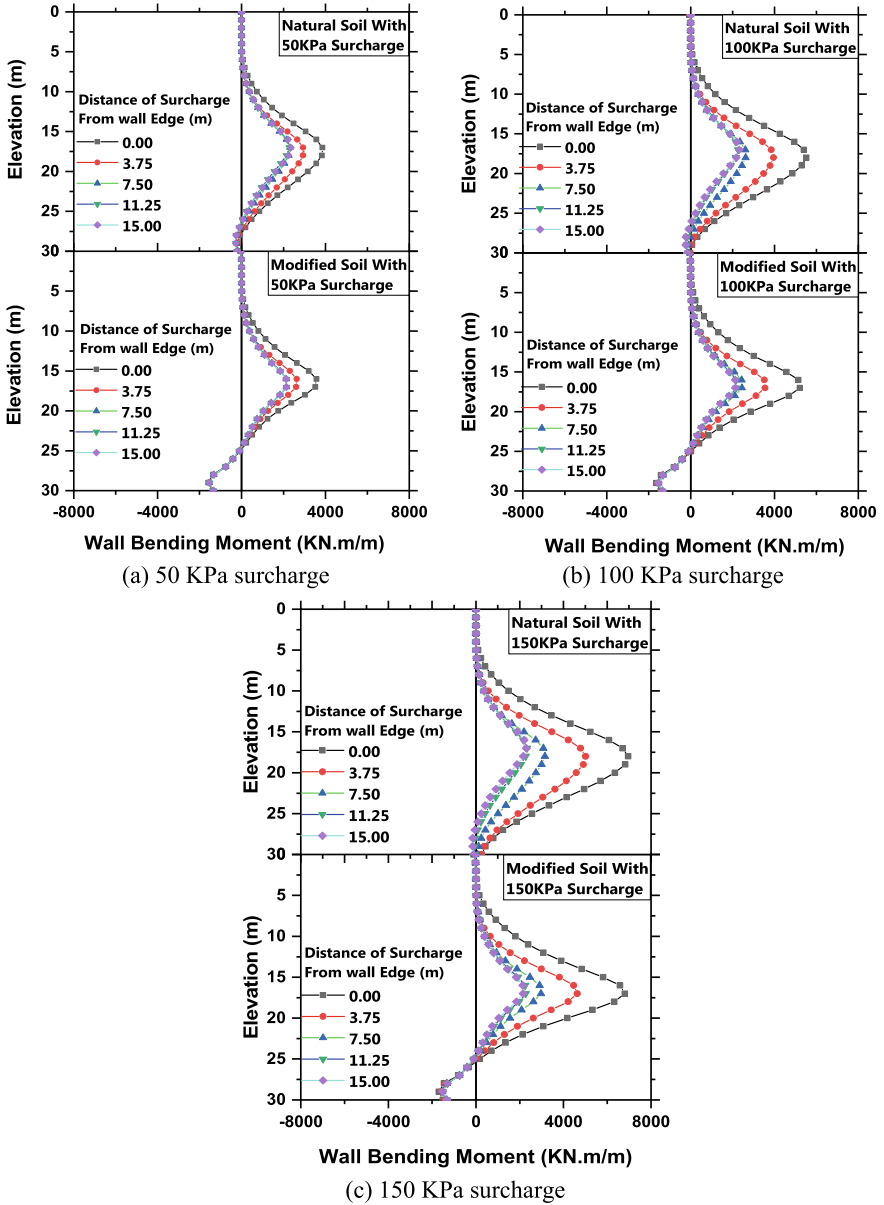


Fig. 35.6 Bending moments of 30 m high wall

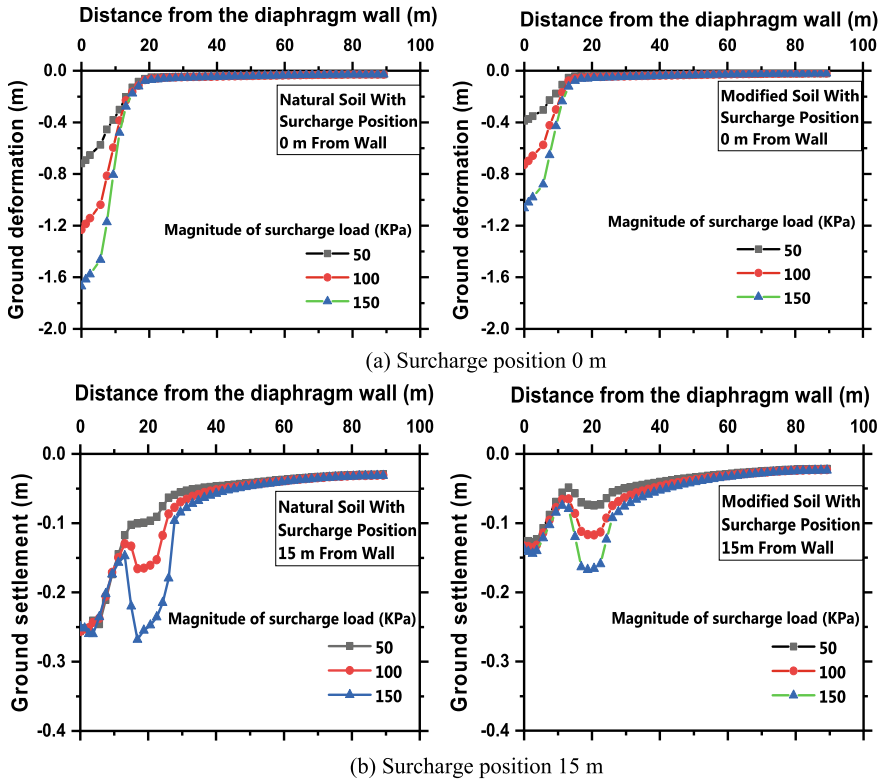


Fig. 35.7 Ground deformation profiles with varying surcharge loads

- Soil modification can effectively reduce wall deformation. However, in the present study, the maximum deflection of the wall reduces by an average value of 0.55 times the deflection obtained in natural soil and this reduction is independent of the magnitude of surcharge load and its position. Higher magnitudes of surcharge load located closer to the wall lead to a higher value of wall deflection.
- Higher magnitudes of surcharge load located closer to the wall lead to a higher value of bending moments. Soil modifications in front-fill soil result in the reduction of maximum bending moment. However, soil modification may lead to the production of the negative bending moment below the dredge level. For all magnitude of surcharge loads, the position of the maximum positive moment was 18 m beneath the top of the diaphragm wall for natural conditions and 17 m beneath the top of the diaphragm wall for modified soil conditions.
- Modified front-fill effectively reduced the maximum ground deformation. Maximum deformations of ground occur below the surcharge. Higher surcharge magnitude results in a higher value of ground deformation, and a higher surcharge distance from the wall gives a lesser ground deformation value.

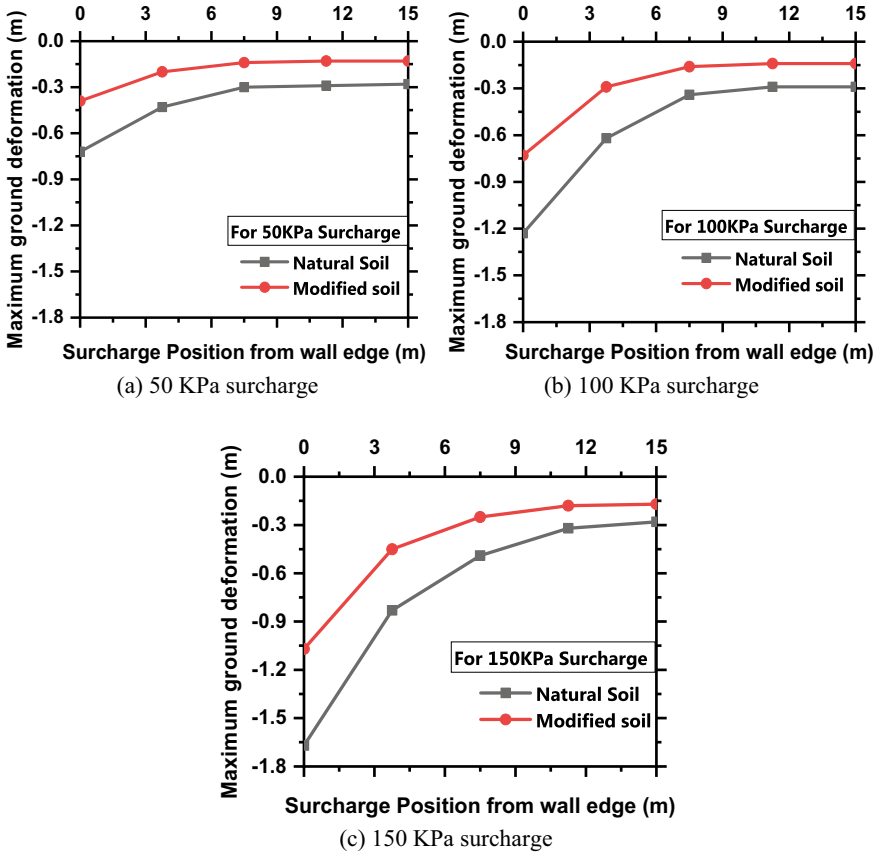


Fig. 35.8 Maximum deformation of ground surface

References

1. Bilgin Ö (2012) Numerical studies of anchored sheet pile wall behavior constructed in cut and fill conditions. *Comput Geotech* 37(3):399–407
2. Bose SK, Som NN (1998) Parametric study of a braced cut by finite element method. *Comput Geotech* 22(2):91–107
3. Burlon S, Mroueh H, Shahrouh I (2013) Influence of diaphragm wall installation on the numerical analysis of deep excavation. *Int J Numer Anal Meth Geomech* 37(11):1670–1684
4. Chen JJ, Lei H, Wang JH (2014) Numerical analysis of the installation effect of diaphragm walls in saturated soft clay. *Acta Geotech* 9(6):981–991
5. Chowdhury SS, Deb K, Sengupta A (2013) Estimation of design parameters for braced excavation: numerical study. *Int J Geomech* 13(3):234–247
6. Emarah DA, Selem SA (2018) A numerical study of anchored sheet piles subjected to different types of sandy soils backfill. *HBRC Journal* 14(3):422–430
7. Hsiung BCB (2009) A case study on the behaviour of a deep excavation in sand. *Comput Geotech* 36(4):665–675

8. Rashidi F, Shahir H (2019) Numerical investigation of anchored soldier pile wall performance in the presence of surcharge. *Int J Geotech Eng* 13(2):162–171
9. Singh AP, Chatterjee K (2019) Ground settlement and deflection response of cantilever sheet pile wall subjected to surcharge loading. *Indian Geotechnical Journal* 1–10
10. Singh M, Singh B (2020) Modelling of diaphragm wall for deep excavation in sandy soil. In: *Proceedings of Indian geotechnical conference 2020*, Andhra University, Visakhapatnam
11. Trautmann CH, Beech JF, O'Rourke TD, McGuire W, Wood WA, Capano C (1983) *Transmission-line structure foundations for uplift-compression loading*. Final report (No. EPRI-EL-2870). Cornell University, Ithaca, NY (USA); GAI Consultants, Inc., Monroeville, PA (USA)

Chapter 36

Gabion Walls—A Remedial Measure for Slope Stabilization



Blacinta Pereira and Wilma Fernandes

Introduction

The purpose of slope protection is to reduce infiltration, to prevent slope erosion due to surface runoff and also to improve slope landscape considering environment friendly measures. Slope stabilization or remedial measures are ways in strengthening the slope stability. Slope stabilization depends on suitable selection of methods, specifications, proper construction procedures, and good maintenance. Various slope stabilization methods include change of geometry, retaining wall, rock filled buttresses, sheet pile wall, gabion wall, reinforced earth wall, crib wall, contiguous bored pile wall, geotextile, soil nailing, and providing slope drainage. Any method can be adopted as remedial measure based on site soil condition, efficiency of method and economical aspect. Gabion walls are present in the civil industry since many years, however within the Indian market the utilization of gabion walls has not gained as much popularity as in the foreign countries. Gabions are preferred not only because of their esthetic but also due to the reduced cost of wall. The main function of any retaining structures or wall is to provide lateral support to soil or the rock mass behind it. Apart from the typical retaining wall, the gabion retaining walls are now gaining attention. A Gabion wall is constructed from rectangular or square cages made of galvanized welded or woven wire mesh filled with stones/boulders. Gabions are mostly used in highways, slope protection, shore protection works, canal linings, bridges, buildings, etc. One of the greatest advantages of gabion walls is it prevents the development of pore water pressure behind the wall. Gabions allow small plants to take roots through it which reinforces the soil and thus improves the life span of

B. Pereira (✉) · W. Fernandes
Civil Engineering Department, Goa Engineering College, Farmagudi, Goa, India
e-mail: blaci712@gmail.com

W. Fernandes
e-mail: wilma@gec.ac.in

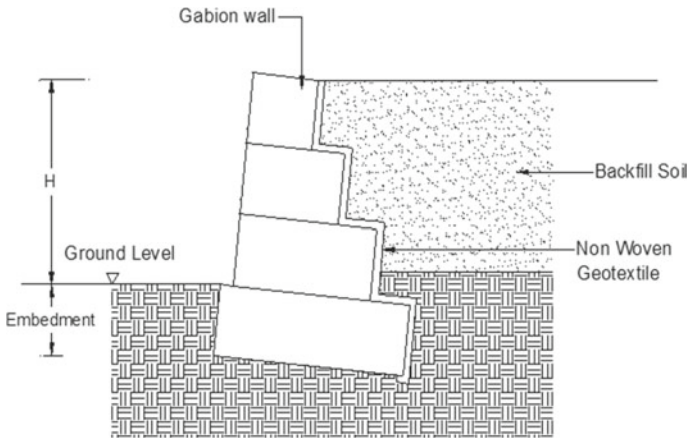


Fig. 36.1 Typical section of Gabion wall with different components

the structure. When compared to conventional solutions, there is also a substantial reduction in carbon footprints [1]. Gabion walls are mass gravity walls made of three main components which are gabion cage, stone/boulders for filling gabion box, filter media and backfill as shown in Fig. 36.1.

Design Principle of Gabion Retaining Wall

The gabion wall are designed in such a way that gabion wire mesh can hold the rocks inside with limited deformation which does not affect internal stability and esthetics. For designing gabion walls limit state principles are used. The gabion wall can be designed with several configurations based on the requirement at the site, such as (i) stepped outside (ii) stepped inside (iii) offset [1].

Advantages of Gabion Retaining Wall

Gabion walls are its flexible and permeable. These qualities allow the gabion wall to deflect and deform in any direction without breaking. Thus gabion can be constructed with a minimum depth of foundation and in areas where differential settlement may occur. Due to permeability in the gabion wall hydrostatic pressure are not developed behind the wall. The gabion wall takes care of slope stabilization by the combined action of draining and retaining. The economical advantages of the gabion are low maintenance, simple in construction and can be constructed with unskilled manpower. For construction of these walls preliminary preparation of foundation bed is not necessary, the surface must be reasonably leveled and smooth. Gabions

are permeable, thus there is no need for expensive drainage. Gabion walls does not require curing time like gravity retaining wall and does not corrode under areas which are constantly or partially submerged. The gabion wall has apparent environmental benefits because it is constructed with materials (cobbles) that will help to preserve the natural ecosystem of the area. Other benefits are that gabion allows plants to grow on its surface, adding to the structure's natural esthetics [2].

Present Study Area

The site is situated at a stretch along the coastline of Nerul village, Goa where a portion of road laid on embankment caved in thereby developing a huge hole along with breaching of retaining wall as seen in Figs. 36.2 and 36.3. The road caved in on June 22nd 2020 during monsoon. Nerul is the village in Bardez taluka in North Goa and is surrounded by rivers on three sides of the village north, west, and east. Nerul village is bordered by the Mandovi River on one side. The road is 7 m in width located along the side of the river with one side of the embankment slope being supported by a retaining wall of height 3.5 m and length of 200 m along the stretch on the riverside and the other side of the road is the land.



Fig. 36.2 A view of the road caved in



Fig. 36.3 A view of breached retaining wall

Objective

The objective of present study is to design and provide a gabion wall as a remedial measure for the above site and prepare a cost comparison between gabion wall and concrete gravity retaining wall for same site condition.

Soil Test and Interpretation

Soil samples collected from failed embankment site was tested in the laboratory for different properties such as cohesion, unit weight, Phi value. The test was done on two soil samples one is the top layer and the other the bottom layer of embankment soil. Laboratory test which includes density test, water content test, grain size analysis, index properties, and direct shear test. From particle size distribution test percentage of silt, sand, and gravel content were as shown in Table 36.1. The soil properties of embankment material have been identified and listed in Table 36.1.

Table 36.1 Basic soil properties

Soil layer	Height (m)	Unit weight (kN/m ³)	c (kN/m ²)	ϕ (degree)	Silt (%)	Sand (%)	Gravel (%)
Top	3.0	14.14	3	40	0.6	75.4	24
Bottom	1.0	12.16	15	38	5.3	89.7	4.77

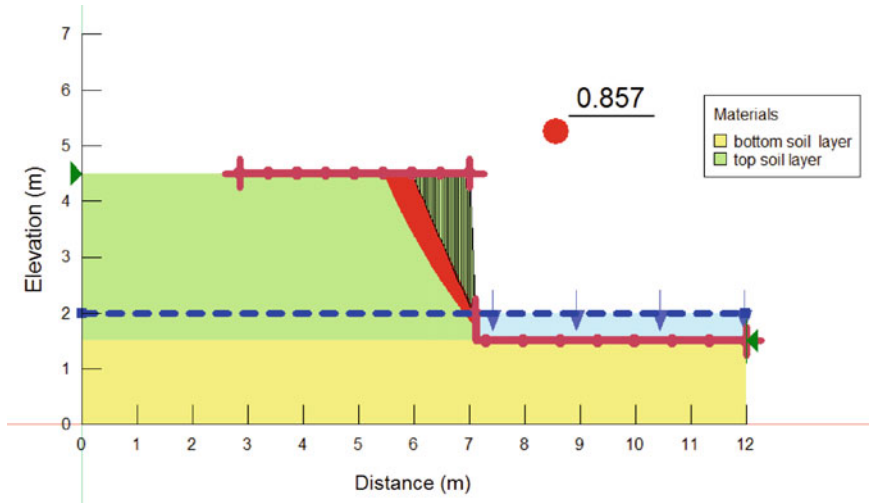


Fig. 36.4 Details of analysis in SLOPE/W showing static factor of safety of slope without retaining structure

Slope Stability Analysis Using Geostudio

For the present study a plane strain 2D model of the embankment was generated in Geostudio SLOPE/W for slope stability analysis. The method used for analysis was the Morgenstern-Price method and the Sine function selected was half sine. The material model considered for the analysis was the Mohr–Coulomb model for soil. The factor of safety for embankment slope without retaining wall was 0.857 as shown in Fig. 36.4.

Suggested Remedial Measures

Gabion Wall

Design of Gabion wall [3].

Step 1: Forces acting on the wall

$$K_a = \frac{\cos^2(\phi - \beta)}{\cos^2 \beta \sin(\delta + \beta) \left[1 + \sqrt{\frac{\sin(\phi + \delta) \sin(\phi - \alpha)}{\cos(\delta + \beta) \cos(\alpha - \beta)}} \right]^2}$$

α slope angle of backfill soil surface = 0°

β inclination angle of face of gabion with vertical = -6°

δ angle of wall friction (δ is usually is taken as ϕ).

ϕ angle of internal friction of back fill soil

K_{a1} 0.167

K_{a2} 0.181

To compute lateral soil pressure, the Coulomb equation is usually used. According to Coulomb theory, the total active pressure on the wall is

$$P_a = \frac{1}{2} K_a \gamma_s H^2$$

where

γ_s density of back fill soil

H wall height

K_a coefficient of active earth pressure

P_a 21.517 kN/m.

P_a is inclined to a line normal to the slope of the back face by the angle δ . The horizontal and vertical components of P_a are as below:

$$P_h = P_a \cdot \cos(\delta + \beta) = 18.247 \text{ kN/m}$$

$$P_v = P_a \cdot \sin(\delta + \beta) = 11.402 \text{ kN/m}$$

Width of wall = $0.7H = 2.45 \text{ m} \approx 2.5 \text{ m}$ (Table 36.2).

Gabion fill density, $\gamma_g = 16 \text{ kN/m}^3$

Weight of the gabion wall, $W_g = 16 \cdot (2.5 + 2 + 1.5 + 1) = 112 \text{ kN/m}$.

Step 2: Sliding Check

$$F \cdot S_{\text{Sliding}} = \frac{F_r}{F_s} \geq 1.5$$

where

F_r resisting force

F_s sliding force

$F_r = W_v \cdot \tan \phi + cB$

Table 36.2 Calculation for weight of Gabion

Layer	Width B (m)	Height h (m)	Area A (m ²)
Bottom layer	2.5	1	2.5
Intermediate layer 1	2	1	2
Intermediate layer 2	1.5	1	1.5
Top layer	1	1	1

$\tan \phi$ coefficient of the sliding friction at base of gabion
 W_v $W_g + P_v = 123.40$ kN/m
 F_r $123.40 * \tan 38^\circ + 15*2.5 = 133.91$ kN/m
 F_s $P_h = 18.247$ kN/m
 $F.S_{\text{sliding}}$ $133.91/18.247 = 7.33 > 1.5$, hence safe

Step 3: Overturning Moment Check

$$F.S_{\text{Overturning}} = \frac{M_r}{M_o} \geq 2$$

where

M_r resisting moment
 M_o overturning moment

The active earth pressure acts at a distance $H/3$ above the base. For a given surcharge the total active pressure above the toe acts at a distance

$$d_a = \frac{H \left(H + \frac{3q}{\gamma_s} \right)}{3 \left(H + \frac{2q}{\gamma_s} \right)} + B \sin \beta$$

$d_a = 1.072$ m

so, the overturning moment is

M_o $d_a \cdot P_h$
 M_o $1.072 * 18.247 = 19.560$ kNm

W_g acts vertically through the centroid of its cross-sectional area. The horizontal distance to centroid of its cross-section area from the toe of the wall (d_g) is calculated from the moment of wall areas (Table 36.3).

$d_g = \Sigma A * x_i / \Sigma A = 1.698$ m.

so, the resisting moment is

$M_r = W_g * d_g + P_v * d_v$
 $d_v = B \cos \beta + d_a \sin \beta$

Table 36.3 Calculation of Horizontal distance from Toe to W_g

Layer	X_i	Y_i	$x_i = (X_i \cos \beta) + (Y_i \sin \beta)$
Bottom layer	1.25	0.5	1.295
Intermediate layer 1	1.5	1.5	1.648
Intermediate layer 2	1.75	2.5	2.001
Top layer	2	3.5	2.354

$$d_v = B \cdot \cos\beta + d_a \cdot \sin\beta = 2.5 \cdot \cos(-6^\circ) + 1.072 \sin(-6^\circ) = 2.374 \text{ m}$$

$$M_r = W_g \cdot d_g + P_v \cdot d_v = 217.244 \text{ kNm.}$$

$$F.S_{\text{Overturning}} = M_r / M_o = 217.244 / 19.560 = 11.10 > 2, \text{ hence safe.}$$

Step 4: Check Bearing Pressure

First check if vertical resultant of forces (W_v) lies within the middle third of the base. If the width of the base is denoted by B , the eccentricity (e) of the W_v from the mid width of the base is

$$e = \frac{B}{2} - \frac{(M_r - M_o)}{W_v}$$

$$e = 0.351$$

The resultant force should lie in the middle third,

$$e \leq B/6 = 0.41 < e$$

If σ_{max} is maximum pressure under the base

$$\sigma_{\text{max}} = \frac{W_v}{B} \left(1 + \frac{6e}{B} \right)$$

$$\sigma_{\text{max}} = 90.82 \leq q_{\text{all}}$$

$$q_{\text{all}} = 600 \text{ kN/m}^2$$

The maximum pressure should not be higher than the allowable soil bearing pressure of base soil, $\sigma_{\text{max}} \leq q_{\text{all}}$ then factor of safety for bearing capacity is

$$F.S_{\text{Bearing capacity}} = \frac{q_{\text{all}}}{\sigma_{\text{max}}} \geq 1$$

$$F.S_{\text{Bearing capacity}} = 600/90.82 = 6.67 > 1 \text{ hence safe.}$$

Final cross section of gabion wall from design analysis is shown in Fig. 36.5 (Table 36.4).

Concrete Gravity Retaining Wall [4]

Designing of gravity retaining wall involves selection of trial dimensions for retaining wall and carrying out various stability checks for analyzing the stability of gravity wall. The retaining wall was analyzed using Coulomb's theory. After analysis factor of safety were found to be as shown in Table 36.5. The dimension of retaining wall which gave a safe factor of safety is with base width of 1.4 m and top width and top

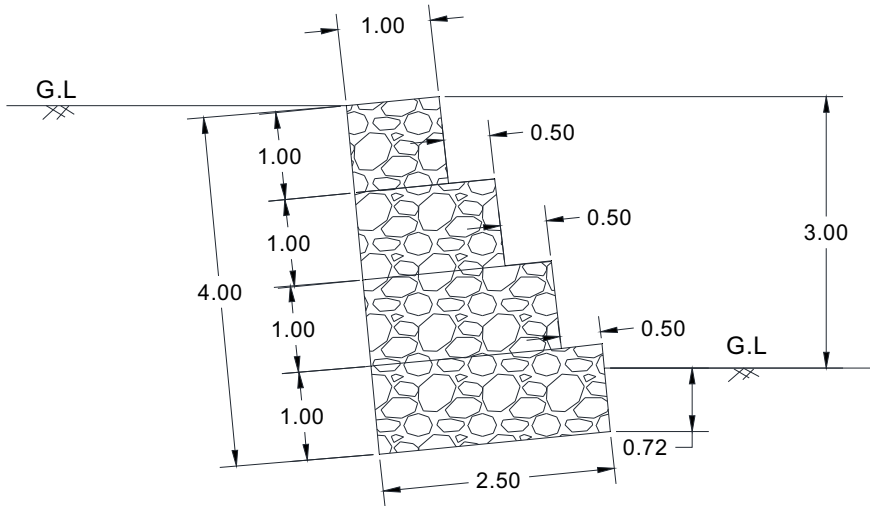


Fig. 36.5 Cross-section of Gabion wall

Table 36.4 Factor of safety for gabion retaining wall

$F.S_{\text{Sliding}} \geq 1.5$	$F.S_{\text{Overturning}} \geq 2$	$F.S_{\text{Bearing capacity}} \geq 1$
7.33	11.10	6.67

Table 36.5 Factor of safety for gravity retaining wall

$F.S_{\text{Sliding}} \geq 1.5$	$F.S_{\text{Overturning}} \geq 2$	$F.S_{\text{Bearing capacity}} \geq 3$
1.517	3.664	6.660

width of 0.5 m. Final cross section of gravity retaining wall from design analysis is shown in Fig. 36.6.

Cost Comparison

The concrete gravity walls are costlier than the gabion walls because of the huge cost involved in the concrete. The cost of gravity retaining includes the cost of excavation, rubble packing and PCC at base, shuttering, placing of concrete, providing weep holes plastering and refilling along with materials used and labor charges. The rates for estimating the total cost are taken from Goa Schedule of Rates [5, 6]. The total cost of the gabion walls consists of site clearance and earthwork excavation at site, gabion boxes (including assembling at site), stones for filling gabion boxes, geotextile provided as a filter at the back of wall, transportation of materials and labor charges [7]. Rate of the gabion box with stone boulders per cubic m was 3584.45 Rs which is

Fig. 36.6 Cross-section of gravity retaining wall

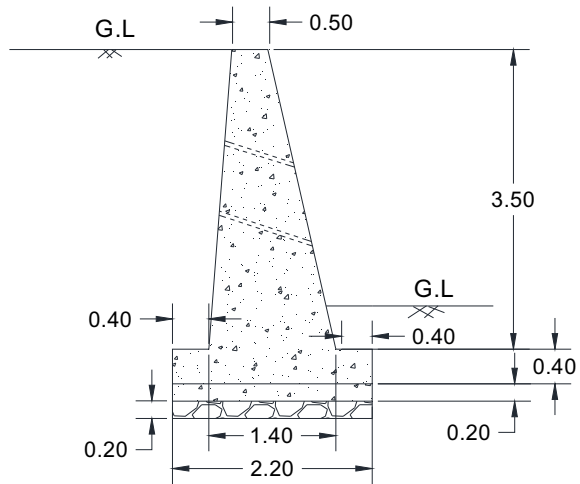


Table 36.6 Cost per running meter length and % variation

Type of retaining wall	Concrete gravity wall	Gabion wall
Total cost (Rs)	7,544,220.50	5,099,730.00
Cost per r.m ($L = 200$ m) (Rs)	37,721.10	25,498.65
Percentage variation in cost (%)	47.93	0

major cost of gabion wall [8]. The total cost and cost per r.m of the concrete gravity retaining wall and gabion wall are shown in Table 36.6.

Conclusion

From the study it was found that the total construction cost of gabion retaining wall was comparatively less as compared to cost of concrete gravity retaining wall. The total cost of concrete gravity wall is 47.93% higher than the total cost of gabion wall. Other benefits of gabion wall as compared to concrete gravity retaining wall are, it does not require curing time for concrete as a result the time required for construction will get reduced. It does not require additional drainage system since gabion wall is a free draining structure with no pore pressure development behind the wall. Thus, it can be seen that gabion retaining walls prove to be the economical and sustainable solution.

References

1. IRC:SP:116-2018 (2018) Guidelines for design and installation of Gabion structures, Indian Roads Congress, New Delhi
2. SubletteWR (1979) A behavioral study of gabion retaining walls, Ph. D. dissertation, University of Arizona
3. Peerdawood CT, Mawlood YI (2010) Analytical study for stability of Gabion walls. *Journal of Pure and Applied Sciences* 22(5)
4. Arora KR (2003) *Soil mechanics and foundation engineering*, 6th edn. Standard Publishers Distributors, Delhi
5. Goa Schedule of Rates for Building Works (2019)
6. Goa Schedule of Rates for Roads & Bridge works (2014)
7. Joshi R (2016) Gabion wall—a cost effective solution. *Journal of Basic and Applied Engineering Research* 3:290–292
8. Analysis of Rate, vol 2, Central Public Work Department, Government of India (2019)

Chapter 37

Stability Enhancement of Railway Embankment Using Geosynthetic Layer



Furquan Ahmad and Pijush Samui

Introduction

Ground improvement enhances the engineering properties of the soil, which is mostly used for embankments, retaining structures, etc. One of the most important considerations in the design and construction of earth and earth supporting structures is the stability of soil mass. The bearing capacity and stability of soils against retaining structures directly depend upon the shear strength of the soil. Throughout the world, there has been an increase in the demand for geotechnical structures day by day which is environmentally friendly, feasible, and more economical. The negative environmental effect which has been caused by the wrenching out of aggregate, to decrease its effectiveness and to make it cost-effective, there is a propensity to use cohesive soil as construction materials. Cohesive soil has been found in abundance and is one of the cheapest construction materials available but due to its lower frictional strength, generation of pore water pressure and compactibility, it should not be used directly as backfill material for the construction of the embankment. Their use can be increased by enhancing its strength by incorporating reinforcing elements such as geosynthetic. Geosynthetic has been used due to its speed of construction, pliability, durability cost-effectiveness, and different site condition adaptability. Adequate clay-geogrid interaction has to be ensured such that stress transfer from soil to reinforcement is done in such a way that the behavior of cohesive soil got improved. The incorporation of geogrid not only enhances the stability of cohesive soil rather also provided sideways drainage and it prevents surplus pore water pressure in saturation cases. Geosynthetic use is well established for material separation and filters [1]. A safe and

F. Ahmad (✉) · P. Samui
Department of Civil Engineering, National Institute of Technology, Patna 800005, India
e-mail: furquana.pg19.ce@nitp.ac.in

P. Samui
e-mail: pijush@nitp.ac.in

economic design of soil reinforcement requires a good understanding of interaction mechanisms that develop between the soil and the reinforcement [2]. Very less no of research has been performed to evaluate the interactions between cohesive soils and geosynthetics significant improvements in the response of clay soils through interfacial enhancement by incorporating geogrids in thin layers of sand [3–10].

Investigating Parameter

The investigating parameter for this work is basically to determine the factor of safety trend with or without incorporating geosynthetic as geogrid in cohesive soil embankment. The input parameters for this test are cohesion value (c), unit weight (γ), angle of shearing resistance (φ) for both the subsoil layer and embankment layer in a normal case as without incorporating anything in between them. When we encapsulate geogrid in it then two more input parameters, pull-out resistance and tensile capacity of geogrid will be added.

Methodology

In this study, a railway embankment is assumed in which the embankment layer is made up of cohesive soil and select the parameter which affects the railway embankment based on the factor of safety criteria. After the selection of parameters, find the range of parameters in which they vary. These parameters need to be used to generate 100 datasets to calculate the factor of safety for the actual dataset. These actual datasets are used to run on the GeoStudio software using the Bishop method to obtain the trend chart of the factor of safety.

Bishop Method for Slope Stability

The simplified Bishop method is used to calculate the factor of safety by a method of slices. This method satisfies the vertical equilibrium force for an individual slice and the overall moment equilibrium about the center of the circular trial surface. As we know, forces acting horizontally are not considered at each slice, and hence, the simplified Bishop method also uses this concept and assumes zero interslice force. The limitation that would be applied to the simplified Bishop method is that all the failure surfaces must be circular (Fig. 37.1).

The factor of safety formula used by the bishop method is:

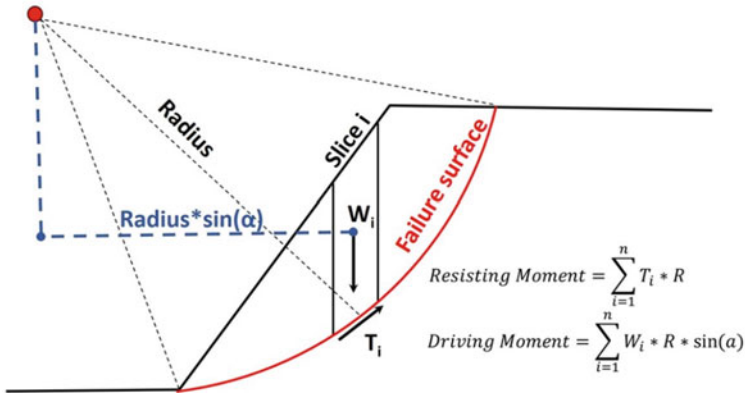


Fig. 37.1 Simplified Bishop’s method for analyzing circular failure in slopes. Source <https://www.geoengineer.org/education/slope-stability/slope-stability-the-bishop-method-of-slices>

$$FS = \frac{1}{\sum W \sin \alpha} \sum \left[\frac{c\beta + W \tan \phi - \frac{c\beta}{FS} \sin \alpha \tan \phi}{m_\alpha} \right]$$

where FS = factor of safety, W = slice weight, α = inclination of slice base, c = cohesion, β = geometric parameter, ϕ = angle of friction, and $m_\alpha = \cos \alpha + \frac{\sin \alpha \tan \phi}{FS}$.

Present Analysis

Assuming a railway embankment of height 6 m in which embankment fill of clayey soil layer is taken which has property ($\gamma = 17 \text{ kN/m}^3$, $c_u = 10 \text{ kN/m}^2$, and $\Phi_u = 26^\circ$) from DFC railway project as shown in Figs. 37.2, 37.3.

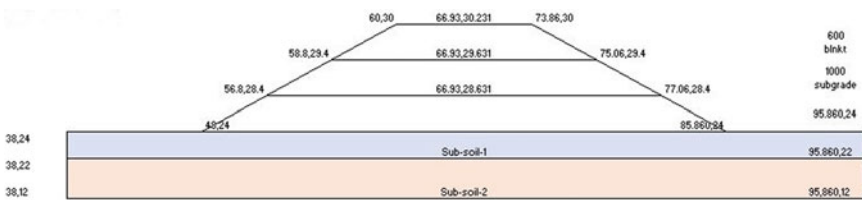
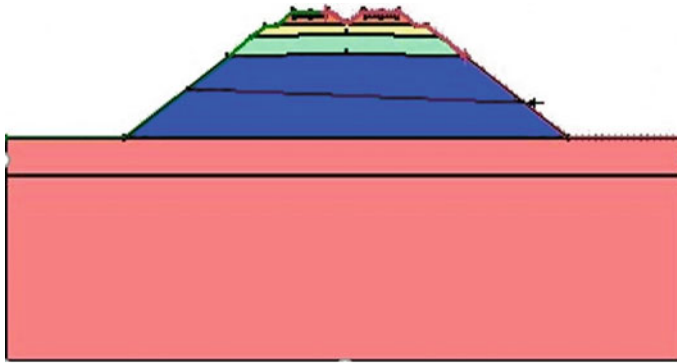


Fig. 37.2 Specification of a railway embankment









color	Name	Unit weight (KN/m ³)	cohesion (kPa)	Phi (°)
	Sleeper	24	50	40
	Ballast Cushion	18	0	40
	Blanket	19	0	32
	Prepared Sub-grade	17	10	26
	Embank fill	20.89	62	10
	Subsoil II	39.5	17.25	15.5

Fig. 37.3 Cross-section of railway embankment with properties

Result

Dataset for A Factor of Safety with or Without Geogrid

See Table 37.1

I have just taken 42 data to show the trend of a factor of safety from 100 datasets but I will show a graph on all the 100 datasets (Fig. 37.4).

Conclusion

The results that have been obtained after performing the analysis on GeoStudio software by the Bishop method of slices indicate that the behavior of cohesive soil has been significantly affected by incorporating geogrid in it.

The conclusions drawn from this present study are as follows:

1. Stability enhancement of cohesive soil has been done by incorporating geosynthetic as geogrid material in it as shown in the graph and observed a significant increase in the factor of safety concerning the normal cohesive soil.

Table 37.1 Factor of safety with or without incorporating geogrid in cohesive soil

SI. No.	fos (clay)	fos (clay + geogrid)
1	2.393	2.681
2	2.393	2.701
3	2.633	2.885
4	2.278	2.591
5	2.767	3.033
6	2.583	2.833
7	2.339	2.564
8	2.801	3.037
9	2.856	3.1
10	2.732	2.996
11	2.825	3.092
12	2.455	2.759
13	1.927	2.228
14	3.053	3.288
15	2.604	2.895
16	2.497	2.688
17	2.581	2.826
18	2.528	2.811
19	2.772	3.037
20	2.819	3.079
21	2.490	2.716
22	2.314	2.638
23	2.129	2.498
24	2.509	2.74
25	2.727	2.979
26	2.657	2.911
27	2.511	2.763
28	2.188	2.42
29	2.419	2.63
30	2.585	2.83
31	2.722	3.007
32	2.559	2.678
33	2.721	3.025
34	1.959	2.386
35	2.582	2.835
36	2.617	2.868
37	1.921	2.194

(continued)

Table 37.1 (continued)

SI. No.	fos (clay)	fos (clay + geogrid)
38	2.208	2.484
39	2.697	3.018
40	2.558	2.84
41	2.545	2.8
42	2.657	2.971

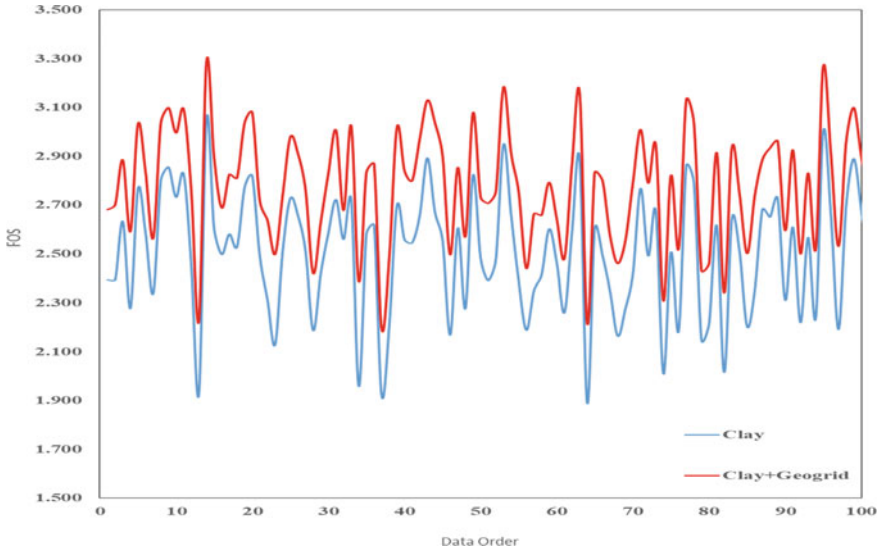


Fig. 37.4 Graph between fos (clay) and fos (clay + geogrid)

2. Due to the pull-out resistance and tensile capacity of the geogrid, the strength of the railway embankment made of cohesive soil got enhanced.

References

1. Faure YH, Baudoin A, Pierson P, Ple O (2006) A contribution for predicting geotextile clogging during filtration of suspended solids. *Geotext Geomembr* 24(1):11–20
2. Giroud JP (1986) From geotextiles to geosynthetics: a revolution in geotechnical engineering. In: *Proceedings of 3rd international conference on geotextiles*, vol 1, Vienna, Austria, pp 1–18
3. Bergado DT, Chai Sampaco CL, Shivashankar R, Alfaro MC, Anderson LR, Balasubramaniam AS (1991) Performance of a welded wire wall with poor quality backfills on soft clay. *ASCE Geotechnical* 908e922. Special publication No.27
4. Abdi MR, Sadrnejad A, Arjomand MA (2009) Strength enhancement of clay by incorporating geogrids in thin layers of sand. *Geotext Geomembr* 27(6):447–455

5. Chen HT, Hung WY, Chang CC, Chen YJ, Lee CJ (2007) Centrifuge modeling test of a geotextile-reinforced wall with a very wet clayey backfill. *Geotext Geomembr* 25:346–359
6. Das BM, Khing KH, Shin EC (1998) Stabilization of weak clay with strong sand and geogrid at sand-clay interface. *Transp Res Rec* 1611:55–62
7. Goodhue MJ, Edil TB, Benson CH (2001) Interaction of foundry sands with geosynthetics. *J Geotech Geoenviron Eng* 27:353–362
8. Elias V, Christopher BB (1996) Mechanically stabilized earth walls and reinforced soil slopes, design and construction guidelines. Federal Highway Administration FHWA-Sa-96-071
9. Fabian KJ, Fourie AB (1986) Performance of geotextile reinforced clay samples in undrained triaxial tests. *Geotext Geomembr* 4:53–63
10. Ingold TS, Miller KS (1982) The performance of impermeable and permeable reinforcement in clay is subject to undrained loading. *Q J Eng Geol* 15:201–208

Chapter 38

Numerical Analysis of Earthen Embankment Resting on Soft Clay Deposit



Anand M. Hulagabali, R. Srujana, A. V. Rachana, and M. Y. Longkumer

Introduction

Background

Embankment is raised from the existing ground level to support railway or road above it [1] whereas the earthen embankment made of impervious core surrounded by permeable substance to form upstream and downstream is constructed to prevent flooding in the low-lying areas. History of embankment construction dates back to 1800s where the road Construction was carried out using Telford and Mc dam techniques. Subgrade below the embankment must support the load of comprised pavement layers and also imposed wheel loads. It is known that soft clay is abundantly found in the coastal regions throughout the country. Due to the expanding population demands, construction of embankment over soft soil deposit is most challenging to the geotechnical engineers according to [2]. However, failure of embankment occurs due to weak subsoil, its seismic proximity and also due to instability of slopes.

Soft clay being highly plastic in nature due to its poor shear strength gives rise to extreme settlements and unacceptable large deformations if embankment is built over it. Considering the problems connected to the embankment on soft soil, parametric analysis is carried out using plaxis2D tool.

A. M. Hulagabali · R. Srujana (✉) · A. V. Rachana · M. Y. Longkumer
Department of Civil Engineering, The National Institute of Engineering, Mysore 570008, India
e-mail: srujanabayari1998@gmail.com

A. M. Hulagabali
e-mail: anandmh@nie.ac.in

Scope of Study

Road embankment constructed on soft clay may lead to potential failure or collapse which would be dangerous to the road users hence it is necessary to analyze them for safety, stability and to determine the parameters that govern the safe construction of embankment on soft soil. Study covers the numerical analysis using PLAXIS tool to analyze the behavior of embankment and to determine the extent of settlement.

Objectives

General objective is to bring the awareness about the problems associated with the construction of an embankment by adopting stage wise construction technique. Plaxis 2D tool is used to demonstrate parametric analysis. Attempts have been made to find the simple and economical construction of embankment. Effect of parameters governing embankment construction over soft clay deposit like height of embankment, slope and location of ground water table is analyzed numerically.

Literature Review

Benmebarek et al. [9] studied on the construction technique of road embankment on sabkha soil in Algeria. Due to symmetry, only half the embankment was modeled in PLAXIS software. This model requires five parameters: young's modulus (E), Poisson's ratio (ν), friction angle (u), cohesion (C), and dilatancy angle (w). Numerical computations show an improvement of about 85% in the bearing capacity of reinforced embankment for rut up to 10 cm and subgrade undrained cohesion about 10 kN/m².

Stimulation of safe height of embankment on soft ground using flex is analyzed by Kaim et al. (2013) analyzed that the settlements cause due to weak Foundation would increase the construction cost. Safe height for embankment construction is between 3 and 5, and ground improvement is adopted by installing geogrid. Parametric analysis is carried out by varying the spacing of reinforcement and height of embankment using PLAXIS tool. It is found that the maximum height for safe construction is 4.9 m by analyzing a case study of Malaysia. Soil considered was of three layers upper middle and lower layers and embankment was considered in drained conditions results are verified using Terzaghi's ultimate bearing capacity equation.

Methodology

Parametric Analysis

A plain strain 15 nodes triangular elements Mohr–Coulomb Criterion model is considered for 2-dimensional finite element analysis. Parametric study is carried out systematically by varying different input parameters which influence the geometry, material and support conditions of the model keeping the rest of the parameters constant. Plaxis 2D version 8.2 is considered for this purpose and complete deformation analysis is carried out in order to determine settlement and failure of embankment. Obtained output is presented graphically for the comparative study of the results. Output results such as horizontal and vertical deformations, total Cartesian stress and strains are computed by varying height, slope of embankment and location of ground water table which influence embankment behavior and its stability. Initially after defining the geometry of the model, it is necessary to set up the boundary conditions and generate the mesh proceeded by plastic calculation and stimulation of results.

A 2 lane 10 m wide embankment of suitable height is built over uniform layer of foundation soil profile of depth 20 m leaving 20 m on either side of the embankment as per the standards set by IRC [3]. Transfer side slope of 1 V:2.5H is provided for the geometry of the model and to drain off the rainwater away from the pavement. For the stimulation of interaction between the different soil structure and for the relative displacement between them, the interface element is applied below the load and interface of embankment and subgrade [4]. Embankment is loaded by means of static uniformly distributed AA system of vertical loading of magnitude 30 kN/m². It is applied only on the central portion of top width of embankment leaving the side offsets of 1.5 m on either side as there is negligible load effect on the shoulders. Model is well defined by generating fine mesh for the accuracy of results. Considering the poor undrained strength of subsoil stage wise construction is adopted by defining model in each stage.

Locally available Marine clay is chosen as foundation soil. Marine clay is typical soft clay and has high compressibility and high plasticity characteristics. Gravel with proper gradation is chosen as embankment filling material which has better engineering properties as compared to the foundation soil adhering to ASTM codes. It is commonly used embankment soil for Highway embankment construction and has good stiffness which helps to mitigate the settlement to certain extent. The soil properties considered for this study is summarized in Table 38.1.

When the soil deposit is loaded the deformation occurs resulting from the load, due the poor permeability of subsoil and rate of compression due to vertical loading is dependent on rate of consolidation. It is well known that the wheel load from the Vehicles gets transferred to the subgrade through the pavement layers which generate shear stress which in turn causes shear failure. Hence, the subgrade should have sufficient shear strength to withstand the imposed load. Assuming normally consolidated condition, it is required to carry out the long-term stability analysis by

Table 38.1 Soil properties considered in the study

Soil	γ -unsaturated (kN/m ³)	γ -saturated (kN/m ³)	E (kN/m ²)	μ	C (kN/m ²)	Φ (degree)	Ψ (degree)
Embankment soil	17	18.9	70,000	0.35	1	32	4
Marine clay	15	15.5	2000	0.26	5	22	0

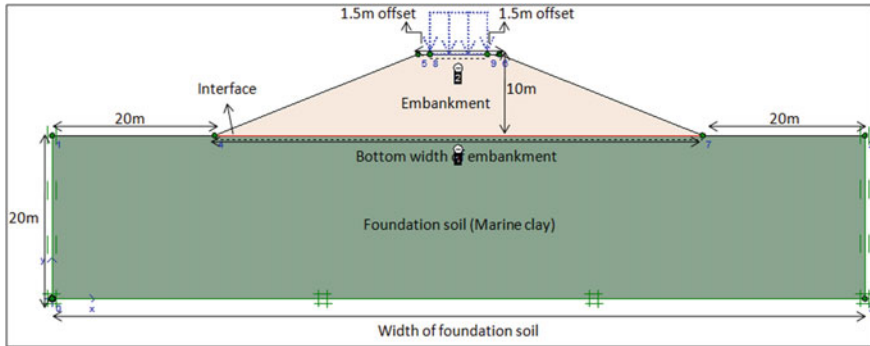


Fig. 38.1 General model

considering the drain condition for granular embankment filling material and short-term analysis using undrained condition for foundation soil. Plastic calculation with increased number of iterations carried out for all stages of this study (Fig. 38.1).

Effect of Embankment Height

Height of embankment has great influence on long-term settlement of embankment resting on soft soil. With increased number of infrastructure projects, there is urge for the utilization of available soft ground and go for higher embankment construction due to limited construction area [5]. It is very much essential to carry out embankment stability analysis by varying embankment height in order to determine safe height governing embankment construction in road project. Shear force caused due to induced traffic loading causes shear failure soon after foundation soil reaches its ultimate bearing capacity [5]. Parametric analysis is carried out by increasing the height of embankment and to learn its stability. Magnitude of settlements caused as a result of loading decreases rapidly with embankment height. Static uniformly distributed live load of 30 kN/m² is imposed on the central portion of embankment with side slope 1:2.5(v:h) omitting ground water table effect. Due to low bearing capacity of weak foundation soil beneath the embankment, it witnesses over compression and undergoes large lateral deformation [6]. Failure of embankment due to soft clay is

reflected in the form of extreme deformations and settlements. The variation of stress, strains deformation with embankment height is depicted graphically from Figs. 38.2, 38.3, 38.4, 38.5, 38.6, 38.7 and 38.8 (Figs. 38.9, 38.10).

Dead load due to comprised pavement layers and induced live load causes large stress to develop in foundation soil (Marine clay). However, this stress gets uniformly distributed throughout the depth of subgrade which is large in dimension (width) which decreases horizontal and vertical deformations with height increment. Due to large overburden pressure caused because of combined traffic loading and dead load causes development of additional vertical stresses which increases with height. Normal stress in both Cartesian axes due to uniform trapezoidal strip loading of embankment also increases with embankment height and are dependent on stress-deformation of subgrade. Strain resulting from vertical loading decreases variably with height and its variation is constant with width and increase tremendously near the extremes due to strain softening behavior of highly sensitive soft clay.

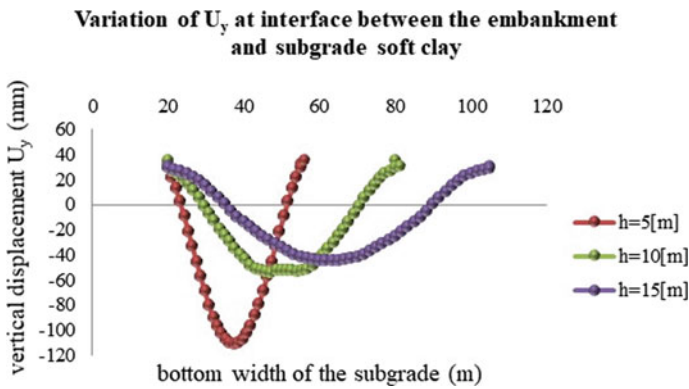


Fig. 38.2 Vertical displacement

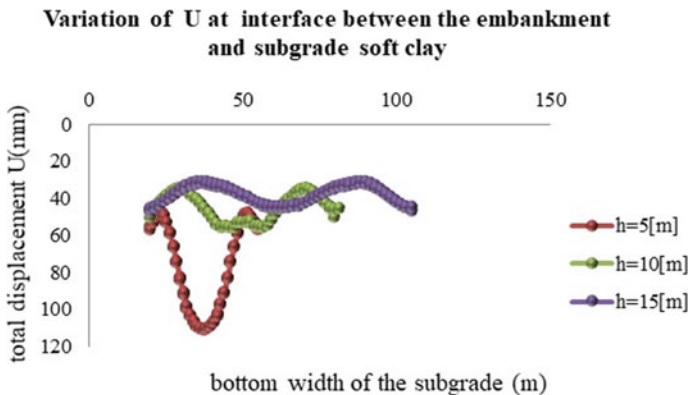


Fig. 38.3 Total displacement

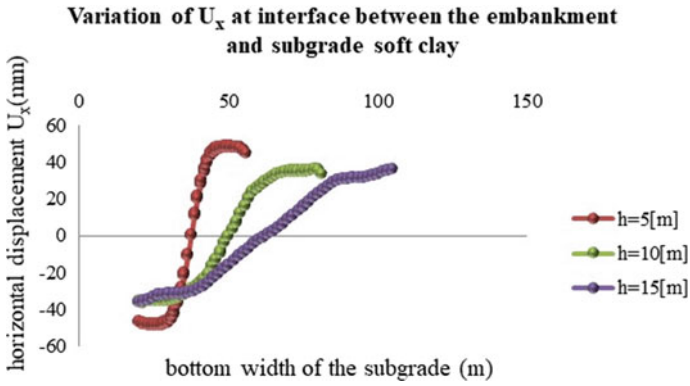


Fig. 38.4 Horizontal displacement

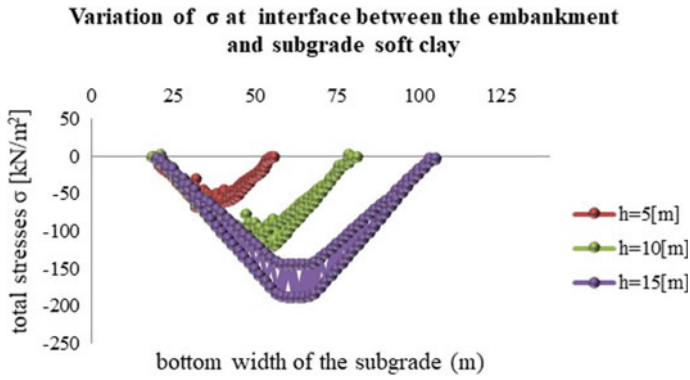


Fig. 38.5 Total stresses

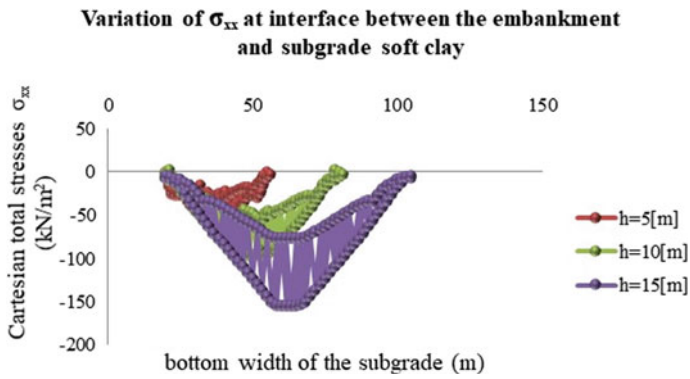


Fig. 38.6 Cartesian stresses σ_{xx}

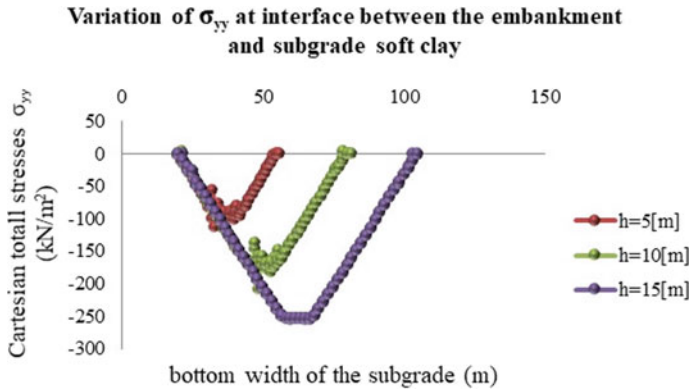


Fig. 38.7 Cartesian stresses σ_{yy}

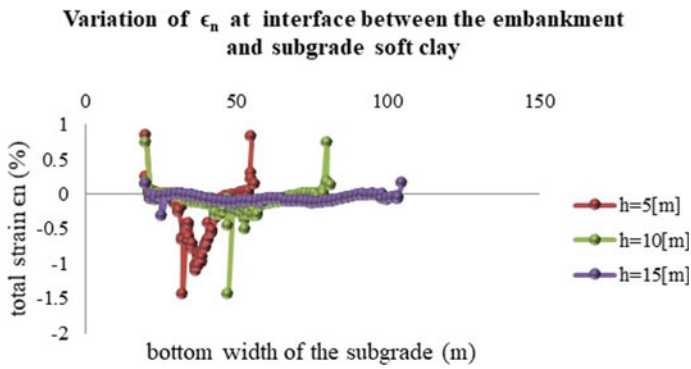


Fig. 38.8 Total strain

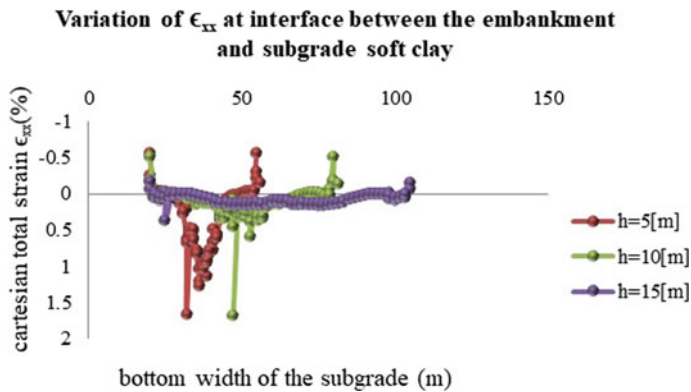


Fig. 38.9 Cartesian strain ϵ_{xx}

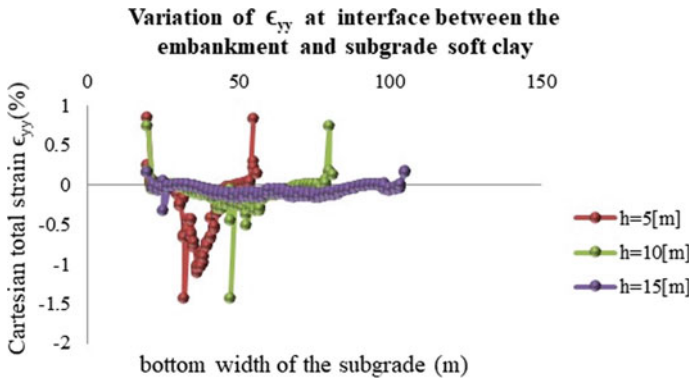


Fig. 38.10 Cartesian strain ϵ_{yy}

Effect of Embankment Slope

Stability of slope has greater influence on stability on Embankment stability. Stability analysis of human-made or natural slopes like embankments or road cuts is done to assess and ensure safe and economic design [7].

Geometry and parameters being a major concern in parametric analysis, Embankment height of 10 m and Surcharge of 30 kPa are kept constant. Slope of Embankment is taken as varying parameter and also by neglecting the effect of ground water table. Total stress method governs the stability as ground water table is omitted because of which pore water generation does not take places. Three models of 3H: 1V, 2.5H: 1V, 2H: 1V of slope angles 18.43° , 21.80° , and 26.56° respectively are analyzed in Plaxis tool by considering Mohr's–Coulomb criteria. The obtained settlements (Vertical deflections) are 102.71 mm, 71.92 mm, 58.38 mm, respectively. The range of settlements attained is indeed high which are hard to accept. Ground improvement techniques need to be adopted to reduce the Settlements. From the depicted results, "As the steepness of slope increases, the Settlement value increases". Variation of total, Cartesian stress and strain including deformations with slope increment are presented graphically from Figs. 38.11, 38.12, 38.13, 38.14, 38.15, 38.16, 38.17, 38.18, and 38.19.

Slopes acts as natural drains as well as point of failure under the influence of rainfall, shear failure, slippage therefore study of all forms of deformation is carried out. As steepness of slope is considered stress developed is less, therefore decrease in total stress and Cartesian stress of x and y directions are obtained in the subgrade soil which depends on self-weight, overburden pressure, and load applied. Increased values of horizontal displacement, vertical and total displacements and negligible variation of total and Cartesian strains are attained.

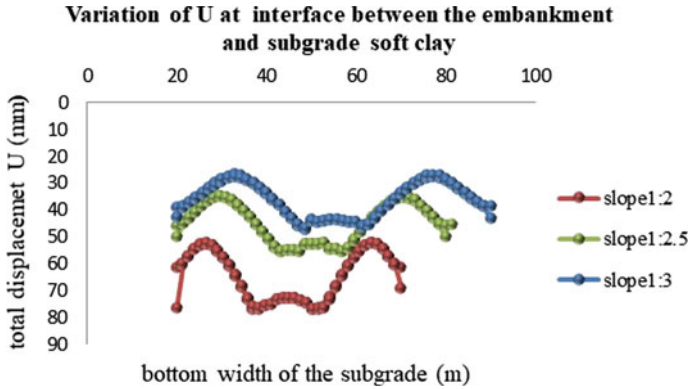


Fig. 38.11 Total displacements

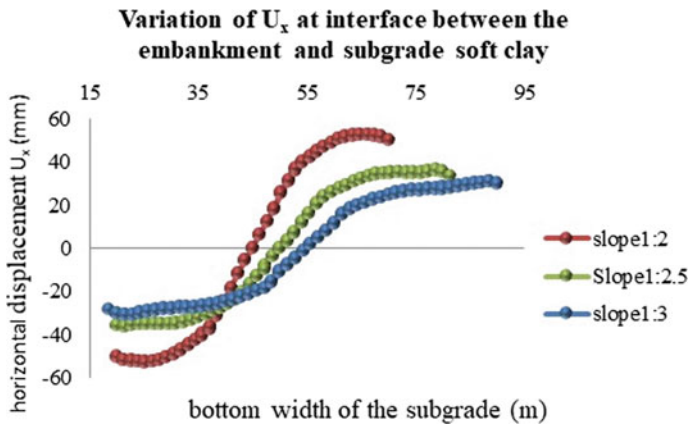


Fig. 38.12 Horizontal displacements

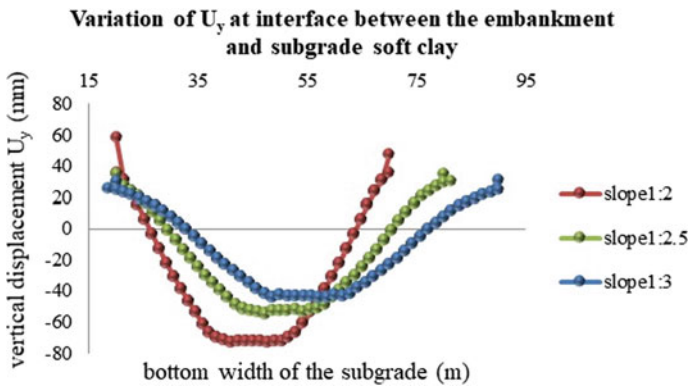


Fig. 38.13 Vertical displacements

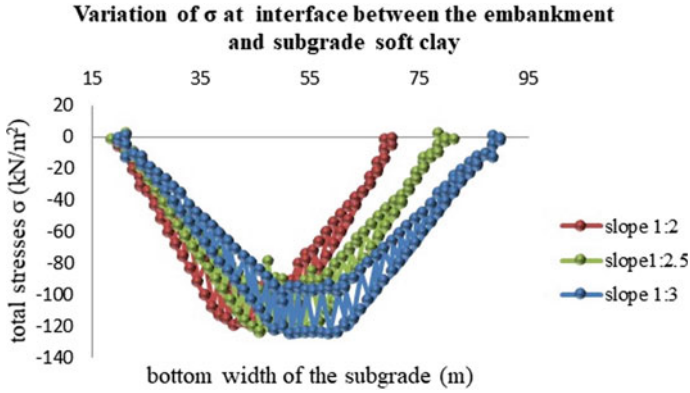


Fig. 38.14 Total stress

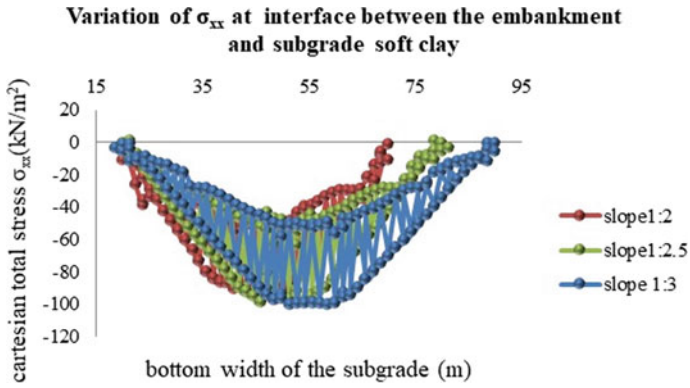


Fig. 38.15 Cartesian total stresses σ_{xx}

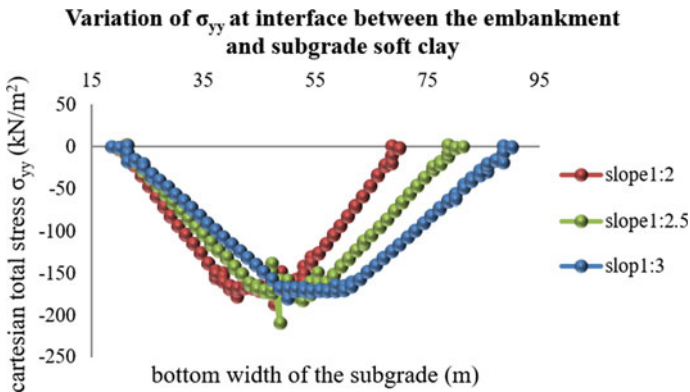


Fig. 38.16 Cartesian total stresses σ_{yy}

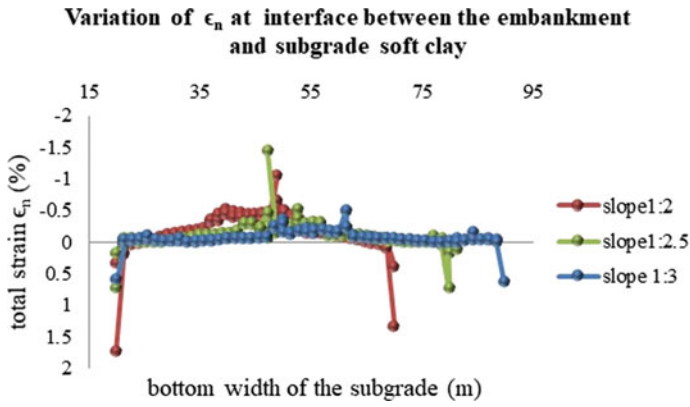


Fig. 38.17 Total strain

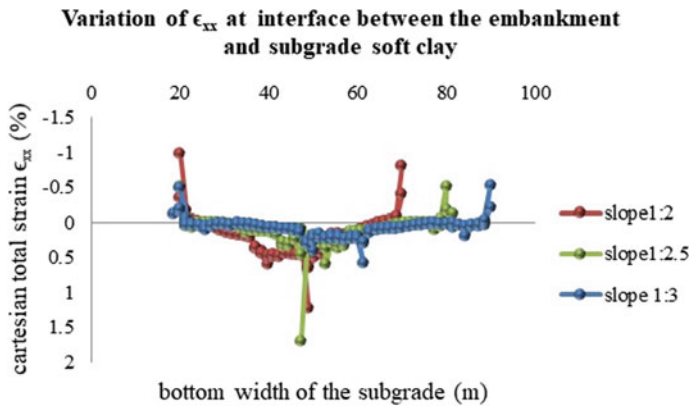


Fig. 38.18 Cartesian strain ϵ_{xx}

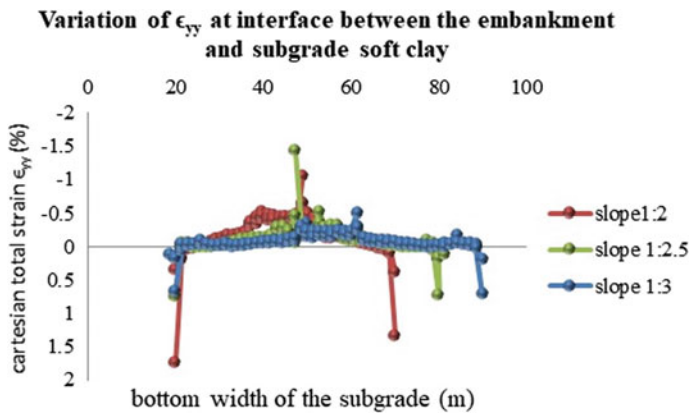


Fig. 38.19 Cartesian strain ϵ_{yy}

Effect of Ground Water Table

The behavior and stability of Embankment resting on Marine clay is analyzed in the presence of ground water table at various locations. The shear strength of soil layers is affected by the ground water level due to the presence of capillary water [8]. It is known that large settlements are caused due to more effective stress developed by lowering the ground water table. For this parametric study, embankment soil properties, subgrade soil properties, height of embankment (10 m), slope of embankment (1V:2.5H), and surcharge load of 30 kN/m² are kept constant throughout and ground water table level at the middle of subgrade, 15 m from bottom of embankment and at the center of embankment were considered and their respective settlements were obtained. Bringing down water table level induces more deformations in the foundation soil. Soft clay being highly compressible in nature and poor undrained shear strength and further gets reduced due to excess pore water pressure. The comparison of numerical analysis on the variable ground water levels clearly shows maximum deformation occurs at the middle of subgrade and minimum settlement is seen by placing water table at the center of embankment. Variation of stress, strain and deformation with respect to location of ground water table is shown by using the graphs from Figs. 38.20, 38.21, 38.22, 38.23, 38.24, 38.25, 38.26, 38.27, 38.28, 38.29 and 38.30.

Effective stress which is significant in determining engineering properties of soil decreases upon rising water table due to buoyancy effect. However due to combined effect of over lying embankment and weight of soil grains above the water table, total stress increases by rising water table. Due to this total stress, Cartesian stress in both *xx* and *yy* direction increases by raising the water table above. However, Marine clay has very high compressibility which further gets increased due to decreased effective stress and its shear strength still decreases resulting in large deformation in both horizontal and vertical direction. Hence by rising water table, Deformation gradually decreases.

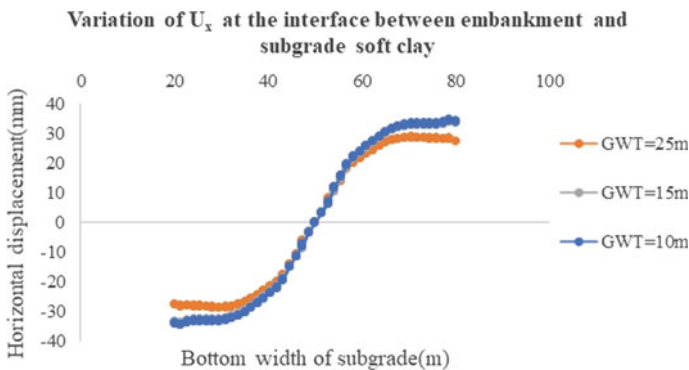


Fig. 38.20 Horizontal displacement

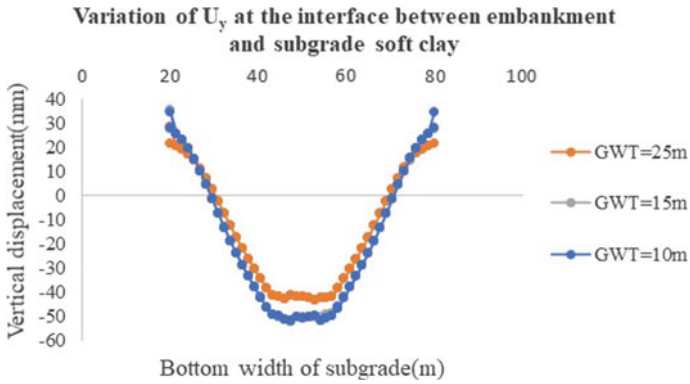


Fig. 38.21 Vertical displacement

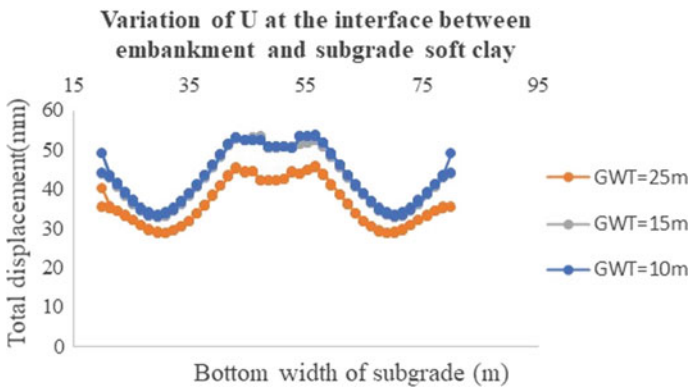


Fig. 38.22 Total displacement

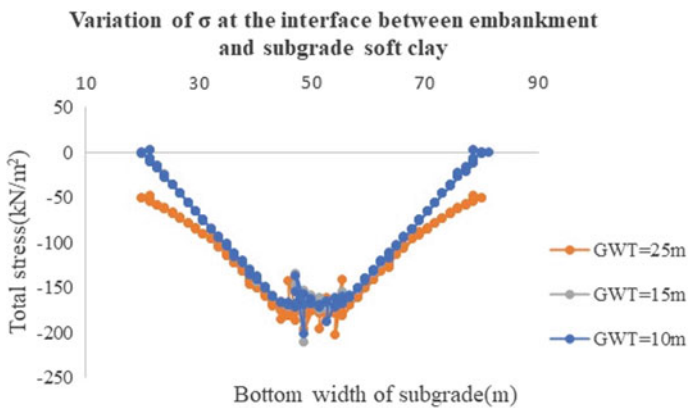


Fig. 38.23 Total stresses

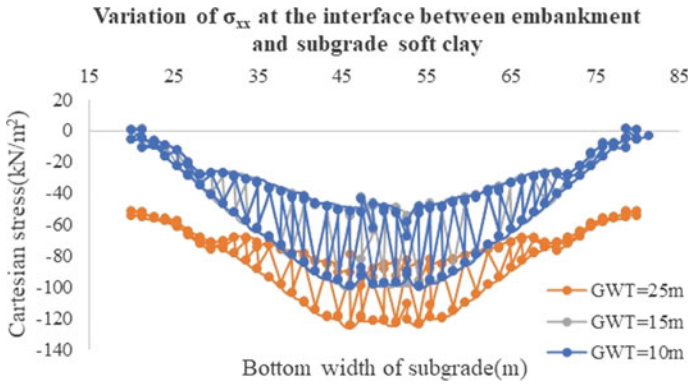


Fig. 38.24 Cartesian stress σ_{xx}

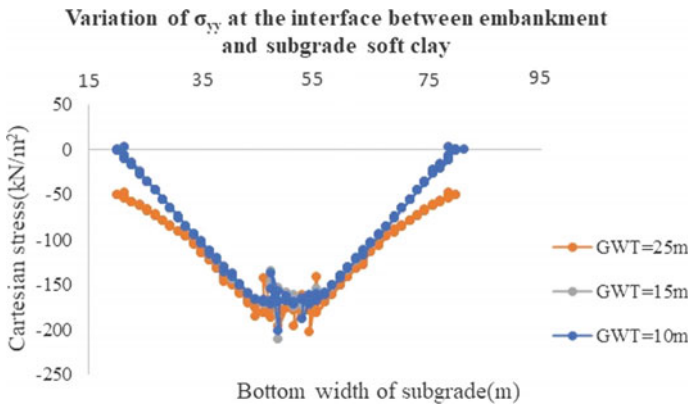


Fig. 38.25 Cartesian stress σ_{yy}

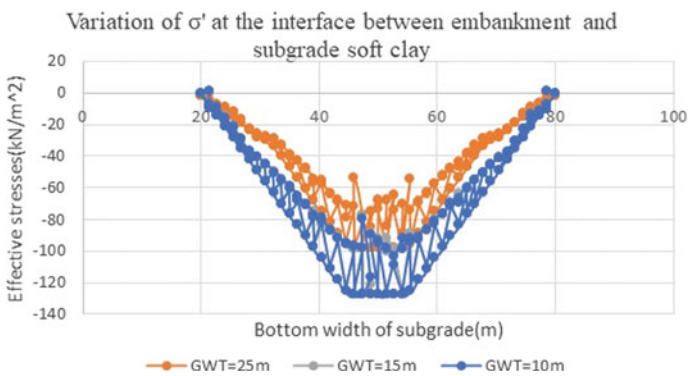


Fig. 38.26 Effective stress

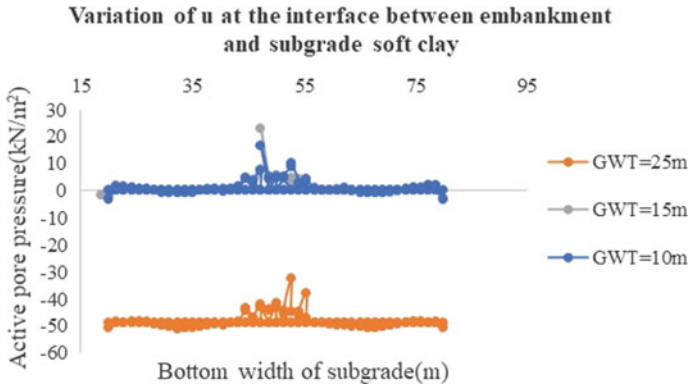


Fig. 38.27 Active pore pressure

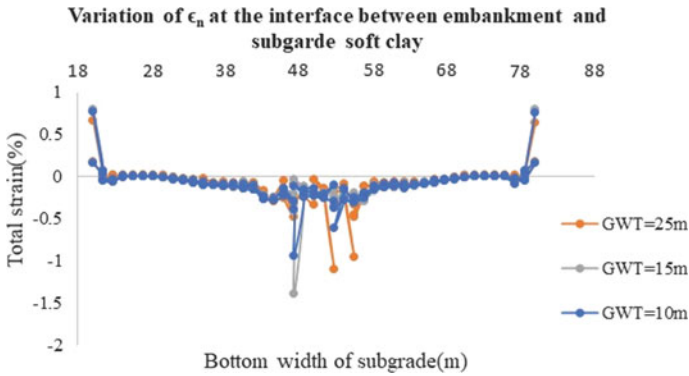


Fig. 38.28 Total strain

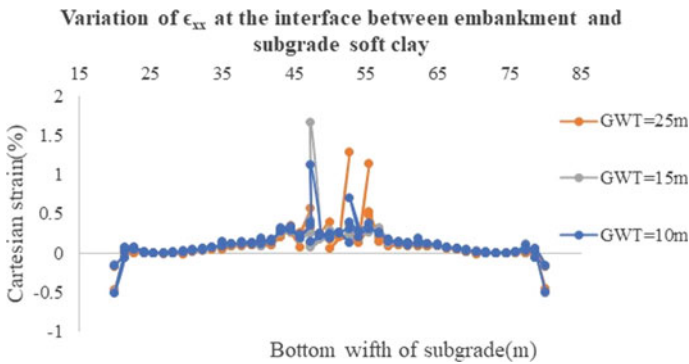


Fig. 38.29 Cartesian strain ϵ_{xx}

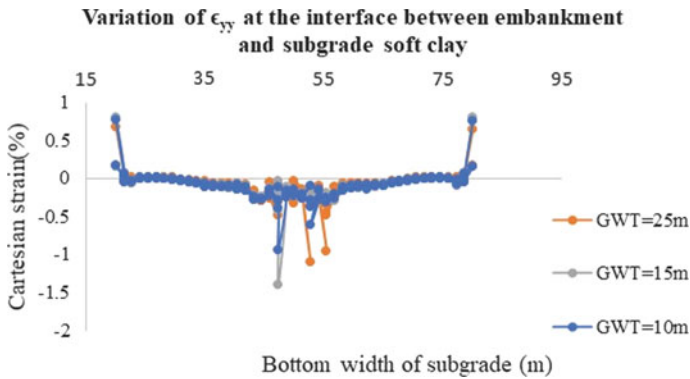


Fig. 38.30 Cartesian strain ϵ_{yy}

Conclusion

As the embankment height increases due to additional stresses developed in the soil the total, Cartesian stresses developed also increases. Magnitude of settlements and strains decreases with increase in embankment height.

Effect of slope study for safe embankment construction shows the increase in total settlements, total and Cartesian strains but the developed total and Cartesian stresses decreases with steepness of slope.

Stresses developed when ground water table is located at the center of embankment are found to be maximum. The deformation is found to be maximum when ground water table is located in middle of foundation soil and least when it is located at the center of embankment.

References

1. Abhishek SV, Madhav MR (2013) Embankments on soft ground an overview. ICTDMU-1, Research gate
2. Wulandari PS, Tjandra D (2015) Analysis of geotextile reinforced road using embankment Plaxis 2D.EACEF-5, Elsevier
3. IRC:SP:73-2007 (2007) Manual of standards and specifications for 2 laning of State Highways. Indian Road Congress
4. Plaxis (2013) User's manual
5. Kaisim F, Marto A, Othman BA, Bakar I, Othman MF (2013) Simulation of safe height of embankment on soft ground using plaxis. Elsevier
6. Carreira M, Almedida M, Pinto A (2016) A numerical study on critical height of embankment supported by geotextile encased granular column. Procedia Engineering 143:1341–1349
7. Sazzad MM, Islam MM (2019) Stability analysis of an earthen dam with internal clay core. J Water Resour. Pollut. Stud 4(1)
8. Latief RH, Zainal AKE (2019) Effect of water table level on slope stability and construction cost of highway Embankment. Engineering Journal 23(5)

9. Benmebarek S, Berraba F, Benmebarek N, Belounar L (2015) Effect of geosynthetic on performance of road embankment over Sabka soils in Algeria: case study. Springer International Publishing, Switzerland

Chapter 39

Study on Soil–Panel Interaction on the Performance of MSE Wall



Anand M. Hulagabali , C. H. Solanki, and G. R. Dodagoudar

Introduction

MSE walls are the retaining walls that can restrain lateral forces by providing alternative layers of reinforcement behind the facing wall, which is compacted with soil to form an integral part to prevent the deformation. The shear stress developed on reinforcement produces tension in reinforcement, which leads to confinement to the soil and results in a decrease in soil deformation and an increase in shear strength of the soil [1, 2]. The stability of the MSE wall depends on the frictional and bearing resistance between the reinforcing elements and the soil [3]. The construction of an MSE wall does not require specialized craftsmanship and skill. The construction procedure is rapid and straightforward. Nonetheless, before the construction of the wall, site-specific material requirements, construction quality control, and a performance monitoring plan are considered [4].

In the numerical modeling of MSE wall, interaction between facing panels and backfill soil plays an important role in governing the performance of the MSE wall [5]. In this study, backfill soil with different stiffness has been considered. Friction coefficient between backfill soil and panel has been varied to understand its effect on the deformations of the wall.

A. M. Hulagabali (✉)
The National Institute of Engineering, Mysore 570022, India
e-mail: anandmh@nie.ac.in

C. H. Solanki
Sardar Vallabhbhai National Institute of Technology, Surat 395007, India

G. R. Dodagoudar
Indian Institute of Technology, Chennai 600036, India

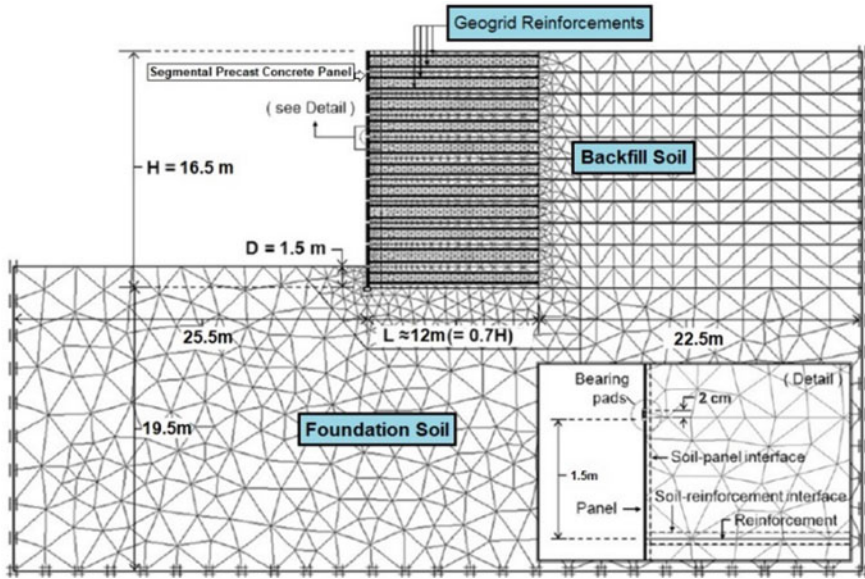


Fig. 39.1 Details of wall geometry used for parametric study

Numerical Modeling

Geometry of the Wall

Parametric study has been carried out to study the effect of backfill and foundation soil stiffness on the wall displacements for different soil–panel friction coefficients. The wall dimensions adopted for the parametric analysis are shown in Fig. 39.1.

Details of wall geometry used for analysis are given in Table 39.1. The height of the wall is considered as 16.5 m. The length of the reinforcements is considered as $0.7 H$ [6]. Bearing pads are modeled in between precast concrete panels. The depth of embedment is 1.5 m. The two-dimensional MSE wall model used in the PLAXIS is shown in Fig. 39.2. Surcharge load of 25 kPa is being applied on the reinforced block.

Material Properties

This parametric analysis takes into account five different backfill soils and three different foundation soils. Because of the susceptibility of soil stiffness to confining pressure, single elastic modulus estimations for soils are widely recognized to be an unsatisfactory mechanical characteristic of soil stiffness. The current study, on the

Table 39.1 Details of wall geometry used for analysis

S No	Properties	Values	Units
1	Height of the wall	16.5	m
2	Type of facing panels	Segmental precast concrete panels	–
3	Thickness of facing panels	0.15	m
4	Segmental panel, EA	11×10^6	kN/m
5	Segmental panel, EI	11×10^3	kN/m ² /m
6	Weight, W	10	kN/m/m
7	Poison’s ratio, μ	0.15	–
8	Type of reinforcement	Ribbed steel strips	
9	Length of reinforcement	12 m	m
10	Spacing of reinforcements	1.5 (middle reinforcements) 0.75 (top and bottom reinforcements)	m
11	Stiffness of reinforcement, EA	88	MN/m

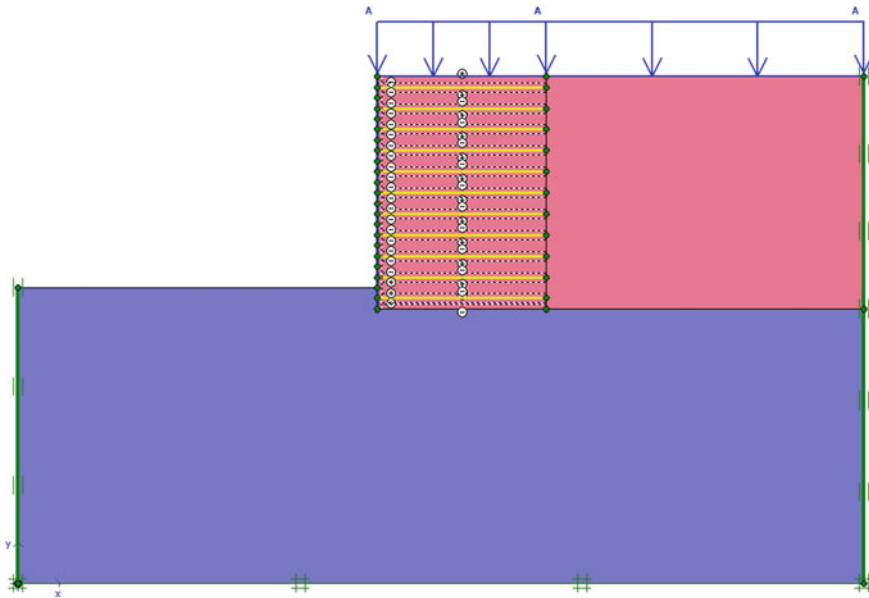


Fig. 39.2 Two-dimensional wall model used for parametric study

other hand, is looking into the effect of relative stiffness of backfill and foundation soil on wall displacements. The lowest value employed in this study for the backfill soil (type 5) does not mean that weakly compacted soils (or very compressible soils) should be used in the construction. Table 39.2 shows the soil type combinations that can be used to test the relative stiffness of the backfill soil and foundation stiffness

Table 39.2 Soil properties used in PLAXIS modeling for parametric study

Material	Parameter		Values	
Reinforced and Retained soil	Unit weight (kN/m ³)		20.8	
	Friction angle (°)		36	
	Cohesion (kPa)		0	
	Dilatancy angle (°)		4	
	Elastic modulus (E _b) (MPa)	Backfill 1		100
		Backfill 2		70
		Backfill 3		50
		Backfill 4		30
		Backfill 5		10
	Poisson's ratio		0.3	
Foundation soil	Unit weight (kN/m ³)		19.73	
	Friction angle (°)		35	
	Cohesion (kPa)		0	
	Elastic modulus (E _f) (MPa)	Foundation soil 1	1000	100
		Foundation soil 2		10
		Foundation soil 3		
	Poisson's ratio		0.3	

in five different instances. The elastic modulus of backfill and foundation soils was altered to see how it affected the wall's performance.

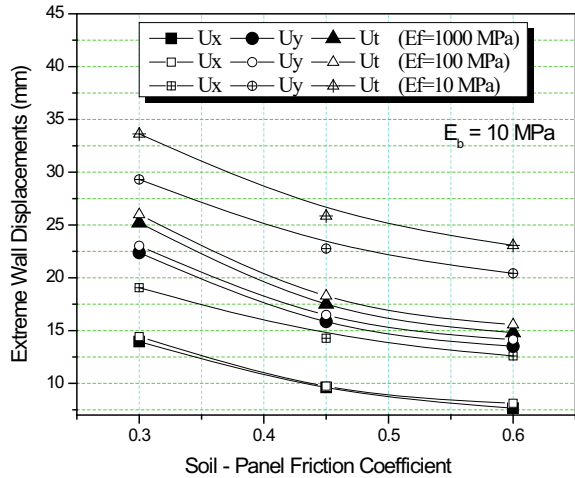
Meshing and Boundary Conditions

Wall is modeled using a two-dimensional finite element method with 1106 elements, 10,050 nodes, and 13,272 stress points. 15-noded triangular elements are used. The average size of the elements is 1.4 m. Very fine elements are used for meshing.

Effect of Soil–Panel Friction on Wall Displacements

The PLAXIS interface elements are used to simulate the strength and stiffness of soil-reinforced elements and soil-concrete facing panels. An interface reduction factor

Fig. 39.3 Variations of wall displacements with interface friction coefficient ($E_b = 10$ MPa)



(R), which is the ratio of the interface shear strength to the shear strength of the surrounding soil, is one of these elements (called the interface friction coefficient here-after). The concrete panel–soil interface is assigned a value of $R = \tan \delta / \tan \phi = 0.3$ [where ϕ is the peak friction angle of the soil (36°), and δ is the concrete soil interface friction angle (12°)] and zero dilatancy angle [7]. Simulations are also carried out using $R = 0.45$ and 0.6 corresponding to $\delta = 18^\circ$ and 24° , respectively. These higher values match values reported in the literature. The reinforcement elements are assumed to be perfectly bonded to the surrounding soil by assigning $R = 1$ (i.e., $\delta = \phi$). It is noted that interface shear is also assumed to be mobilized between the front of the wall facing and the foundation soil over the embedment depth $D = 1.5$ m. Extreme horizontal, vertical, and total deformations of the wall are shown in Figs. 39.3, 39.4, 39.5, 39.6 and 39.7.

From Figs. 39.3, 39.4, 39.5, 39.6 and 39.7, results are representing the variation of extreme horizontal, vertical, and total displacements for different backfill and foundation soil stiffnesses. Variations in displacements are analyzed for soil–panel friction coefficients (0.3, 0.45, and 0.6).

From Fig. 39.3, it is clear that the horizontal maximum displacements (here-after referred as U_x), vertical displacements (U_y), and total displacements (U_t) are 19.06 mm, 29.31 mm, and 33.62 mm, respectively, for the modulus of elasticity of foundation (E_f) 10 MPa, modulus of elasticity of backfill (E_b) 10 MPa, and coefficient of soil–panel coefficient (R) 0.30. Also, the minimum U_x , U_y , and U_t are 7.65 mm, 13.51 mm, and 14.81 mm, respectively, for $E_f = 1000$ MPa, $E_b = 10$ MPa, and $R = 0.60$.

Figure 39.4 shows that maximum U_x , U_y , and U_t are 9.89 mm, 14.2 mm, and 17.13 mm, respectively, for $E_f = 10$ MPa, $E_b = 30$ MPa, and $R = 0.30$. Also, the minimum U_x , U_y , and U_t are 2.72 mm, 4.71 mm, and 5.20 mm, respectively, for $E_f = 1000$ MPa, $E_b = 30$ MPa, and $R = 0.60$. Figure 39.5 shows that maximum U_x , U_y , and U_t are 8.0 mm, 11.7 mm, and 13.8 mm, respectively for $E_f = 10$ MPa and $E_b =$

Fig. 39.4 Variations of wall displacements with interface friction coefficient ($E_b = 30$ MPa)

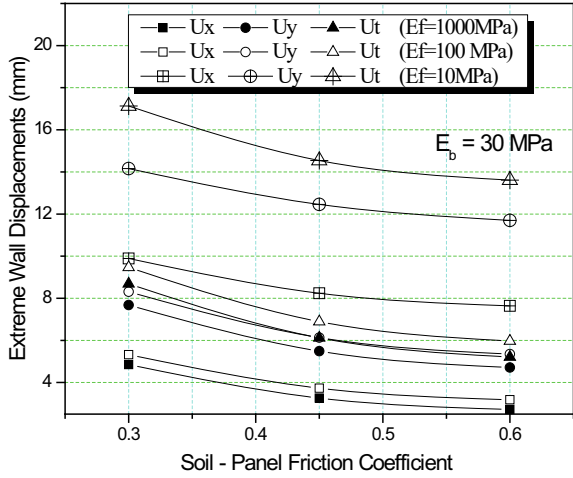
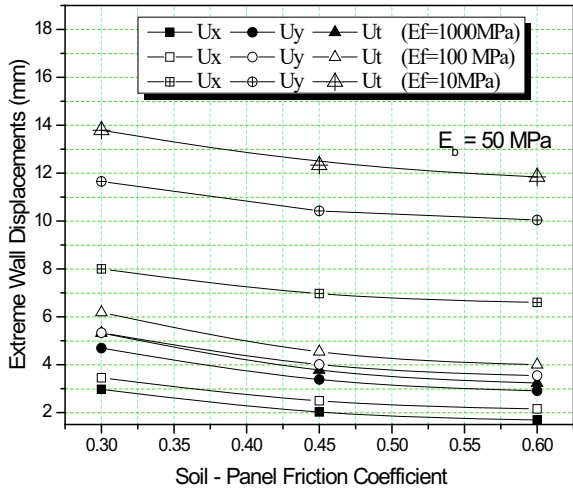


Fig. 39.5 Variations of wall displacements with interface friction coefficient ($E_b = 50$ MPa)



50 MPa. Also, the minimum U_x , U_y , and U_t are 1.69 mm, 2.91 mm, and 3.23 mm, respectively, for $E_f = 1000$ MPa, $E_b = 50$ MPa, and $R = 0.60$.

Figure 39.6 clearly shows that maximum U_x , U_y , and U_t are 7.3 mm, 10.2 mm, and 12.5 mm, respectively, for $E_f = 10$ MPa, $E_b = 70$ MPa, and $R = 0.30$. Also, the minimum U_x , U_y , and U_t are 1.25 mm, 2.10 mm, and 2.50 mm, respectively, for $E_f = 1000$ MPa, $E_b = 70$ MPa, and $R = 0.60$. For greater soil–panel friction coefficient, horizontal, vertical, and total wall deformations are less compared with lesser friction coefficient. With the increase in modulus of elasticity of backfill and foundation soil, wall deformations are reduced significantly. Figure 39.7 shows that maximum U_x , U_y , and U_t are 5.76 mm, 9.13 mm, and 10.48 mm, respectively, for

Fig. 39.6 Variations of wall displacements with interface friction coefficient ($E_b = 70$ MPa)

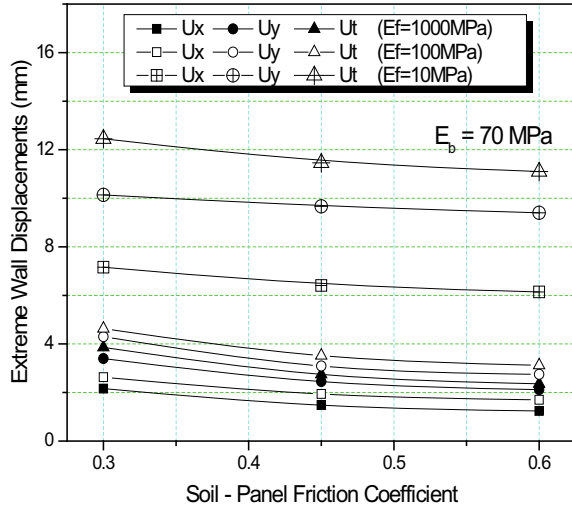
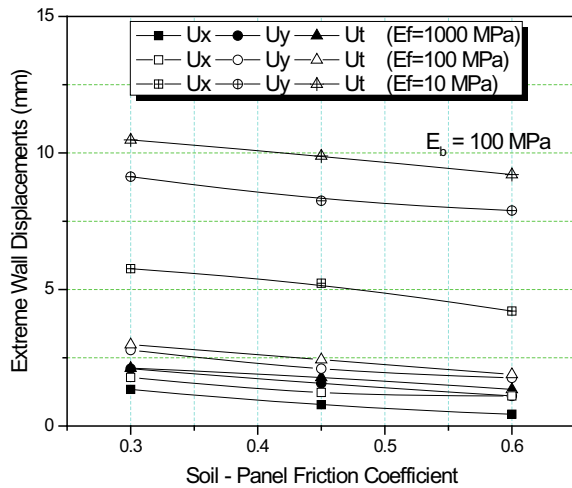


Fig. 39.7 Variations of wall displacements with interface friction coefficient ($E_b = 100$ MPa)



$E_f = 10$ MPa and $E_b = 100$ MPa. Also, the minimum U_x , U_y , and U_t are 0.43 mm, 1.1 mm, and 1.34 mm, respectively, for $E_f = 1000$ MPa, $E_b = 100$ MPa, and $R = 0.60$.

As the modulus of elasticity of backfill soil increased from 10 to 100 MPa, horizontal and vertical displacements decreased as seen in Figs. 39.8 and 39.9. It is clear from the analysis that, soil chosen for backfill and foundation should have more modulus of elasticity. Soils such as gravel or sand mixed with silt are more preferred for this purpose.

Fig. 39.8 Extreme horizontal displacements ($E_f = 1000$ MPa)

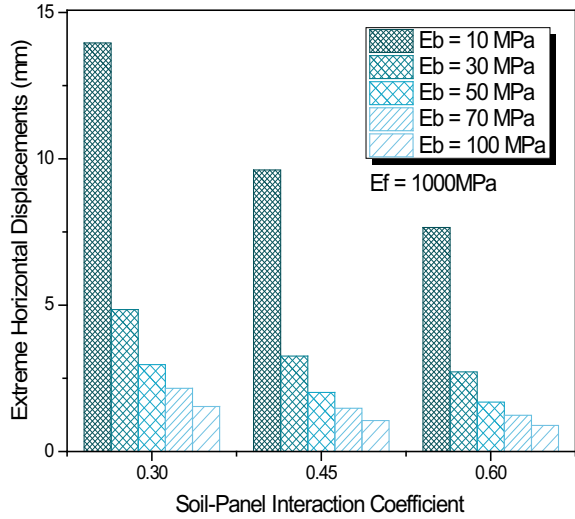
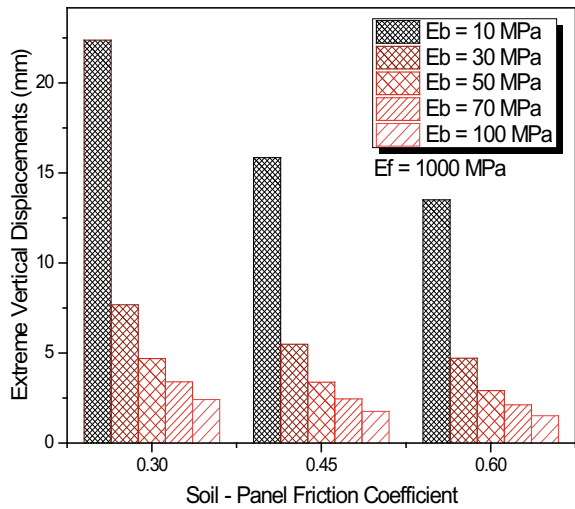


Fig. 39.9 Extreme vertical displacements ($E_f = 1000$ MPa)



Conclusions

From the above results, it is clear that, as the coefficient of interaction between soil and reinforcement increased from 0.3 to 0.6, displacements (U_x , U_y , and U_t) are decreased. Also, there is a vital role of backfill and foundation soil stiffness on the displacements of the wall. It is clear from the analysis that, soil chosen for backfill and foundation should have more modulus of elasticity. Soils such as gravel or sand mixed with silt are more preferred for this purpose.

References

1. Koerner RM, Koerner GR (2013) A data base, statistics and recommendations regarding 171 failed geosynthetic reinforced mechanically stabilized earth (MSE) walls. *Geotext Geomembr* 40:20–27
2. Koerner RM, Koerner GR (2018) An extended database and recommendations regarding 320 failed geosynthetic reinforced mechanically stabilized earth (MSE) walls. *Geotext Geomembr* 46(6):904–912
3. Kibria G, Sahadat HMD, Khan MS (2014) Influence of soil reinforcement on horizontal displacement of MSE wall. *Int J Geomech* 14(1):130–141
4. Hulagabali AM, Solanki CH, Dodagoudar GR, Konnur SS, Shettar MP (2018) Analysis of mechanically stabilised earth (MSE) retaining wall using finite element and AASHTO methods. *Journal of Engineering and Technology, American Society for Engineering Education*, 6:139–150 (Special issue-emerging trends in engineering technology)
5. Yu Y, Bathurst RJ, Miyata Y (2015) Numerical analysis of a mechanically stabilized earth wall reinforced with steel strips. *Soils Found* 55(3):536–547
6. FHWA-NHI-10-024 (2009) Design and construction of mechanically stabilized earth walls and reinforced soil slopes—volume I. Federal High Way Administration (FHWA), I
7. Rahmouni O, Mabrouki A, Benmeddour D, Mellas M (2016) A numerical investigation into the behavior of geosynthetic-reinforced soil segmental retaining walls. *Int J Geotech Eng* 10(5):435–444

Chapter 40

Effect of Different Compressible Inclusions on Lateral Earth Pressure Reduction in Rigid Retaining Wall



L. Anandha Raj and M. Muttharam

Introduction

Performance of the earth retaining structures is important in infrastructure development, railways, highways, and other places where required to retain the soil mass. In design, the free-standing retaining wall is designed based on active earth pressure condition by assuming the full friction mobilized along the failure plane surface by considering a required amount of deformation takes place for reaching the active earth pressure state during construction of the retaining wall. But in field conditions like bridge abutments, basement walls, and box culverts, the mobilized friction not fully develops and the Rankine failure plane does not occur. It leads to a higher amount of earth pressure coefficient which is taken for design. By introducing the readily compressible material as a vertical inclusion at the wall-backfill interface, the inclusion material gets compressed by earth pressure and backfill soil laterally deforms. This mechanism of lateral earth pressure reduction is initially proposed by Karpurapu and Bathurst [1] called the “Control Yielding Technique”. In earlier days, Partos and Kazaniwsky [2] conducted a field study on lateral earth pressure reduction on a rigid non-yielding wall using compressible inclusions. Controlling the compaction-induced earth pressure on earth retaining structure with geofoam inclusion was studied by Ravees and Filz [3], and large-scale physical model tests were conducted with cohesionless backfill. Similar to cohesionless backfill, cohesive soil also exerts a higher lateral earth pressure in addition to horizontal swell pressure under saturated conditions. Ikizher et al. [4] attempted to study the lateral earth pressure reduction on the wall from the expansive soil as backfill by using compressible inclusion. Ethylene Polystyrene Styrofoam (EPS) geofoam, an elastic

L. A. Raj (✉) · M. Muttharam
Department of Civil Engineering, Anna University, Chennai 600025, India
e-mail: anandhar.lenin@gmail.com

material initially introduced by Horvath [5], is used for filler material in embankment construction. A small-scale physical model study is carried out by Ertugrul and Trandfir [6] with geofoam as a compressible inclusion material in a rigid wall. Reddy and Krishna [7] conducted a shake table test on the modeled wall with 34 rubber tire chips as a compressible inclusion material for finding the effectiveness of tire chips as inclusion material in seismic conditions. Ni et al. [8] conducted a small-scale physical study and proposed a different analytical solution that defines the lateral earth pressure reduction using geofoam material. Liu et al. [9] conducted a field study on lateral earth pressure in retaining walls with woven textile bags filled up with expansive soil as an inclusion material. The functional parameters in the lateral earth pressure reduction technique are inclusion material properties such as the thickness of inclusion material, elastic modulus, and backfill characteristics. In this paper, the intended study is to compare the effect of different compressible inclusion materials such as EPS geofoam with different densities, fly ash, and rubber tire chips behind a rigid non-yielding wall on lateral earth pressure by numerical modeling using finite element code-based software PLAXIS 3D with cohesionless backfill.

Validation of Numerical Model

Before performing the numerical analysis, proper validation of the created numerical model is required. In this study, the created numerical model using PLAXIS 3D is validated through the experimental results of Ertugrul and Trandfir [6] by developing a numerical model of a retaining wall having a dimension of 0.7 m height and 1 m length with a base plate thickness of 0.05 m as shown in Fig. 40.1.

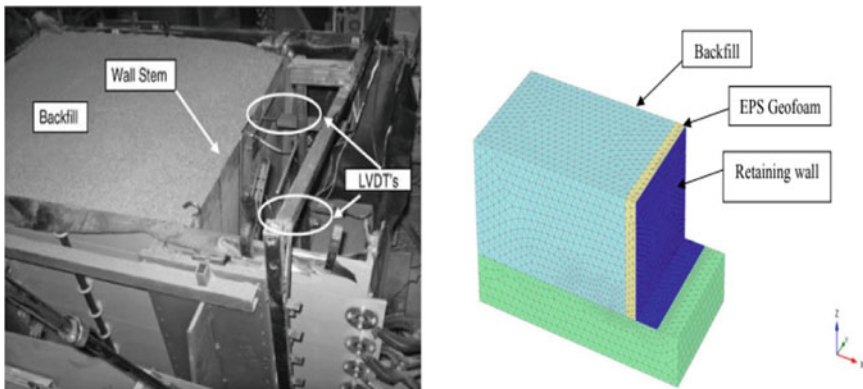


Fig. 40.1 FE model of experimental setup of Ertugrul and Trandfir [6]

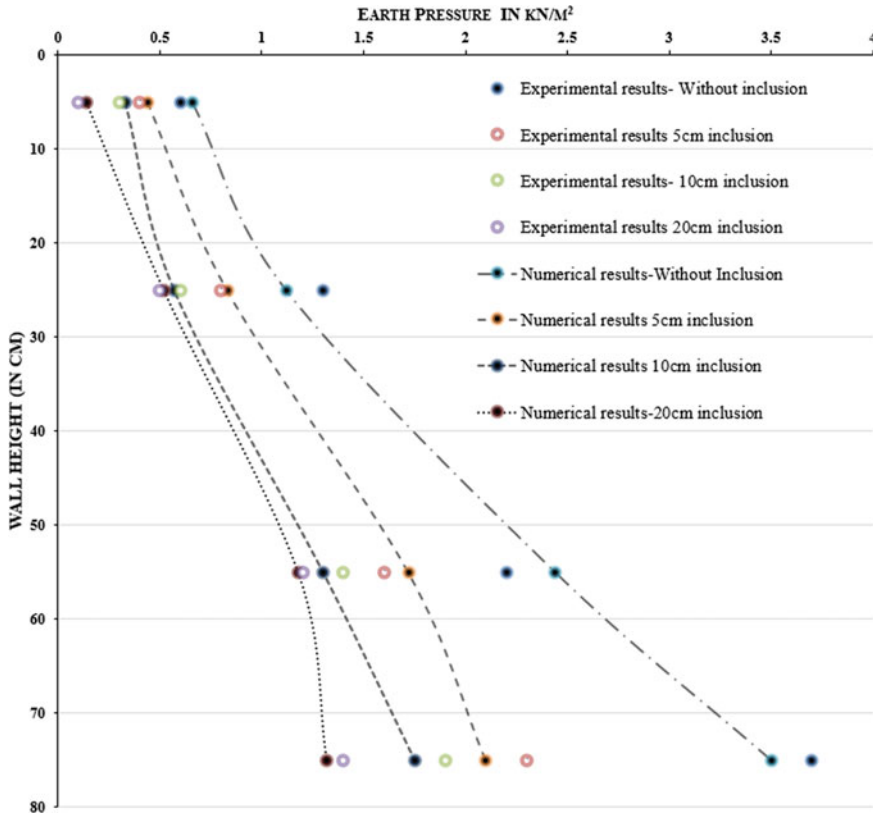


Fig. 40.2 Validation of created model through experimental results

Results of the numerical analysis obtained by considering very fine mesh discretization that gave the better convergence with the different thicknesses in Ethylene Polystyrene Styrofoam (EPS) geofoam of 5 cm, 10 cm, and 20 cm concerning wall height are shown in Fig. 40.2. In most cases, the deviation of the numerical results of Ertugrul and Trandfir [6] be less than 10% which is acceptable.

Numerical Modeling

In general, the retaining wall length was more than 50 m, the wall behavior is considered as plane strain condition (as infinite long plane strain problem), and a two-dimensional numerical tool is enough for analyses. If the retaining wall length is less than 50 m, the bending moments and lateral displacements of the soil along the wall length were quite different due to end corner effects. In the case of rigid

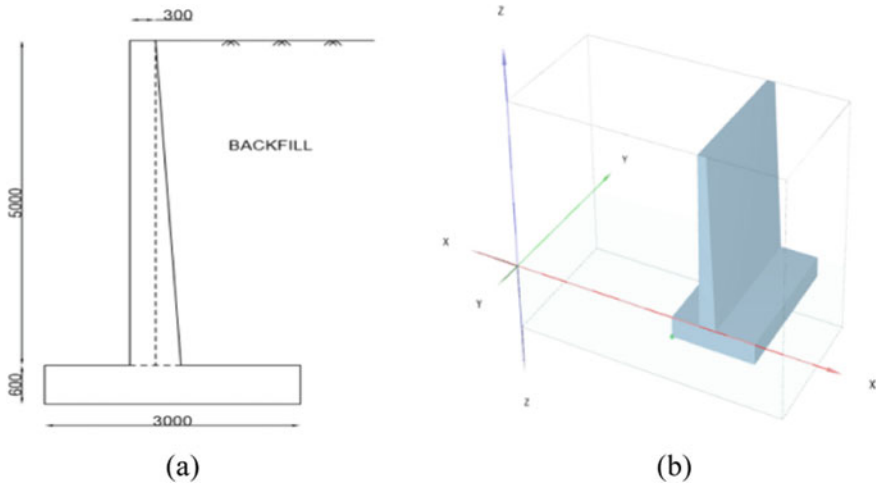


Fig. 40.3 a Cross-sectional view of a wall. b 3D numerical model of retaining wall

retaining structures, where highly lateral movements are restrained like bridge abutments, basement walls, etc., are in three dimensional state of stress conditions. Hence in this study, a 3D analysis tool is used through finite element code-based software PLAXIS 3D for better results. The numerical model of the cantilever retaining wall has 5 m high from the base and 7 m length is modeled with cohesionless soil as a backfill are shown in Fig. 40.3.

A cohesionless backfill soil and the foundation layer soil were modeled as homogenous, isotropic, and elasto-plastic which are characterized by Mohr–Coulomb yield function. All the inclusion materials like EPS geofoam, rubber tire chips, and fly ash are characterized by linearly elastic. To define interface stiffness at the backfill-inclusion material interface in the modeling, the interface strength reduction factor ($R_{\text{-Inter}}$) is used. The direct shear test was performed on geofoam to backfill and fly ash to backfill interfaces, and interface friction angle was observed as 29° and 18° , respectively. An interface stress reduction factor ($R_{\text{-Inter}}$) for the sand-geofoam, sand-fly ash, and sand-tire chip interfaces is 0.6, 0.65, and 0.7, respectively, taken based on the shear tests conducted and results reported on previous studies conducted by Khan and Meguid [10] and Balunaini et al. [11] for the input parameters in the numerical modeling. The parameters involved in the constitutive modeling for the materials are summarized in Table 40.1. The wall material is considered as rigid condition restrained to the horizontal material.

A created numerical model is discretized as a 10-noded tetrahedral element, and the appropriate function is applied for the analyses. An analysis is run through in 5 different phases for simulating the actual field condition by initial activation of the foundation soil, installing the rigid retaining wall, and the 3 stage-wise placings of backfill. The model has been analyzed with different inclusion materials which are EPS geofoam at different densities of 12, 15, and 20 kg/m³ and fly ash and rubber

Table 40.1 Constitutive model properties of materials involved

Model	Backfill	Foundation	EPS 12	EPS 15	EPS 20	Fly ash	Tire chips
	Mohr–Coulomb		Linear elastic				
Unit weight (γ , kN/m ³)	16	17.5	0.109	0.141	0.18	13	7.845
Young’s modulus (E , kPa)	30,000	55,000	1500	2500	4000	2000	1000
Poisson’s ratio (μ)	0.3	0.33	0.025	0.025	0.025	0.2	0.3
Friction angle (ϕ , degrees)	38	42.5	–	–	–	22	–
Dilatancy angle (ψ , degrees)	9	14	–	–	–	3	–

tire chips at different thicknesses of 50, 100, and 150 cm, respectively. Based on the results, the earth pressure distribution profile is obtained through lateral pressure measured in selected stress points at a regular interval of 0.5 m along the 5 m high wall. The lateral earth pressure distribution profile obtained by numerical analysis through created retaining wall numerical model with compressible inclusions as different densities of EPS geofom, rubber tire chips, and fly ash is shown in Figs. 40.4, 40.5, 40.6, and 40.7, respectively.

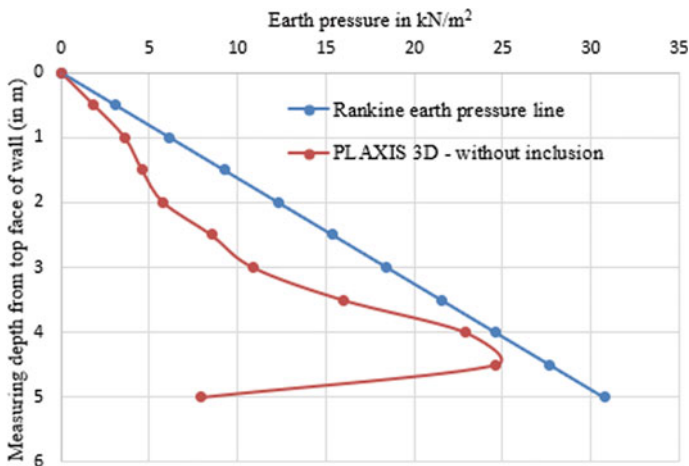


Fig. 40.4 LEP distribution on the wall without the inclusion

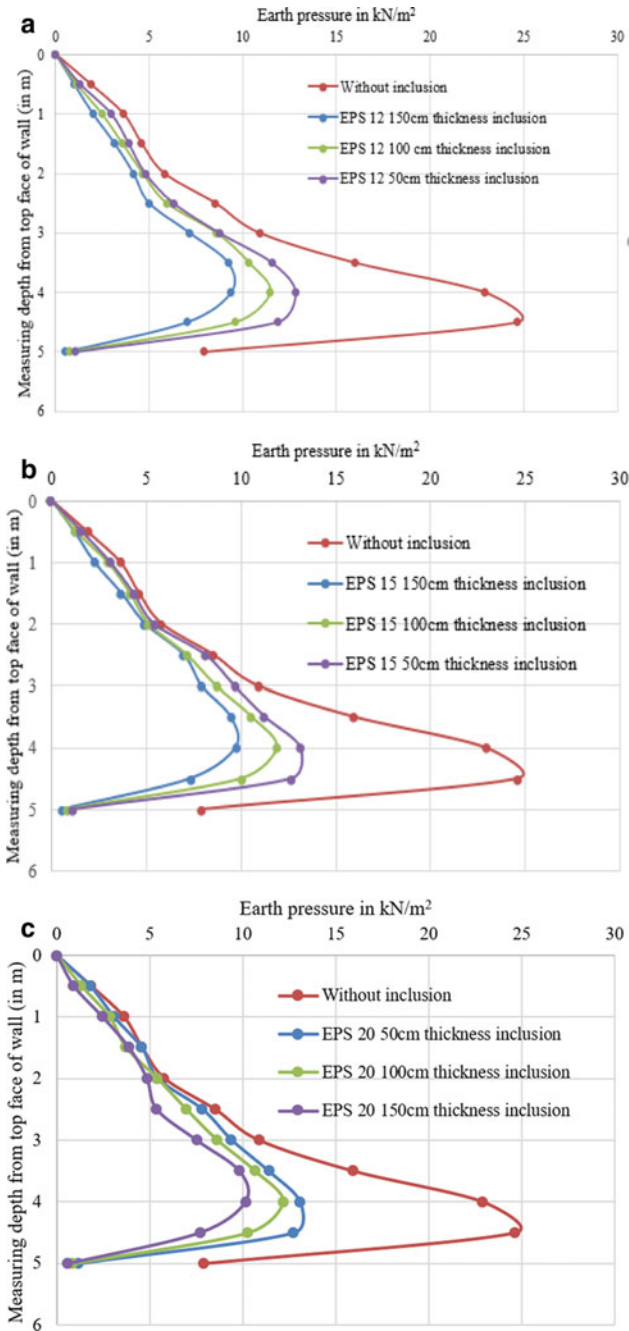


Fig. 40.5 a LEP distribution on the wall with EPS 12 inclusion. b LEP distribution on the wall with EPS 15 inclusion. c LEP distribution on the wall with EPS 20 inclusion

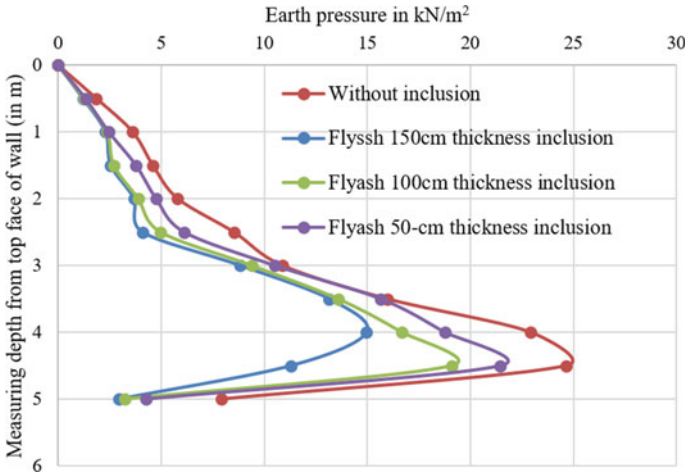


Fig. 40.6 LEP distribution on the wall with fly-ash inclusion

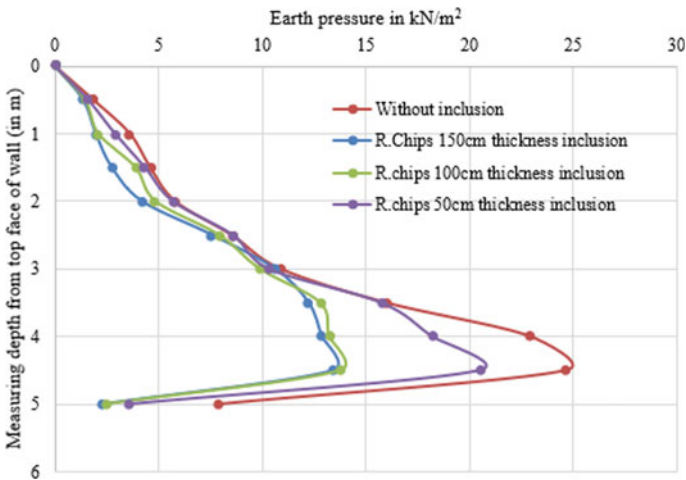


Fig. 40.7 LEP distribution on the wall with tire chip inclusion

Results and Discussions

The total earth pressure force exerted from the cohesionless backfill is obtained based on calculating the area of the lateral earth pressure distribution curve by using the best-fitting straight line. The total earth force calculated through the lateral earth pressure profiles for different inclusion materials with varying thicknesses is summarized in Table 40.2. The term “Isolation efficiency” is calculated for representing the amount of lateral earth pressure reduction by introducing the compressible inclusion at the

Table 40.2 Comparison of lateral earth pressure reduction on the wall with different inclusion material

Material	Thickness (cm)	Actual earth pressure measured (kN/m)	Amount of EP reduced (kn/m)	Isolation efficiency (%)
Water inclusion		66.15		
EPS 12	50	26.89	39.26	59.35
	100	25.8	40.275	60.88
	150	19.133	47.017	71.07
EPS 15	50	27.6	38.55	58.27
	100	26.64	39.57	59.72
	150	20.5	45.65	69
EPS 20	50	29.25	36.9	55.78
	100	26.35	39.798	60.16
	150	21.35	44.8	67.77
Fly ash	50	56.8	9.294	14.04
	100	49.99	16.16	24.42
	150	38.13	28.012	42.34
Rubber tire chips	50	52.11	14.04	21.22
	100	31.752	34.39	52
	150	30.07	36.08	54.5

wall-backfill interface as:

$$\text{Isolation efficiency}(\%) = \frac{\text{Amount of earth pressure reduced with inclusion}}{\text{Amount of earth pressure measured with inclusion}} * 100$$

By comparing all the inclusion materials, EPS geofoam having different densities efficiently reduces the earth’s pressure. By increasing the thickness of inclusion material, lateral earth pressure effectively reduced more than 50% of the actual earth pressure which acts on the wall. The lower density material EPS 12 should readily compressible and perfectly elastic at initial strain range reduces actual earth pressure of 71.07% was observed compared to the EPS geofoam at higher densities. A vertical surface settlement on backfill having EPS geofoam as inclusion was minimum because of its better volume stability and free from dilatancy effect.

By considering fly ash as an inclusion material, the actual earth pressure was reduced up to 30–40% at higher thickness. Further, rubber tire chips are considered as inclusion material at the wall-backfill interface, and the actual earth pressure was reduced up to 20–50% depending upon the thickness and initial elastic range of the material. In both fly ash and rubber tire chips as an inclusion material, the surface settlement was observed in the range of 10–50 mm. Comparing the results of

lateral earth pressure distribution profiles with the inclusion of EPS geofoam, fly ash, and rubber tire chips under surcharge loading conditions, EPS geofoam effectively redistributes the earth pressure uniformly at the mid-height of the wall due to the soil arching effect. Among all compressible inclusion materials considered in this study, EPS geofoam preferably with lower density satisfies in all aspects to reduce the lateral earth pressure on the rigid retaining wall. Also, other materials such as fly ash and tire chips as an inclusion material effectively reduce the lateral earth pressure with the drawback of volume instability and dilatancy effect.

Conclusion

The effect of different compressible inclusion on the reduction of lateral earth pressure acting on a rigid non-yielding retaining wall has been investigated through a created numerical model by finite element code-based software PLAXIS 3D. The tests were carried out by considering different compressible inclusion materials in different thicknesses of 50, 100, and 150 cm at the wall-backfill interface. EPS geofoam material with lower density and higher thickness effectively reduces the lateral earth pressure compared to the other inclusion materials considered. Tire chips and fly ash as an inclusion material placed at the wall-backfill interface reduce the lateral earth pressure up to 40% and 25%, respectively. In numerical modeling of retaining walls, predicting the behavior of inclusion materials at the wall-backfill interface under the lateral earth pressure conditions is quite complex; hence, all inclusion materials are characterized as linearly elastic. Rubber tire chips and fly-ash inclusions are particulate materials not able to place the wall-backfill interface without any packing. In that case, inclusion materials are packed in woven geotextile bags at the required density before placing them in field conditions. It is quite complex, to stimulate the inclusion materials with the packed condition. These two are limitations in this study, but both these limitations give conservative results by comparing them to field studies.

References

1. Karpurapu R, Bathurst RJ (1992) Numerical investigation of control yielding of soil retaining structures. *Geotext Geomembr* 11(2):115–131
2. Partos AM, Kazaniwsky PM (1987) Geofoam reduces lateral earth pressures. In: *Proceedings of geosynthetics, industrial fabrics association international*, New Orleans, pp 628–639
3. Reeves JN, Filz GM (2000) Earth force reduction by a synthetic compressible inclusion. Virginia 210 Tech., Department of Civil Engineering, Blacksburg, VA, USA
4. Ikizher SB, Aytekin M, Nas E (2008) Laboratory study of EPS geofoam used with expansive soils. *Geotext Geomembr* 26(2):189–195
5. Horvath JS (1997) The compressible inclusion function of EPS Geofoam. *Geotext Geomembr* 15:77–120

6. Ertugrul OL, Trandafir AC (2011) Reduction of lateral earth forces acting on rigid retaining walls by EPS geofoam inclusions. *J Mater Civ Eng ASCE* 23(12):1711–1718
7. Reddy SB, Krishna AM (2017) Tire chips as compressible inclusions in earth retaining walls. In: *Proceedings of the institution of civil engineers ground improvement*. June 2017
8. Ni P, Mei G, Zhao Y (2017) Displacement-dependent earth pressures on rigid retaining walls with compressible geofoam inclusions: physical modeling and analytical solutions. *Int J Geomech, ASCE* 17(6):04016132
9. Liu S, Fan K, Xu S (2018) Field study of a retaining wall constructed with clay-filled soil bags. *Geo-textiles and Geomembranes* 47:87–94
10. Khan MI, Meguid MA (2018) Experimental investigation of the shear behavior of EPS Geofoam. *International Journal of Geosynthetics and Ground Engineering* 4:1–12
11. Balunaini U, Mohan VKD, Prezzi M, Salgado R (2014) Shear strength of tire chips–sand and tire shred–sand mixtures. *Proceedings of Institution of Civil Engineers—Geotechnical Engineering* 167(6):585–595

Chapter 41

Restoration of Breached Ash Dyke Embankment in Constrained Site Conditions



Vinod Kumar Mauriya

Introduction

In thermal power plants, unutilized ash is disposed of in well designed, constructed, and maintained ash ponds in slurry form. The scheme for ash disposal in the ash pond in one of the plant was envisaged with spillway for taking out the decanted water from inside lagoon to existing overflow lagoon (common OFL with other adjacent lagoons) for further recirculation back to plant. For safety against overtopping, a free board of 1.5 m as per codal provisions has been provided between the maximum ash fill level and top of dyke embankment. For collection of any seepage water through internal drainage of dyke embankment, toe drain is provided at periphery of dyke for collection and recirculation back to the plant.

Design of Ash Pond

Considering the site conditions and operational constraints to ensure early availability of lagoon for ash slurry discharge, Starter dyke was constructed for the height of 6.6 m. The ultimate height of dyke is 15.6 m comprising of Starter dyke of maximum 6.6 m height to be constructed with compacted earth and 3 subsequent upstream raisings of 3 m (effective height) each using ash as main construction material with an earth cover. Considering the maximum flood water level, the Starter dyke was protected with downstream slope protection up to top level. Following Figs. 41.1 and 41.2 indicate the inside view and downstream side view of ash pond, respectively.

V. K. Mauriya (✉)
NTPC LTD, EOC Noida, Gautam Buddha Nagar 201301, India
e-mail: vkmauriya@ntpc.co.in



Fig. 41.1 Inside area of ash pond in 1st raising



Fig. 41.2 Downstream side view of ash pond

Design Considerations

Ash dykes are built based on accepted engineering standards of design and construction. As per the established practice, the ash dyke raising is done on consolidated state (through consolidation process) of dry ash bed achieved in the hydraulically deposited ash. As per practice, during raising in the non-operative lagoon, the hydraulically deposited top layer of the ash bed for a depth of about 1.0–2.0 m has to be dry to ensure safe and stable construction of each upstream raising. The deformation and drainage

behaviors of the foundation bed below raising dyke are dependent on the state of consolidation. The compression of the raising dyke embankment resting on consolidated strata would be very small and would occur quickly and is generally completed during construction of dyke embankment. However, when the embankment rests on unconsolidated strata, long-term settlement will occur due to consolidation of the underlying foundation strata.

Construction and Operation of Raising Dyke

During construction of raising dyke, the lagoon shall be inoperative, whereas due to plant's functional constraints during construction of 1st raising dyke, the ash slurry discharge in the part of the lagoon was continued. As a consequence, the ash bed acting as foundation of the raising dyke could not be completely dry and as a result could not gain sufficient strength to support the raised embankment. Based on the detailed inspection of completed works, raised dyke was cleared for operation with ash slurry discharge.

Dyke Embankment of Starter Dyke and Raising Dyke

The design of ash dyke is carried out as per codal provisions of earth dam and prevailing engineering practices. The dyke embankments are designed for ultimate heights (starter dyke and subsequent raisings) based on ground topography, foundation soil, availability of construction materials, etc. The embankments are analyzed and designed as water retaining structures, and dyke stability is checked for static and earthquake cases as per IS Codes. The elements of the ash dyke are designed on the basis of design criteria available for earthen embankment dams resulting technically sound and structurally sustainable structure. The supernatant from the ash dykes is recycled back to the plant to comply zero liquid discharge.

Decanted Water Evacuation System

Water Escape Structures (WES wells). In this case, the dyke of the ash pond is constructed to use the existing overflow lagoon (OFL) common with other adjacent lagoons. Due to constructional constraints in integrating the WES system (decanted water evacuation system) with the operating water-filled OFL, originally, envisaged WES wells could not be constructed. Therefore, the envisaged WES provision is subsequently deleted, and existing spillway (on common dyke with OFL) is considered for evacuation of decanted water similar to practice adopted in other lagoon.

Spillway. As spillway was already existing in the Starter dyke toward OFL side (common dyke with OFL), the adequacy including discharge capacity was reviewed, and it was observed that existing spillway is having more than the required discharge capacity; therefore, no additional spillway was provided in this ash pond due to constructional and operational constraints in integrating the new spillway with the operating water-filled OFL. However, in raising dykes, new spillway was envisaged at the immediate upstream of the existing spillway toward OFL side (on starter dyke) to achieve constructional advantage.

Design of Spillway in Raising Dyke. To achieve the constructional and operational advantages, the crest length of box culvert spillway in 1st raising dyke is considered same as that of existing spillway in starter dyke. Further, to ensure 1.5-m freeboard, the standard box size and other standard dimensions are adopted similar to the recent practice followed in other running plants. Based on the same, the detailed capacity calculations of box culvert spillway in 1st raising dyke is worked out. Though with the same crest length as that of existing downstream spillway in Starter dyke, the discharge capacity is found more than the required discharge capacity; the crest length was adopted same as that of existing spillway to achieve the constructional and operational advantages.

As per practice, to protect the spillway from floatation displacement due to buoyant forces, the spillway is provided as a grade slab over dyke surface with key at center of dyke embankment and properly anchored at downstream with existing spillway and at upstream with strip footing at the heel of dyke embankment. Through this, the hydraulic jump is avoided, and uplift forces acting at the interface between the structure and foundation become negligible compared to the vertical forces acting on the interface between the structure and foundation.

Additional provisions. As pond ash is having the geotechnical properties similar to soil, therefore, it is used as main material for construction of 1st raising dyke with top cover of natural soil to prevent surface erosion. However, inside the lagoon, in general, spatial variation of the pond ash characteristics is observed. Near the slurry discharge point, the ash is predominantly sand sized, while near the decant pond zone, the ash is predominantly silt sized. Strength parameters are largely influenced by the percentage of coarse ash particles. It is observed that as the percentage of bottom ash varies in the pond ash, the strength parameters and compaction behavior of pond ash varies. Though the pond ash with soil cover meets the dyke stability requirements, compacted earth was envisaged in the dyke embankment below the spillway to mitigate the implication of spatial variation of pond ash (if any) and to enable better compaction at interfaces between RCC and dyke embankment to have better resistance against the internal erosion.

Incidence of Breach of Ash Dyke Embankment

During operation of 1st raising dyke of ash pond, ash dyke embankment breached from spillway portion and settlement of spillway cum culvert structure resulted in



Fig. 41.3 Breached dyke view from top

ash water gushing toward OFL. The breached section view is presented in following Fig. 41.3.

Review of Original Design and Formulation of Restoration Scheme

Review of Original Design

The original design document prepared before issue of construction drawing of 1st raising dyke has been reviewed after breach incident. After detailed review, it was observed that envisaged design philosophy has the adequate factor of safety in static as well as seismic cases (IS 7894 1), and no change in the basic design is required; however, restoration scheme is to be formulated considering prevailing constrained site conditions. Further, it is also observed that adopted design principles in the design of dyke embankment of 1st raising is already in practice and performing well at other plants. Also, no issue from any plants has been reported so far on the distress related to similar design. Following Figs. 41.4 and 41.5 show the adequate factor of safety in static and seismic cases as per codal provisions.

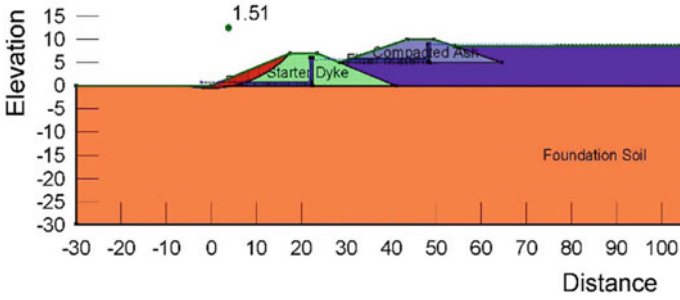


Fig. 41.4 F actor of safety in static case

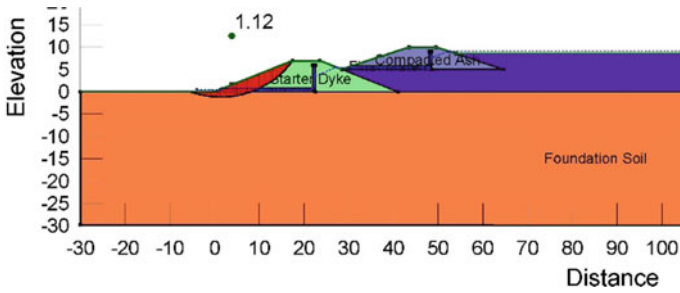


Fig. 41.5 Factor of safety in seismic case

Design of Restoration Scheme

As the heavy flow of water eroded the base as well as the sides of embankment at spillway portion at the time of breach, therefore, the restoration scheme drawing is formulated considering the actual prevailing constrained site conditions and requirement of early restoration. This involved the foundation improvement using geogrid, geotextile, compacted earth, stone aggregate in the affected breach area and adjoining influence area. Additionally, as the restoration dyke section is of limited length compared to original construction length and the same is to be re-constructed in the constrained working conditions, some additional measures are also adopted to ensure sustainable restoration of damaged dyke section. However, the basic design of dyke and spillway (material, dyke formation level, slopes, number of spillway boxes, etc.) in the restoration drawing is kept same as per original design. Restoration scheme incorporates following measures for early and safe restoration considering prevailing site conditions.

- (i) The debris are removed carefully after barricading the area. All loose material below spillway crest and adjoining area is removed.

- (ii) Before undertaking repair works, a coffer dam was provided for isolating the construction area with rest of the area of lagoon filled with ash slurry to prevent surface water flow from adjoining area to construction area.
- (iii) Providing trench drain/sumps with adequate dewatering arrangement at periphery of construction area to remove the subsurface seepage water to keep the construction area dry.
- (iv) Foundation preparation from consolidated ash bed level with foundation improvement using biaxial geogrid, geotextile, compacted earth, stone aggregate in the affected breach area and adjoining influence area.
- (v) Re-construction of dyke embankment using materials as per originally envisaged design
- (vi) Re-construction of box culvert spillway at original location
- (vii) Considering present site conditions, to enhance safety against piping through interface of RCC spillway walls and adjoining embankment, RCC keys perpendicular to the side walls projecting toward the embankment were provided to increase seepage/piping path.
- (viii) Though the dyke was designed with adequate factor of safety, plant requested to lower the spillway invert to (–) 2.5 m in place of existing practice of (–) 1.5 m to enable early recirculation of decanted water from inside lagoon. The same was also incorporated with suitable flexible opening at inlet of spillway.

The revised construction drawings were issued for restoration of breach section. The breached section has been successfully restored, and the lagoon is under operation with ash slurry discharge. Following Fig. 41.6 indicates upstream view of re-constructed spillway in dyke embankment.



Fig. 41.6 Upstream view of re-constructed spillway in dyke embankment

Conclusion

The site conditions evolved after breach necessitated additional measures to restore the breach section. This involved the foundation improvement using geogrid, geotextile, compacted earth, stone aggregate in the affected breach area and adjoining influence area. The posed challenges of creating construction area dry were overcome by providing additional measures in restoration scheme, and finally, restoration is successfully completed, and restored dyke section with spillway structure is presently under successful operation.

Reference

1. IS 7894 (2002) Code of practice for stability analysis of earth dams. Bureau of Indian Standards, New Delhi